

AD-787 547

PROCEEDINGS OF THE FLUIDIC STATE-OF-THE-ART
SYMPOSIUM HELD AT NAVAL ORDNANCE LABORATORY,
WHITE OAK, MARYLAND ON 30 SEPTEMBER -
3 OCTOBER, 1974
VOLUME 11

HARRY DIAMOND LABORATORIES

1974

DISTRIBUTED BY:

NTIS

National Technical Information Service
U. S. DEPARTMENT OF COMMERCE

AD 787547

FLUIDIC
STATE-OF-THE-ART

SYMPOSIUM

1974

30 SEPTEMBER - OCTOBER

D D C
RECEIVED
OCT 23 1974
RECEIVED
D



Reproduced by
NATIONAL TECHNICAL
INFORMATION SERVICE
U S Department of Commerce
Springfield VA 22151

VOLUME II

U.S. Army Materiel Command
Harry Diamond Laboratories
Washington, D.C.

DISTRIBUTION STATEMENT A

Approved for public release;
Distribution Unlimited

REPORT DOCUMENTATION PAGE		READ INSTRUCTIONS BEFORE COMPLETING FORM
1. REPORT NUMBER	2. GOVT ACCESSION NO.	3. RECIPIENT'S CATALOG NUMBER
4. TITLE (and Subtitle) Proceedings of the Fluidic State-of-the Art Symposium, 30 Sep - 3 Oct 74, Vol. II		5. TYPE OF REPORT & PERIOD COVERED
7. AUTHOR(s) Various		6. PERFORMING ORG. REPORT NUMBER
9. PERFORMING ORGANIZATION NAME AND ADDRESS		8. CONTRACT OR GRANT NUMBER(s) HDL Proj. No. 302531
11. CONTROLLING OFFICE NAME AND ADDRESS		10. PROGRAM ELEMENT, PROJECT, TASK AREA & WORK UNIT NUMBERS
14. MONITORING AGENCY NAME & ADDRESS (if different from Controlling Office)		12. REPORT DATE
		13. NUMBER OF PAGES 642
		15. SECURITY CLASS. (of this report) Unclassified
		15a. DECLASSIFICATION/DOWNGRADING SCHEDULE
16. DISTRIBUTION STATEMENT (of this Report) Unlimited		
<div style="border: 1px solid black; padding: 5px; display: inline-block;"> DISTRIBUTION STATEMENT A Approved for public release; Distribution Unlimited </div>		
17. DISTRIBUTION STATEMENT (of the abstract entered in Block 20, if different from Report)		
18. SUPPLEMENTARY NOTES		
19. KEY WORDS (Continue on reverse side if necessary and identify by block number) Fluidics; fluierics; miniature fluid amplifier; bistable fluid amplifier; laminar flip-flop; moving part fluidic devices; fluidic pressure-flow interface; fluidic sensors; fluidic acoustic sensor; vortex rate sensor; laminar jet rate sensor; fluidic G sensor; pneumatic rate/acceleration sensor; fluidic non-contact gaging; rotational speed control; fluid amplifier scaling; heat and mass transfer in fluidic		
20. ABSTRACT (Continue on reverse side if necessary and identify by block number) This volume contains twenty-one papers for a total of 642 pages.		

circuits; thrust of free and submerged jets; particles in fluidic devices; supersonic boundary layer.

SECURITY CLASSIFICATION OF THIS PAGE(When Data Entered)

Volume II

<i>A Miniaturized Fluid Amplifier in Integrated Circuits</i> T. Jansen, Automatic Switch Co., Florham Park, New Jersey	1
<i>Downstream Control of a Jet</i> H. P. Lin, Stone and Webster Engineering Corp., Boston, Mass. F. R. Swenson, University of Stirling, Scotland	29
<i>The Laminar Flip-Flop</i> T. Drzewiecki, Harry Diamond Labs, Washington, D.C. F. Manion, Harry Diamond Labs, Washington, D.C.	51
<i>Projects on Moving Part Fluidic Devices Carried Out at Sir George Williams University</i> C. C. K. Kwok, Sir George Williams University, Canada	67
<i>A Fluoric Pressure or Flow Interface</i> E. C. Hind, University of New South Wales, Australia	101
<i>Survey of Sensors, Part I</i> A. Schmidlin, Picatinny Arsenal, Dover, New Jersey	113
<i>Survey of Sensors, Part II</i> J. M. Kirshner, Harry Diamond Labs, Washington, D.C.	187
<i>The Fluidic Acoustic Sensor</i> B. B. Beeken, Automatic Switch Co.	261
<i>Performance and Application of the Vortex Rate Sensor</i> James O. Hedeon, Honeywell, Inc.	295
<i>Theoretical Analysis of Two-Dimensional Laminar Jet Rate Sensor</i> P. L. Jacobs, U.S. Army Missile Command, Redstone Arsenal, Alabama	319
<i>Development of a Laminar Angular Rate Sensor (LARS)</i> R. Young, General Electric Co., Philadelphia, Pennsylvania	357

ic

<i>Mathematical Modeling and Computer Aided Design of a Fluidic G Sensor</i>	
Charles A. Belsterling, Franklin Institute Labs, Philadelphia, Pennsylvania	
A. E. Schmidlin, Picatinny Arsenal, New Jersey	413
<i>Pneumatic Rate/Acceleration Sensor</i>	
C. J. Bell, Mississippi State University	
L. R. Hester, Mississippi State University	453
<i>Fluidic Non-Contact Gaging</i>	
W. R. Schurman, Monsanto Research Corp., Miamisburg, Ohio	463
<i>A Fluidic Sensor Applied to the Hydraulic Control of Rotational Speed</i>	
R. J. Stuart and R. W. Mayne, State University of New York at Buffalo, Buffalo, New York	497
<i>A Fluid Amplifier Reynolds Number</i>	
T. M. Drzewiecki, Harry Diamond Labs, Washington, D.C.	525
<i>Effects of Aspect Ratio and Low Reynolds Number on Recovery and Flow Regimes in a Plane-Wall Diffuser</i>	
A. S. Dighe, University of Bombay, India	
A. T. McDonald, Purdue University	541
<i>Heat and Mass Transfer as Control Parameters in Fluidic Circuits</i>	
Sui Lin, Sir George Williams University, Montreal, Canada	567
<i>Thrust and Associated Phenomena of Free and Submerged Jets</i>	
Ernest Taylor, Monsanto Textiles Co.	595
<i>Flow of Particles in a Submerged Fluidic Device</i>	
Pah I. Chen, Portland State University, Oregon	
M. L. Marcott, Bureau of Sanitary Engineering, City of Portland, Oregon	601
<i>Supersonic Boundary Layer Control and Its Application</i>	
R. B. Thompson, University of New Castle Upon Tyne, England	609

A MINIATURIZED FLUID AMPLIFIER IN
INTEGRATED CIRCUITS

T. Jansen
Chief Fluidics Engineer

Automatic Switch Company
Florham Park, N.J. 07932

SUBMITTED TO HARRY DIAMOND LABORATORIES SYMPOSIUM, 1974

SYMBOLS

$$\alpha = f\left(\frac{l_s}{d_s Re}\right)$$

$$\rho = \text{density, lbm/ft}^3$$

$$\mu = \text{dynamic viscosity, lbm/ft-sec.}$$

$$d_s = \text{emitter diameter, in.}$$

$$k = \text{ratio of specific heats}$$

$$l_s = \text{emitter length, in.}$$

$$L = \text{cavity length, in.}$$

$$P_o = \text{pressure recovery}$$

$$\Delta p = \text{emitter pressure drop, psf.}$$

$$Q_s = \text{mass flowrate, standard ft}^3/\text{sec, scc/min.}$$

$$Q_o = \text{collector flowrate, scc/min.}$$

$$R = \text{gas constant, } \frac{\text{lb-ft}}{\text{lbm}^\circ\text{R}}$$

$$Re = \text{Reynolds number, } \frac{\bar{u}_m d_s \rho}{\mu}$$

$$T = \text{absolute temperature, } ^\circ\text{R}$$

$$\Delta t = \text{response time, sec.}$$

$$\bar{u}_m = \text{average emitter velocity, ft/sec.}$$

$$u_c = \text{emitter centerline velocity, ft/sec.}$$

$$x_c = \text{constant velocity core length, ft.}$$

$$x_o = \text{virtual origin, ft.}$$

$$\nu = \text{Kinematic viscosity, ft}^2/\text{sec.}$$

INTRODUCTION

This paper describes a miniaturized flow mode (laminar - turbulent flow) amplifier and its application in integrated fluidic circuits.

Power consumption, response time, pressure recovery, operating range, temperature effects and interconnections are discussed.

Miniaturization offers distinct advantages in cost and packaging density, in addition to higher speed capability and reduced power consumption.

An integrated circuit assembly is shown in Figure 1(a) and an exploded view in 1(b). Individual parts are accurately located on tooling pins, and sandwiched between aluminum end plates by means of a single nut on a threaded manifold.

A 2.5" diameter formed aluminum cover provides protection against ambient contamination. While the entire system is protected by a .1 micron filter, an additional 25 micron nylon filter protects the module during handling. This filter is located inside the supply manifold.

In the photographs of Figure 1, a total of 84 amplifiers are integrated into an 8-in^3 package, yielding a packaging density of about $.1\text{-in}^3$ per amplifier.

The improved packaging density over an identical handwired circuit is best illustrated in Figure 2. The particular circuit is a 1-decade binary coded decimal down counter, complete with numerical display, such as used in fluidic batch controllers.

The Amplifier - A General Discussion

The amplifier discussed is an improved, miniaturized version of the flowmode amplifier described in Reference (1).

The amplifier is digital, of the flowmode (laminar - turbulent flow) type. See Figure 3.

Pressure recovery at the collector of a laminar jet produced by the emitter yields a "1" in the "on" state, typically 15-inches of water.

A control port signal of about 4-inches of water pressure and 10 cc/minute flow induces turbulence with a resultant pressure recovery of less than .3 inches of water in the "0" or "off" state. The amplifier has a fan-in of 4.

The amplifiers are arranged in a radial array of 12 as shown in Figure 4, injection molded of ABS.

With molding parameters held within practical limits, the discs are mass produced with very uniform results.

1. Power Consumption

Amplifier power consumption is usually expressed as,

$$\text{power consumption} = Q_s \Delta p$$

where Q_s = mass flowrate

Δp = emitter pressure drop.

With a relatively short emitter ($l_s/d_s = 28$) and Reynolds number ($Re = \frac{\bar{u}_m d_s \rho}{\mu}$) ranging from 700 to 1232, the emitter velocity profile is nearly fully developed, and the emitter pressure drop, Δp , is given by Langhaar (Reference 2) as,

$$\Delta p = \alpha \left(\frac{1}{2} \rho \bar{u}_m^2 \right)$$

$$\text{where } \alpha = f\left(\frac{l_s}{d_s Re}\right)$$

ρ = air density

\bar{u}_m = average emitter velocity

The emitter pressure flow curve is shown in Figure 5. It is seen that, typically, power consumption is 25 milliwatt (at 1.5 psig) which compares very favorably with any other commercially available fluid amplifier.

An important conclusion may be drawn simply if it is momentarily assumed that the emitter length is just sufficiently long to produce a fully developed velocity profile. Then,

$$\Delta p = \frac{32 \mu l_s \bar{u}_m}{d_s^2} + 2.3 (1/2 \rho \bar{u}_m^2)$$

from which it can be easily shown that

$$Q_s \Delta p \sim Re^2$$

Since a minimum critical Reynolds number exists below which the jet cannot be made turbulent (Reference 3, 4), power consumption has a definite lower limit for this type of device.

2. Response Time

Response time for a particular circuit is governed by amplifier response characteristics, interconnecting line lengths and circuit complexity.

Circuit complexity and configuration are the basic restraints on speed. An 8 amplifier binary counter stage has been cycled up to 550 cps, with maximum speed of a 55 amplifier counter at 160 cps.

Amplifier Response

Neglecting transient delays and considering only amplifier "on" and "off" transport delays as defined in Figure 6, the pertinent terminology is shown in Figure 7. Refer to Ref. 5 for further details.

The emitter flow exits into a constant velocity core, X_c , beyond which the jet flow is fully developed and the center-line velocity decays in inverse proportion to the distance from the virtual origin, $X + X_0$. (Reference 5,6).

Transport delays are based on laminar transport times, following W. Hayes (Reference 5).

TABLE I TRANSPORT DELAY TIMES

SUPPLY PRESSURE Δp	Q_s	\bar{u}_m	u_c	$\frac{u_m d}{\nu}$	$\frac{d_s Re}{16}$	Core Length X_c	X_c/u_c	$\int_{X_c}^{\infty} \frac{dX}{u_c} \Delta t_2$	Total Delay Δt
psig	acc/min.	ft/sec	ft/sec	-	in.	in.	msec.	msec.	msec.
1.0	115	152	304	700	.39	.025	.0069	.054	.061
1.5	155	204	408	950	.53	.034	.00695	.036	.043
2.0	185	244	488	1190	.66	.043	.00734	.027	.034
2.5	200	264	528	1232	.69	.045	.0071	.025	.032

NOTE: $X_c = .004d Re$

ν = Kinematic viscosity, ft^2/sec .

Total transport time, Δt , is the sum of core and developed jet delays and is given in Reference 5 as,

$$\Delta t = \frac{x_c}{u_c|_{x=0}} + \int_{x_c}^L \frac{dx}{u_c}$$

Calculated values of Δt as a function of supply pressure are shown in Figure 8 and Table I.

Measurements of above response time using the smallest pressure probes available confirmed these values only in a general way. Large corrections, in the order of .1 to .2 msec., were necessary to account for acoustic delays in probe connecting lines.

Oscilloscope traces using a Kistler probe at the control and a hot wire at a collector cross-section are shown in Figure 9.

3. Pressure Recovery

Pressure recovery is an important characteristic, determining fan-out capability, and compatibility with other amplifiers and output devices. A minimum fan-out of 4 is available.

Pressure recovery data for the amplifier is shown in Figure 10, where the experimental points represent the full range of data for 12 amplifiers molded in a single plastic disc, 2-inches in diameter.

No theoretical pressure recovery information is available on jets issuing from a parabolic cross-section type of channel, and bounded entirely by a flat cover plate. However, it is valuable to compare the data with experimental and theoretical work done on tubular turbulence amplifiers (Reference 6, 7, 8).

The experimental data is not unexpectedly somewhat below that predicted for the open, tubular turbulence amplifier because of the cover plate's proximity to the jet's boundary.

What is of particular interest is the fact that for practical purposes, the theoretical results provide reasonable pressure recovery estimates for the bounded jet.

Collector characteristics for a loaded amplifier are shown in Figure 11.

4. Operating Pressure Range

Operating pressure range, at room temperature, is from 1.0 to 2.5 psig, the low limit determined by collector and control port characteristics, with negligible pressure drop in connecting lines.

The high limit is established by the maximum Reynolds number at which the collector still sees a laminar stream.

As Figure 12 shows, the maximum Reynolds number, Re_{max} , is a fairly weak function of emitter length, being about 1250 for the present amplifier with an emitter length to diameter ratio of 28. The emitter is of (approximately) parabolic cross-section, about .0102 in. wide and .0078 in. deep. The cross-sectional area was obtained by placing a grid overlay over an enlarged photo of a thin slice of material containing the cross-section and counting squares. The emitter diameter, d_s , is an equivalent diameter, based on the above cross-sectional area.

Long emitters tend to dampen out disturbances in the supply flow and allow the laminar jet greater reach before spontaneously breaking up into turbulent flow. Long emitters also aid in establishing paraboloidal velocity profiles, producing inherently more stable jets than uniform profiles.

However, since Re_{max} is only lightly dependent on emitter length, the packaging density was considerably improved by keeping the emitter as short as possible, in this case 28 diameters.

It is seen that the "peak out" Reynolds number for various planar devices fall below the data for the open turbulence amplifier (Reference 6). Excellent alignment of emitter and collector in the planar amplifiers is offset by the need for a jet enclosure. It is easily demonstrated that even though a shroud shields the amplifier from ambient noise, the maximum operating Reynolds number is somewhat reduced also.

5. Temperature Effects

Supply Air - Temperature changes in the air supply affect response time and operating pressure range.

The dynamic viscosity of air, μ , varies with absolute temperature, T , as

$$\mu \propto T^{1/2}$$

while the density variation is,

$$\rho \propto T^{-1}$$

In order to maintain a constant Reynolds number, the operating pressure (Figure 13) must be varied as T^2 . Amplifier response time varies then as emitter velocity, as follows:

$$\Delta t \sim T^{3/2}$$

Ambient Temperature Changes

Since the components in the assembly have different coefficients of expansion, bi-metal discs are used which maintain a constant compressive load on the assembly under varying ambient temperatures.

6. Interconnections

Interconnections between amplifiers consist of .015" wide channels etched through in .015" thick stainless steel discs, contained between gaskets of polyester film.

Etched circuits were chosen for flatness, dimensional accuracy and smoothness.

A square cross-section was chosen for several reasons:

- The pressure drop for a rectangular section has a minimum value when the aspect ratio is 1 (Ref.9).
- Small aspect ratios are difficult, if not impossible, to etch, while large aspect ratios are uneconomical space-wise.

A single channel, .015 x .015, carrying flow to four amplifiers has approximately a .10 psi pressure drop for each inch of such track when operating the integrated circuit at 1.3 psig. It should be noted that the pressure drop per unit length for a square duct is 13% greater than for a round duct of the same cross-sectional area.

Simple, symmetrical circuits are then expected to operate at a somewhat wider pressure range than complex, non-symmetrical circuits which may involve longer lines.

A three dimensional computer model for a layout of this type circuitry is presently not available.

Impedance Matching

Since these integrated circuits are capable of operating in excess of 500 cps, the line carrying the trigger signal to the circuit (from an air sensor, for instance), must be properly selected when cycling at speeds in excess of 200 to 300 cps.

When the line is not matched to the load, i.e., when the line characteristic impedance is not matched to the load impedance, the reflected wave interferes with the incident wave and the signal distorted. Signal distortion results in pressure levels at certain frequencies which are much higher or lower than the original static (d-c) pressure.

Figure 14 and 15 show the amplitude variation with frequency at the end of a .055 ID sensor line of 6" and 24" length, respectively, terminated by a .031 ID input connector to the circuit.

When the line is matched to the load, the pressure decays in a simple exponential function along the line, and is independent of frequency for any particular location along the line.

The load impedance is expressed as,

$$Z_L = \frac{dp}{dq}$$

while the line impedance (cross-sectional) is given by,

$$Z_{SO} = \frac{(KRT)^{\frac{1}{2}}}{\text{Cross.Area.}} \quad (\text{Ref. 9})$$

Impedance matching for circular and rectangular fluidic lines has been extensively treated by Schaedel (Ref.9).

REFERENCES

1. R.F. O'Keefe, "Development and Application of a new Jet Interaction Fluid Amplifier", ISA Conference 1967.
2. H.L. Langhaar, "Steady Flow in the Transition Length of a Straight Tube", ASME Trans., J. of Appl. Mech. V64, 1942
3. E.N. Dac. Andrade, "The Sensitive Flame", Proc. of the Physical Soc., Vol. 53, Pt. 4, July 1941
4. A Viilu, "An Experimental Determination of the Minimum Reynolds Number for Instability in a Free Jet", ASME Trans., J of Appl. Mech., September 1972.
5. W. Hayes, "Static and Dynamic Performance Characteristics of Fluidic Turbulence Amplifiers", National Research Council (Canada) 1969.
6. A.C. Bell, "An Analytical and Experimental Investigation of the Turbulence Amplifier", Doctoral Thesis, M.I.T. 1969.
7. E. Bendor, "The Performance of Flow Mode Amplifiers", Fluidics Quarterly, June 1973.
8. T. Jansen & S. Winnikow, "Pressure Recovery Characteristics of a Laminar Free Jet", Fluidics Quarterly, January 1971.
9. H. M. Schaedel, "The Behavior of Transmission Lines and Nozzles in Fluidic Networks"; "A Theoretical Investigation of Fluidic Transmission Lines with Rectangular Cross-Section", Third Cranfield Fluidics Conference, Turin, 1968.
10. H.A.M. Verhelst, "On the Design, Characteristics, and Production of Turbulence Amplifiers", paper, Second Cranfield Fluidics Conference, January 1967.

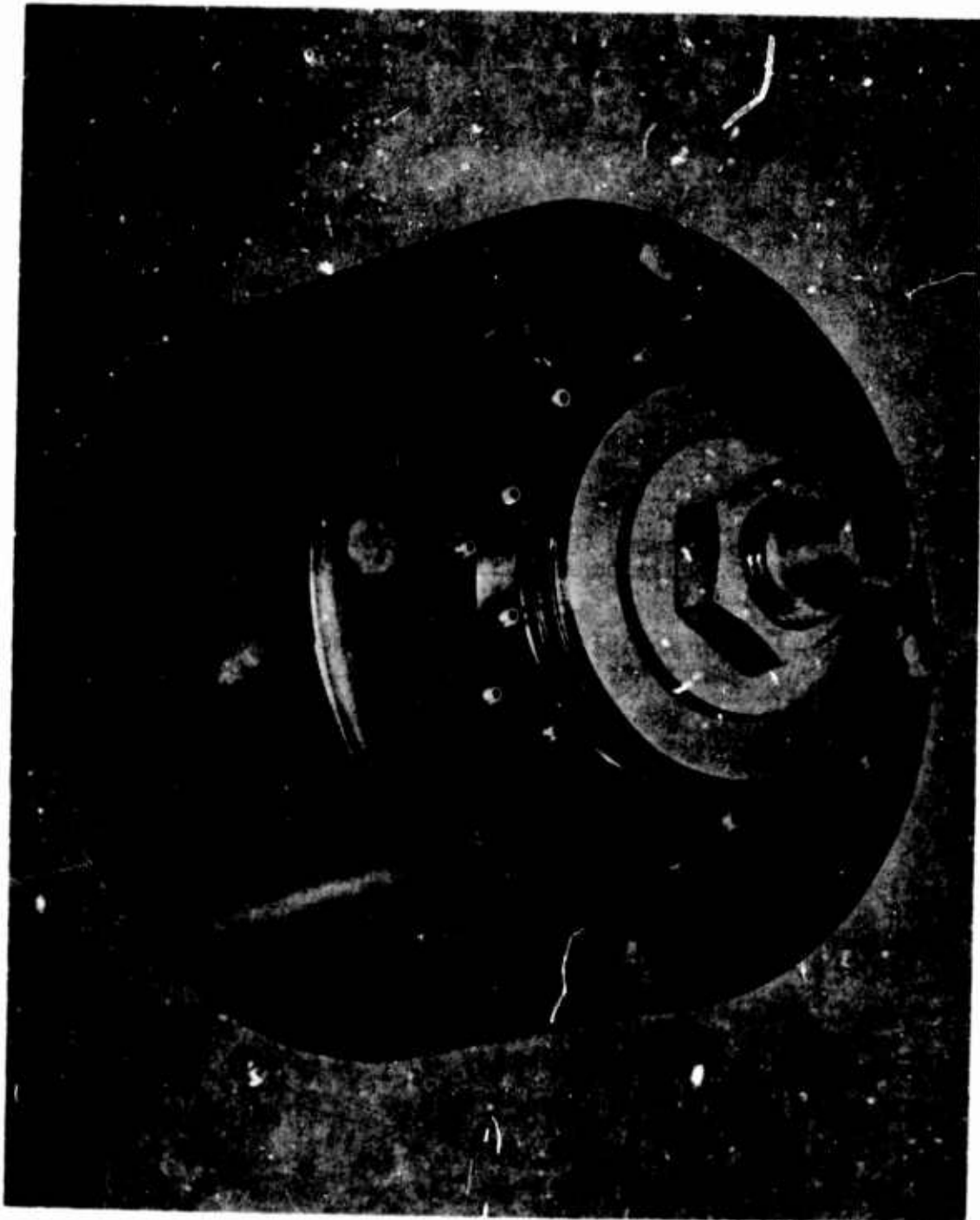


Fig. 1(a) A MINIATURE INTEGRATED CIRCUIT

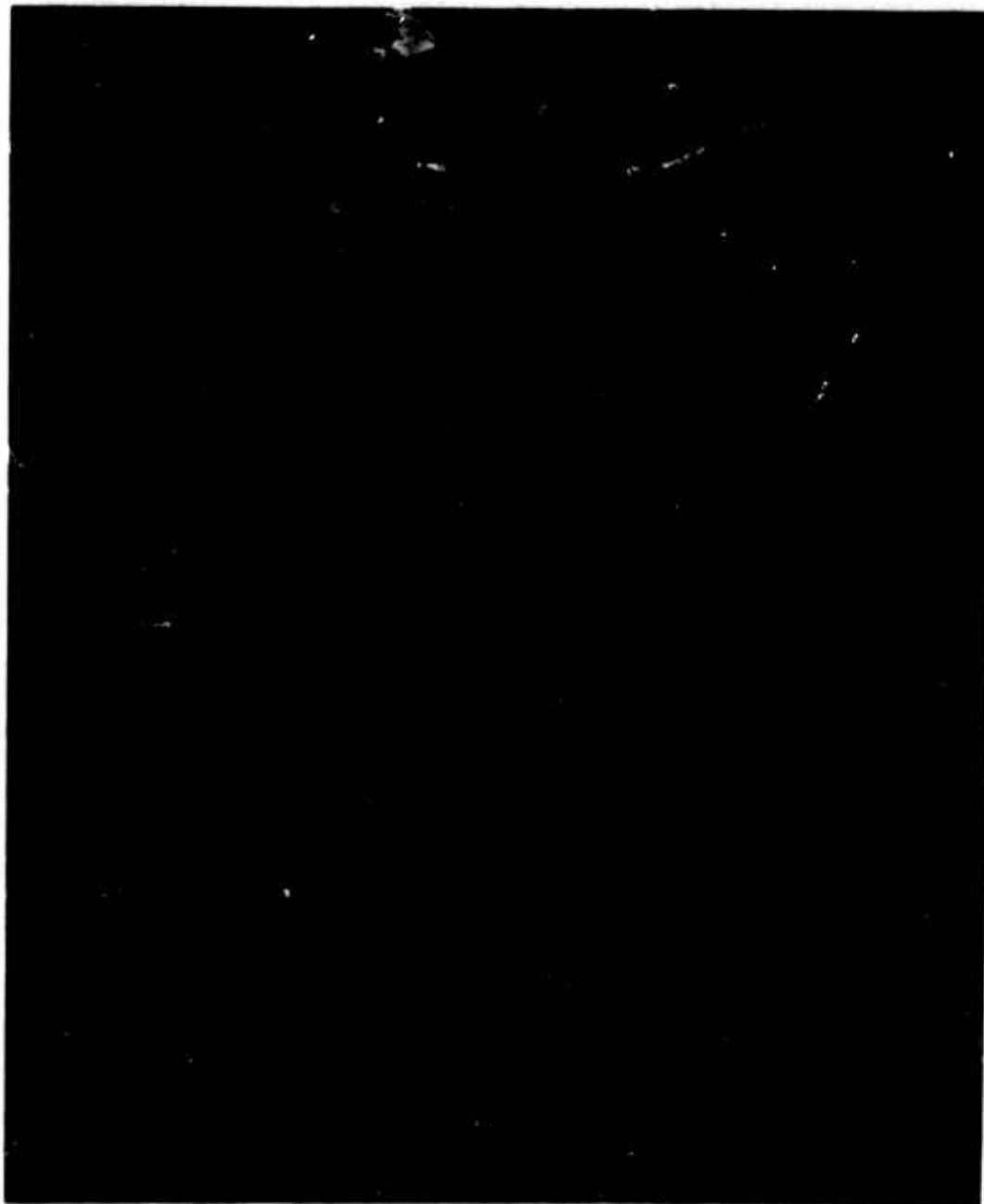


FIG. 1(b) EXPLODED VIEW

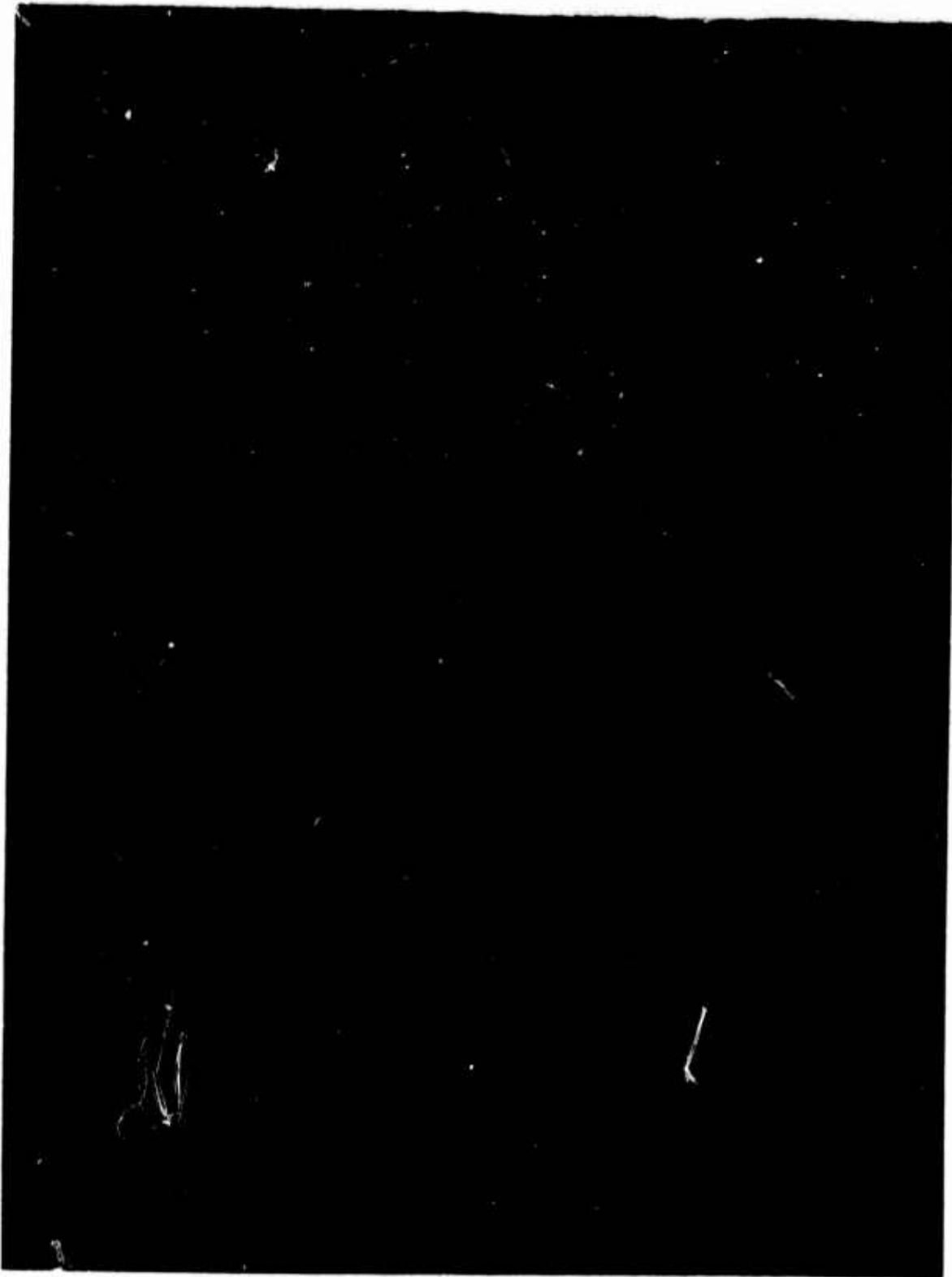


FIG. 2 - SIZE COMPARISON - INTEGRATED AND
HANDWIRED CIRCUITS

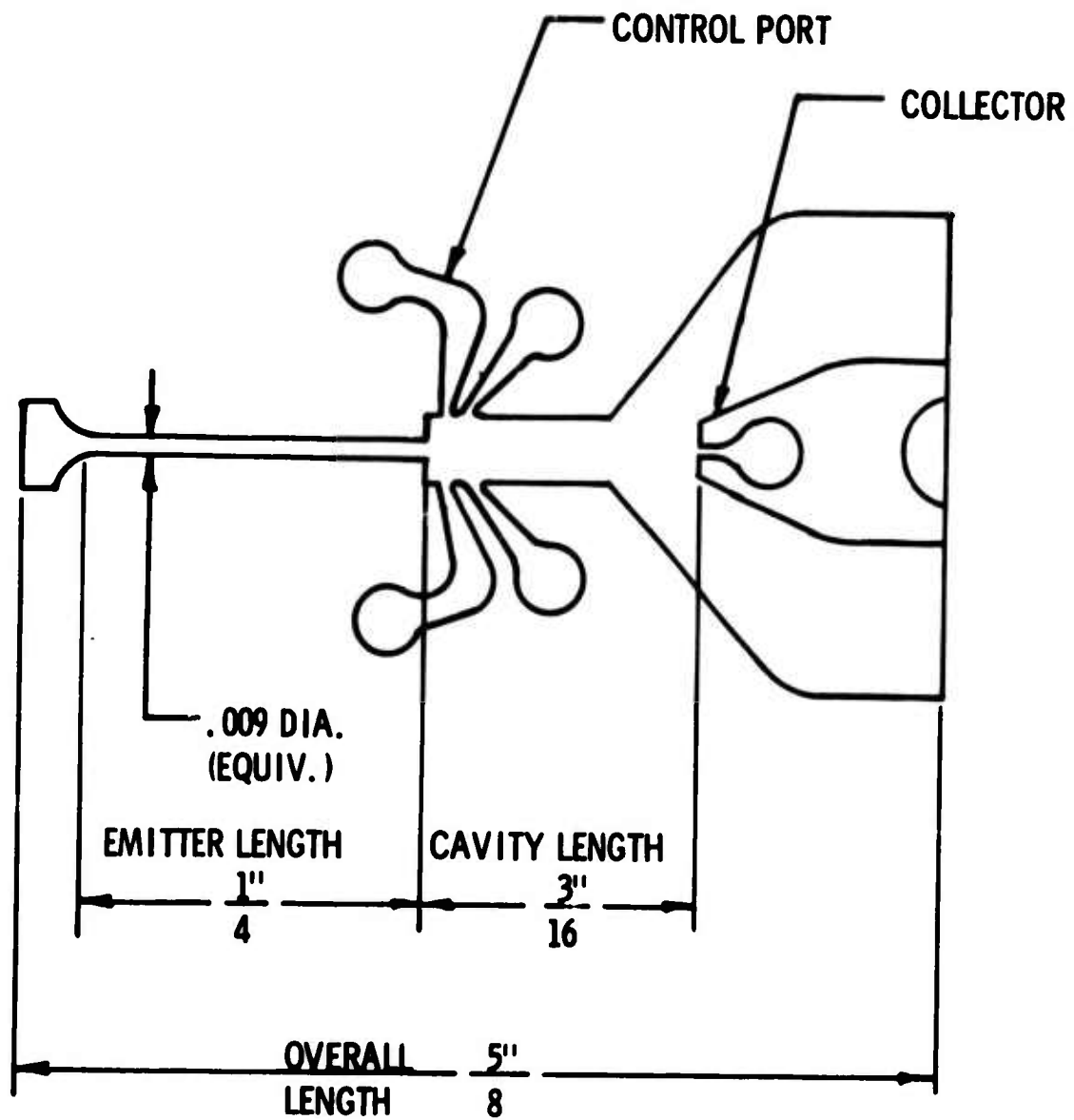


FIG 3 AMPLIFIER GEOMETRY

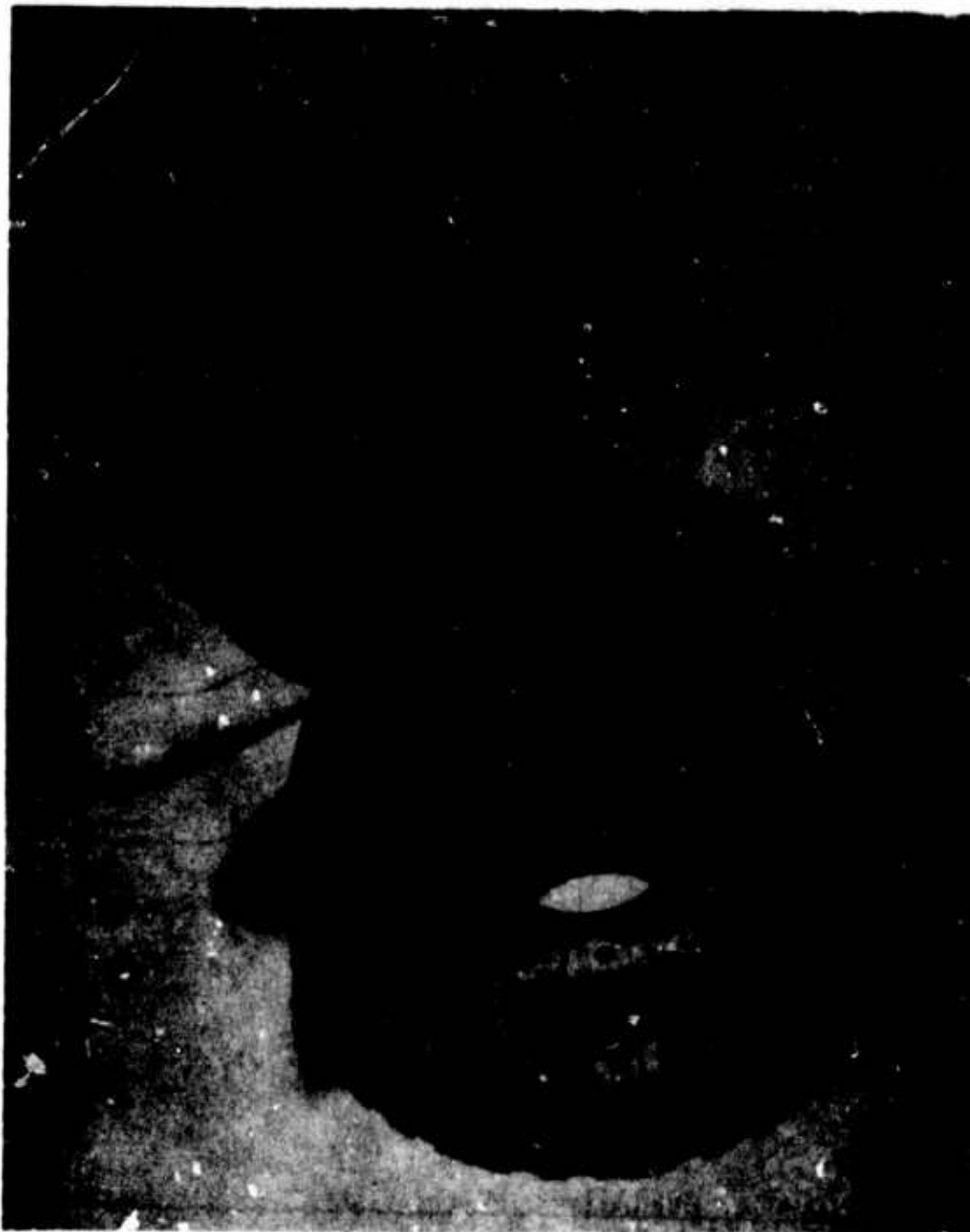
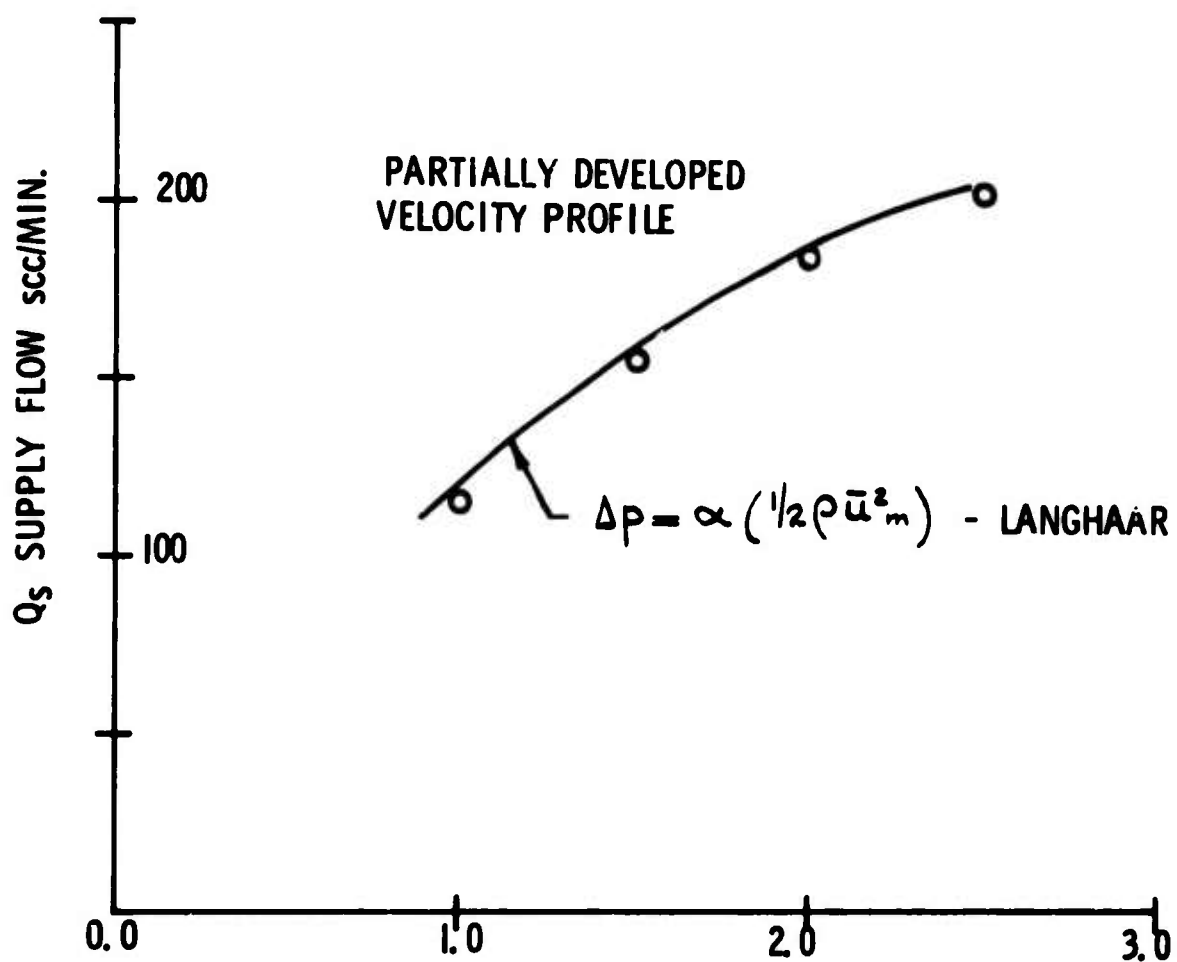


FIG. 4 - PARTS SHOWING RADIAL AMPLIFIER ARRAY, GASKETS,
AND STAINLESS STEEL CIRCUIT BOARD.



Δp, SUPPLY PRESSURE, PSIG
FIG. 5 EMITTER CHARACTERISTICS

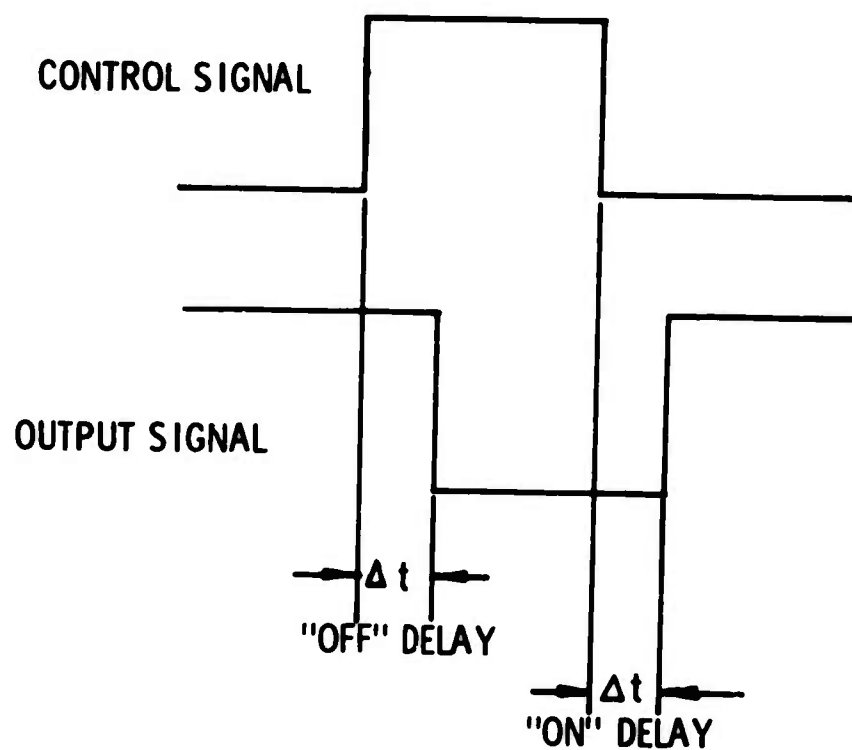


FIG. 6 DEFINITION OF "ON" & "OFF" DELAY TIMES, Δt

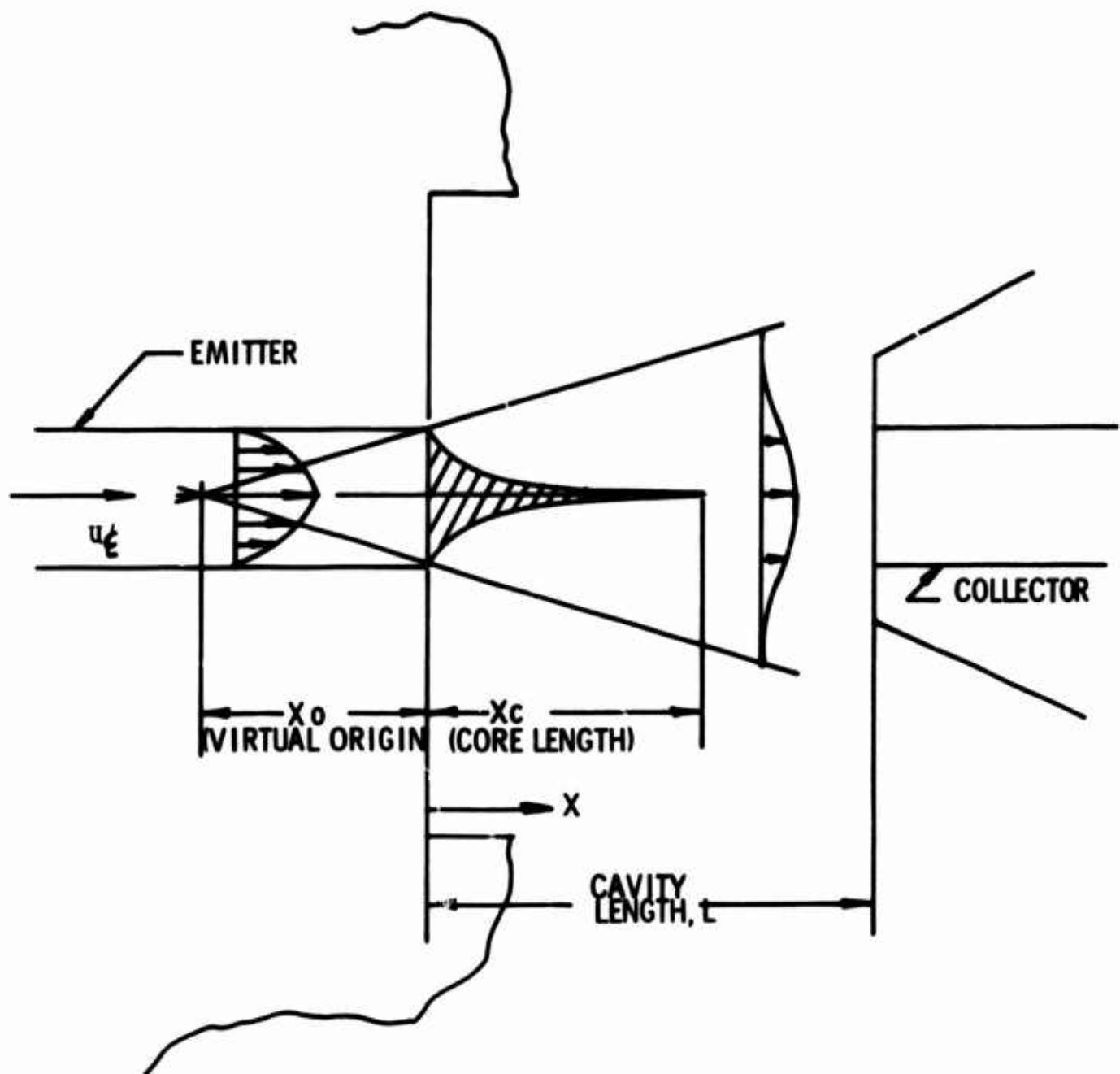


FIG. 7 TERMINOLOGY

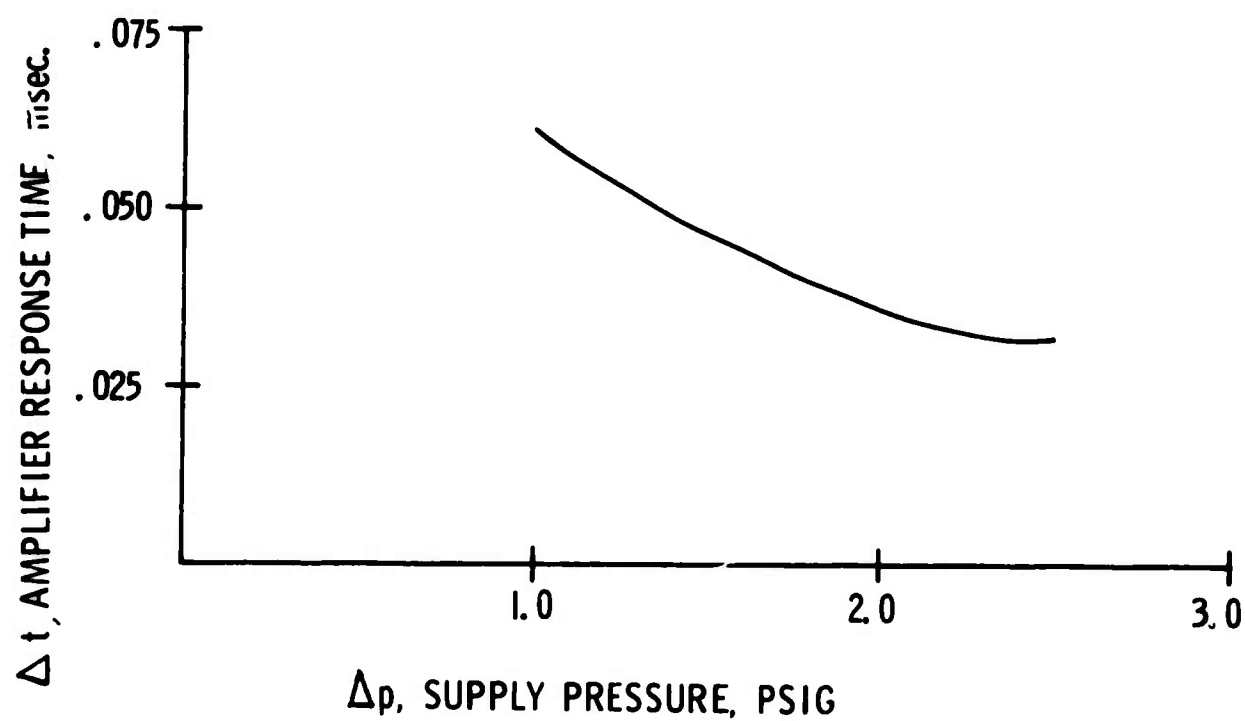


FIG. 8 AMPLIFIER RESPONSE (TRANSPORT DELAY)
TIME VARIATION WITH SUPPLY PRESSURE



FIG. 9 - INPUT/OUTPUT OSCILLOSCOPE TRACES;
1 MSEC./CM; $\Delta p = 1$ PSI

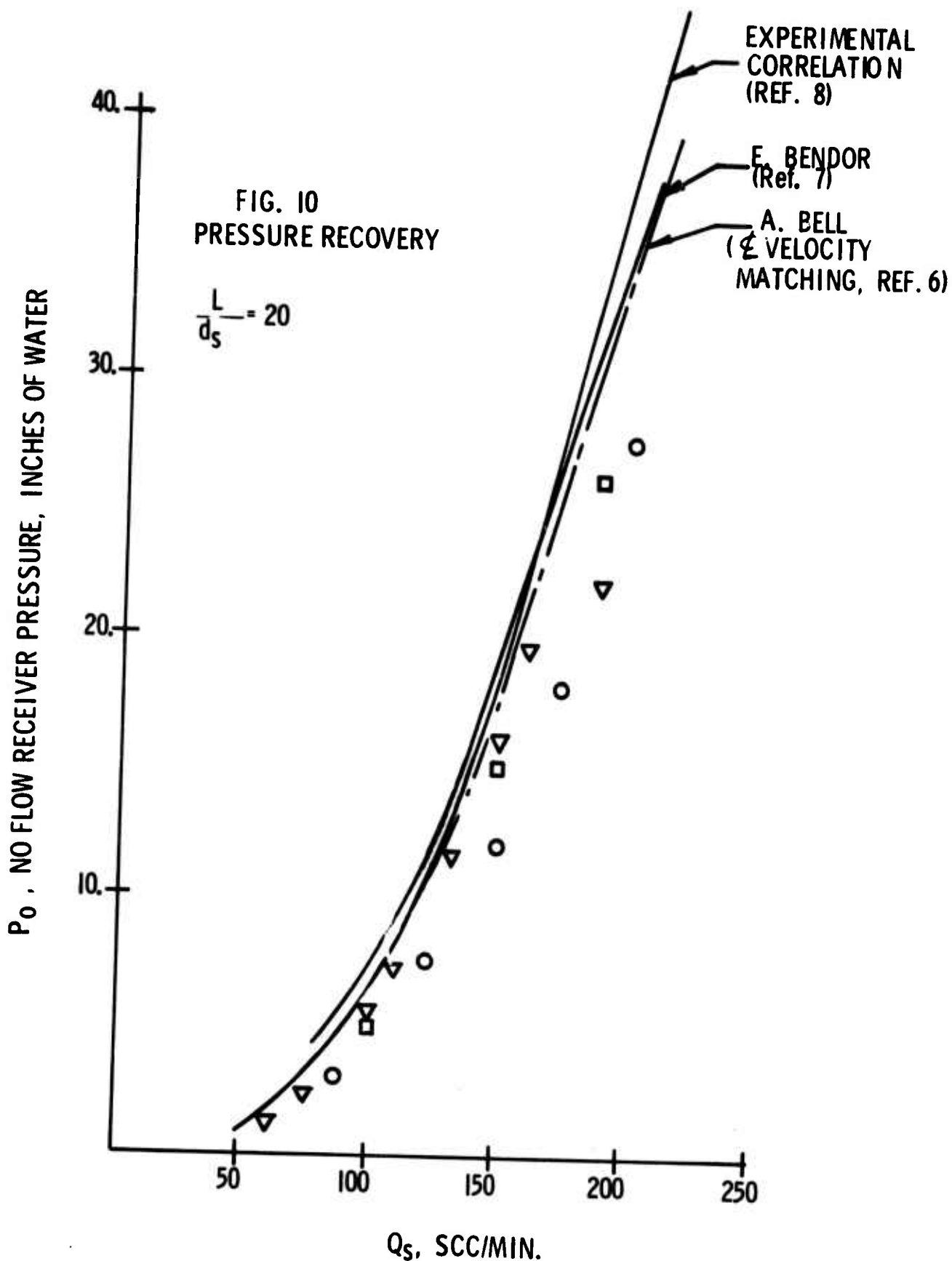


FIG. 10 PRESSURE RECOVERY

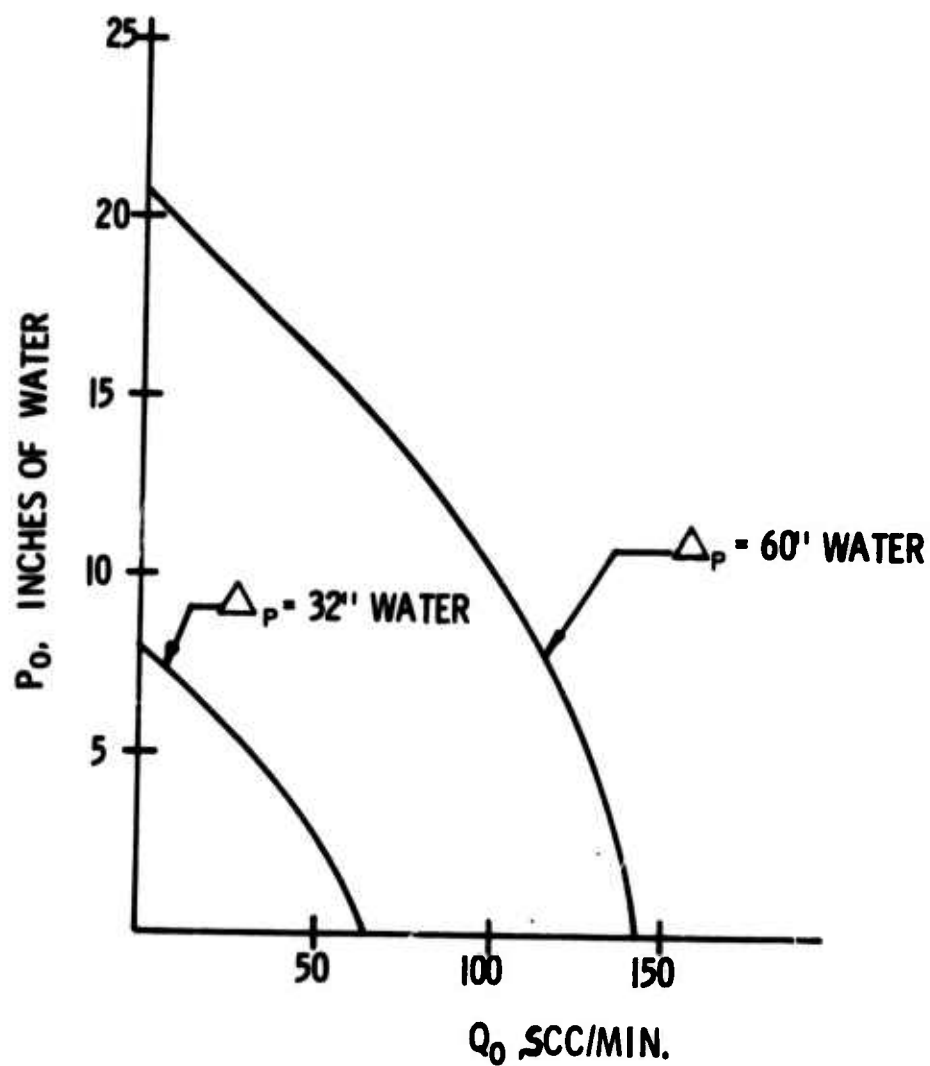


FIG. II COLLECTOR CHARACTERISTIC

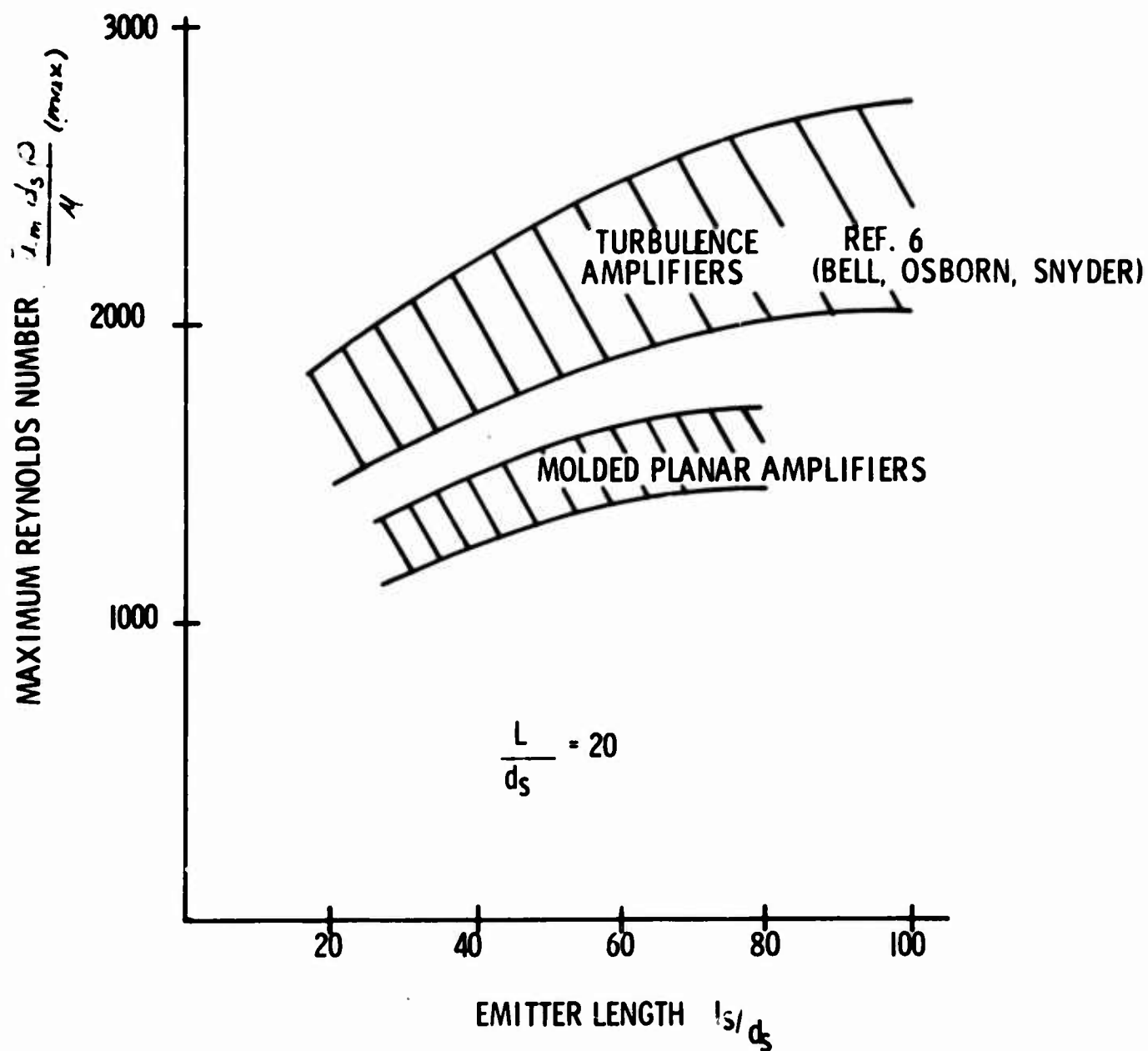


FIG. 12 MAXIMUM REYNOLDS NUMBER AS A FUNCTION OF Emitter LENGTH

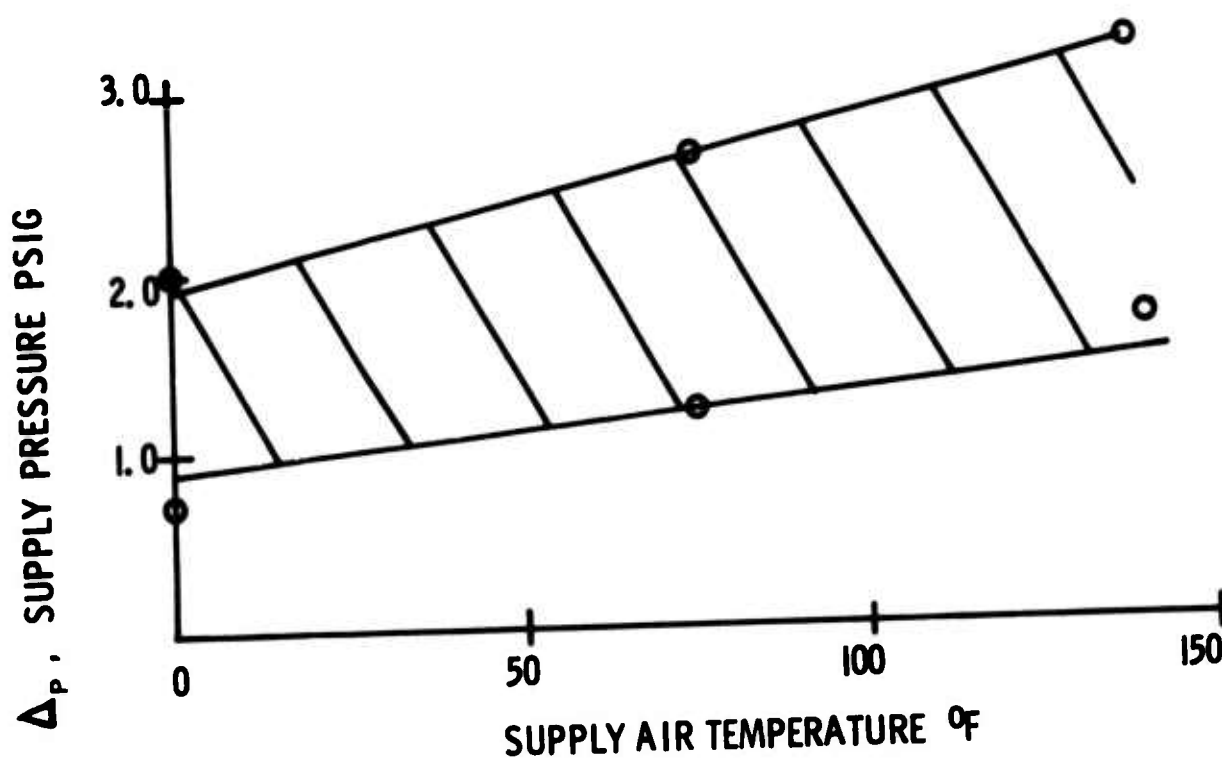


FIG. 13 OPERATING PRESSURE RANGE VARIATION WITH AIR SUPPLY TEMPERATURE

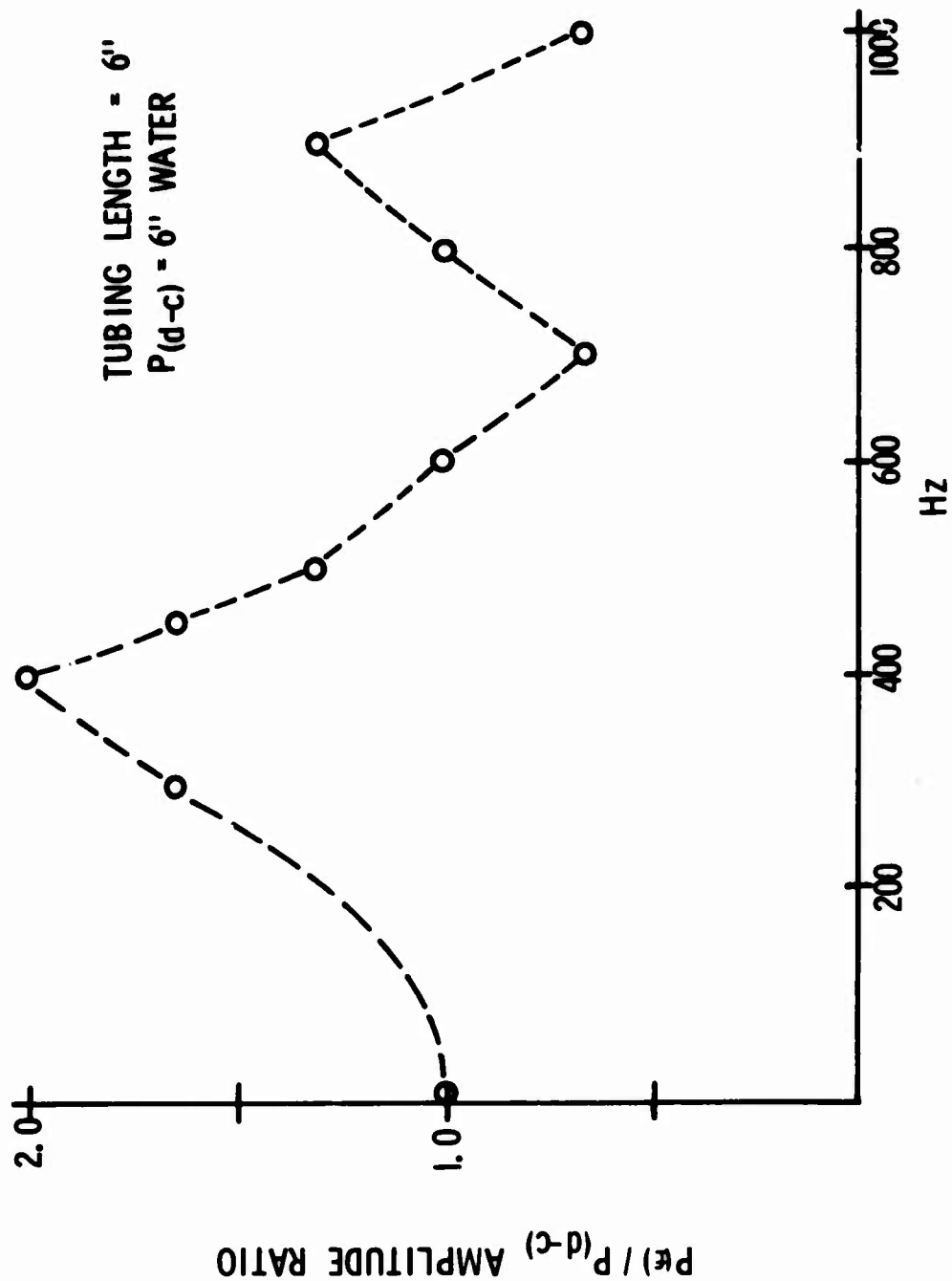


FIG. 14 AMPLITUDE VARIATION AT END OF .055 I. D.
SENSOR LINE (L = 6")

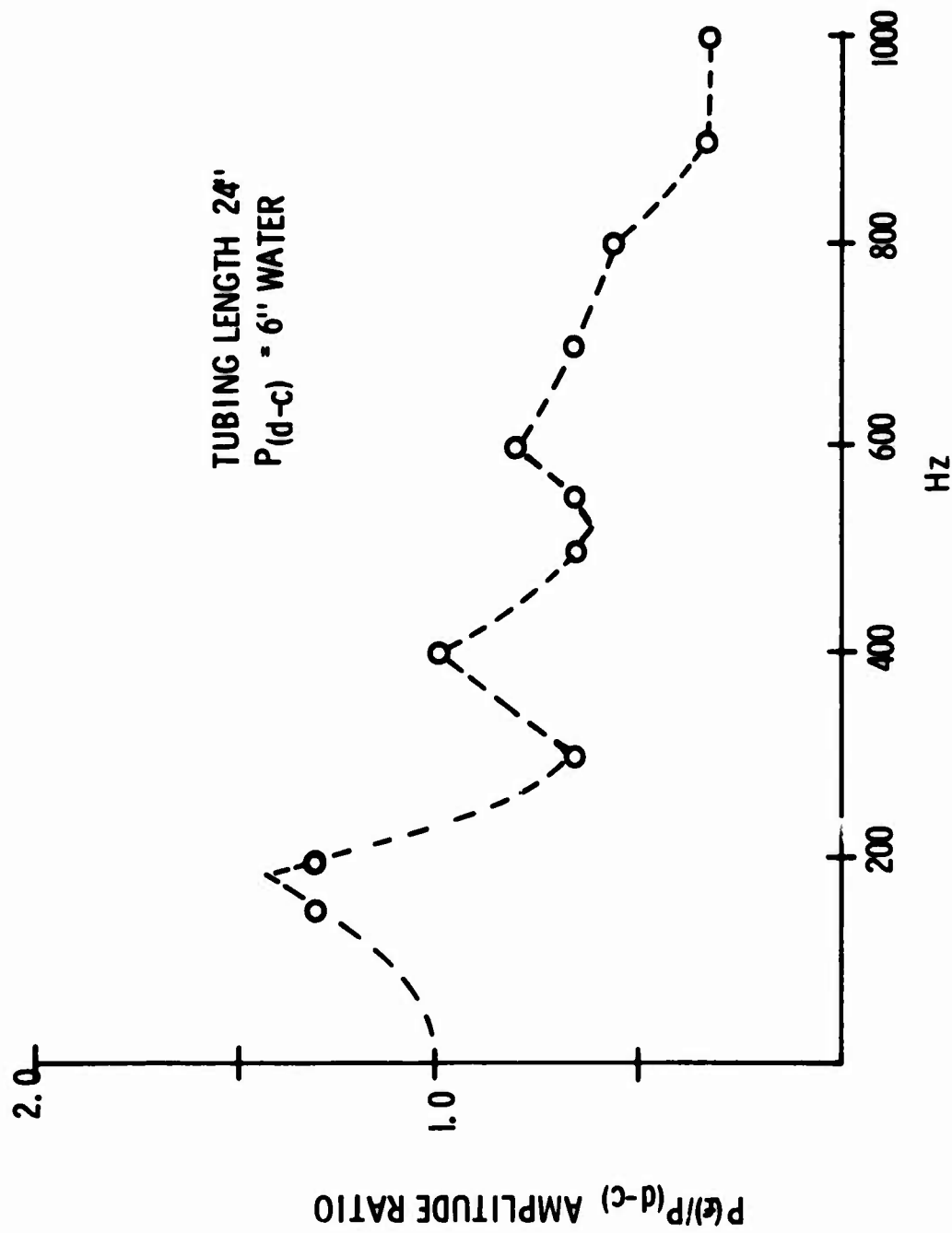


FIG. 15 AMPLITUDE VARIATION AT END OF .055 I. D.
 SENSOR LINE (L = 24")

DOWNSTREAM CONTROL OF A JET

H.P. Lin, Stone & Webster Engineering Corp., Boston, Massachusetts
F.R. Swenson, Department of Industrial Science, University of Stirling,
Stirling, Scotland

both formerly with the Department of Mechanical Engineering,
University of Missouri-Columbia, Columbia, Missouri

ABSTRACT

Supply jet attachment switching by a control jet located downstream in the supply jet flow field is discussed. At many control jet nozzle locations switching is possible both to the opposite sidewall and from the opposite wall to the sidewall nearest to the control nozzle. The influences of control jet direction and control nozzle location on the type of switching, and the influences of the flow splitter location and the control jet flow, location and direction on the two output parameters - minimum control flow for switching and switching time - are discussed and examples given from experimental results. Comparisons are made with the performance of normal upstream-controlled devices.

NOMENCLATURE

- b = width of the control jet nozzle (mm)
- B = width of the supply jet nozzle (mm)
- D = offset distance of the sidewalls (mm)
- h = depth of diffuser section and both jets (mm)
- L = length of the sidewalls (mm)
- P = increasing pressure (n/m^2)
- Q_c = flow rate of control jet (dm^3/s at standard conditions)
- $Q_c/Q_{c\min}$ = ratio of control flow to the minimum control flow for switching to occur
- Q_c/Q_s = ratio of control flow to supply flow
- $(Q_c/Q_s)_{\min}$ = minimum ratio of control flow to supply flow for switching to occur
- Q = flow rate of supply jet (dm^3/s at standard conditions)
- t = switching time interval (s)
- U_o = mean velocity of supply jet
- X_o = downstream coordinate of control nozzle (mm)
- X_{sp} = downstream coordinate of flow splitter (mm)
- Y_o = lateral coordinate of control nozzle (mm)
- α = inclination angle of sidewalls ($^\circ$)
- β = included angle of flow splitter ($^\circ$)
- ψ = direction angle of control nozzle ($^\circ$)
- τ = nondimensional switching time = $U_o t/B$

Introduction

The two most commonly used methods for moving the attachment of a supply jet from point of initial attachment to the opposite wall, a switching action, are to deflect the supply jet either with the momentum of a high-speed jet directed laterally to the supply jet as shown in Figure 1 or with an increase in the pressure in the separation zone between the attached supply jet and the wall of attachment as shown in Figure 2. Moses and Comparin (1) and Carbonaro (2) have presented earlier in this Symposium comprehensive reviews of the literature on both wall attachment and on the influences of changes in geometric and flow variables on the performance of devices designed on the basis of these two methods for controlling attachment switching.

A conventional design feature of nearly all devices using either of these two methods is that the control flow issues from ports located in the sidewalls of the diffuser for the supply jet. In most of the devices designed for subsonic flows in the supply jet these control ports are located upstream in the diffuser at the exit plane of the supply jet nozzle as is shown in Figures 1 and 2. In devices designed for supersonic flows in the supply jet these control ports are usually located downstream of the supply jet nozzle, but are still located in the sidewalls at the boundary of the supply jet flow field.

An alternative to placing the control jets in the sidewalls is to locate them downstream in the supply jet flow field. Potential advantages to these locations compared to control jet locations in the boundary of the flow field are comparable or better performance levels with a reduction in element width and an increase in the ease of manufacture due to the vertical introduction of the control flow directly into the flow field.

One recently reported application of the alternative set of locations for the control jet is the use by Tesar (3) of a control jet directed laterally from the trailing edge of a blade located in the supply jet flow field to generate supercirculation on the blade and thus to switch attachment flows in ventilation ducts. Another application of this alternative was made by Lance and Swenson (4) who used the unsymmetrical flow issuing from a vertically-oriented single-inlet vortex diode to control attachment switching. The switching performance was found to be sensitive to the direction of the region of peak velocity in the diode outlet flow.

Lin (5) continued the theme of Lance and Swenson's investigation but used the more compact and more highly directional flow issuing from a moveable, rotatable control nozzle. His complete report includes a review of the literature on the movement of the attachment point of the supply jet and on attachment switching. In addition it includes

¹ Numbers in parentheses designate references at the end of the paper.

a theoretical analysis of the movement of the jet attachment point due to control flows from nozzle locations inside of the separation zone, and experimental evidence of the deflection of a supply jet by a downstream control jet. This present paper is based upon the last portion of his investigation and discusses the influence of control nozzle location and direction on the type of switching that is observed and the influences of flow splitter location and control jet flow, location and direction on the switching performance. The evidence and conclusions are illustrated for a symmetrical two-dimensional supply nozzle and diffuser geometry, first without a flow splitter and then with a symmetrical splitter.

Geometric and Flow Parameters

The geometric parameters for the symmetrical two-dimensional nozzle and diffuser for the supply jet are shown in Figure 3. The principal parameters are the nozzle width B and height h , and the sidewall inclination angle α , offset D and length L_w . The principal flow parameter for the supply jet is the flow rate Q . For the experimental results presented in this paper the parameters with fixed values are the nozzle width $B = 4.76$ mm, aspect ratio $h/B = 4.26$, sidewall length $L_w/B = 26.6$ and sidewall inclination angle $\alpha = 15^\circ$.

The geometric parameters for a control jet located downstream in the supply jet flow field are the nozzle width b , downstream distance X_o , lateral distance from the diffuser section centerline Y and the angular direction ψ of the control nozzle opening, as shown in Figure 4. The flow parameter for the control jet is the flow rate Q . The fixed value parameter is the nozzle width $b/B = .13$. The control nozzle height is the same as the height of the supply nozzle, h .

The nozzle opening direction angle is also the direction of the control jet and ψ is measured from a reference line parallel to the diffuser centerline with 0° in the downstream direction and, as viewed from above the diffuser section, the positive sense of rotation is away from the diffuser centerline. The supply nozzle, diffuser and the flow splitter are symmetrical in the half-planes above and below the extended centerline of the supply nozzle for these experiments, so that results obtained for a control nozzle location and direction in one half-plane are the same for the mirror image location and direction in the other half-plane.

Air is the fluid used in the experiments and the flows exhaust from the diffuser directly to atmosphere without internal vents or bleeds. Also the control flow is at a constant value during a switching process.

Switching Types and Output Performance Parameters

The types of switching are named for the sidewall to which the attachment is moved. Thus, far-side switching is from the sidewall nearest to the control nozzle to the farthest sidewall as shown in Figure 5, and near-side switching is to the sidewall closest to the control nozzle as shown in Figure 6.

Two important performance parameters for downstream control are the control flow for switching to occur and the switching time. The control flow for switching to occur is a measure of the device control sensitivity and for each control nozzle location and direction is measured by slowly increasing the control flow until switching just occurs. The switching time is the time interval from the start of control flow until the supply jet comes to rest at its final position on the wall of reattachment. The sensor for switching time measurements is a reluctance-type differential pressure transducer with one side connected to a piezometric opening in the wall of the control flow tubing and the opposite side connected to a piezometric opening near the end of the wall of reattachment. The time interval measurements are made from traces of the differential pressure on records from recording oscillographs and a memory oscilloscope.

Switching Performance without Flow Splitter

Figure 7 shows a plot of the ratio of the control flow to the supply flow Q_c/Q_s versus the control jet direction and illustrates the use of the control flow required for switching to trace switching curves which are the boundaries of the far-side and near-side switching regions. The minimum control flow for switching to occur at that control jet location and supply flow rate is measured as the shortest radial distance from the plot origin to a switching curve. In Figure 7 the minimum occurs for far-side switching and is a control flow to supply flow ratio of 0.12 at a control jet direction of 270° for a supply jet flow rate equivalent to $1.03 \text{ dm}^3/\text{s}$ at standard atmospheric conditions.

Two conclusions that are illustrated in this graph are (1) that both far-side switching and near-side switching can occur at the same control jet location, but only for different ranges of control jet location and for control flows above different minimum values, and (2) there are combinations of control jet directions and flows for which switching does not occur.

The variation with control jet location of the minimum value for switching to occur is illustrated in Figure 8 in which the minimum control flow ratios at control nozzle locations on four lateral traverses are shown for both near-side and far-side switching. The lowest of these local minima determines the dominant type of switching and the optimum control nozzle location for the given geometry

and supply flow. In Figure 8 this optimum location is at $X/B = 9.33$, $Y/B = 1.33$ for a control flow ratio of $Q_c/Q_s = 0.01$ and is for far-side switching.

The variation of switching time with control jet direction at a given control jet location and for a range of control jet direction values including the direction for minimum control flow for switching is shown in Figure 9. The switching time results are in the nondimensional form $\bar{t} = U t/B$, where U is the mean velocity of the supply jet, t is the measured time interval for switching, B is the supply nozzle width and the ratio B/U is a nominal transport time. The sharp dip in the switching time curve is typical and the minimum values for switching times and the control flow for switching usually occur at the same control jet direction.

Switching Performance with Flow Splitter

The addition of a symmetrical flow splitter to the supply jet nozzle and diffuser geometry completes the configuration for a simple straight-walled bistable fluid amplifier. The location of the flow splitter in the diffuser is specified by X_s , the distance from the plane of the supply nozzle exit to the leading edge of the splitter, as shown in Figure 10. For the experimental results presented in this paper the included angle β of the triangular flow splitter is 30° which is equal to 2α , the included angle between the two sidewalls of the diffuser.

The influence of the location of the flow splitter on the minimum control flow for switching to occur is illustrated in Figure 11. The effect of the location of the splitter is different for each type of switching as is seen in the movement of the switching curves in Figure 12. At locations far from the control jet the splitter has negligible effect on the switching curves, but when the splitter is moved nearer to the control jet the switching curves for far-side switching first are moved away from the origin and then towards the origin, resulting in a rise and then a sharp drop of the minimum control flow required for switching as is well illustrated in Figure 11. The changes to the near-side switching curve are nearly opposite to those for the far-side switching curve, with a sharp increase in the control flow required for switching as the flow splitter is moved closer to the control jet.

The variation of switching times with flow splitter location is illustrated in Figure 13. These changes follow a similar trend to that for the minimum control flow for switching.

The experimental results shown in Figures 7-9 and 11-13 are typical in that switching performance and the optimum control nozzle location and control jet direction vary slowly with changes in the supply flow rate.

Comparison with Upstream Control of Switching

Positive switching as either momentum switching or pressure switching is the most common type of upstream switching control and corresponds to far-side switching in downstream control devices. The nearest equivalent to near-side switching in downstream control devices is suction switching in upstream control devices which is described by Drzwiecki (6). Suction switching occurs due to low pressures in the region of the control port in the wall opposite to that of wall attachment. The low pressure can be caused either by entrainment of fluid from a blocked control port into the amplifier in devices with low offsets (close sidewalls) or by sucking of flow out of the amplifier in devices with either large offsets ($D/B > 5.0$) or small wall offsets. A distinctive difference between near-side switching and suction switching is that near-side switching occurs for a positive control flow signal into the device from outside the device.

The minimum control flow to supply flow ratio for switching in downstream control devices compares favorably with the ratio for upstream control devices of about the same physical size and similar geometry. The low value of $Q_c/Q_s = .01$ for far-side switching in Figure 8 is in the same range of values as the inverse, .01, of the flow gain of about 100 reported by Markland (3) as the approximate performance level of Tesar's jet flap devices, and also of the low values reported in the literature for positive switching by Colborne and Williams (7) of .007 ($D/B = 0.0$) and Foster and Jones (8) of .01 ($D/B = 1.5$, square-ended splitter).

The minimum non-dimensional switching time of $\tau = 186$ from Figure 13 for far-side switching ($Q_c/Q_s = 0.18$, $Q_c/Q_{cmin} = 1.8$, $D/B = 2.0$) compares not too unfavorably with the value of $\tau = 105$ for positive switching ($Q_c/Q_s = 0.18$, $Q_c/Q_{cmin} = 6.4$, $D/B = 0.625$) with the interpolation of results reported by Ozgu and Stenning (9) who used a similar definition of switching time to that used in this paper. The ratio Q_c/Q_{cmin} of the actual control flow to the minimum control flow for switching is a relative measure of the control flow.

General Conclusions

The control of supply jet attachment is possible for control nozzle locations downstream in the supply jet flow field. The type of switching, minimum control flow rate for switching to occur and the switching time are all dependent upon control jet direction as well as control jet flow and control nozzle location. The switching time and minimum control flow rate for switching to occur are different for far-side and near-side switching and also vary with flow splitter location.

The values of the performance parameters for downstream control devices are comparable to those for similar upstream control devices, with the potential advantage of smaller elements and, because of the dependence of switching thresholds on both direction of the control jet and the level of the control flow, angular and flow inputs can be combined to control outputs in moving-part devices.

Although evidence and conclusions for only bistable switching devices are presented in this paper, control jets at downstream, in-the-flow locations can be used also in proportional devices.

Acknowledgments

Financial support for this project was provided by the University of Missouri-Columbia and the National Science Foundation under NSF Grant GK 27771. Secretarial and library support for the preparation of this paper was provided by the University of Stirling.

REFERENCES

1. Moses, H.L. and R.A. Comparin, "The Effect of Geometric and Fluid Parameters on the Static Performance of Wall-Attachment Type Fluid Amplifiers," Proceedings of the Fluidics State-of-the-Art Symposium, Harry Diamond Laboratories, September 1974.
2. Carbonaro, M., "The Effect of Geometric and Fluid Parameters on the Dynamic Characteristics of Wall Attachment Type Fluid Amplifiers," Proceedings of the Fluidics State-of-the-Art Symposium, Harry Diamond Laboratories, September 1974.
3. Tesar, V., "Stabilized Fluidic Oscillator," Czech. Patent No. 148 266, 15 April, 1973 (In Czech), summarized in Fluidics Feedback, Vol. 7 No. 6, Nov/Dec 1973, p.131. See also E. Markland, "The First International Conference on Applications of Fluidics," Fluidics Feedback, Vol. 7, No.6, Nov/Dec 1973, p.120.
4. Lance, G.M. and F.R. Swenson, "Vortex Induced and Forced Switching of Two-Dimensional Jets," ASME Paper No. 70-WA/Flcs-13, Nov. 1970.
5. Lin, H.P., "Downstream Control of Jet Attachment Switching," Ph.D. Thesis, University of Missouri-Columbia, May 1973.
6. Drzwiecki, T.M., "Prediction of the Dynamic and Quasi-Static Performance Characteristics of Fluoric Wall-Attachment Amplifiers," Fluidics Quarterly, Vol. 5, No.2, April 1973, pp.96-126.
7. Colborne, W.G. and C.J. Williams, "Experimental Study of Switching in a Bistable Fluid Amplifier," ASME Paper 72-FE-11, March 1972.

8. Foster, K. and N.S. Jones, "An Examination of the Effect of Geometry on the Characteristics of a Turbulent Reattachment Device," First Cranfield Fluidics Conference, Paper B1, 1965.
9. Ozgu, M.R. and A.H. Stenning, "Switching Dynamics of Bistable Fluidic Amplifiers with Low Setbacks," Transactions of the ASME, Journal of Dynamic Systems, Measurement, and Control, Vol. 94, No. 1, March 1972, pp. 21-29.

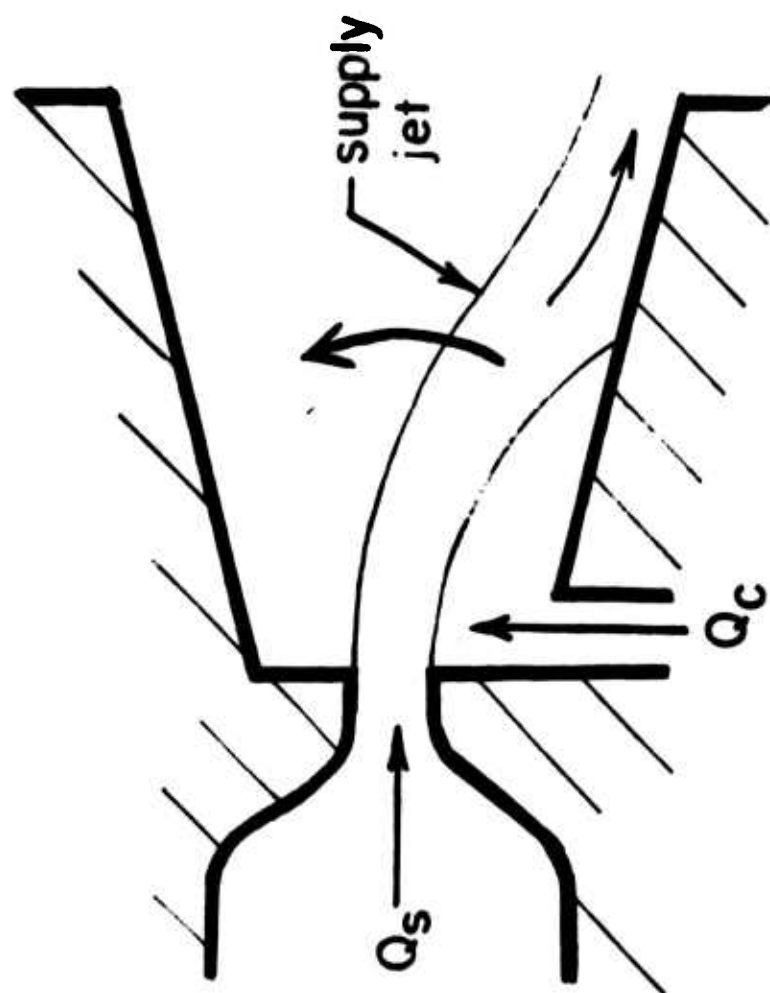


Figure 1. Momentum Switching

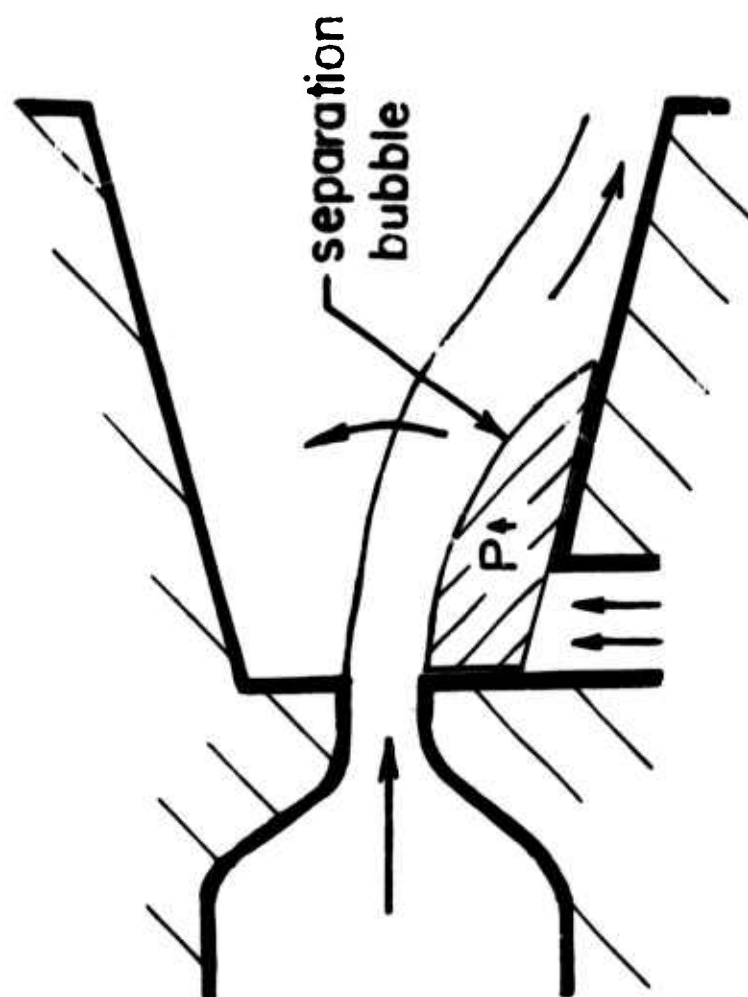


Figure 2. Pressure Switching

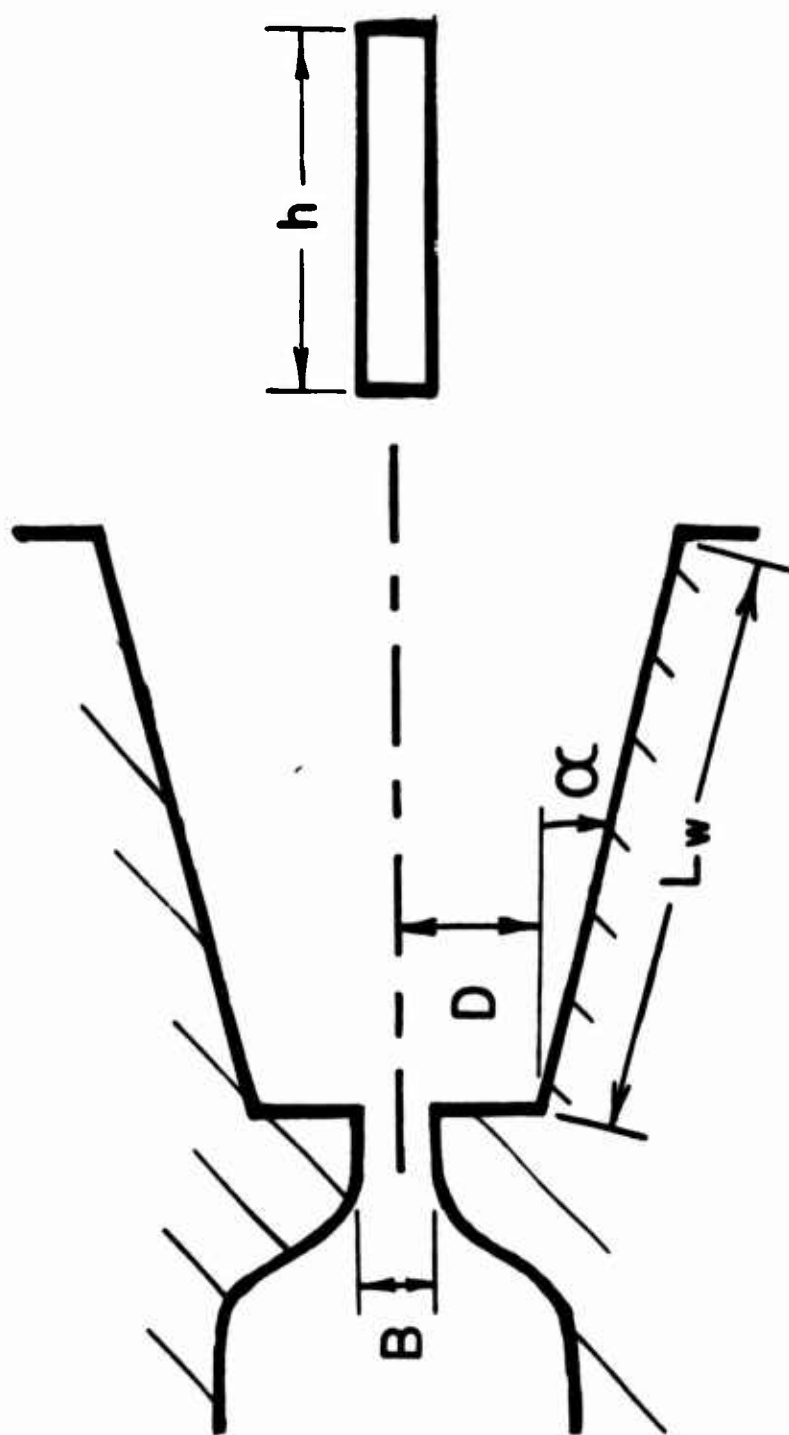


Figure 3. Geometric Parameters for Supply Jet

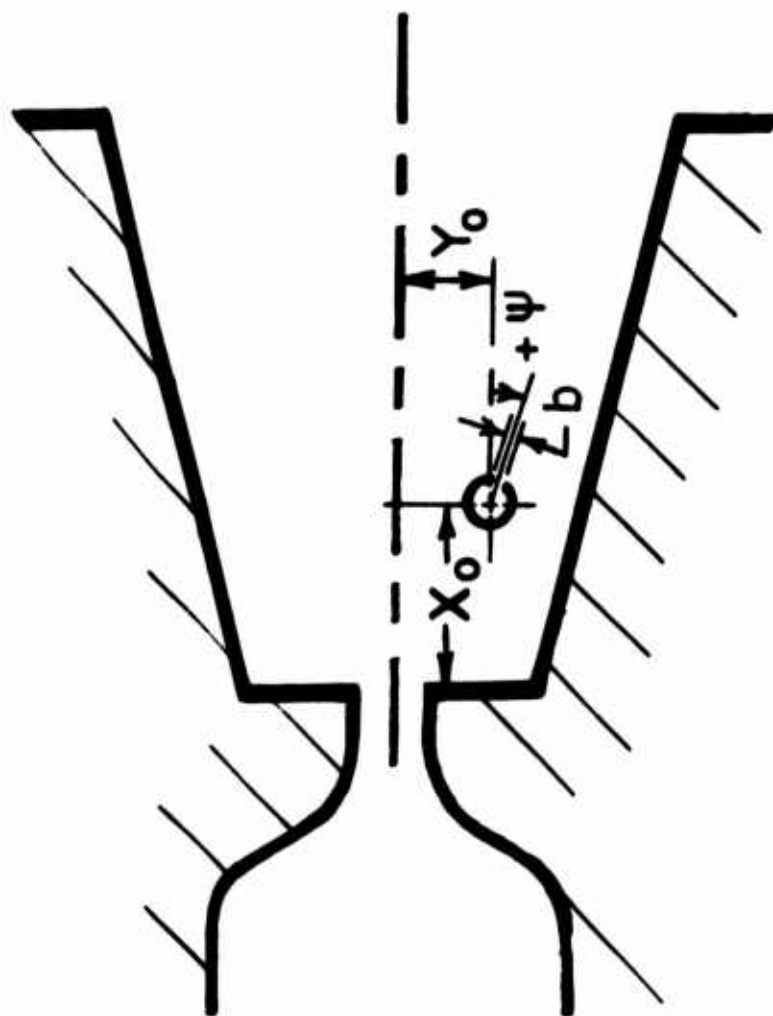


Figure 4. Geometric Parameters for Control Jet

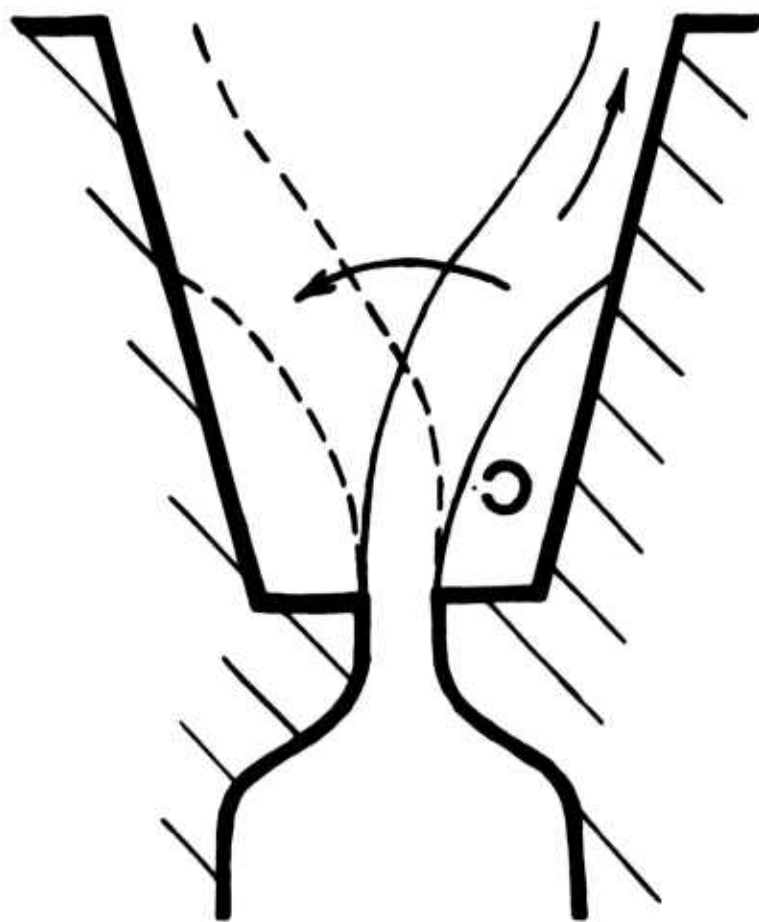


Figure 5. Far-Side Switching

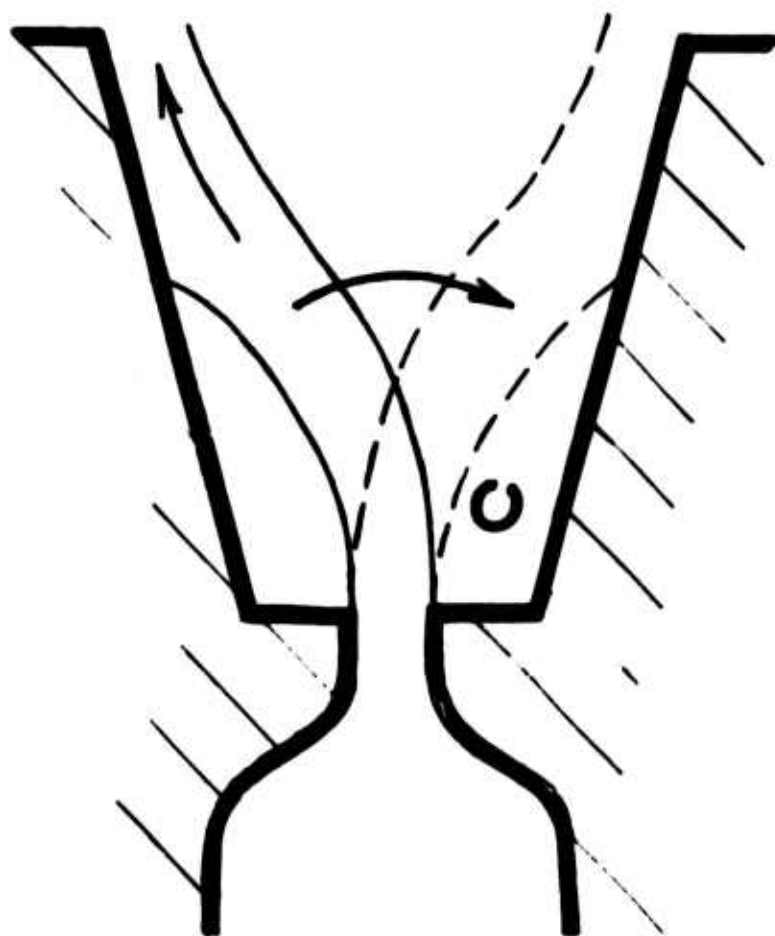


Figure 6. Near-Side Switching

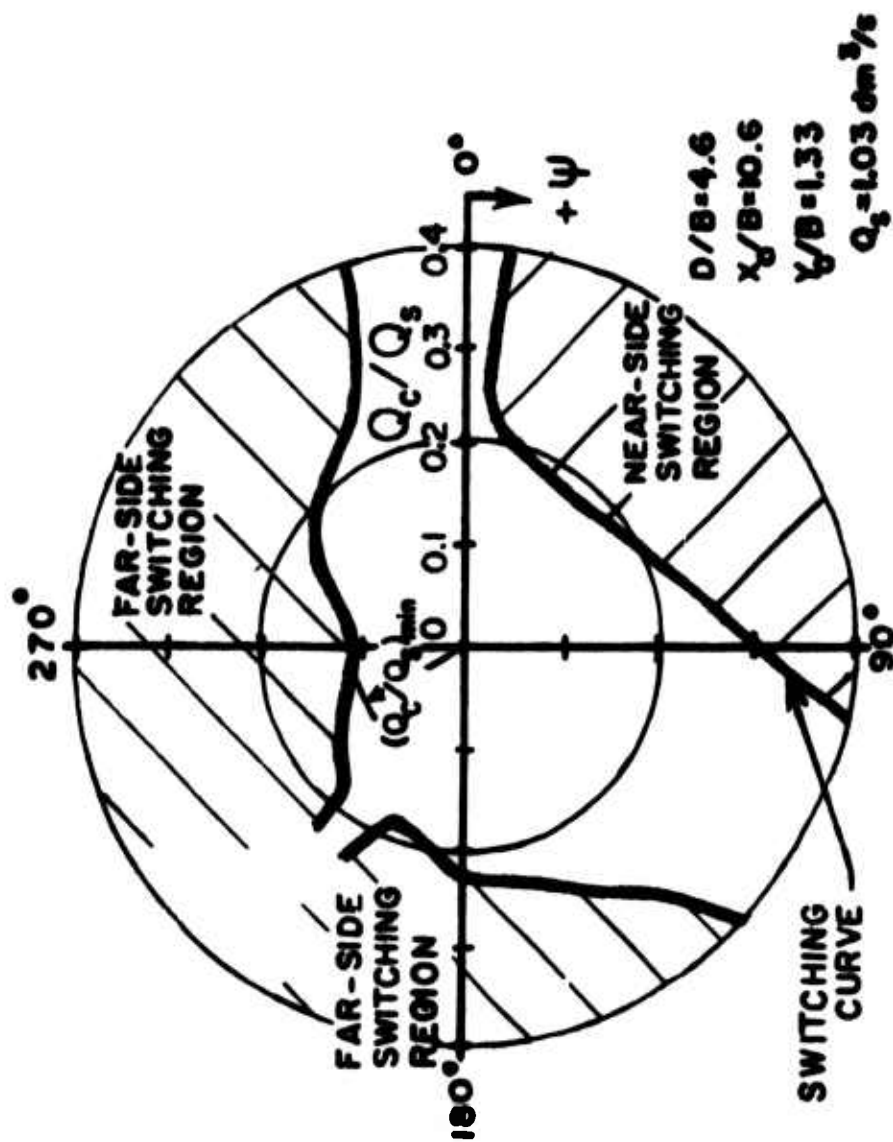


Figure 7. Switching Regions and Typical Changes of the Ratio of Control Flow to Supply Flow for Switching to Occur due to Changes in Control Jet Direction

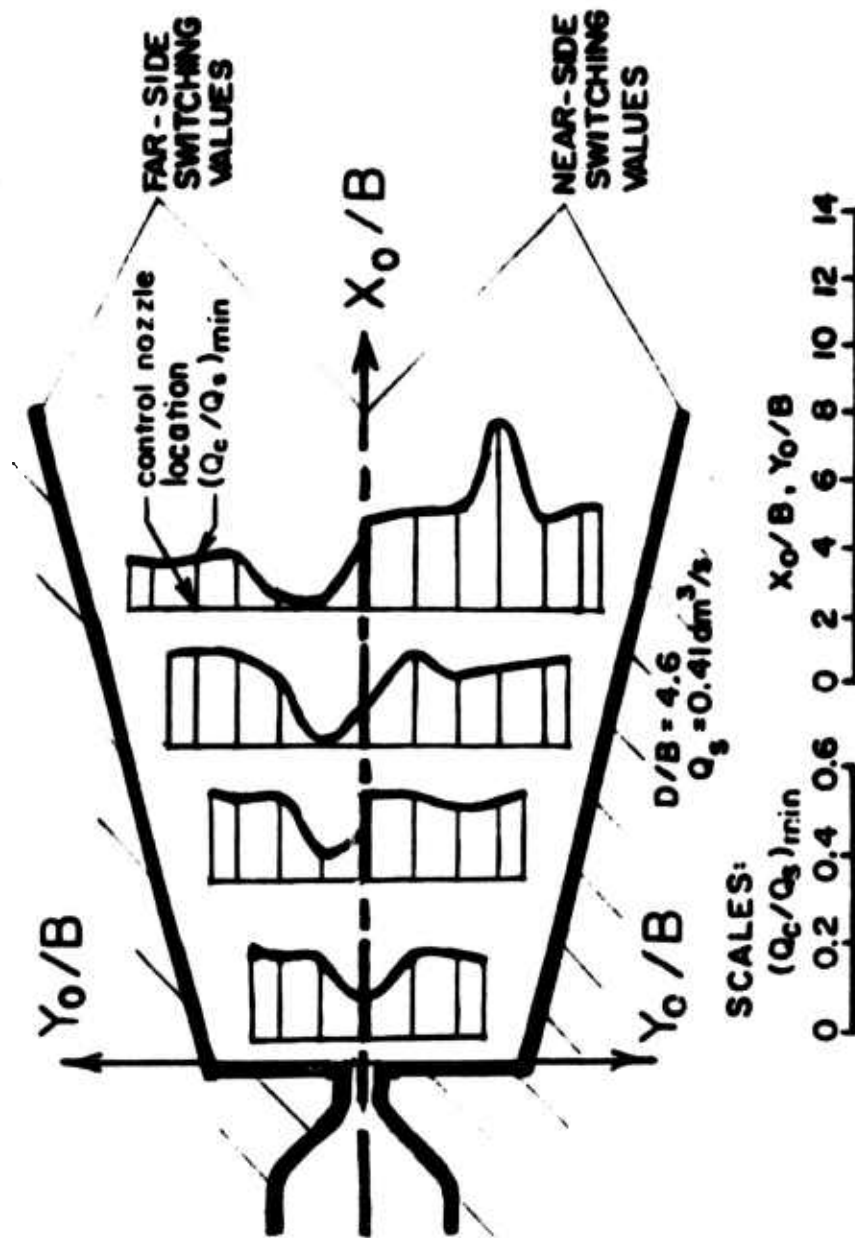


Figure 8. Typical Changes of the Minimum Ratio of Control Flow to Supply Flow for Switching to Occur due to Changes in Control Jet Nozzle Location

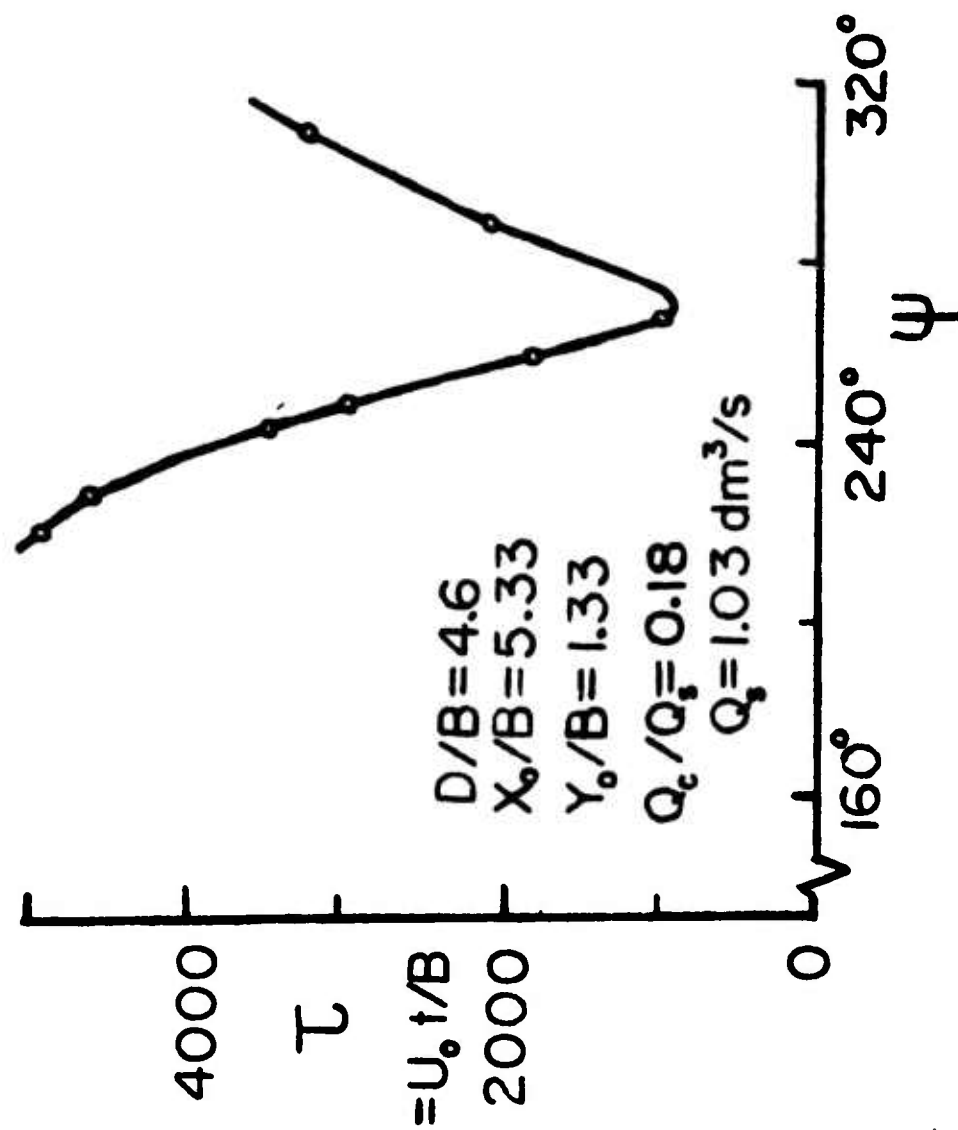


Figure 9. Typical Switching Time Changes due to Changes in Control Jet Direction

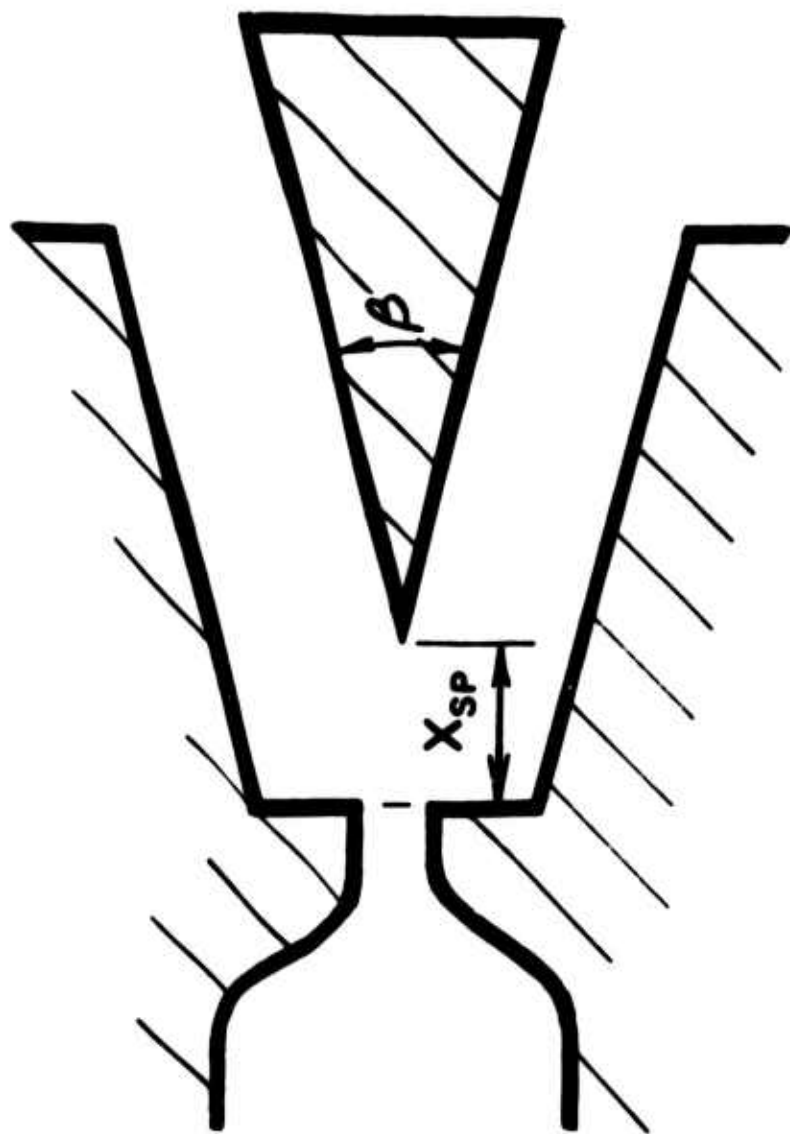


Figure 10. Geometric Parameters for Flow Splitter

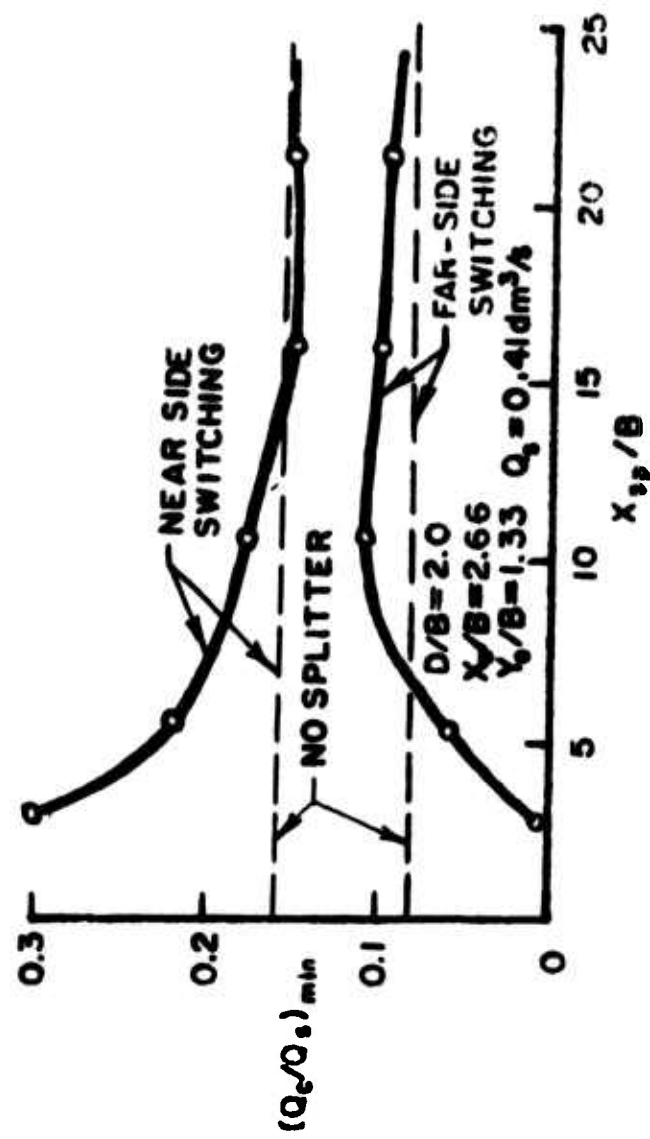


Figure 11. Typical Changes in Minimum Ratio of Control Flow to Supply Flow for Switching to Occur due to Changes in Flow Splitter Location

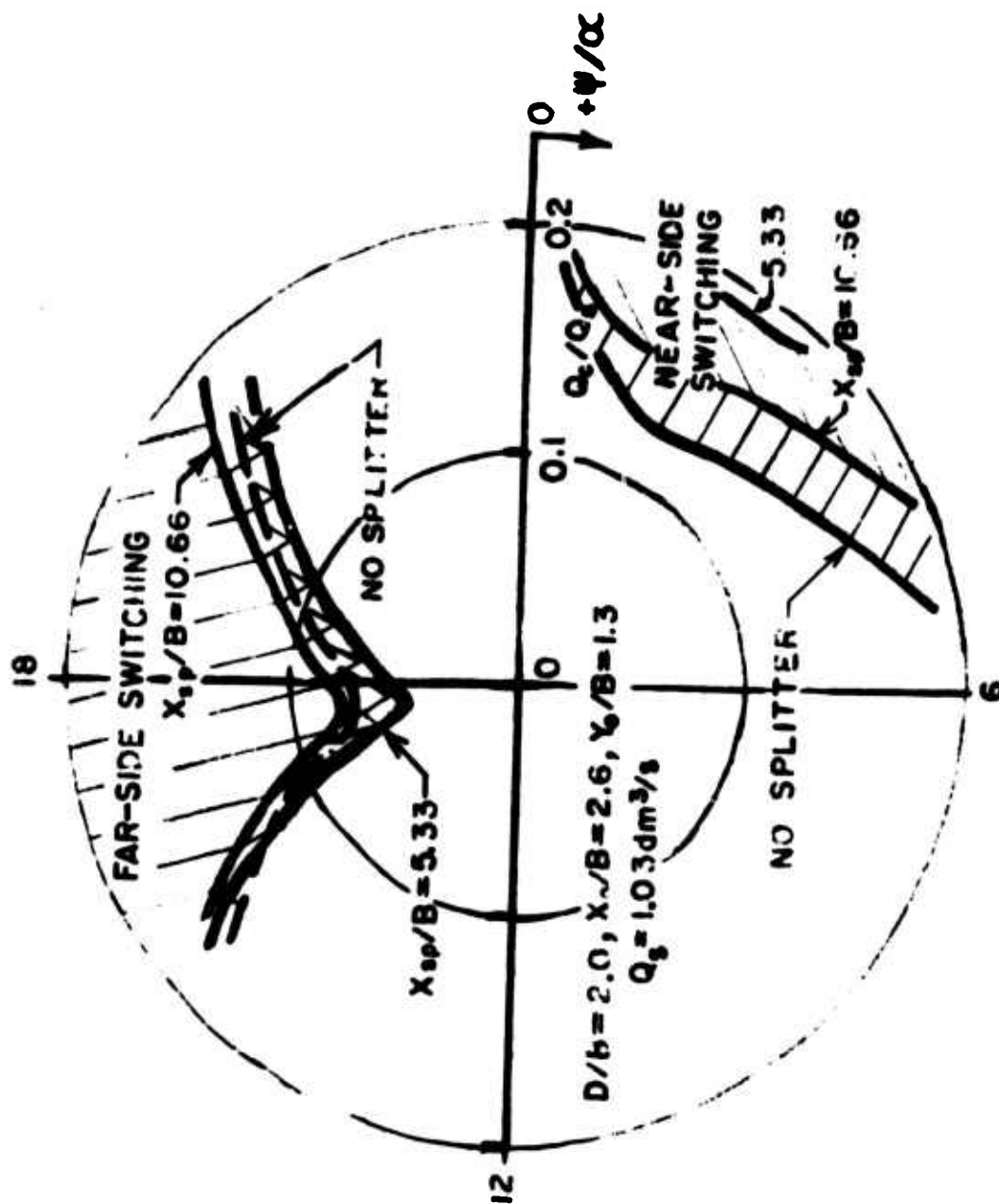


Figure 12. Typical Changes in Switching Curves due to Changes in Flow Splitter Location

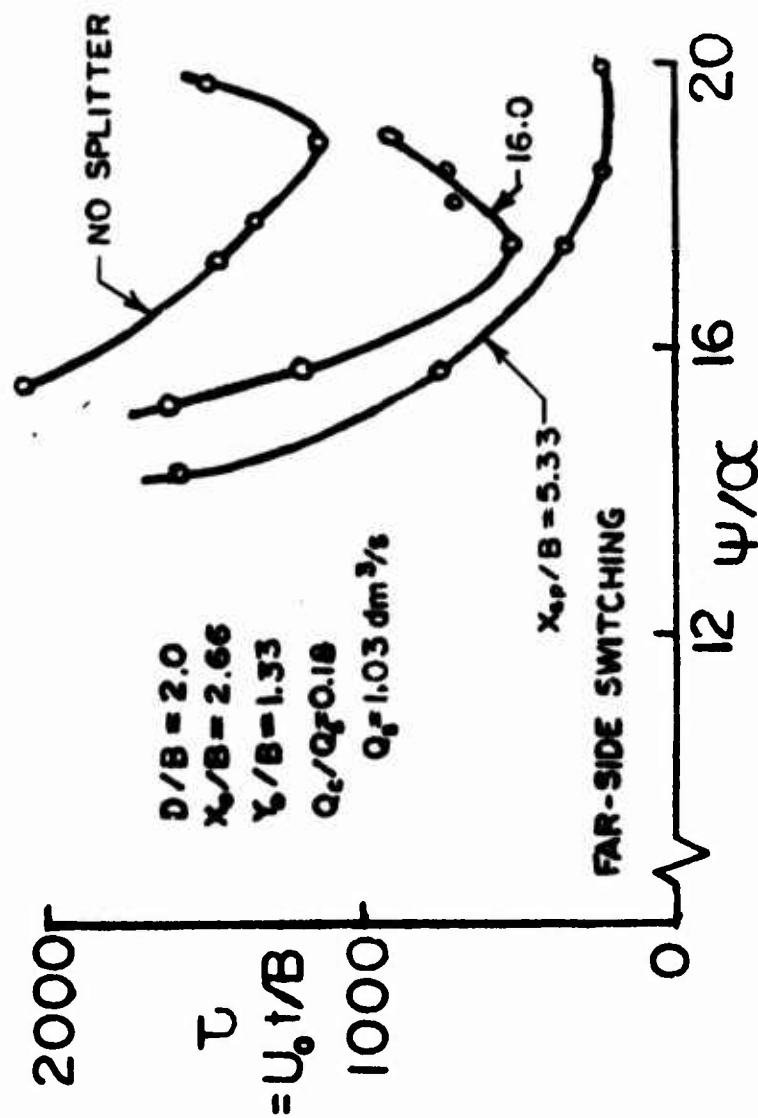


Figure 13. Typical Changes in Switching Times due to Changes in Flow Splitter Location

THE LAMINAR FLIP-FLOP

by

TADEUSZ M. DRZEWIECKI
FRANCIS M. MANION

Submitted for Presentation at:
The Harry Diamond Laboratories
Fluidic State-of-the-Art Symposium
30 Sep - 4 Oct 1974
Adelphi, Maryland

ABSTRACT

This paper describes the design of a fluidic, laminar flip-flop that does not use the Coanda effect, but rather an instability of jet position due to vent pressurization. If vent flow is allowed to enter the control region in excess of that demanded by entrainment, and the control port is vented to ambient, then any small perturbation will cause more flow to enter one side and less on the other, increasing the pressure differential and causing the jet deflection to increase until it reaches a stable position on one side or the other. This phenomenon has been put to use in the laminar flip-flop. The prototype device has a pressure gain of 15, a fanout of 8 and a power consumption of 3.5 mW for a 1.0 mm x 0.5 mm supply nozzle device. Frequency response is estimated at 90 Hz. A smaller device with a 0.5 x 0.5 mm nozzle has measured frequency response of about 180 Hz. The static characteristics compare favorably with the best that turbulent fluidics has to offer but with an improved low-power consumption of over an order of magnitude less than that of currently available devices with prospects of yet another order of magnitude reduction seen. In addition, since the flow is laminar and has virtually no random fluctuations switching occurs at a discrete control pressure point as opposed to a zone as in turbulent devices. The availability of such a precision flip-flop now makes it possible to consider accurate timers and counters, pulse-duration modulators, and analog-to-digital converters.

1. INTRODUCTION

Flueric logic devices have, since their introduction in 1959, fallen primarily into three distinct categories: the Coanda effect or wall attachment devices; the turbulence amplifiers, and impact modulators. Each of these devices operates at some stage in the turbulent-flow regime, and all but the turbulence amplifiers require considerable continuous operating power, in the order of 0.5 watts. The necessity of a continuous supply of fluid, if excessive, makes fluerics at best an unattractive choice when considering large, complex or mobile circuitry. Because of this, much effort has been expended in lowering the power consumption of flueric logic devices. One such attempt by Walker and Trask [1] resulted in a laminar NOR gate that operated at several milliwatts of power but with a fairly low fanout of about 3. It became obvious that low power was almost synonymous with laminar flow. Several studies of laminar wall attachment [2, 3] showed that one could obtain a Coanda-type flow even in the laminar regime; however, no practical flueric devices were forthcoming.

At the same time as the search for low-power logic devices was going on, much progress was being made in the development of laminar, proportional amplifiers [4, 5]. Manion and Mon [4] showed that a laminar proportional amplifier can exhibit dynamic ranges and signal to noise ratios of several orders of magnitude greater than comparable turbulent devices, as well as having improved gain characteristics. As this amplifier was being developed a theoretical analysis was also developed. As a result of the analysis, it was discovered that the input resistance may become negative due to internal feedback. This negative input resistance makes a laminar bistable device possible. Since these laminar proportional amplifiers operate at very low powers (from 0.1 mW upwards), the bistable device if feasible would also operate at this low power.

This paper presents a discussion of the operating principle, a simple analysis predicting bistability and dynamic response, and some preliminary prototype experimental data, for laminar flip-flops. In addition several applications and advantages of laminar flip-flops are discussed.

2. OPERATING PRINCIPLE

Consider the laminar proportional amplifier (LPA) shown in figure 1



Figure 1. A Laminar proportional amplifier

The flow field can be visualized readily and under normal operating conditions, with the vents at ambient pressure, appears as shown in the photograph in figure 2. The jet emanates from the supply nozzle and splits evenly on the splitter.

When a sufficient pressure differential is applied at the controls, flow from the control is exhausted to the vents through the space defined by the jet edge and the downstream edge of the control channel. This space may be considered to be a variable orifice which changes in area as the jet is deflected. Consider, however, that the vents can be maintained at a pressure higher than the pressure at the jet edge. In this case, if we consider one side, flow passes from the vent region to the jet edge reducing the flow required through the control passage (R_c in figure 3). However, consider the case where the control ports are maintained at ambient pressure and the jet is centered. In such a case the flow entrained by the portion of the jet in the control region, Q_c , must be supplied from both the upstream vent and the control port, which means that the pressure at the jet edge, P_j , is lower than ambient (when the vent is at ambient pressure). Now if the vent pressure P_v is increased to the point where the flow entrained by the jet is equal to the flow from the vent Q_v , then the flow through the control port, Q_c , will be zero. The jet is still centered because there are no excess flows and entrainment is satisfied. If the vent pressure is now further increased so that there is flow entering from the vent in excess to that demanded by entrainment, then a metastable situation occurs. The excess flow, over and above entrainment, now exits through



the control port; hence, the pressure at the jet edge is above ambient (remember that the control port is at ambient pressure). The flows can be easily visualized by the aid of the simple equivalent circuit for the input to the amplifier shown in figure 3.

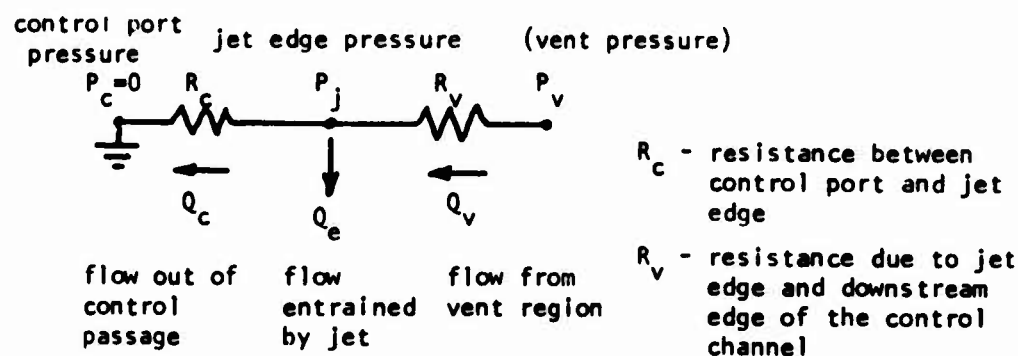


Figure 3. Equivalent circuit of one side of LPA input

If the jet should move slightly, by any perturbation, to one side or the other, increasing the vent width on one side and decreasing it on the other, then more flow enters the wider space and less through the narrower space. Since the control resistance, R_c (fig. 3) is constant, this means that for more control flow out (equal to the excess of vent flow, by continuity), the jet-edge pressure must increase on the side with more flow and conversely must decrease on the side with less flow. This of course is then an applied pressure differential to the jet so that it continues deflecting until it is in a position which completely blocks the vent flow on one side. Clearly, then, only the states are stable for which the jet is deflected, and it blocks the downstream edge of the control channel, hence the jet position is bistable.

3. DESIGN

To obtain an input-output device operating on the above principle, it is necessary to modify the LPA in three ways: First, provide a pressure supply to the vents; second, ground the control ports; and third provide a means of pressurizing the controls, despite their grounded condition, in order to flip the jet to another state:

Pressurizing the vents is readily accomplished by collecting the vents in a junction and supplying an independent pressure source or by using bleed flow through a resistor from the supply port of the amplifier.

Grounding the control ports and providing a means of pressurizing the controls can be accomplished with a single modification. In the bistable mode, flow is outward from the controls. If this flow forms a jet and is exhausted across a vent, the grounding function is performed. If a new jet is formed to axially impinge on the control outflow jet, the back pressure of the outflow jet will be increased, hence providing pressurization of the control to flip the jet. Figure 4 shows schematically the first prototype LFF built.



Figure 4. First prototype laminar flip-flop

In this device the vent pressure was controlled from an independent, outside source.

Later designs differ only in that bleed flow from the supply is fed to the collected vents by resistor laminates placed in the cover plate of the device, and the supply nozzle width $b_s = 0.5$ mm.

4. ANALYSIS

The analysis presented here is intended to show how the bistable phenomenon occurs and how one can estimate the pressures and other such parameters to predict its occurrence. This analysis is not intended to be a thorough study of this phenomenon; this will come in a later report.

The equivalent circuit (figure 3) for the flows of this element exists on each side of the jet. As a result, two flow summations must be written. In these equations the vent to jet edge resistance R_v is an area times the square root of the pressure difference. For mathematical simplicity all quantities have been normalized,

flows by the supply flow Q_s , pressures by the supply pressure P_s , dimensions by the supply nozzle width b_s .

$$Q_{c1} - Q_{e1} + (b_v + \delta') \sqrt{P_v - P_{j1}} = 0 \quad (1)$$

$$Q_{c2} - Q_{e2} + (b_v - \delta') \sqrt{P_v - P_{j2}} = 0 \quad (2)$$

where Q_c is the input flow, Q_e is the entrained flow, $Q_v = (B_v \pm \delta') \sqrt{P_v - P_j}$ is the flow from the vent region to the jet edge, b_v is the spacing between the jet and the control edge labeled in figure 2 and δ' is the jet deflection due to P_j' - the small change in jet edge pressure (fig. 2 and 3). Subscripts 1 and 2 identify the side of the jet in question (e.g. right or left).

$$\text{Let } Q_{c1} = Q_c + \frac{Q_c'}{2}, Q_{c2} = Q_c - \frac{Q_c'}{2}, Q_{e1} = Q_e + \frac{Q_e'}{2}, \text{ etc.,}$$

$P_{j1} = P_j + \frac{P_j'}{2}$, and $P_{j2} = P_j - \frac{P_j'}{2}$, where primed (') quantities refer to small perturbations about the unprimed quantity. Thus, note that

$$\sqrt{P_v - P_{j1}} \text{ is approximately equal to } \sqrt{P_v - P_j} \left(1 - \frac{P_j'}{4(P_v - P_j)}\right).$$

Substituting these terms and taking the difference between equations (1) and (2) we get

$$Q_c' - Q_e' - b_v \left(\frac{P_j'}{2\sqrt{P_v - P_j}} \right) + 2 \delta' \sqrt{P_v - P_j} = 0 \quad (3)$$

From reference [4], the lateral displacement of the jet at the control downstream edge is

$$\delta' = \frac{b_c^2}{4c_\theta} P_j'$$

where b_c is the control nozzle width and c_θ is the momentum flux discharge coefficient. The resulting combination with equation (3) results in

$$\delta' = \frac{Q_c'}{a_1 + \frac{b_v}{2k_c \sqrt{P_v - P_j}} - 2 \sqrt{P_v - P_j}} \quad (4)$$

where $a_1 \delta' = Q_e'$ and $k_c = b_c^2/(4c_\theta)$

The input flow Q'_c is defined as

$$Q'_c = \frac{P'_c - P'_j}{R_c} = \frac{P'_c}{R_c} - \frac{\delta'}{k_c R_c} \quad (5)$$

where R_c is the control line resistance.

Using equations (4) and (5) and multiplying through by $\frac{\sqrt{|P_v - P_j|}}{k_c R_c}$ the input admittance $\frac{\partial Q'_c}{\partial P'_c}$ is found to equal

$$\frac{\partial Q'_c}{\partial P'_c} = \frac{1}{R_c} \left\{ \frac{\frac{b_v}{2k_c} + a_1 \sqrt{|P_v - P_j|} - 2(P_v - P_j)}{\frac{b_v}{2k_c} + (a_1 + 1/k_c R_c) \sqrt{|P_v - P_j|} - 2(P_v - P_j)} \right\} \quad (6)$$

The bistable phenomenon occurs when this slope is negative. (Note, if $P_v = P_j$ then $\frac{\partial Q'_c}{\partial P'_c} = \frac{1}{R_c}$). The numerator decreases to zero and then becomes negative at a larger value of $|P_v - P_j|$ for typical parameters. For example let $b_v = 0.25$, $k_c = 8.86$, $a_1 = .0668$ when the jet is centered then the slope will be zero or negative when $(P_v - P_j) > 0.0104$.

The numerator is negative while the denominator is still positive, giving a negative slope. If the denominator becomes negative the input inductance coupled with the jet displacement compliance results in a limit cycle oscillation whose excursion is limited by the entrainment derivative with displacement.

A more thorough discussion of this phenomena (denominator equal to zero) will be the subject of another report. This report evaluates the slope of the input admittance characteristic to determine if the device will be bistable. This can be accomplished by evaluating the slope with the jet centered.

Equation (6) therefore defines the condition when the negative slope occurs and which parameters determine this slope.

The effect of downstream control edge clearance, control width (k_c is determined by b_c^2), the entrainment and the pressure difference is given in equation (6).

The dynamic response of a digital device is usually characterized by a switching time that is a decreasing function of the control power. Analytic studies of Coanda-type devices such as that by Goto and

Drzewiecki [6] derive this relation and verify it experimentally. It is not usual to consider digital frequency response, but if one does, the limiting frequency at which a wall attachment device can operate is determined by the amplitude of the input signal. For example, if a device switches in one ms at a control pressure amplitude of $0.1 P_s$, then the maximum frequency of a switch-switch-back function would be 500 Hz ($f = 1/(2\tau_{sw})$, τ_{sw} = switch time). If the same device switches in 0.5 ms at a control pressure of $0.3 P_s$ then the maximum frequency would be 1000 Hz. At each of these frequencies the maximum output pressure equal to the static pressure recovery is recovered. So for a square-wave input, the maximum operating frequency is a function of the input amplitude. A Bode plot of the output pressure would then consist of a family of curves, each dropping off at different frequencies for different input amplitudes.

The dynamic response of the laminar flip-flop is tied closely to the dynamics of the LPA which have already been analyzed successfully [4]. Because of this the dynamic response of the LFF will be discussed in terms of the known frequency response of the LPA rather than to rework the analysis in terms of step responses and switching times.

To estimate, analytically, the flip-flop frequency response one may consider the following arguments. When the LPA is operated in its digital mode as a LFF and the jet deflection excursion is such that the jet position varies from just at saturation to saturation (i.e. where each output just reaches a maximum pressure recovery without ringing) it can be assumed that the jet is critically damped (damping ratio $\zeta = 1.0$). Assuming then a second-order response for the LPA results in a transfer function, T ,

$$T = \frac{1}{\frac{s^2}{\omega_n^2} + 2\zeta \frac{s}{\omega_n} + 1} \quad (7)$$

Substituting $j\omega$ for the Laplace variable s , where $j = \sqrt{-1}$, ω is radian frequency, and $\zeta = 1.0$, the output amplitude, A , is just the vector sum of the real and imaginary parts of the transfer function.

$$A = 1/\sqrt{(\omega/\omega_n)^2 + 4(\omega/\omega_n)^2} \quad (8)$$

To calculate the -3db point (break point frequency) set $A = 0.707$ which results in $\omega/\omega_n|_{-3db} = 0.644$. The natural (or resonant) frequency f_n

of the LPA (therefore also of the LFF) has been found by Manion and Mon [4] to be

$$f_n = 0.01 \bar{V}_s / b_s$$

or rewritten, noting that the average supply velocity $\bar{V}_s = c_d \sqrt{2(P_s - P_v)/\rho}$ where c_d is the supply nozzle discharge coefficient and ρ the fluid density,

$$f_n = 0.01 c_d \sqrt{2(P_s - P_v)/\rho} / b_s \quad (9)$$

Note that pressure, flow and dimensions are not normalized here. Using equation (9) and noting that $\omega/\omega_n|_{-3db} = f/f_n|_{-3db} = .644$ (since $f = \omega/2\pi$), then the breakpoint or maximum operating frequency for the LFF is approximated by the expression

$$f_{-3db} = 0.00644 c_d \sqrt{2(P_s - P_v)/\rho} / b_s \quad (10)$$

The minimum switch time can be estimated as

$$\tau_{sw} = 0.5/f_{-3db} \quad (11)$$

5. PROTOTYPE CHARACTERISTICS

The device depicted in figure 4 was tested statically; the supply and input impedances, the blocked output pressure transfer characteristic, and the output impedance characteristic were measured at a supply Reynolds number based on nozzle height of about 10^3 . Figure 5 depicts graphically the measured characteristics.

The blocked-pressure gain is the change of an output pressure divided by the switch pressure. The fan-out (number of like units that can be driven simultaneously by one output) is the output flow, at an output pressure equal to the switch pressure, divided by the switch flow at switch pressure. The power consumption is the product of the supply pressure and the supply flow. These three characteristics are obtained from the data in figure 5 and are listed in Table I in comparison with a high performance, wall attachment turbulent flip-flop described by Warren [7] and also in ref [8], and with the lowest power consumption, commercially available flip-flop [8].

As can be seen, the laminar flip-flop compares well with the highest gain/fanout device and has, over an order of magnitude, lower power consumption than the lowest power consumption, commercially available device and almost three orders of magnitude lower than the high-performance device.

Assuming that for the same Reynolds number the characteristics remain the same, the power consumption can be further reduced by yet another order of magnitude to about 0.25 mW if one uses a 0.25 mm x 1.0 mm ($\sigma = 4$) nozzle, and down to about 0.1 mW if the Reynolds number $h_s \sqrt{2P_s/\rho} / \nu$ is reduced by half.

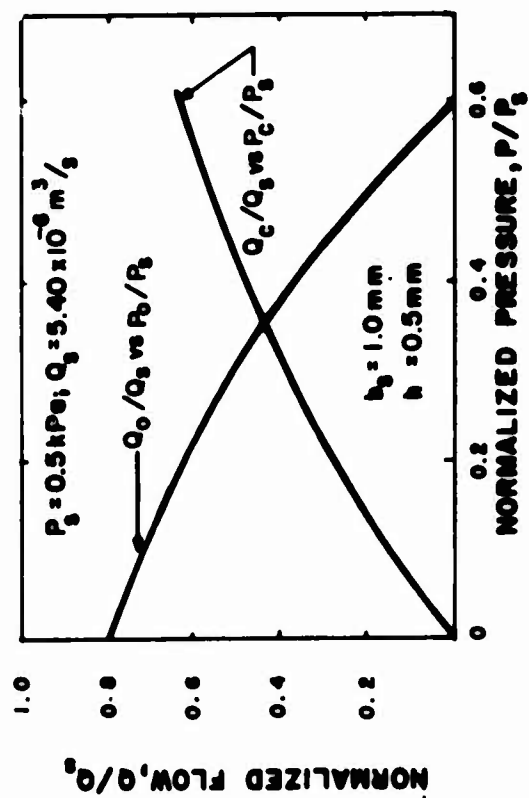
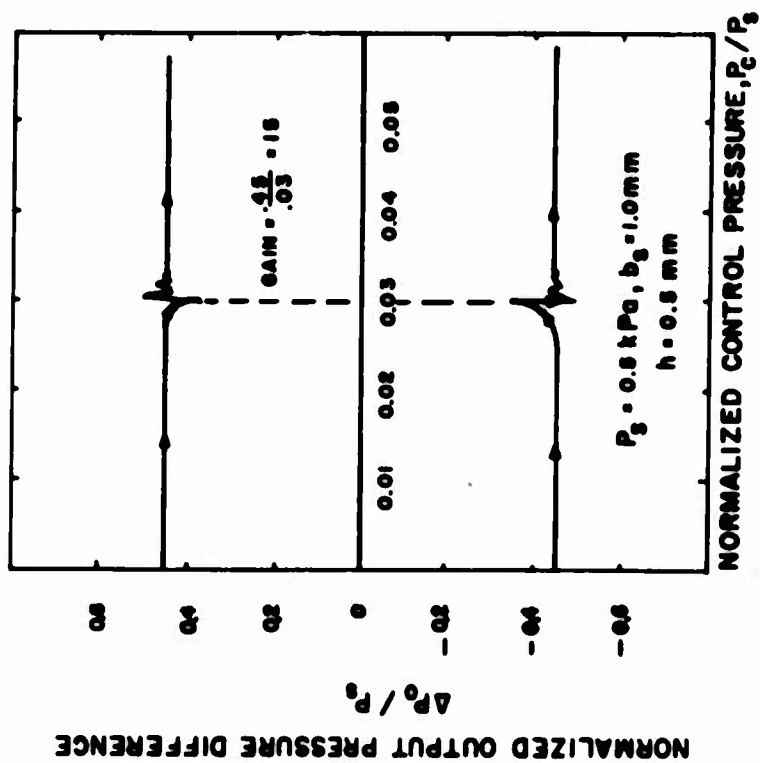


Figure 5. Experimental characteristic of prototype laminar flip-flop

Table 1. Comparison of LFF performance to typical turbulent devices

	LFF	TFF [7, 8], HDL	TFF [8], Commercial
Gain, G_p $\Delta P_o / P_{sw}$	15	17	3.5
Fanout $Q_o / Q_{sw} _{P_{sw}}$	8	10	3
Power $P_s Q_s$ (watts)	0.0035	1.37	0.064

The frequency response of the device in figure 4, as estimated from the expressions in section 4 and the current dimensions and supply pressure, is roughly 90 Hz.

Dynamic tests conducted on a smaller device, operating as a feedback oscillator with varying lengths of feedback lines (to change the frequency) result in a Bode plot, logarithm of amplitude versus frequency, as shown in figure 6.

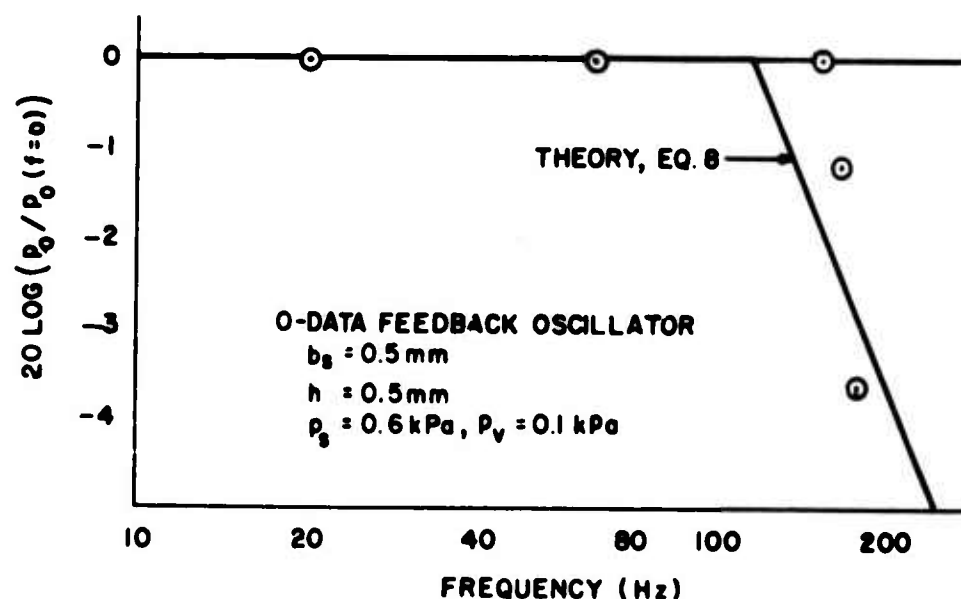


Figure 6. Bode Plot of LFF Response

While this testing method gives very conservative data because as the output amplitude starts to fall so does the input, it is nonetheless an easy test to perform. From section 4 and eq. (10) since the LPA -3db frequency is 290 Hz for this geometry, then the LFF -3db point should occur at 185 Hz since $f/f_n|_{-3db} = .644$. From figure 6 one can

see that the conservative data yields about 178 Hz as the -3db frequency. This frequency compares well with the published specifications of many commercial flip-flops, which are usually about 200 Hz.

6. DISCUSSION

In addition to the advantages of a laminar, low power, logic device, already mentioned in the introductory paragraphs, there are other benefits which accrue because of the laminar nature of the flow. The most important of these is accuracy. In turbulent digital devices one must consider, in reality, the probability of switching because as the switching condition is slowly approached turbulent fluctuations in the stream may have enough energy, at one instant or another, to cause a switch. Usually when making measurements on turbulent flip-flops a switching zone is encountered rather than a discrete switching point [8]. The laminar device, however, does not have this problem - it virtually has no noise or turbulence at all, and as a result has a well-defined switching point. This means that extremely accurate Schmitt triggers, counters, adders and analog-to-digital converters can be made. In addition such systems as pulse-duration modulators and digital information transfer systems can be effectively utilized.

Another advantage of laminar flow is the ability to scale the devices to virtually any size, since the laminar flows obey the well behaved laws of Reynolds number scaling; whereas, similar turbulent devices of different size rarely, if ever, operate the same way unless fully established turbulent flows are present, and then they consume a lot of power.

Other advantages of laminar devices include the eventual likelihood of acceptable solutions of equations of motion and the ability to make measurements on large models with different working fluids and relate them immediately to the actual size devices.

7. CONCLUSIONS

A laminar flip-flop (LFF) was designed and built based on analytic findings from the study of laminar, proportional amplifiers. Essentially the device operates due to a physical instability when the vents are pressurized, resulting in only two stable positions of the jet. It is not a Coanda effect device - no attachment walls are used.

This device performs as well as, or better than, any turbulent flip-flop from the standpoint of static and dynamic characteristics but has a more than an order of magnitude lower-power consumption with

the possibility of yet another order of magnitude reduction to about 0.1 mW.

The concept of the laminar flip-flop has led to the possibility of extremely accurate, low-noise digital systems heretofore impossible due to the random nature of the flow in turbulent devices. Such systems include, but are not limited to, such devices as Schmitt-triggers and analog-to-digital converters.

8. REFERENCES

1. Walker, M. L., and Trask, R. P., "Feasibility Study of a Laminar NOR Unit," Advances in Fluidics, ed. F. T. Brown, ASME, NY, 1967.
2. Comparin, R. A., Jenkins, W. C. and Moore, R. B., "Jet Reattachment at Low Reynolds Number and Moderate Aspect Ratio," ASME paper 67-FE-25, May 1967.
3. Fahnestock, M. R., "A Theoretical Study of Laminar Jet Wall Reattachment," Research Report No. 12, Systems and Control Lab., Penn. State Univ., Oct 1970.
4. Manion, F. M. and Mon, G., "Fluerics 33: Design and Staging of Laminar Proportional Amplifiers," Harry Diamond Labs Technical Report, HDL-TR-1608, Sept 1972.
5. Mon, G., "Laminar Proportional Amplifier," Proc. 6th Cranfield Fluidics Conference, Cambridge, England, March 1974.
6. Goto, J. and Drzewiecki, T., "Fluerics 32: An Analytical Model for the Response of Flueric Wall Attachment Amplifiers," HDL-TR-1598, June 1972.
7. Warren, R. W., "The Digital Fluid Amplifier," Proc. IFAC/IFIP Symposium, Munich, Germany, Oct 1965.
8. Drzewiecki, T. M., "Test Report on Flueric Logic Devices," Harry Diamond Labs Technical Report, HDL-TR-1601, July 1972 (Distribution limited to U.S. government agencies only. Request for copies must be sent to HDL).

PROJECTS ON MOVING PARTS FLUIDIC DEVICES CARRIED OUT AT
SIR GEORGE WILLIAMS UNIVERSITY

by Clyde C.K. KWOK

The area of fluid controls has been developed at Sir George Williams University since 1967. Part of the research efforts have been concentrated in the moving parts fluidic devices which include also diaphragm elements and components. It is the objective of this report to present the most up-to-date information on some of the most interesting research projects carried out in the area.

Description of the projects will be presented in the following order:

- (1) Hybrid Magnetic/Fluidic Pulse Shortener;
- (2) Vortex Flowmeter;
- (3) Valve Block for Air Massaging Application;
- (4) Diaphragm/ejector Schmitt Trigger;
- (5) Liquid Oscillator.

Results of some of the projects strongly demonstrated the advantages and inherent potentials as well as some unique solutions offered to practical problems by the fluidic technology.

Hybrid Magnetic Pulse Shortener

In many fluidic logic control circuits, there exists the requirement for pulse shorteners or special devices capable of producing short pulses for precise duration when supplied with step or other forms of input pulses. At present, this special function in most cases can be performed by using active fluidic bistable and monostable amplifiers with suitable delay lines. This approach, however, is considered unattractive because of the difficulty usually associated with choosing the suitable delay lines as well as the relatively high power consumption. A new scheme was proposed [1]. The basic configuration of this device consists of a short cylindrical chamber with an input and an output port located symmetrically at the top and bottom surfaces of the chamber as shown in Fig. 1. A permanent ring magnet is attached to the bottom surface and a thin metal disc is placed inside the cylindrical chamber.

When there is no input pressure signal, the metal disc is held onto the permanent magnet. Upon the application of a pressure signal, the pressure force will lift the metal disc away from the magnet. Once they are separated, the pressure force will be acting on the entire surface of the disc instead of the area corresponding only to that of the input port. At the same time, the magnetic attractive

force decreases inversely as the squares of the distance between the metal disc and the pole of the permanent magnet. As a result, there is a snap effect and the disc moves very rapidly towards the output port. This movement generates a compression pulse, the duration of which is dependent only on the motion of the disc and is independent of the input pulse length. When the input pressure pulse has expired, the disc returns to the bottom surface due to the attractive force of the ring magnet.

In order to achieve the optimum design criteria, an analysis of the dynamic characteristics of the disc when subjected to both the magnetic and input pressure forces under various possible loading conditions was carried out. The mathematical model for the system was developed using an incremental quasi-steady state approach. Equations describing the mathematical model were derived from the basic thermodynamic and fluid dynamic relations such as continuity equation, equation of state and the equation of motion. The mathematical model was further modified in non-dimensional form and reduced to the following five governing equations.

$$(P_1 - P_2) - \frac{\kappa}{(X + X_0)^2} - W_x = \frac{d^2 X}{d\tau^2} \quad (1)$$

$$P_2 \phi_2^{-\gamma} = \text{constant} \quad (2)$$

$$\phi_2 (1 - \Delta + X) = \text{constant} \quad (3)$$

$$\frac{d\phi_2}{d\tau} = \frac{-A_0 C_d \sqrt{2\alpha P_2 \phi_2 \left[\frac{\gamma}{\gamma-1} \right] \left\{ \left[\frac{1}{P_2} \right]^{\frac{\gamma}{\gamma-1}} - \left[\frac{1}{P_2} \right] \frac{\gamma+1}{\gamma} \right\}}}{1 + \Delta - X} \quad (4)$$

$$\frac{dP_2}{d\tau} = \frac{P_2}{\phi_2} \frac{d\phi_2}{d\tau} \quad (5)$$

where

$$P_1 = \frac{\text{input pressure } p_1}{\text{atmospheric pressure } p_\infty}$$

$$P_2 = \frac{\text{output or chamber pressure } p_2}{\text{atmospheric pressure } p_\infty}$$

$$\phi_2 = \frac{\text{mass density of air inside chamber } \rho_2}{\text{mass density of atmospheric air } \rho_\infty}$$

$$X = \frac{\text{distance travelled by disc } x}{\text{chamber length } L}$$

$$X_0 = \frac{\text{location of imaginary magnetic pole from the surface of magnet } x_0}{\text{chamber length } L}$$

$$A_0 = \frac{\text{area of orifice } a_0}{\text{area of disc } A}$$

$$\Delta = \frac{(\text{length of output port passage } l)(\text{area of output port } a)}{(\text{chamber length } L)(\text{Area of disc } A)}$$

$$\alpha = \frac{\text{mass of disc } M_D}{L A \rho_\infty}$$

$$K = \text{magnetic constant } K$$

$$\tau = \sqrt{\frac{L A \rho_\infty}{M_D}} \text{ (time } t)$$

$$W_x = \frac{\text{weight of disc } W_D}{\rho_\infty A}$$

and the magnetic constant K and imaginary pole X_0 were determined experimentally [1] using the relationship

$$x_0 = \frac{L}{\frac{p_a}{p_b} - 1} \quad (6)$$

and

$$K = p_b A (x_0 + L)^2 \quad (7)$$

where p_a and p_b were experimentally observed pressure levels where the disc was separating away and attracting towards the magnet respectively. The theoretical response of the pulse shortener for a given geometry was obtained by solving the above mentioned non-dimensional mathematical model using the fourth-order Runge Kutta numerical method.

The original experimental model shown in Fig. 2 having a chamber diameter and length of 0.63 in. and 0.1 in. respectively was subjected to step pressure input signals and different frequencies. The input and output pressure wave forms were recorded for different output port loading conditions. A typical set of experimental pressure traces is shown in Fig. 3a. The same set of data was used to compare with the theoretically predicted results in Fig. 3b.

A sensitivity study of the effects of various independent para-

meters, namely, the input pressure, chamber length and diameter, output port diameter and output port passage length as well as the magnetic force, was undertaken. Results revealed an important finding of this pulse shortener that above an input pressure level of 16.5 psia, the output characteristics for this particular pulse shortener under study is insensitive to the variation of the input signal amplitude. The effects of other geometric parameters on the pulse shortener performance characteristics were also computed and critically analysed. These detailed information together with the computer program are given in Ref. [2].

Vortex Flowmeter

Flow measurement and monitoring are important in many industrial applications. There always exist requirements for a low cost reliable flowmeter. An unconventional concept to utilize the vortex principle in measuring flow rate was tried [3]. The basic device shown in Fig. 4 consists of a thin cylindrical chamber with tangential inlets and central outlet. A free ball is contained within the circular track of the chamber. When fluid flows in, due to the tangential inlet configuration, a vortex will be generated. The swirling flow causes the ball to rotate along the track. The frequency of rotation of the ball, measured by a simple light emitting diode arrangement, provides direct information of the flow rate.

An analysis, assuming a laminar, incompressible irrotational flow, was carried out in an attempt to analyse the motion of the ball inside the vortex chamber [4]. Forces and moments acting on the sphere were found and may be summarized as follows:

- (i) The drag D , calculated by assuming the flow is irrotational and the sphere is stationary, is found to be

$$D = 12 \pi \mu R V \quad (8)$$

where μ , R , V are the fluid viscosity, the sphere radius and the stream velocity respectively.

- (ii) The mechanical friction F , opposite to the direction of motion, is acting at the two points of contact of the sphere and the track as shown in Fig. 5.

- (iii) The moment of mechanical friction M_z about the axis of rolling which is given by

$$M_z = \ell \cdot F \quad (9)$$

where ℓ is the distance between the point of contact and the rolling axis of the sphere.

- (iv) The total moment on the sphere M_f , formed by assuming a rotating sphere in a stationary incompressible flow, expressed in terms of the sphere radius R , fluid viscosity μ and rotational angular velocity, ω is given by

$$M_f = -8 \pi \mu R^3 \omega \quad (10)$$

Under steady state conditions, the above forces and moments are balanced. Solving the above equations, the frequency of rotation, N of the sphere about the axis of the chamber is given by

$$N = \frac{R_0}{2 \pi^2 d_0^2 R_t^2 [1 + \frac{2}{3} (\frac{R}{\ell})^2]} Q \quad (11)$$

where d_0 is the diameter of the inlet port, R_t and R_0 are the track means radius and vortex chamber radius respectively, and Q is the flow rate.

During experimental investigations, it was found that the ball did not start moving inside the chamber until a certain minimum flow rate was reached to overcome the static frictional effects between the ball and the wall. Since the static friction was very difficult to evaluate and was not considered in the formulation of the theory, equation (11) was modified to the form

$$N = \frac{R_0}{2 \pi^2 d_0^2 R_t^2 [1 + \frac{2}{3} (\frac{R}{\ell})^2]} [Q - Q_0] \quad (12)$$

where Q_0 is the minimum volume flow rate required to overcome static friction. Detailed derivations of the theory are presented in Ref. [4].

Experiments were conducted using water to investigate the effects of changing the geometric configurations, mass and size on the ball and flow rate on the performance of the flowmeter. A typical set of experimental data showing the variation of frequency with ball diameter as compared with theory is shown in Fig. 6. They all indicate linear characteristics between the volume flow rate and the frequency of rotation of the ball.

Valve Block for Air Massaging Application

A massaging unit in the form of a belt with air pockets to be strapped around one's body or limb was investigated [5]. Such a unit is useful for reducing fatigue level and stimulating the blood circulation of a person suffering from confinement for a long period of time.

At the present stage of development, the emphasis is on the design and performance of an integrated valve block which, together with the air pockets in the belt, operates as an oscillator. The air pockets,

serving as the charging capacitors in the delay paths, undergo continual cycles of inflation and deflation in groups. The resulting expansion and contraction in the pocket volumes thus contribute to the production of a massaging effect. Two types of moving part logic elements are contained in the valve block, the inverter and repeater. These elements have to have a low pressure gain, wide hysteresis band and a relatively high flow capacity. A design using the poppet and spool valve combination was evolved. Basically, the inverter and repeater are identical in physical configuration except in the external connections. The operation of the repeater and inverter valves are shown in Figs. 7 and 8 respectively.

Each valve has a piston assembly sliding inside a cylindrical cavity which is separated from the control chamber by means of a diaphragm. The top end of the piston rod is firmly secured onto the diaphragm so that the piston will be directed to move up and down according to the force balance across the diaphragm. The lower and larger end of the piston rests against the valve seat, and there are two port openings leading to the cylindrical cavity. In this application, the output ports are always connected to the air pocket, which is essentially a blocked load. Consequently, as a unique feature of the valve design, no return spring is required. For the experimental prototype, 3 repeater valves and one inverter valve were accommodated inside a valve block. An exploded view of the valve block is shown in Fig. 9.

Normalized static switching characteristics of the valve functioning as a repeater and as an inverter are shown in Figs. 10a and 10b respectively. In both sets of characteristics, the normalized switching pressure $\left(\frac{P_C}{P_S}\right)$ is plotted as a function of the supply pressure P_S .

Preliminary analysis of the repeater and inverter valve operation using force balance equations across the diaphragm yield the following expression:

$$\frac{d\left(\frac{P_C}{P_S}\right)}{dP_S} = - \left(\frac{f}{A_{eff}}\right) \cdot \frac{1}{P_S^2} \quad (13)$$

where A_{eff} is the effective area of the diaphragm and f is the frictional force between the O-ring and the cylindrical cavity, acting upwards against the downward movement of the piston assembly. Eq. (13) provides correct indication of the slope of characteristic curves given in Figs. 10a and 10b.

Typical output waveform of the valve block is shown in Fig. 11. For an application such as the air massage device serving a special therapeutic purpose, it is difficult to assess its performance in terms of quantitative criteria. However, with the oscillator block connected to the air-belt having air pockets of a volume of approximately

5 cu. in. each, the "working" frequency is in the region of 2 Hz. This frequency depends on the material of the air-belt and how tight it is strapped to the body, etc. So far, the massaging effect produced has been considered sufficiently satisfactory to warrant continued development of the concept in conjunction with personnel in the area of physiotherapy.

Diaphragm-Ejector Schmitt Trigger

The pneumatic Schmitt Trigger is a pressure switching device which can be turned on and off using predetermined, adjustable control pressures. A Diaphragm-Ejector Schmitt Trigger (DEST) consisting of a diaphragm-ejector step-up relay "A" and a passive diaphragm element "B" interconnected was designed and is shown schematically in Fig. 12. P_o and P_s represent the output and supply pressure respectively. One of the chief functional characteristics of the device is the availability of independently adjustable trigger pressure levels. This function enables the possible application of the device in the on-off control of parameters such as flow rate, temperature, liquid level, etc. and also in accept-reject testing of production components.

The operation of the Diaphragm Ejector Schmitt Trigger may be described as follows: Assuming that the device is initially in the OFF state, the pressures $P_1(\text{off})$ and $P_3(\text{off})$ in cavities 1 and 3 respectively will be determined by the pressure divider circuit consisting of the ejector-nozzle flow restriction and the adjustable restrictor R_1 . In this state the diaphragm in the "B" element will be deflected to close the seat B2, due to the action of pressure $P_3(\text{off}) [= P_1(\text{off})]$.

Also, since the seat pressure P_{A1} and $P_1(\text{off})$ are now equal to each other, the output pressure in the OFF state, $P_o(\text{off})$, is determined from the ejector-sensor characteristic of Fig. 13. In order to switch the device on, the control pressure must be increased to a value $P_1(\text{on})$ which just exceeds $P_1(\text{off})$. Thus, the magnitude of switch on control pressure $P_1(\text{on})$ is predetermined by the setting of R_1 . When the device is switched on, the sensor seat A1 is closed by the relay diaphragm and the pressures P_{A1} and P_o quickly become equal to the supply pressure P_s . It is assumed here that the restrictors R_o , R_2 and the load do not draw any significant flow, thereby approximating the zero-output-flow requirement of the ejector-sensor. Subsequent to the switching on of the relay diaphragm, the pressures P_3 and P_1 begin to decrease due to discharge through R_1 , while the pressure P_{B2} in seat B2 is increased to the value $P_o(\text{on}) [P_s]$. As a result, the "B" - element diaphragm is switched so as to close the seat B3. The pressure P_2 in cavity 2 then increases to a value $P_2(\text{on})$ determined by $P_o(\text{on})$, and by the pressure divider circuit consisting of R_o and R_2 . Since the pressure $P_2(\text{on})$ is communicated via the diode D_1 to cavities 3 and 1, the pressure P_1 reaches the value $P_1(\text{on}) = P_2(\text{on})$. Assuming that area A_{A1} is much smaller than the diaphragm area the pressure $P_1(\text{on})$ determines the magnitude of $P_1(\text{off})$, to which the control pressure must now be reduced

in order to obtain switch-off. Thus it may be seen that $P_i(\text{on})$ and $P_i(\text{off})$ required for switching the device on and off, respectively, can therefore be set independently by means of the adjustable restrictors R_1 and R_2 . The diode D also ensures the control of pressure $P_i(\text{off})$ through restrictor R_1 alone.

A DEST unit using 1-inch diameter rubber diaphragms was constructed from plexiglass with the sensor dimensions shown in Fig. 13. The characteristic shown in the figure also represents the experimental sensor characteristics. A photograph and the construction of the device are shown in Figs. 14 and 15, respectively. The device was tested over a supply pressure range of 5 to 50 psig (34.5 to 345 kN/m²) and the repeatability and minimum available hysteresis were found to be about 1.5% and 1% of P_s , respectively. Deterioration in repeatability was sometimes observed, but was traced to a shift in the values of $P_i(\text{off})$ and $P_i(\text{on})$, probably caused by poor flow stability in the control restrictors. Predictable switching was obtained up to repetition frequencies in the region of 15 Hz [with $P_s = 10$ psig (69 kN/m²), $P_i(\text{on}) = 1.4$ psig (9.55 kN/m²), and $P_i(\text{off}) = 1.16$ psig (8 kN/m²)], which is adequate for most mechanical automation applications.

The chief functional characteristic of the device is the availability of independently adjustable trigger (control) pressures. In addition to the above feature, the DEST has the following advantages over the fluidic Schmitt Trigger: (1) greater adjustable hysteresis range, (2) higher pressure recovery, together with the possibility of obtaining a vacuum output in the OFF state, and (3) probably lesser susceptibility to contamination. The major disadvantage of the DEST is that it is a diaphragm-operated moving part device, and hence has limitations in parameters such as response time, lifetime, operating temperature, etc.

Nevertheless, in less severe environments, it could be utilized to provide on-off pneumatic control, for example, in low cost automation. A few typical industrial applications using this Diaphragm Ejector Schmitt Trigger are listed below:

- Liquid Level Control System;
- Pulse Width Modulation Type Control System;
- Timing Circuits;
- Liquid Mixture Density Control System.

Detailed information on the above systems as well as the design considerations for the Diaphragm Ejector Schmitt Triggers are presented in Refs. [6] and [7].

Liquid Operated Oscillator

The search for a simple, liquid-operated oscillator was initiated because of the requirement for a special type of dental syringe known as a "waterpic" which produces strong pulsating jets of water at approximately 15 cps for cleaning teeth as well as massaging the gums. After some initial experimentations with no-moving parts pure fluidic devices, the approach was not pursued due to high pressure drop across the power jet nozzle and the difficulties in obtaining low frequency oscillation due to high wave propagational velocity in liquids. An entirely different oscillator concept was subsequently conceived utilizing mainly the inertia effects of the liquid to control the opening and closing of the diaphragm valve as described in Refs. [8] and [9].

The basic operational principle of the oscillator can be explained by first referring to the illustration in Fig. 16. The supply inlet, which is connected to the pressure source, is designed to incorporate an ejector system consisting of a supply nozzle which directs the flow into a receiver. This ejector chamber is connected to the output line of the oscillator. The other end of the receiver is connected to a seat chamber located inside the vent chamber. There is a vent tube connection between the vent chamber and the atmosphere. A diaphragm is positioned so as to control the flow of fluid from the seat chamber into the vent chamber. A spring with a force-adjusting screw is provided on the other side of the diaphragm to keep it in proper position.

Operation of the early designs of oscillator prototypes was based on the inertia effect of the liquid in the vent tubes. First, consider the diaphragm to be at the uppermost deflected position, flow entering the receiver tube will have an almost free path to the vent chamber, and the pressure of the latter will be built up rapidly. According to the Law of Continuity, flow entering the vent chamber must flow out through the vent tube. In other words, movement of the whole column of liquid contained within the vent tube is accelerated. During this phase of operation, the output channel, which is connected to the ejector chamber, is experiencing a negative pressure due to the venturi effect of the ejector system. At this point, the spring is being compressed, exerting a force which tends to close the diaphragm against its seat. Furthermore, it can be seen that as maximum flow into the vent chamber is achieved, the fluid velocity between the diaphragm and the seat is at its highest value and, according to the Bernoulli's relation, pressure will decrease correspondingly. The reduction in static pressure in that region causes the diaphragm to start moving downwards. When this happens, the cross-sectional flow area between the seat and the diaphragm will be reduced. This will decrease the flow into the vent chamber and further reduce its pressure. This reduction of pressure causes an additional downward deflection of the diaphragm resulting in a further decrease of flow into the vent chamber. Eventually, the diaphragm will snap onto the seat blocking the entire flow into the vent chamber. However, before the snap closing of the

diaphragm, the whole column of liquid within the vent tube has been accelerated. Due to the inertia of the liquid, the sudden closing of the diaphragm cannot produce an immediate stoppage of the moving liquid within the vent tube. The liquid in the tube continues to move, thus creating a strong vacuum within the vent chamber which pulls the diaphragm further downwards against the seat. This effect creates an even tighter closing of the diaphragm against its seat and diverts all the supply flow into the output line.

As soon as the fluid in the vent tube has come to rest, the pressure in the vent chamber returns from sub-ambient to ambient. At this time, the total force acting on the diaphragm, including that due to the supply pressure acting on the valve seat, will be high enough to overcome the force exerted on the opposite face of the diaphragm by the now-extended spring, and the diaphragm valve commences to open again. Fluid then starts to flow into the vent and its pressure will be built up. This build-up of pressure in the vent chamber causes a further upward deflection of the diaphragm and more flow will be entering the chamber. When this occurs, the output pressure at the outlet drops and becomes sub-ambient due to the strong venturi effect created in the ejector chamber. The cycle is thus repeated.

It can be seen that both the diaphragm and spring stiffnesses affect the oscillation to a certain degree; however, the main governing parameter for the oscillation phenomenon is the inertia of the column of liquid in the vent tube. Changing the geometric configuration of the vent tube strongly affects the operation of the oscillator.

In an attempt to understand the effects of various design parameters affecting the operation of the oscillator, an analytical study was carried out by S. Sankar (Ref. [10]) using the linear graph technique. The oscillator was subdivided into three systems:

- (1) The fluid system comprising the inlet nozzle, seat chamber and valve seat, vent chamber and vent tube;
- (2) The mechanical system consisting of the spring and a mass which represents the lumped mass of the diaphragm and the spring retainer;
- (3) The linkage between the fluid and the mechanical system.

The schematic representation of the linear graph for the liquid operated oscillator is shown in Fig. 1/. A set of 14 equations together with the definition of the symbol used are given in Table 1. The equations are derived assuming that the fluid is incompressible, the deflection of the diaphragm uniform and velocity heads are negligible compared to the pressure heads (except in the vent tube).

The analytical model was further extended to include a feedback

path between the vent and the spring chamber as described in Ref [11]. This modification not only improves the performance of the oscillator but also enables it to operate over a large range of supply pressures.

The type of liquid operated oscillator described above is relatively simple to construct and there is considerable leeway in the tolerances of the fluid passages. Except for the diaphragm and the spring, which operates on a very small displacement, there are no other moving parts and the reliability should be excellent. Furthermore, the instantaneous output pressure magnitude, due to the inertia effect of the liquid, which can sometimes be 60% above that of the steady state supply pressure, makes this oscillator particularly attractive for use in many cleaning applications. Detailed descriptions of a dental syringe (Fig. 18), and oscillating showerhead (Fig. 19), and a car wash apparatus (Fig. 20) presented in Refs. [9] and [11] represent some typical applications of the oscillator concept.

CONCLUSION

Five interesting projects on moving parts devices carried out at Sir George Williams University have been described. It is the intention of this paper to indicate some of the advantages and flexibility offered by moving parts fluidic components, and the various potential application areas. More important, highlights of the theoretical analysis for each component developed was referenced and discussed. This is to be consistent with the main theme of this Symposium that the fluidic technology has gone through the growing period and is now reaching maturity. "It has become a Science rather than an Art".

REFERENCES

- [1] Chan, W.W.L. Hybrid Magnetic/Fluidic Pulse Jan. 1972
Kwok, C.K. Shortener;
duPlessis, M.P. Fluidic Quarterly, Vol. 4, No. 1,
pp. 85-100.
- [2] Chan, W.W.L. Magnetic Fluidic Pulse shortener; April 1971
M.Eng. Research Thesis, Sir George
University.
- [3] Kwok, C.K. An Experimental Investigation of 1972
Farag, E. the Vortex Flowmeter;
Nastou, D. ISA International Conference
Paper 825.
- [4] Kwok, C.K. Investigation of a Vortex Flow- March 1974
Nastou, D. meter;
6th Cranfield Fluidics Conference,
Cambridge, England.
- [5] Cheng, R.M.H. Development of a Valve Block for March 1974
Kwok, C.K. Air Massaging Applications;
6th Cranfield Fluidics Conference,
Cambridge, England.
- [6] Suresh, N. The Diaphragm-Ejector Schmitt- October 1973
Lin, S. Trigger and its Applications;
Callaghan, J.C. ISA-73 International Conference,
Paper 73-832.
- [7] Suresh, N. Design Considerations for October 1973
Lin, S. Diaphragm-Ejector Schmitt-Trigger;
Callaghan, J.C. Fluidic Quarterly.
- [8] Kwok, C.K. Fluid Oscillator and Pulsating October 1972
Dental Syringe Employing Same;
U.S. Patent 3,698,416.
- [9] Kwok, C.K. A Fluid Oscillator and Its Appli- June 1972
cations;
Paper A-7, Fifth Cranfield Fluidics
Conference, Uppsala, Sweden.
- [10] Sankar, S. Simulation of a Diaphragm Type August 1971
Fluid Oscillator;
M.Eng. Thesis, Sir George Williams Univ.
- [11] Kwok, C.K. A Liquid Operated Oscillator; October 1973
Cheng, R.M.H. ISA International Conference.

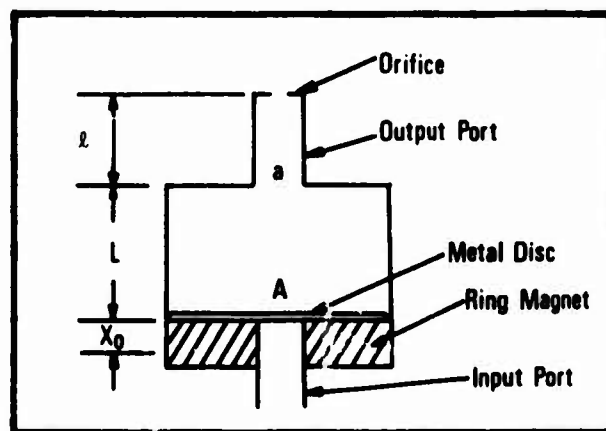


FIG. 1: Schematic Diagram of Magnetic/
Fluidic Pulse Shortener

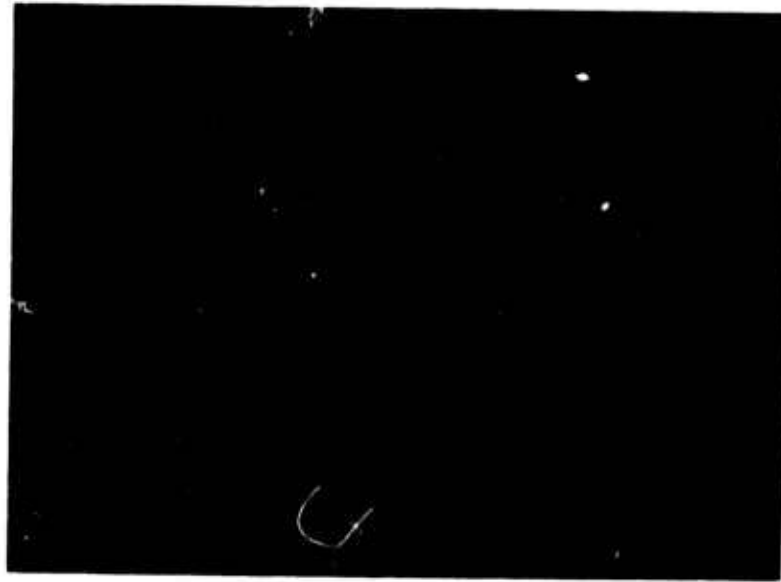


FIG. 2: Pulse Shortener Test Model

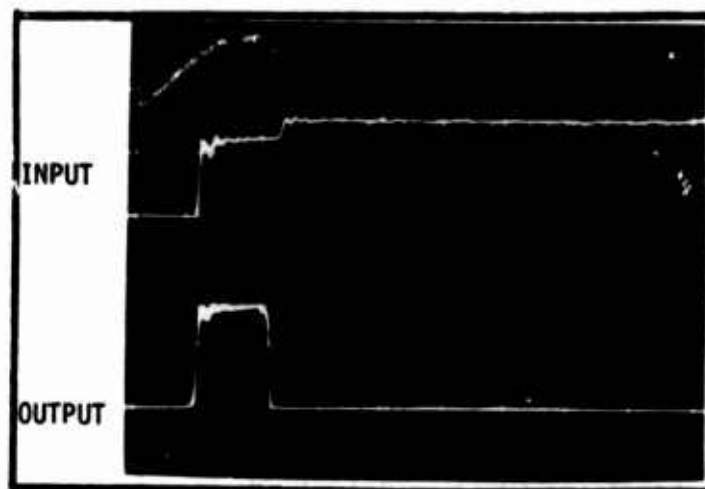


Fig. 3a:

$p_1 = 16.02 \text{ psia}$

Orifice diameter
= 0.03"

Disc thickness
= 0.0078"

Time base
= 10 ms/div.

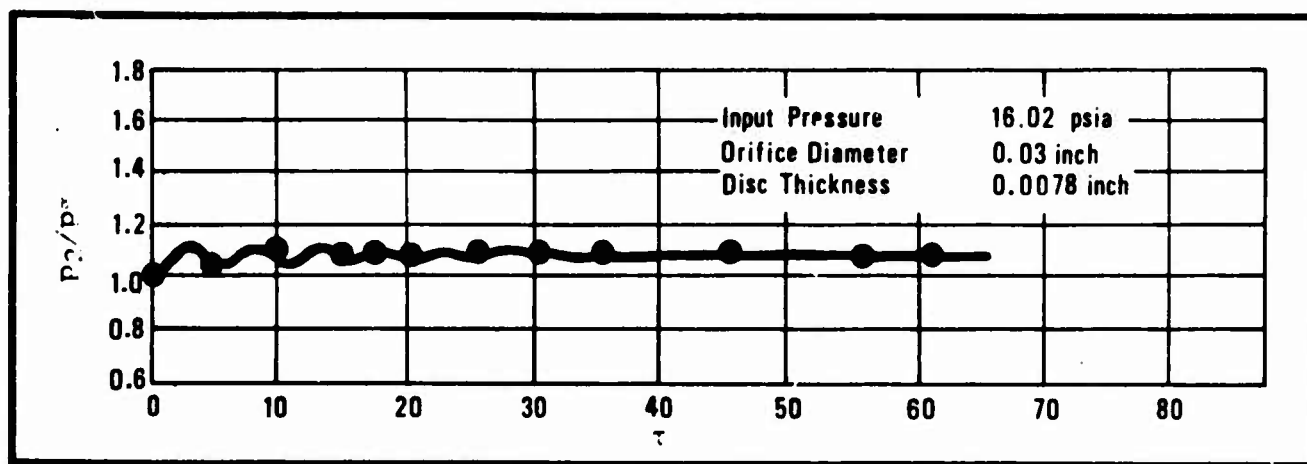


Fig. 3b: Input pressure = 16.02 psia;

Orifice diameter = 0.03";

Disc thickness = 0.0078".

FIG. 3: Typical results of the Magnetic/
Fluidic Pulse/Shortener.

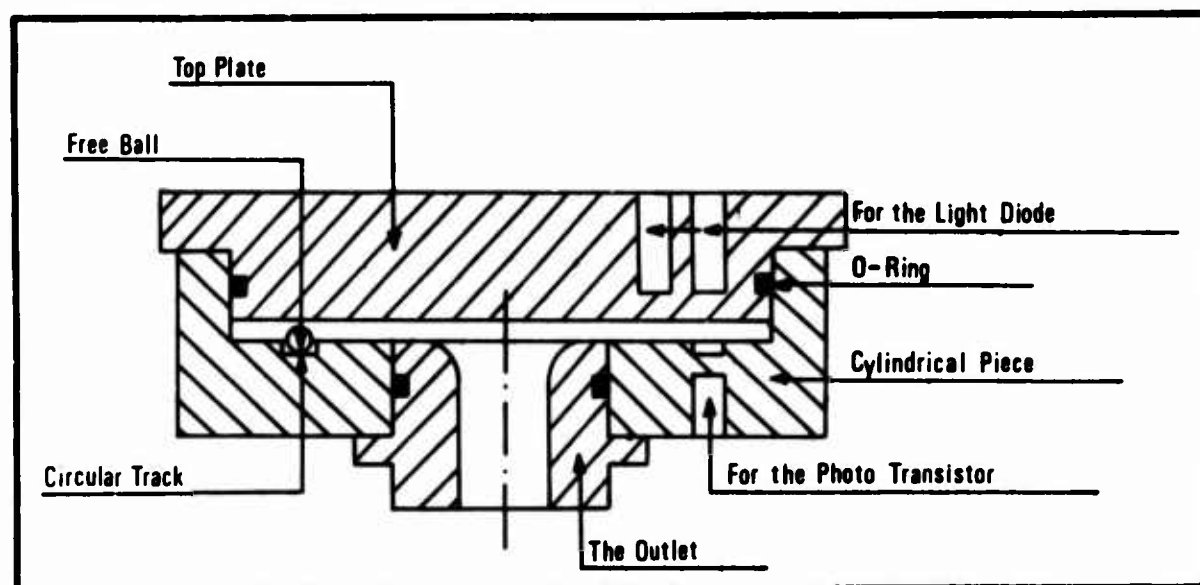
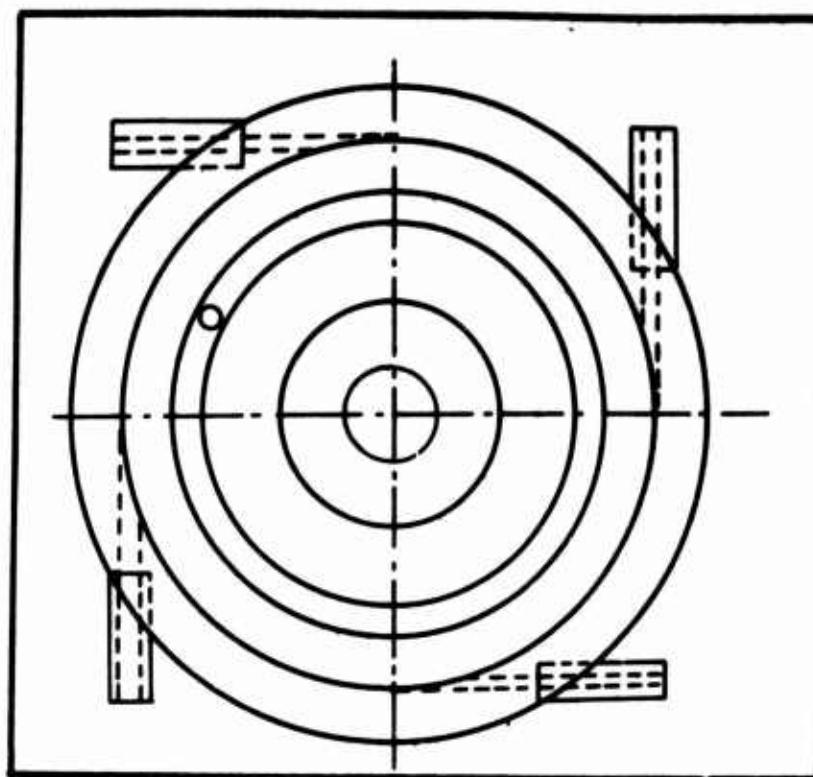


FIG. 4: Experimental Model of Vortex Flowmeter

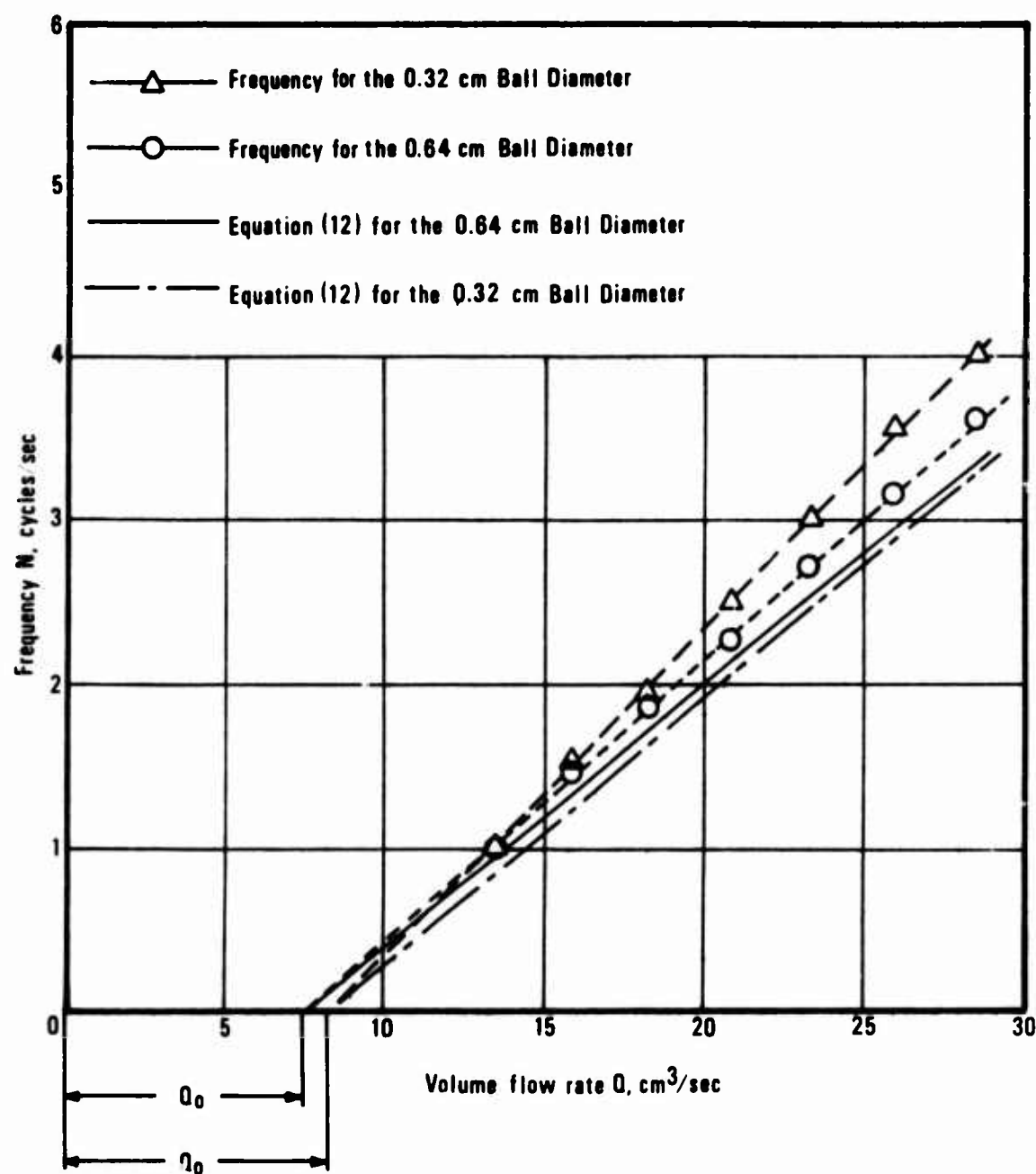


FIG.6: Variation of Frequency with Ball Diameter
(Outlet Diameter = 0.64 cm, track mean
radius = 2.86 cm).

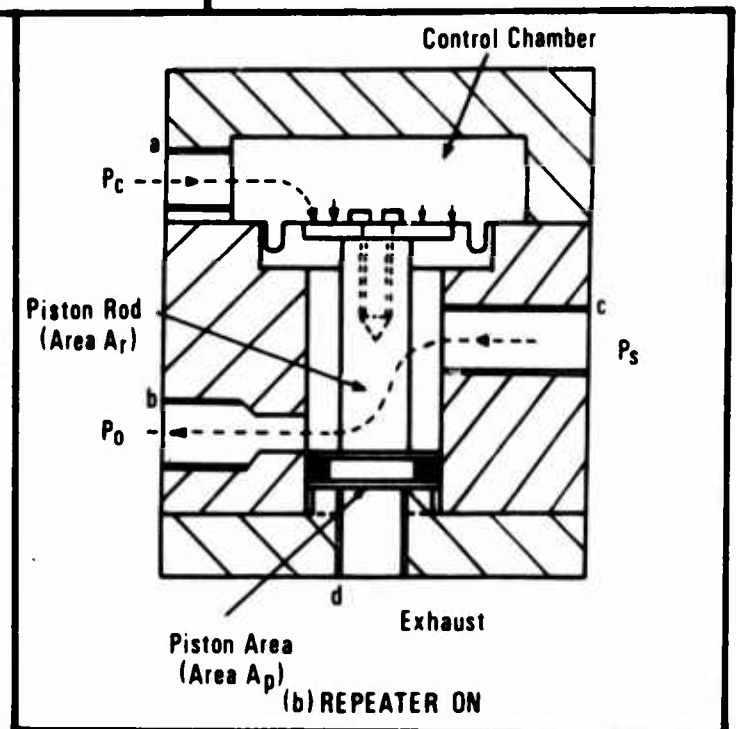
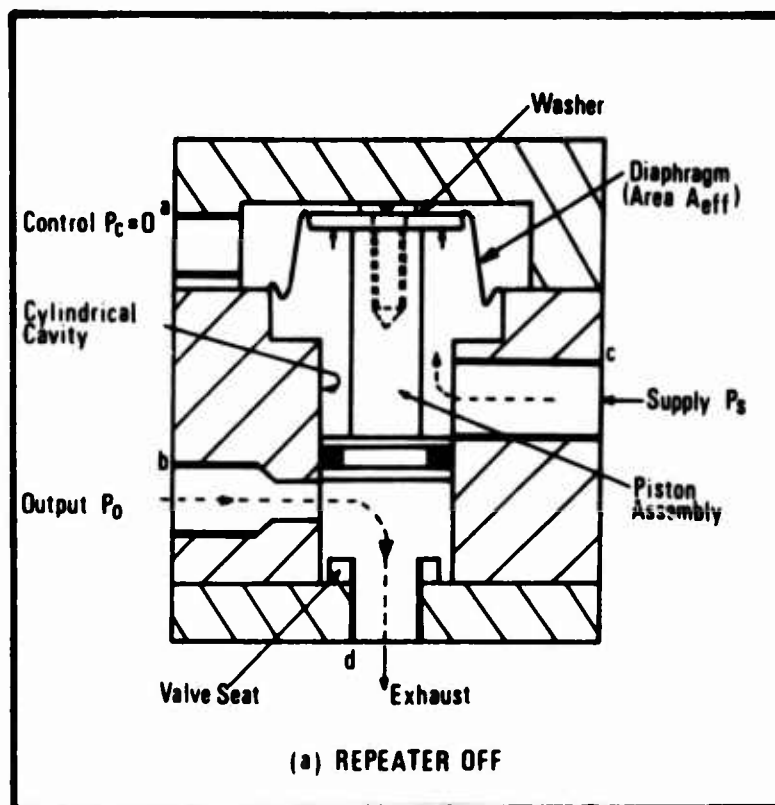


FIG. 7: Operation of a Repeater Valve

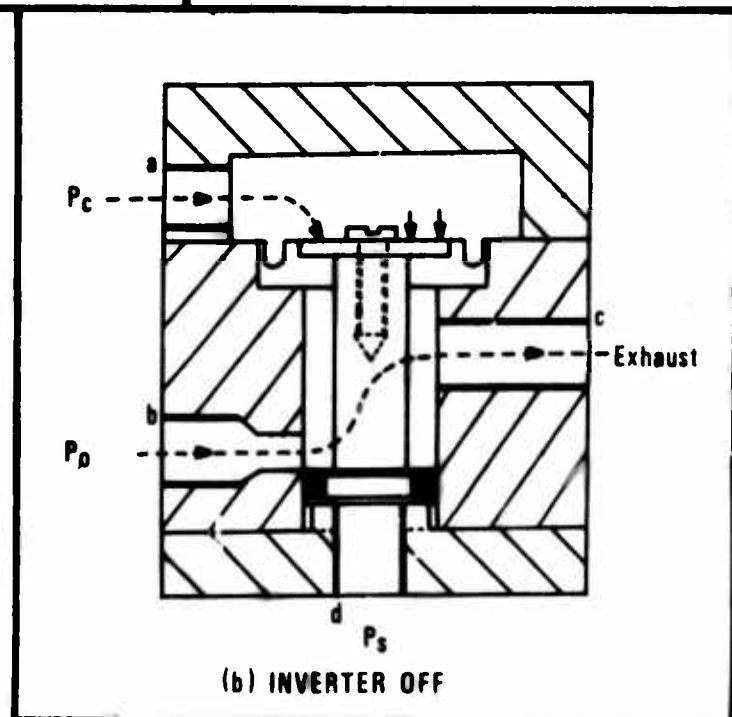
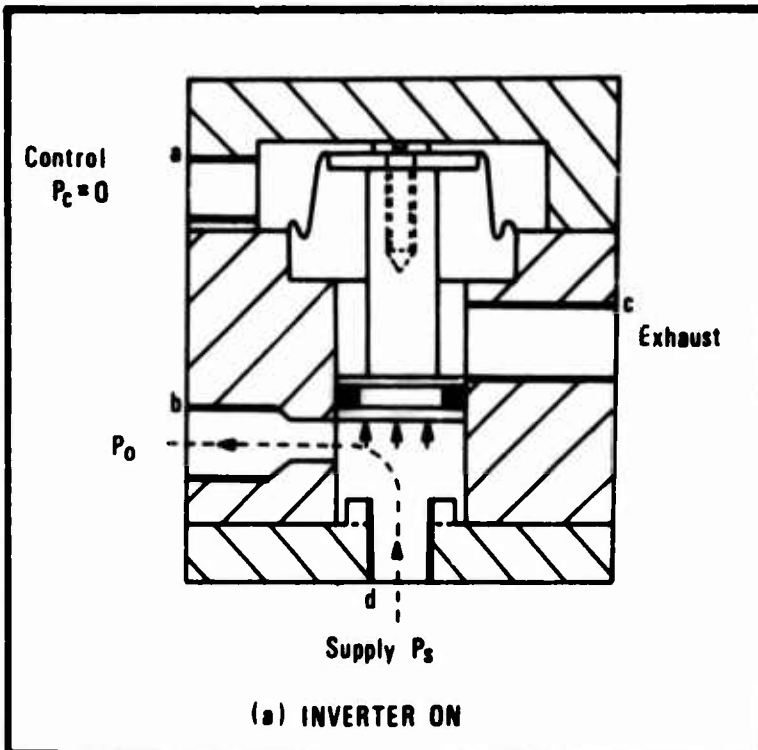


FIG. 8: Operation of an Inverter Valve

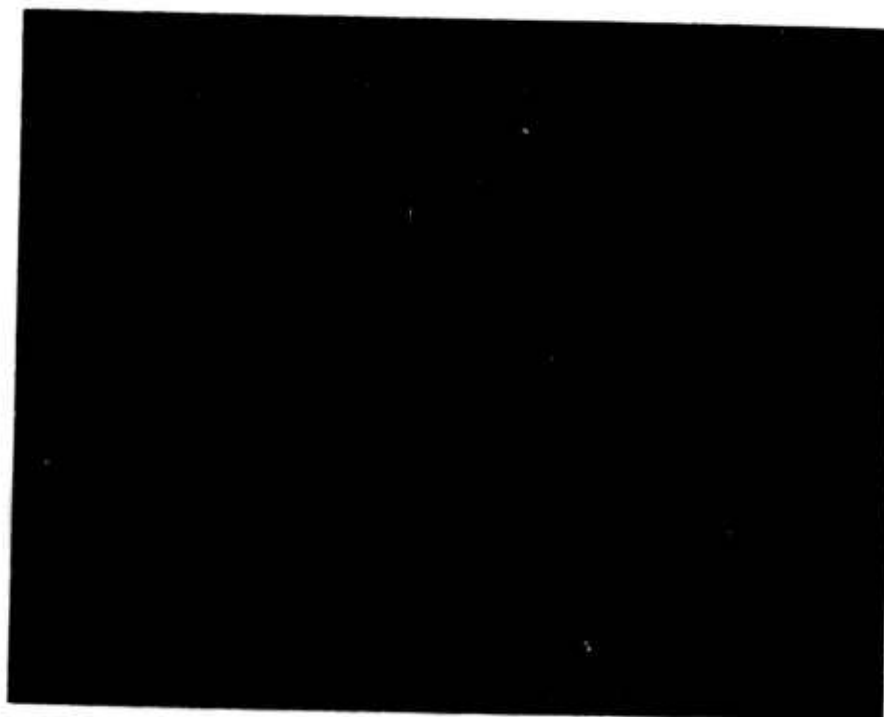


FIG. 9: Exploded View of Valve Block

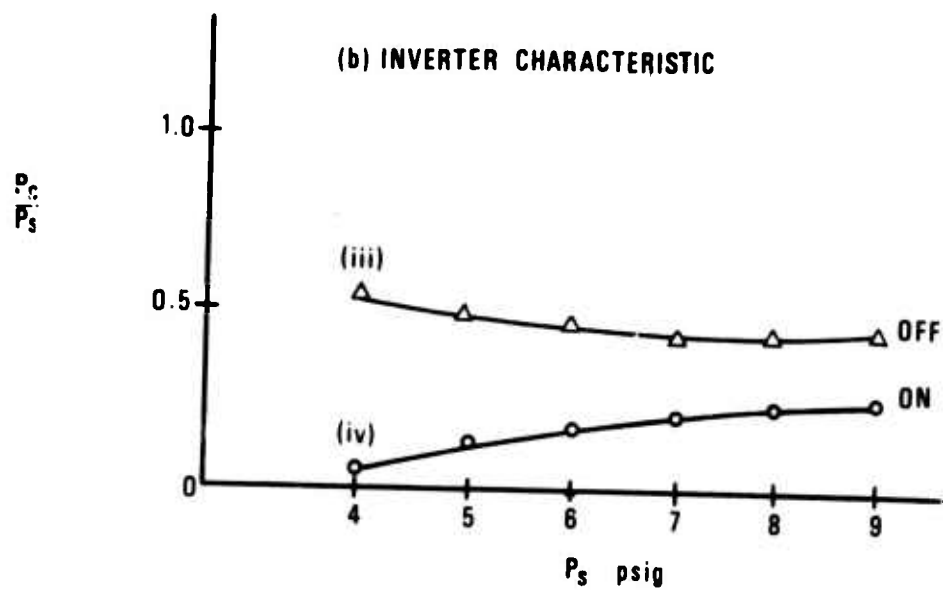
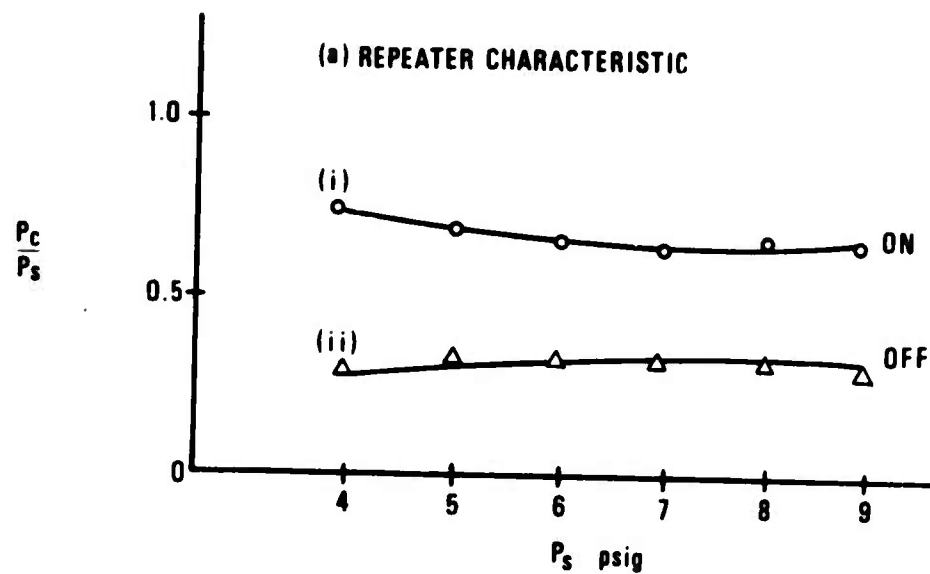
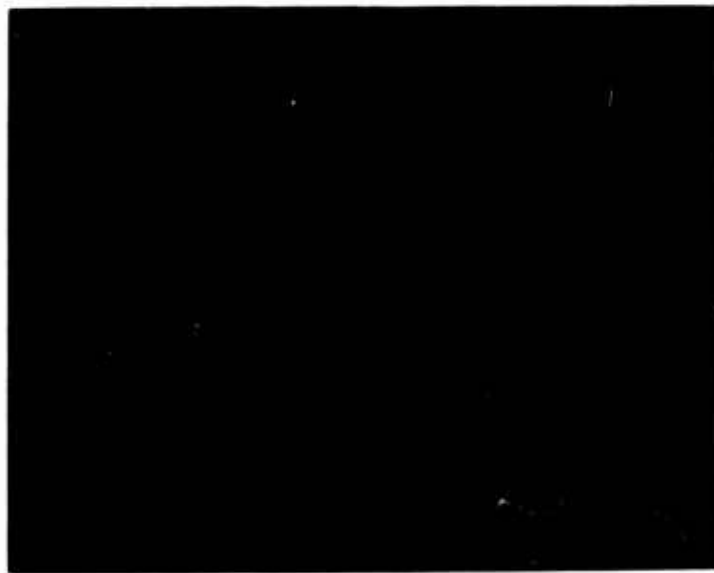


FIG. 10



INVERTOR I

REPEATOR R_1

REPEATOR R_2

REPEATOR R_3

$P_s = 12'' \text{ Hg}$

Frequency of oscillation = 16 Hz

FIG. 11: Output of Oscillator

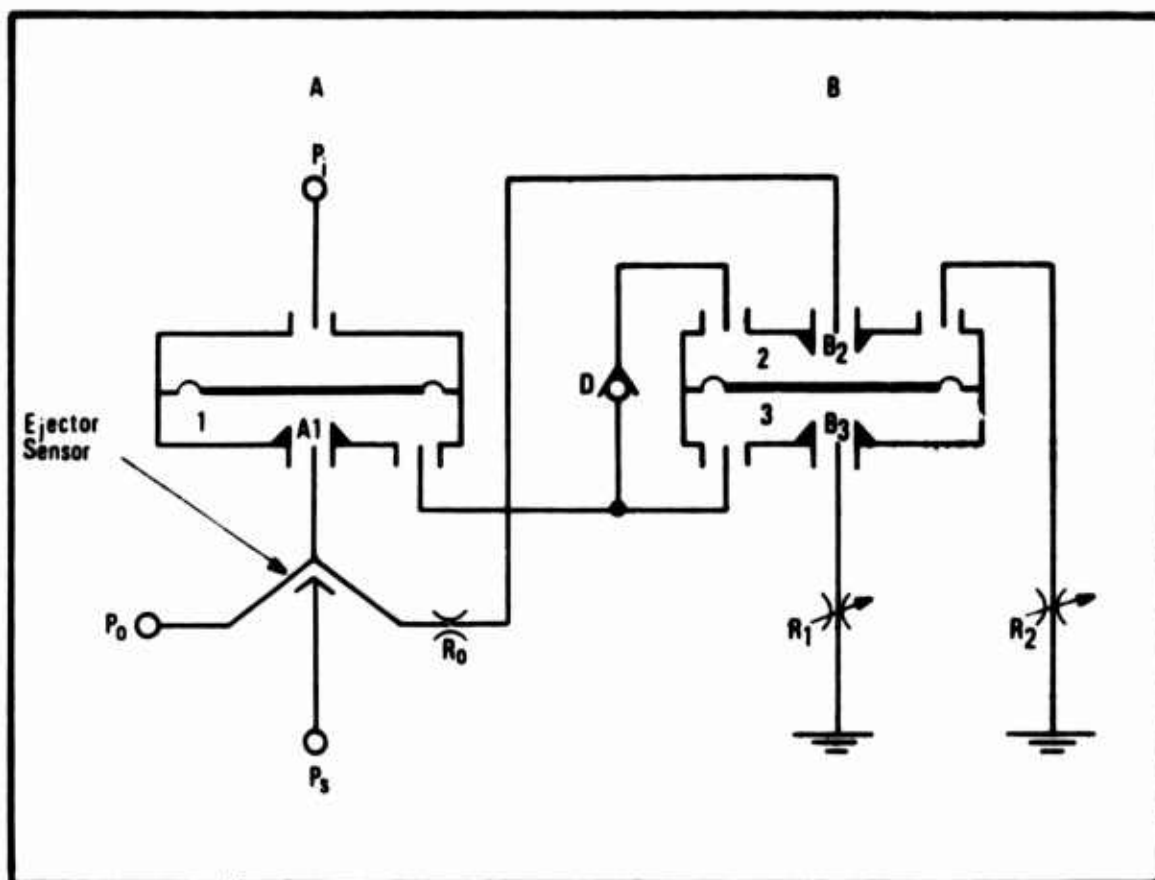


FIG. 12: Schematic of the Diaphragm-Ejector Schmitt Trigger

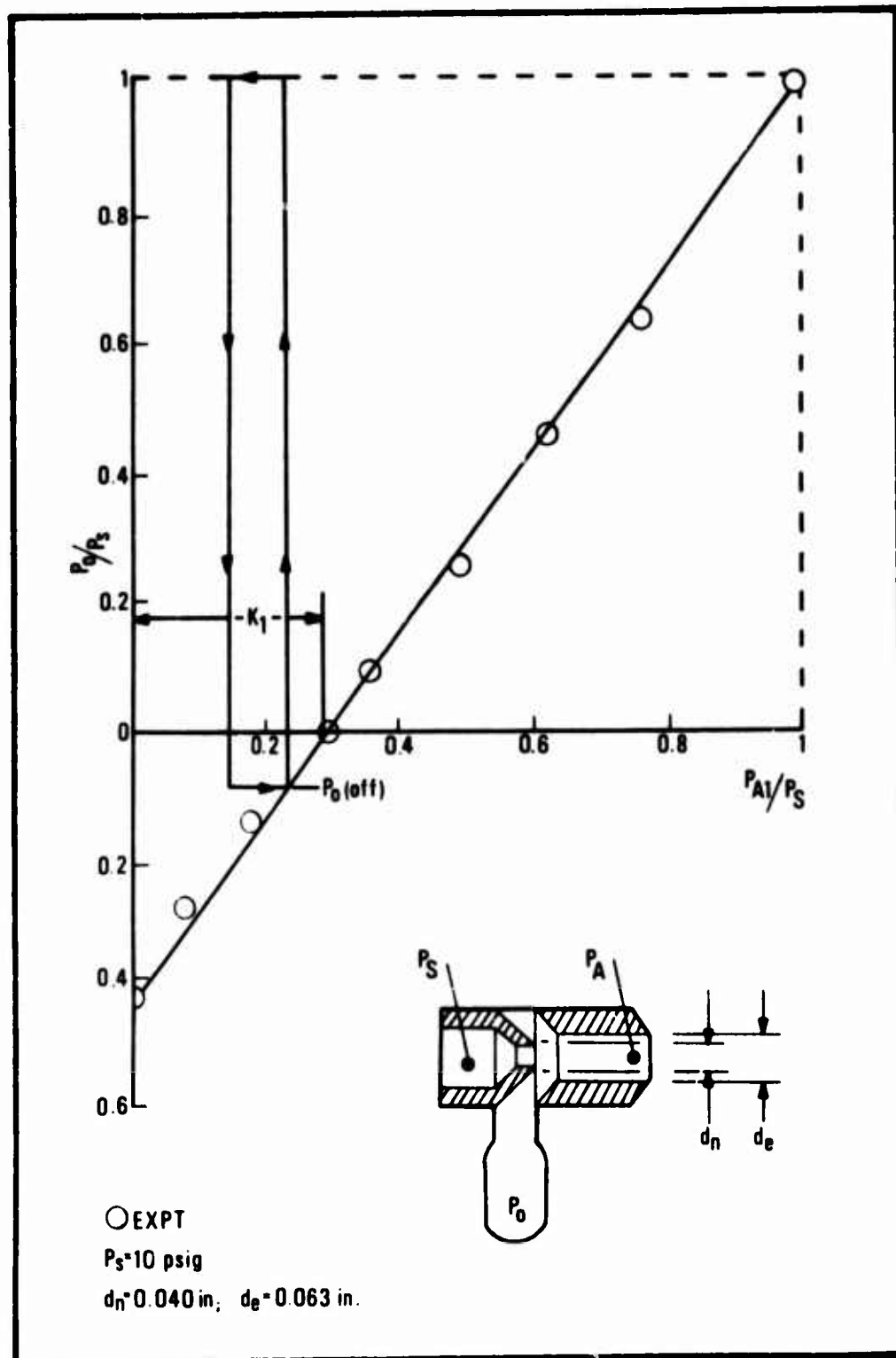


FIG. 13: Geometry and Back-Pressure Characteristic of the Ejector-Sensor

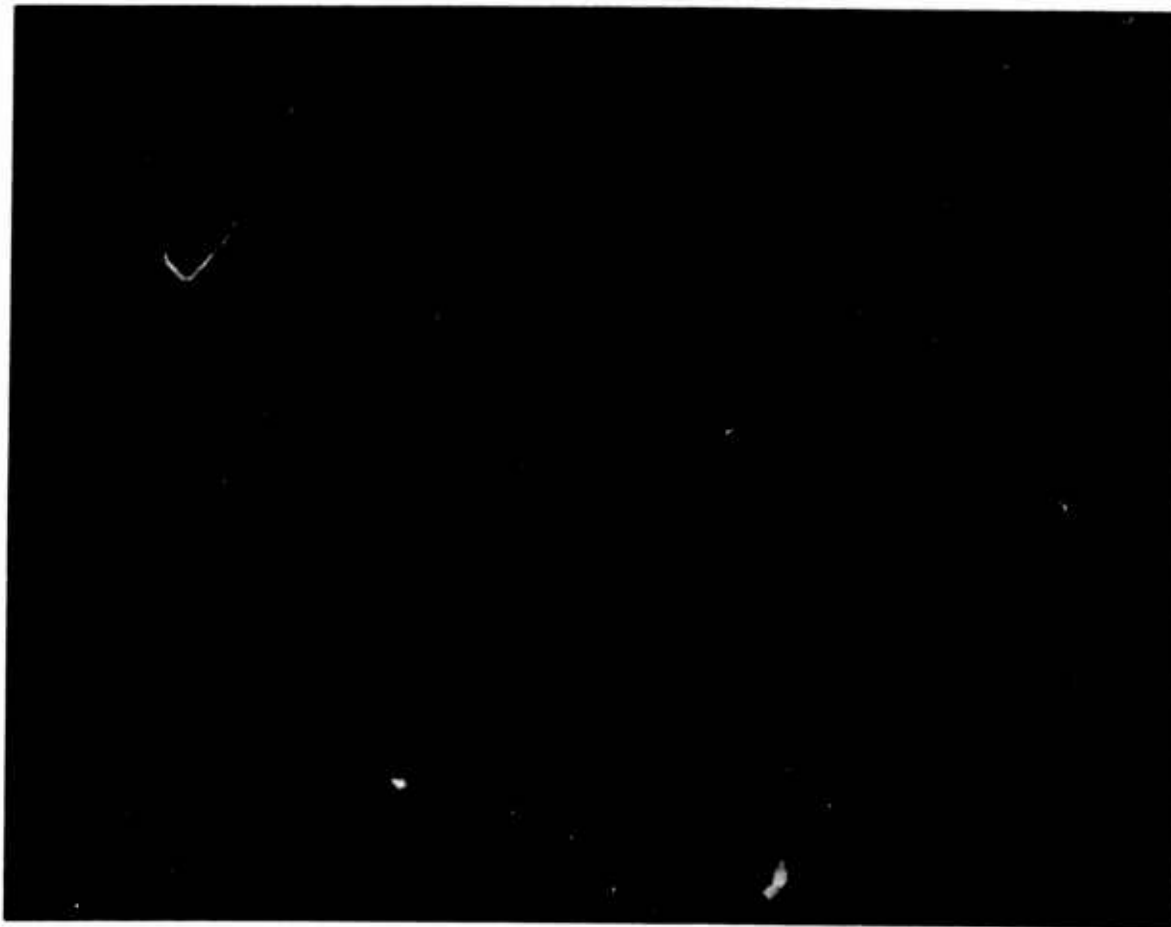


FIG. 14: Photograph of the Diaphragm-Ejector
Schmitt-Trigger.

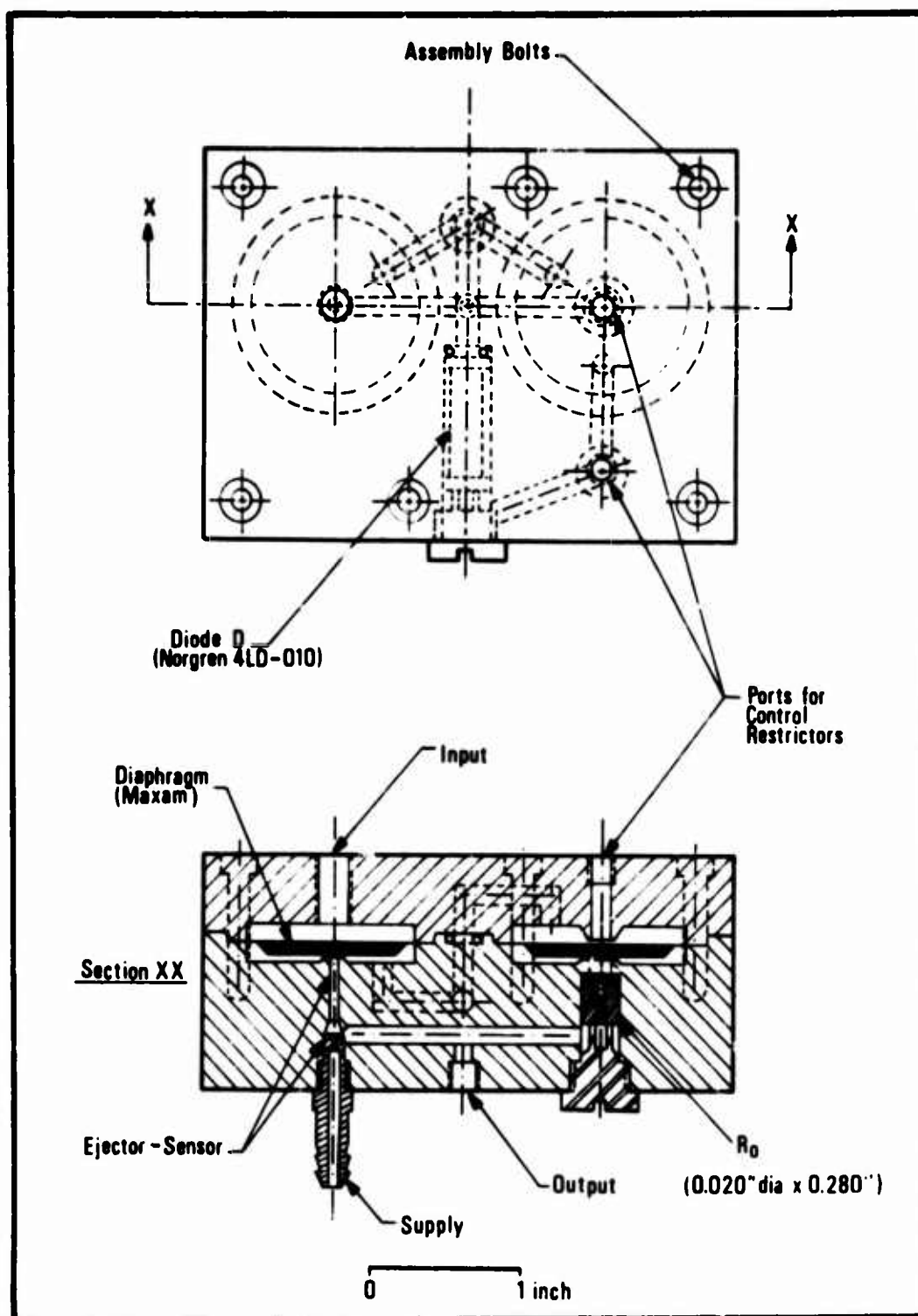


FIG. 15: Construction of the DEST

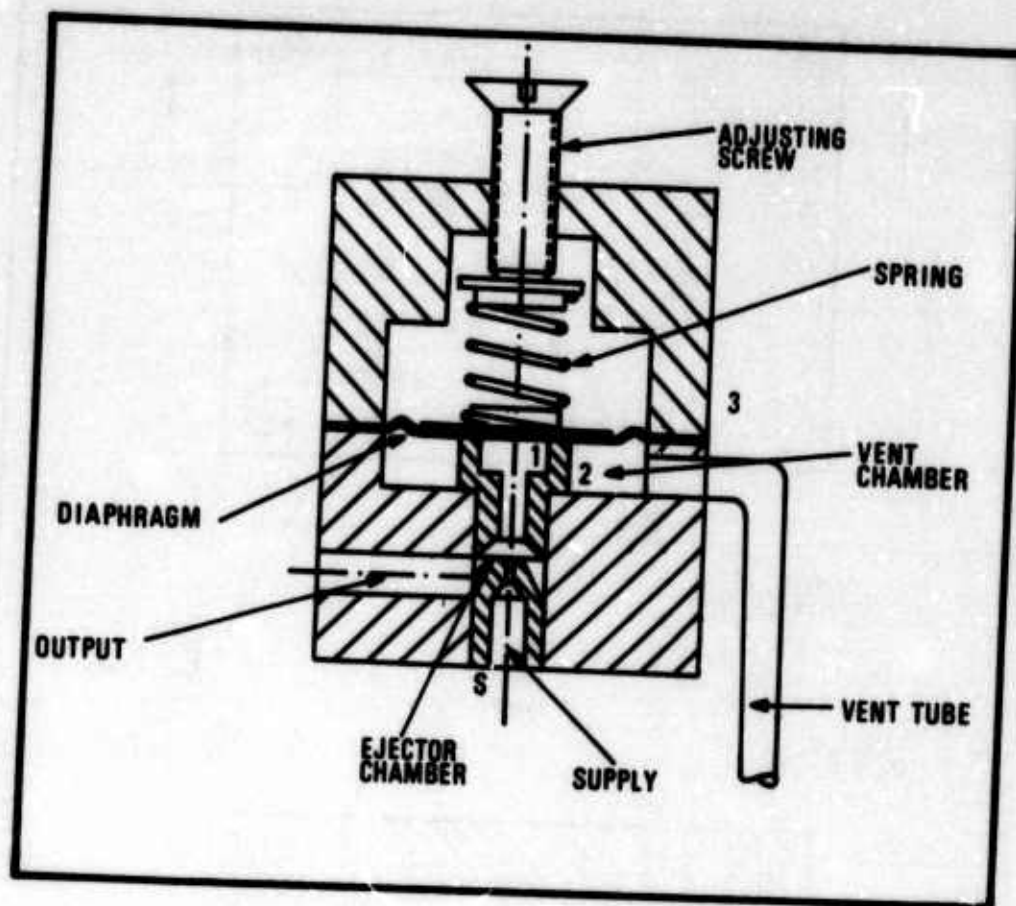


FIG. 16: Schematic Diagram of Liquid Operated Oscillator

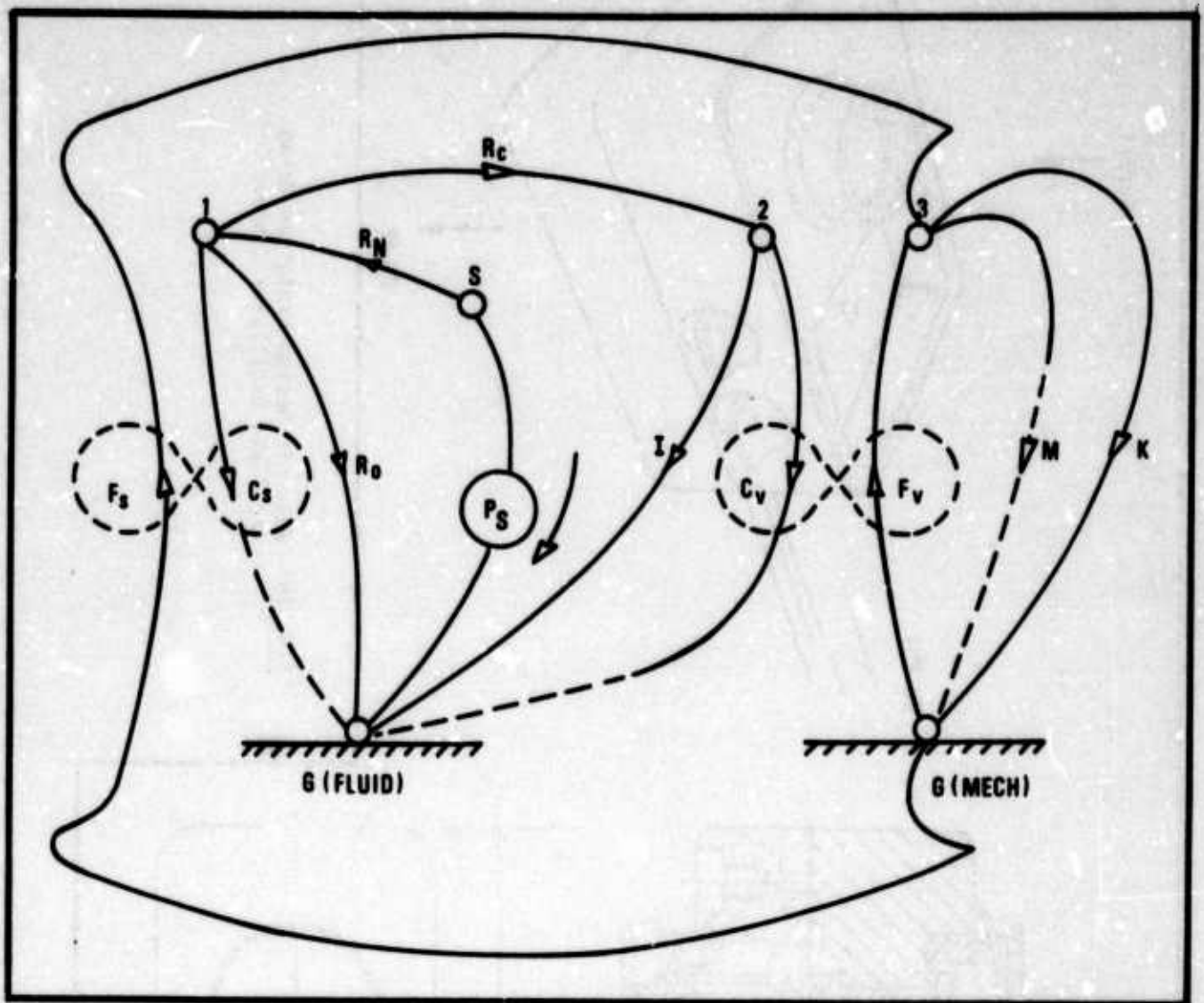


FIG. 17: Linear Graph of Fluid Oscillator

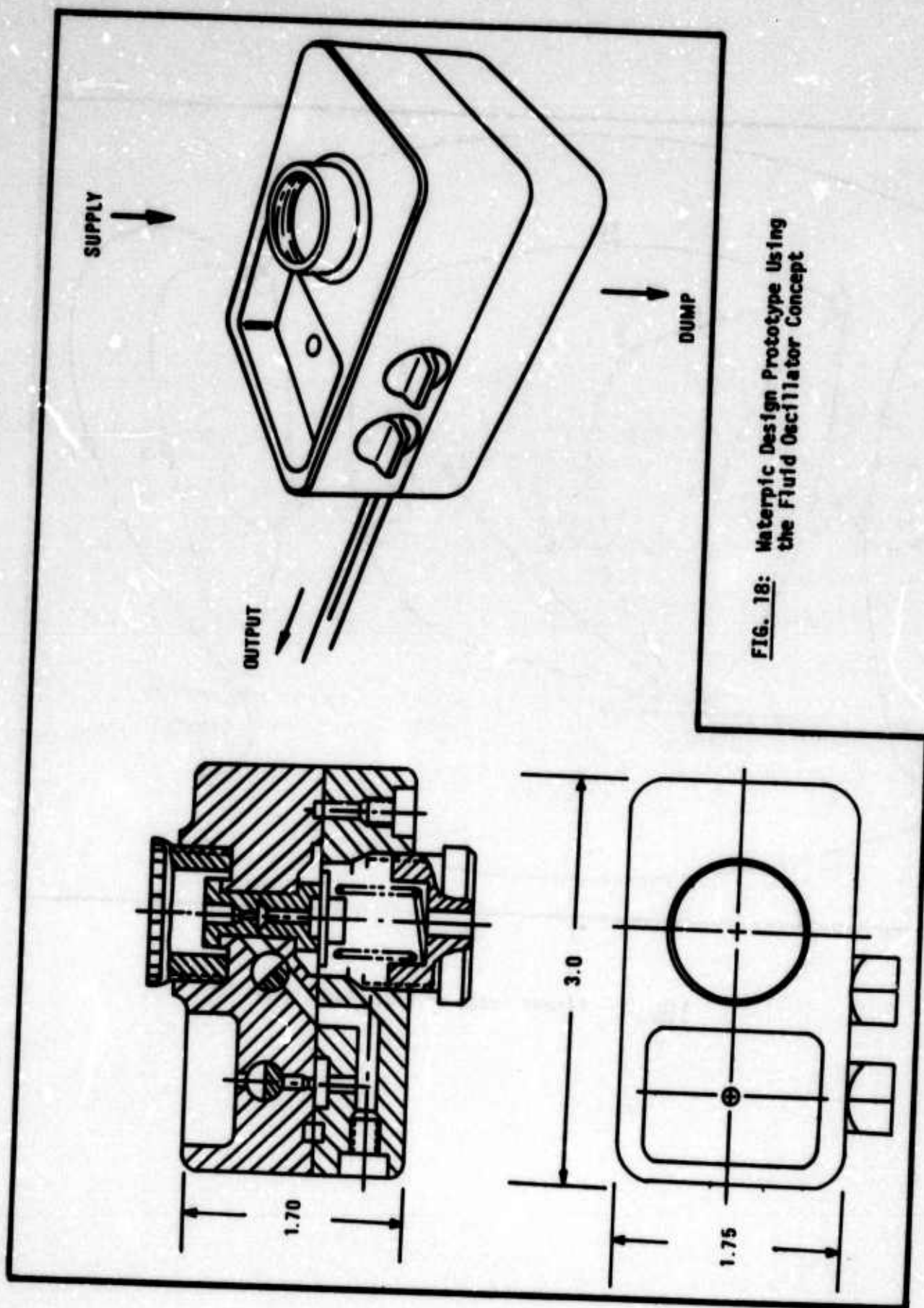


FIG. 18: Waterpic Design Prototype Using the Fluid Oscillator Concept

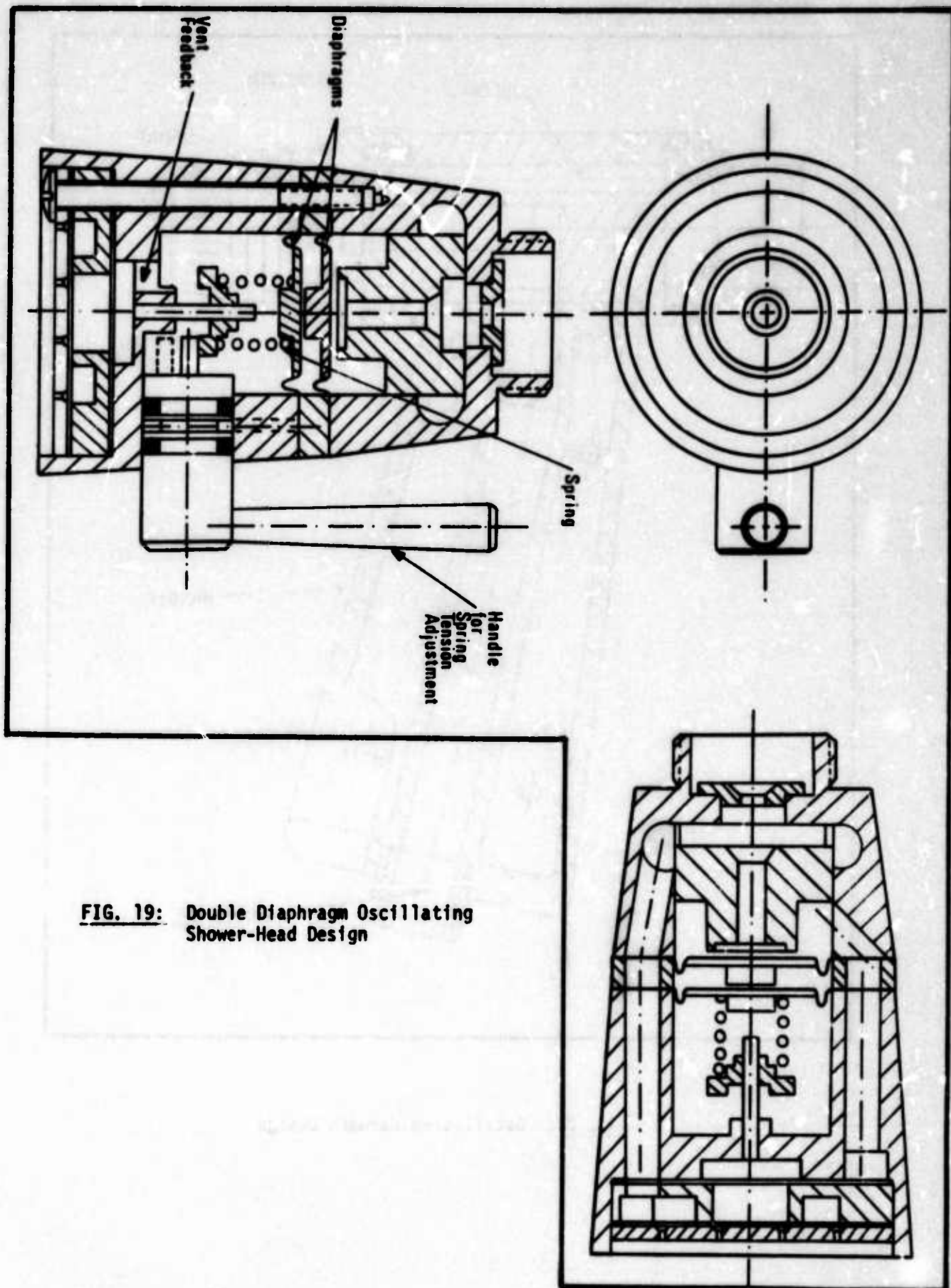


FIG. 19: Double Diaphragm Oscillating Shower-Head Design

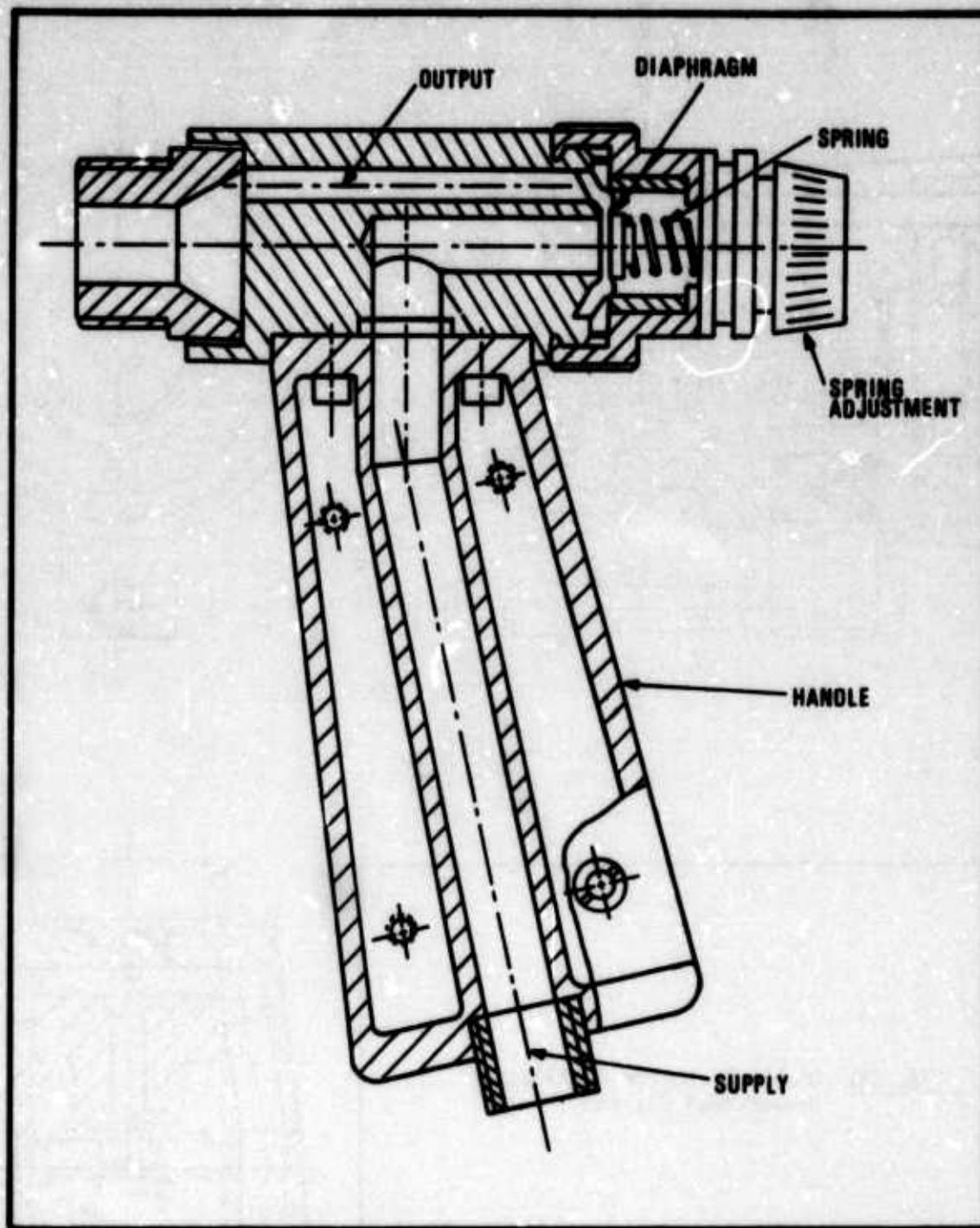


FIG. 20: Oscillating Carwash Design

TABLE I

<u>Fluid Oscillator System Equations</u>		REMARKS
Continuity at Vertex S	$Q_S = Q_{Rn}$	Q_{Rn} flow through supply nozzle
Continuity at Vertex 1	$Q_{Rn} - Q_{Ro} - Q_{Rc} - Q_{Cs} = 0$	Q_{Cs} incremental flowrate into seat chamber
Continuity at Vertex 2	$Q_{Rc} - Q_I - Q_{Cv} = 0$	Q_{Cv} incremental flowrate into vent chamber
Elemental Equation for R_n	$P_S - P_s = R_n(P_S, P_s)Q_{Rn}$	R_n is a non-linear function of P_S & P_s
Elemental Equation for R_o	$P_s = R_o(P_s)Q_{Ro}$	R_o is a non-linear function of P_s
Elemental Equation for R_c	$P_s - P_v = R_c(P_s, P_v)Q_{Rc}$	R_c is a non-linear function of P_s & P_v
Elemental Equation for inertance in vent tube	$P_v = I \frac{dQ_I}{dt}$	I is inertance in vent tube = $\frac{\rho L}{A_y}$
Gyrator relationship I	$\dot{y} = \frac{1}{A_s} Q_{Cs}$ $F_s = A_s P_s$	\dot{y} = velocity of diaphragm F_s = force at seat chamber
Gyrator relationship II	$\dot{y} = \frac{1}{A_v} Q_{Cv}$ $F_v = A_v P_v$	A_v = X-sectional area of vent chamber F_v = force in the vent chamber
Continuity Equation at Vertex 3	$F_s + F_v - F_m - F_k = 0$	F_m = force due to mass F_k = force due to spring
Elemental Equation for the diaphragm	$F_m = M \frac{d\dot{y}}{dt}$	M = lumped mass of the diaphragm
Elemental Equation for the spring	$\dot{y} = \frac{1}{K} \frac{dF_k}{dt}$	K = spring stiffness

Subscripts: c curtain area;
I vent tube;
n supply nozzle;
o output orifice;
s seat chamber;
S supply;
v vent chamber.

Symbols: Q volume flow rate of fluid;
L length of vent tube;
P density of fluid;
R fluid resistance;
y diaphragm displacement;
A cross sectional area.

A FLUERIC PRESSURE OR FLOW INTERFACE

E.C. Hind *

Abstract

The interface device, which has no moving parts, will cause the pressure and/or flow rate of one fluid to vary in accordance with the pressure and/or flow rate of another fluid.

Basically, the device consists of a chamber containing an interface region with provision for discharge of the two fluids. The controlled fluid is admitted to the chamber through a restriction and the controlling fluid is admitted unrestricted. Possible uses for the device are:

1. As an active interface between gas and liquid systems by converting gas pressure to liquid pressure and vice versa.
2. As a valve in kind by controlling the flow of liquid by gas pressure.
3. As a flow meter by converting liquid flow rate into gas pressure.
4. As a mixing valve by controlling the proportions of two fluids in a discharge flow by means of the pressure or flow rate of one fluid.

Introduction

The purpose of this paper is firstly to describe a type of interface device, which has no moving parts, and which will cause the pressure and/or flow rate of one fluid to vary in accordance with the pressure and/or flow rate of another fluid; and secondly, to present characteristic curves for one interface geometry with air pressure or flow rate controlling water pressure or flow rate and vice versa. The characteristics are presented for the interface device with and without resistance type loads on the controlled fluids.

The interface was initially developed to allow a conventional pneumatic controller, operating over the standard signal range of 3-15 psi (or 20 - 100 k Pa), to drive a water operated vortex flow modulator. Although initially the aim was to convert a gas pressure into a liquid pressure, studies of the device during the

* University of New South Wales, Australia.

past two years have shown that it may be used in the following additional applications:

- . To vary liquid flow rate by means of gas pressure.
- . To vary liquid pressure or flow rate by means of gas flow rate.
- . To vary gas pressure or gas flow rate by means of liquid pressure.
- . To vary gas pressure or gas flow rate by means of liquid flow rate.
- . To control the proportions of the two fluids in a discharge flow by means of the pressure or flow rate of one of the fluids.

In a recent paper R.L. Woods* has described a most interesting interface amplifier which converts gas pressure to liquid pressure without moving parts, with no intermixing of fluids and with no measurable control flow. However, the amplifier operates on very small subambient pressures and so the feasibility of using an aspirator to convert the output signal range from a conventional pneumatic controller into an acceptable subambient pressure range would need to be investigated.

Basic Nature of Interface Device

Basically the device consists of a chamber containing an interface region and provision for discharge of the two fluids from the interface region. The chamber has two inlets. The controlling fluid is admitted to one inlet unrestricted and the controlled fluid, which comes from a constant pressure supply, is admitted to the other inlet, through a restriction. The discharge from the interface region may go to atmosphere, to drain or to a device or system requiring a mixture of the two fluids. In addition an outlet may be provided for the controlled fluid between the restriction and the interface region. This controlled fluid outlet would be connected to a device or load driven by the controlled fluid such as the control port of a fluid amplifier.

Explanation of Operation

In the simplest embodiment of the device the discharge occurs through an aperture in the side wall of a tube containing the common surface of the two fluids. Fig. 1 shows this arrangement when air is the controlling fluid and water is the controlled fluid.

* Woods, R.L. *A Fluero Gas-to-Liquid Interface Amplifier*, Journal of Dynamics Systems, Measurement and Control, Trans-ASME, June 1973, pp. 196-199.

Consider the effect of an increase in air pressure; this will force the common surface down, increasing the flow rate of air and reducing the area of the aperture for water discharge. This will reduce the water flow rate through the aperture and increase the water pressure to values which correspond to the new air pressure. If the water side is connected to a load the increase in water pressure will result in an increased flow rate of water through the load resistance and the net change in water flow rate will be the difference between the decrease in flow of water through the aperture and the increase in flow rate through the load resistance.

If the air pressure is reduced the common surface rises reducing air flow rate, increasing water flow rate through the aperture and reducing water pressure.

If the air flow rate is increased the common surface is forced down, reducing water flow rate through the aperture, resulting in an increased water pressure and an increased air pressure.

If the air flow rate is decreased the common surface moves up, increasing water flow rate through the aperture and reducing water pressure and air pressure.

Experimental Operating Characteristics

The operating characteristics depend on the geometry in the interface region, the resistance of the restriction in the controlled fluid line, the load resistance and the controlled fluid supply pressure. It is assumed that sufficient flow of the controlling fluid is attainable at the controlling fluid pressure. This will be so if sufficient flow of the controlling fluid is available to maintain a controlling pressure of 15 psig with zero controlled fluid flow, i.e. with an unrestricted aperture.

The procedure for matching the controlled fluid restriction (variable for test purposes) to the interface device with or without a load resistance was to set a small controlling fluid flow and open the controlled fluid restriction so that the output pressure was 1 or 2 psi. The controlling fluid pressure was then increased towards 15 psi. If output pressure oscillations became evident at high pressure it was necessary to increase the controlled fluid flow rate by either reducing the resistance of the controlled fluid restriction or increasing the supply pressure of the controlled fluid. Satisfactory operation was considered to exist when the signal range limits could be exceeded by 1 or 2 psi at each end without excessive oscillation and without either air entering the water line or water entering the air line to the interface region.

Various interface devices have been tested. In the case of the simple tube and aperture interface the following aperture shapes have been

tested with the tube vertical and air admitted at the top and water at the bottom: circular holes, square with sides parallel to tube axis, triangle with apex at the top, triangle with apex at the bottom, longitudinal slot, transverse slot. Other devices include vortex amplifiers with air driving water and water driving air; and a pair of concentric small bore tubes one inserted into the other with various amounts of overlap.

The interface device, consisting of a pair of vertically opposed triangles with a common apex and bases both across the tube, exhibited the most nearly linear characteristics. This was so when controlled pressures and flows were plotted against either liquid or gas controlling pressure and when both pressure and flow characteristics were considered.

Figures 2, 3, 4 and 5 show the characteristics for this type of aperture with equilateral triangles of side approximately $1/16$ inch cut into the side of a tube of $3/16$ inch inside diameter.

Figures 2 and 3 are for air controlling water with a water supply pressure of 30 psig. Figure 2 shows water pressure psi, water flow rate cc/min through the restriction, and air flow rate ft³/hr at N.T.P., plotted against controlling air pressure psi. The characteristics are shown for no load (full lines) and driving a small bore tube of length 1.875 inch and inside diameter 0.042 inch as a water load (dashed lines). Figure 3 shows controlled water pressure and water flow rate plotted against controlling air flow rate with and without the water load resistance.

Figures 4 and 5 are for water controlling air with an air supply pressure of 22.5 psig. Figure 4 shows air pressure, air flow rate through the restriction, and water flow rate plotted against controlling water pressure. The characteristics are for no load (full lines) and driving a small bore tube of length 1.875 inch and inside diameter 0.024 inch as an air load (dashed lines). Figure 5 shows controlled air pressure and air flow rate plotted against controlling water flow rate.

Pressure gains indicated at the measuring points are about 0.94 and are no doubt influenced by pressure drops in the line and fittings between each pressure gauge and the interface device. As force balance across the area of the common surface is necessary pressure gains measured in the interface region could be expected to be very nearly unity and should not depend on the shape of the aperture. The experimental evidence for apertures in tube type interfaces certainly suggests that the pressure gain does not depend on aperture shape. Measured pressure gains for air controlling water were found

to be less than unity and to be mainly in the range 0.90 to 0.97 while pressure gains for water controlling air were often unity (to better than 0.1 psi over the signal range), but could vary to below a gain of 0.9 for this type of device.

The shape of the aperture, in an aperture and tube type device, does influence the shape of the controlled flow versus controlling pressure characteristic, although the way in which the shape influences the characteristic is not at this stage clear.

Oscillations can be troublesome and for some types of interface they reach a maximum of 0.4 psi peak to peak. In isolates cases, the oscillations can reach 2 psi peak to peak. In contrast, some interfaces produced no oscillation over the whole of the signal range. In this respect triangular apertures with air controlling were very good. The relationship between aperture size and tube size seemed to have some bearing on the amount of oscillation; smaller apertures giving less oscillation, e.g. a 3/32 inch diameter aperture in a 3/16 inch diameter tube produced significant oscillations, particularly with water controlling, whereas a 1/16 inch diameter hole in a 3/16 inch diameter tube produced small oscillations only near the top of the range and no oscillations over the remainder of the range. Concentric tubes (e.g. air tube of 0.040 inch I.D., 0.063 inch O.D., length 1.875 inch and water, 0.069 inch I.D., length 1.875 inch with about 0.25 inch overlap) with air driving showed no oscillation, with water driving oscillations of 0.1 psi occurred only in the range of 13 to 15 psi.

There is no doubt that on some occasions the oscillations were due to the presence of air bubbles trapped in the water line in the vicinity of the water pressure gauge. In other cases, oscillations were eliminated by increasing the flow of the controlling or controlled fluid. Some oscillations were probably due to instability in the flow through the aperture.

A few interface devices appeared to produce a discontinuity in the water flow rate characteristic when air was the controlling medium.

Limitations on Use

When the combined flow from the interface region is not being used the device will be acceptable provided there is no objection to the mixing of the two fluids, to the venting of gas from the mixed discharge, or to the draining of liquid from the mixed discharge. In this case, it will be necessary to tolerate sacrificial flows, although these are widely accepted in pneumatic and hydraulic systems.

Conclusion

An interface device, without moving parts, has been described which will cause the pressure and/or flow rate of one fluid to vary in accordance with the pressure and/or flow rate of another fluid. Characteristic curves have been presented for one interface geometry based on water or air pressure input signal ranges of 3 - 15 psi with either air pressure or air flow rate controlling water pressure or water flow rate, and with either water pressure or water flow rate controlling air pressure or air flow rate. Although the device described here is still under development, it is clear that satisfactory interfaces can be developed for any of the above mentioned conversions and that a reasonably linear general purpose interface is also possible.

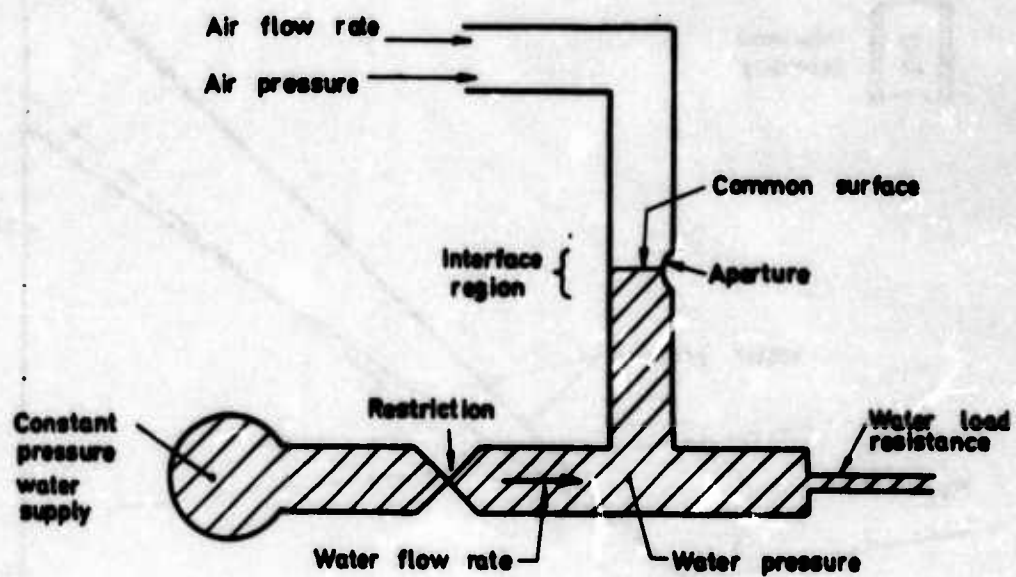


FIGURE 1

Simple embodiment of interface device with air pressure or flow rate controlling water pressure or flow rate.

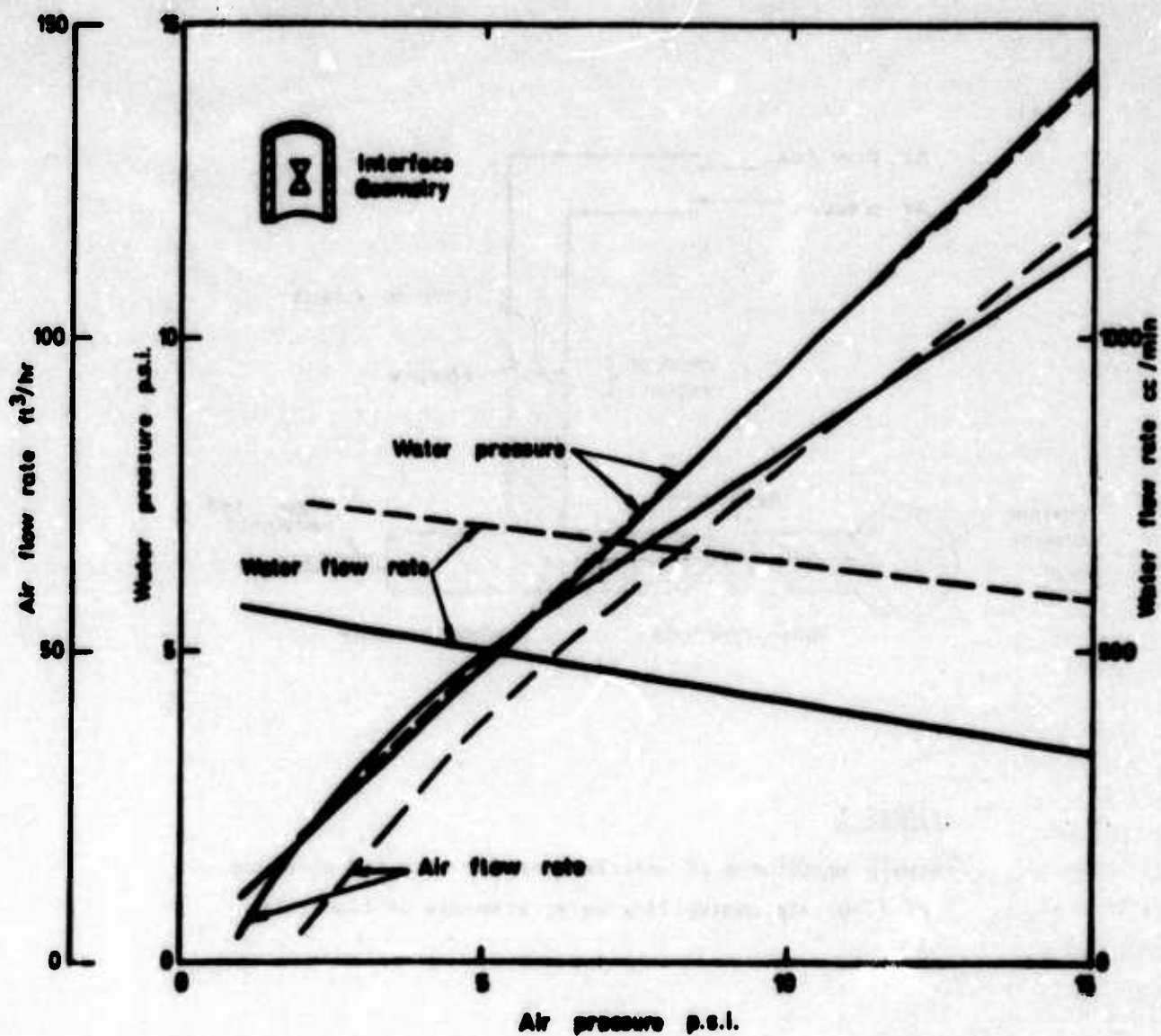


FIGURE 2

Characteristics for air pressure controlling water pressure and water flow rate.

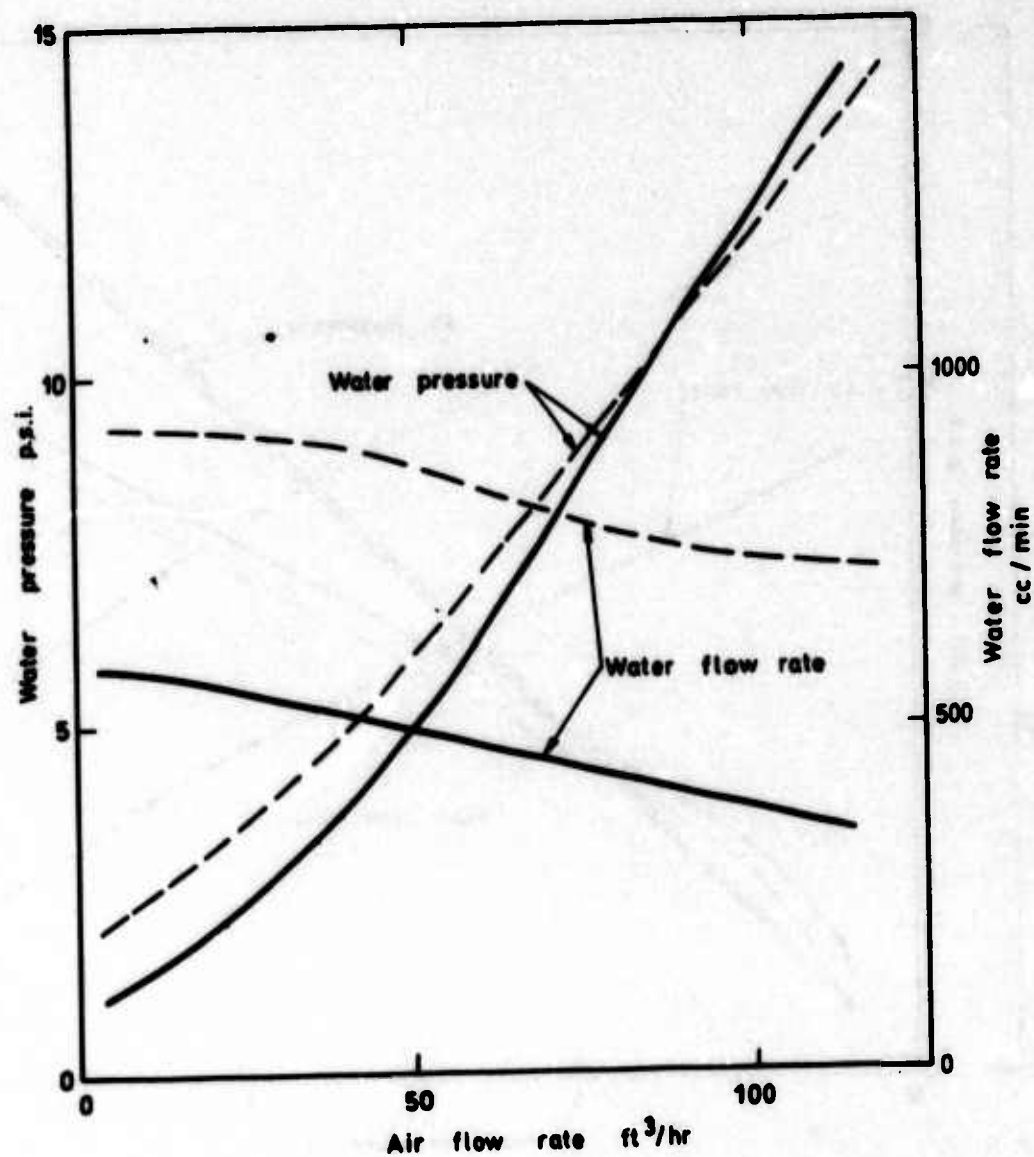


FIGURE 3

Characteristics for air flow rate controlling water pressure and water flow rate.

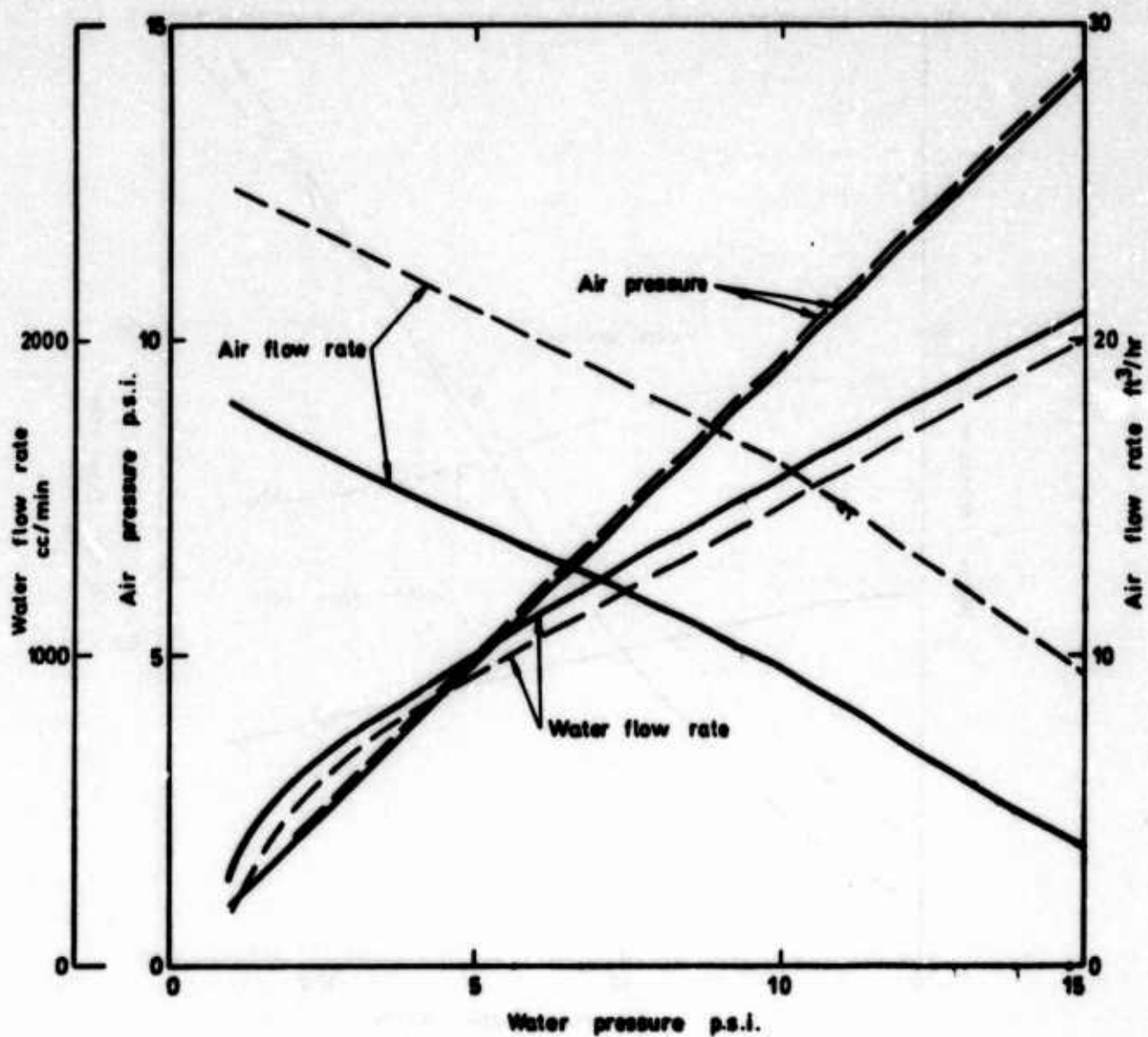


FIGURE 4

Characteristics for water pressure controlling air pressure and air flow rate.

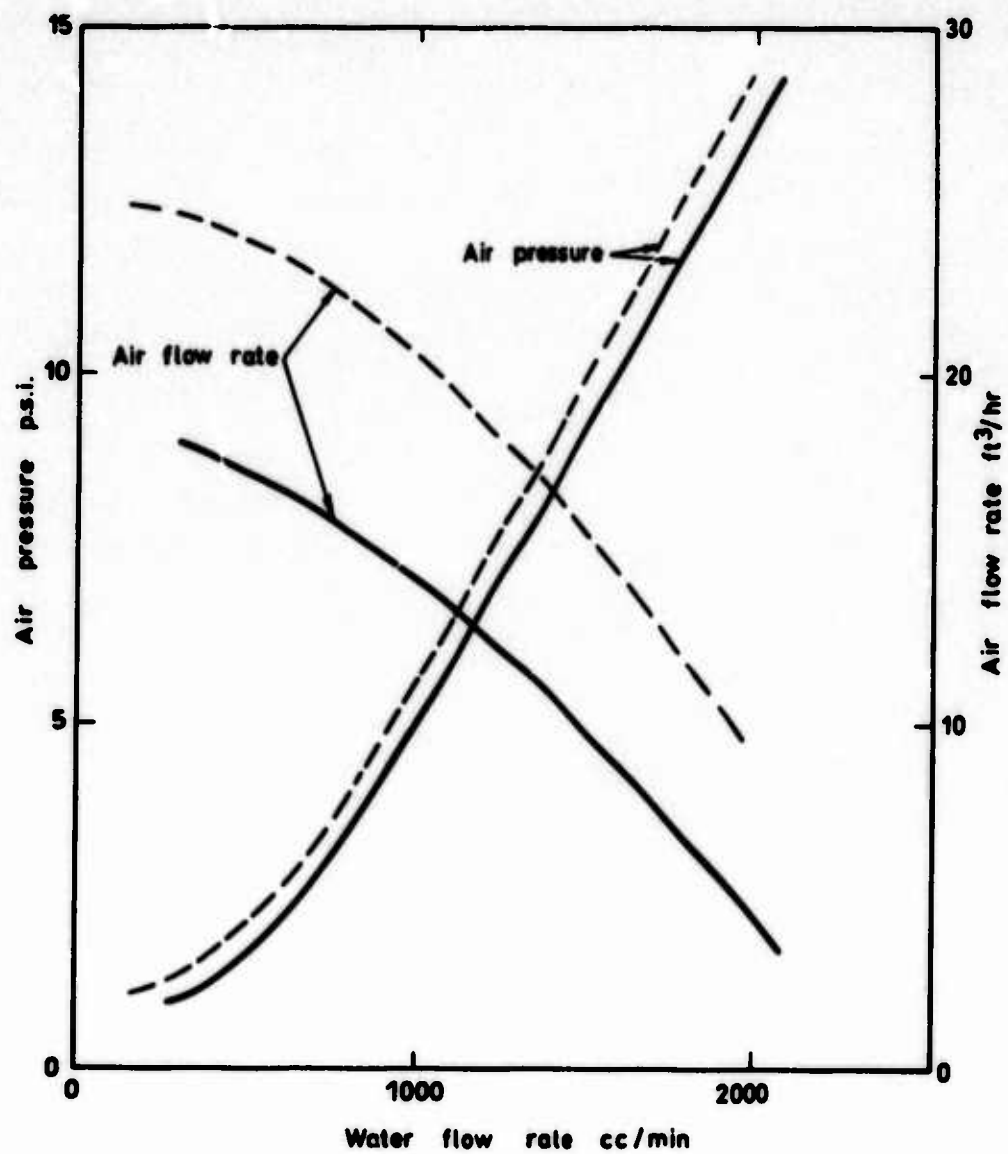


FIGURE 5

Characteristics for water flow rate controlling air pressure and air flow rate.

FLUIDIC SENSORS

PART I

Albertus E. Schmidlin
Picatinny Arsenal

PART II

Joseph M. Kirshner
Harry Diamond Laboratories

ABSTRACT

These two papers discuss many of the available fluidic sensors and the phenomena that make them possible. Included are various types of proximity sensors, angular rate sensors, accelerometers, temperature sensors, concentration sensors, flow temperature sensors, concentration sensors, flow sensors, and level sensors. Part I is devoted primarily to the description of devices and of their operating characteristics. Part II discusses some additional devices and gives the theoretical analysis for several.

PAPER FOR HDL FLUIDICS STATE OF THE ART SYMPOSIUM

SEPTEMBER 1971

FLUIDIC SENSORS - A SURVEY

PART I

BY

ALBERTUS E. SCHMIDLIN *

* Concept & Effectiveness Division, NDED, Picatinny Arsenal, Dover, N.J.
07801

LIST OF FIGURES

- FIGURE 1 BLOCK DIAGRAM OF SENSOR
- 2 NOZZLE FLAPPER AND KEY
- 3 PROXIMITY SENSORS - 2 Plates
- 4 INTERRUPTIBLE SENSORS
- 5 FLUIDIC EAR
- 6 FLUIDIC EAR AND OJ PROXIMITY SENSOR - 2 Plates
- 7 LIQUID LEVEL SENSOR
- 8 ANGULAR RATE SENSORS
- 9 AXISYMMETRIC RATE SENSOR
- 10 RATE SWITCH
- 11 VORTEX RATE SENSOR
- 12 HYBRID RATE SENSOR
- 13a SCHEMATIC - ANALOG RATE GYRO
- 13b ANALOG RATE GYRO
- 14 DUAL FLUID ACCELEROMETER
- 15 FLUERIC ACCELEROMETER
- 16 FLUERIC ACCELEROMETER - TEST RESULTS - 2 Plates
- 17 SCHEMATIC - HYBRID ACCELEROMETER
- 18 FLUIDIC ACCELEROMETER
- 19 FLUIDIC ACCELEROMETER - TEST RESULTS
- 20 FLUIDIC ACCELEROMETER AND TEST RESULTS - 2 Plates
- 21a FLUIDIC ACCELEROMETER WITH DAMPING
- 21b FLUIDIC ACCELEROMETER WITH JET PIPE
- 22a FLUIDIC G SENSOR
- 22b G SENSOR SCHEMATIC

- FIGURE 23 G SENSOR TEST RESULTS**
- 24 FEEDBACK OSCILLATOR**
 - 25 PERIOD OF OSCILLATION VS. VOLUME**
 - 26 FLUIDIC CIRCUIT**
 - 27 DIGITAL ACCELEROMETER**
 - 28 SCHEMATIC - VIBRATING STRING ACCELEROMETER**
 - 29a TEST RESULTS - VIBRATING STRING ACCELEROMETER**
 - 29b VIBRATING STRING ACCELEROMETER**
 - 30 ATTITUDE GYRO - TAPP**
 - 31 ATTITUDE GYRO**
 - 32a FREE ROTOR GAS BEARING GYRO**
 - 32b FREE ROTOR GAS BEARING GYRO**
 - 33 ATTITUDE GYRO**
 - 34 JET EDGE RESONATOR CONCENTRATION SENSOR - 2 Plates**
 - 35 PASSIVE GAS CONCENTRATION SENSOR**
 - 36 PASSIVE GAS CONCENTRATION SENSOR - TEST RESULTS**

FLUIDIC SENSORS
by
Albertus E. Schmidlin

INTRODUCTION

Fluidic technology has proved to be a viable means for systems implementation in industrial, commercial and military systems. Necessarily the fluidic system would not reach this stage of usefulness if totally isolated from its surroundings. It must receive input signals from its environment, act upon these and provide control outputs if it is to serve a useful purpose. The input to the system is provided by sensors. The objective of this paper is to present a state of the art survey of sensors, both having extensive use in operating systems and those still in the R&D phase.

At the outset a sensor should be defined in broad terms. Consider the block diagram in Figure 1. Here we see the sensor represented by the Block S. It receives input signals and power as shown. It provides an output as a function of the input. A generalized input might be represented by the function F_{in} . This function can be dependent upon many variables although in a specific case the number is limited. In fact a perfect sensor responds to only one variable, the variable of interest, and is not responsive to all of the others. Unfortunately, perfect sensors are difficult to design. Although a device might respond primarily to one variable, spurious outputs may occur as a result of other variables in the system.

Let us define these variables. The variables x, \dot{x}, \ddot{x} and $\alpha, \dot{\alpha}, \ddot{\alpha}$ represent linear and angular expressions for the displacement, velocity and acceleration, respectively. These may be inertial variables used to represent the position of a vehicle in flight, or of a machine or part of a machine in motion. This is the case where the application involves inertial control of a system. On the other hand x can represent a physical dimension. An example is a piece part being machined, and could represent the angular position of connected mechanical linkages in a machine. The symbol ϕ is an on/off function. It represents a yes or no, presence or absence, a zero or one. Switches, push buttons and start/stop devices are in this category. "A" represents another physical, dimensional variable, namely; area. An example is the cross sectional area of a circular hole or the projected area created by an object in a passage of a fixed size.

The variables T, P, Q and C represent properties of the fluid -- temperature, pressure, flow and concentration or purity. These variables are especially significant because they define the fluid itself. Fluidics is particularly advantageous to use where fluid itself is being controlled. Finally, the variables E and I introduce electrical signals in the expression. A device which responds to these inputs is a transducer rather than a sensor; these variables are included to complete the generalized expression.

The output, F_{out} is necessarily very simple. It consist of fluidic potentials only. Hence, pressure, P, flow, Q and frequency, are the only variables to be expected in this signal. The great number of parameters in the F_{in} function illustrate the difficulty in preparing a comprehensive paper on the subject of fluidic sensors. Hence, this paper is only a beginning and is an invitation for other authors to present their knowledge and experience in this very interesting and necessary part of fluidic technology.

PROXIMITY SENSORS

The first sensor to be discussed is perhaps the simplest. It is an on/off device which responds to δ (or x) in the generalized function. It is a push button and provides a switching function upon the application of the input signal. The simplest implementation of the push button is one where the finger is used as the flapper of a nozzle/flapper valve as shown in Figure 2 (Reference 1). Placing the finger over the nozzle produces a pressure and flow output from the vertical leg of the device. Manufacturers also make a fluidic element called a Key (Reference 2) or Back Pressure Switch (Reference 3) which performs a similar function. By placing an object over port C, in Figure 2 (b), the switching function is accomplished. The basic difference between these two devices is that (a) is proportional and (b) is digital. This means that partial covering of the nozzle will produce a proportional pressure increase at the output while partial covering at C, will produce no switching in output until it reaches the prescribed degree. Output pressure and flow are functions of the input conditions. Devices of this type are available for supply pressures between 1.25 and 5.0 psig, consume between 42cu. in. per minute and 0.3 scfm and provide output pressures between 20% and 40% of the supply. Manufactures package these devices in numerous combinations with push buttons, toggles, etc., including colors and styles.

The next group of devices is a family of position or proximity sensors. The flapper/nozzle principle can be applied here also with the flapper being replaced by the object being sensed. Other devices are as shown in Figure 3 (Reference 3). The cone-jet sensor uses an annular nozzle, connected to the supply port, surrounding a sensing hole, connected to the output port, as shown in the figure. The high-velocity jet of supply air converges after leaving the nozzle, enclosing a bubble of low pressure within the flow cone. Therefore, the pressure at the sensing opening into the base of the cone is normally slightly below atmospheric. When an object enters the flow cone, a portion of the supply jet is reflected from the object back into the bubble region, increasing the pressure at the output port. The change is inversely proportional to the gap between the object and the nozzle.

In comparison to the back-pressure sensor, the cone-jet achieves sensing gaps as much as ten times greater for an equivalent flow consumption. Edges, steps, grooves, small-diameter objects and cloth or screen mesh can be sensed with precision by this device because of the convergent shape of the jet. Efficient pressure recovery permits sen-

using a distance of up to 1/8".

The sensor is nearly immune to external contamination since the output flow is principally supply air recovered from the interior of the flow pattern. If desired, positive purging can be achieved by introducing a small flow between the sensor output and the control input of its switching component.

A different principle of proximity sensing is used in the vortex sensor, which employs a vortex chamber to produce a swirling flow in the shape of a diverging cone. This high-velocity flow field entrains air from the surrounding atmosphere. Air entrained from the center of the vortex is normally replaced by ambient air drawn in through the open top, as shown in Figure 3, thus maintaining equal (atmospheric) pressure inside and outside the cone. However, the approach of an object acts to restrain the free supply of ambient air to the center of the vortex and a reduced pressure region forms there, since entrainment continues. This region may be sensed as vacuum by an output tap at the apex of the cone, or as a decreasing, but positive, pressure by a tap offset from the apex.

The output signal is analog, proportional to the gap between sensor and object, but limited in range and gradual in slope. For this reason, the vortex sensor can be used only with a high gain fluidic amplifier or the fluidic Schmitt trigger, an extremely sensitive switch with very narrow hysteresis. This combination provides an effective sensing range up to 1/2".

Contamination of the external parts of the vortex sensor from ambient air is likely and is not a dangerous condition. The positive output pressure prevents contaminants from entering the internal parts of the sensor or the Schmitt trigger; localized contaminant build-up can be cleaned away periodically as required.

The third type of proximity sensor is the OJ sensor. This is a longer-range sensor (Reference 4) employing an annular nozzle to create a diverging flow of air, as shown in Figure 3. If there is no obstruction, mutual attraction causes the sides of the air stream to converge, enclosing a central bubble that contains a slight vacuum. This signal is sensed through an opening in the raised centerpiece at the point where the air stream makes the sharpest turn. The output signal under this condition is approximately 0.10 psi vacuum.

This flow pattern remains stable as long as it is unobstructed, but the intrusion of any object diverts part of the flow and bursts the bubble. The output pressure rises abruptly to near-atmospheric when the air stream shifts away from the output opening.

As long as the object is present, this condition is a stable one, so the response of the OJ sensor to the presence of an object is digital, rather than analog. The device exhibits a considerable hysteresis because the air stream cannot converge again, once the bubble is broken,

until the entire bubble zone is free of obstruction.

The range of the OJ sensor is approximately 1-1/8" and remains relatively constant, regardless of changes in supply pressure. An interface valve is supplied with each sensor to convert the OJ output to a signal compatible with the back-pressure switch mentioned earlier.

Another type of object sensor employs the obscuration or interruption principle. The fluidic interruptible jet sensor, in its simplest form, employs an air stream projecting from a transmitting nozzle across a gap to a receiver. As long as the flow is unimpeded, sufficient pressure is recovered by the receiver, as shown in Figure 4, to hold a switching element in the "on" condition. When an object enters the jet, the output pressure at the receiver is reduced, changing the state of the switching element to signal the event. This sensor can be built into the structure of a mechanism. The basic parameters for such a design are given in Figure 4 (Reference 3). Air consumption limitations dictate a sensing gap no greater than 0.75" to 1.0".

Another obscuration scheme employs a beam rather than a stream which is interrupted by the object. The beam consists of a high frequency (50 kHz) wave which is transmitted to a receiver, a Fluidic Ear, (Reference 5). The signal is delivered when the inaudible 50 kHz sound is received and the signal becomes zero when the sound is interrupted; maximum separation between transmitter and receiver is a function of supply pressure, 60 inches being attainable at a supply pressure of 1.6 psig, as shown in Figure 4. Response time is 2 milliseconds and objects as small as 1 square inch are detectable at a separation distance of 5 inches.

In the reflex mode, shown in Figure 5, a non absorbing surface, positioned to satisfy the law of reflection (angles of incidence and of reflection equal and in the same plane), deflects the acoustic wave into the sensor amplifier of the sensor circuit. The acoustic energy causes this amplifier to go off which in turn allows the output amplifier to go on.

By using interferometric techniques, the resolution can be improved by at least two orders of magnitude. One sensor, in Figure 5, uses a reflecting surface in the primary radiation field to form an image that produces a secondary radiation field. The super-position of the two fields forms a pattern of dead zones or fringes.

When the reflecting surface changes position with respect to the sensor system, the fringes shift, passing over the mouth of the sensor. Output pressure of the sensor circuit drops to zero when the null point of the fringe is centered in the mouth of the sensor. Using this technique displacements as small as .001 inch can be measured. This sensor is described in more detail in another paper devoted entirely to it. A summary of the various types of object sensors is given in Table I. Photos of typical off the shelf hardware are shown in Figure 6.

TABLE I

Component	Range	Differential Travel (Hysteresis)	Senses	Minimum Object Size	Response Time "On"	Flow Consumption At 5.0 Psig
Limit Switch	Requires Actuator Motion	0.003"-0.007"	Solids	Not Applicable	0.10Sec	0.12 Scfm
Back Pressure Switch	Contact	0-0.003"	Solids Liquids	1/16"x1/16"	0.10Sec	0.09 Scfm
Position Sensor	To-0.010"	0.002"-0.020"	Solids Films	1/16"x1/16"	0.10Sec	0.30 Scfm
Cone-Jet Sensor	To 1/8"	0.004"-0.030"	Solids Films	1/4"x 1/4"	0.03Sec	0.72 Scfm
2X Vortex Sensor	To 1/2"	3/16"-5/16"	Solids	3/8"x3/8"	0.25Sec	0.66 Scfm
OJ Sensor Set	To 1-1/8"	1/2"-3/4"	Solids Liquids	1-1/2"x1-1/2"	0.30Sec	1.3 Scfm
Interruptible Jet Sensor	1/2"	0.010"-0.030"	Solids Fabrics Fluids	1/32"x1/32"	0.05Sec	0.60 Scfm

A logical progression from proximity sensors is to sensor systems which employ these devices. Sensors which count can be implemented by using a proximity sensor (or an interruptible jet, a fluidic ear, etc.) in conjunction with a counting circuit. The great number of such combinations rules out the possibility of covering all these in this paper. A potential user can easily find manufacturers who will define his products and will design a system to satisfy his requirements. A few examples of sensor systems which are available in a package will be given. For example, a liquid level sensor can be implemented by using a back pressure sensor and a bubble pipe. One manufacturer advertises the system in Figure 7 with the switching characteristics shown (Reference 6).

A sensor for continuously monitoring the size of a wire filament or yarn can be implemented. This is accomplished by passing the wire through a passage of fixed area and measuring the differential area between the wire and the hole. Schematically the circuit is similar to the nozzle/flapper combination except here the wire obscures part of the passage area, thereby developing a pressure output as a proportional function of size. The unique feature of this sensor is the ability to monitor the size of the filament as it is moving through the manufacturing process.

An unusual measuring device is the hot forging sensor (Reference 7). The fluidic non-contacting gage is a system designed for taking measurements on a rotating hot shell body. An arm supported like a lever has a nozzle on one end from which an air jet pressure supports the arm at a given distance above the rotating shell. As the high and low areas of the rotating shell move under the jet, the lever action transmits the up and down motion to the opposite end of the arm where an appropriate fluidic back pressure sensor measures the dimensional change in the shell.

A successful demonstration of the fluidic non-contacting gage was made at the Scranton Army Ammunition Plant in which the external runout of a hot shell forging was measured.

In feeding paper to printing presses or in automated packaging, two sheets are often mistakenly fed to the machine instead of one. Many printing and packaging machines have to negotiate sheets as thin as $0.05 \pm 0.1\text{mm}$. A fluidic sensor designed for these thicknesses was described by F.G. Bavagnoli of Politecnico di Torino of Italy at the Fourth Cranfield Fluidics Conference held in Coventry, England. The basic element of the fluidic sensor is an inhibited OR-NOR gate. The inhibitor signal divides between two channels which are connected to two sensing heads during operation. When a single sheet passes, the suction forces it toward one sensing head, leaving the other head free. When two sheets pass, both sensing heads are blocked. This induces the gate to switch which in turn actuates an indicator or shutoff device.

RATE SENSORS

There is a simple concept presented in the literature which senses the rotational speed of spur gears (Reference 8). The primary sensor

is an interruptible jet through which the teeth of the gear travel. A jet of air emanates from the emitter nozzle. When the gear rotates, air transported between gear teeth has a tangential velocity proportional to the angular speed which deflects the emitter jet. Gear teeth block the emitter jet periodically. Thus, the deflected jet comes through the gear as a pulsed signal at a frequency equal to the number of gear teeth times the angular speed. The output collector then receives the deflected jet, and the passive fluidic/circuit of the collector filters out the high-frequency signals caused by the gear-teeth interruptions. The result is an average analog output pressure signal that is a function of the angular speed.

There are other devices for sensing angular rates of rotation which inherently are much more sensitive than the device just described. They are also more complicated and expensive and are better suited for use in inertial guidance and control to sense the angular pitch or yaw rate of a vehicle rather than the rotational rate of a shaft. In the latter case one wished to determine the shaft speed with respect to a fixed position on the machine. In the former case one desires to know the pitch rate of the vehicle with respect to a fixed reference such as the stars (or the earth). In this case the entire system including the sensor, the power source and the control system are inside the vehicle. If these devices were used to measure the speed of a shaft, only the sensor itself would be part of the rotating system and means would be needed to provide flow into and out of the moving shaft by means of rotating couplings or pneumatic slip rings. Hence, plumbing such applications becomes unduly complicated.

Two types of devices are available for onboard measurement of the angular rate of a vehicle. One of the earliest schemes for a fluidic angular rate sensor uses a rigid jet pipe nozzle and is sometimes called a garden hose device. The principle in this scheme was first presented more than 30 years ago (Reference 9). It is based on the concept that a jet of fluid will be deflected from its initial straight line path if the system is subjected to angular rotation (the Coriolis effect) and can be used to make on-board measurements of vehicle motion. In this way output signals, which are a function of angular rate of rotation, are generated. The garden hose device principle is shown in Figure 8 (Reference 10). A jet of fluid issues from a jet pipe rigidly mounted on the instrument (as shown at the origin of the XYZ axes). The tube is aligned with respect to a target (pickoff) located some distance away from the origin leaving an unconfined fluid stream between the tube exit and pickoff. In the absence of all inertial body forces and motion, the fluid jet strikes the pickoff "on target". If there is motion of the vehicle such as rotational velocity, w , about the Z axis or linear acceleration, y , along the Y axis, there will be a deflection of the jet from the line of sight. This is an example of a device which is sensitive to two different inputs. Owing to this angular rate/linear acceleration coupling, this principle cannot be used in its simplest form in a general-purpose instrument. As a linear accelerometer, it will have an error due to angular rates of rotation and as an angular rate sensor

it will have an error due to linear acceleration.

In a practical form of the device the acceleration sensitivity can be nullified. If the jet pipe and pickoff are totally enclosed, the jet will discharge into a region which is filled with fluid. Therefore, this ambient fluid, as well as the unconfined jet, will be subjected to the acceleration. The net result is the cancellation of the acceleration sensitivity. The fluidic laminar angular rate sensor will be discussed in greater detail in a paper devoted only to that subject.

Work has also been done on an axisymmetric laminar jet angular rate sensor (Reference 11). This device was constructed in a two-axis version; that is, two pairs of outputs were provided to provide output signals from the pitch and yaw axes of a vehicle. Several design features of the sensor deserve mention. As is shown in Figure 9, the sensor consists of two co-axial tubes. The power jet flows inside the inner tube. This tube, called the entrainment tube serves to partially protect the power jet against outside disturbances. It and the outer case provide a convenient method of returning entrainment flow to the power jet. A set of holes at the junction of entrainment tube with the power nozzle admit entrainment flow to the jet. The jet can thus have a close-fitting wall around it which helps its stability. Since entrainment flow is furnished at the power nozzle exit, the jet does not have to perform as an ejector. Excess return flow is dumped to ambient by a set of axial vent holes in the power nozzle block.

Another device is the fluid vortex angular rate sensor. It is based on the conservation of angular momentum and uses a gaseous or liquid fluid. Upon entering the device, the fluid is given the angular rotational rate of the instrument housing. A typical configuration is shown in Figure 8 (Reference 10). There is a continuous flow of fluid into the manifold, radially through the coupler and vortex chamber and axially out of the drains. If there is a component of angular rotation around the axis of the device, the coupler superimposes a tangential velocity onto the radial flow, thereby creating a vortex. The amplification of the circumferential velocity in this vortex is a function of the radial velocity. For an inviscid incompressible fluid the angular momentum will be conserved. This creates a swirling flow as depicted in Figure 8. A suitable pickoff device senses this tangential velocity component.

Since the velocity increases hyperbolically at small radii, it is potentially possible to detect small rates of rotation of the device. In the ideal case, the circumferential velocity approaches infinity as the fluid approaches the center of the vortex. For a real fluid, viscous effects change this distribution of angular momentum. The velocity curve follows the ideal (inviscid) case for large radii but it soon reaches a maximum value at a critical radius. Inside of this radius the circumferential velocity no longer increases. Hence, for design purposes it becomes important to predict the location of this point. This requires an understanding of the flow field, including the effects of viscosity.

The two devices described here are available in many sizes for both liquid and gaseous fluids. The sensitivity extends from a threshold of less than 0.1 degrees per second to a full scale range of 3000 degrees per second. Photos of hardware are shown in Figures 10 and 11 (Reference 12). Other characteristics of the vortex angular rate sensor are as follows:

TABLE II
VORTEX RATE SENSOR CHARACTERISTICS

(Data From Previous Programs)

Parameter	Pneumatic		Hydraulic	
Range ($^{\circ}$ /sec)	3000	2000	500	100
Threshold ($^{\circ}$ /sec)	0.1	0.05	0.05	0.2
Frequency Response (CPS) (90° Phase Shift)	15	8.3	25	5
Transport Delay (Sec)	0.05	0.030	0.010	0.050
Output level (Psi)	0.2	0.3	15	10
Scale Factor (Psi/ $^{\circ}$ /sec)	0.004	0.002	0.005	0.003
Noise P-P	0.01% FS .2 $^{\circ}$ /sec	0.0005% FS 0.01 $^{\circ}$ /sec	0.2% FS 0.1 $^{\circ}$ /sec	0.5% FS 0.5 $^{\circ}$ /sec
Null offset ($^{\circ}$ /sec)	Adjustable to 1 $^{\circ}$ /sec	Adjustable to 1 $^{\circ}$ /sec	Adjustable to 1 $^{\circ}$ /sec	Adjustable to 1 $^{\circ}$ /sec
Linearity (% FS)	2.0	2.5	1.0	1.0
Pressure Drop (Psi)	10	8	60	60
Flow	1.0 SCFM	0.4 SCFM	4.0 CIS	2.0 CIS
Size (Inch)	6D x 1	3D x .8	2.5D x 20	2.5D x 1.5
Weight (lbs.)	1.5	.3	0.7	0.5
Temp. Effects (% SF/ $^{\circ}$ F)	0.1	0.08	0.1	0.1
Regulation (\pm %)	1	1	1	1
Reliability (hours MTBF)	-	-	50,000	50,000
Accel. Eff.	neg.	05 $^{\circ}$ /sec/g	-	-
Vibration Eff.	neg.	neg.	neg.	neg.
Shock Eff.	neg.	neg.	-	-
Noise Eff.	neg.	neg.	-	-
Radiation Eff.	Hard	Hard	-	-

HYBRID RATE SENSORS

An interesting implementation of the Coriolis effect laminar jet principle is in a hybrid device which utilizes an electrical pick off to sense the fluid flow field as it is influenced by the rate of rotation (Reference 13). An air pump (Figure 12) connected to a long, small-diameter tube creates a laminar air jet which, when undisturbed, flows along the centerline of the drift tube which houses the device. When the device is subjected to an angular rotation about an axis perpendicular to the centerline of the jet, the inertial properties of the air jet cause it to be deflected laterally. The magnitude and sense of the deflection are proportional to the magnitude and sense of the input angular rate. The two tiny thermistor deflection sensors are positioned symmetrically about the undisturbed air jet and separated a distance approximately equal to the jet nozzle diameter. The thermistors are electrically connected into a simple bridge circuit (as shown in the sketch) which provides enough current to cause self-heating of the two thermistors. In the undisturbed state the bridge is balanced and the meter indicates zero. When the air jet is deflected away from its normal centerline position, the velocity of the air flowing by one thermistor (toward which the jet is deflected) is greater than the velocity of air flowing by the opposite thermistor. This causes an unbalance in the cooling of the two thermistors. Since the thermistor resistance increases with decreasing temperature, the electronic bridge becomes unbalanced; this unbalance is indicated by a positive deflection of the meter. When the air jet is deflected in the opposite direction by a negative input angular rate, the other thermistor is cooled, thus unbalancing the bridge in the opposite sense. This causes the meter to indicate a negative value. Thus the device yields an indicated output, the magnitude and sense of which are proportional to the input angular rate about a particular axis.

The significant characteristics of this device are as follows:
Size: 1-inch in diameter x 3 inches long + 2 cu. in. of electronics
Weight: 3 oz. plus 3 oz. of electronics (2.8 watts)
Range: Up to 2000°/sec.
Frequency Response: Up to 70 HZ
Threshold Resolution: 0.005% of full scale, 0.005°/sec minimum

Some of the fluidic devices mentioned earlier are limited to single-axis instruments. Therefore, in a multi-axis system individual sensors would be required for each axis. There are many applications for two-axis rate sensors. Typical cases are stabilized platforms for aircraft, missiles, armament, telescopes and other instruments. A simple scheme is available for two-axis rate sensing using a hybrid device. Bread-board systems of two-axis, fluidic-output rate gyros have been developed. The rate gyros provide a gas output signal proportional to the input rate about each of two orthogonal axes. Some can be built with either a conventional analog output, or a Pulse-Direction-Modulated (PDM) output. PDM signals are particularly useful in fluidic control systems, since they are easier to amplify and transmit than analog signals.

There are several implementations of this principle by different manufacturers. One typical rate gyro design is shown in Figure 13A (Reference 10). The rotor is suspended on a spherical, pressurized bearing restrained by two pairs of pneumatic springs, which are produced by pressurized torquing cavities located on two orthogonal axes. In the analog mode, the pneumatic springs must be deflected when the gyro is precessed at the input rate. When the pneumatic springs deflect, a pressure differential, which is proportional to the torque required to precess the rotor, and therefore proportional to the input rate, develops across them. In the slightly more complex PDM mode, the rotor position is sensed by a fluidic pickoff (not shown). The two torquer pairs operate continuously and cause the rotor to precess back and forth at a constant rate between two limits determined by the pickoff. When the input rate is zero, the angular distance between the rotor precession limits is the same in both the clockwise and counter-clockwise directions. Since the precession rates are equal, the transit times are also equal; however, in the presence of an input rate, the angular distances between the limits are not equal. When the rotor precesses in the same direction as the input rate, the pickoff limit attached to the gyro frame rotates in the same direction, and the total angular travel is greater than that for zero input rate. When the rotor precession opposes the input rate, the frame rotates towards the rotor and the angular distance is reduced. The PDM signal is actually two on-off signals that are never on simultaneously.

Test results indicate that this instrument can provide either a pulse-duration modulated or an analog pressure signal, having a full scale input of 0.1 revolutions per second. Resolution is 0.1 percent of full scale with a linearity of less than 2%. A photograph of an alternate design is shown in Figure 13B (Reference 6). Major design goals achieved in this device were both the development of a stable air bearing configuration, as well as a demonstration of the feasibility of closing fluidic damping and torquing loops around the gyro rotor. A scale factor of 0.2 psi/deg/sec was measured. The gyro loops were operated with sufficient gain to give a 40 rad/sec gyro bandwidth while still retaining adequate nutation damping. The loops were operated stable over a rotor speed range of 3000 to 5000 rpm.

FLUIDIC ACCELEROMETERS - ANALOG

One of the most needed instruments in aerospace guidance and control is the accelerometer. Fluidic accelerometers (devices having a minimum number of moving parts), which utilize a physical mass of solid material and produce output signals in fluid form, are available. This output can be used in fluidic amplifiers and logic devices to perform the necessary signal processing.

Fluidic accelerometers, which eliminate the solid proof mass and use a purely fluid phenomenon, are not state-of-the-art devices, in the same sense as other fluidic sensors such as vortex angular rate sensors, fluid temperature sensors, etc. Hence, the art of deriving a fluid

output proportional to acceleration has received concentrated investigation. The main factor is to conceive a scheme in which a large output signal is derived from the fluid due to acceleration. By using a liquid jet in the garden hose device described earlier, one may derive a large enough signal at the pickoff from the high kinetic energy in the liquid stream. However, this idea suffers from two problems. The angular rate sensitivity must be compensated for and the power supply for the liquid jet becomes prohibitive in some application.

Many schemes become feasible when two fluids of different densities are used; technically, jet devices then become feasible. Principles which utilize the body force on the heavy fluid as a proof mass can be applied. A light fluid is used as the signal transmission fluid and to provide a low density ambient atmosphere around the jet. Recent work on the viscous vortex angular rate sensor has yielded a new form of flueric accelerometer (Reference 14). By providing a manifold divided into two halves, see Figure 14, a flow field composed of two different fluids is created. These fluids enter at A and B, respectively. If A is more dense than B the body forces due to acceleration will create a swirling flow. The swirl will be as shown for downward body forces with fluid A entering on the left and fluid B entering from the right. This would be the case for the device resting on the lab bench in the earth's gravitational field, or for the case of the device accelerating upward. The sensitive axis is along the vertical line OO' passing through the partitions in the manifold as shown.

Testing of this device has shown a threshold of 10^{-4} G and a full scale range of 1/2G (Reference 14).

In general, dual fluid concepts are not readily accepted because of the need for two sources of fluid power rather than one. Applications in closed systems for long-flight durations have the added complication of separating the two fluids before returning them to their respective reservoirs. The ideal flueric accelerometer would utilize a heavy fluid (liquid) as a proof mass and a light fluid (gas) as a signal transmission medium; the ultimate feasibility of such a scheme would depend upon a means for capturing the heavy fluid so that only one fluid power source, the gas, would need replenishment in the system. As a result of studies, a flueric acceleration sensor, based on a new principle was invented. It uses a heavy liquid (mercury) in a configuration that produces large hydrostatic pressure gradients proportional to and aligned with the acceleration vector. The mercury is contained in a capsule with porous walls; its surface tension prevents seepage through the pores; hence, the mercury charge is held fixed. Gas flow is maintained inward through one wall of the porous capsule and emerges through other walls. The gas passes through the mercury in the form of small bubbles. The gas pressure required to maintain flow depends primarily upon the pressure required to form bubbles at the entrance interface between the liquid mercury and the porous wall. Since this pressure is a function of the local hydrostatic pressure, it provides a measure of the acceleration. A schematic is shown in Figure 15 (Reference 15).

In tests of the experimental model, the output signal pressure was determined as a function of the acceleration imparted to the device. Figure 16 depicts the response of the accelerometer in the range from 0-100g's. The maximum output differential pressure was approximately 20 percent of the supply pressure of 25 psig, and the mercury volume was 0.4 cc or 25 percent of the total internal volume of the porous cylinder. It is observed from Figure 16 that the output pressure increases monotonically with increasing acceleration up to the point where saturation occurs. The acceleration range over which the output signal increases monotonically depends upon the ratio of the volume of mercury to total cylinder volume, i.e. the ratio must decrease to broaden the range. The signal output was nearly identical for increasing and decreasing acceleration and hysteresis was determined to be less than .01 psi. No noise data were specifically recorded. Figure 16 provides insight into the dependence of the operating range of the accelerometer on supply pressure, and the volume of mercury encapsulated within the device. The accelerometer yields a linear output over the greatest range for a supply pressure of 40 psig. The maximum acceleration for which linearity is maintained is in excess of 100 g's. As the supply pressure is decreased, the range of linearity decreases proportionately, e.g., for a supply of 10 psig, the accelerometer exhibits linearity up to approximately 35 g's. Linearity at low g-levels (below 10 g's) was obtained and Figure 16 shows the output signal pressure as a function of acceleration for a supply of 2 psig. Linearity was exhibited over the entire range and the maximum output signal pressure was 0.34 psig. The data were obtained for both acceleration and deceleration, and as seen from Figure 16, the hysteresis was approximately 0.01 psi. Preliminary data indicated that the threshold of the accelerometer was approximately 0.08 g's. Only a small variation in threshold was observed for two supply pressures, 10 and 40 psig.

For some applications, higher scale factors are required from the instrument without the use of amplification. This can be done in a hybrid device using a solid proof mass. There are several implementations of devices of this type by different manufacturers; typical of these is the schematic drawing shown on Figure 17 (Reference 10). A proof mass, M, is supported between two end plates, E, on a cylindrical gas bearing. A continuous flow of gas streams from the gas supply through the restrictor A_0 , where the pressure drops from P_0 to P_1 (or P_2) depending on which side is being discussed. It then enters the forcing cavity of diameter d. It escapes through the peripheral area at h_1 and h_2 and then is vented through the end plates to the atmosphere. When an acceleration is applied to the case, it moves relative to the proof mass. This causes the gaps to change, h_1 becomes smaller and h_2 becomes larger. As a result, a pressure differential across the proof mass develops in the forcing cavities. This differential is maintained by the supply at a pressure P. The pressure differential acting on the forcing cavity area creates a force that just balances the inertial reaction, causing the proof mass to accelerate with the case in the steady state. The output ($P_1 - P_2$), is linearly related to the acceleration. The scale factor is a function of the geometry and mass and is therefore constant. The proof mass is

supported on a cylindrical gas bearing made to minimize friction forces on the proof mass. In addition, it affords a restraintless suspension of the proof mass. The One "G" fluidic accelerometer shown in Figure 18 was tested against a typical performance specification. Figure 19 shows the output pressure versus input acceleration. The data points are shown. The two extreme lines show the performance envelope, as defined by the maximum signal error of $\pm 5\%$ F.S. and the maximum g error at zero output pressure of ± 0.002 g. These results illustrate that a high scale factor can be attained.

Other designs are available from other manufacturers. A different design proved that a high G range device is feasible. Figure 20 shows a photograph and typical test results on this device. (Reference 16).

The cylindrical seismic mass is supported radially by flexures which are designed to provide rigid lateral and angular support of the mass. Axial support is from gas thrust bearings that oppose the acceleration forces on the seismic mass.

Under the influence of axial acceleration forces, a pressure differential is built up between the two gas bearings to support the seismic mass. The change in pressure differential is linearly related to the acceleration with a high degree of precision. The output is taken from circumferential grooves in each gas bearing.

The accelerometer with ranges up to 400 g, has been built in both steel and aluminum, and normally operates at supply pressures of 150 to 200 psig. However the device can operate on supply pressures as low as 20 psig for low acceleration ranges.

Output pressure levels are 20 to 70 percent of the absolute supply pressure. Frequencies of the spring mass system are from 100 to 3000 cps, depending upon the range. Exact system response may be designed to suit any specific application.

Accelerometer gains range from 0.02 to 0.4 psid/g. If higher gains are required, the accelerometer may be provided with a fluidic proportional amplifier which will boost the differential pressure output to as much as 2 psid/g.

Still another implementation of the seismic mass fluidic accelerometer showed accuracies suitable for inertial navigation systems could be attained (Reference 17). The cylindrical seismic mass is supported on a fluid film, the equivalent of a hydrostatic bearing. An acceleration force tends to displace the mass along the sensitive axis. This motion causes a decrease in the gap between the mass and the pad, increasing the resistance to flow and the pressure on the pad in a manner as described earlier. The resetting pressure differential balances the acceleration force and this pressure differential, which is measured at the signal pressure ports, is proportional to acceleration.

A development model was designed, fabricated and tested and a final model was built. The results showed the following operating characteristics: (Reference 17)

Scale factor: 9.12 inches water per G
1-G linearity: 6×10^{-4} G
Null uncertainty: $\pm 2.2 \times 10^{-4}$ G
Null repeatability: $\pm 2.5 \times 10^{-4}$ G
Threshold: 5×10^{-5} G
Maximum Input: 9 G
Dynamic range: 2×10^{-5}

Later development incorporated a "squeeze film" damping technique that has increased the damping ratio from less than 0.05 to 0.7. The unit is shown in the photo in Figure 21a.

Figure 21b (Reference 6) shows yet a different design. In this device acceleration applied along the sensitive axis results in a deflection of seismic mass and jet pipe relative to the signal pickoff probe. The signal pressure is amplified and applied to the nulling nozzles, to produce a force to restore the mass to its neutral position. The restoring force is proportional to the differential pressure. Closed loop operation maintains the restoring force equal to the acceleration force. The scale factor (psi per g) is then a function of the seismic mass and of the area of the nulling nozzle.

In some specialized applications, it is desirable to sense the acceleration of a vehicle by a special purpose device. This unit has neither the precise performance nor the complexity of the accelerometers just described. In the flight of an aerospace vehicle, the performance during the boost phase has a direct effect on the trajectory of the flight. A major factor here is the propulsion system. Its performance can be monitored using onboard instruments by sensing pressure, temperature, fuel flow, etc. The most direct way to measure the performance of the engine is to measure the acceleration produced on the vehicle. A hybrid accelerometer was conceived which would sense the launch acceleration. The objective was to devise a high reliability, low cost device to monitor the time when a minimum acceleration of the vehicle is reached. A design having a minimum number of moving parts and imposing a minimum power drain on the gas supply was desired.

The Fluidic G Sensor and schematic are shown in Figure 22 a & b (Reference 18). The conversion of a sensed acceleration into a representative pressure signal is the basic operational function. Referring to Figure 22 the sensor consists of a seismic mass, a flat, unbonded elastomer diaphragm, and a variable vent plate. The inlet, outlet, and variable vent resistors shown are sized to ensure subsonic flow. Initially, supply pressure, P, passes through the fixed flow inlet resistor into the chamber forcing the diaphragm off its seat and permitting the fluid to escape out the variable vent. As acceleration is applied, the force acting upon the sensing mass will force the diaphragm down changing

the distance x and partially blocking the variable vent. The chamber and orifice above the seismic mass act as a damper to restrain the motion of the mass under dynamic conditions.

At a fixed acceleration level, a force balance is created in which the force on the mass due to the chamber pressure balances the acceleration force and the mass comes to rest. The value of this pressure is a measure of acceleration and is transmitted to the fluidic system. A detailed computer analysis of mass motion, fluid flow, vent area calculations, etc., are included in a separate paper. Results of tests are shown in Figure 23. The "G" sensor is an example where high accuracy is not required and where an analog signal is tolerable. In the complete system the signal is transmitted to a Schmitt trigger which switches at a discrete "G" level. Typically, this system is active for only a matter of seconds.

FLUIDIC ACCELEROMETERS - DIGITAL

In other specialized applications, the acceleration measurement is used in a computation scheme. Here, the device is active for an extended time period and accuracy is important. For example, the accelerometer signal may be integrated once (or twice) in a calculation of increments of velocity (or distance). It is desirable here to integrate a digital rather than an analog signal in order to preserve accuracy. Therefore, accelerometer concepts which yield digital outputs are of interest. Two devices under development are described in the following section.

Previously developed pneumatic accelerometers exhibited unacceptable sensitivity to environmental temperature changes and supply pressure variations. Both of these parameters affected performance in a non-linear fashion and were hard to compensate. In order to provide acceptable performance characteristics under these conditions, a proof-of-principle model of a unique concept for a fluidic accelerometer was analyzed. The accelerometer concept studied was unique in that acceleration was measured as a ratio of two frequencies generated by two fluidic oscillators. The idea was that when ratios are used, environmental influences which modify frequency will affect both oscillators identically, thus keeping the ratio of the frequencies constant.

The testing of this proof-of-principle model (PPDA) indicated several areas which required further development, namely, linearity and hysteresis (Reference 19). A follow-on program was instituted to reduce the nonlinearities and hysteresis by redesign of the device.

The basic concept for this digital accelerometer concept uses the ratio of two frequencies as a measure of acceleration expressed by $a = KN_1/N_2$. Thus frequencies N_1 and N_2 are generated by fluidic oscillators of identical design which will be affected identically by temperature and pressure variations.

The digital accelerometer consists of proof mass which is suspended by a spring in a cylinder. This mass responds to acceleration, moving two identical pistons in cylinders causing changes in volume (and capacitance) in the feedback circuit of a relaxation oscillator as shown in Figure 24. When a variable capacitance (or volume) is placed in the feedback line of a fluidic oscillators, as in the figure, the output frequency of the oscillator is a function of this capacitance. This function is generally non-linear, and accounts for the non-linear behavior of other fluidic accelerometer concepts, where direct conversion of proof mass motion into output frequency is used.

This accelerometer circumvents the problem by utilizing variations in oscillator period rather than oscillator frequency. Certain types of fluidic feedback oscillators previously developed exhibited a linear relationship (Figure 25) between variations in volume and period of oscillation. By using the change in volume created by the proof mass motion as a feedback volume for the oscillator, a linear relationship between acceleration and oscillator period exists.

The accelerometer concept is completed by processing the acceleration sensitive oscillator signals together with a high frequency, free-running oscillator signal, through a fluidic AND gate as shown in Figure 26. The number of pulses, N , from the free running oscillator, seen as an output and the AND circuit per period T of the volume controlled oscillator, will be in direct proportion to the acceleration, a . A fluidic counter accumulates the number of pulses, N , admitted through the AND gate and is reset after each period T .

A photograph of the sensor is shown in Figure 27.

The second principle utilizes a vibrating system which is acceleration sensitive (Reference 20). The digital fluidic vibrating string sub-assemblies are packaged diametrically opposite in a common housing. Each vibrating string subassembly consists of a round wire, wire terminations, a tension spring, a seismic mass, an input pressure nozzle, a receiver, and a nozzle and receiver support plate. The housing, in addition to providing a means for mounting the vibrating subassemblies, also accommodates a beat frequency detector element and a fluidic filter capacitor. A manifold network is an integral part of the housing. This network directs the input air supply to the nozzles and beat detector and the output pulses from the receivers to the various fluidic elements. A schematic diagram of the device is shown in Figure 28. The device operates in the following manner: A flow of gas (Air) at 5 psig, is introduced into the input port of the device and directed by the nozzles towards the midpoint of each wire, thus creating a disturbing force. This disturbing force excites each wire in a transverse mode of vibration at its fundamental natural frequency. The gas flow exciting the input nozzles is periodically interrupted by the wire motion, resulting in a sinusoidal pressure pulse (of the same frequency as the wire) which is detected by the receiver. The sinusoidal pulses from each receiver are then fed to the beat frequency detector element through the manifold

network, and a modulated pressure signal containing the sum and difference frequencies is obtained. This modulated signal is demodulated by the pneumatic filter capacitor and a difference frequency is generated at the output port of the device.

The natural frequency of each wire is directly proportional to the square root of the tension in each wire. As acceleration is applied along the input axis of the device, the tension in each wire changes by virtue of the acceleration forces on the seismic mass attached to each string assembly. The tension in one wire is increased, thus raising its natural frequency, while the tension in the other wire is decreased thus reducing its natural frequency. The beat difference frequency which appears at the output port of the device is proportional to the acceleration and therefore can be used as a direct measure of the absolute acceleration applied. The device could also be used as an integrator to provide a measure of the velocity change acquired during a specific time interval by an accumulated frequency difference count.

Typical performance results are shown in Figure 29a (Reference 20) and a photo is shown in Figure 29b.

ATTITUDE GYROS

In many aerospace systems it is desirable to control the attitude of the vehicle. Hence an attitude gyro is needed. A means for sensing the attitude with a fluoric device (no moving parts) has not yet been demonstrated and perhaps this objective is the most difficult to achieve.

For control of a vehicle about two axes, a two-degree-of-freedom gyro is a necessity. This function is best performed by elements having a few moving parts. The term "hybrid" fluidic sensor is used to describe a sensor in which a mechanical moving element is introduced into a pure fluid component to obtain performance beyond the current state-of-the-art for fluoric devices. The use of a limited number of "hybrid" fluidic devices in a fluoric system has certain advantages over the fluidic approach at this time. Such devices provide simplicity, low cost, and are less affected by severe environmental conditions.

A Two Axis Pneumatic Pickoff (TAPP) gyroscope was successfully tested several years ago by the Army using Little John missiles as test vehicles. The miss-distance from the aiming point was negligible (Reference 10).

The gyroscope rotor, supported on a gas bearing, is the only moving mechanical part. The gyroscope contains a spin-up, bearing, and pick-off gas supply bottle; a squib ignited activator; a unique internal regulator; a gyro rotor and gas bearing assembly; a two-axis pneumatic pickoff, and a fluoric summing module. Versions are available which provide either analog or digital pneumatic output. These meet rigid performance specifications in operating environments over 1200 G's continuous or shock loads and non-operating shock loads 10 times greater. A photo of the TAPP gyro is shown in Figure 30 (Reference 21).

An attitude gyro of a different design is shown in Figure 31 (Refer-

ence 6). This unit includes automatic sequencing for startup and uncaging and is adaptable for use on stable platforms. The gyro parameters and the drift characteristics are as follows:

GYRO PARAMETERS

Size:	1½ inches diam. by 2 1/8 long
Weight:	0.3 lbs
Angular Freedom:	+ 10°
Readout Range:	Linear to + 3°
Scale Factor:	Uncompensated - 0.8 psi/deg Compensated - 0.6 psi/deg
g Capability:	100 g @ 35 psig supply
Spin Time:	100 RPM/sec/psi above cage pressure
Operating Speed:	Uncompensated - 6000 to 15,000 RPM Compensated - 3000 to 5000 RPM
Caging Pressure:	30 to 40 psig

GYRO DRIFT CHARACTERISTICS

100 g CAPABILITY

	SN #1	SN #2 Uncomp.	SN #2 Comp.
Bias Drift	10°/hr	10°/hr	50°/hr
Erection Drift			
in Phase #1	90°/hr/deg	165°/hr/deg	55°/hr/deg
#2	72°/hr/deg	240°/hr/deg	90°/hr/deg
Quad. #1	24°/hr/deg	100°/hr/deg	25°/hr/deg
#2	50°/hr/deg	80°/hr/deg	40°/hr/deg
G Sensitive			
Spin Axis	360°/hr/g* @ 6000 RPM	300°/hr/g @ 6000 RPM	*Rotor was not mass balanced
Readout			
Scale Factor	0.8 psi/deg	0.8 psi/deg	0.6 psi/deg
Noise (100Hz BW)	20 arc min	20 arc min	20 arc min
Bandwidth	300 rad/sec	300 rad/sec	300 rad/sec
Cage Repeatability	1.0 millirad	1.0 millirad	1.0 millirad

A third attitude gyro design is pictured in Figures 32 and b. Tests of this unit provided the following results (Reference 22).

FLUIDIC GYRO TEST RESULTS

Drift Bias	84 Degrees/Hour
Acceleration Sensitive Drift	1.17 (SA), 0.31 (IA) Degrees/Hour/msec ⁻²
(Acceleration) ² Sensitive Drift	0.018 Degrees/Hour/m ² sec ⁻⁴
Auto-Erection	1.0 Degrees/Hour/Hz/rad
Alignment Error	1.0 mrad (maximum)
Uncage Error	1.0 mrad (maximum)
Pickoff	
Threshold	1.0 mrad
Null Offset	1.5 mrad
Flow Impact Bias	1.0 Degrees/Hour
Linearity 0 - 2 Degrees	0.28 Percent

TABLE III

SENSOR	OPERATIONAL CHARACTERISTICS		RELIABILITY & USAGE FACTORS		
	ACCURACY F.S.	RESPONSE READOUT SEC	LIFE @3000°F	MAINT.	COST
THERMOCOUPLE	+4.8%	.07-1.5 Point Total	100 Hr	Very Good	Very Good
FLUIDIC SENSOR	+2.5%	.01 Point Total	100 Hr	Good	Good
ULTRASONIC AIR GAP	+2.9%	.01 Average Static	5000Hr	Poor	Good
ELECTRON BEAM	+2.5%	.01 Average Static	1000Hr	Poor	Good
OPTICAL IM- MERSED TARGET	+2.3%	.07 Point Total	150 Hr	Good	Good
RESISTANCE	+5.1%	.07-1.5 Point Total	100 Hr	Very Good	Very Good
LASER TECHNIQUES	+2.5%	.01 Point Static	5000Hr	Poor	Poor
PNEUMATIC	+7.0%	.1-1.0 Point Total	200 Hr	Poor	Good

FLUIDIC GYRO TEST RESULTS - con't

	2 - 5 Degrees	1.85 Percent
Scale Factor		0.025 Ncm ⁻² /Degrees
Angular Freedom		+ 10 Degrees
Maximum Pickoff Angles		+ 5 Degrees
Spin-Up Time		4 Seconds
Operating Time		60 Seconds

A fourth attitude gyro design is shown in Figure 33 (Reference 23). The overall size of this gyro is $2\frac{1}{2}$ " in diameter and $3\frac{1}{2}$ " long. The objectives were to develop a fluid pickoff that used the natural rotor boundary layer as the power source for the sensor, improve gyro uncage repeatability to achieve a 0.5-mrad 1σ value, develop new lapping methods to advance the state of the art of rotor cavity fabrication, and verify gyro performance in a simulated missile vibration environment.

TEMPERATURE AND CONCENTRATION SENSORS

An important characteristic of fluidics is the dependency of the performance of certain fluidic elements on the properties of the fluid. This is particularly significant in the case of gases. Here the effects are so pronounced that some devices can be used to detect changes in these properties and therefore become sensors of that property of the gas. Of particular significance is the effect of acoustic properties on the frequency of a fluidic oscillator. Since the speed of an acoustic wave is a function of the molecular structure and the density and temperature, the fluidic oscillator becomes a basic building block for sensing gas temperature or for detecting changes in concentrations of a mixture of gases of different densities.

There are two basic oscillator designs, the jet-edge resonator cavity and delay line relaxation oscillator. Both have been used as temperature/concentration sensors. Typical of the applications of the jet-edge cavity resonators is the carbon dioxide concentration sensor (Reference 24). The physical configuration of this device and the performance characteristics are as shown in Figure 34. Devices having a similar physical configuration have been applied extensively for temperature measurement of gases. These devices can be designed for use over a wide temperature range from room temperature to 4000° F and above.

A typical application is in the aircraft jet engine. Here the measurement of the turbine inlet gas temperature is particularly important for the optimum control of the engine parameters. The fluidic sensor excels among all other types in accuracy and response time while holding good ratings in maintenance, weight and cost (Reference 25). A comparative evaluation is shown in Table III.

These devices are digital in nature, that is, the fluidic signal is a series of pulses, a frequency or a differential frequency.

Other devices produce analog signals, that is, signals which are steady but modulated. Typical among these is a passive flueric gas concentrator sensor that can be used to determine the concentration of a gas relative to a reference gas mixture. The sensor is composed of linear (viscosity dependent) and nonlinear (density dependent) fluid resistors connected in a bridge circuit. The bridge output is a differential pressure signal proportional to the unknown concentration. The low output signal of the sensor is amplified by a high-gain laminar proportional amplifier. The sensor is capable of sensing from extremely low concentrations to full gas concentrations with good linearity and low noise. (Reference 26). The schematics and geometry are as shown in Figure 35. The operating characteristic is as shown in Figure 36.

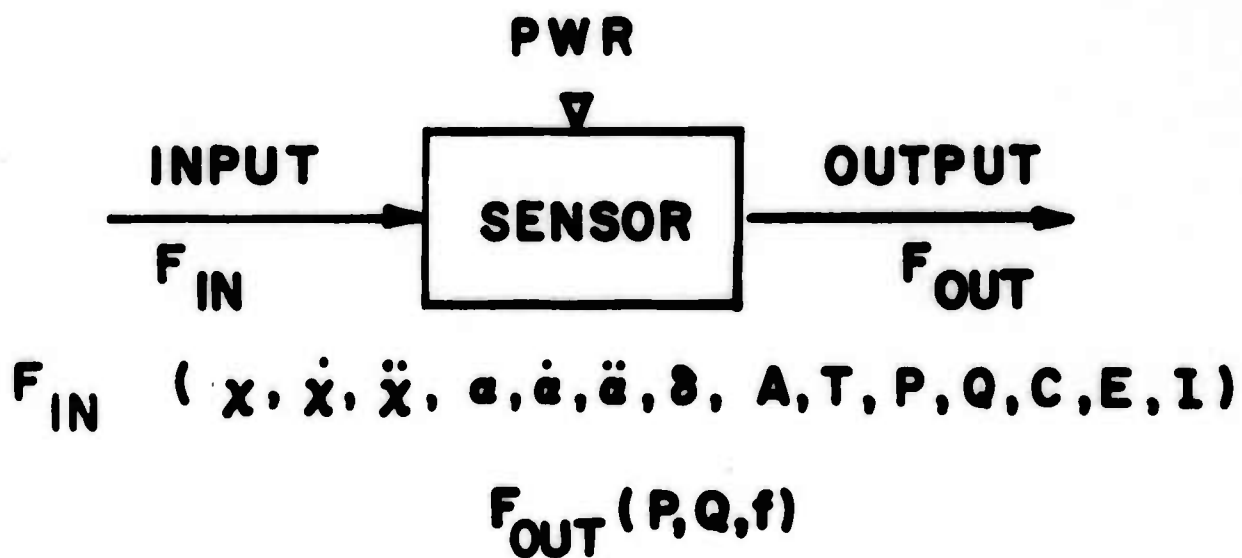
REFERENCES

1. Higgins, P.T., "How to Interface with Fluidics", Bendix Electrical Components Division, December 1968
2. "Fluidics Components, Circuits and Systems", Catalog 1170, Bowles Fluidics Corporation
3. "Fluidics Industrial Control Modules, Sensors and Interfaces" Corning Fluidic Products
4. Belsterling, C.A., "Sensing with Air", ISA Conference and Exhibit, October 1970, Philadelphia, Pa.
5. Beeken, B.B. "An Acoustic Fluidic Sensor", 23rd Annual ISA Conference October 1968
6. "Fluid Power Control Competence", General Electric Co.
7. Swartz, E., "A Fluidic Non-contacting Gage", Harry Diamond Laboratories, personal communication
8. Katz, S. and Hastie, E., "Fluidic Sensing of Rotational Speed Using Spur Gears", ASME Gas Turbine and Fluids Engineering Conference, San Francisco, March 1972
9. Ziebolz, H., Instruments, September 1942
10. Schmidlin, A.E., "Fluidic Inertial Instruments", ISA Aerospace Conference, Las Vegas, May 1969
11. Griffin, W.S., Coultas, R.K., "The Axisymmetric Laminar Jet Angular Rate Sensor", ASME Gas Turbine and Fluids Engineering Conference, San Francisco, March 1972
12. Evans, R.A., "Fluidic Technology", Honeywell Government and Aeronautical Products Division, January 1971
13. "Superjet", Hamilton Standard Division of United Aircraft, private communication
14. Ostdiek, A.J., Harry Diamond Laboratories, personal communication, (also Sampson Patent, Honeywell)
15. Rakowsky, E.L., Schmidlin, A.E., De Santis, M., "A Fluoric Accelerometer", Journal of Dynamic Systems Measurement and Control, June 1973
16. "Pneumatic Seismic Mass Accelerometer", Bendix Research Laboratories
17. Evans, R.A., "Fluidic Accelerometers", Honeywell Government & Aeronautical Products Division, personal communication
18. Schmidlin, A.E., Staley, C.H., "Military Fluidics", Ordnance, November-December 1972
19. Bravo, V., "Development of an Improved Digital Accelerometer", Martin Marietta Aerospace, October 1973
20. Clark, W.K., "Testing & Evaluation of a Fluidic Vibrating String Accelerometer", AVCO Systems Division, November 1973
21. Chiafulio, D., Singer - Kearfott Division, personal communication
22. Brodersen, R., "Externally Pressurized Gas Bearings for Inertial Guidance Platforms and Gyros", BHRA Sixth International Gas Bearing Symposium, Southampton, V.K. March 1974
23. Rodgers, A., Widner, R.K., "Spherical Hydrostatic Gas Bearing Gyro Phase II", U.S. Army Missile Command Technical Report RG-72-20 November 1972
24. Villarroel, F., and Joyce, J.W., "Fluoric Carbon Dioxide Concentration Sensor", ASME Winter Meeting, November 1970

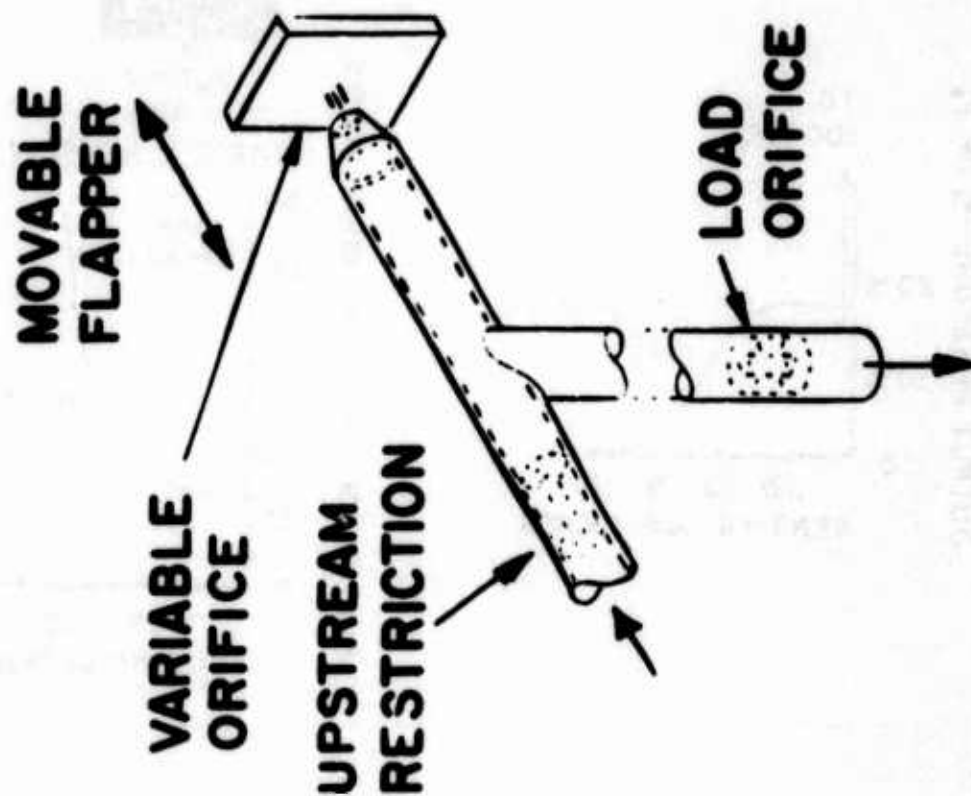
REFERENCES

24. Small, L.L., "Turbine Engine Sensors for High Temperature Applications", ASME Gas Turbine and Fluids Engineering Conference, San Francisco, March 1972
26. Villarroel, F., and Woods, R.L., "Analog Fluoric Gas Concentration Sensor", HDL-TM-73-9, June 1973

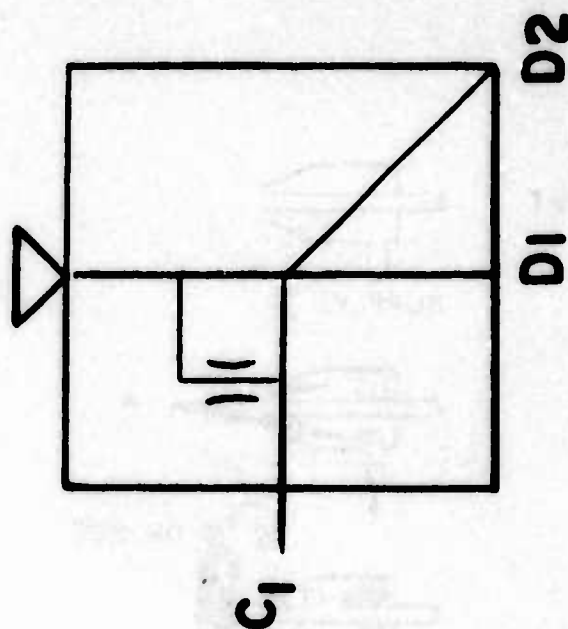


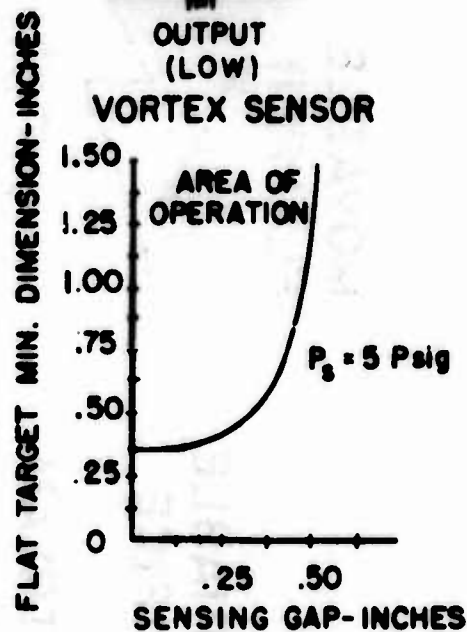
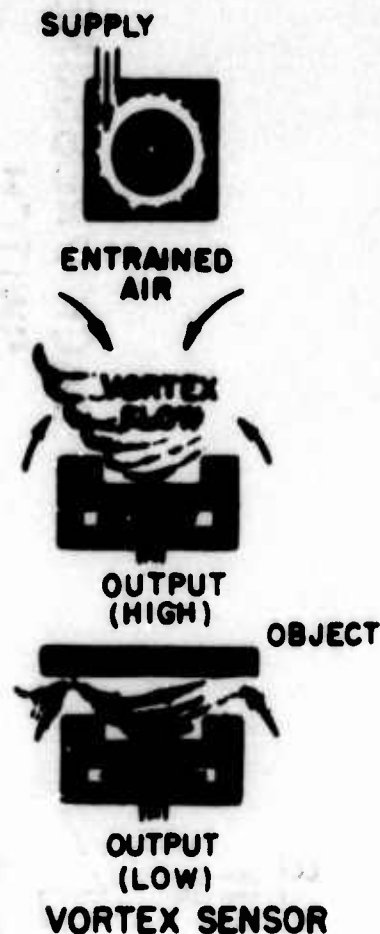
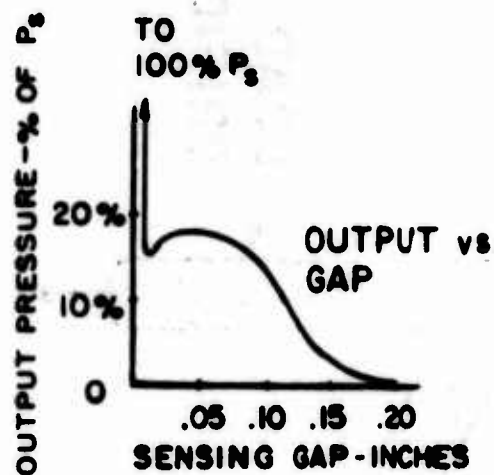
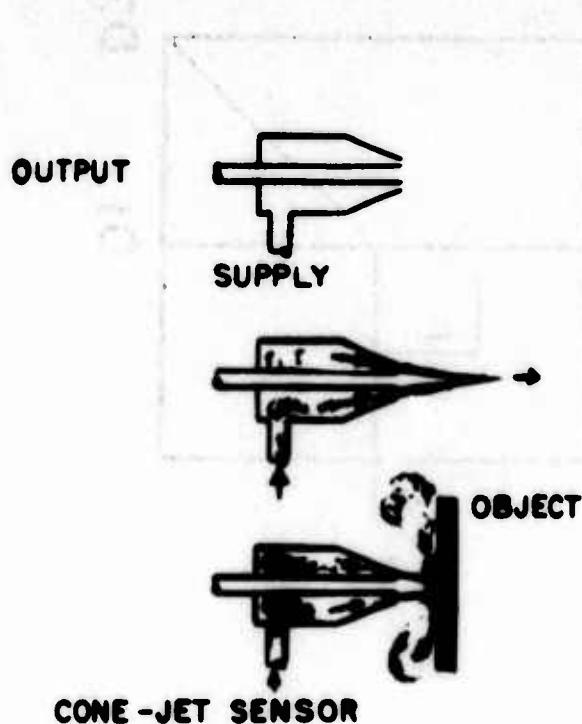


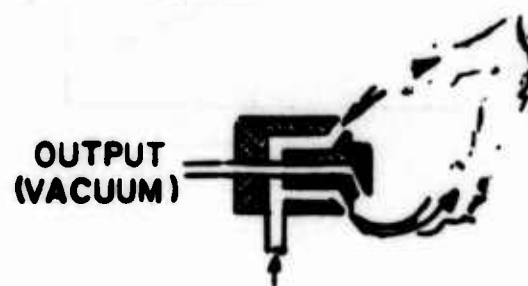
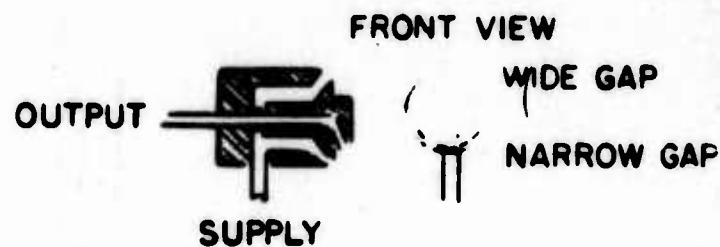
1 BLOCK DIAGRAM OF SENSOR



**BACK PRESSURE
SWITCH**







OJ PROXIMITY SENSOR

MODEL	NOMINAL SENSING DISTANCE	OUTPUT SIGNAL AT 3 PSI SUPPLY PRESSURE		AIR CONSUMPTION AT 3 PSI SUPPLY PRESSURE
		NEG	POS	
A	0.12 INCH		3 IN. H ₂ O	0.7 SCFM
B	0.3 INCH	4 IN. H ₂ O		0.4 SCFM
C	0.7 INCH	4 IN. H ₂ O		0.75 SCFM
D	1.2 INCH	4 IN. H ₂ O		1.4 SCFM
E	.3 INCH	PROPORTIONAL		0.9 SCFM

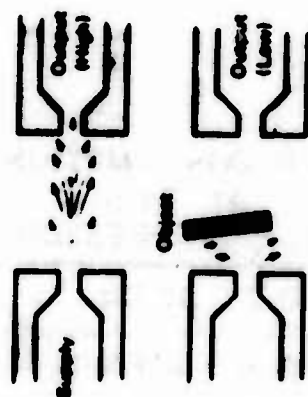


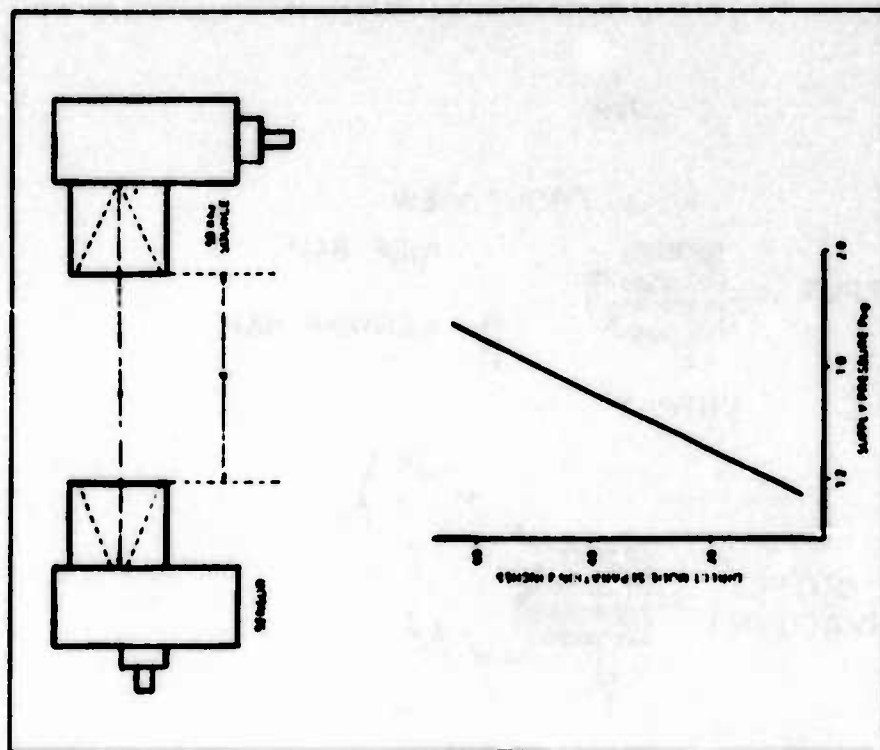
Figure 10. Interruptible Jet Sensor



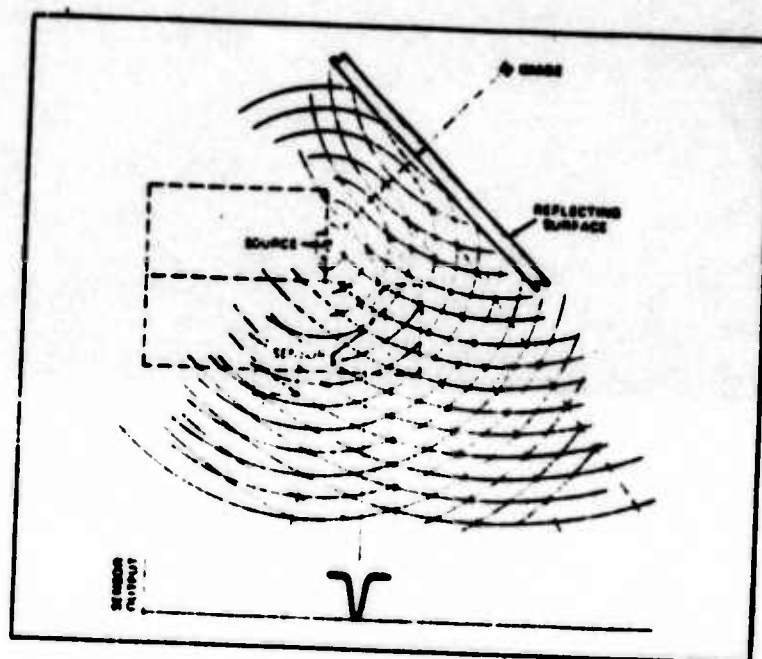
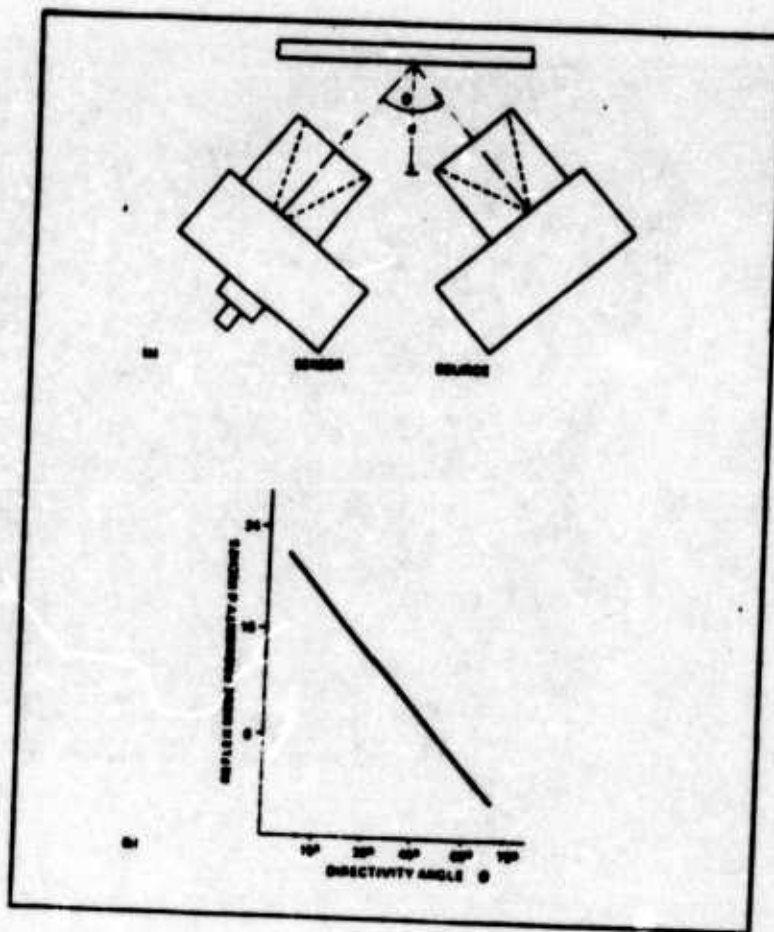
For Acceptable Efficiency:

- $A_1 > 0.4A_2$
- $0.8A_2 < A_3 < 1.5A_2$
- $10A_3 < A_4 < 20A_3$
- $20 < A_5 < 50$
- $D < 100$
- $50 < A_6 < 120$

Design Parameters for Interruptible Jet



4. INTERRUPTIBLE SENSORS



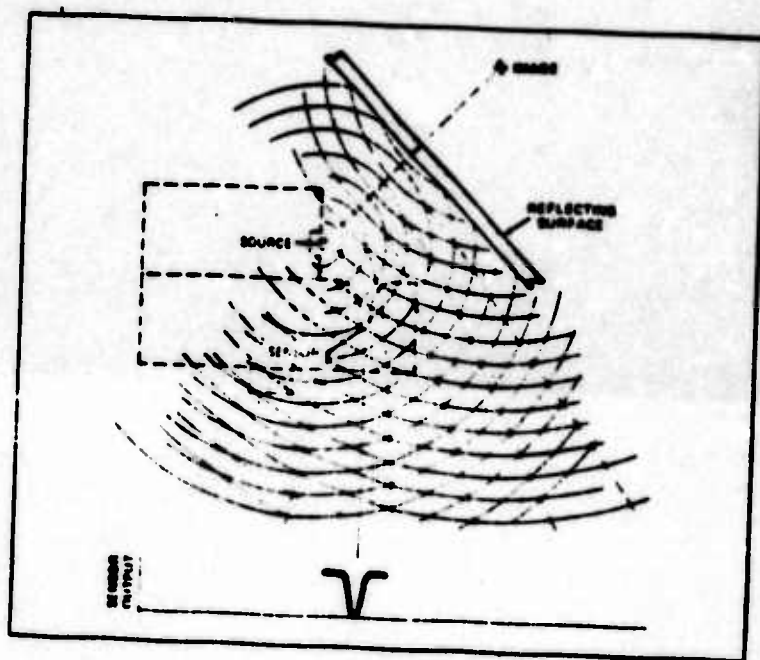
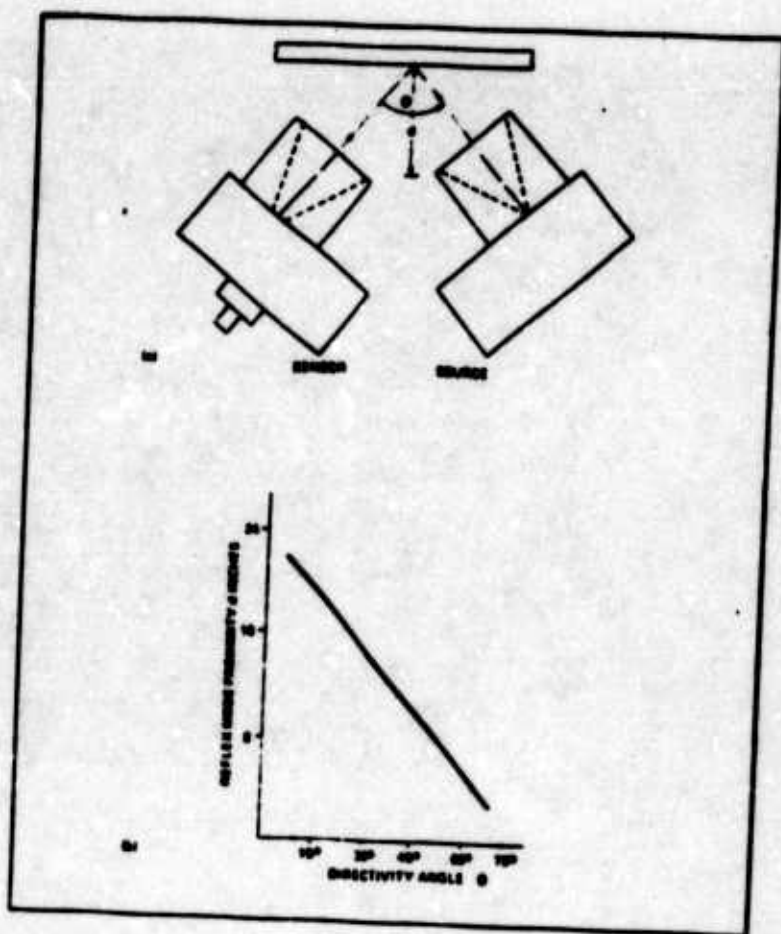


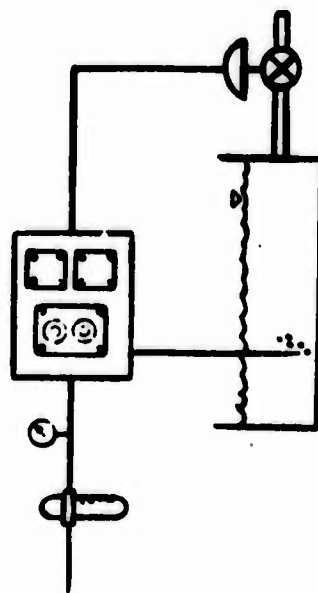


FIGURE 6. FLUIDIC EAR AND OJ PROXIMITY SENSOR (1 of 2)

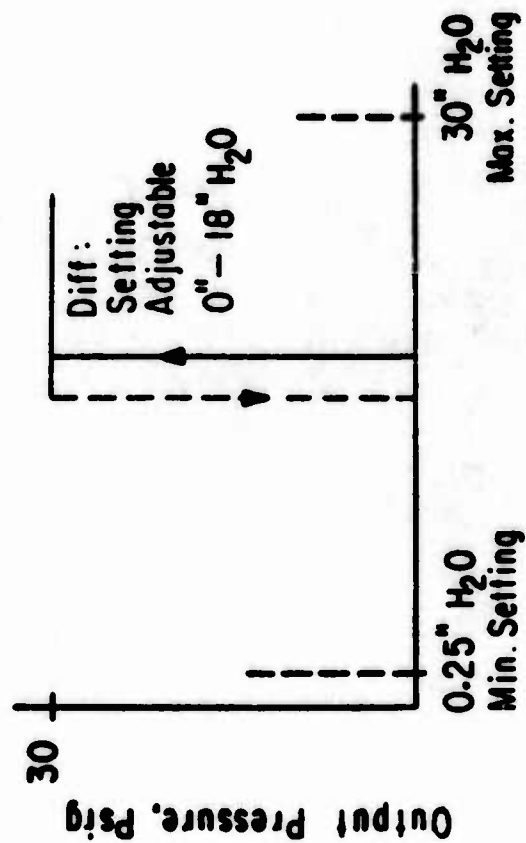


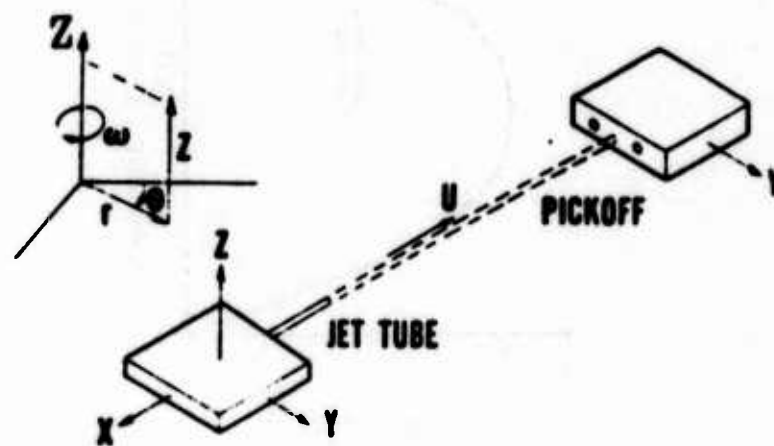
FIGURE 6. FLUIDIC EAR AND OJ PROXIMITY SENSOR (2 of 2)

INSTALLATION DIAGRAM

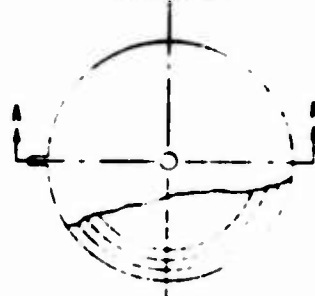
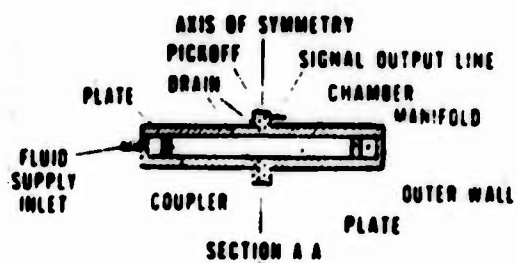


SWITCHING CHARACTERISTIC





GARDEN HOSE DEVICE

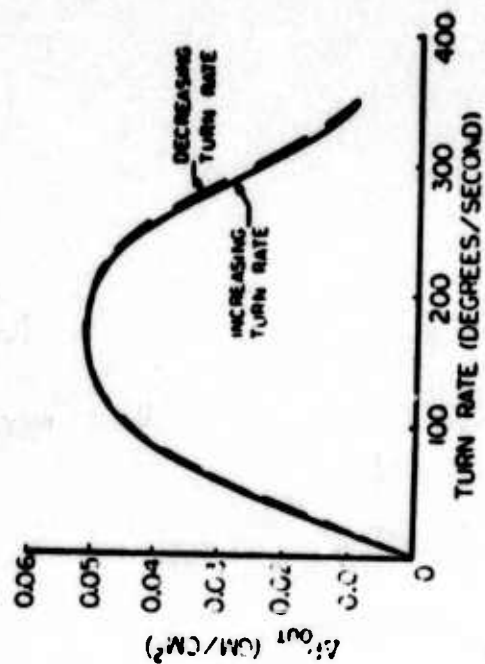
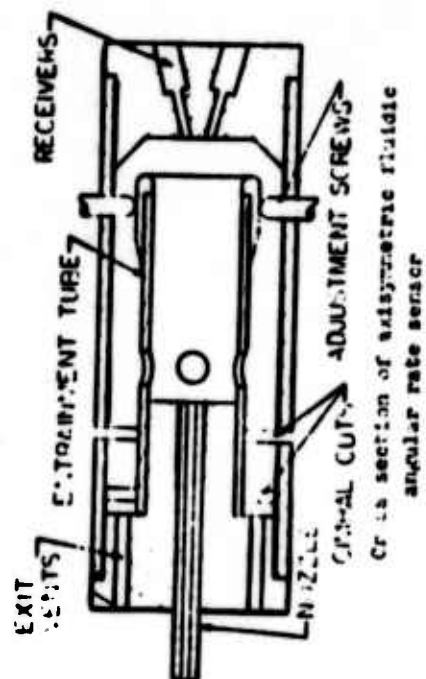


ANGULAR RATE SENSOR



SWIRLING FLOW IN SENSOR

8 ANGULAR RATE SENSORS



9 AXISYMMETRIC RATE SENSOR

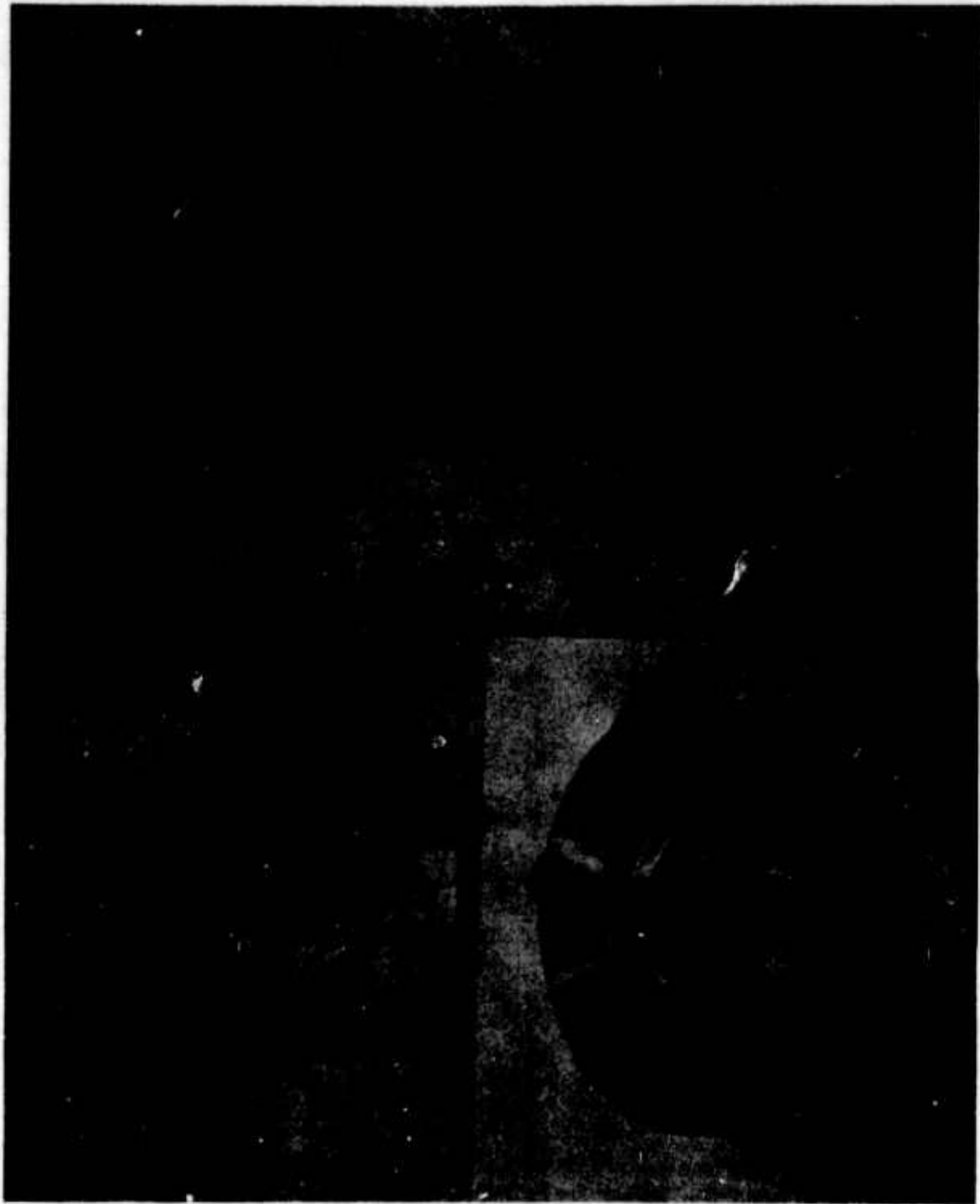


FIGURE 10. RATE SWITCH

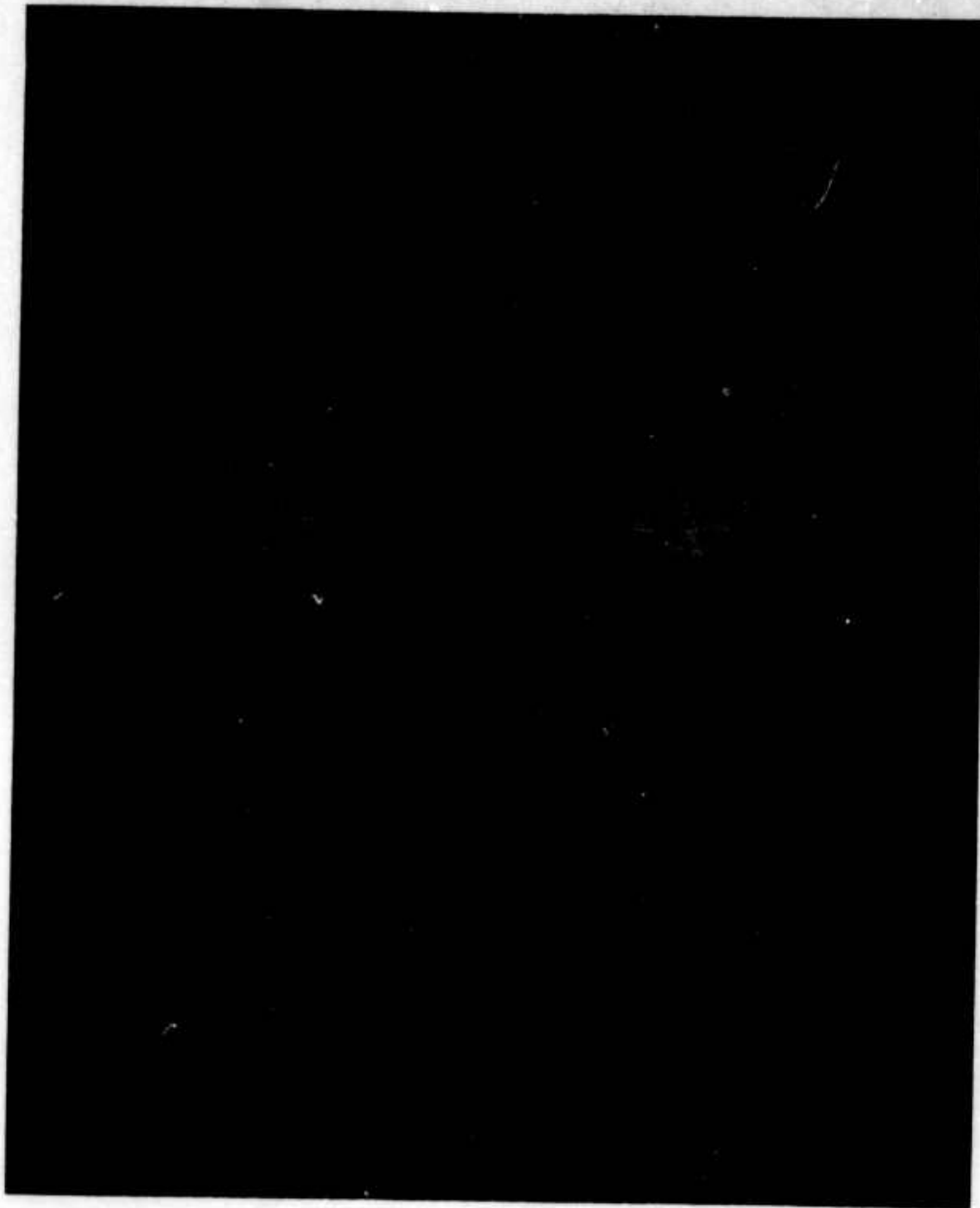
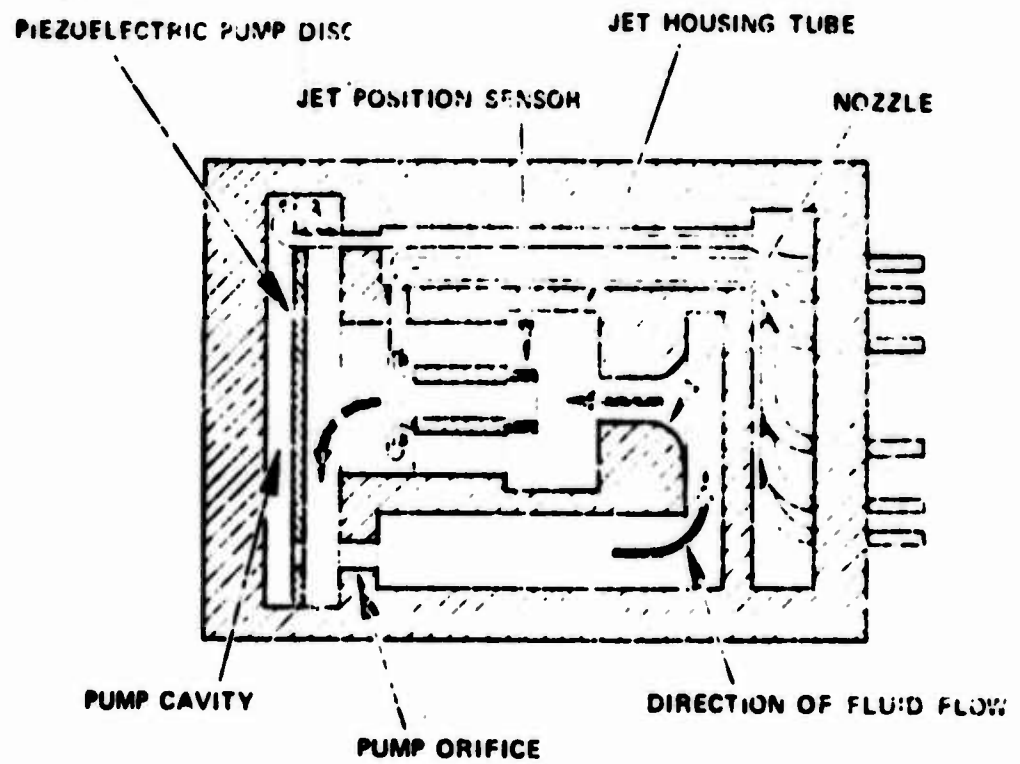
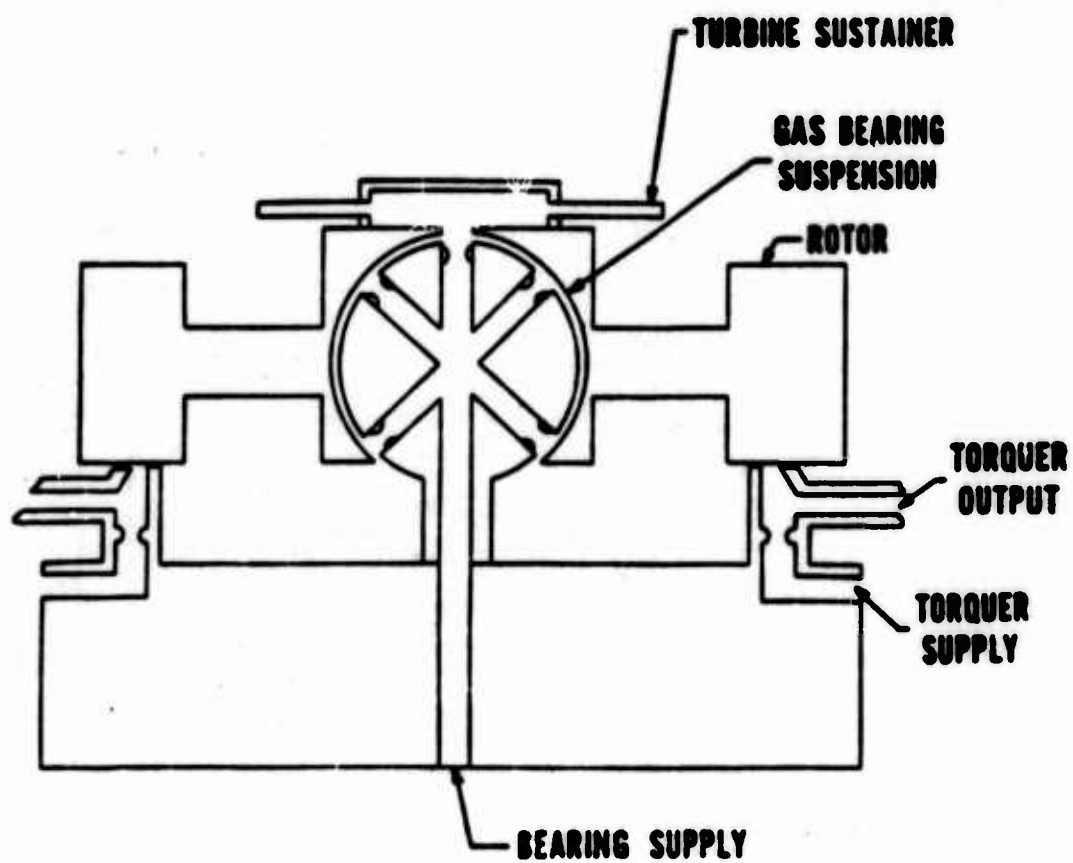


FIGURE 11. VORTEX RATE SENSOR



12 HYBRID RATE SENSOR



13a SCHEMATIC - ANALOG RATE GYRO

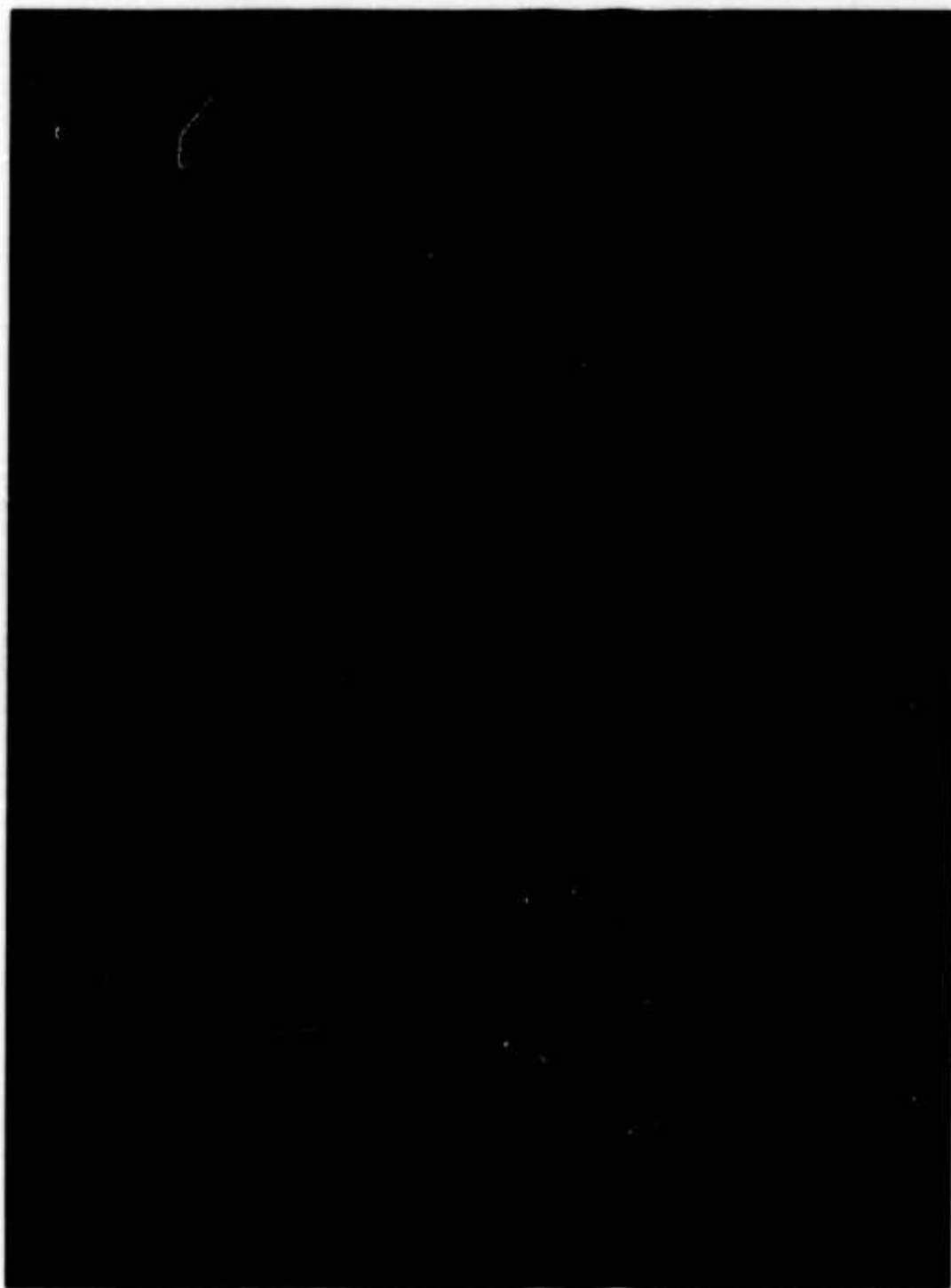
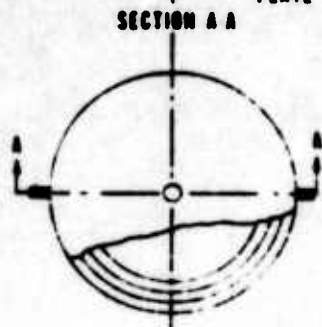
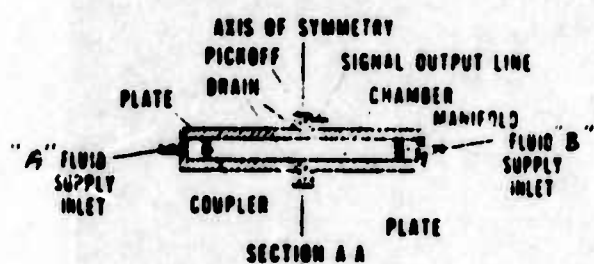
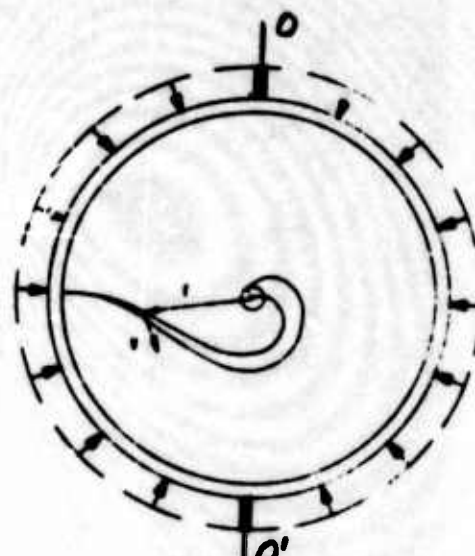


FIGURE 13b. ANALOG RATE GYRO

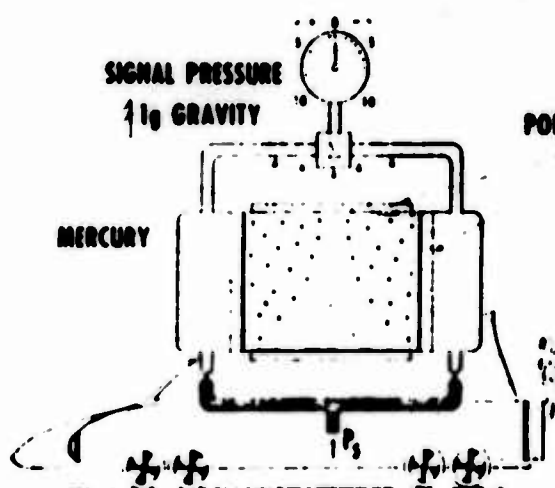
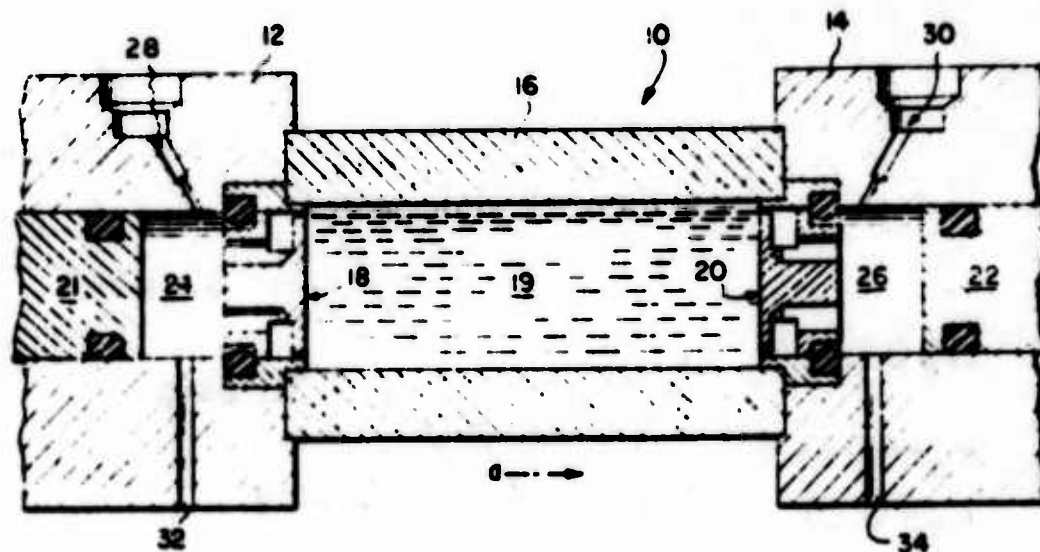


ACCELEROMETER

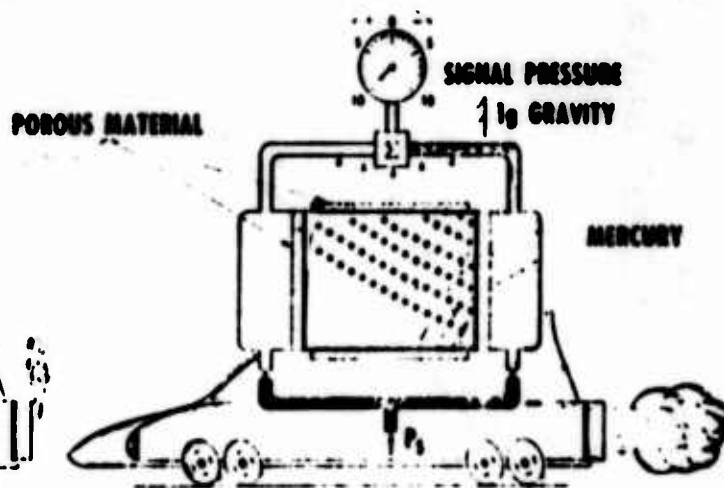


SWIRLING FLOW IN SENSOR

14 DUAL FLUID ACCELEROMETER

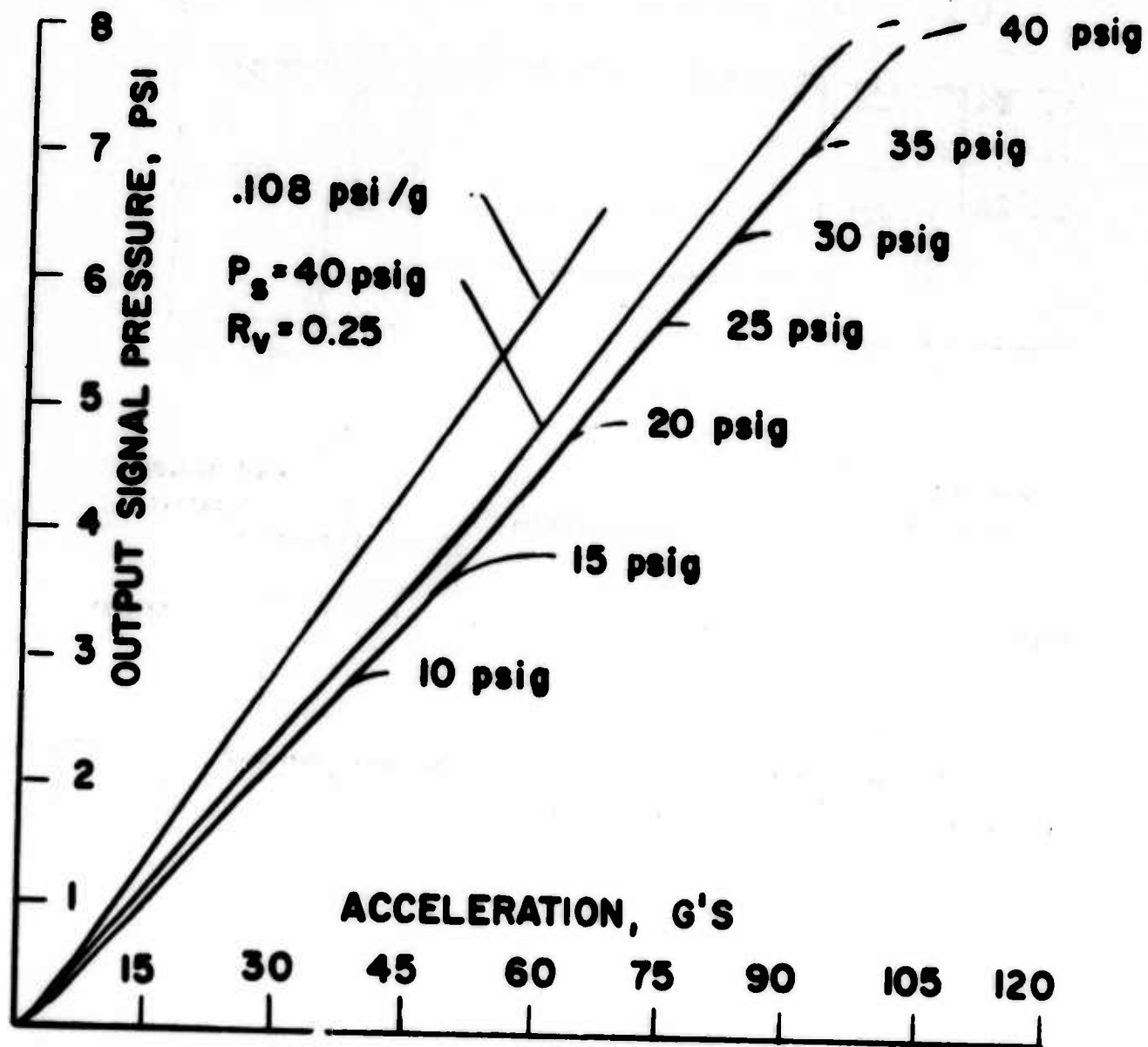


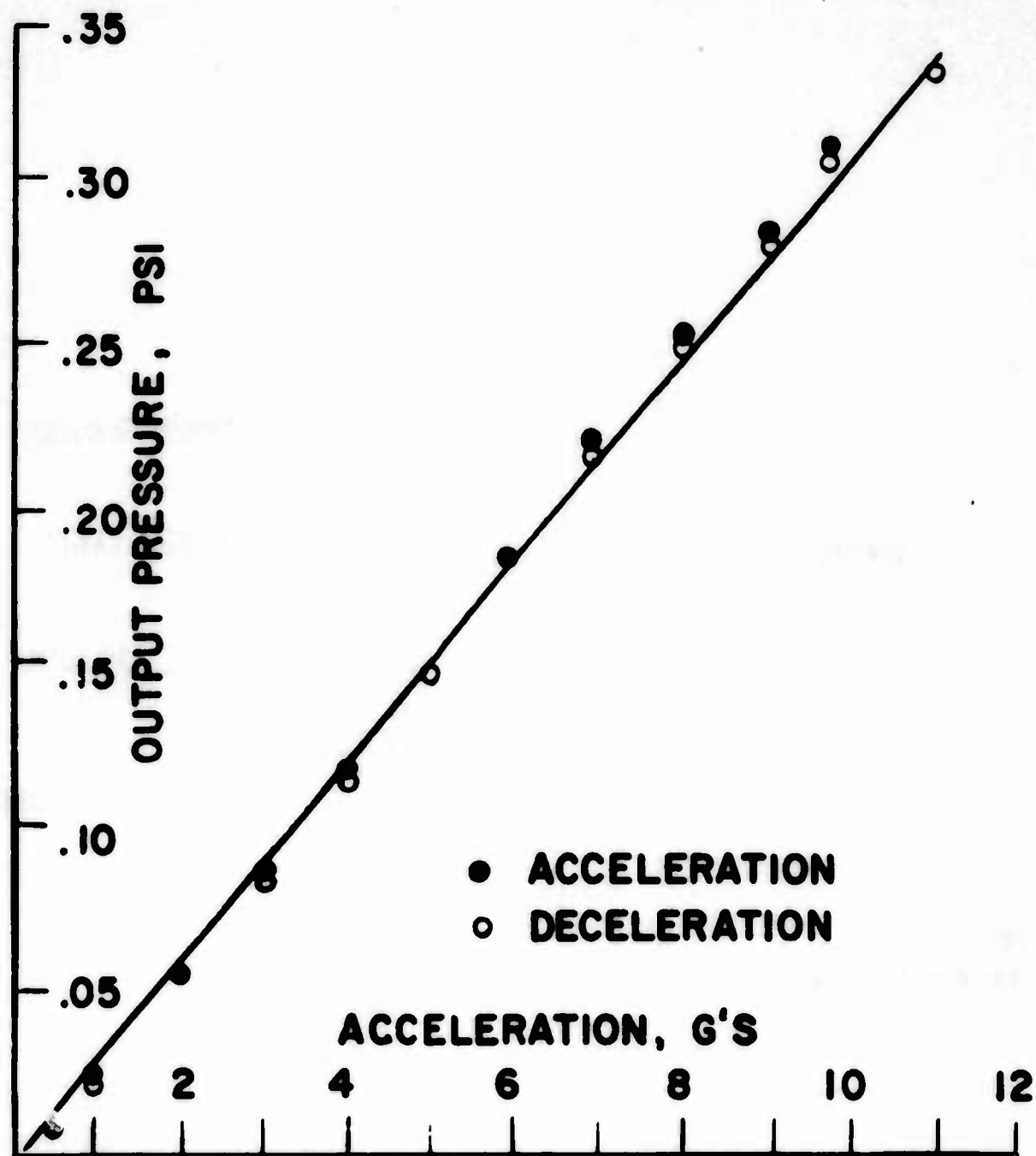
NO LONGITUDINAL MOTION



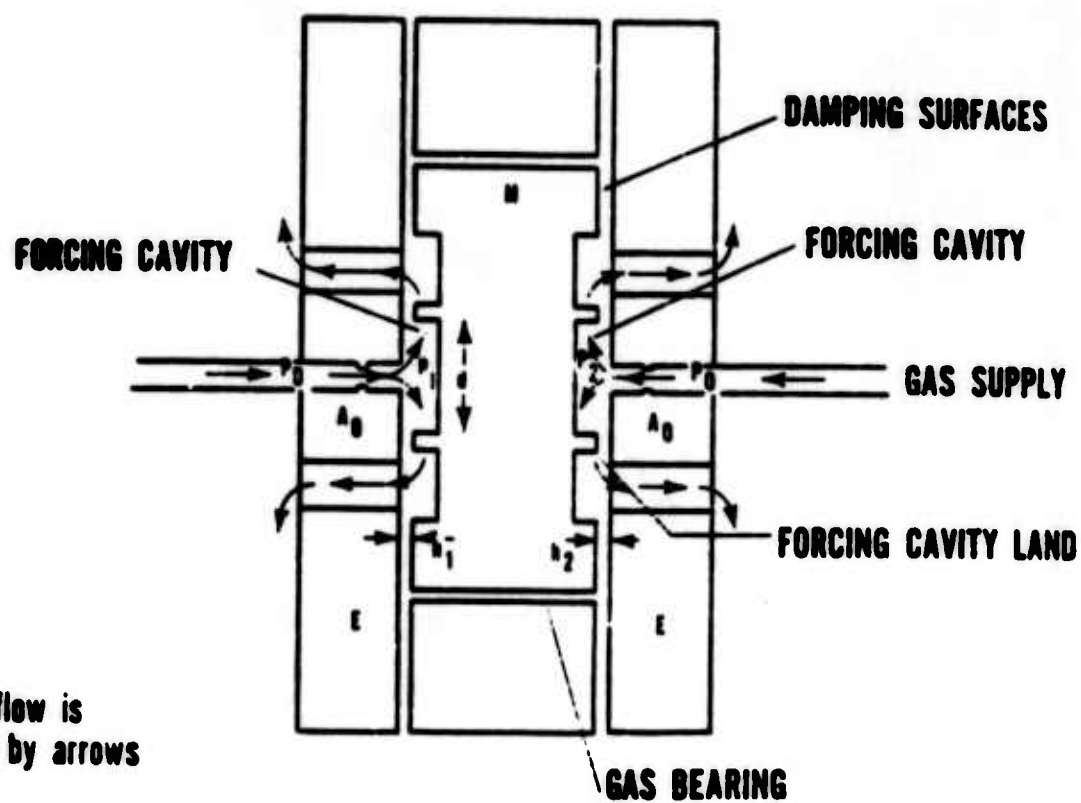
10g LONGITUDINAL

15 FLUIDIC ACCELEROMETER





The gas flow is indicated by arrows



17 SCHEMATIC - HYBRID ACCELEROMETER



FIGURE 18. FLUIDIC ACCELEROMETER

19 FLUIDIC ACCELEROMETER - TEST RESULTS

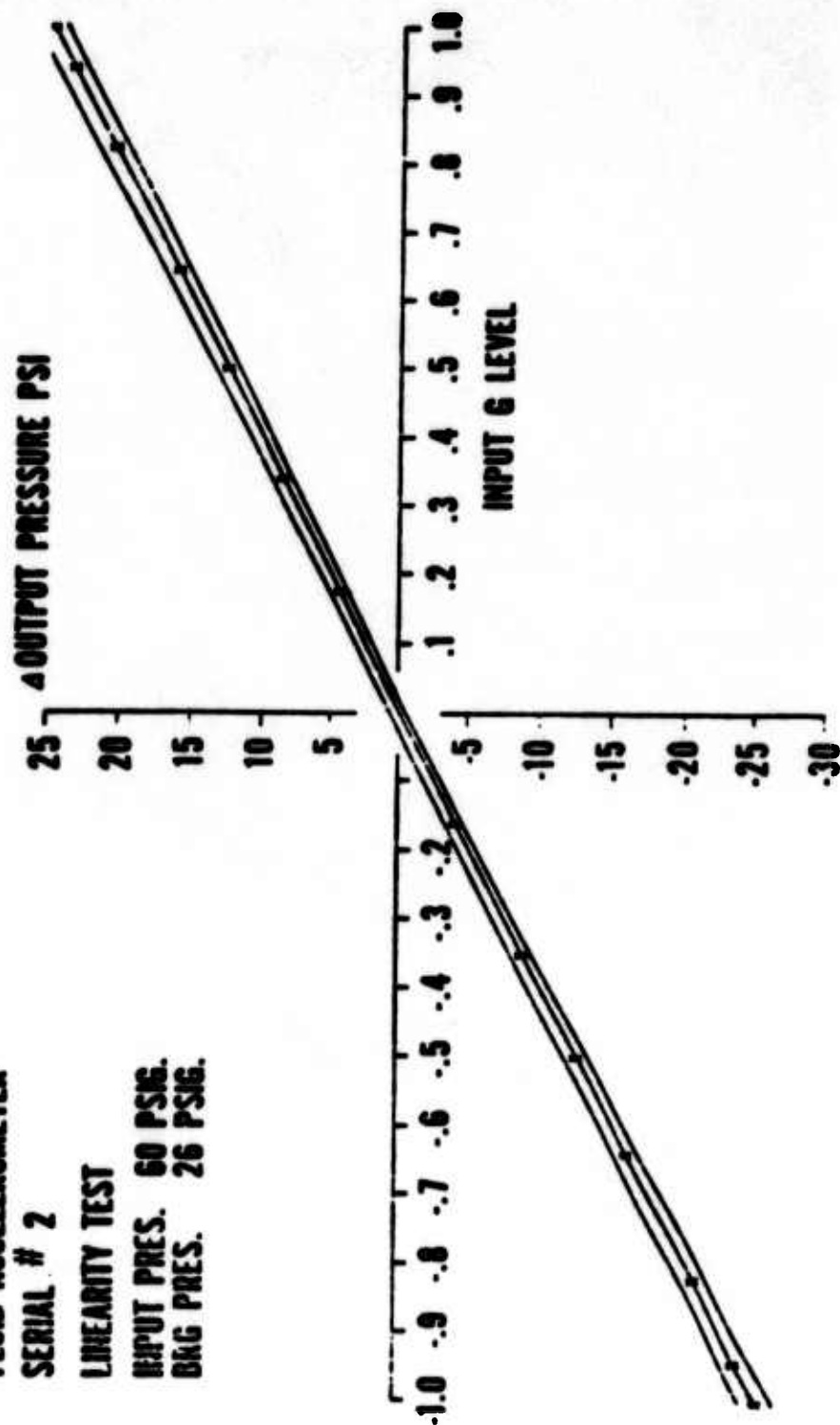
FLUID ACCELEROMETER

SERIAL # 2

LINEARITY TEST

INPUT PRES. 60 PSIG.

BKG PRES. 26 PSIG.



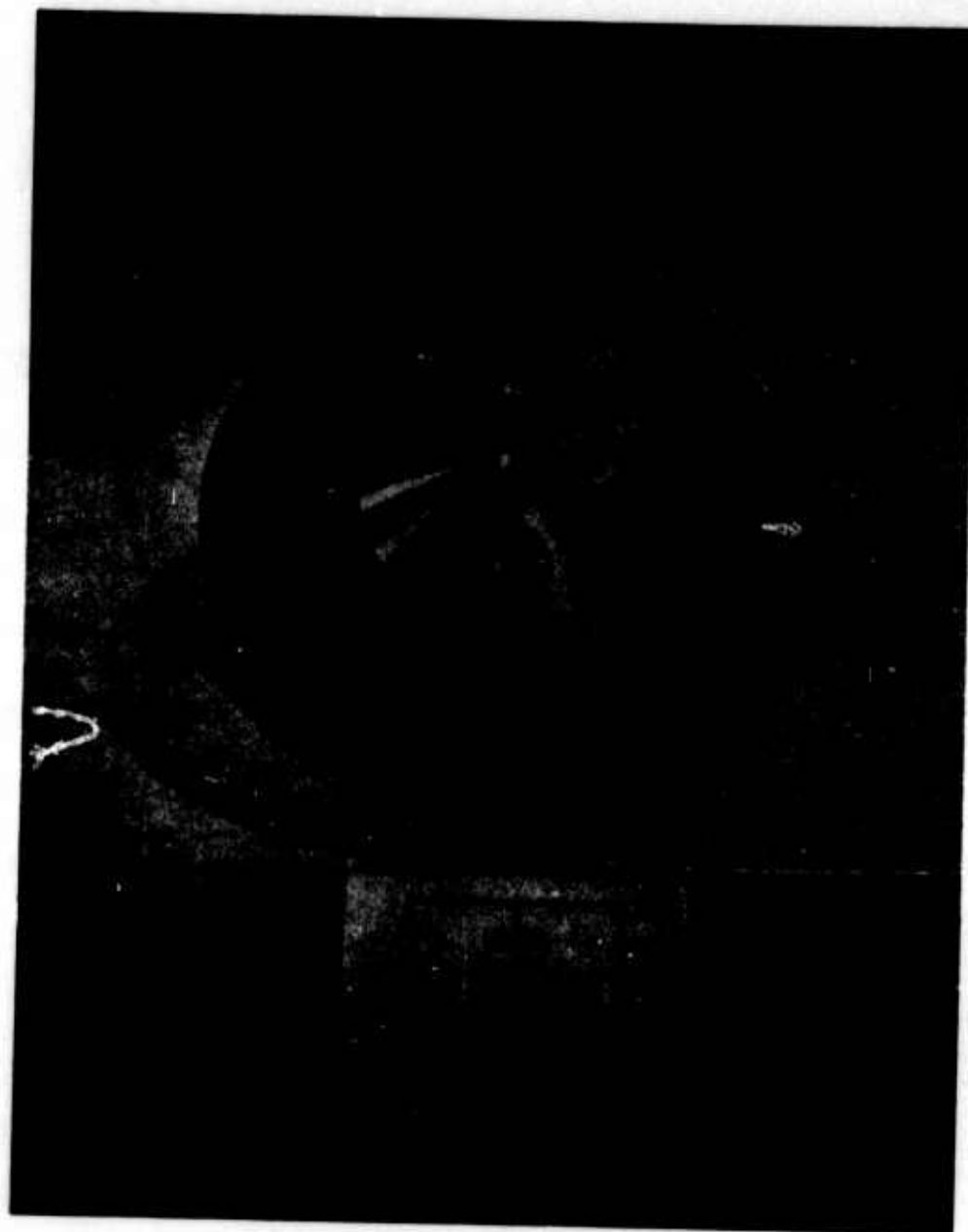
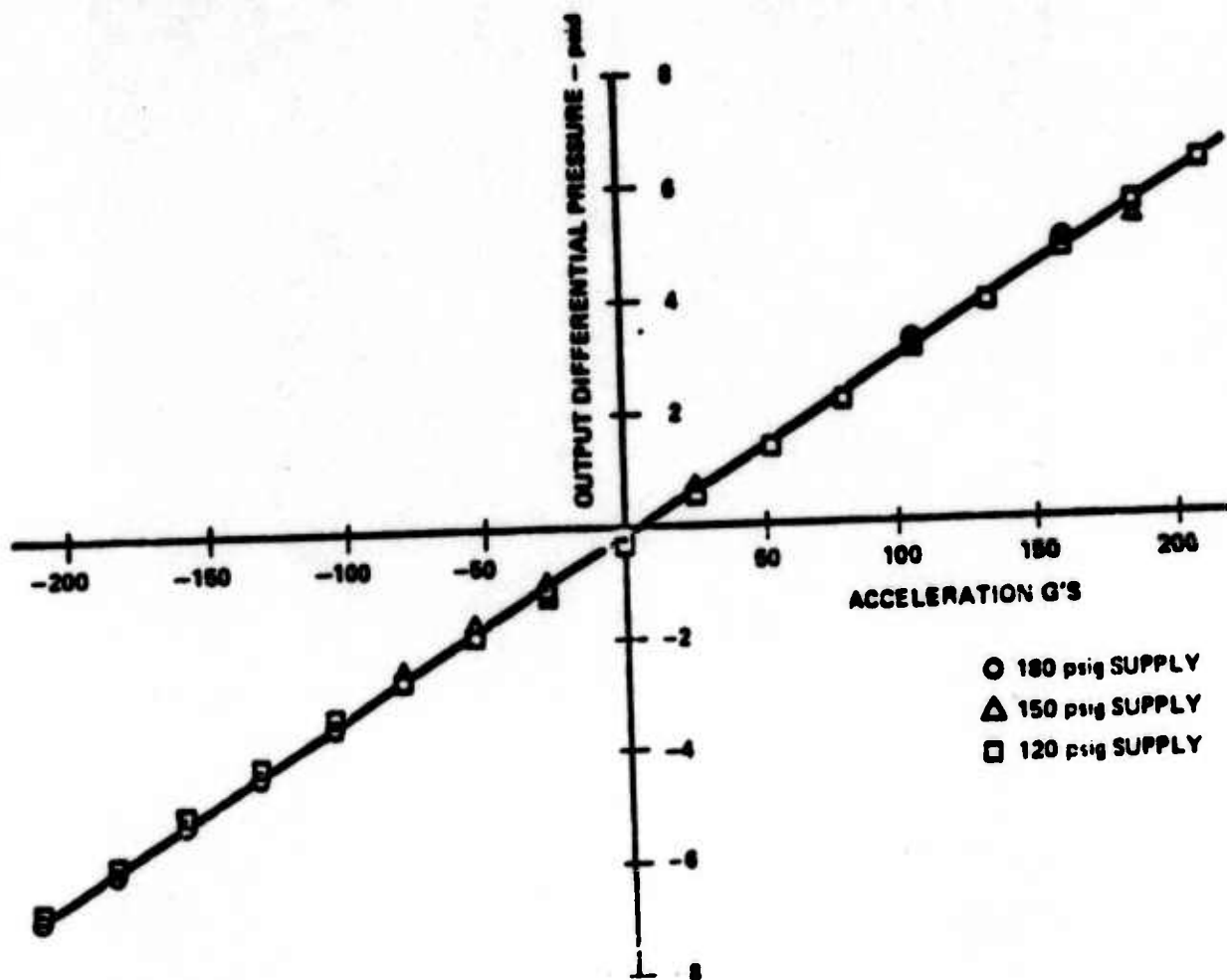


FIGURE 20. FLUIDIC ACCELEROMETER AND TEST RESULTS (1 of 2)



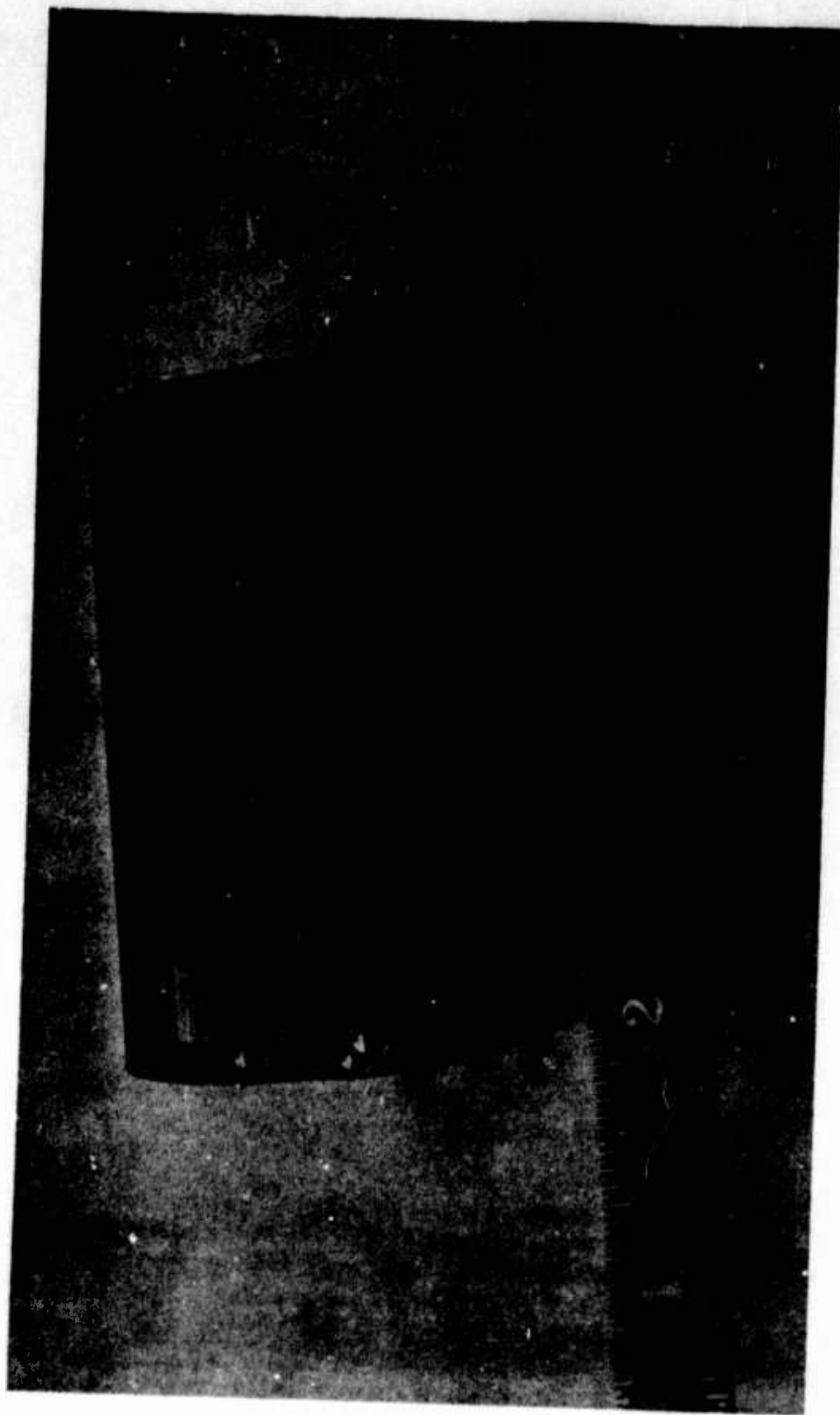


FIGURE 21a. FLUIDIC ACCELEROMETER WITH DAMPING

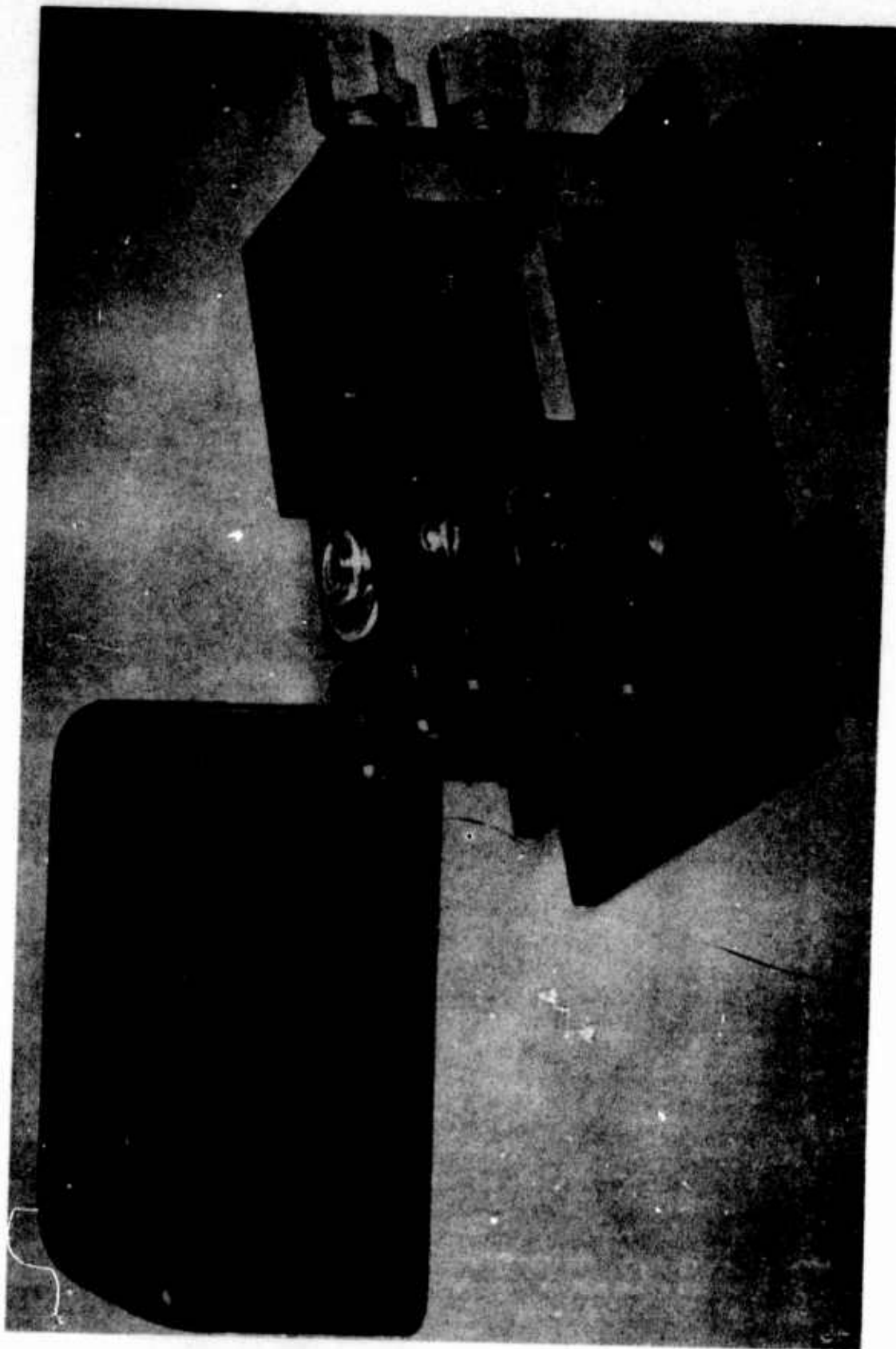


FIGURE 21b. FLUIDIC ACCELEROMETER WITH JET PIPE

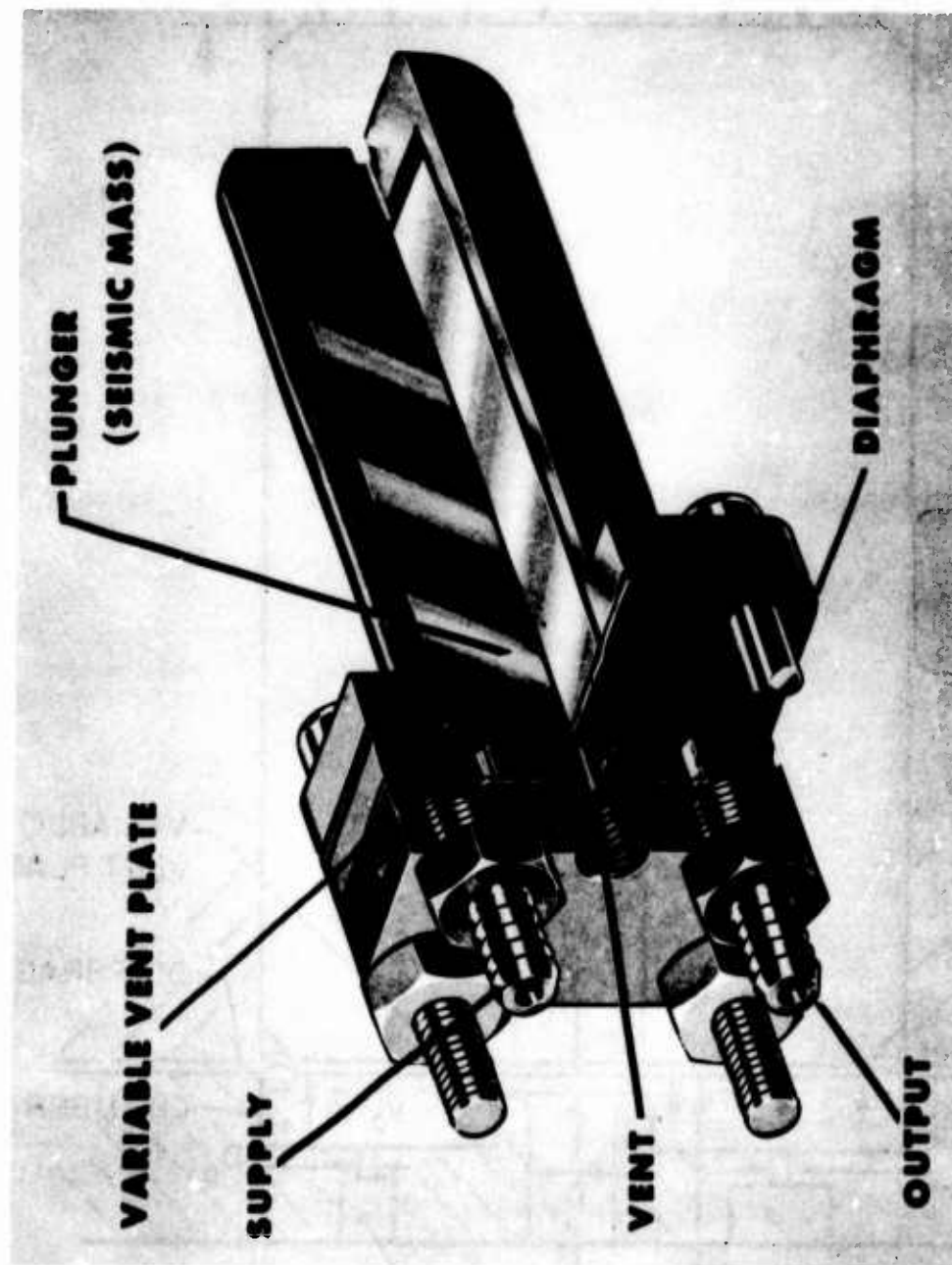
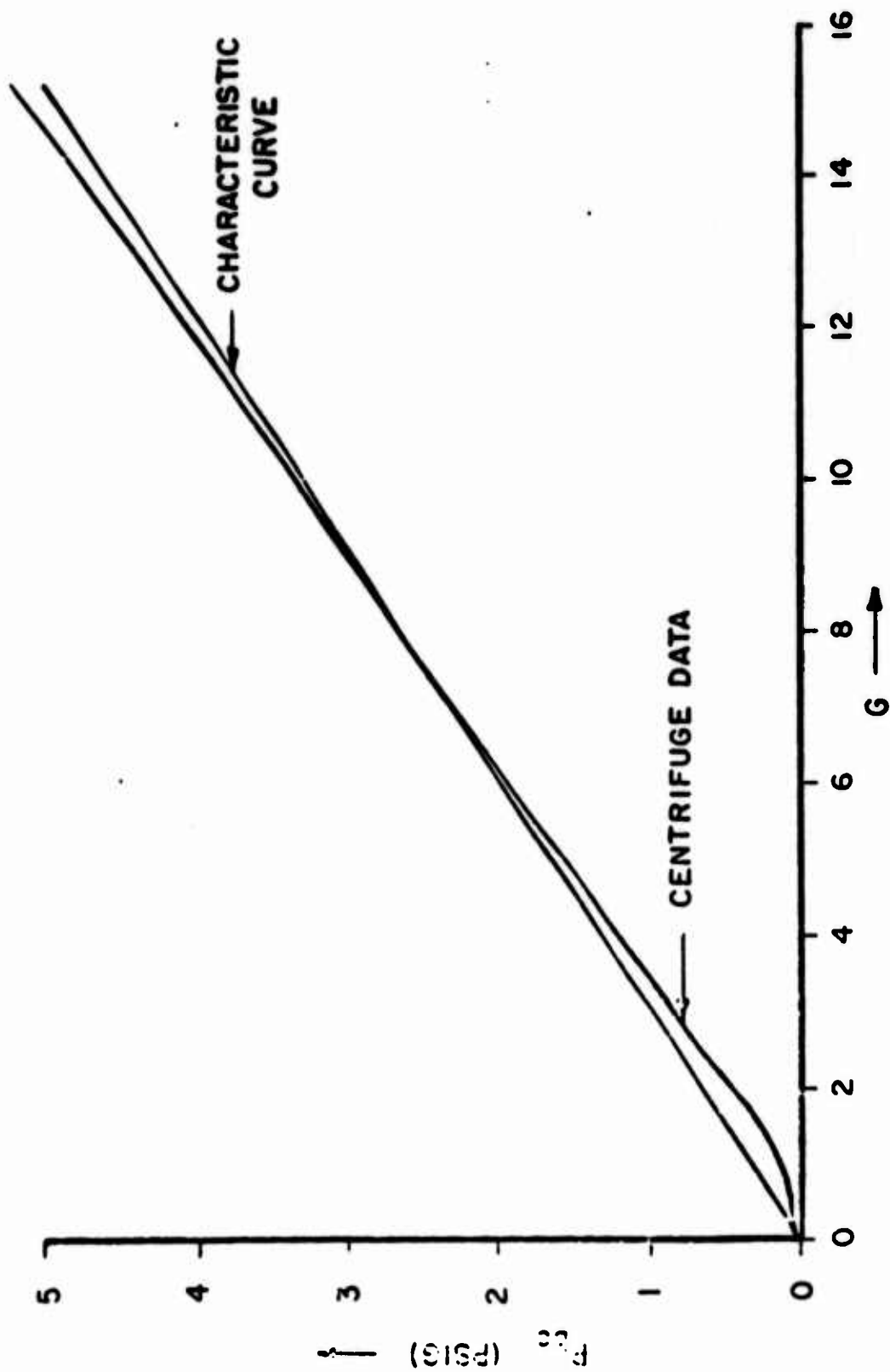
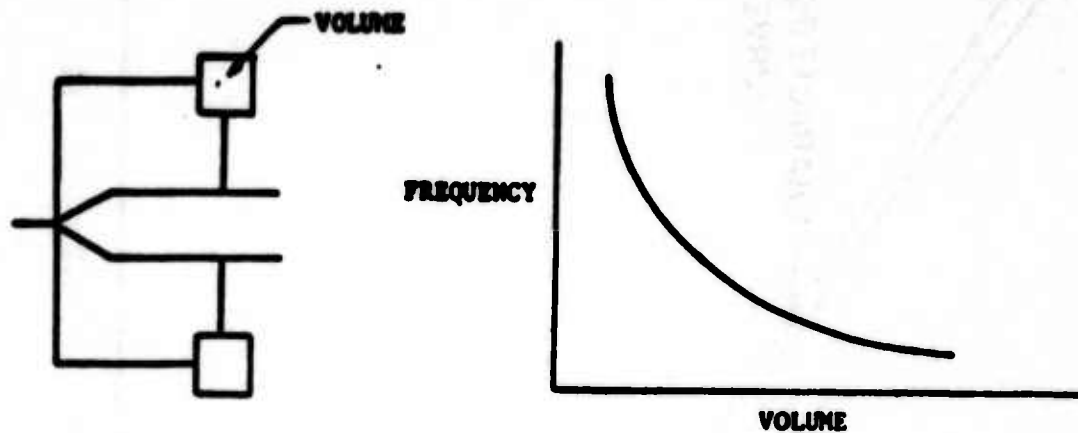


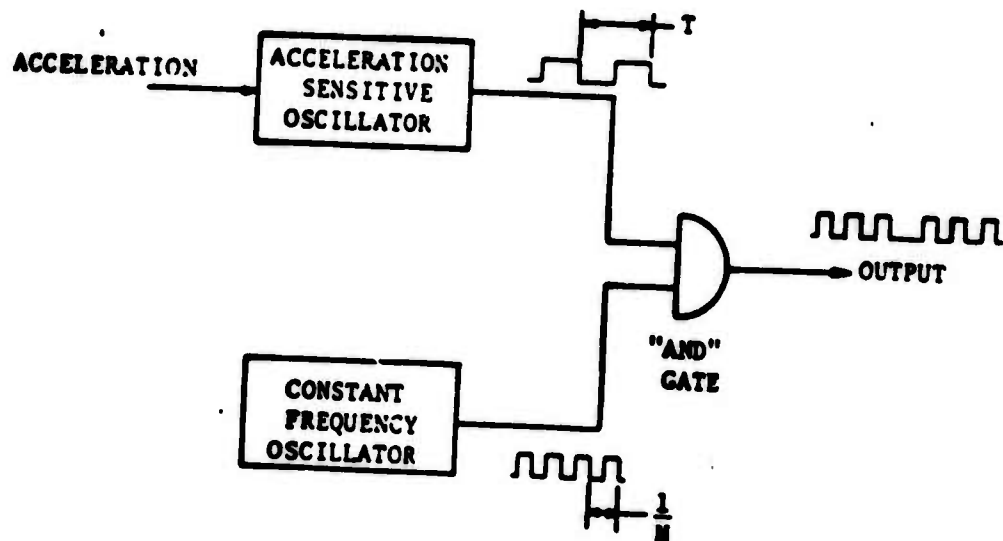
FIGURE 22a. FLUIDIC G SENSOR



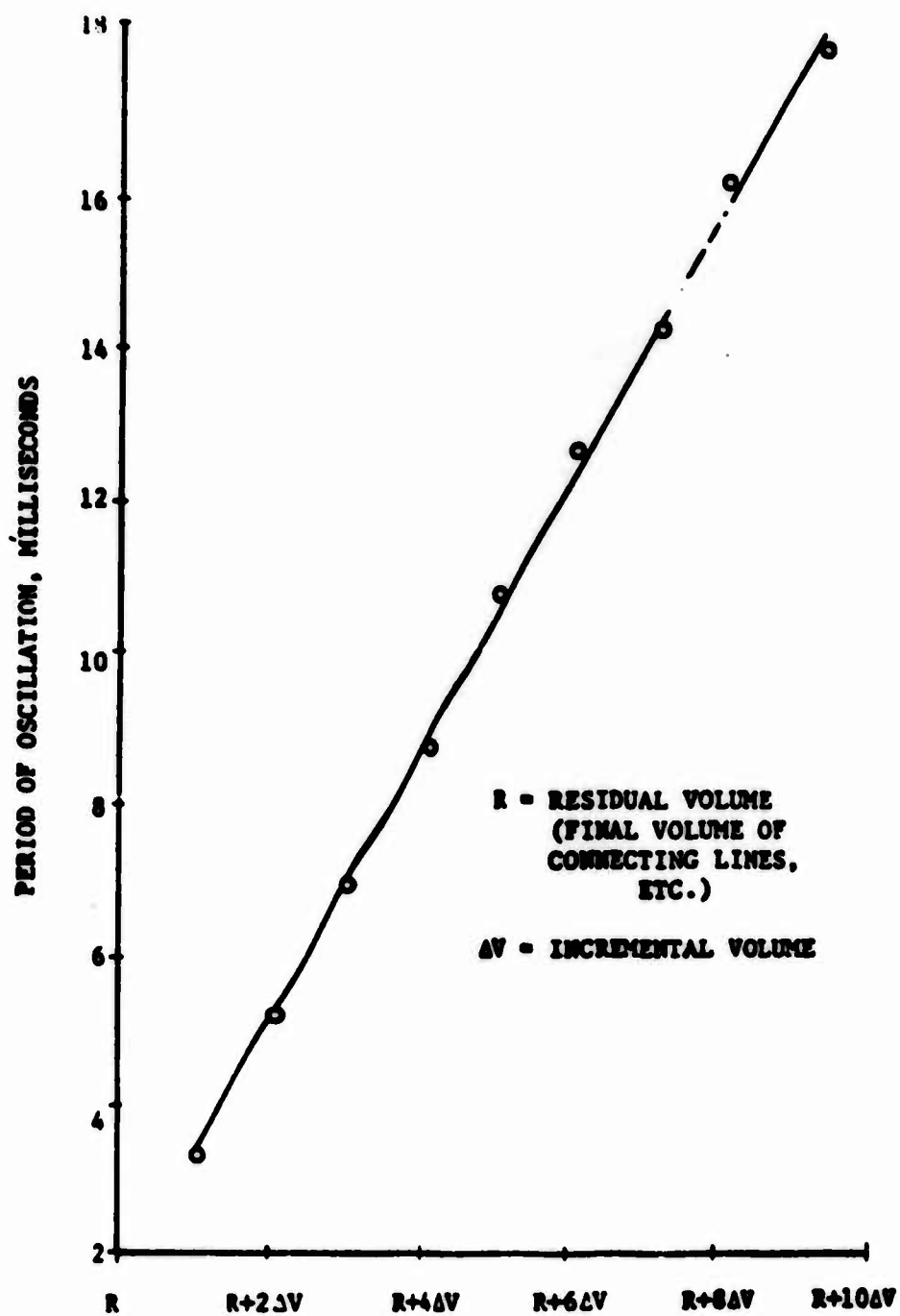
**BOTTOM CHAMBER PRESSURE vs G LEVEL
15 G SENSOR**



24 FEEDBACK OSCILLATOR



26 FLUIDIC CIRCUIT



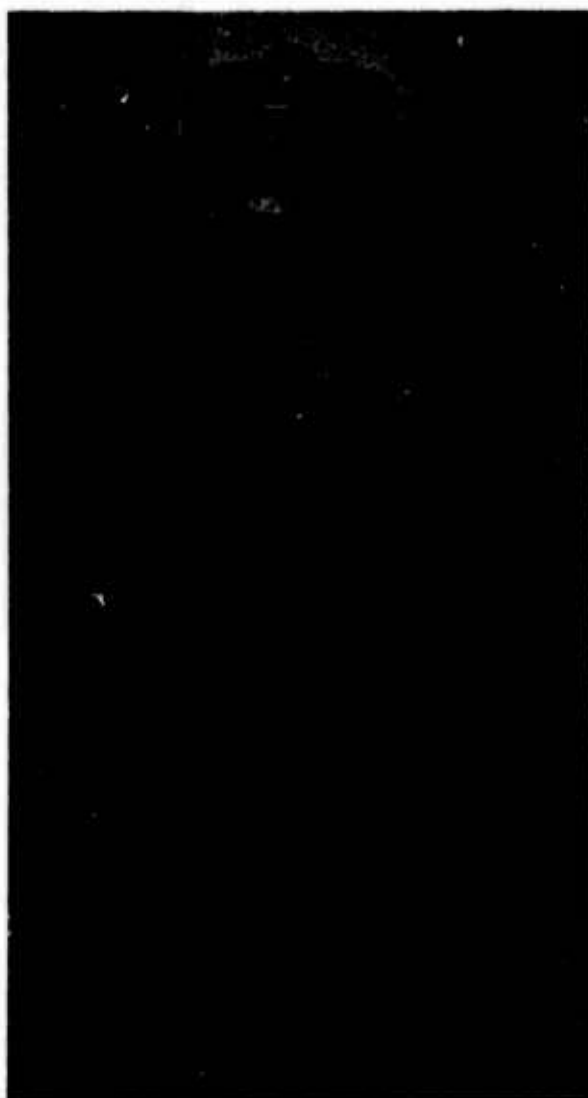
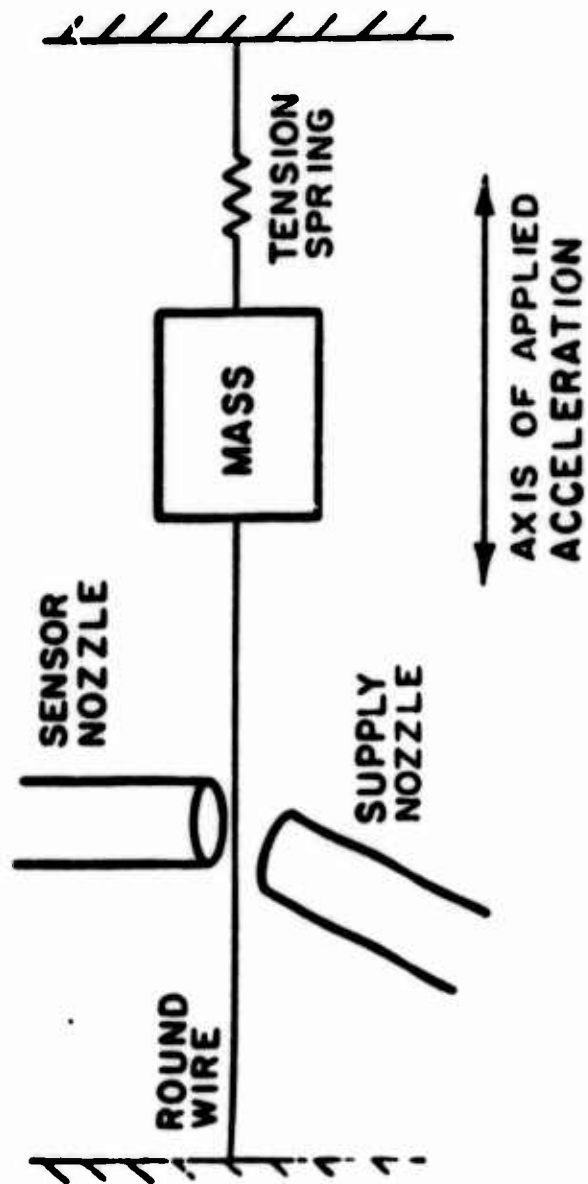
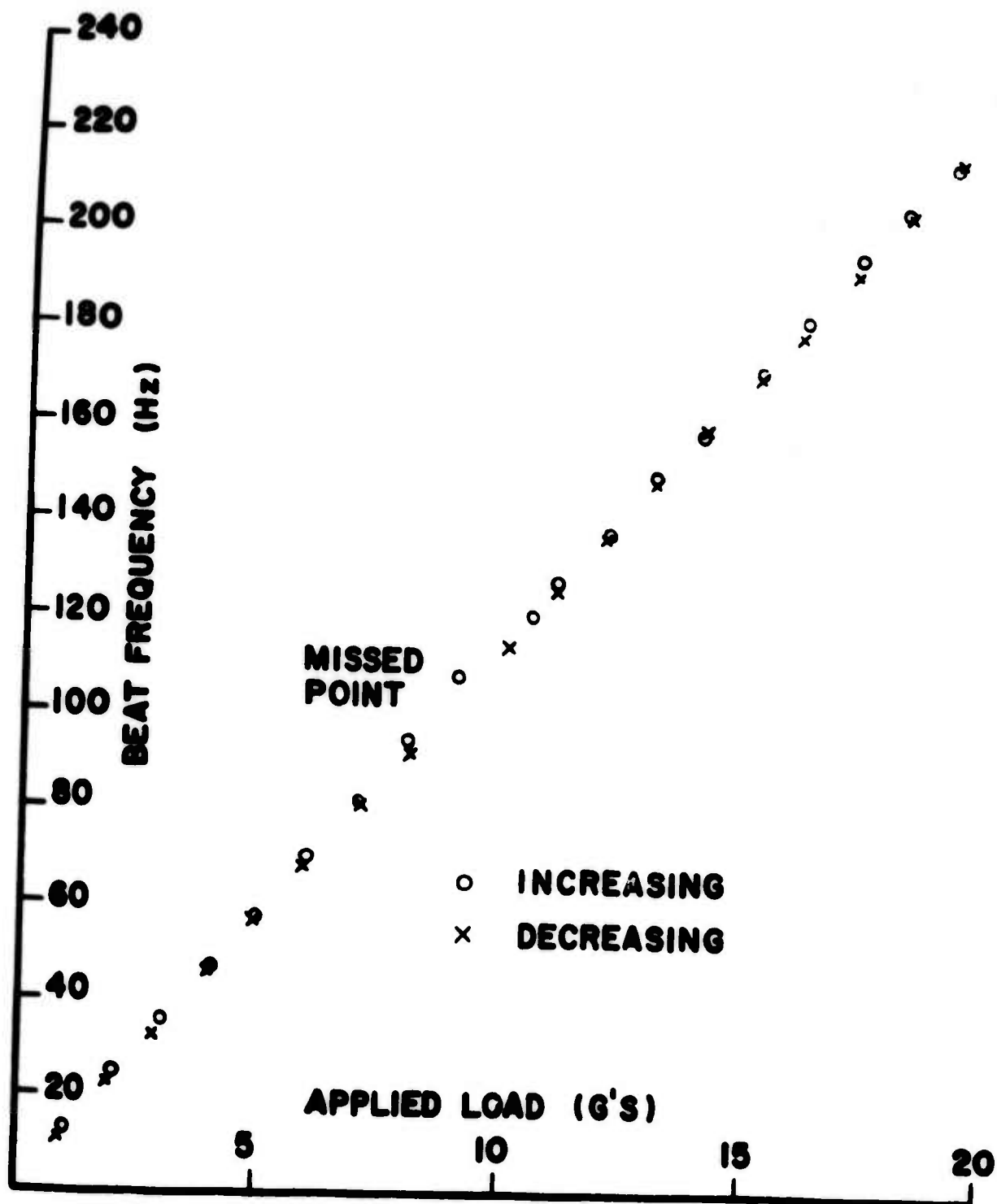


FIGURE 27. DIGITAL ACCELEROMETER



28 SCHEMATIC - VIBRATING STRING ACCELEROMETER



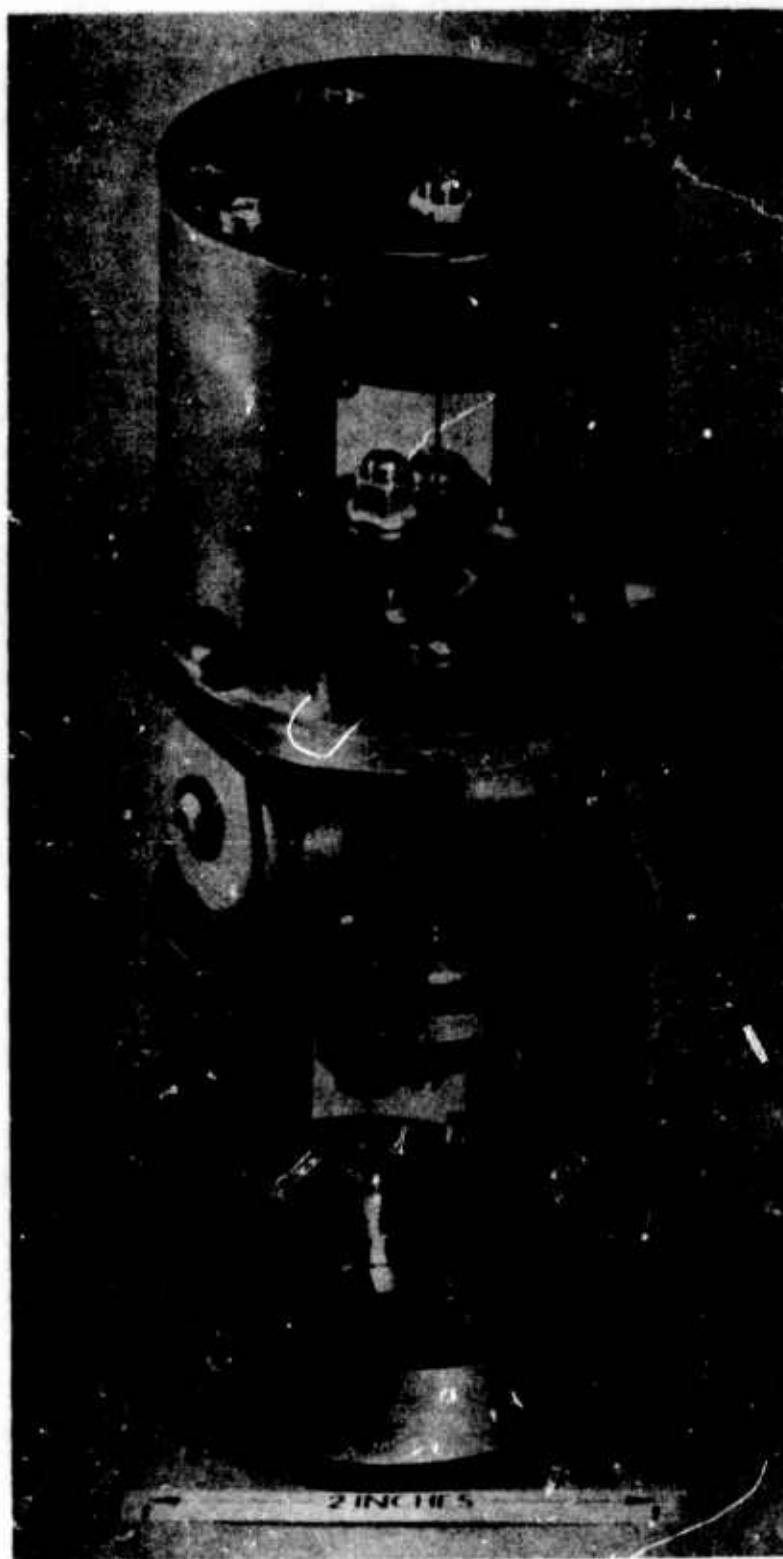


FIGURE 29b. VIBRATING STRING ACCELEROMETER

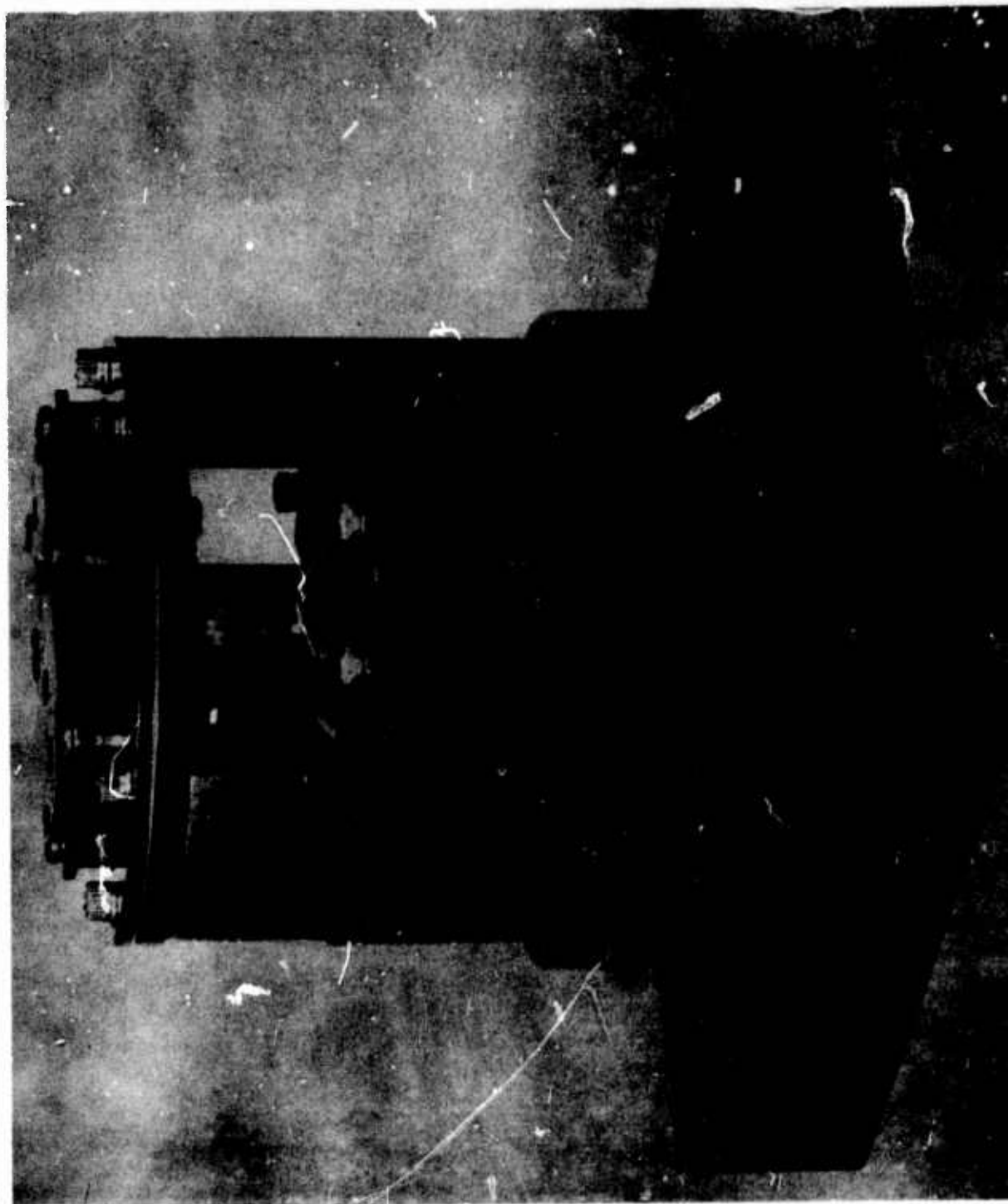


FIGURE 30. ATTITUDE GYRO - TAPP

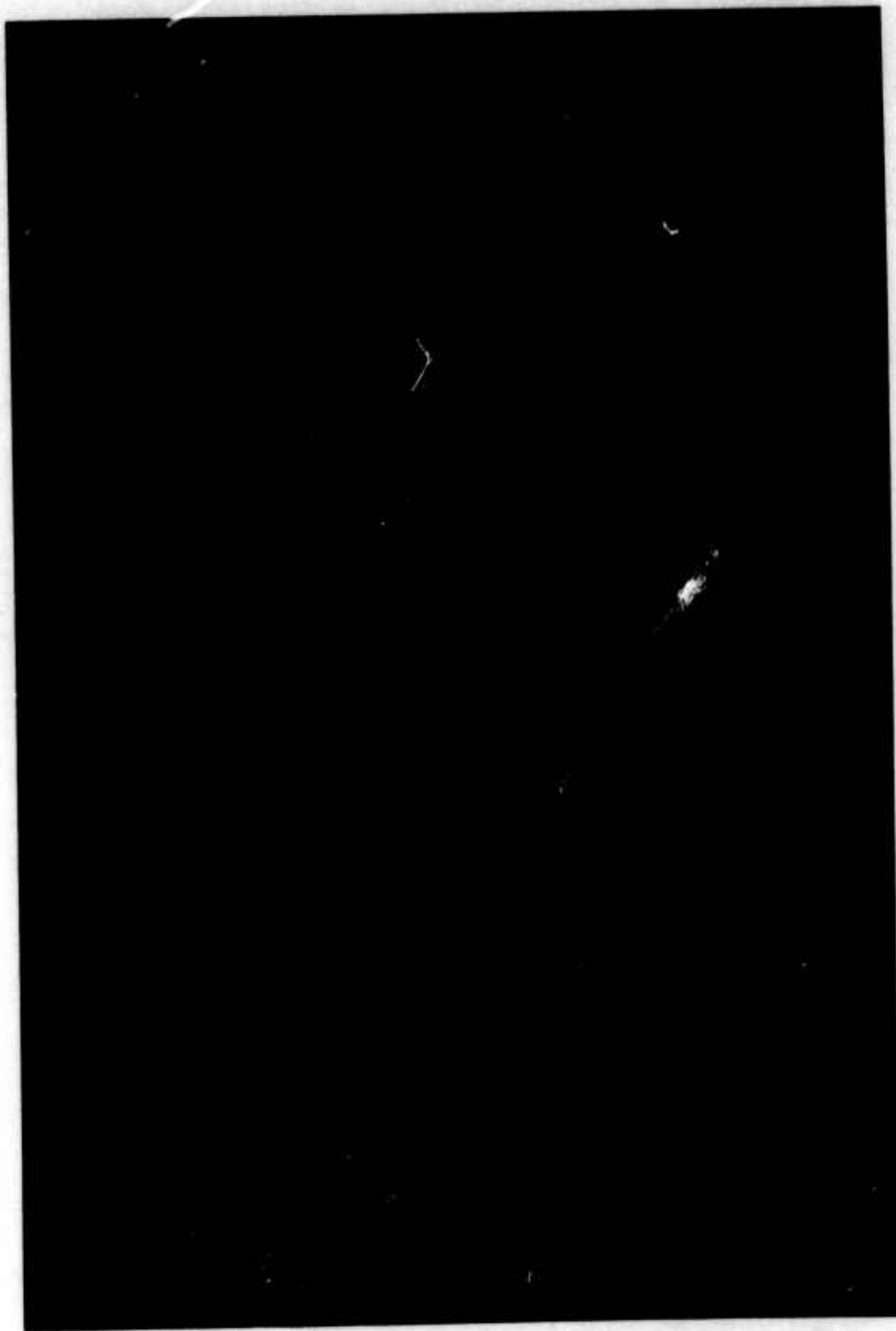


FIGURE 31. ATTITUDE GYRO

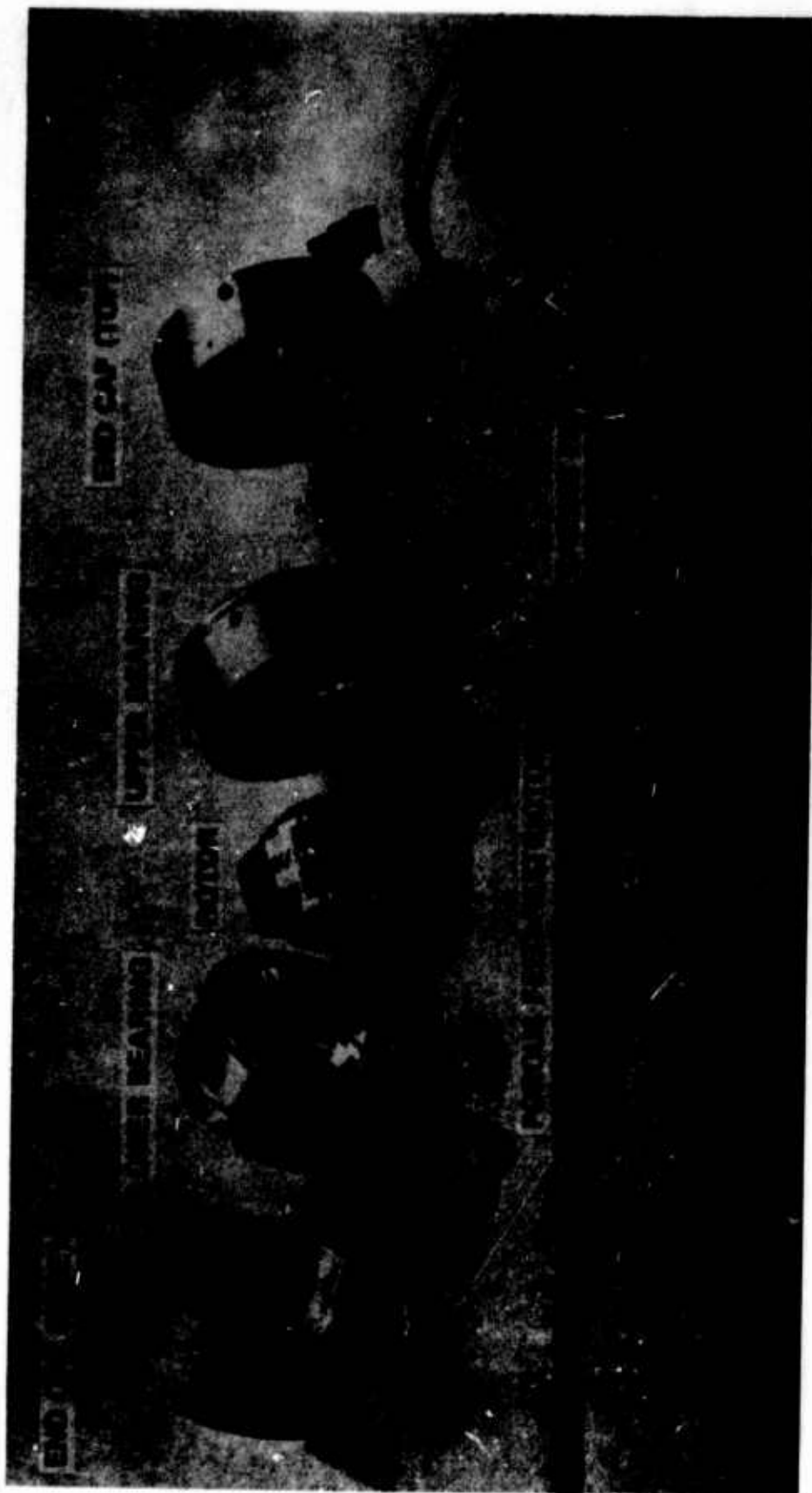
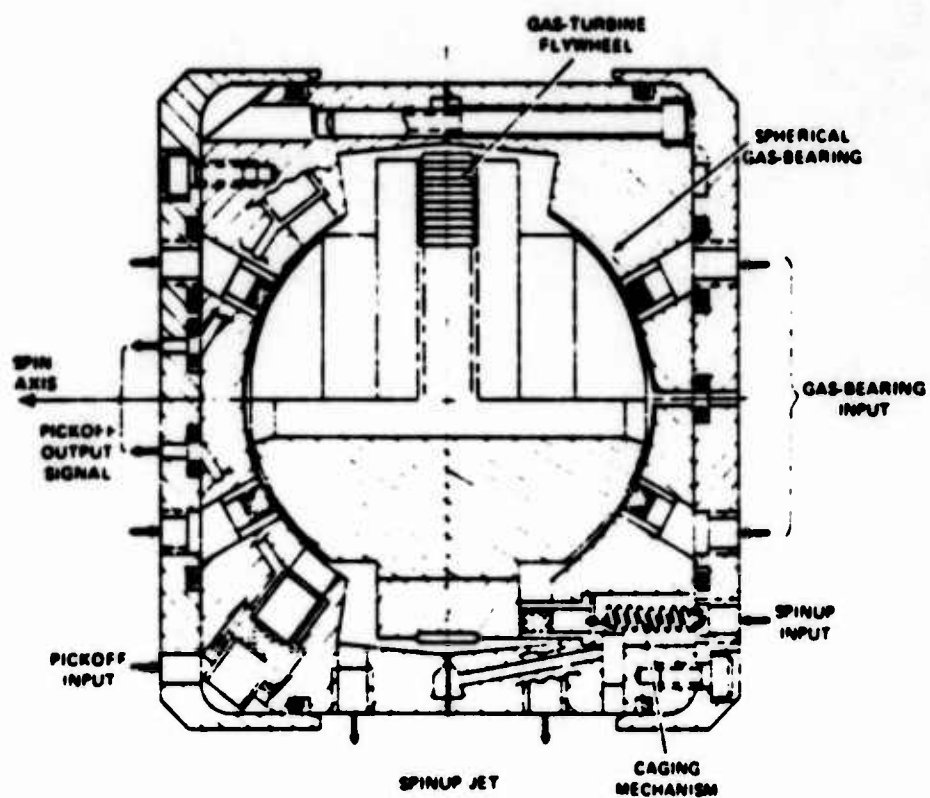


FIGURE 32a. FREE ROTOR GAS BEARING GYRO



32b FREE ROTOR GAS BEARING GYRO

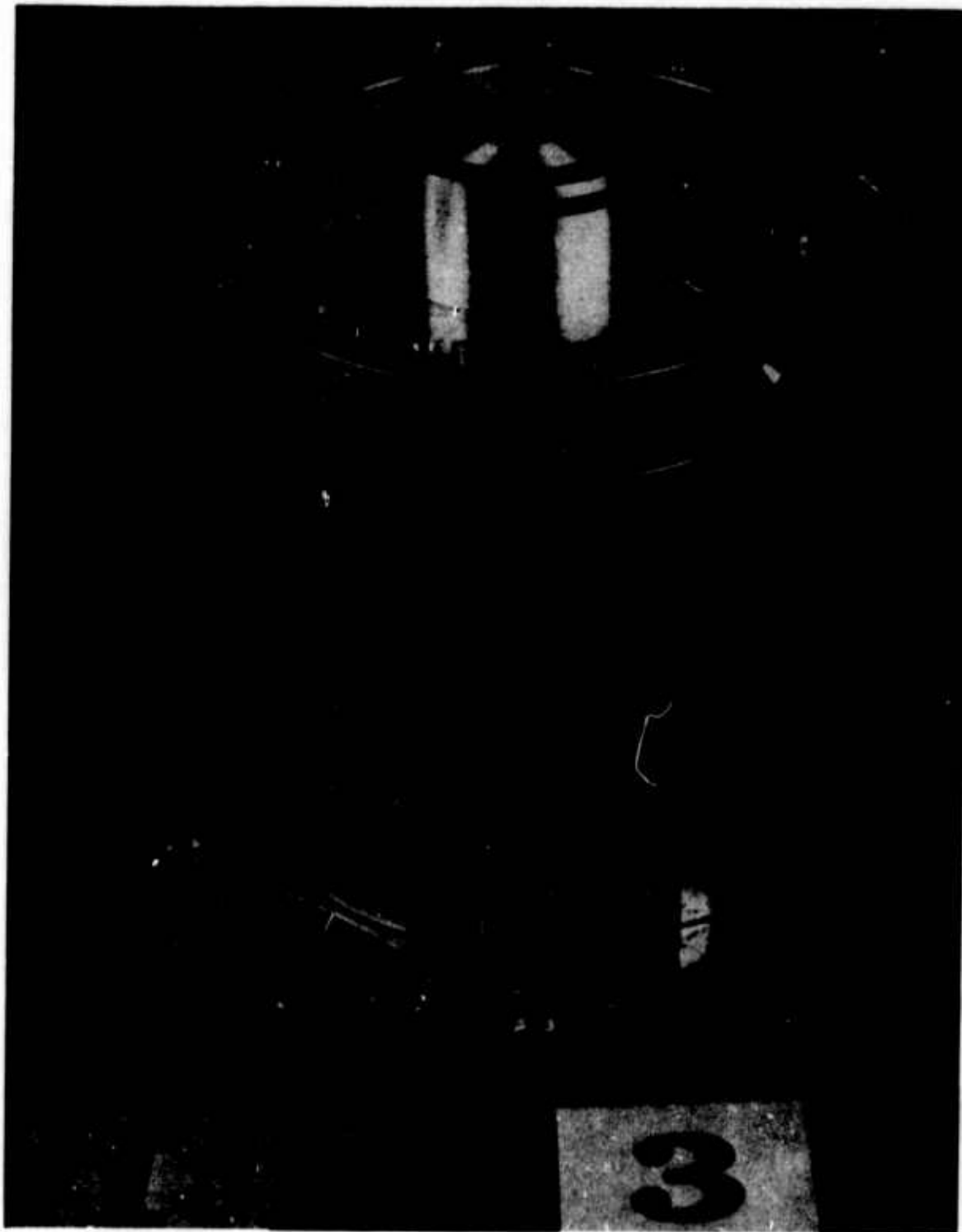
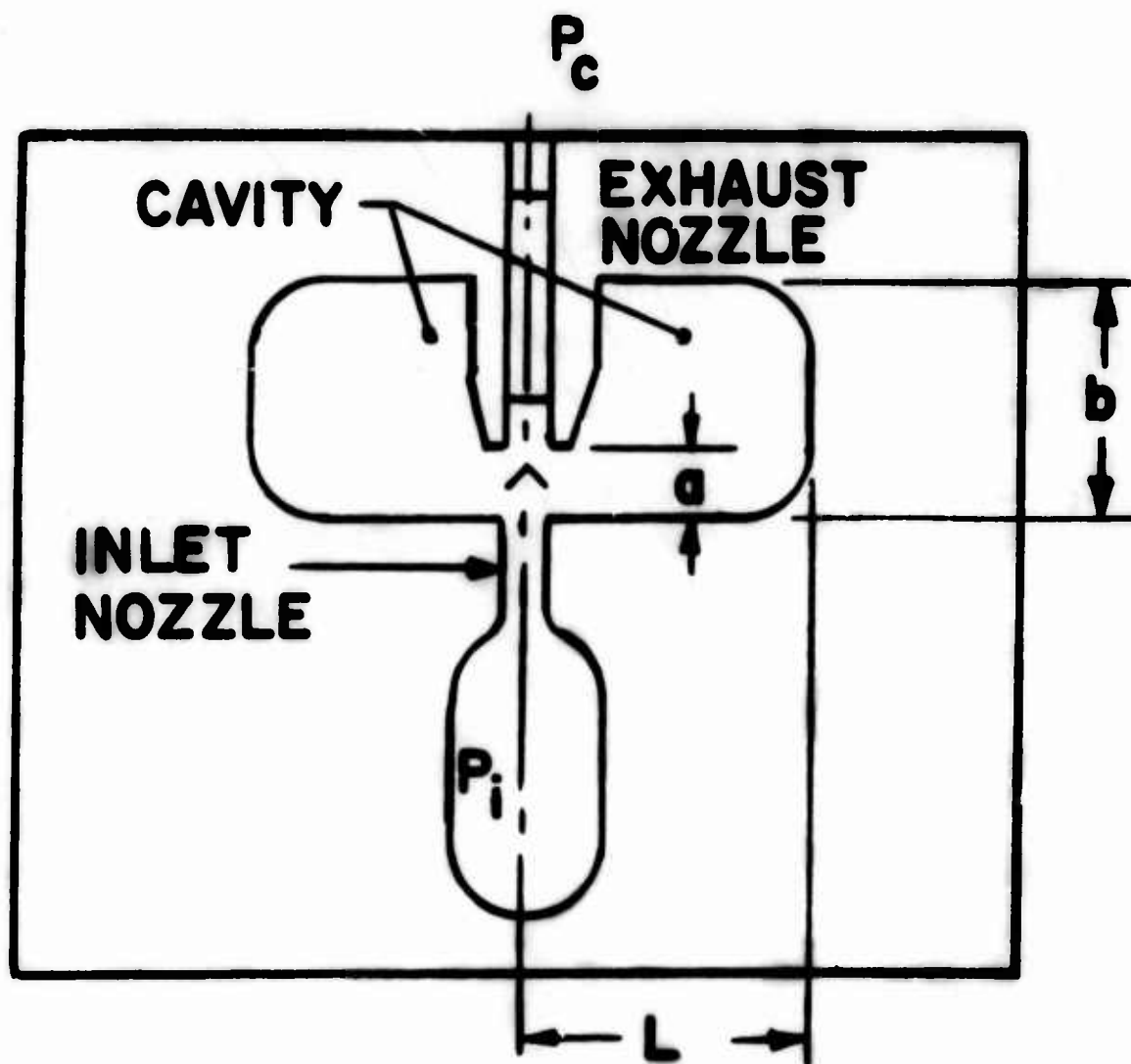
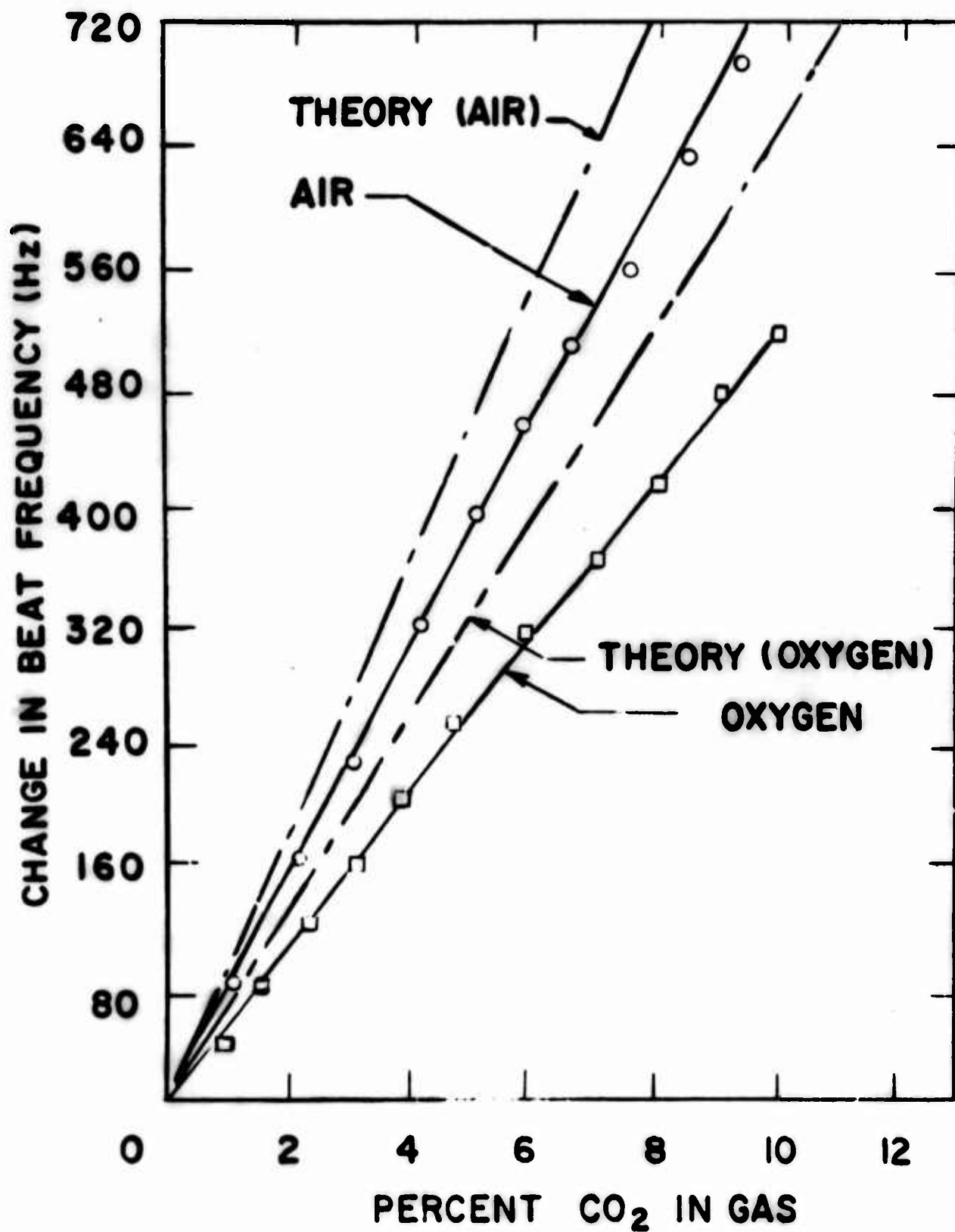
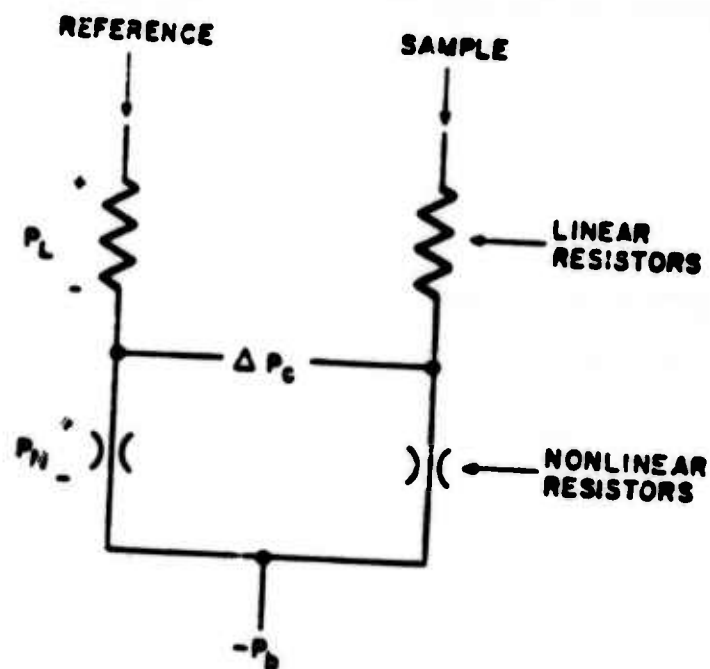


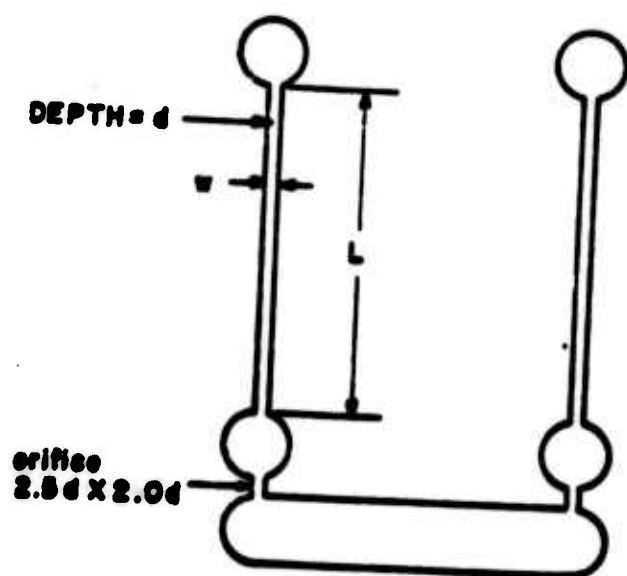
FIGURE 33. ATTITUDE GYRO





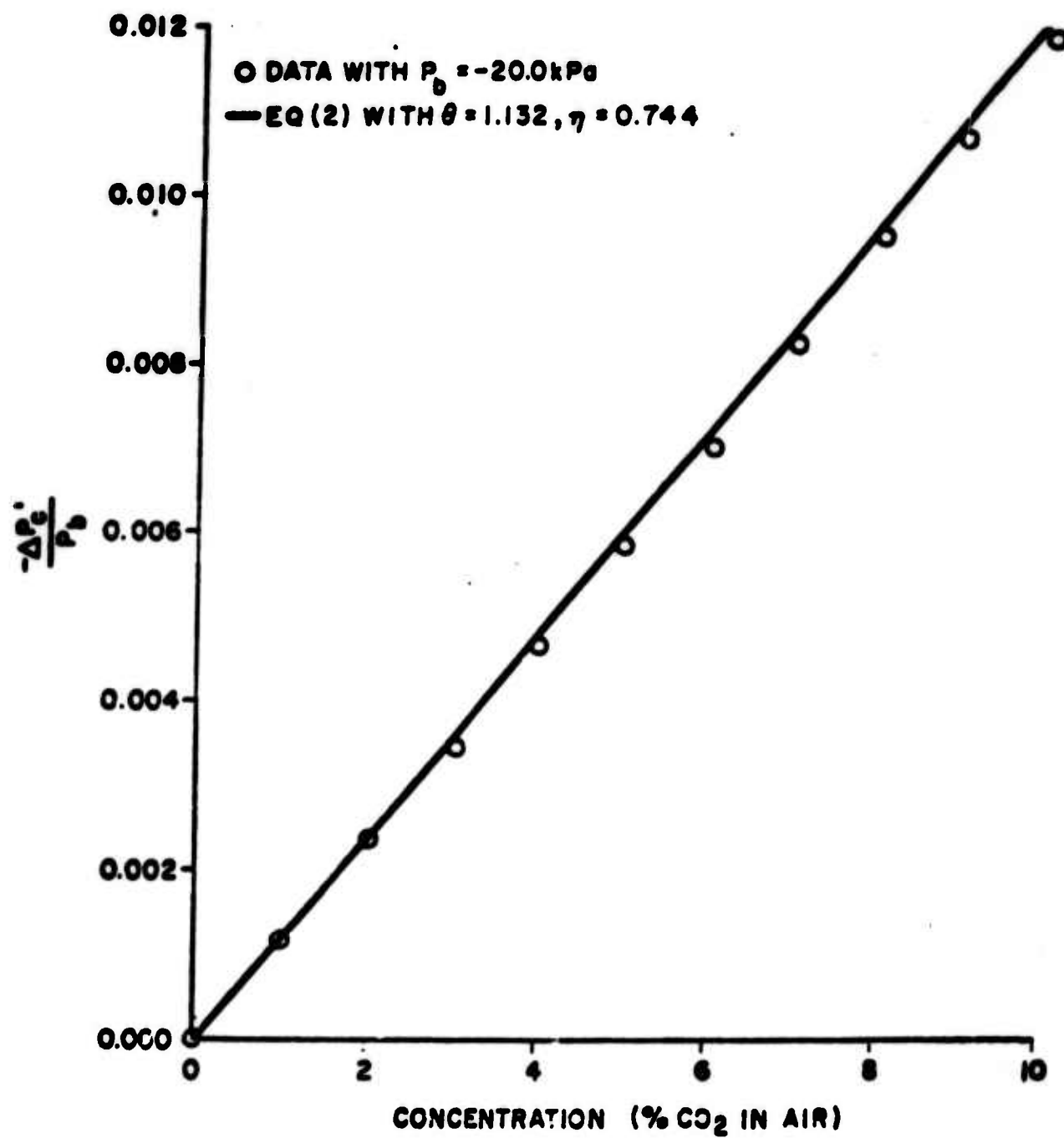


c. SCHEMATIC REPRESENTATION



d. SENSOR GEOMETRY ($w=12.5d$, $L=250d$, $d=0.01016$ cm = 0.004 in.)

36 PASSIVE GAS CONCENTRATION SENSOR - TEST RESULTS



FLUIDIC SENSORS - A SURVEY

PART II

by

**Joseph M. Kirshner
Fluidics Systems Research Branch
Harry Diamond Laboratories**

**Prepared for
HDL Fluidics State-of-the-Art
Symposium
30 Sept - 04 Oct 74**

NOMENCLATURE

a	constant
a_s	speed of sound
b	constant
c	speed of wave propagation
c_d, c_{d1}, c_{d2}	discharge coefficients
C_T	see equation 41b
d	diameter
D	antenna directivity
f	frequency
f_l	frequency for laminar jet length of l
f_s	most sensitive frequency
F	force
h	vortex chamber height
k	see equation 48
k_o	see equation 7
k_1, k_2	constants
l	length
m	see equation 41c
N_M	Mach number
N_R	Reynolds number
N_S	Strouhal number
p	pressure
p_a	ambient pressure
p_b	pressure at sudden enlargement (fig. 1)
p_B	see equation 44

p_o	output pressure
p_{o1}, p_{o2}	see figure 1
p_s	supply pressure
p_L	pressure drop across linear resistor
p_N	pressure drop across nonlinear resistor
p_T	total signal pressure
q	volume flow
r	radial distance
r_c	radius of coupling ring
r_d	drain radius
r_h	radius of reflecting surface
R_1, R_2	resistances
R_g	gas constant
t_{dro}	fill time
T	period
T_a	absolute temperature
u	flow velocity
u_d	stream velocity
u_e	see figure 1
u_i	see figure 1
u_o	see figure 1
u_r	radial velocity
u_{rc}	radial velocity at coupling ring
u_{rd}	radial velocity at drain
u_{rel}	relative velocity between rate sensor housing and fluid
u_θ	tangential velocity

$u_{\theta c}$	tangential flow velocity at coupling ring
$u_{\theta cT}$	tangential velocity at coupling ring at threshold angular velocity
$u_{\theta d}$	tangential velocity at drain
$u_{\theta s}$	tangential velocity at rate sensor housing
$u_{\theta sc}$	tangential velocity of coupling ring
w	see figure 1
β_i	see figure 41c
γ	ratio of specific heats
θ	angle, also defined in equation 46
θ_b	angular beam width
λ	wavelength
μ	viscosity
ν	kinematic viscosity
ρ	density
τ_s	switching time
ψ	flow angle
ψ_{Th}	threshold flow angle
ω	angular velocity
ω_{Th}	threshold angular velocity

1.0 INTRODUCTION

Sensors are an important component of fluidic systems and appreciable work has been done in an attempt to obtain sensors that are compatible with and can take advantage of the fluid signal amplification possible by the use of fluid amplifiers. Because a great deal of literature has appeared and is still appearing in this area, we have allocated two papers to this subject. Even so, we have not covered the topic fully. Although we have made some effort to avoid duplication between the two parts, there is some overlap which we hope will prove useful. Part I provides engineering data on many of the important sensors. In Part II, a number of devices are described and some are analyzed.

2.0 PROXIMITY SENSORS

Part I describes several types of proximity sensors.

In all of these devices the static characteristic (back pressure as a function of distance between object and probe) depends on the specific geometry including the resistance of the probe, the resistance in the supply line, the resistance associated with the signal readout, and any jet entrainment or venturi effects.

An analysis and data showing the improvement in the characteristic when jet entrainment is used is given by Brychta and Suresh [1]*. In the analysis that follows, the assumptions differ slightly from theirs and therefore the results are also somewhat different.

Let us consider the back-pressure sensor geometry shown in figure 1. In effect the sensor is two resistances in series (a half-bridge circuit). The two resistances are: 1) a fixed upstream resistance formed by an orifice of diameter, w , and a sudden enlargement to diameter, d , and, 2) a variable downstream resistance that depends on the distance, l . A source of pressure, p_s , is supplied to the half-bridge circuit. The sensor output pressure, p_o , may be received at stations A or B. The pressure at each output station is generally not the same.

In figure 1, as the jet leaves the nozzle of diameter w and expands into the region of diameter d , the velocity decreases from u_j to u_e and a low pressure region, p_b , is formed near the nozzle.

The pickoff regions A and B are assumed to draw negligible flow in this analysis; however, if the flow to the pickoff is not small compared to that through the probe, the analysis must be modified. When the pick-off flow can be assumed negligible, the static pressure p_{o1} is approximately equal to p_e and the static pressure p_{o2} is approximately equal to p_b .

*Numerals in brackets indicate reference number.

We associate a discharge coefficient c_{d1} with the nozzle and a discharge coefficient c_{d2} with the region between the probe and the object whose distance is being sensed.

Assuming lossless steady incompressible flow we then have the following approximate equations:

Energy

$$p_s = p_b + \frac{\rho u_1^2}{2} \quad (1)$$

$$p_e + \frac{\rho u_e^2}{2} = \frac{\rho u_o^2}{2} \quad (2)$$

Continuity

$$c_{d1} u_1 \frac{w^2}{4} = \frac{u_e d^2}{4} = u_o l d c_{d2} \quad (3)$$

where l is the object distance (fig. 1).

Note that the flow is affected by l only if $l \leq \frac{d}{4c_{d2}^2}$ consequently the maximum range of the probe is one-fourth its diameter.

Momentum

$$p_b + \rho u_1^2 \frac{w^2}{d^2} = p_e + \rho u_e^2. \quad (4)$$

Now the substitution of the continuity equation (equation 3) into the energy and momentum equations (1, 2, and 4) yields.

$$p_s = p_b + \frac{\rho c_{d2}^2}{2c_{d1}^2} \frac{16u_o^2 l^2 d^2}{w^4} \quad (5a)$$

$$p_e = \frac{\rho u_o^2 c_{d2}^2}{2} \left(\frac{1}{c_{d2}^2} - \frac{16l^2}{d^2} \right) \quad (5b)$$

$$p_b = p_e + 16\rho u_o^2 l^2 c_{d2}^2 \left(\frac{1}{d^2} - \frac{1}{w^2 c_{d1}^2} \right) \quad (5c)$$

The addition of equations 5a and 5c results in:

$$p_s = p_e + 16\rho u_o^2 l^2 c_{d2}^2 \left(\frac{1}{d^2} - \frac{1}{w^2 c_{d1}^2} + \frac{d^2}{2c_{d1}^2 w^4} \right) \quad (6)$$

We may eliminate ρu_o^2 from equation 6 by using the expression for ρu_o^2 provided in equation 5b. Thus,

$$\frac{p_e}{p_s} = \frac{\frac{1}{c_{d2}^2} - \frac{16l^2}{d^2}}{\frac{1}{c_{d2}^2} + 16k_o \frac{l^2}{d^2}} \quad (7a)$$

$$k_o = 1 - \frac{2d^2}{w^2 c_{d1}^2} + \frac{d^4}{c_{d1}^2 w^4} \quad (7b)$$

where $l \leq \frac{2}{4c_{d2}}$.

To find the pressure relation involving p_b we substitute pu_o^2 from equation 5b into equation 5c to obtain

$$\frac{p_b}{p_e} = \frac{\frac{1}{c_{d2}^2} + \frac{16l^2}{d^2} (1 - \frac{2d^2}{w^2 c_{d1}^2})}{\frac{1}{c_{d2}^2} - \frac{16l^2}{d^2}} \quad (8)$$

The multiplication of equations 7a and 8 produces:

$$\frac{p_b}{p_s} = \frac{\frac{1}{c_{d2}^2} + \frac{16l^2}{d^2} (1 - \frac{2d^2}{w^2 c_{d1}^2})}{\frac{1}{c_{d2}^2} + 16k_o \frac{p^2}{d^2}} \quad (9)$$

Figure 2 shows the pressure ratios p_e/p_s and p_b/p_s from equations 7a and 9 plotted against the normalized gap distance $4l/d$ for several values of d/w . The assumption here is that $c_{d1} = 1.0$ and $c_{d2} = 0.8$. Several points of interest appear:

1. The sensitivity (slope of the curve) $d(p_b/p_s)/d(4l/d)$ is in general greater than or equal to the sensitivity, $d(p_e/p_s)/d(4l/d)$.
2. Small values of $\frac{d}{w}$ (close to unity) result in higher sensitivity at the longer ranges whereas larger values of $\frac{d}{w}$ increase the near range sensitivity at the expense of the longer range sensitivity.
3. The curves are most linear for $1 < \frac{d}{w} < 2$.

3.0 OBJECT DETECTING SENSORS

When the presence or absence of an object is to be detected, as for counting, proximity sensors can of course be used if the range of the sensor is adequate or an emitter and a catcher can be used for longer ranges as illustrated in figure 3a or figure 4 of part I. In this case an object passing between the emitter and the catcher interrupts the jet, thereby changing the pressure in the catcher which is then indicated in the measuring device. This type of device has the drawback that foreign particles may enter the catcher along with the flow from the emitter and may eventually cause a failure to occur in the measuring device. At the cost of additional flow, particle ingestion may be prevented by using one of the back-pressure sensing devices such as indicated in figure 2 of part I instead of the catcher. This results in

the configuration of figure 3b. It is apparent that the configuration of 3b is essentially the same as that of an impact modulator which can, therefore, be modified to act as a sensor.

The range of detection may be increased by using a fluid amplifier in the vicinity of the catcher instead of a passive device or by allowing the emitter jet to deflect a second jet when the object is not present. A detector of this type is discussed by Jacobs and Baker [3]. The principle of operation is very similar to that of a velocity sensor which we discuss later, but a venturi shape is used to increase the deflection of the detecting jet.

3.1 Thread Detectors

Where surrounding conditions are sufficiently calm to permit it, long ranges at relatively low pressures and flows can be obtained by the use of laminar jet emitters. These are also particularly useful for the detection of small objects which may cause negligible pressure drop when placed in a turbulent stream. If, however, the emitter parameters are such as to yield a laminar jet, then turbulence can be triggered by even a very small object such as a thread. When the jet becomes turbulent the pressure received by the catcher drops drastically. A device of this kind can be used, for example, to detect the breaking of a thread (fig. 4).

Impact devices, apparently very similar to the impact modulator NOR element have been used as thread sensors in Japan according to K. Izawa [4]. The rapidly moving thread carries with it a boundary layer of air thick enough to appreciably affect the jet which is allowed to impinge upon it. The opposing jet will then cause the interaction region to move out of the output chamber resulting in zero output signal. If the thread breaks, the jet which was formerly impeded by the cylinder of thread and air will have sufficient momentum to force the interaction region back into the chamber resulting in a nonzero output.

3.2 Acoustic Ear

As noted in part I, the longest range fluidic sensor is the acoustic ear [5,6,7], which uses a beam of ultrasonic sound instead of a jet and which has a range of about 5 meters.

The acoustic beam may be generated by a fluidic oscillator or by a piezoelectric crystal and is detected by a jet sensitive to the transmitted frequency, that is, a transition device is designed [8] with the proper nozzle width and jet velocity so as to be sensitive to the desired frequency.

To determine the frequency to which the jet is most sensitive let us note that the data on jet stability show that the Strouhal number, N_s , for maximum jet sensitivity is proportional to the square root of the Reynolds number, N_R , for Reynolds numbers greater than 150. Thus from the data we may write

$$N_s = A(N_R)^{\frac{1}{2}} \quad (10)$$

where $N_s = f_s d/u_o$, $N_R = u_o d/\nu$, f_s is the most sensitive frequency in Hz, d is the nozzle diameter, u_o is the exit velocity, ν is the kinematic viscosity, and A is an experimental constant. The constant A may take on a wide variety of values that depend on the jet nozzle geometry and the geometry of the chamber that supplies the nozzle. In assembling the data of many investigators, Rockwell [9] presents bounds for those cases when the Reynolds number is between 200 and 10,000. These bounds are equivalent to

$$0.007 < A < 0.015; \text{axisymmetric-jet} \quad (11a)$$

$$0.002 < A < 0.008; \text{two dimensional jet} \quad (11b)$$

As an example suppose that we have an axisymmetric air jet of diameter 0.7 mm and an exit velocity of 75 m/sec. We want to approximate the frequency to which the jet is most sensitive. The Reynolds number of the given jet is 3540. Therefore, from equation 10 and the condition on A in equation 11a, the Strouhal number has the limits $0.42 < N_s < 0.89$.

Now from the definition of Strouhal number we find the sensitive frequency range as $45,000 \text{ Hz} < f_s < 95,000 \text{ Hz}$.

For a particular geometry the jet will have a most sensitive frequency. However, to some extent the jet is sensitive to a relatively broad band around this particular frequency. This broad band sensitivity is partially due to the fact that the velocity of the jet decreases and its width increases with downstream distance. As a result the length of the laminar region tends to decrease as the frequency increases.

If at a given frequency, f_s , the length of the laminar portion is l , then if the distance to the sensor receiver is less than l , the sensor output will be unchanged for frequencies less than f_s , but will be drastically reduced for a band of frequencies somewhat higher than f_s .

An opening, in the form of a horn, built into the housing of the sensor allows the beam to impinge on the jet. To the extent possible, the geometry of this opening should be chosen so that its impedance is least at the sensitive frequency of the jet. This will narrow the band of frequencies to which the sensor is sensitive.

The range of the sensor depends, on the transmitter power, the absorption by the air of the energy associated with a particular frequency, the antenna gain, and on the receiver sensitivity.

If the beam width, θ_b , of the major lobe of the transmitted beam is defined as the angle between the points at which the intensity becomes zero then, [10]

$$\sin \frac{\theta_b}{2} = 0.61 \frac{\lambda}{r_h} \quad (12)$$

where λ is the wavelength of the radiation and r_h is the radius of the reflected surface.

The directivity or gain of the antenna, D , which is intensity in the given direction divided by the intensity which would result from an isotropic source [11] is given by

$$D = \frac{\left(\frac{2\pi r_h}{\lambda}\right)^2}{1 - \frac{J_1\left(\frac{4\pi r_h}{\lambda}\right)}{\frac{2\pi r_h}{\lambda}}} \quad (13a)$$

where $J_1\left(\frac{4\pi r_h}{\lambda}\right)$ is the Bessel function of the first kind of order one.

$$\text{For } \frac{4\pi r_h}{\lambda} \gg 1 \quad D \approx \left(\frac{2\pi r_h}{\lambda}\right)^2 \quad (13b)$$

For $\frac{r_h}{\lambda} > 1$, the error in 13b is less than about 20%.

The sensor may be used in either the direct or the reflex mode. In the direct mode, the beam passes directly from the transmitting oscillator to the receiver, except when interrupted by the object to be sensed. In the reflex mode, both transmitter and receiver are side by side and face in the same direction. The beam goes off into space unless an object causes it to be reflected into the receiver.

Kishel [12] gives a method for sharply limiting the band to which an acoustic detector is sensitive. Two transition devices are mounted close to each other so that the beam affects both jets. By using different gap lengths and slightly different pressures, the band of frequencies to which each of the devices is sensitive is different. For example, transition device A cuts off (zero output) at frequency f_{A1} and remains off for all frequencies between f_{A1} and f_{A2} , but is on again for all frequencies above f_{A2} . Transition device B is off for all frequencies between f_{B1} and f_{B2} but is on for all other frequencies where

$$f_{A1} < f_{B1} < f_{A2} < f_{B2}$$

The outputs of the two devices then go to a simple logic circuit which yields an output only when A is on and B is off. This occurs only for frequencies, f_N , where

$$f_{A2} \leq f_N \leq f_{B2}$$

4.0 FORCE SENSORS

It is apparent that proximity sensing may be used in conjunction with other components to obtain other types of sensing. For example, a force sensor can be obtained by holding a flapper against the probe by the force of a spring. The distance that the flapper can be moved away from the probe by a second force, which is to be measured, will then depend on the magnitude of the force, and of course the signal obtained will be a function of the distance and, therefore, of the force.

4.1 Pulse Width Modulated Force Sensor

A more sophisticated variation of a force transducer given by Daruk and Rukhadze [13] is accomplished through pulse-width modulation. In their version (fig. 5), the applied force is balanced by increased pressure in the bellows so that the equilibrium position of the flapper is the same for all applied forces.

In figure 5 the two unconnected outlets of a bistable switch are both vented to ambient and the topmost outlet is connected through a resistor R_1 to the bellows and to the readout device.

If the nozzle is initially closed by the flapper, jet entrainment through the two open outlets will cause the jet to flip to the topmost one. Part of the flow from this outlet is fed back through a high resistance R_2 to the opposite control where it helps hold the jet over. Flow from the topmost outlet also feeds to the bellows causing it to inflate and thereby move the flapper lever away, thus opening the nozzle. Since the flow entrained through the open nozzle is greater than the flow through the high resistance R_2 , the jet is flipped to the bottom outlet, thus removing the flow into the bellows so that the spring tends to again close the flapper against the nozzle initiating a new cycle.

As functions of time, figure 6a indicates the motion of the flapper, figure 6b shows the pressure at the topmost outlet of the amplifier, and figure 6c gives the pressure at the output and in the bellows. The average pressure \bar{p} is a measure of the applied force.

4.2 Strain Gage

Another type of force sensor is the fluidic strain gage. Drzewiecki [14,15] has pointed out that since tensile stress along the length of a tube stretches it, its resistance to flow changes. This change in flow resistance may be used to measure an applied force.

Figure 7 illustrates the relationship between the pressure change and the length change. Although Drzewiecki has described many forms of the device, figure 8 illustrates only one of them. In the configuration shown, a metal tube is coiled around a cylinder in a helix. A force on the cylinder causes it to expand, resulting in stretching the length of the metal tube.

5.0 VELOCITY SENSORS

A fluid velocity sensing device [16] is shown in figure 9. The device is placed in the fluid whose velocity it is desired to measure so that the flowing fluid strikes the supply jet perpendicularly. This causes the jet to be deflected and varies the amount of the jet caught in the two catchers that are placed symmetrically about the main jet. The velocity sensitivity can be varied by altering the supply-jet pressure and, consequently, the jet velocity. Whereas, lowering the power-supply velocity increases the sensitivity of the device, it also decreases its range since the jet will eventually be deflected beyond the catcher.

5.1 Fluidic Devices Using the Vortex Shedding Phenomenon

A circular cylinder whose axis is perpendicular to flow past it, causes the flow on both sides of the cylinder to break up into eddies which are shed alternately from each side.

For a range of Reynolds numbers between about 40 and 150, the eddies are stable; that is, they proceed, in a regular pattern for an appreciable distance downstream of the cylinder, along two approximately parallel planes. This stable condition is known as a Karman vortex street after Theodore von Karman who first developed a theory for this phenomenon.

The Strouhal number, N_s , is defined as

$$N_s = \frac{fd}{u}$$

where f is the shedding frequency, d is the cylinder diameter and u is the free stream velocity. Because N_s varies in a known way with Reynolds number, it was pointed out by Roshko [17] that the velocity of a stream can be determined by measuring the frequency of vortex shedding. This frequency can be determined by detecting the oscillations downstream of the cylinder, with hot wires, [18], or by an ultrasonic beam [19]. The oscillations may also be measured by mounting a detector within the cylinder itself. Sharpsteen [20] discusses the use of a fluid amplifier within the cylinder. The controls of the amplifier lead to holes on opposite sides of the cylinder, the holes being situated in the vicinity where the eddies are formed.

For Reynolds numbers between about 150 and 10^5 , the Strouhal number is approximately constant so that the frequency is proportional to the velocity. Unfortunately, the eddy shedding is not stable over these Reynolds numbers so that the measurements must be made close to the cylinder, and there is appreciable noise.

The alternate shedding of vortices causes an alternating force on the cylinder. This force is perpendicular both to the cylinder axis and to the flow velocity and tends to cause the cylinder to vibrate. This transverse force per unit length F , is given approximately [21] by

$$F = 0.73 \rho d \frac{u^2}{2} \quad (14)$$

where ρ is the density. Since this force is applied as an essentially square wave in time, the amplitude of the fundamental is $4/\pi$ times the above.

Vortex shedding can thus be used to vibrate a body. The vibrating of the body causes a coupling of the resonant frequency of the object with the eddy-shedding frequency, tending to alter both frequencies somewhat. If the object is not very stiff, the frequency of the system will be close to the resonant frequency of the body. The resulting oscillations can be destructive of buildings, bridges, and even of power-lines; however, they have also proven useful, as in the vibrating string accelerometer.

5.2 Vortex Precession

Another method of measuring fluid velocity depends on vortex precession [18,22]. The device consists of a tube having a converging section followed by a constant area section and a diverging one.

Vanes at the entrance force the flow to swirl forming a vortex tube, shaped in a fairly tight spiral that moves down the center of the tube until the diverging portion is reached; at this point the spiral opens up taking on the form of a conically wound, spiral spring, with the vertex pointing upstream. The whole spiral rotates about its own axis as the flow proceeds downstream. A sensor in the wall of the diverging portion, senses the vortex tube everytime the tube passes the sensor as the coil rotates (or precesses). Since the precession rate depends on the flow velocity, measurement of the frequency of rotation gives the flow velocity.

5.3 Oscillator

Velocity can also be measured using a fluidic oscillator. This will be discussed in conjunction with temperature sensing. (Section 14.0)

6.0 ANGULAR POSITION SENSORS

The proximity sensor may also be adapted for use as an angular position sensor by the use of a tilted collar as has been pointed out by Fox [23].

This concept is illustrated in figure 10. Because of symmetry, there is an ambiguity involved in that a particular pressure can correspond to either of two angular positions. This ambiguity can be eliminated either by the use of two probes some angle apart (e.g. 90°) or by making the collar as a single spiral of a helix.

6.1 Code Wheel

A more accurate but more complex technique is the use of a collar containing coding [25]. This coding can be in the form of holes or of channels etched, machined, or drilled sufficiently close together in angle to yield the required angular sensitivity. This collar is perpendicular to the shaft (fig.11).

6.2 Jet-Receiver

The angular position of a body rotating only through a small angle can be measured accurately by a method due to Bright [26].

This concept involves placing a nozzle on the rotating body so that it points out toward a set of two receivers similar to those of a fluid amplifier. A center dump may also be incorporated between the two receivers. If the nozzle points so that it is centered between the two receivers, the outputs will be balanced. When the nozzle deviates from the center position one receiver will have a larger output.

6.3 Counting

Holes or slits placed at equal angles around on circumference of a disc may also be used to indicate angular position by counting the number of jet interruptions caused by turning of the disc. This concept has been used by Welk to determine the position of an automobile steering wheel [27].

7.0 TWIST MEASURING DEVICE

The twist in a rotating shaft can be measured by attaching the type of discs described in 6.3 at two positions along a bar. Twisting of the bar will change the phase of the interrupted signals from one disc as compared to the other [28].

8.0 ANGULAR RATE SENSORS

8.1 Fan Type

A pressure sensor can be adapted to measuring rotation speed. One configuration is simply to mount a blower or fan blade on the end of the shaft or to have the speed of a blower or fan blade controlled by the rotating shaft. Then, as is shown in figure 12a it is only necessary to measure the air velocity caused by the rotating fan which results in a dynamic pressure. This dynamic pressure will of course be a function of the rotation speed of the fan.

8.2 Blade Counter

If more accuracy is desirable at the expense of a more sophisticated and complicated system, the sensor may be placed close enough to the plane

of the blades so that the pulsation caused by the passage of the blade past the sensor is easily detectable (fig. 12b).

8.3 Jet Deflection or Interruption

Another method of measuring the angular velocity is to use the air velocity caused by the boundary layer around a rotating disk to deflect a jet [29] as shown at top of figure 13. This deflection may be made more efficient by using a gear [30] instead of a disk as is shown at the bottom of figure 13. The pressure picked up by the catcher shown in the bottom of figure 13 may be smoothed and used directly to measure the angular speed, or here again, a more sophisticated system can be used and the frequency measured to obtain more accurate results.

8.4 Pulse Propagation Time

An angular rate-control device discussed by Katz [31] and Iseman [32] controls the angular rotation rate of a disc by comparing the time it takes a pulse to propagate along a fixed length of line with the time it takes the disc to make one revolution.

The comparison is accomplished by injecting a pulse into the line through a hole in the rotating disc and accepting the pulse out of the line through a second hole (at a different distance from the axis) in the disc. If the disc deviates from the proper speed, the length of the received pulse will change.

8.5 The Vortex Rate Sensor

Still another technique for determining angular rate is the use of the vortex rate sensor, which is particularly useful when the angular rate is very small.

In its original form [33] the vortex rate sensor (fig. 14) consists of a circular chamber. An outer manifold surrounds a porous coupling ring through which flow enters and (when the angular rate is zero) moves radially toward the drain at the center. A pickoff which may be placed in the drain or just upstream of it is used to detect the flow angle. The purpose of the coupling ring is twofold; it is intended to cause the radial flow to be uniform from all directions, and it imparts the tangential velocity of the solid device to the fluid passing through it. Various types of coupling devices have been tried, including sintered metals, porous ceramic materials, layers of wire screens of various meshes, grille structures (like those on an automobile radiator), large numbers of small balls, spaced washers, etc. All have problems of one type or another and contribute appreciably to the threshold and accuracy limitations of the sensor.

If some angular velocity is imparted to the device, the fluid will take on the angular velocity of the device as it moves through the coupling ring and will spiral in toward the drain with a tangential velocity, u_θ .

which increases as it moves toward the drain and is given for inviscid flow by

$$u_{\theta} = \frac{k_1}{r} \quad (15)$$

where k_1 is a constant
 r is the radial distance from the axis.

If the radius of the coupling ring is r_c , and $u_{\theta c}$ is the tangential velocity at the coupling ring, then from equation 15

$$u_{\theta} = \frac{u_{\theta c} r_c}{r} \quad (16)$$

The solid portions of the device have a tangential velocity $u_{\theta s}$ which obeys the equation

$$u_{\theta s} = k_2 r \quad (17)$$

where k_2 is a constant.

Thus, since the coupling ring tangential velocity is equal to that of the fluid at $r = r_c$

$$u_{\theta sc} = u_{\theta c} = k_2 r_c$$

so that

$$u_{\theta s} = \frac{u_{\theta c}}{r_c} r$$

At the radius r , the relative velocity, u_{rel} , between the housing and the fluid will be

$$u_{rel} = u_{\theta} - u_{\theta s} = \frac{u_{\theta c} r_c}{r} - \frac{u_{\theta c} r}{r_c}$$

$$u_{rel} = u_{\theta c} \left(\frac{r_c}{r} - \frac{r}{r_c} \right)$$

thus at a point where $\frac{r_c}{r} = 10$

$$u_{rel} = u_{\theta c} (10 - 0.1) = 9.9 u_{\theta c}$$

The pickoff, or sensing element, is rigidly attached to the solid body of the device. Thus, the flow variable that the pickoff must sense is the relative velocity, u_{rel} . Furthermore, since the relative velocity increases as the radius decreases, the pickoff should be placed at a small radial position, r , for maximum sensitivity.

Various types of pickoffs have been tried, including pitot tubes, and a number of devices, usually placed in the drain, that measure angle of attack. An angle of attack pickoff of one type [34] is illustrated in figure 15. Other variations are given by Sarpkaya [35], Ogren [36],

Doyle [37], Jones [38], Scudder, et al. [39] and others. In some cases a stage of fluid amplification is built as an integral part of the rate sensor.

To gain some insight into the importance of the various parameters, let us consider the geometry of figure 14 and assume steady incompressible inviscid flow.

The continuity equation is

$$\frac{d}{dr} (ru_r) = 0 \quad (18)$$

The radial momentum equation for inviscid flow is

$$\frac{d}{dr} \left(\frac{u_r^2}{2} + \frac{p}{\rho} \right) = \frac{u_{\theta}^2}{r} \quad (19)$$

Now from 18

$$ru_r = r_c u_{rc} \quad (20)$$

where u_{rc} is the radial velocity at the coupling ring.

The substitution of equations 16 and 20 into equation 19 yields

$$\frac{d}{dr} \left\{ \frac{r_c^2 u_{rc}^2}{2r^2} + \frac{p}{\rho} \right\} = \frac{r_c^2 u_{\theta c}^2}{r^3} \quad (21)$$

Equation 21 integrates to

$$p_s = p + \frac{\rho r_c^2}{2r^2} (u_{rc}^2 + u_{\theta c}^2) - \frac{\rho}{2} u_{\theta c}^2 \quad (22)$$

where p_s is the supply total pressure.

In equation 22 the terms containing $u_{\theta c}^2$ are centrifugal force terms. For a given supply pressure the centrifugal force terms tend to decrease the signal available in the drain region. The total signal pressure, p_T , available at the drain ($r = r_d$) is therefore (assuming ambient pressure at the drain):

$$p_T = p_a + \frac{\rho r_c^2 u_{rc}^2}{2r_d^2} \quad (23)$$

Thus at the drain, from equations 22 and 23 we obtain for $r_d \ll r_c$

$$p_T = p_s - \frac{\rho r_c^2 u_{\theta c}^2}{2r_d^2} = p_a + \frac{1}{2} \rho u_d^2 \quad (24)$$

where r_d = radius of drain;

u_d = axial velocity in drain.

For a given supply pressure, the total pressure available at the drain depends on the tangential velocity $u_{\theta c}$ and on the ratio of the coupling ring radius to the drain radius. It is apparent that for any given ratio there is a tangential velocity for which the dynamic pressure $\frac{\rho u_d^2}{2}$ becomes zero. Thus, the maximum angular velocity that can be sensed depends on the coupling ring to drain radius ratio. Although equation 24 assumes inviscid flow, the result still holds qualitatively unless the height is so small that viscous effects predominate.

8.5.1 The Angle of Attack Pickoff

Using the assumption of potential flow, the classical solution for the pressure distribution around a circular cylinder in a stream of uniform velocity u_d is

$$p(\theta) = p_a + \frac{1}{2} \rho u_d^2 (1 - 4 \sin^2 \theta) \quad (25)$$

This distribution is illustrated in figure 16.

From equation 25 we find that the pressure gradient is

$$\frac{dp}{d\theta} = -4\rho u_d^2 \sin\theta \cos\theta \quad (26)$$

As may be readily found from equation 26, the pressure gradient $\frac{dp}{d\theta}$ is greatest when $\theta = 45^\circ$; consequently, if the stream angle changes from zero by some small amount, the largest change of pressure will occur at $\theta = 45^\circ$.

Although real flow is viscous so that the above solution is not exact, it does indicate that maximum sensitivity to a slight change in flow angle should be obtained by measuring the pressure at an angle of approximately 45° to the flow. The pickoff, therefore, has a small hole in it which is set at approximately 45° to the flow, when the probe is inserted into the drain. Ideally the hole should draw no flow since this will change the pressure distribution in its vicinity.

A type of pickoff is illustrated in figure 15. It contains an inner partition dividing it into two sections and is inserted in the drain with the holes at 45° to the axis as in figure 14. When the angular rate is zero, the flow in the drain is essentially vertical and both holes in the sensor make an angle of 45° with the flow. The pickoff shown uses an external plate to increase sensitivity.

When an angular velocity, ω , is imparted to the sensor, the flow spirals through the drain in a helical fashion so that the flow strikes one hole at an angle greater than 45° and the other one at an angle less than 45° . The pressure therefore increases on one side of the pickoff

partition and decreases on the other side. This pressure difference is thus a measure of the angular velocity.

The change in the difference in pressure produced across the pickoff partition, divided by the change in angular rate, is the sensitivity. In general one would like to make the sensitivity large. Now from equation 26, for a small change, $\Delta\theta$, in flow angle, the change in pressure, Δp , is given by

$$\Delta p = -4 u_d^2 \sin\theta \cos\theta \Delta\theta$$

and at 45°

$$\Delta p = -2\alpha u_d^2 \Delta\theta.$$

The difference in pressure between the two sides of the pickoff ($\Delta_2 p$) is then

$$\Delta_2 p = 2|\Delta p| = 4\alpha u_d^2 \Delta\theta \quad (27)$$

where α is a loss coefficient.

Now the change in angle, $\Delta\theta$, is given by

$$\sin \Delta\theta = \frac{u_{\theta d}}{u_d} = \frac{r_c}{r_d} \frac{u_{\theta c}}{u_d}$$

where $u_{\theta d}$ is the tangential velocity at the drain.

For small $\Delta\theta$

$$\Delta\theta \approx \sin\Delta\theta = \frac{r_c}{r_d} \frac{u_{\theta c}}{u_d} \quad (28)$$

Inserting equation 28 into 27

$$\Delta_2 p = 4\alpha \rho \frac{r_c}{r_d} u_d u_{\theta c} = 4\alpha \rho \frac{r_c^2}{r_d} u_d \omega \quad (29)$$

The substitution of u_d from equation 24 into equation 29 yields

$$\Delta_2 p = 4\alpha \rho \frac{r_c^2}{r_d} \omega \left[\frac{2(p_s - p_a)}{\rho} - \frac{r_c^4 \omega^2}{r_d^2} \right]^{\frac{1}{2}} \quad (30)$$

It is seen from equation 30 that the output signal initially increases approximately linearly for small ω , but as the second term under the radical becomes comparable to the first term, $\Delta_2 p$ reaches a maximum and then eventually decreases as the angular velocity ω increases.

The sensitivity is the derivative of equation 30 with respect to ω , and for small ω is given by

$$\left. \frac{d\Delta_2 p}{d\omega} \right|_{\omega \rightarrow 0} = 4\alpha \rho \frac{r_c^2}{r_d} \left[\frac{2(p_s - p_a)}{\rho} \right]^{\frac{1}{2}} \quad (31)$$

At least as important as the sensitivity is the threshold; that is, the smallest angular velocity that can be detected above the noise at a given bandwidth (or response time).

The fill time is the chamber volume divided by the volume flow. For inviscid flow the fill time t_{dro} is given for $r_c \gg r_d$ as

$$t_{dro} \approx \frac{r_c}{2u_{rc}} \quad (32a)$$

where u_{rc} is the radial velocity at the coupling ring.

The threshold angular velocity ω_{Th} is given by

$$\omega_{Th} = \frac{u_{\theta cT}}{r_c} \quad (32b)$$

where $u_{\theta cT}$ is the tangential velocity at the coupling ring radius ($r = r_c$) corresponding to the threshold angular velocity.

The product of the threshold angular velocity and the fill time is then

$$\omega_{Th} t_{dro} = \frac{u_{\theta cT}}{2u_{rc}} \quad (32c)$$

The flow angle ψ for the vortex devices is defined by $\tan \psi = \frac{u_{\theta}}{u_r}$. We may specialize this equation to define the threshold flow angle as

$$\tan \psi_{Th} = \frac{u_{\theta cT}}{u_{rc}} \quad (32d)$$

hence for small flow angles

$$\psi_{Th} \approx \frac{u_{\theta cT}}{u_{rc}} = 2 \omega_{Th} t_{dro} \quad (32e)$$

Since the pickoff of the sensor actually measures flow angle, it follows that the important consideration is not ω_{Th} or t_{dro} but their product; that is, we should be able to detect a smaller angular velocity by increasing the fill time.

In analogy with the inviscid case, we define the threshold angle for a sensor as the product of the threshold angular velocity and the response time. It is a figure of merit for the rate sensor. Threshold angles of the order of 10^{-3} degrees have been obtained.

A third factor is the null shift. When the angular velocity is zero, the difference signal out of the pickoff should be zero, but in general the signal is not zero and moreover the null shift varies with time (drift).

Null shift is due to asymmetries in the sensor, the most significant of which are usually due to inaccurate placement of the pickoff in the drain, slight differences between the two sides of the pickoff, particularly the holes, and asymmetry of the coupling ring. The most undesirable effect associated with the null shift is that it is pressure dependent. As a result, null shift is a major source of low frequency noise (drift) that comes from small fluctuations in the supply pressure. This causes variations in the amount of flow-field asymmetry and results in appreciable drift for small changes in pressure. The effect of pressure variation on the flow-field asymmetry is much greater than, and should not be confused with, the relatively small effect that occurs due to a small change of supply pressure as indicated in equation 31.

The circular pickoff is a major source of noise due to the shedding of vortices that occurs when there is flow past a circular cylinder. Although an appreciable portion of the resulting oscillation occurs over a narrow band of frequencies, there is also considerable broad-band noise. This vortex shedding can be minimized by streamlining the pickoff.

Another major source of noise is turbulence both within the chamber and in the drain. A great deal of the noise is generated as the fluid turns from the chamber into the drain.

The increase of tangential velocity according to the $1/r$ law is based on the assumption of inviscid flow. For real flow a boundary layer forms near the top and bottom plates that retards the flow so that the tangential velocity does not increase as fast as $1/r$. If we define the momentum efficiency as the momentum actually delivered to the pickoff, divided by the initial momentum, then in general the efficiency decreases as the top and bottom plates of the chamber are brought closer together. For this reason, the original designs of the vortex rate sensor used bottom-to-top plate distances greater than the boundary layer thickness, and a number of the earlier papers [35, 40] deal with this aspect. Recently however, Ostdiek [41] has pointed out advantages resulting from top and bottom plate distances appreciably less than the boundary layer thickness that outweigh the disadvantages of loss in sensitivity. These are the decrease in noise and in time response.

The response (fill) time for the inviscid sensor is essentially determined by dividing the chamber volume by the volume flow into or out of it

$$t_{dro} = \frac{\pi r_c^2 h}{\pi r_d^2 u_d} \quad (33a)$$

The expressions given for the fill time in equations 32a and 33a are equivalent. This can be proven by noting that from continuity $u_d = 2u_{rd} h/r_d$ and then applying equation 20. For low angular velocities ($u_{\theta c} \approx 0$), the substitution of equation 24 into equation 33a leads to

$$t_{dro} = \frac{r_c^2 h}{r_d^2 \left[\frac{2}{\rho} (p_s - p_a) \right]^{1/2}} \quad (33b)$$

This equation shows that for a fixed volume flow (or for a fixed supply pressure) the response time is proportional to the chamber height and that reducing the height reduces the time constant.

For the inviscid case considered, the drain radius is the determining factor for the volume flow at a given pressure, the volume flow being unaffected by the chamber size; however, when the plates are closer together than the boundary layer thickness, the effect of viscosity becomes appreciable so that the volume flow is no longer determined only by the drain area; we can then no longer be sure that the time constant is proportional to the height for a fixed pressure. On the other hand, we can still make a similar statement with respect to a fixed volume flow.

Actually the response time will decrease faster than the height for a fixed volume flow because for plates close together, the plates are closely coupled to the fluid by the boundary layer so that the angular velocity information is applied to the fluid from every point on the plates. This effect makes the coupling ring unnecessary and reduces the time constant.

The vortex rate sensor is primarily used to detect or measure small angular velocities. As has been pointed out (eq. 30), the output becomes non-linear for large angular rates. The linear range can be extended, however, by application of the technique for using feedback to null the device. In order to use this method, it is necessary to provide a counter rotation so that the output of the sensor is near zero. This counter rotation can be applied as proposed by Senstad [42] by using an electrolyte for the fluid and passing a current through it. A coil wound around the outer diameter of the sensor provides an axial magnetic field that acts on the moving charged-fluid particles causing them to move in the direction perpendicular to both the charge flow and the magnetic field; namely, in a circular path around the sensor.

The fluid signal from the pickoff is converted into an electrical signal that controls the polarity and amount of current through the electrolyte so as to attempt to make the pickoff output zero. The current necessary to cause this null is a measure of the angular velocity.

8.6 Variations of the Vortex Rate Sensor and Pickoffs

8.6.1 Ridged Double Drain

Schmidlin and Rakowsky [43] have devised a double drain that feeds directly into a fluid amplifier as illustrated in figure 17. Raised ridges arranged in a spiral manner placed around these drains tend to cause the flow to swirl down the drains, one clockwise and the other counterclockwise when there is no motion of the device itself. The two

drains feed the two controls of the fluid amplifier. Under conditions of no angular rotation, the flow into both controls is the same, resulting in a balanced output from the amplifier. Rotational flow in a drain effectively increases the resistance of the drain. If angular rotation causes the whole device to turn, then the circulation in one of the drains will increase and the circulation in the other will decrease, thereby increasing the resistance of one drain and decreasing the other. The resistance of the spiral ridges to the flow will also be different for the two drains. The flow will, therefore, no longer be balanced and the amplifier will become unbalanced since the flow into its controls will differ.

The device will saturate at values of angular rate equal to the angular rate that will cause zero rotation in one of the drains.

8.6.2 Plate and Pitot Tubes

This type of pickoff [44] is placed in the drain or just downstream of the drain. As illustrated in figure 18, the device essentially consists of a plate which closes off part of the drain, and two pitot probes placed as illustrated. Flow not having any swirl will cause the same pressure in each of the two pitots. However, as a result of a swirl given to the flow, the effect of the plate will be to shade the helical flow in such a way as to decrease the flow into one of the pitots with respect to the flow into the other.

8.6.3 Double Vortex Chamber Oscillator

This device [45] (fig. 19) uses two vortex chambers, one on either side of amplifier that is part of an oscillator circuit. The oscillation is obtained by feeding the outputs back to the controls. In addition to flow leaving from the conventional outlets, which in this case are used to provide the feedback to cause the oscillation, there is a second output to a set of vortex devices, one on each side of the amplifier as shown in figure 19. These vortex devices also feed back to the interaction region. Rotation of the entire device causes a circulation in the same direction in both vortical regions on either side of the amplifier. One of these will, therefore, be in the same direction as the flow from the amplifier; whereas, the other will be in the opposite direction. This will, therefore, cause a pressure difference across the amplifier resulting in departure from the symmetrical "sinusoidal" signal obtained when the device is not rotated (see fig. 19).

8.6.4 Application to a Drive Shaft

In most applications of the vortex rate sensor, one is concerned with very low angular rates. At low rates, the resistance drop across the sensor (from input to output) due to swirl is relatively small; at large angular rates, however, the pressure drop between the input and the output becomes large enough to be measured. This method is used, for example, to measure the speed of rotation of a drive shaft [46].

As figure 20 illustrates, a disc or wheel integral with the drive shaft provides the vorticity that causes a resistance drop between input and output. The input and output are then applied to the controls of a fluid amplifier.

8.6.5 Spherical Pickoffs

Sarpkaya [47] has designed a vortex rate sensor that uses vanes to obtain uniform input flow and to couple the sensor rotation to the fluid. The pickoffs consist of two spheres each supported by signal transmission tubes. This arrangement allows two additional degrees of freedom compared to the cylindrical pickoff, since the holes in the spheres can be translated and/or rotated with respect to each other. Sarpkaya states that this arrangement has resulted in increased sensitivity, more accurate nulling, less noise, and improved linearity.

9.0 ACCELEROMETERS

Most fluidic accelerometers involve a mass of some solid as well as the fluid. Even in those cases where only fluid is used, a diaphragm is usually involved. There is, however, one type that we will discuss that uses two different fluids and no diaphragm, and there are several types that use a single fluid directly affecting a fluid amplifier.

9.1 Seismic Mass

We first consider those types of accelerometers involving a solid seismic mass. A number of these are of the proximity sensor type. In this type of device the mass is situated between two proximity sensors such as shown in figure 21. A typical device measures the acceleration along the axis of two proximity sensors. Under acceleration, the ball moves toward one of the sensors and away from the other, causing pressure signals to arise as is usual in proximity sensors of this type [48].

The mass may also be inserted into a circuit [49] that includes one or more fluid amplifiers as illustrated in the figure 22. The mass used is a cylinder rather than a ball. When there is no acceleration the cylinder is midway between the two controls and the output of each of the two fluid amplifiers is balanced. Some part of each of the last stage outputs is fed back as illustrated. When acceleration causes the cylinder to move closer to one side than the other, the flow will be restricted causing the pressure in the side nearest the cylinder to increase, thereby deflecting the amplifier jets. This increases the feedback in a way that tends to further increase the pressure on the side nearest the cylinder. It is, therefore, necessary that care be taken in the design so that the gain is not large enough to cause saturation at too small values of the acceleration.

9.2 Vibrating String Accelerometer

The operation of the vibrating string accelerometer [50, 51] is based upon the fact that the vibration frequency of a string is dependent upon the tension. If, as is shown in figure 23a, an acceleration is applied in the direction A, the force on the mass will change the tension in the string. Air is blown past the string from a nozzle into a receiver opposite the string, resulting in Karman vortices being shed from the string which causes it to oscillate. Coupling of the resonant frequency of the string with the vortex oscillations force the oscillations to take on essentially the resonant frequency of the string. The vibration of the string in front of the receiver openings (fig. 23b) causes an output signal of the same frequency. By using two pairs of nozzles and receivers on opposite sides of the proof mass, a difference frequency is obtained.

10.0 ANGULAR ACCELEROMETERS

The principles used in the linear accelerometers can in general also be used for angular accelerometers. This is particularly true for fluid types such as those described by Schmidlin in part I. Schmidlin discusses [52] using one or more loops, filled with mercury, connecting the two controls of a fluid amplifier, as an angular accelerometer.

Depending upon the resistance in the loop, connecting together the two controls may cause oscillation. The device can still be used in that case as shown by Munch [53]. When there is no angular acceleration the signal out is sinusoidal. When an angular acceleration is present the waves become distorted in the same way as the rate sensor of Neradka [45]. Of course it is then necessary to process the signal in order to determine the acceleration.

Angular acceleration can also be measured by a device due to Colston [54]. This device also depends on loops or windings; however, these windings are interposed between two stages of fluid amplifiers and are perpendicular to the plane of the amplifiers.

11.0 PRESSURE DETECTING DEVICES

In certain processes it is necessary that a particular action should occur if a preset pressure level is reached. One way of doing this is to bias one control of a bistable switch, using a reference pressure so that the unit will switch when the pressure of the other control exceeds it. The comparison may also be made in a proportional amplifier, the output of which may then be used for actuation of some device or to switch a bistable device.

By using the geometry of figure 24, a band of pressure in the vicinity of the reference pressure may be selected [55]. If the unknown pressure is close to that of the reference pressure, the flow exits through A.

If the unknown pressure is either sufficiently less than or more than the reference pressure, the flow exits through B.

The need for an auxiliary reference pressure can be avoided by taking advantage of the different flow-pressure relations in a linear and a nonlinear resistor. The source to be measured is fed to one control of an amplifier through a linear resistor and to the other control through a nonlinear resistor. If the source and reference pressures are equal the amplifier outputs are equal. At low pressures, the flow through the nonlinear resistor will be less than that through the linear resistor (fig. 25). If the source pressure is greater than the reference pressure, the flow through the nonlinear resistor will be greater than that through the linear resistor. This concept has been used to obtain a pressure regulator by White and Kirshner [56, 57].

12.0 LEVEL SENSORS

These sensors are usually adaptations of a proximity and/or pressure sensor. In general if a number of tanks are to be filled with a liquid, the liquid itself is used in the fluid amplifiers sensing and controlling the level. When the desired level is attained, as indicated by some pressure threshold, the liquid is switched to another tank or to a reservoir [58, 59, 60]. If the system is one that requires that the liquid flow be shut off, then the sensing is done with air which actuates the valves to start or stop the flow of liquid [61, 62].

12.1 Acoustic Ear

The acoustic ear may be used to measure the distance to the top of the liquid or granular solid level, using an interference pattern to determine the distance between the sensor and the top of the material to be measured [63]. The sensor is situated vertically above the container of material. As the level of the material in the container rises, the distance between the sensor and the top of the material changes. As this distance decreases, the pressure intensity due to the interference-pattern receiver at the amplifier alternately increases and decreases, forming a wave pattern. The wave pattern is, however, not of constant amplitude because the intensity also changes not only because of interference, but also because the distance that the signal must travel decreases. As a result, the peaks of the signal grow successively larger as the distance decreases as shown in figure 26. The amplifier is set so that at the desired level the intensity of the peak reached will be sufficient to actuate turn off the material being supplied to the container.

12.2 Biased Amplifier

A method of sensing liquid level is to use a properly biased bistable amplifier to fill the container. One outlet of the amplifier empties into the container. The other goes back to the reservoir. One amplifier control is connected to a sensing tube which is perpendicular to and normally out of the liquid. While the container is being filled the amplifier

is biased in the direction causing the flow to move into the container. Air is being drawn through the sensing tube into the amplifier control. When the level of the liquid becomes high enough to cover the open end of the sensing tube, the pressure is lowered on that side of the amplifier which, therefore, flips so that the flow is now back into the reservoir instead of into the container [59, 60, 64].

12.3 Aspirator Fine Control

Aspiration through the sensing tube may be used to control the liquid level more accurately where that is desirable. In general there will be some liquid left in the outlet line when the liquid level has covered the sensing tube. This liquid will drain into the container changing the level somewhat. Suction caused by entrainment can be used to remove this excess fluid [66].

12.4 Proximity Sensor

A proximity sensor perpendicular to the liquid may also be used as a means of flipping an amplifier [66]. Air from a source supplies both the amplifier control and a tube. When the tube opening is above the liquid level, the tube resistance is low. When the water level rises to cover the tube opening, the resistance to flow becomes high and sufficient pressure and flow is then available to flip the amplifier. When the water level covers the tube, air from the tube bubbles through the water. This is, therefore, commonly called a bubbler tube type of sensor.

12.5 Interrupted Jet Sensor

An interrupted jet sensor such as shown in figure 3 can also be used as a liquid-level sensor. The sensor is positioned in the liquid so that it is perpendicular to the surface of the liquid with the emitter on the bottom. As long as the surface of the liquid is below the emitter, air from the emitter moves into the catcher. When the liquid level covers the emitter, the flow of air is interrupted causing a signal [67].

Interrupted jet sensors of the simple type (fig. 3a) are used to detect the level of oil-air foam mixtures according to a patent by Meyer [68]. The sensor is situated at the desired liquid level. The pressure recovery decreases as the foam mixture covers the jet receiver combination. In order to compensate for changes in pressure that may occur for environmental reasons, a second sensor is completely immersed within the liquid. The pressure recovery of the two sensors are then compared in an amplifier. The differential pressure indicates the presence or absence of the foam at the upper device.

12.6 Signal Propagation Time

The capacitance, or signal propagation time of a tube immersed in a liquid, has also been used to change the frequency of an oscillator as a function of the liquid level. The frequency of oscillation increases

because as the liquid rises in the tube its capacitance [69, 70] is changed.

13.0 TEMPERATURE SENSORS

In contrast with the many other types of temperature sensors, fluidic temperature sensors measure the temperature of a fluid in motion. Like the more conventional devices, however, the measurement is made on some parameter that is a function of the temperature.

When it is feasible, the gas whose temperature is desired, is moved through the temperature sensor. This technique gives the fastest response time. In other cases the sensor is used as a probe inserted into the material whose temperature is required, in which case the gas within the sensor must be allowed to approach thermal equilibrium with its surroundings.

13.1 Flow-Resistance Temperature Sensor

In the flow-resistance temperature sensor (fig. 27), the temperature of the flowing gas is determined by measuring the pressure drop across B-C [71]. It is more or less obvious that this requires that the pressure drop between A and B and/or C and D change in a different way with temperature than does the pressure drop between B and C.

One way of doing this is to place an orifice resistor between A and B and a capillary resistor between B and C as shown in figure 27.

For an orifice, the pressure drop Δp is given by

$$\Delta p = \frac{\rho u^2}{2} = \frac{8 \rho q^2}{c_d^2 \pi^2 d^4} \quad (34a)$$

where d is the orifice diameter.

For laminar flow in a capillary tube that exits into a sudden enlargement and has a uniform velocity input, it can be shown that [72]

$$\Delta p = \frac{128 \mu l q}{\pi d^4} + \frac{8 \rho q^2}{\pi^2 d^4} \quad (34b)$$

where, in equation 34, u is the axial velocity, q is the volume flow, d is the tube diameter, c_d is the discharge coefficient, μ is the viscosity and l is the length of capillary.

For most gases, μ is an exponential function of temperature over at least a limited range, i.e.,

$$\mu = \mu_0 T_a^n \quad (35a)$$

where μ_0 and n are positive constants (for air, $n = 0.76$ over an appreciable range) and T_a is the absolute temperature of the gas.

Furthermore, from the ideal gas law

$$\rho = \frac{p}{R_g T_a} \quad (35b)$$

where R_g is the gas constant.

Now, p , ρ , and T_a will actually be functions of position along the duct; however, for our purposes we shall use the averages over the duct volume and assume that equation 35b holds approximately for the average values.

Now, if the volume flow, q , is kept constant, the pressure drop across an orifice as a function of temperature, (from equations 34a and 35b), is of the form

$$\Delta p = a T_a^{-1} \quad (36)$$

whereas, the pressure drop across a capillary duct is of the form

$$\Delta p = b_1 T_a^n + b_2 T_a^{-1} \quad (37)$$

It follows from equation 36 that the pressure drop across the orifice decreases* with temperature; whereas, except at extremely low temperatures (when equation 37 no longer holds in any case) the pressure drop across the capillary increases with temperature since the first term for the most practical cases is numerically appreciably greater than the second. The factors that make the capillary (linear) term of equations 34b or 37 large with the respect to the square-law term also increase the capillary resistance so that a high sensitivity is associated with a large resistance. If this pressure drop is to be used as an input to a fluidic control system, it will be a high impedance source and the device into which it feeds must have a high input impedance.

Very often an even more important consideration is the time constant of the system arising from the high resistance, necessitated by the above requirement, coupled with the volume capacitances of the fluid lines.

When the measurement is made by immersing a probe, through which gas is flowing, into the medium to be measured, the internal gas is hot only downstream of the point of immersion so that the pressure drop will be different than for the case discussed above, where the measured gas flows through the resistance.

13.1.1 Bridge Type Resistance Temperature Sensors

Haspert has reported [73] the use of a fluidic bridge for measuring small temperature changes due to the passage of current through a wire. The sensor consists of two parallel sets of orifice and capillary resistors

*Note that this is not true if mass flow rather than volume flow is held constant.

in series (fig. 35 of part I). The wire is in the vicinity of one of the orifices and the bridge becomes unbalanced when the gas temperature changes due to passage of current through the wire.

13.1.2 Infrared Sensor

The infrared sensor [74] uses four laminar resistors each of which is zig zagged back and forth on a quadrant of a circular disk so as to substantially cover that quadrant. The four resistors together consequently cover the entire circular disk. The resistor covered disk is positioned on the axis of a parabolic reflector such that when the infrared source is on the reflector axis, the beam will be focused at the center of the disk and all four quadrants will be equally affected. If the heat source is off axis, the beam too will be off axis and the direction will be sensed by heating of the quadrant (or quadrants) upon which the beam falls. The resistors on diagonally opposite quadrants are connected to fluid amplifier inputs, the outputs of which provide an indication of the position of the beam.

13.2 Fluidic Oscillator Temperature Sensors

The frequency of a fluid oscillator [75, 76, 77, 78] depends on the speed of wave propagation. Since the speed of wave propagation in a gas depends on temperature, the frequency of oscillation is a measure of the temperature. The obvious approach is to use a fluid amplifier or a bistable switch together with a feedback circuit. The bistable switch used as an oscillator is shown in figure 28. The method of operation is as follows: If the jet is, for example, on the right-hand side, some of the flow will be returned through the feedback loop on the right-hand side to the right-hand control where it will switch the jet to the left-hand side. This in turn will now cause some of the flow to be returned through the left-hand feedback loop through the left-hand control and again switch the jet back to the right-hand side, thus completing the cycle.

The period of oscillation T will be

$$T = \frac{2l}{c} + 2\tau_s \quad (38)$$

where

- τ_s is the switching time and is inversely proportional to the jet velocity,
- c is the speed of wave propagation,
- l is the length of one loop.

If the duct is not too small, then the speed of wave propagation c will be approximately equal to the speed of sound a_s , given by

$$a_s = (\gamma R_g T_a)^{\frac{1}{2}} \quad (39)$$

where γ is the ratio of specific heats.

If we assume that the switching time τ_s is negligible, the frequency of oscillation, f , is then given from equations 38 and 39 by

$$f = \frac{1}{T} = \frac{(\gamma R_g T_a)^{\frac{1}{2}}}{2l} \quad (40)$$

The derivative of the logarithm of (40) shows that a change in frequency is related to a change in temperature by

$$df = \frac{f}{2T_a} dT_a .$$

Thus, for a given temperature the change in frequency is proportional to the frequency of oscillation. This means that to increase the sensitivity, it is necessary to increase the frequency at which the oscillator is operating; consequently, the feedback path should be short. (Making the feedback path short makes it necessary to take the switching time into account in relating temperature and frequency).

The feedback path is shortest if a resonant chamber or internal feedback is used instead of the external ducts. This configuration together with the high speed of oscillation eliminates wall attachment so that the switching time need not be considered.

13.2.1 Cavity-Type Oscillators

Gottron and Gaylord early in 1962 [75] found on examining the frequencies present in an oscillator built with external feedback that not only the frequency due to the line length was present but that a much higher frequency also existed. This higher frequency was quickly attributed to cavity resonance. Further experiment seemed to indicate that the frequencies were related both to edgetone frequencies and to the resonant frequencies of the cavities. This type of temperature sensor is often called an edgetone-cavity oscillator.

Since this oscillator is actually a special case of a beam deflection amplifier, equations (details will be published elsewhere) based on previous discussions [72, 79] of the beam deflection amplifier are presented.

Assuming rectangular cavities of breadth b_T and length l (in direction of the jet) on each side and that the nozzle-splitter distance is also l , then for an assumed constant jet velocity u and nozzle width b , the following expression relating the various parameters with the frequency is obtained:

$$\tan \frac{\beta_l}{2} = \frac{\beta_l}{2} \frac{1 - C_T \beta_l^2 (1 + 2m)}{1 - C_T \beta_l^2 (1 + m)} \quad (41)$$

where

$$C_T = \frac{b_T^2 N_M^2}{3l^2}; \quad N_M^2 = \frac{\rho u_o^2}{\gamma p} = \frac{u_o^2}{\gamma R_g T_a}$$

$$m = \frac{3b}{4b_T}$$

$$\beta_L = \frac{\omega l}{u_0}$$

ω = angular frequency

N_M = mach number:

Expression 41 is plotted in figure 29 for the first two modes of oscillation.

Although an infinite number of modes are possible from equation 41, considerations of the gain around the loop cause the higher modes of oscillation to drop out as C_T increases so that for $C_T > 0.045$ only the fundamental exists. It is interesting to note that this model predicts that for values of C_T near zero, the frequency of oscillation is the edgetone frequency.

Although quantitatively incorrect, the results do agree qualitatively with experiment with respect to the effect on the frequency of velocity, chamber length and breadth, and temperature. It is believed that the major reason for lack of quantitative agreement is the assumption of constant jet velocity. In addition to omitting the velocity dependence of the jet, the theory also neglects nonlinear effects that cause distortion of the wave at high amplitudes resulting in harmonics.

If the frequency is considered as a function of pressure it is apparent that as the pressure increases, a maximum frequency must eventually be reached when the flow becomes sonic somewhere in the system, since for pressures higher than that causing sonic flow, the velocity remains constant unless the temperature is changed.

When used as a temperature sensor, the flow should preferably be sonic in the sensor input or output line so that the Mach number in the oscillator is relatively independent of pressure. Then as the speed of sound changes, the velocity will change in the same way and because β_L is constant, the frequency will be proportional to the velocity and consequently proportional to the speed of sound.

The design is optimum if, when the flow is choked, the value of C_T is such that only the undistorted fundamental is present and its amplitude is maximum. This value must be slightly greater than 0.045 according to the linear analysis presented, so as to eliminate the higher modes, but must actually be appreciably greater than 0.045 to eliminate the modes of oscillation due to wave distortion.

13.2.2 Response Time of Oscillator Temperature Sensors

Very often an important consideration in a temperature sensor is its response time, i.e., the time that it takes to approach some fraction

of the final temperature when the temperature changes in the form of a step. When the temperature sensor is used as a probe to measure the temperature of its surroundings, the important considerations are to keep the mass flow through the sensor small and the walls thin.

When the gas, whose temperature is to be measured flows through the sensor, the physical considerations entering into the response time of the sensor can be essentially determined by examining the geometry of the system and considering the material of which it is made. The first relatively obvious requirement is that the sensor should be placed as close as is feasible to the point at which the temperature is to be measured and if possible the lines should be insulated.

Any distance between the point where the measurement is desired and the temperature sensor will allow the gas to exchange heat with its surroundings (the duct); and since in general the duct will never come up to the gas temperature because of its heat losses, the temperature at the sensor will not only take appreciable time to arrive at equilibrium, but will also be in error.

A second contributor to response time is the flush out time, the time involved in cleaning out or exhausting the gas at the old temperature. To the extent that the old gas tends to remain in the chamber and mix with the new gas, the response will be delayed. Therefore, the device must be designed to be flushed out by the incoming gas. A final important factor contributing to the response time is heat transfer between the walls of the oscillator and the gas by radiation and, to a lesser extent by conductivity.

When one attempts to read out the temperature or transfer this information to some other point, the advantages of the frequency technique compared with the resistor method become apparent. Temperature gradients in the readout system will affect the output of the resistor method (pressures and flows) to an unknown extent leading to erroneous results, but this will not affect an output frequency. Thus, the frequency signal can be transmitted for some distance without altering the frequency and may be used as a fluid control signal.

If this signal is to be carried over an appreciable length of line, several considerations are important. In general we desire a high signal-to-noise ratio. A temperature sensitive oscillator not only has to contend with random noise but because of the nonlinearities involved, harmonics of the frequency corresponding to the temperature also appear. If this signal is to be used in a servo system, then it is necessary that the ratio between the amplitude of the fundamental and the next harmonic be fairly large. This ratio can be kept reasonably large by careful attention to the design of the oscillator and to the fluid lines, and the matching of the oscillator to the fluid lines. In some cases it may be necessary to add acoustic filters to filter the harmonics or to decrease their amplitudes.

In many cases it is necessary to convert the oscillating signal into a d.c. pressure proportional to frequency. Some circuits to do this are discussed by Sutton and Chapin [80].

The time response of temperature sensing oscillators is discussed by McMillan and Pamperin [81] who model it as the sum of two first-order lags

$$G(s) = \frac{k_1}{1 + \tau_1 s} + \frac{k_2}{1 + \tau_2 s}$$

where τ_1 is the time delay associated with the flush-out time and τ_2 is the delay associated with the thermal inertia of the body.

The authors give typical time constants as

$$\begin{aligned}\tau_1 &= 0.01 \text{ seconds} \\ \tau_2 &= 2.0 \text{ seconds.}\end{aligned}$$

The second time constant may be compensated for by a lead circuit, according to the authors.

14.0 VELOCITY METER OR FLOWMETER

An oscillator can be used as a flowmeter [82, 83] over some velocity range because the frequency is velocity dependent for the lower velocities.

For example, if we examine figure 29, we note that for C_T sufficiently small, β_l is approximately constant.

Since $\beta_l = \frac{\omega l}{u} = \frac{2\pi f l}{u}$, it follows that for $\beta_l = \text{constant}$, the frequency f is proportional to the velocity. Thus, for low velocities, the frequency will increase approximately linearly with velocity. If a cavity oscillator is used to measure velocity, it is apparent that the geometry should be chosen such that $C_T \approx .03$ for the highest velocity to be measured and, in general it is seen that figure 29 equations 41 indicate that for an oscillator intended for use as a flowmeter, the ratio b_T/l should be made small so as to extend the linear region; whereas, for an oscillator intended as a temperature sensor, the ratio b_T/l should be large so that the frequency can be made pressure insensitive at lower pressures.

The external feedback type of oscillator (fig. 28) has some advantages over the cavity type when used as a flowmeter. This type of oscillator can be designed to give a long linear range of frequency vs. velocity and tends to provide a cleaner signal at low velocities than does the cavity type oscillator. The reason for the cleaner signal is that the cavity type has many modes of oscillation competing for the energy at low velocities, as compared with the external feedback type.

Now the period of oscillation T is given in equation 38 as

$$T = \frac{2L}{c} + 2\tau_s$$

where τ_s is the switching time. This switching time is inversely proportional to the jet velocity, i.e.,

$$\tau_s = \frac{kL}{u}$$

where L is the nozzle to splitter distance. A fast switching device has a value of k between one and two, but in some devices k can be appreciably greater. If a long linear range is desired, then k should be large and the feedback line should be as short as possible so that τ_s is large compared to the time for feedback. This will result in a long linear range.

15.0 RESISTANCE BRIDGE CONCENTRATION SENSOR

The bridge configuration used for temperature sensing can also be used to determine the concentration of a known impurity in a gas. (See fig. 35 of part I).

An equation, relating the concentration of gas it is desired to measure, is obtained by Villaroel and Woods [34] as follows:

The pressure drop across the linear resistor is given by

$$p_L = a\mu q \quad (42)$$

where μ = viscosity;
 q = volume flow;
 a = constant dependent on geometry.

The pressure drop across the nonlinear resistor is given by

$$p_N = b\rho q^2 \quad (43)$$

where ρ = density;
 b = constant dependent on geometry.

The pressure drop across the two resistors in series, p_B , is held constant and

$$p_B = p_{LS} + p_{NS} = p_{LR} + p_{NR} \quad (44)$$

where the subscripts S and R indicate the halves of the bridge through which pass respectively the sample and reference gases.

From equations 42 and 43 we have for the reference gas

$$P_{NR} = b\rho_R \frac{P_{LR}^2}{a^2\mu_R^2} \quad (45)$$

A similar equation holds for the sample gas.

From equations 44 and 45

$$1 = \frac{P_{LR}}{P_B} + \frac{P_{NR}}{P_B} = \frac{P_{LR}}{P_B} + \frac{b\rho_R P_B}{a^2\mu_R^2} \frac{P_{LR}^2}{P_B^2}$$

Defining

$$\theta \equiv \frac{b\rho_R P_B}{a^2\mu_R^2} \quad (46)$$

$$\frac{P_{LR}}{P_B} = \frac{\sqrt{1 + 4\theta} - 1}{2\theta} \quad (47)$$

Then defining

$$\begin{aligned} \Delta p_c &\equiv P_{LS} - P_{LR} \\ k &\equiv \frac{\rho_S \mu_R^2}{\rho_R \mu_S^2} \end{aligned} \quad (48)$$

After finding $\frac{P_{LS}}{P_B}$ from equations 44 and 45, we obtain

$$\frac{\Delta p_c}{P_B} = \frac{\sqrt{1 + 4k\theta} - 1}{2k\theta} - \frac{\sqrt{1 + 4\theta} - 1}{2\theta} \quad (49)$$

If the bridge is to be used to measure the amount of a known impurity in a known gas, for example excess CO_2 in air, then air is used as the reference gas and excess CO_2 in air is the sample gas. For small amounts of CO_2 , k will be approximately equal to unity. On the assumption that $k \approx 1$, $G(\theta)$ defined below, can be approximated from equation 49 as

$$G(\theta) \equiv \frac{\Delta p_c}{P_B} \approx \frac{\sqrt{1 + 4\theta} - 2\theta - 1}{2\theta\sqrt{1 + 4\theta}} \left(\frac{k - 1}{k} \right) \quad (50)$$

From equation 46, θ is a constant whose value depends on the geometry of the resistors, the characteristics of the reference gas and the pressure across the bridge; whereas, k is the parameter that is sensitive to the concentration of the impurity.

The function $G(\theta)$ has a maximum at $\theta = 1.207$ where

$$G(\theta) = \frac{\sqrt{1 + 4\theta} - 2\theta - 1}{2\theta\sqrt{1 + 4\theta}} \quad (51)$$

Consequently maximum sensitivity is obtained if, for the particular reference gas being used, resistor geometries and the pressure p_g is chosen such that $\theta = 1.207$.

The above analysis assumes that both the linear and nonlinear resistances are pure; in actual fact, however, the linear resistances will have some nonlinearity and vice versa. Villaroel and Woods show that this impurity of the resistances can be accounted for by a multiplicative factor η .

A plot of $G(\theta)$ for CO_2 is given in figure 36 part 1.

16.0 IN CONCLUSION

The sensors described in parts 1 and 2 by no means include all the fluidic sensors. New types are continually being devised, most often by adapting, modifying, or combining one or more existing sensors to a new use, and occasionally by applying for the first time some fluid phenomenon that had previously escaped recognition as a means of sensing.

Seemingly unrelated improvements in fluidic devices (such as low noise laminar amplifiers) often make possible new or improved sensors. Thus, we can continue to look forward not only to the capability of better sensing techniques to improve current devices, but to the possibility of measuring fluid properties in ways not thought of as yet.

REFERENCES

1. Brychta, O. and Suresh, N., "New Pneumatic Signal Generator," ASME Paper #71-WA/FIcs-4, December 1971.
2. Moses, H. L., Small, D. A. and Cotta, G. A., "Response of a Fluidic Air Gauge," ASME Paper #68-WA/FE-16, December 1968.
3. Jacobs, B. E. A. and Baker, P. J., "The Development of Fluidic Sensors for Application in Steel Handling," Paper R4, Fourth Cranfield Fluidics Conference, 17-20 March 1970.
4. Izawa, Keisuke, Tokyo Institute of Technology, as reported at the Fluidics Round Table Discussion, IFAC June 1969.
5. Beeken, Basil B., "Acoustic Fluidic Sensor," Instruments and Control Systems, February 1970.
6. O'Keefe, Robert F., "Importance of Fluidics to Air Control Technology," National Conference on Fluid Power 20 October 1971.
7. Beeken, B. B., "Long Range Fluidic Acoustic Sensor," paper 72-WA/FIcs-8, November 1972.
8. O'Keefe, Robert F., "Development and Application of a New Jet Interaction Fluid Amplifier," 22nd ISA Conference, 11-14 September 1967, Preprint #15-2-MCID-67.
9. Rockwell, Donald O., "The Macroscopic Nature of Jet Flows Subjected to Small Amplitude Periodic Disturbances," Chemical Engineering Progress, pp 99-107, Vol. 67, No. 109, 1971.
10. Kinsler, L. and Frey, A., "Fundamentals of Acoustics," page 169, Second Edition, John Wiley and Sons, Inc.
11. Ibid, page 174.
12. Kishel, J. F., "Fluid Apparatus for Detecting Acoustic Signals," US Patent 3,529,615, 22 September 1970.
13. Daruk, A. S. and Rukhadze, V. A., "Pneumatic Force Transducer," US Patent 3,472,257, 14 October 1969.
14. Drzewiecki, T. M., "Fluidic Strain Gage Concepts," HDL-TR-1575, December 1971.
15. Drzewiecki, T. M., "The Fluidic Load Cell," HDL-TR-1622, June 1973.
16. Tanney, J. W., "Three Fluidic Sensors Using Unbounded Turbulent Jets," Paper #R1, Fourth Cranfield Fluidics Conference, 17-20 March 1970.

17. Roshko, Anatol, "On the Development of Turbulent Wakes from Vortex Streets," TN2913, NACA 1952.
18. Bailey, S. J., "Two New Flowmeters Have No Moving Parts," Control Engineering December 1969.
19. Campbell, R. J., "New Vortex Flowmeter Uses Ultrasonics," Control Engineering July 1973.
20. Sharpsteen, James T. "Fluid Amplifier Measures Flow Velocity," Control Engineering January 1966.
21. Ruedy, R., "Vibrations of Power Lines in a Steady Wind," Canadian Journal of Research, Vol. 13, Section A, 1935.
22. Rodely, Alan E., "The Swirl Flowmeter," Journal of the Southern California Meter Association March 1968.
23. Fox, H. L., "Direct Fluidic Sensor," Instrumentation Technology, September 1967.
24. Levin, G. A., "Pneumatic Sensing Device with Digital Readout," US Patent 3,239,142, 08 March 1966.
25. Nightingale, R. A., "Angular Position Indicators for Rotatable Shafts," US Patent 3,433,238, 18 March 1969.
26. Bright, Lawrence, S., "Fluidic Angular Position Transducer," US Patent 3,620,239, 16 November 1971.
27. Welk, Horace B. Jr., "Fluidic Angular Displacement Sensor," US Patent 3,776,043, 04 December 1973.
28. National Research Development Corporation British Patent Spec 1,214,061, 02 December 1970.
29. Leathers, J. W. and Davis, J. C. H., "A New Rotational Speed Sensor for Fluidics," Paper T3, Fourth Cranfield Fluidics Conference, 17-20 March 1970.
30. Katz, S. and Hastie, E., "Fluidic Sensing of Rotational Speed Using Spur Gears," ASME Joint Gas Turbine Fluid Engineering Conference, March 1972.
31. Katz, S., "Speed Sensor and Regulator for Prime Movers," US Patent No. 3,260,271, 12 July 1966.
32. Iseman, Joseph M., "Angular Velocity Regulation with a Fluid Interaction System," HDL Fluid Amplification Symposium, Vol. III, May 1964.
33. Bowles, R. and Horton, B., "Fluid Vortex Transducer, US Patent 3,417,624, 24 December 1968.

34. Burke, J. F., Scudder, K. R. and Dunn, J. L., Pick-off for Fluid Angular Rate Sensor, US Patent 3,454,023, 08 July 1969.
35. Sarpkaya, Turgut, "A Theoretical and Experimental Investigation of the Vortex-Sink Angular Rate Sensor", Proceedings of the Third HDL Fluid Amplification Symposium, Vol. 2, October 1965.
36. Ogren, H. D., "Vortex Rate Sensor," US Patent 3,202,237, 31 August 1965.
37. Doyle, R., "Vortex Rate Sensor," US Patent 3,240,060, 15 March 1966.
38. Jones, D. R., "Readout for Vortex Amplifier," US Patent 3,272,213, 13 September 1966.
39. Scudder, K. R., Burke, J. F., and Dunn, J. L., "Fluid Angular Rate Sensor," US 3,365,955, 30 January 1968.
40. Sarpkaya, T., Goto, J. M. and Kirshner, J. M., "A Theoretical and Experimental Study of Vortex Rate Gyro," Advances in Fluidics ASME, May 1967.
41. Ostdiek, Arthur J., "Viscous Vortex Rate Sensor," HDL-TR-1555, November 1971.
42. Senstad, P. D., "Magnetically and Electrically Rebalanced Vortex Rate Sensor," US Patent 3,230,765, 25 January 1966.
43. Schmidlin, Albertus E. and Rakowsky, Edward L., "Angular Rate Sensor," US Patent 3,530,725, Patented 29 September 1970.
44. Brooks, John D., "Helical Fluid Signal to Pressure Signal Converter," US Patent 3,336,932, 22 August 1967.
45. Neradka, Vincent F., "AC Vortex Rate Sensor," US Patent 3,529,613, 22 September 1970.
46. Przybylko, S. J., "Vortex Analog Speed Sensor," US Patent 3,342,196, 19 September 1967.
47. Sarpkaya, Turgut, "A Pneumatic Vortex Angular Rate Sensor-Analysis and Experiments," Second IFAC Symposium on Fluidics, 28 June - 2 July 1971, Prague, Czechoslovakia.
48. Fish, V. R. and Lance, G. M., "An Accelerometer for Fluidic Control Systems," ASME Publication 67-WA/FE-29, ASME Winter Annual Meeting, 12-17 November 1967.
49. Bauer, Peter, "Uniaxial Accelerometer Controlled Fluidic Amplifier," US Patent 3,543,782, 1 December 1970.
50. Schmidlin, Albertus E. and Evans, John L., "Fluidic Accelerometer," US Patent 3,581,579, 1 June 1971.

51. Clark, W. K., Lederman, W. and Smith, M. S., "The Fluidic Vibrating String Accelerometer," presented at the IFAC Symposium on Fluidics, 4-8 November 1968.
52. Schmidlin, A. E., "Flueric Accelerometer," US Patent 3,577,786, 4 May 71.
53. Munch, Otto R., "Fluidic Accelerometer," US Patent 3,712,324, 23 Jan 73.
54. Colston, John R., "Accelerometer," US Patent 3,450,145, 17 June 1969.
55. Bauer, Peter., "Pressure Band Detector," US Patent 3,340,885, 12 Sep 67.
56. White, H. N. and Kirshner, J. M., "Fluid Pressure Regulator and Reference," US Patent 3,457,936, 29 July 1969.
57. White, Harry N., "Flueric Pressure Regulation Using a Resistance Set Point," Vol. 4, HDL Third Amp Symp, October 1965.
58. Adams, R. B., "Level Control Apparatus," US Patent 3,267,949, 23 Aug 66.
59. Manion, F. M., "Automatic Fill Valve," US Patent 3,277,914, 11 Oct 66.
60. Boothe, W. A., "Liquid Level Control Means," US Patent 3,404,700, 8 Oct 68.
61. Kirchmier, W. O., "Liquid Level Controller," US Patent 3,463,278, 26 Aug 69.
62. Jones, D. R., "Liquid Level Sensor," US Patent 3,467,122, 16 Sep 69.
63. O'Keefe, Robert F. and Beeken, Basil B., "Fluidic Acoustic Techniques for Level Detection and Control," Instrument Society of America International Conference and Exhibit, 15-18 Oct 73.
64. Shinn, Jeffery N., "Means to Control the Admission of Liquid into a Container," US Patent 3,392,741, 16 Jul 68.
65. Hanaoka, Masanori, "Liquid Level Controlling Apparatus," US Patent 3,702,122, 7 Nov 72.
66. Hisada, Takeo, Nakajima, Fumio, Nishi, Takeshi and Sugiyama, Kunro "Liquid Level Detecting Apparatus," US Patent 3,680,579, 1 Aug 72.
67. Wilson, J. N. and Dumont, R. S., "Fluidic Liquid Level Sensor," p 835, Instrument Society of America International Conference and Exhibit, 15-18 October 1973.
68. Meyer, Arthur Stivers, "Multiple-Jet Liquid Level Detector," US Patent 3,590,843, 6 July 1971.
69. Sowers, Edwin U. III, "Fluidic Liquid Level Detector," US Patent 3,542,050, 24 November 1970.

70. McKinnon, M. G., Wilson, J. N. and Besant, R. W., "Fluidic Position Sensor," US Patent 3,690,339, 12 Sep 72.
71. Kirshner, J. M., "Fluid Thermometry," IEEE Transactions of Industrial Electronics and Control Instrumentation, July 1969.
72. Kirshner, J. M. and Katz, S., "Design Theory of Fluidic Components," Academic Press, Jan 1975.
73. Haspert, J. K., "Flueric Sensor for RF-Induced Currents in Bridge Wires," HDL-TM-69-5, March 1969.
74. Zaginailoff, Ralph G., "Fluidic Infrared Sensing Device," US Patent 3,598,136, 10 Aug 71.
75. Gottron, Richard N. and Gaylord, Wilmer, "Pneumatic Thermometer," US Patent 3,706,227, 19 Dec 72.
76. Carter, Vondell, "Flueric Temperature Sensor," US Patent 3,667,297, 6 Jun 72.
77. Zoerb, Edward G., "Cooled Temperature Sensitive Oscillator," US Patent 3,707,979, 2 Jan 73.
78. Bailey, Ronald G., "Fluidic Sensor," US Patent 3,587,603, 28 Jun 71.
79. Kirshner, J. M., "Fluerics 35. Jet Dynamics and Its Application to the Beam-Deflection Amplifier," HDL-TR-1630, July 1973.
80. Sutton, Trevor G. and Chapin, Donald W., "Fluidic Characteristic Sensor," US Patent 3,570,514, 16 Mar 71.
81. McMillan, John G. and Pamparin, Ralph, H., "Application of Fluidic Sensors for Measurement of Turbine Inlet Temperature," Automotive Engineering Congress, 10-14 Jan 72, S.A.E. Number 720158.
82. Andrelev, N., "Fluidic Oscillator Measures Flow," Control Engineering, September 1973. page 56.
83. Tippetts, J. R., Royle, J. K. and Ng, H. K., "An Oscillating Bistable Fluid Amplifier for Use as a Flow Meter," Proceedings of the 2nd IFAC Symposium on Fluidics, 28 Jun - 02 Jul 71.
84. Villaroel, Fernando and Woods, Robert L., "An Analog Flueric Concentration Sensor Applicable to Respiratory Gases," Paper 73-WA/Bio-9, ASME Winter Annual Meeting, 11-15 Nov 73.

LIST OF FIGURES

- Figure 1 Possible Pickoff Positions on a Back Pressure Sensor
- Figure 2 Output Pressure vs Separation Distance
- Figure 3 Interrupted Jet Sensors
- Figure 4 Thread (Small Object) Sensor
- Figure 5 Pneumatic Force Transducer
- Figure 6 Transducer Response Curves
- Figure 7 Fluidic Strain Gage
- Figure 8 Fluidic Strain Gage
- Figure 9 Velocity Sensor
- Figure 10 Angular Position Sensor
- Figure 11 Angular Position Coding Wheel
- Figure 12 Fan Type Angular Speed Sensors
- Figure 13 Angular Speed Sensors
- Figure 14 Vortex Rate Sensor
- Figure 15 Angle of Attack Pickoff
- Figure 16 Pressure Distribution About Pickoff
- Figure 17 Vortex Rate Sensor with Dual Drain
- Figure 18 Plate and Pitot Drain Arrangement
- Figure 19 Vortex Rate Sensor Oscillator
- Figure 20 Drive Shaft with Vortex Rate Sensor
- Figure 21 Accelerometer with Fluidic Output
- Figure 22 Fluidic Accelerometer
- Figure 23 Vibrating String Accelerometer
- Figure 24 Pressure Band Detector
- Figure 25 Resistance Cross-over Pressure Reference
- Figure 26 Intensity as a Function of Distance

LIST OF FIGURES (CON'T)

- Figure 27 Capillary and Orifice Resistors in Series
- Figure 28 External Feedback Oscillator
- Figure 29 Normalized Frequency β_k as a function of the Oscillator Parameter C_T



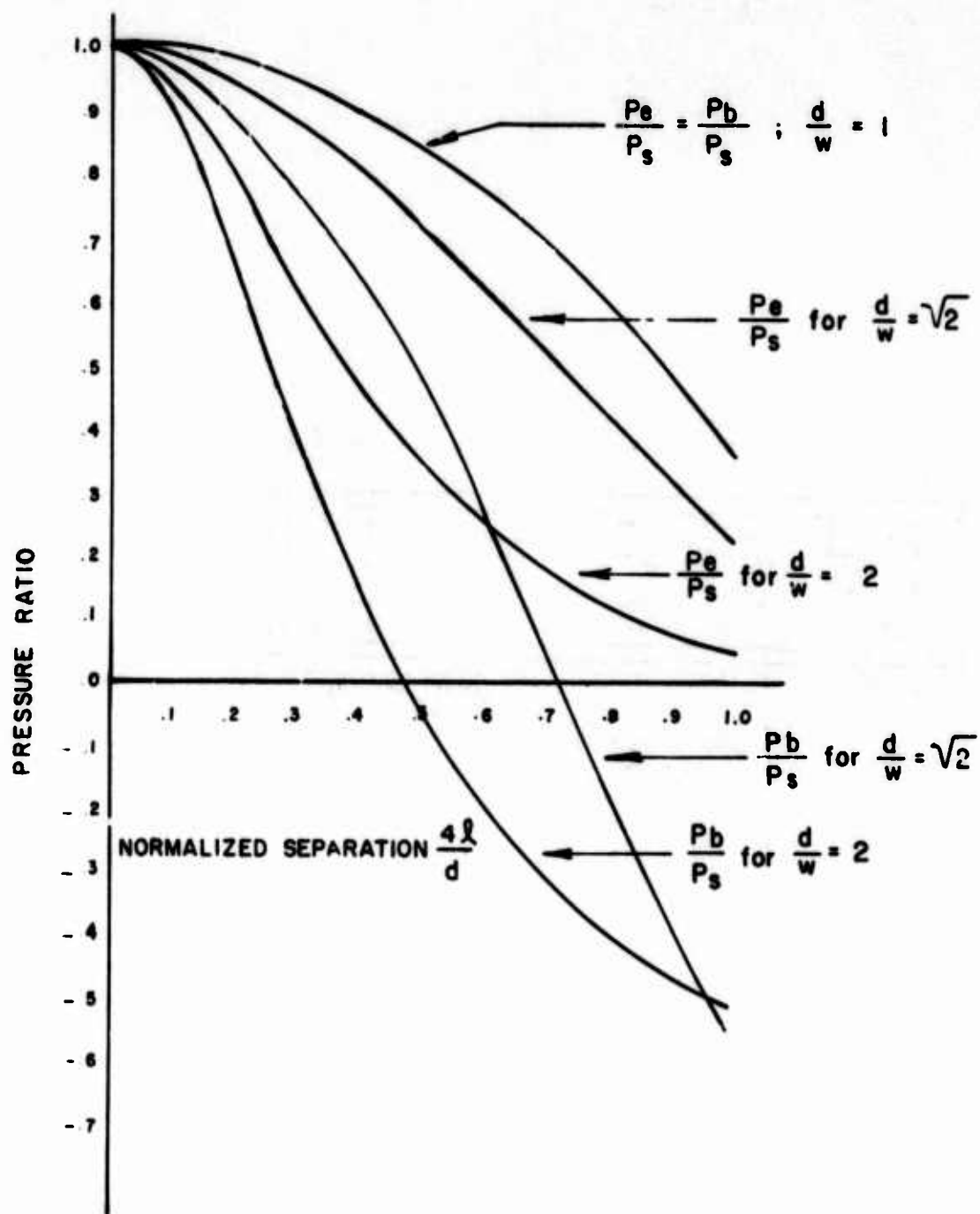
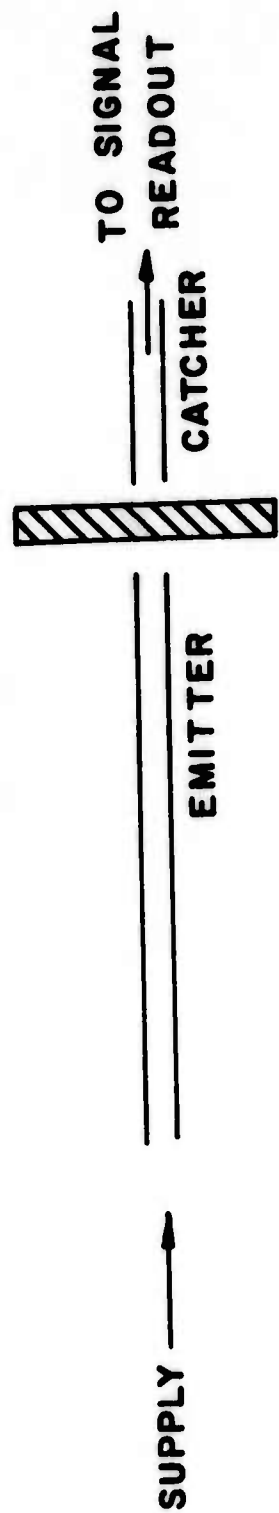
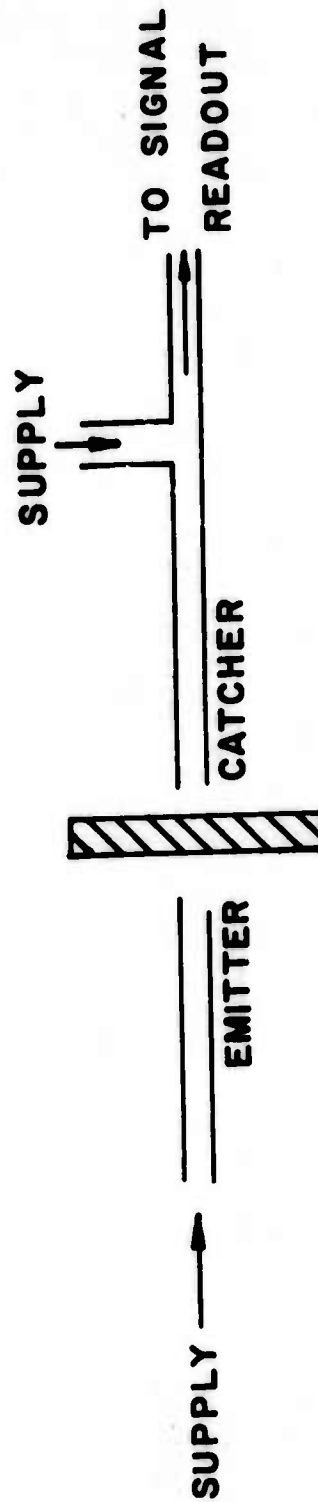


Fig. 2 Output Pressure vs Separation Distance



a. INTERRUPTED JET SENSOR



b. INTERRUPTED JET—BACK PRESSURE SENSOR

Fig. 3 Interrupted Jet Sensors

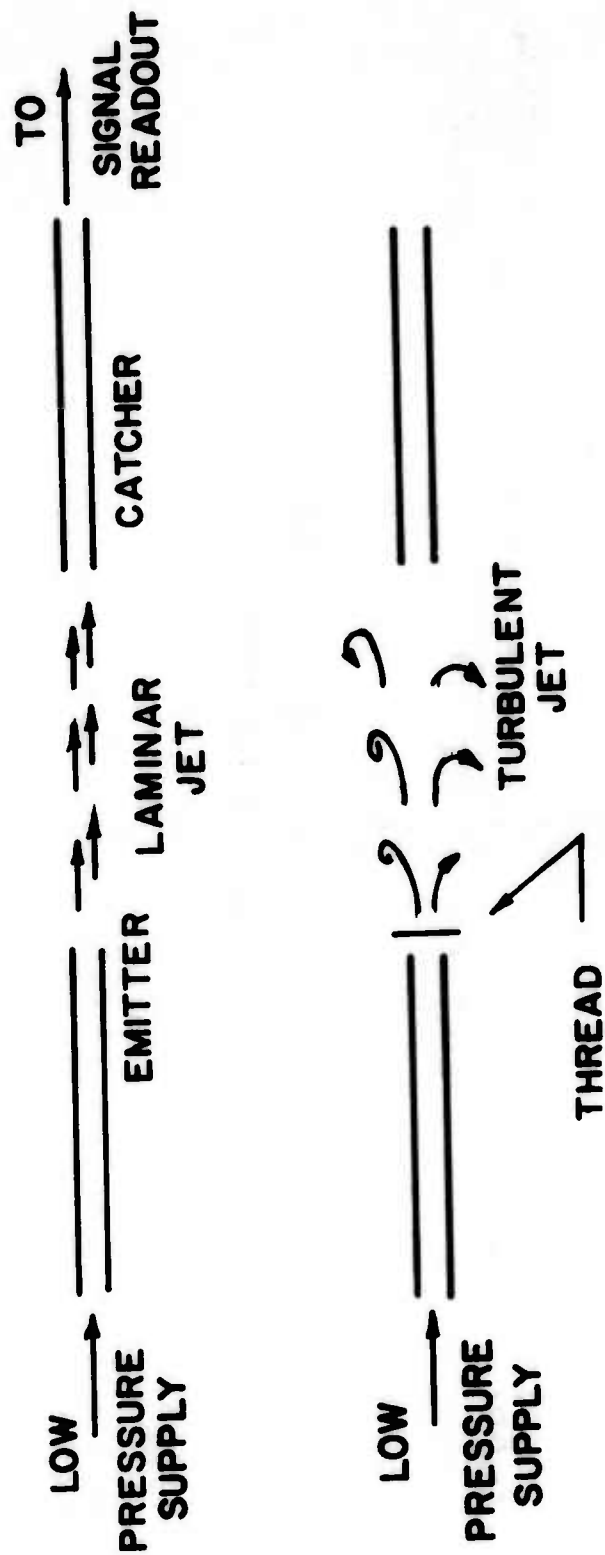


Fig. 4 Thread (Small Object) Sensor

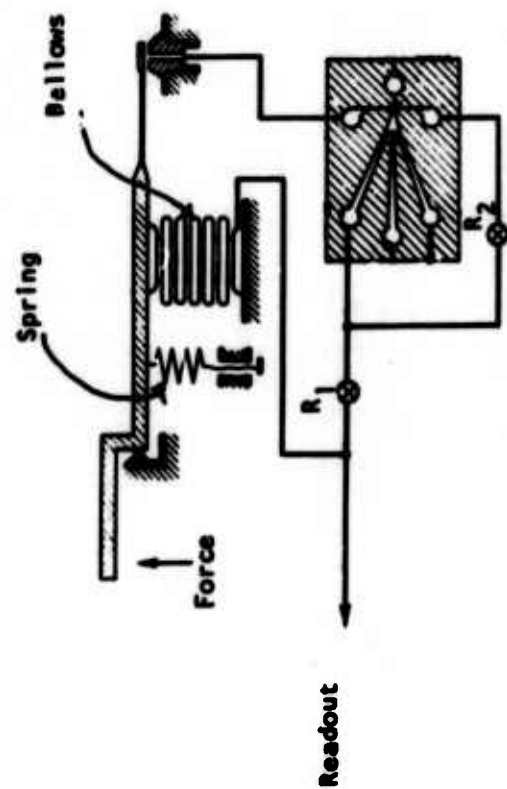


Fig. 5 Pneumatic Force Transducer

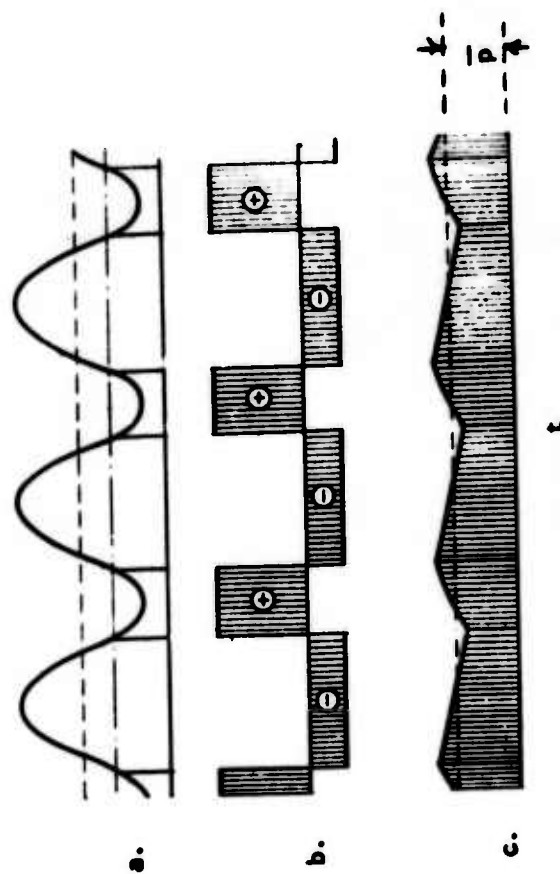
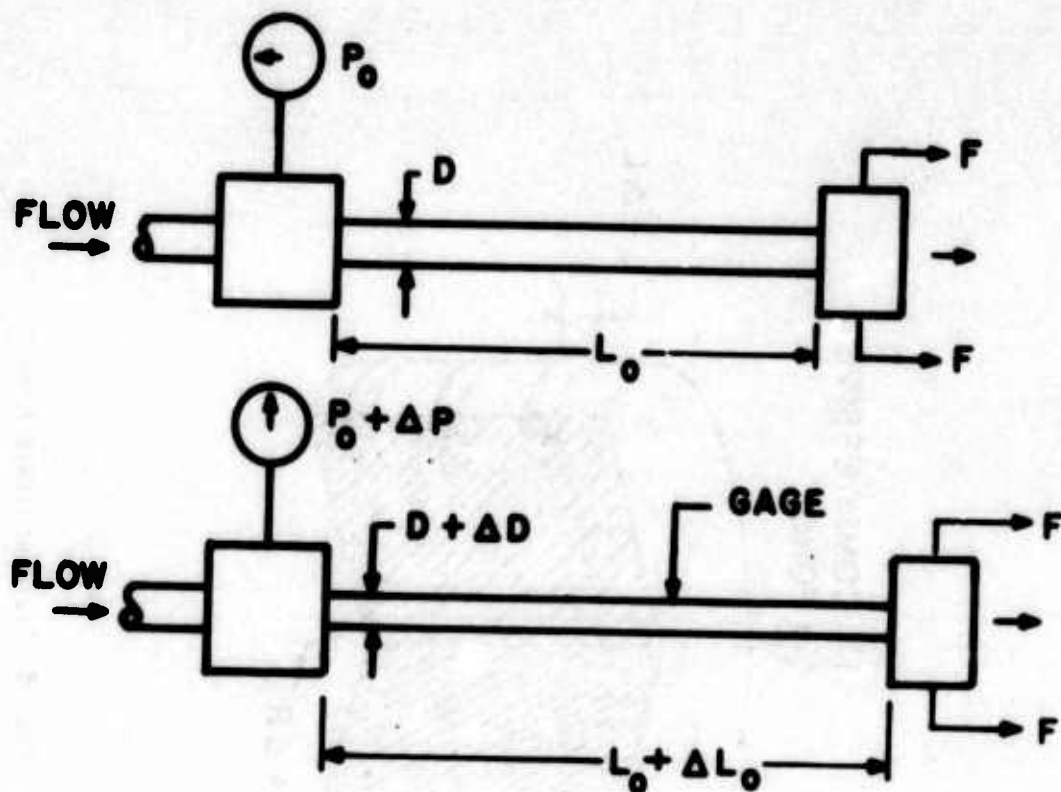


Fig. 6 Transducer Response Curves



$$\frac{\frac{\Delta P}{P_0}}{\frac{\Delta L}{L_0}} = 1 + 4\epsilon \left\{ \begin{array}{l} = 3.0 \text{ RUBBER} \\ = 2.2 \text{ STEEL} \end{array} \right.$$

ϵ - POISSON'S RATIO

Fig. 7 Fluidic Strain Gage

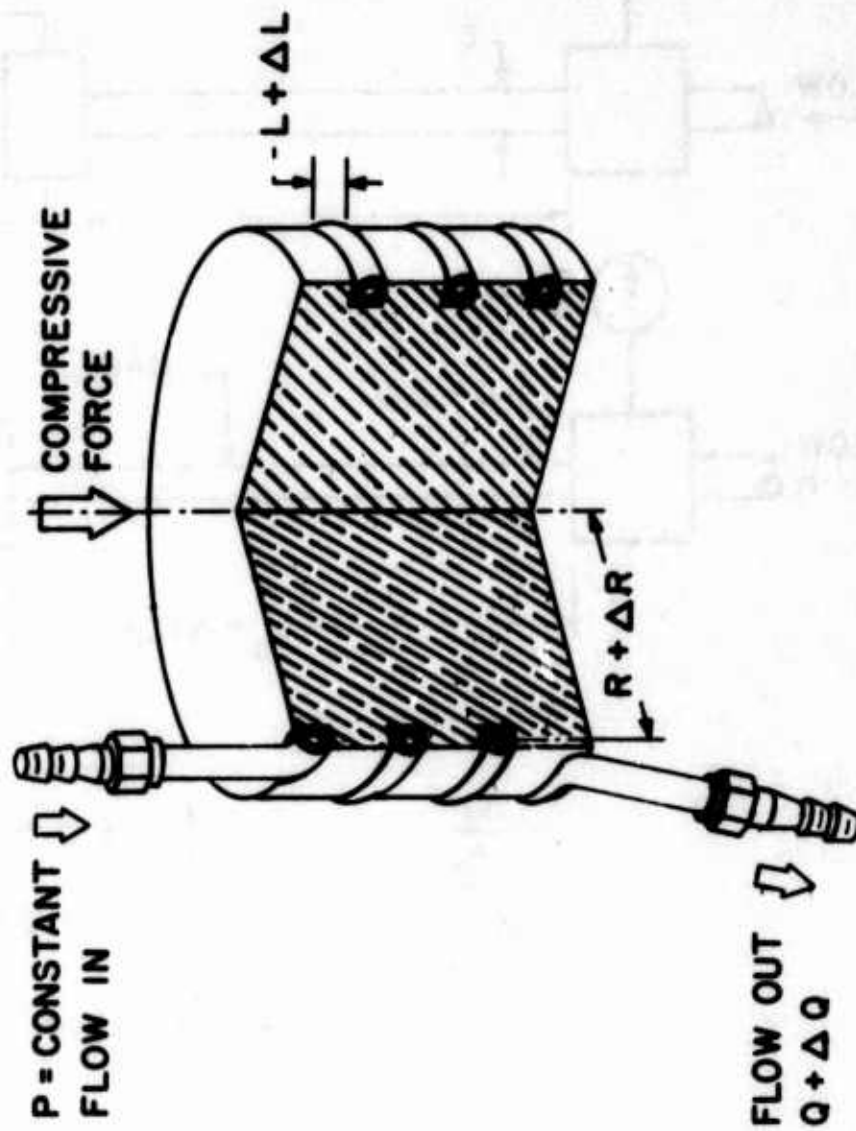


Fig. 8 Fluidic Strain Gage

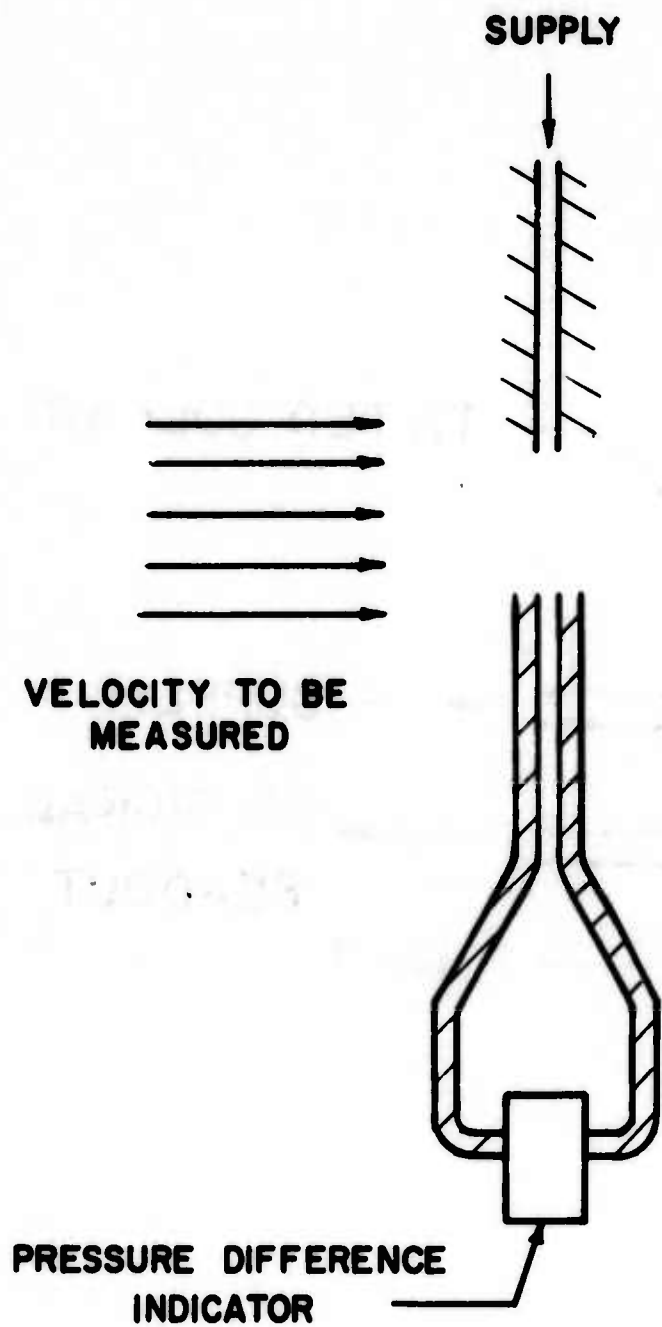


Fig. 9 Velocity Sensor

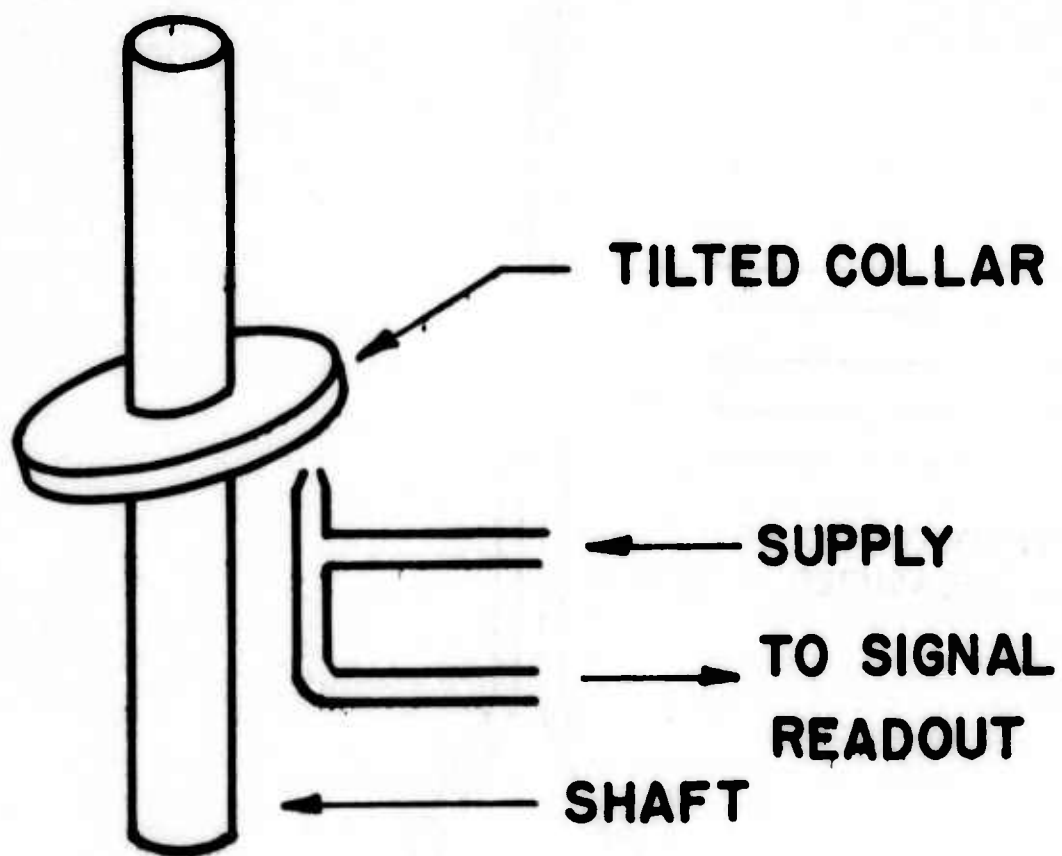


Fig. 10 Angular Position Sensor

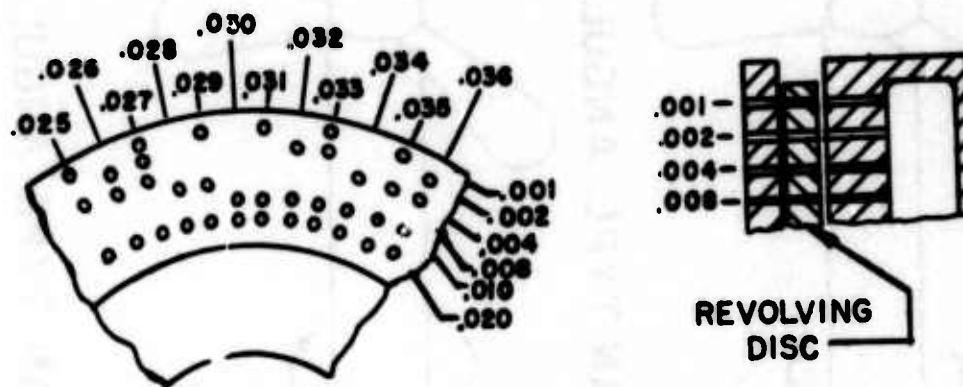
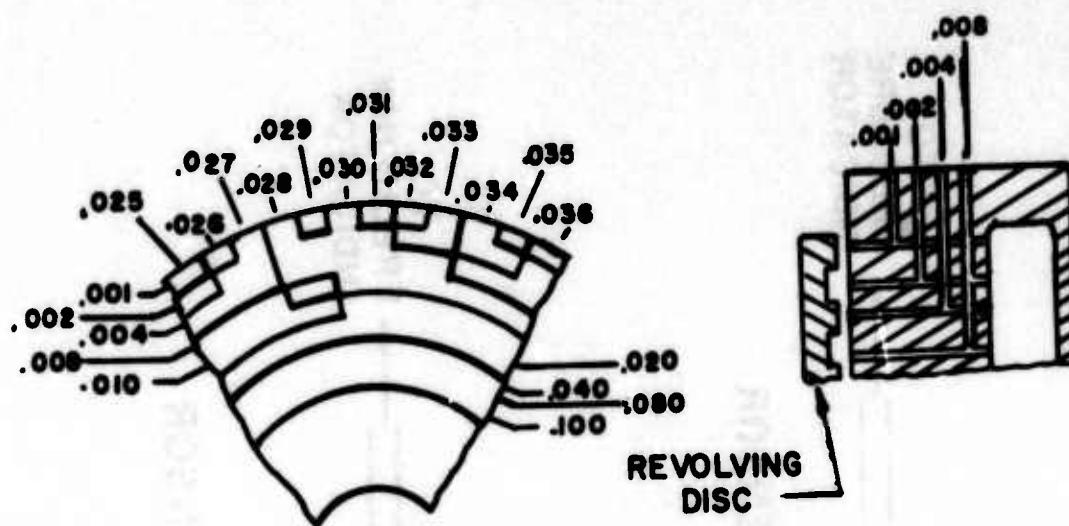
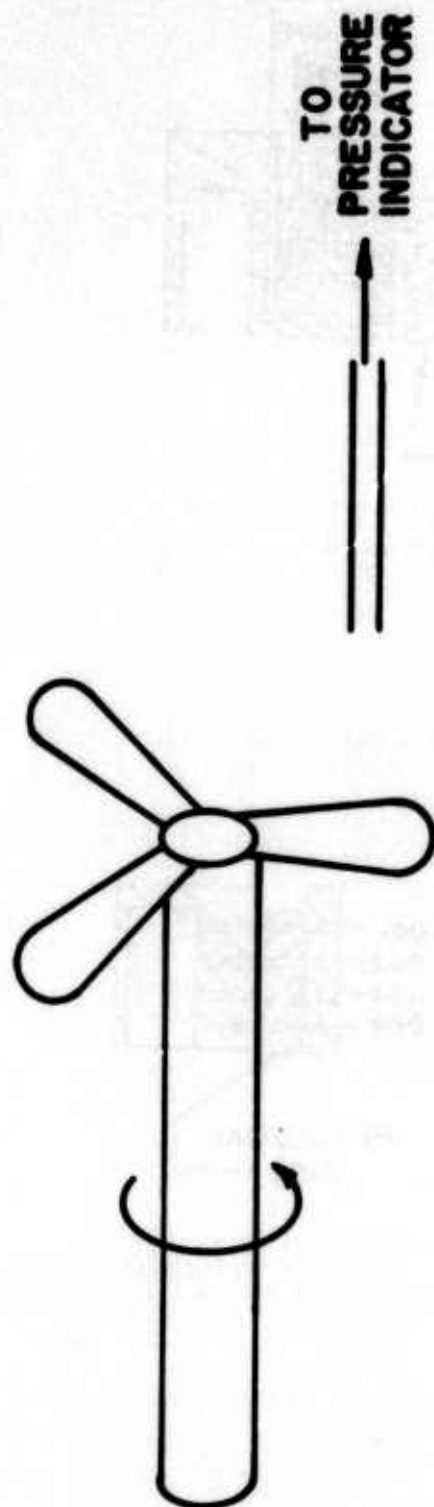
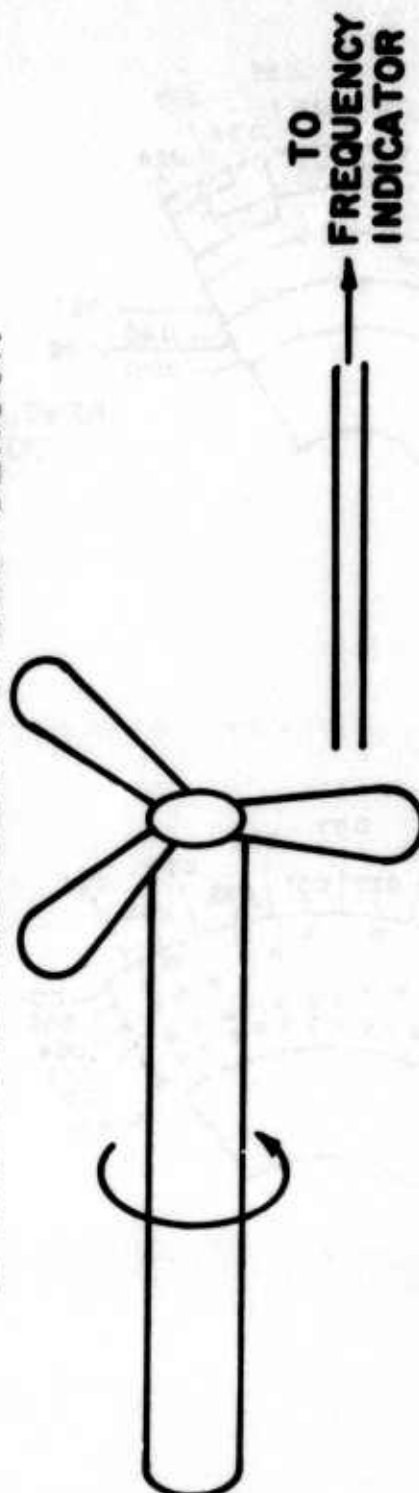


Fig. 11 Angular Position Coding Wheel

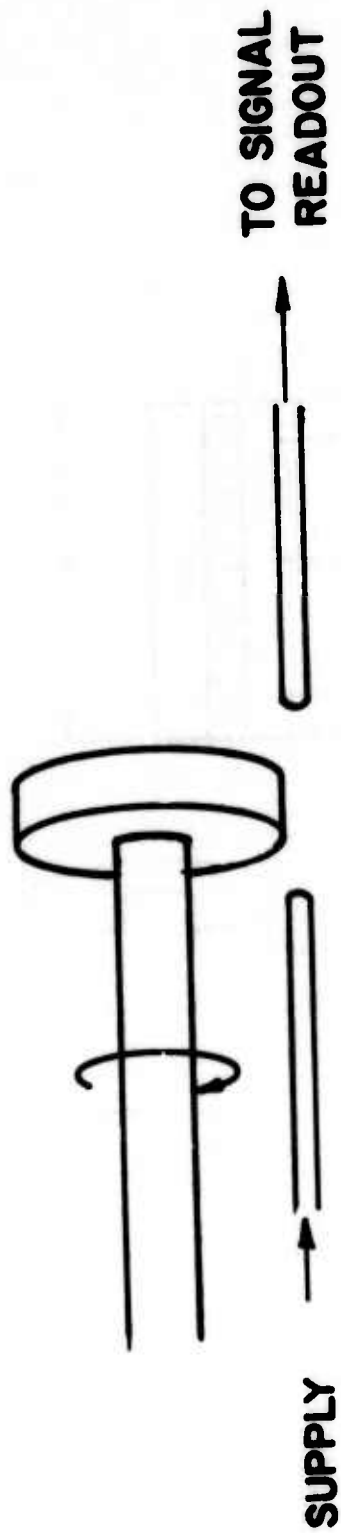


a. FAN TYPE ANGULAR SPEED SENSOR

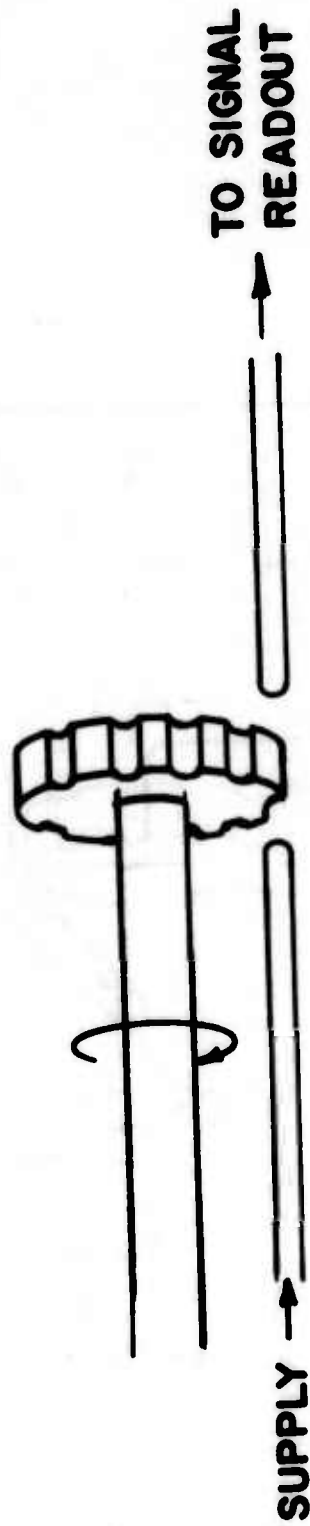


b. FAN TYPE ANGULAR SPEED SENSOR

Fig. 12 Fan Type Angular Speed Sensors



BOUNDARY LAYER ANGULAR SPEED SENSOR



GEAR TYPE ANGULAR SPEED SENSOR

Fig. 13 Angular Speed Sensors

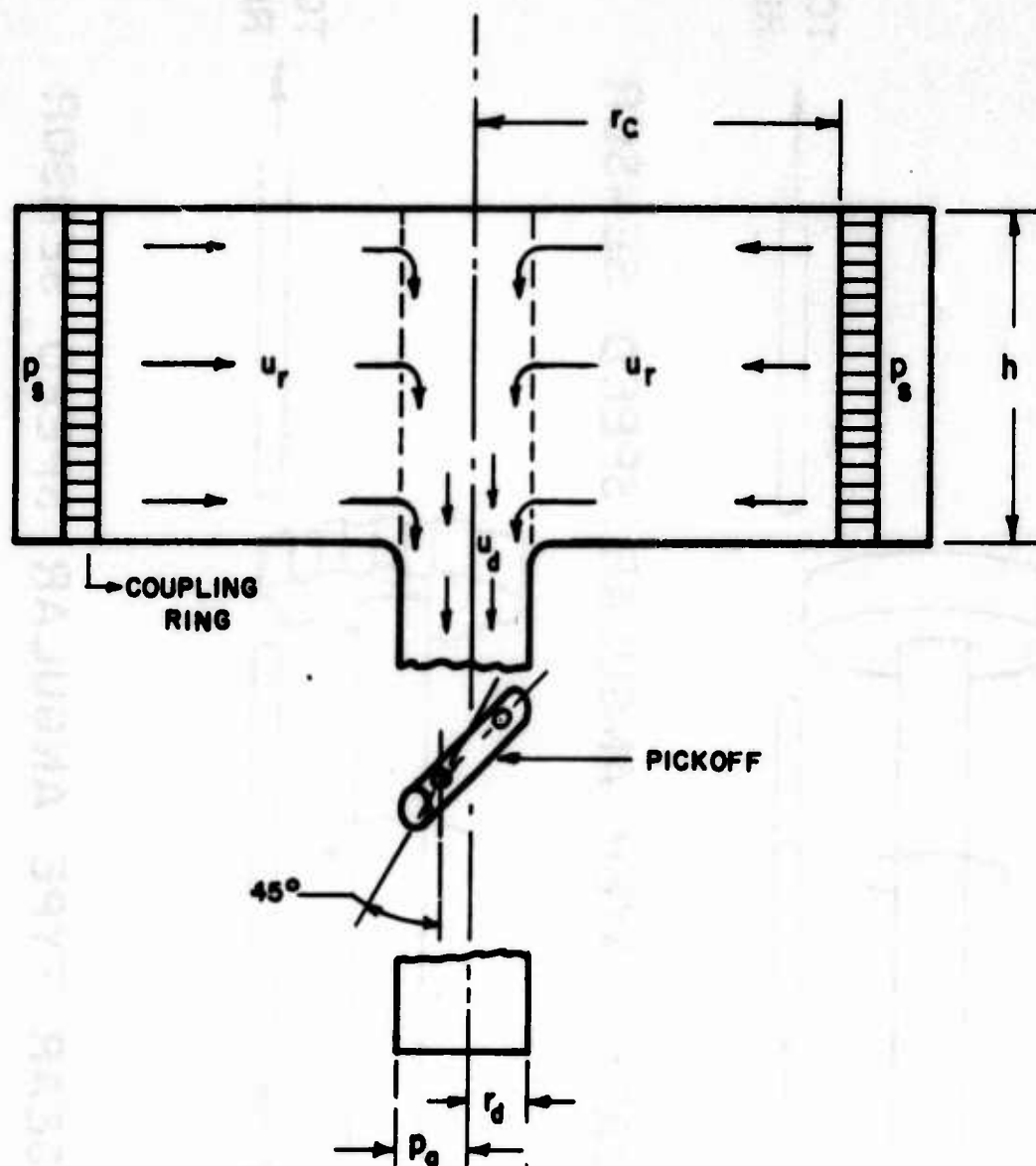


Fig. 14 Vortex Rate Sensor

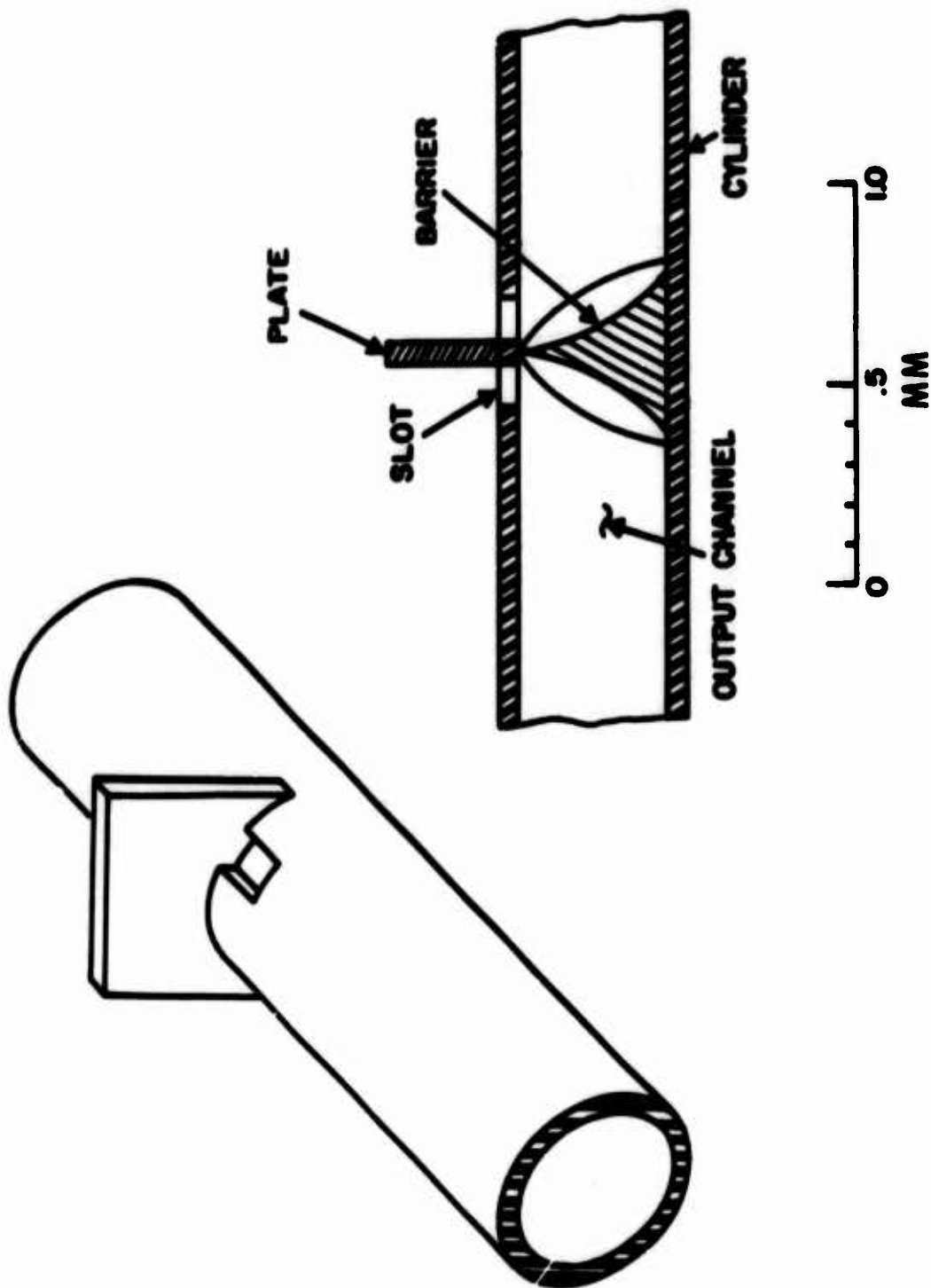


Fig. 15 Angle of Attack Pickoff

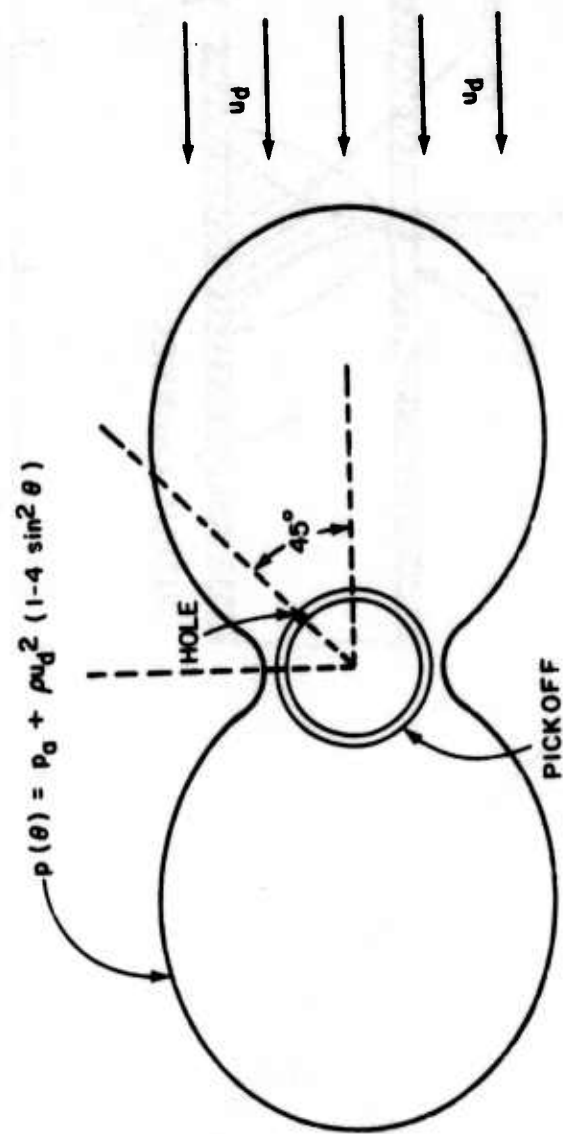


Fig. 16 Pressure Distribution About Pickoff

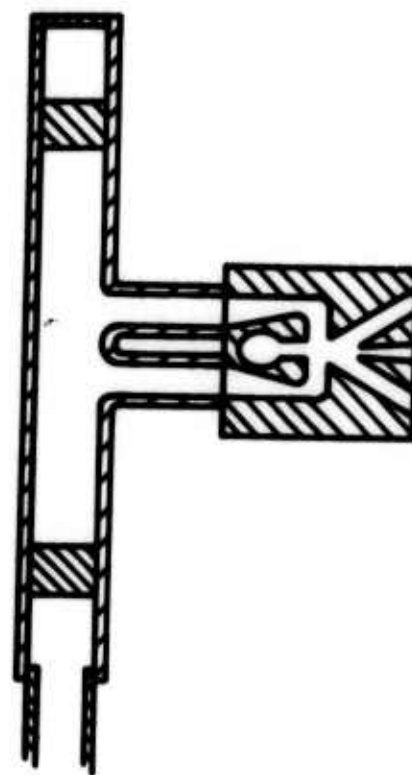
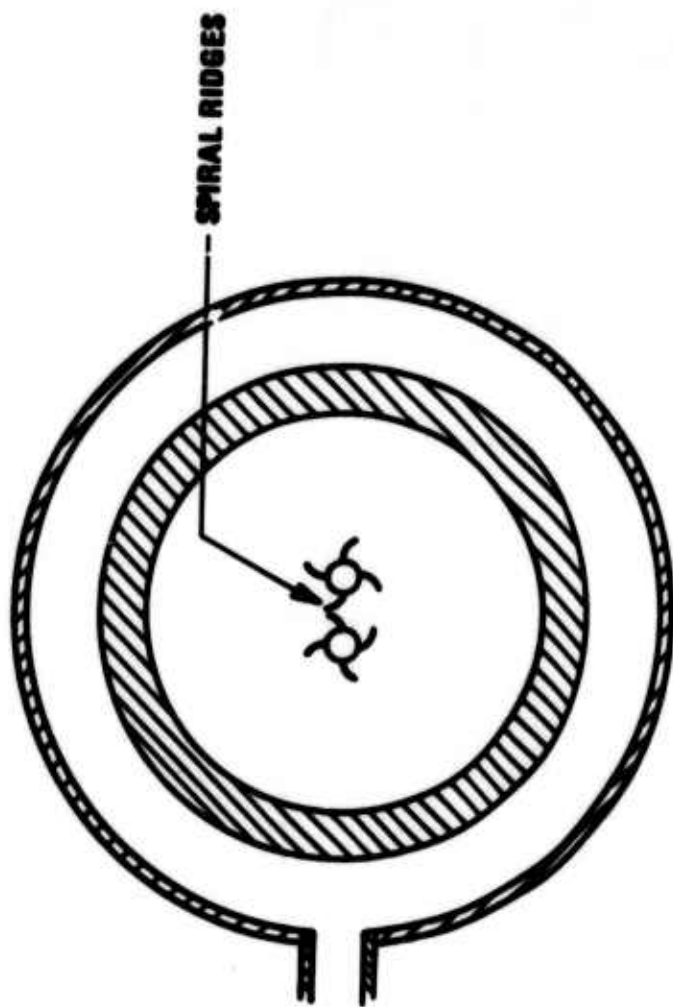


Fig. 17 Vortex Rate Sensor with Dual Drain

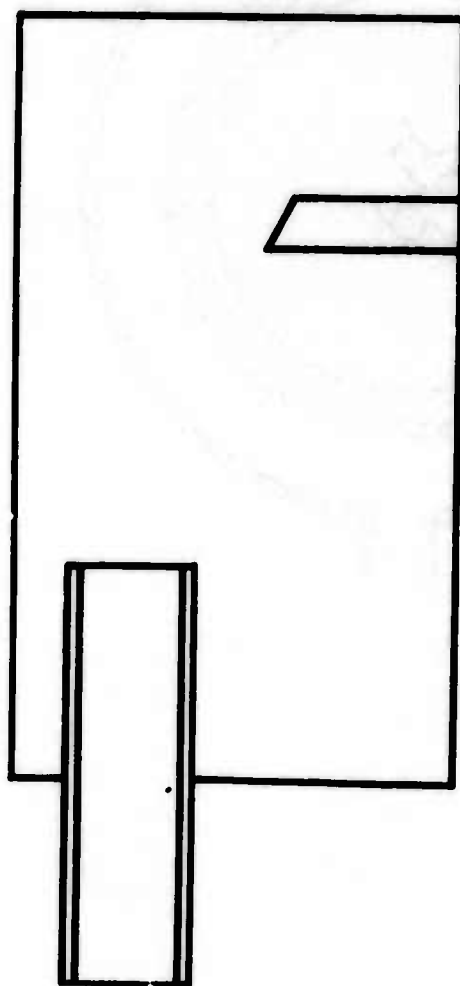
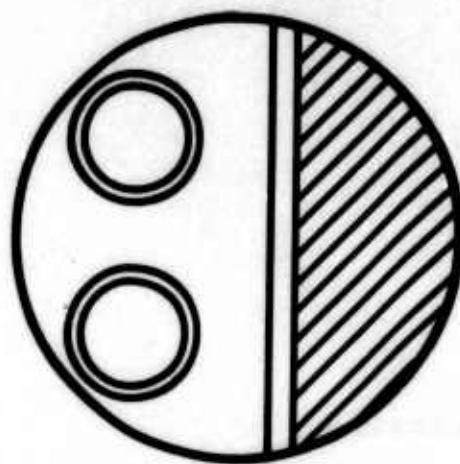


Fig. 18 Plate & Pitot Drain Arrangement
248

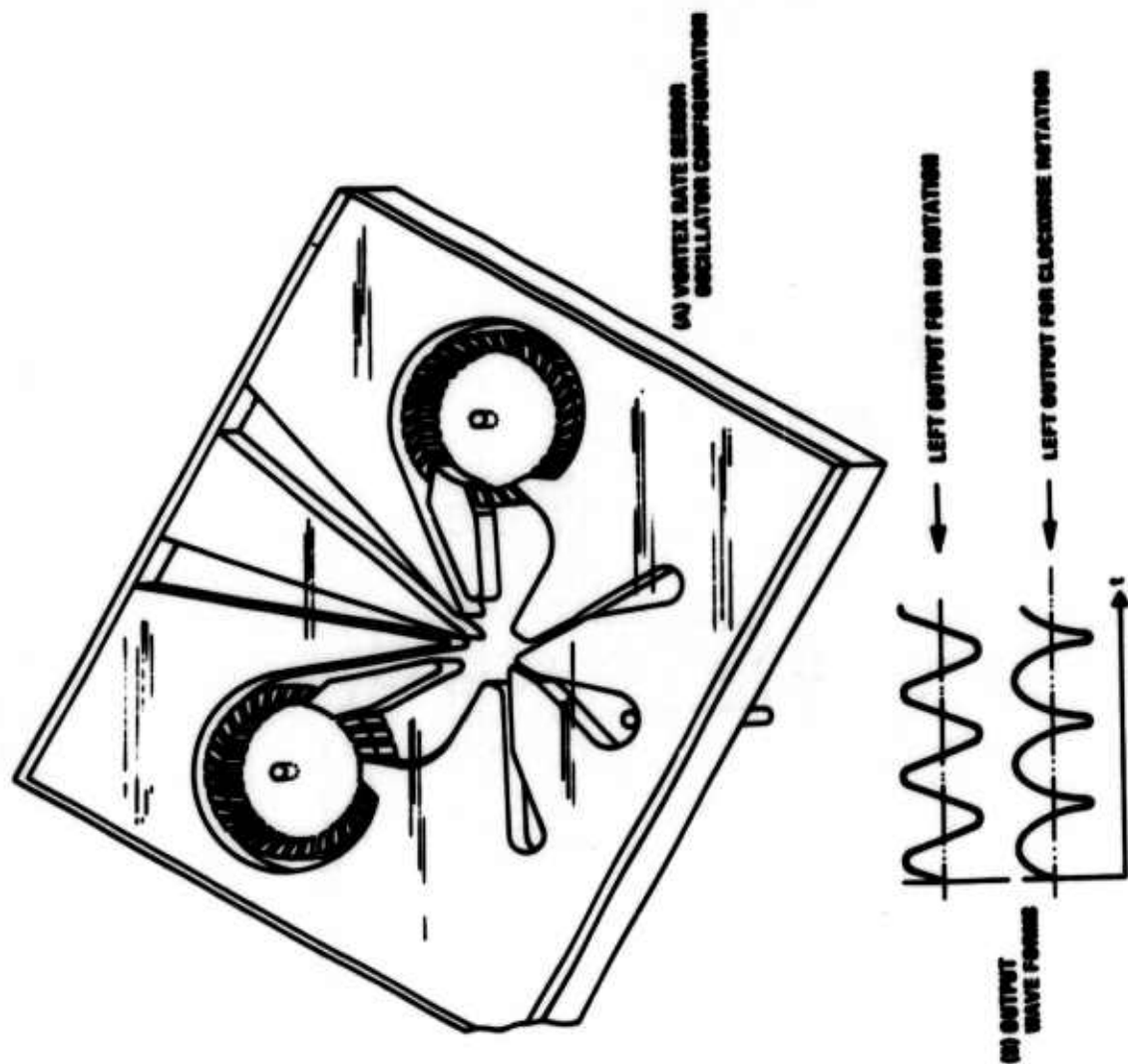


Fig. 19 Vortex Rate Sensor Oscillator

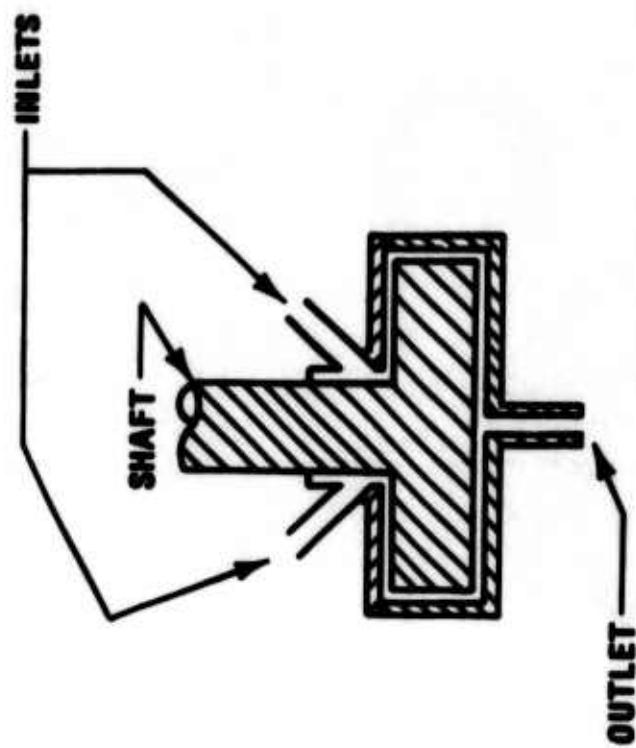


Fig. 20 Drive Shaft with Vortex Rate Sensor

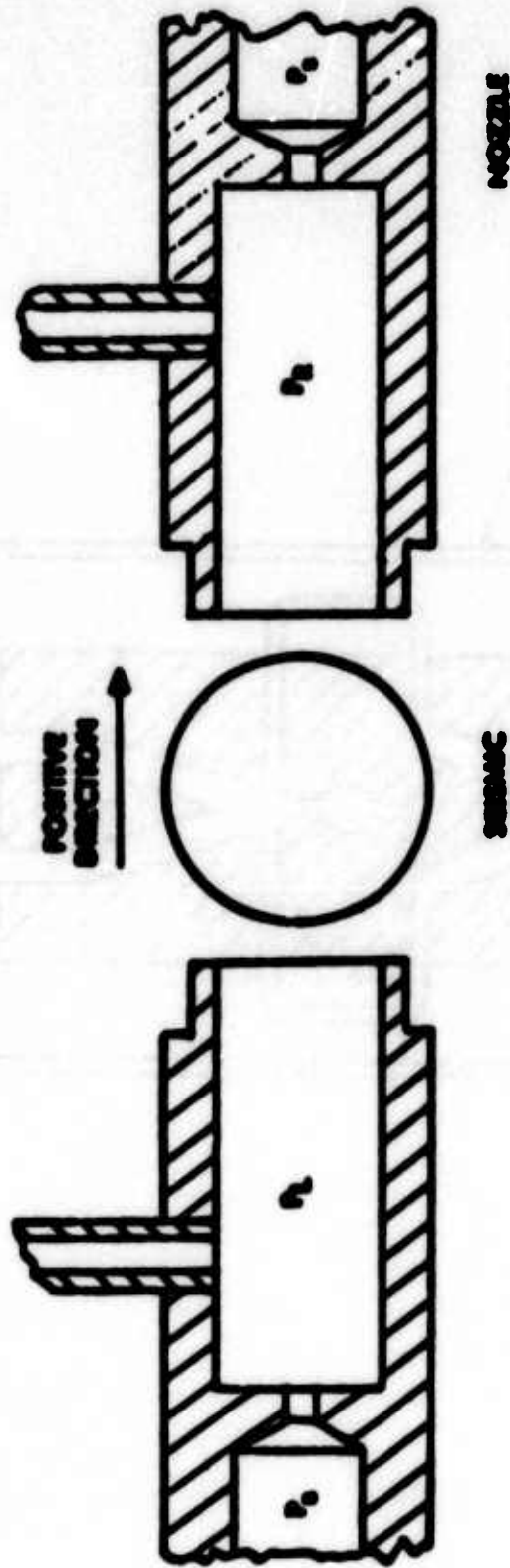


Fig. 21 Accelerometer with Fluidic Output

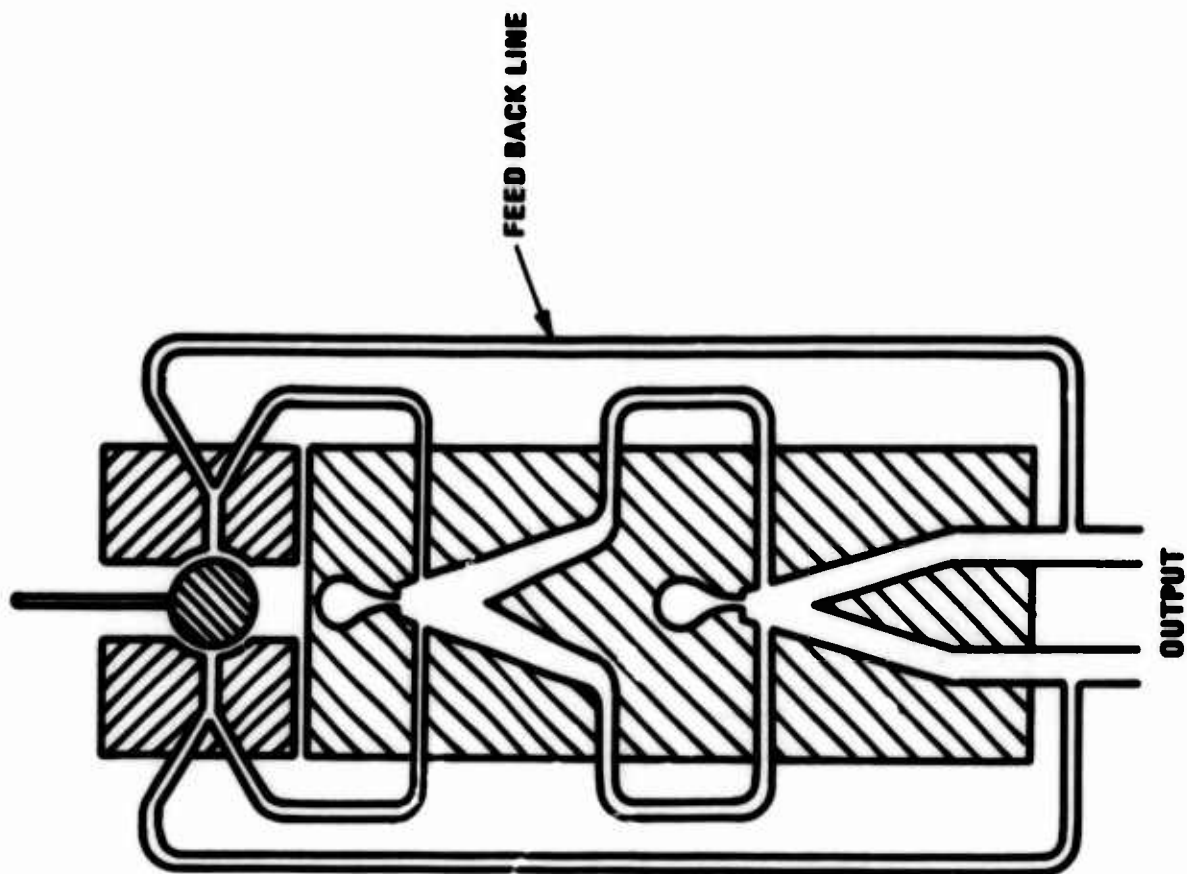


Fig. 22 Fluidic Accelerometer

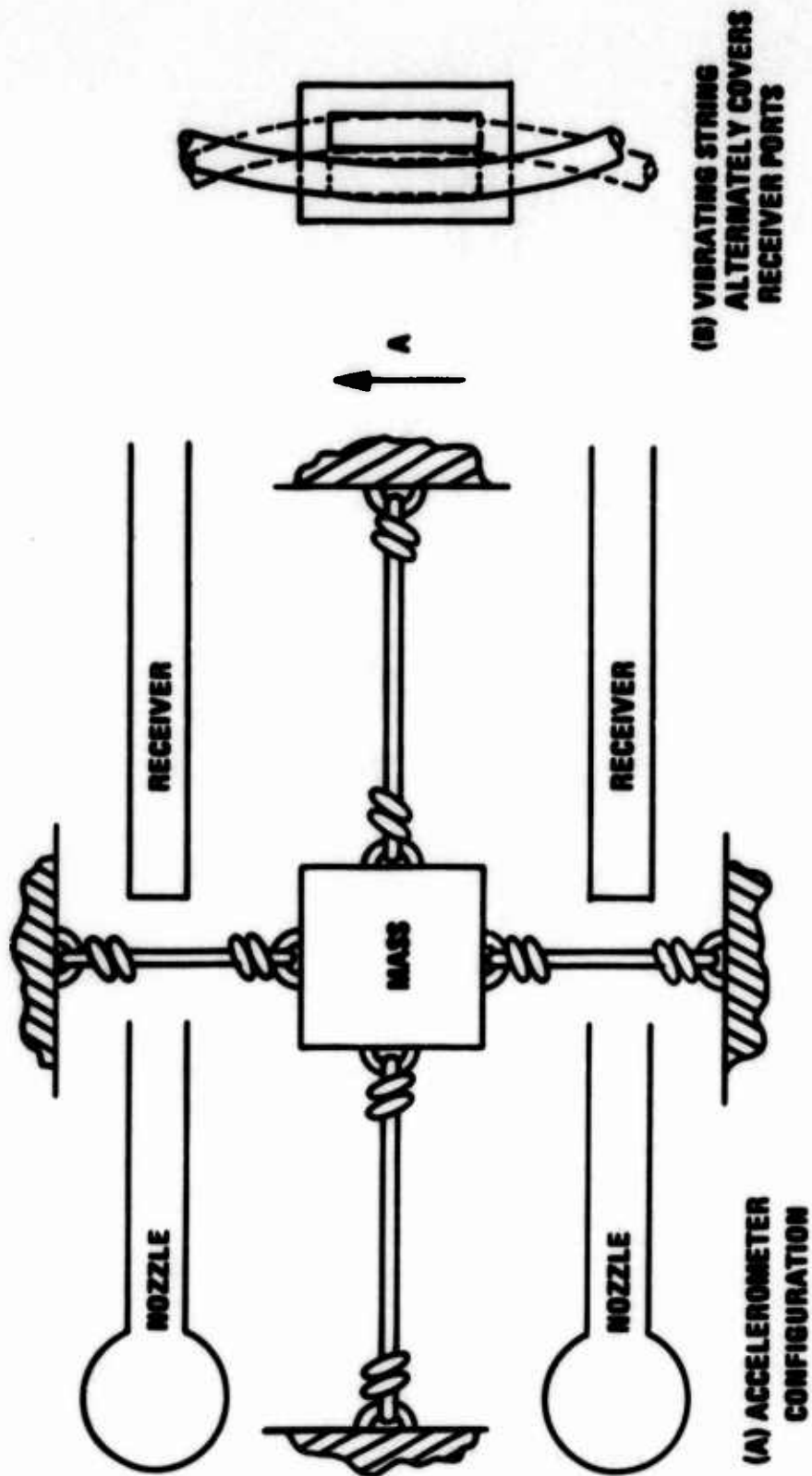


Fig. 23 Vibrating String Accelerometer

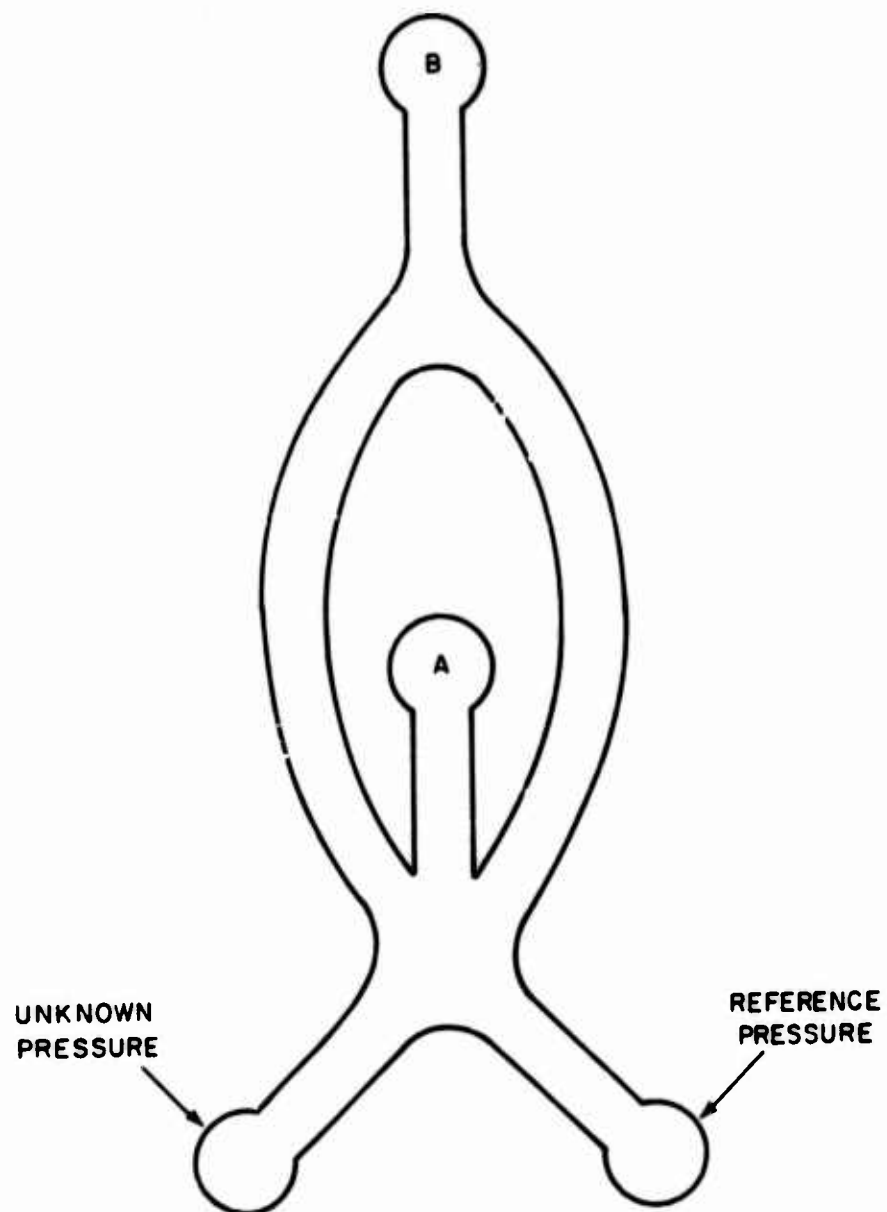


Fig. 24 Pressure Band Detector

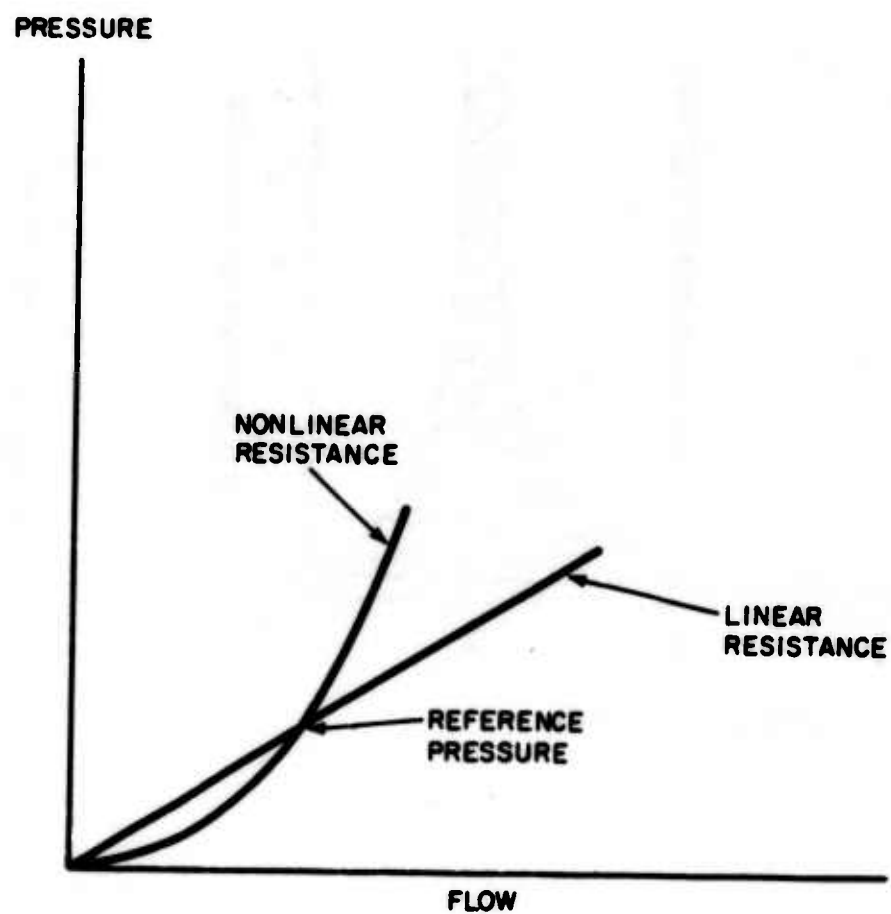


Fig. 25 Resistance Cross-over Pressure Reference

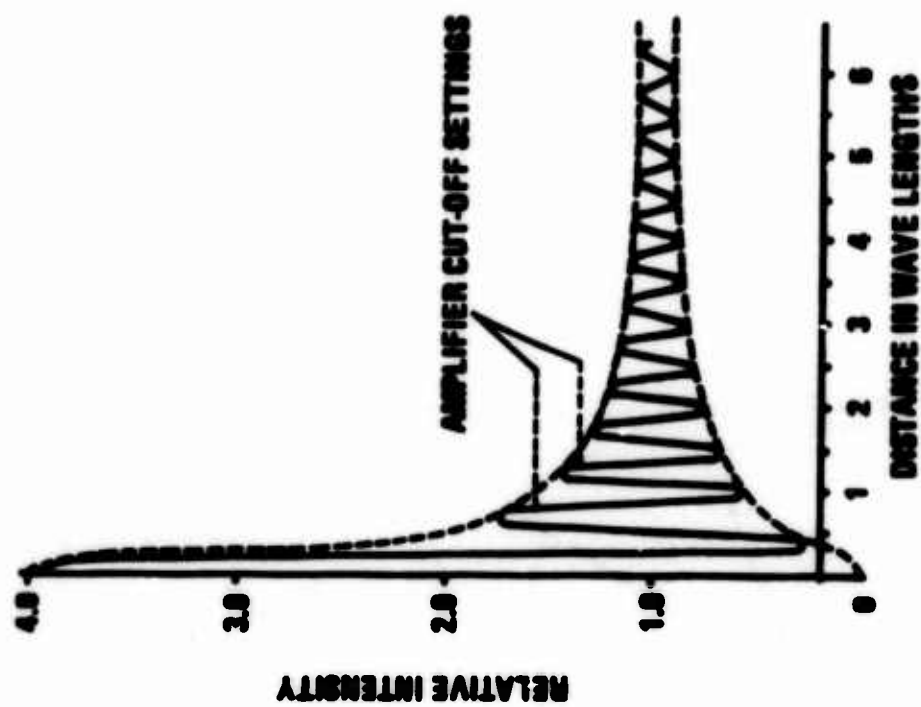


Fig. 26 Intensity as a Function of Distance

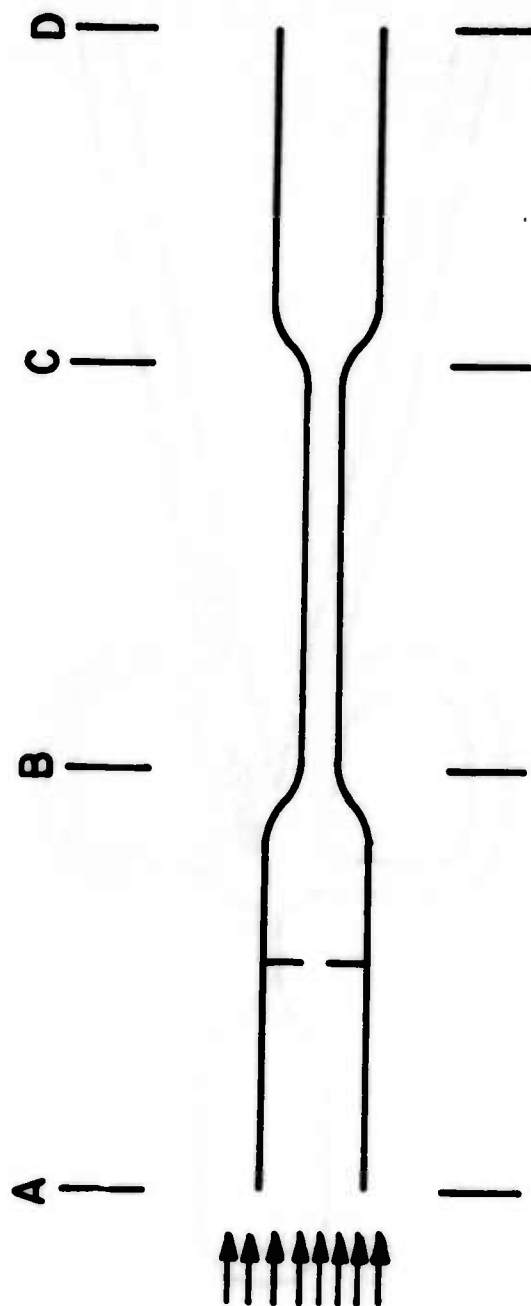


Fig. 27 Capillary & Orifice Resistors
in Series

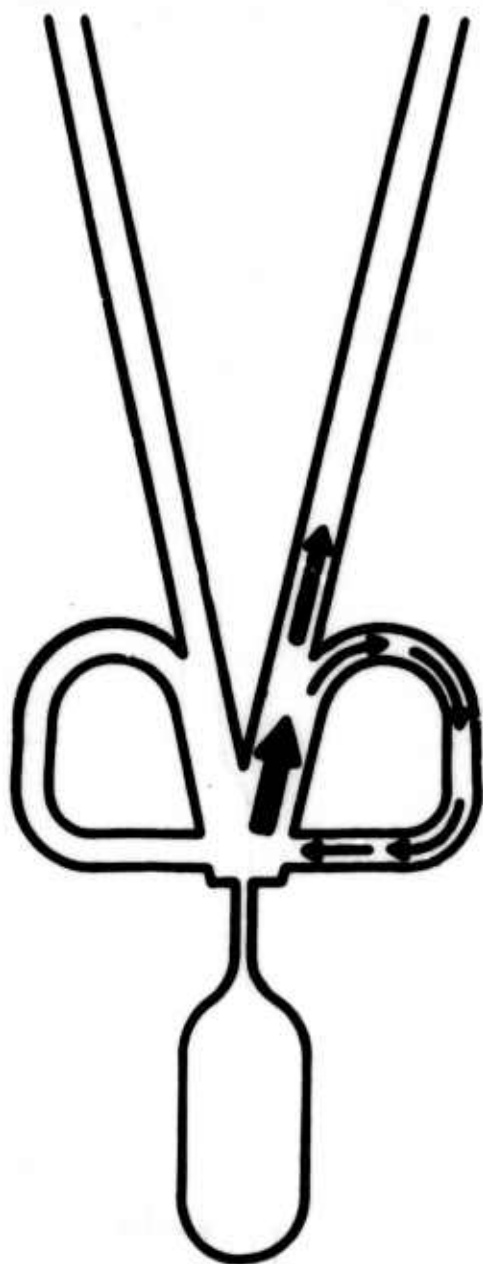


Fig. 28 External Feedback Oscillator

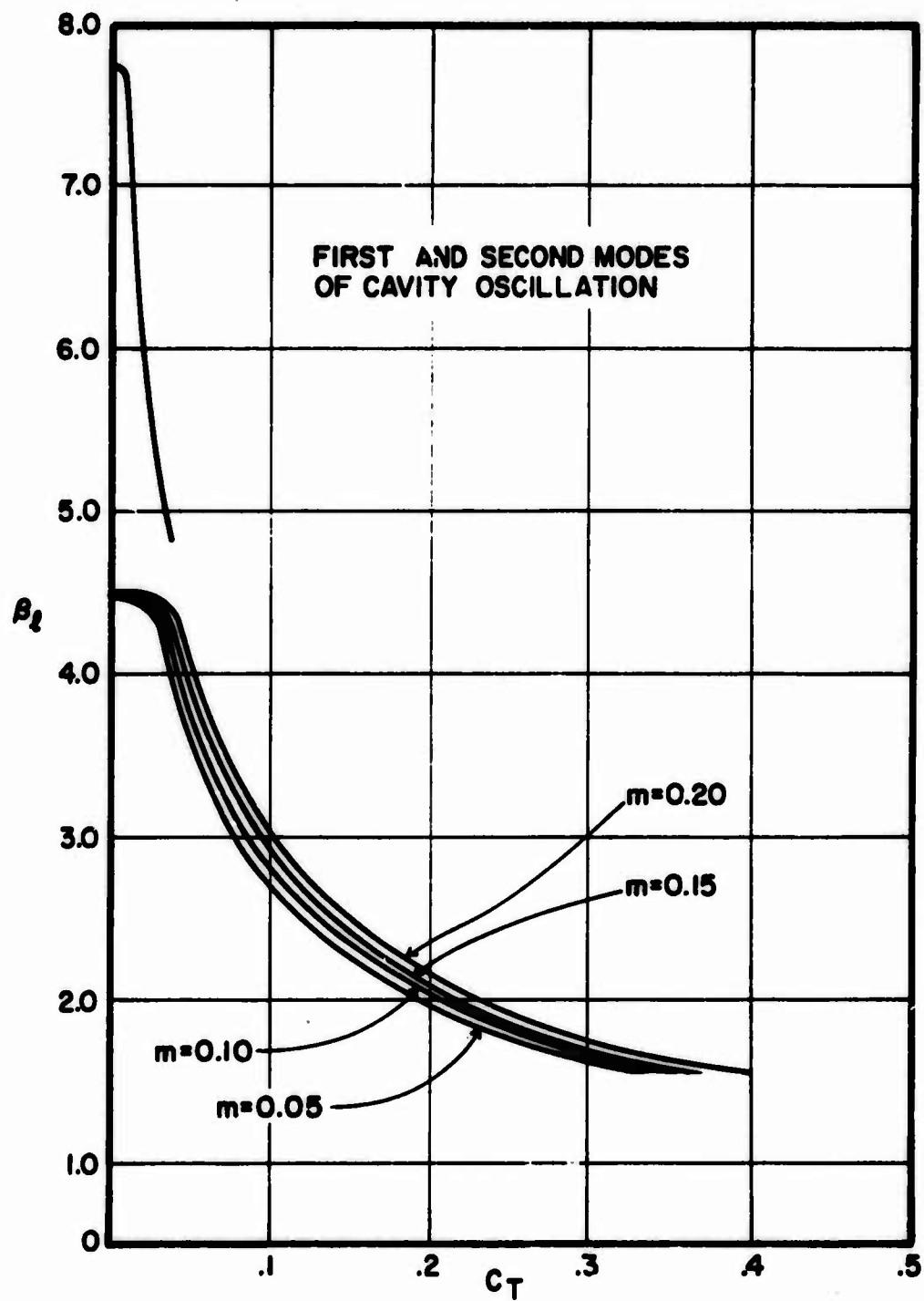


Fig. 29 Normalized Frequency β_L as
a function of the Oscillator
Parameter C_T

THE FLUIDIC ACOUSTIC SENSOR

Basil B. Beeken, B.S., M.S., M.A.T.,
Yale University
Director, Air Controls Research
Automatic Switch Company
Florham Park, New Jersey

ABSTRACT

A fluidic sonic generator utilizing edgetone principles and a sensor dependent upon the acoustic disturbance of laminar flow are described. How the two components are coupled to create the fluidic analogy to the photocell is explained. Various system configurations along with optional characteristics are outlined. Also included is a discussion of target resolutions and environmental influence.

THE FLUIDIC ACOUSTIC SENSOR

Introduction

It has been known for nearly a century that a free laminar jet, or stream, subjected to acoustic perturbations will become turbulent. Tyndall¹ first observed this in 1867 in his so-called "sensitive flame" experiments. Later, as reported by Rayleigh², he used smoke for a visual study of the stream itself and correctly interpreted the observed effects as a result of turbulence induced by the acoustic waves impinging upon the stream. The first U.S. Patent on a device utilizing this phenomenon was issued to C. Bell³ some 20 years later. Others followed subsequently.

In 1962 Raymond Auger⁴ of the U.S. demonstrated acoustic sensitivity as a property of his "turbulence amplifiers". They could be shut-off (made to go turbulent) in the region of 8 khz. This incidentally was considered at the time as detrimental to their use as control devices in an area of high level machine noise.

R. O'Keefe⁵ in 1967 described a "flow mode" device utilizing laminar stream properties for use as a fluidic digital amplifier. The structure of this device lent itself to production of arrays on a flat sheet and has since become known as the Flowboard AmplifierTM, abbreviated FB Amplifier.

This unit was found to be sensitive only to a narrow band of frequencies well above the audible range and out of the normal machine noise spectrum. He revealed that by design, one could fix the range of frequencies to which the device was most sensitive. That is, by proper variation of the geometry, such a device could be designed to response to a specified narrow band of frequencies. It is this device that serves as the sensing element of the fluidic acoustic sensor.

For an air driven acoustic source, various types were investigated resulting in the choice of an edgetone device.

The Sensor (Soni-Ceiver)

As a compromise between practical considerations, high sensitivity, and resolution of a reasonably small target, the region of 50 khz was chosen as the operating frequency.

What resulted was an amplifier of similar proportions but only 1/4 the size of the Flowboard Amplifier (Figure 1). As in the Flowboard Amplifier, the long narrow emitter channel serves to generate the parabolic velocity profile, which provides a stable jet attached to the upper plate and issuing across the short distance of the interaction chamber to the collector. In the normally stable mode, the collector receives a substantial portion of the stream energy and is registered at the output. When the stability of the jet is broken down by a control jet of lower energy in the complex manner described by R. O'Keefe⁵, relatively little energy is received by the collector and registered at the output. Utilized as an acoustic sensor, the instability is caused by the incident acoustic energy of the proper frequency directed at the jet where it issues from the emitter. A small aperture in the bottom of the interaction chamber at that point allows for the sound entry. The exponential horn opening out through the backside of the block containing the amplifier provides for efficient transmission of the acoustic energy through this opening. The frequency response of such a device (output pressure versus frequency) is shown in the graph of Figure 2.

Because of the smaller dimensions of the element just described, the power consumption and, therefore, its output is substantially lower than that of a standard Flowboard, (FB) Amplifier. However, its output is sufficient to control a FB Amplifier at the same supply pressure. In order to provide a package with a high enough level for fan-out and transmission through long lines, a standard Flowboard Amplifier was added to serve as a stage of amplification for this purpose.

The photograph of Figure 3 shows a top view of the complete sensor package with the cover plate removed. Figure 4 shows two views of the assembled unit, which is fabricated from an ABS plastic by a molding process.

In order to prevent contamination of the sensing element from dust and oil ingested through the throat of the exponential horn, a thin mylar window (.00015 inches thick) is positioned across the mouth of the horn.

The placement is judiciously chosen to insure a maximum standing wave ratio on the sensor side of the window. This results in an optimum coupling across the membrane with a minimum loss of acoustic energy.

The Source (Soni-Emitter)

For reasons outlined by B. Beeken⁶ in 1968, an edgetone device was developed for use as the acoustic source.

A double edge is oriented in the stream to provide a push-pull effect. Open ended resonator columns are used in conjunction with the edges to fix the frequency at the desired value. The open end of one of the resonator columns serves as the emission source in a direction lateral to the jet. The unit is represented in the schematic of Figure 5. This configuration essentially latches the lateral oscillation of the jet between the orifice and the edges, somewhat, like a taut wire vibrating in its fundamental mode. The length of the resonating column is, as might be expected, approximately $1/2$ a wave length less the end corrections. The output intensity at one end of the resonating column is significantly increased, about 3 db, by appropriately reflecting the energy from the end of the other resonating column back through the jet and in phase with the emission from the unblocked column. Figure 6 shows graphs of the frequency and intensity characteristics of such a unit with a .020 x .040 inch throat.

The Horn System

The operating frequency of a fluidic acoustic source is approximately 52 khz. The wave length, therefore, is about $1/4$ inch. From the dimensions given in the schematic of Figure 2, the emission aperture of the resonator cavity is roughly equivalent to a circular cross-section with a diameter of approximately $1/4$ of a wave length.

As such, it turns out to be essentially a spherically radiating point source.

Spherical radiation wastes much of the energy lateral to the axis of the generator. Therefore, a properly designed

conical horn section was appended to direct more of the energy along the axis. For a 52 khz wave, a reasonable compromise between the ideal and practical resulted in a horn of about 1 inch in length with a mouth diameter of 2 wave lengths or 1/2 inch. This provided sufficient directivity to span 4 feet and actuate the sensor. Figure 7 reveals the internal structure of the acoustic source with the horn appended. The material is again an ABS molded plastic.

The polar plot calculated for this unit is shown in Figure 8 along with that actually measured for comparison. The first side lobe is down about 18 db and is a factor to be considered in very short range reflex applications. The angular beam width at the 3 db points is approximately 30°.

The sensor element is similarly fitted with a horn to provide an antenna gain characteristic along the axis of the system, which by the reciprocity principle is similar to the emission characteristics of the generator.

Figure 9 shows the ABS plastic components of the system completely assembled. For applications in industrial environments where protection by a rugged enclosure is mandatory, cast aluminum housings are provided (Figure 10). Air supply and signal tubing are routed through standard electrical type sealtite conduit firmly anchored by standard connectors to the enclosure.

Fluidic Ear as a Sensing System

What has been developed is a fluidic sensor with no moving parts. An acoustic analog to the photocell or electric eye, the terms sonicell or Fluidic Ear have been coined. As a simple presence or proximity sensor, it may be used in either a direct or reflex mode schematically represented in Figure 11a and b.

In the direct mode when an acoustically opaque object is placed in the beam from the generator, the acoustically sensitive element in the sensor circuit resumes its normally "on" state and thus turns off the output amplifier. The spanning range in this mode is a function of the supply pressures, both common and separate, as seen by the data of Figures 12 and 13.

In Figure 14 is shown the supply pressure and flow characteristics. At a common nominal supply pressure of 1.4 psig, the system requires about 1.4 watts (joules/second) to operate. Figure 15 shows the range of output pressures available from the device.

For the reflex mode, a suitable reflecting surface positioned to satisfy the law of reflection will deflect the acoustic energy into the sensor turning the output amplifier on. Figures 16 and 17 show the assembled ABS package and its rugged industrial enclosure, respectively.

Resolution of a target is, of course, a function of the wave length. It turns out, empirically for this system, that the minimum for any dimension of the obstructing target can be no less than four wave lengths or about 1 inch. For effective scattering of the acoustic energy and reliable actuation of the sensor, the target cross-section should be no less than about 1 square inch.

The Paraboloid System and Extended Range

The span limitation of the system described above is due primarily to the simple acoustical beaming techniques employed in the system. The conical horns used have aperture dimensions of only two wave lengths, and therefore, the spread of the sound energy due to the beam angle is significant. The loss of the acoustic energy lateral to the axis of the system due to the beam spread is what contributes significantly to the limited spans.

Since the band in which the sensor is most sensitive is centered about 52 khz, the frequency of the generator must remain fixed. Improvement of the directivity (reduction of beam spread) and the resulting increase in span can only be implemented by an increase in the radiation aperture.

For the reasons outlined by B.Beeken⁷ in 1972, a paraboloid system was adopted.

The source is mounted with its aperture at the focal point of the paraboloid as shown in Figure 18a. The radiation pattern measured for this array is shown in Figure 19, along with that calculated theoretically, assuming a point source and, therefore, a uniform intensity across the face

of the paraboloid. Clearly, considerable improvement in directivity and side lobe suppression was achieved in this design.

The receiver section of the system was similarly provided with a paraboloid antenna and for compactness a Cassegrain structure was adopted. See Figure 18b.

The Convex secondary reflector re-directs the energy back along the axis through the aperture at the vertex. This aperture is shadowed by the secondary and constitutes an unused portion of the paraboloid.

The secondary reflector is placed so that its focal length coincides with that of the paraboloidal reflector. A flange at the back serves nicely as a mount for the receiver horn section. The energy is thus effectively focused into the sensor unit.

The Production Unit

Rugged cast aluminum housings were fabricated incorporating the paraboloid surfaces. They are shown in the photograph of Figure 20. Note that the paraboloids are an integral part of the housing. The wave length involved is about $1/4$ " so that the rough surfaces of the paraboloids are sufficiently smooth to provide a near perfect acoustic reflecting surface. This system allows for spans of up to 16 feet.

The active elements of the paraboloid system are the same as those for the standard horn systems; the power consumption remains the same. The graphs of Figure 21 and 22 reveal the span dependence on supply pressures.

One implementation of the parabolic system is in its use as an Area Coverage Sensor. A curtain of 50 khz acoustic waves is created by folding the 3-inch diameter collimated beam back and forth using a sawtooth array of 45° angle plane reflectors (Figure 23).

The Area Coverage Sensor, thus generated, senses the presence of objects with a projected area of at least 3 square inches anywhere within the area covered.

For applications where the system is considered for personnel detection as a safety device, monitoring circuitry has been developed which provides a continuous check on the sensor to assure proper function.

Resolution and Environmental Considerations

For wave phenomena the resolution of the object under illumination is a function of wave length alone. System geometries and object shapes do not alter this basic principle. Therefore, there is a minimum specification for target cross-sectional dimensions. Empirically it turns out that the acoustically opaque object must present at least the equivalent of a 3.0 square inch cross-section, regardless of its shape, anywhere across the 3.0 square inch diameter collimated beam.

For the larger spans the extent to which cross air flows can be tolerated must be considered. Air being the medium through which and by which the acoustic energy is being transmitted, its displacement cannot be more than that which would divert the beam by about 1/2 a beam width. For a uniform velocity at 90° across a 10 ft. span, this turns out to be approximately 14 ft./second.

Severe temperature gradients in a direction other than the direction of propagation must also be considered. According to Snell's law, refraction of waves occurs where changes in propagation velocities take place and where the angle of incidence is other than normal. Since the velocity of sound in air is proportional to the square root of the temperature, a temperature gradient oblique to the direction of propagation can cause the sound beam to bend or refract.

For the relatively simple case of a uniform temperature gradient, normal to the beam, calculations show that for the beam to be diverted 1/2 a beam width in a 10-foot span, the temperature gradient must be greater than 6°F/foot.

REFERENCES

1. Tyndall, Phil. Mag., Vol. XXVIII, pp. 92, 1867
2. Rayleigh, J.W.S., Theory of Sound, Vol. II, pp. 403, Dover Pub. New York, 1945
3. Bell, C.A., U.S. Patent No. 336,203, Feb. 16, 1886, U.S. Patent Office
4. Auger, R.M., "Turbulence Amplifier Design and Application", Proceedings of the Fluid Amplifier Symposium DAFL, October 1962.
5. O'Keefe, R.F., "Development and Applications of a New Jet Interaction Fluid Amplifier", 22nd Annual ISA Conference, Preprint No. 15-2-MCID-67, Chicago.
6. Beeken, Basil B., "An Acoustic Fluidic Sensor", 23rd Annual ISA Conference, Proceedings Vol. 23 Part II, October 23-31, 1968, New York USA.
7. Beeken, Basil B., "Long Range Fluidic Acoustic Sensor", ASME Winter Annual Meeting, Preprint 72-WA/FLCS-8, November 26-30, 1972, New York USA

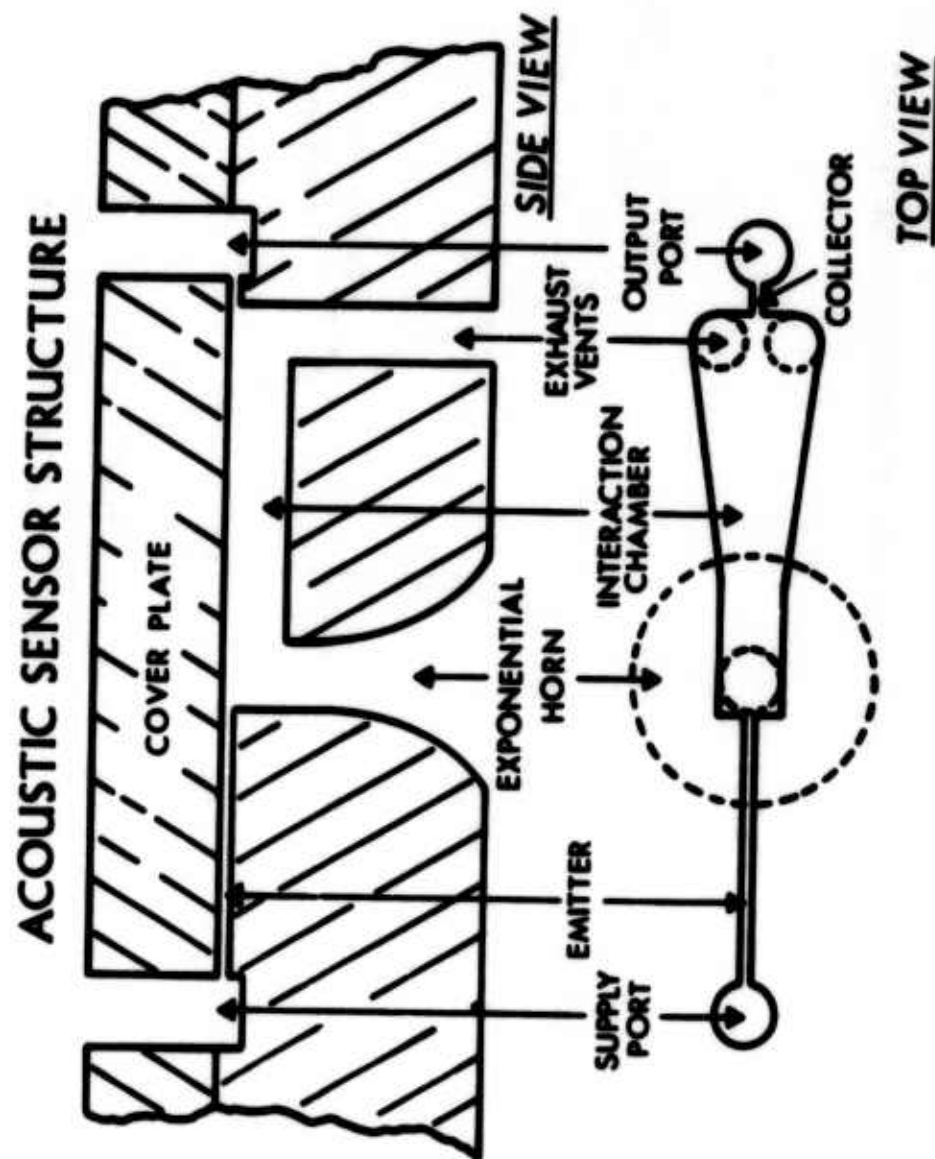


FIGURE 1

Acoustic Sensor Frequency Response

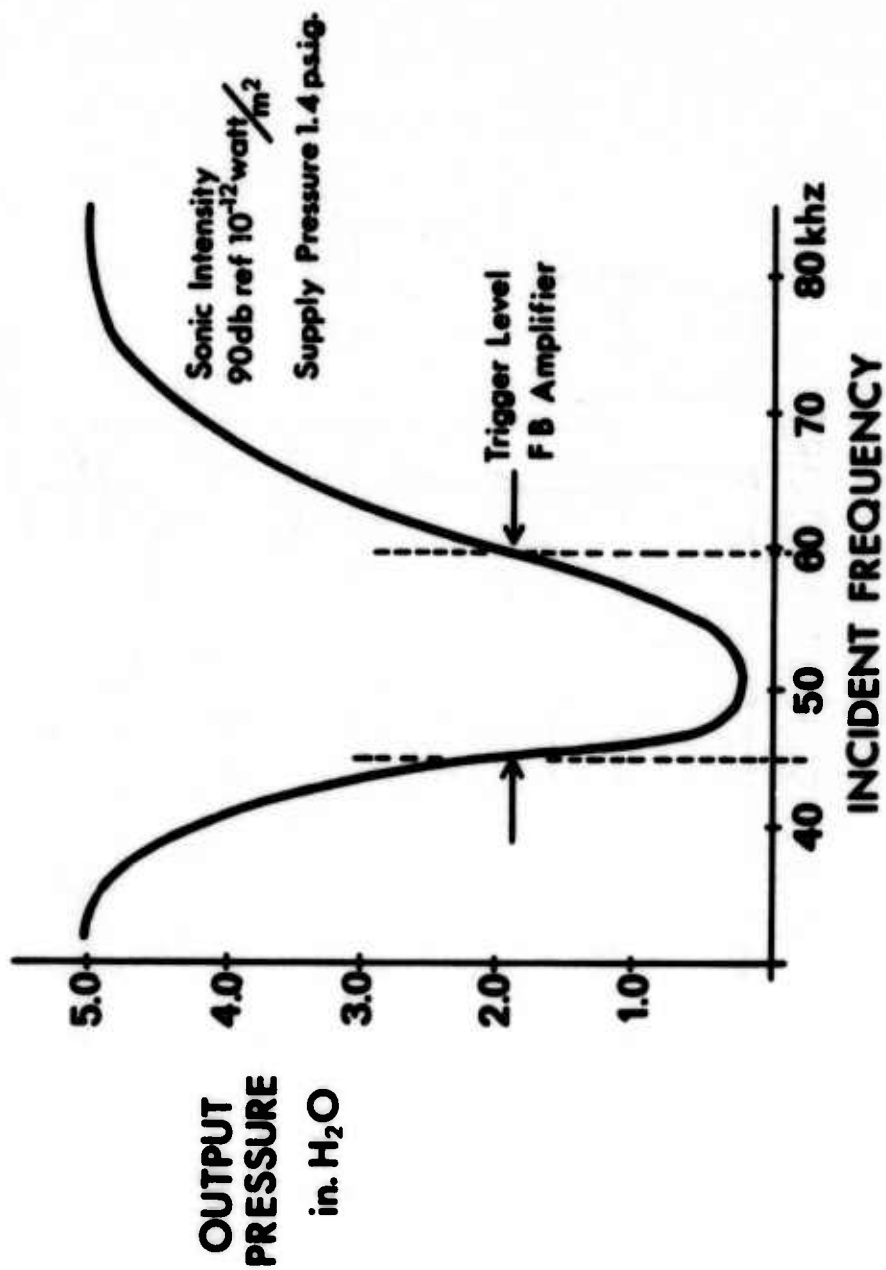


FIGURE 2

SENSOR CIRCUIT



FIGURE 3

SENSOR PACKAGE

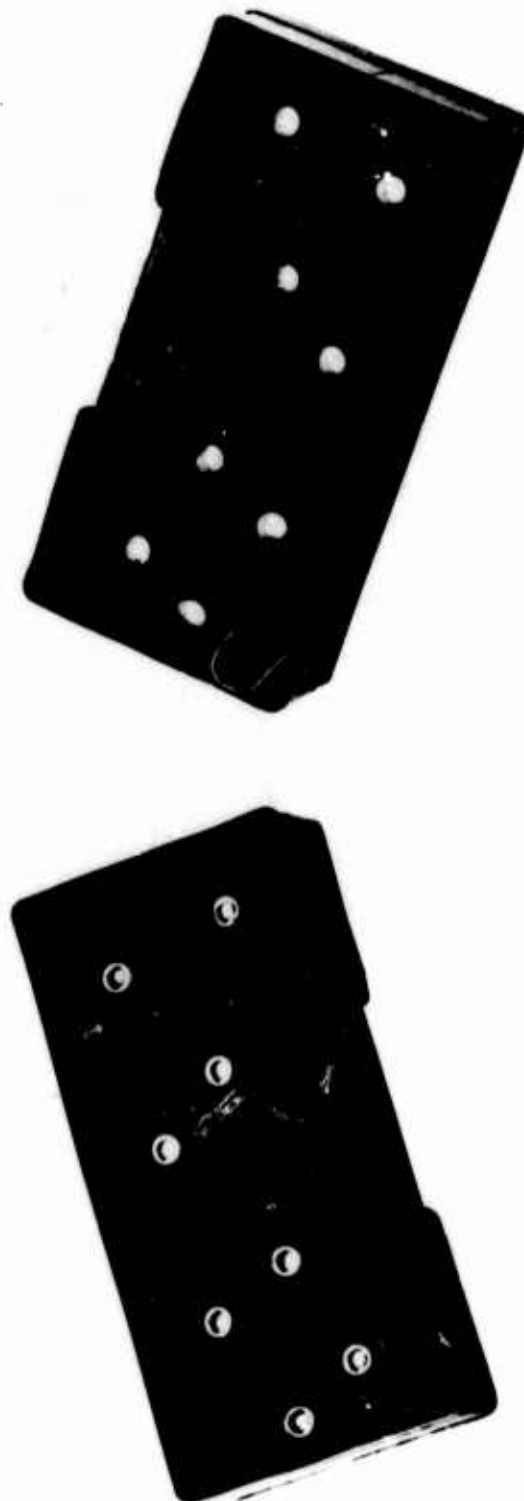


FIGURE 4

GENERATOR STRUCTURE SCHEMATIC

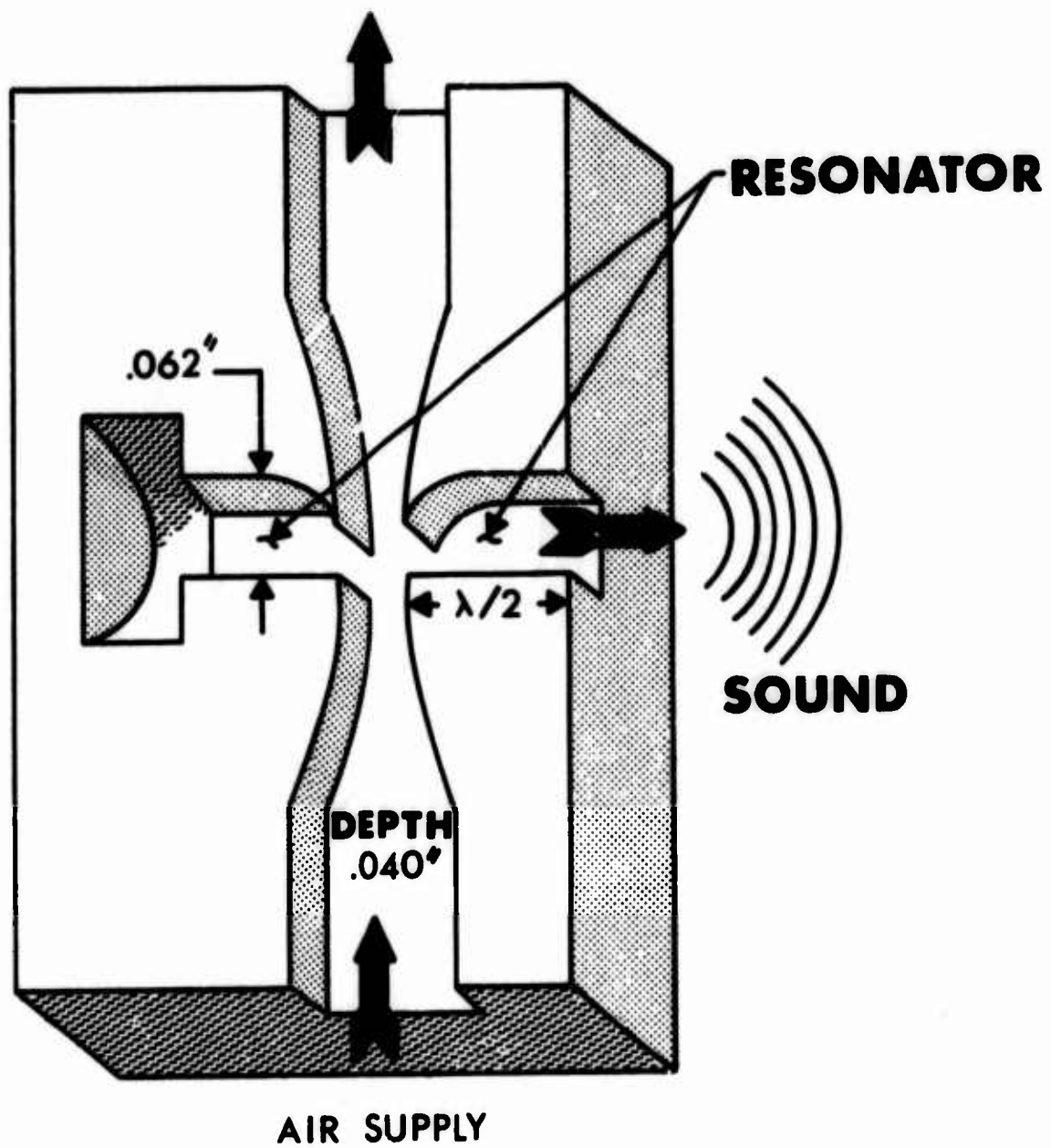


FIGURE 5

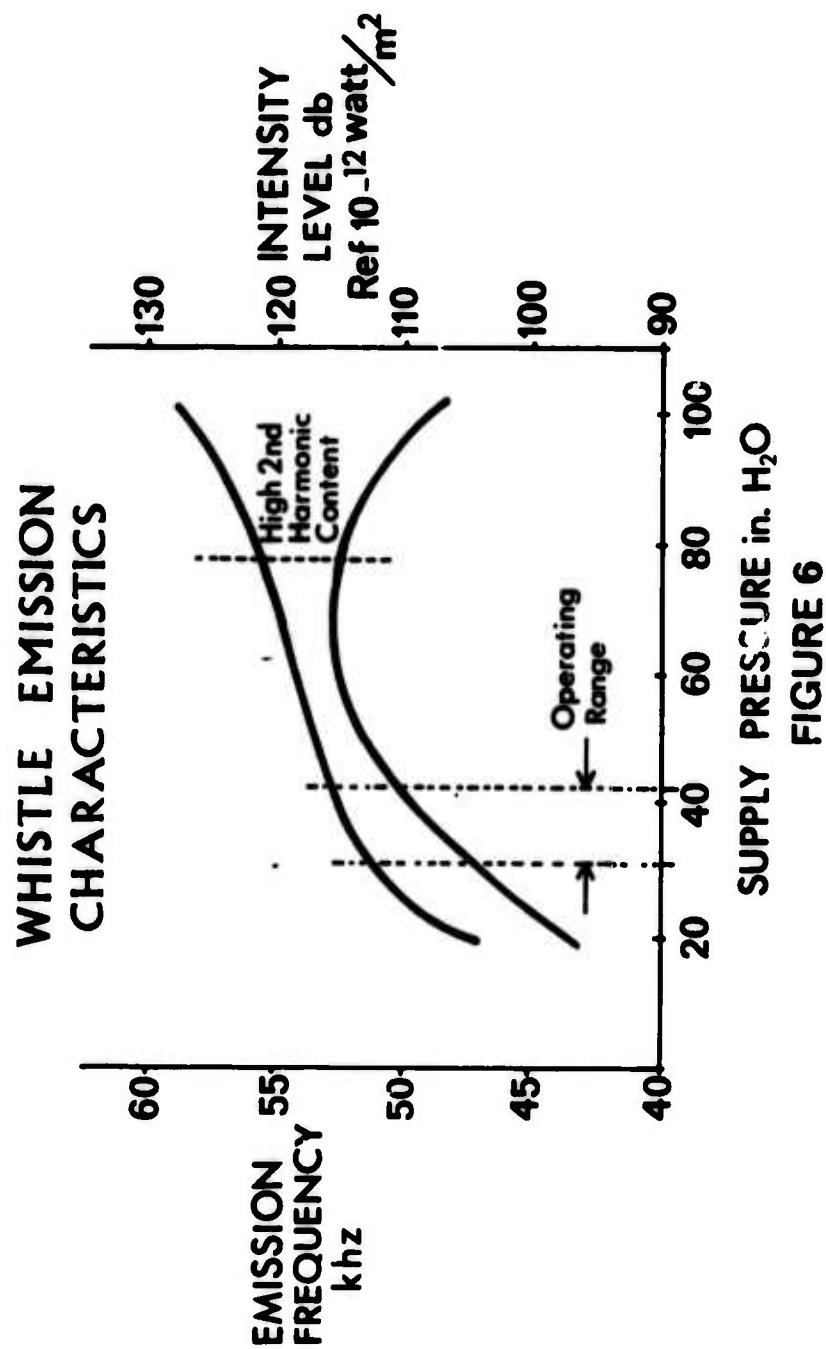


FIGURE 6

EMITTER DETAIL



FIGURE 7

**POLAR DIAGRAM OF RADIATION INTENSITY
FROM GENERATOR WITH HORN**

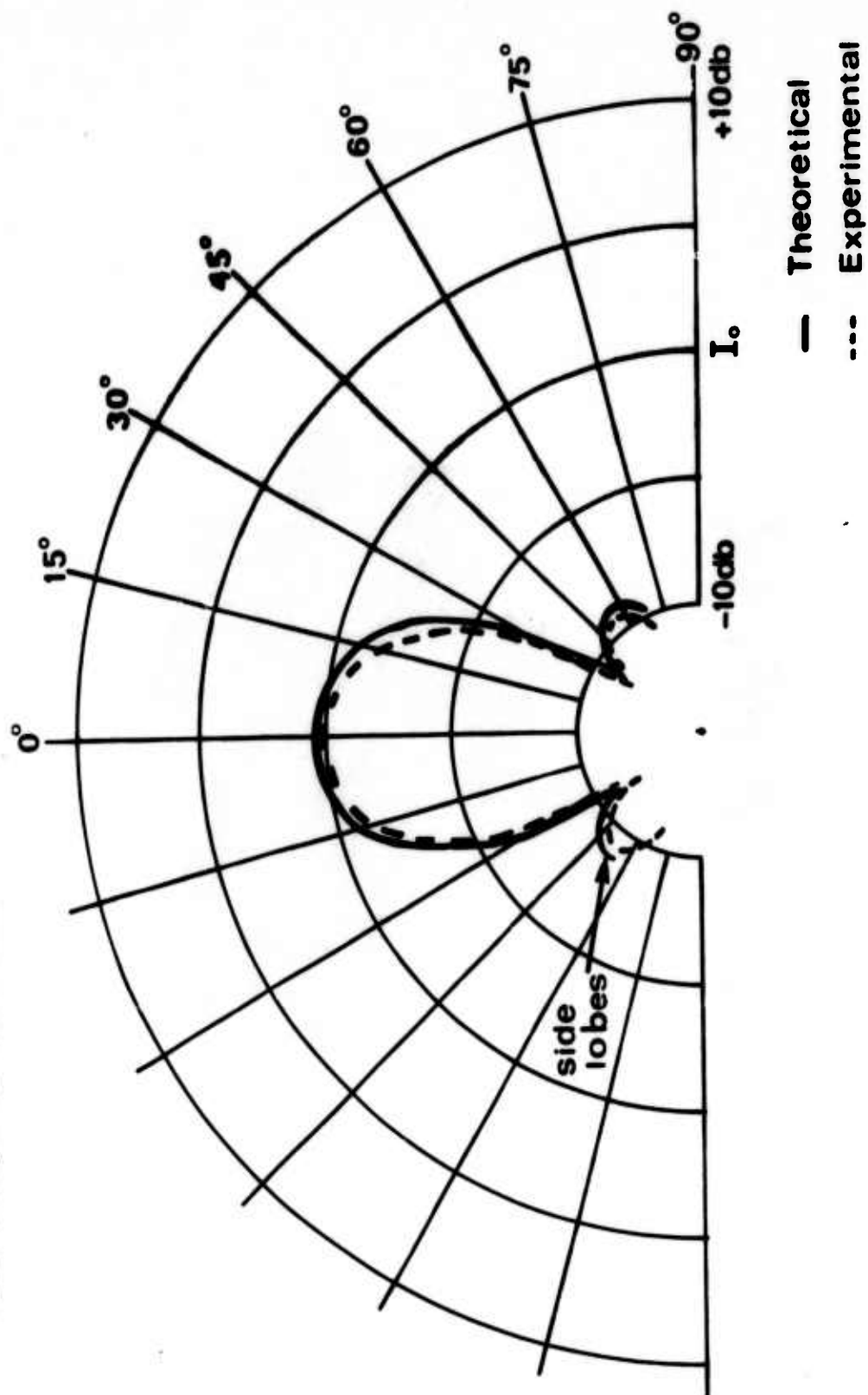


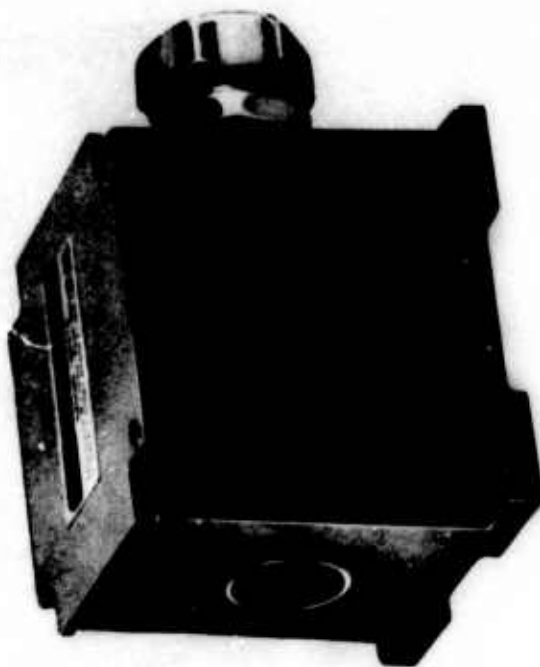
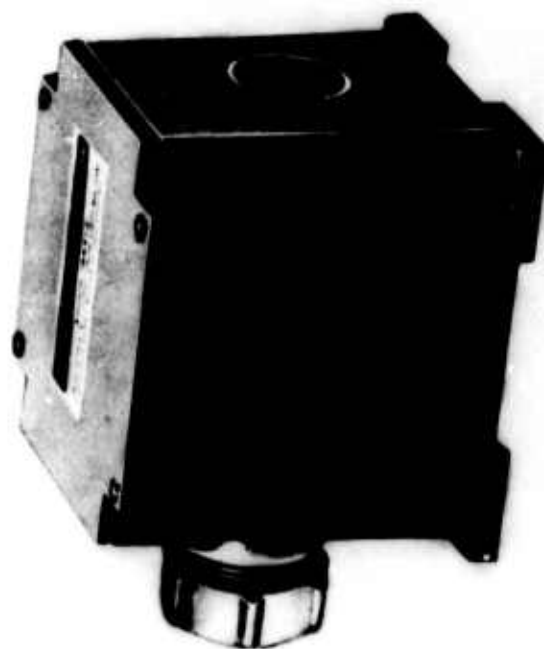
FIGURE 8

FLUIDIC EAR DIRECT MODE



FIGURE 9

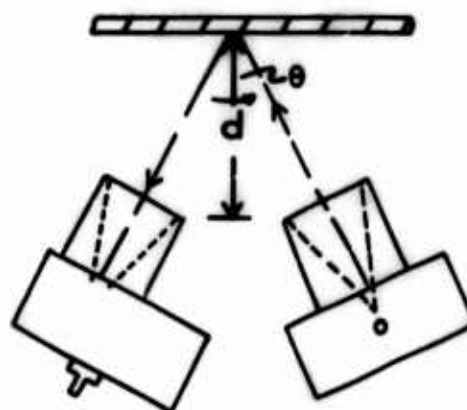
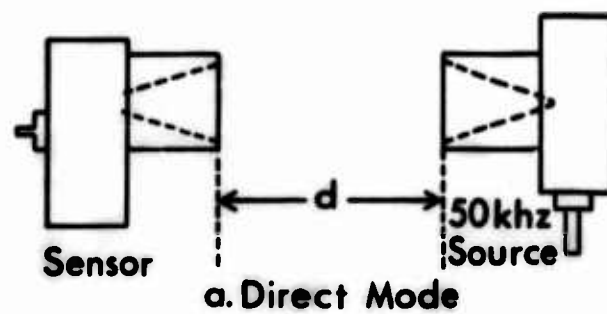
***FLUIDIC EAR
Industrial Enclosure***



Direct Mode

FIGURE 10

FLUIDIC EAR OPERATING MODES



b. Reflex Mode

FIGURE 11

FLUIDIC EAR

Max. Span For Separate Supply Pressure

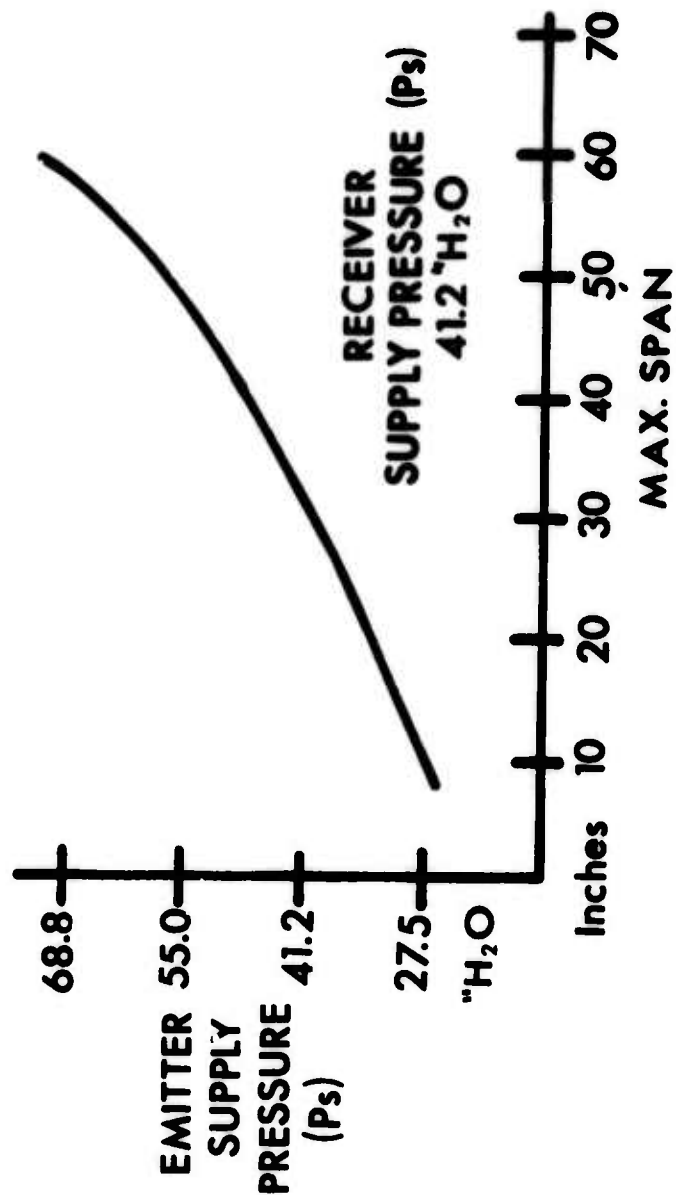


FIGURE 12

FLUIDIC EAR **Max. Span For Common Supply Pressure**

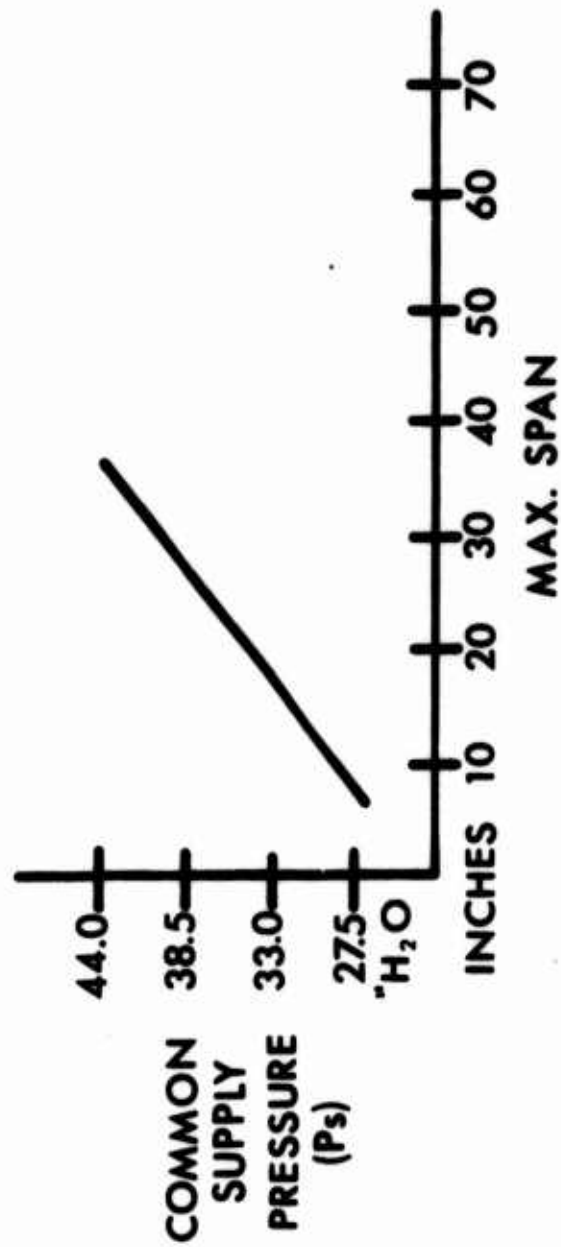


FIGURE 13

FLUIDIC EAR POWER CONSUMPTION

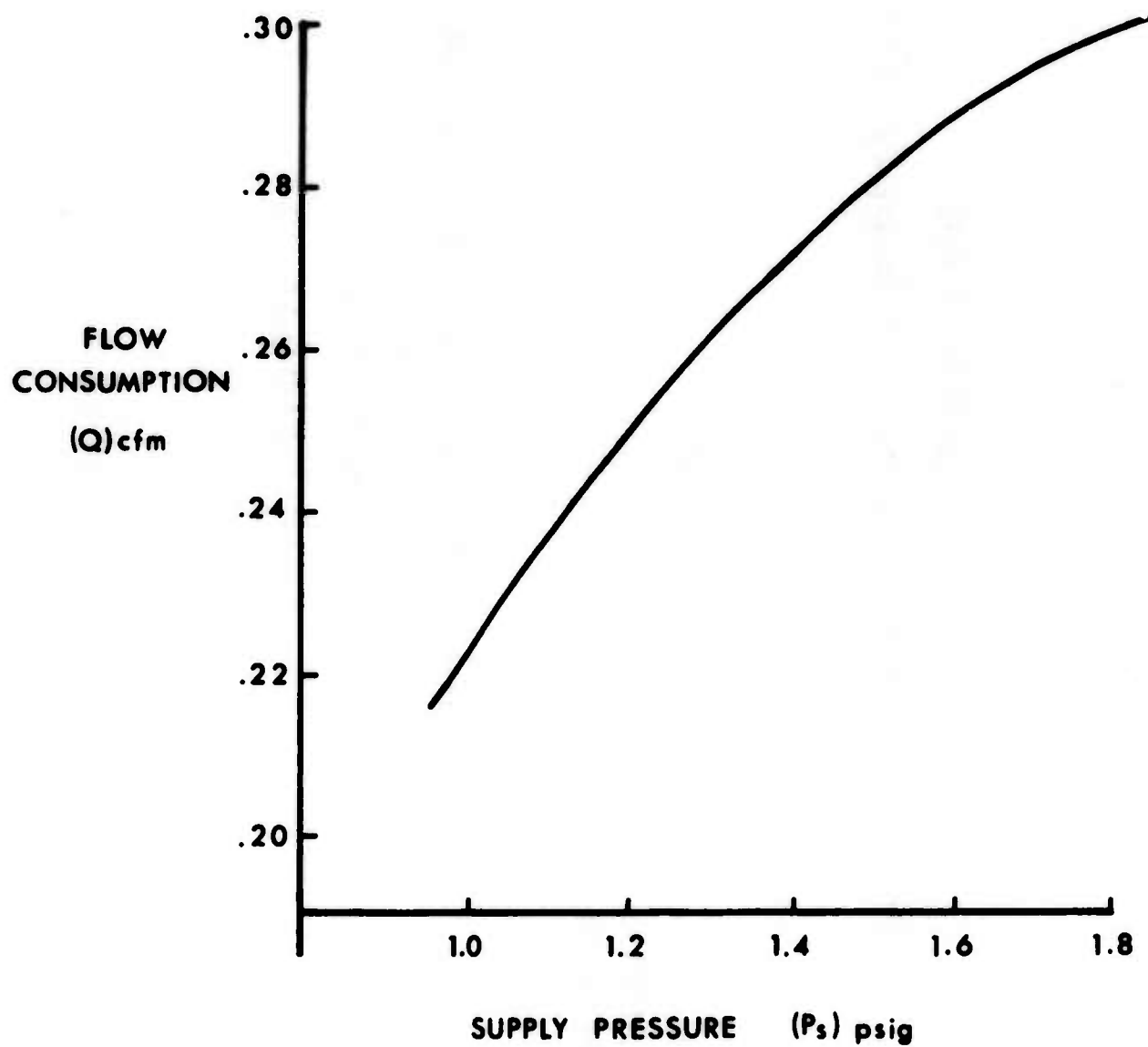
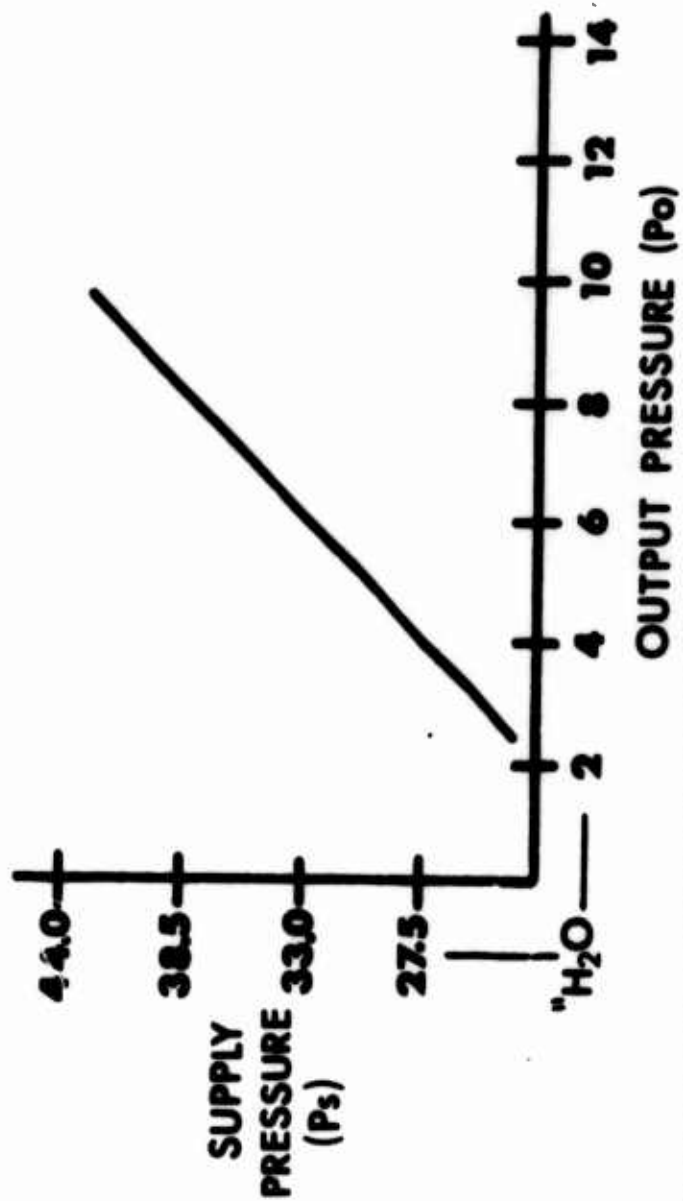


FIGURE 14

STANDARD FLUIDIC EAR



RECEIVER OUTPUT PRESSURE VS SUPPLY PRESSURE

FIGURE 15

FLUIDIC EAR



Reflex Mode

FIGURE 16

FLUIDIC EAR
Industrial Enclosure



REFLEX MODE

FIGURE 17

PARABOLIC EAR SYSTEM SCHEMATIC

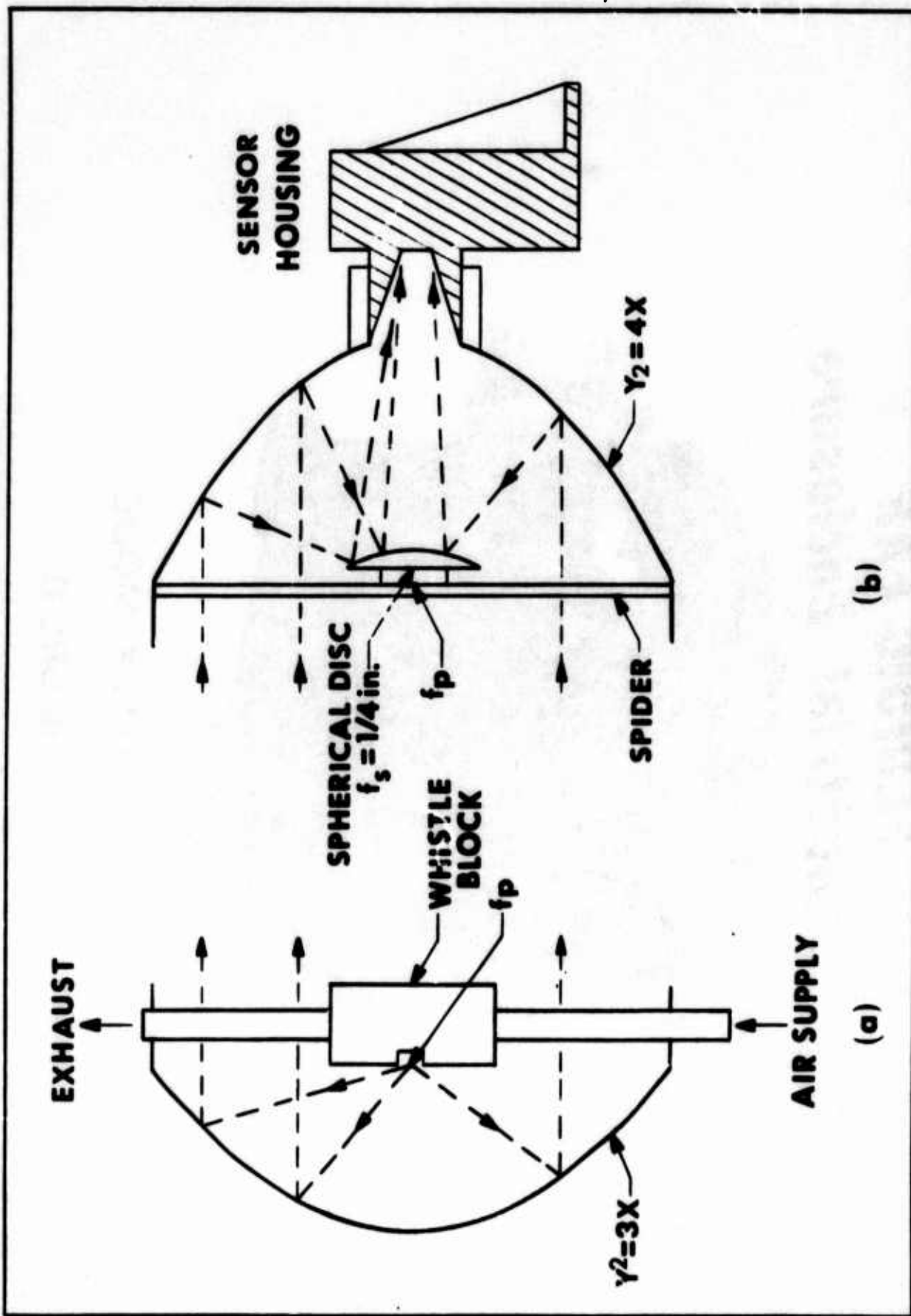


FIGURE 18

**POLAR DIAGRAM OF RADIATION INTENSITY
FROM GENERATOR WITH PARABOLOIDAL REFLECTOR**

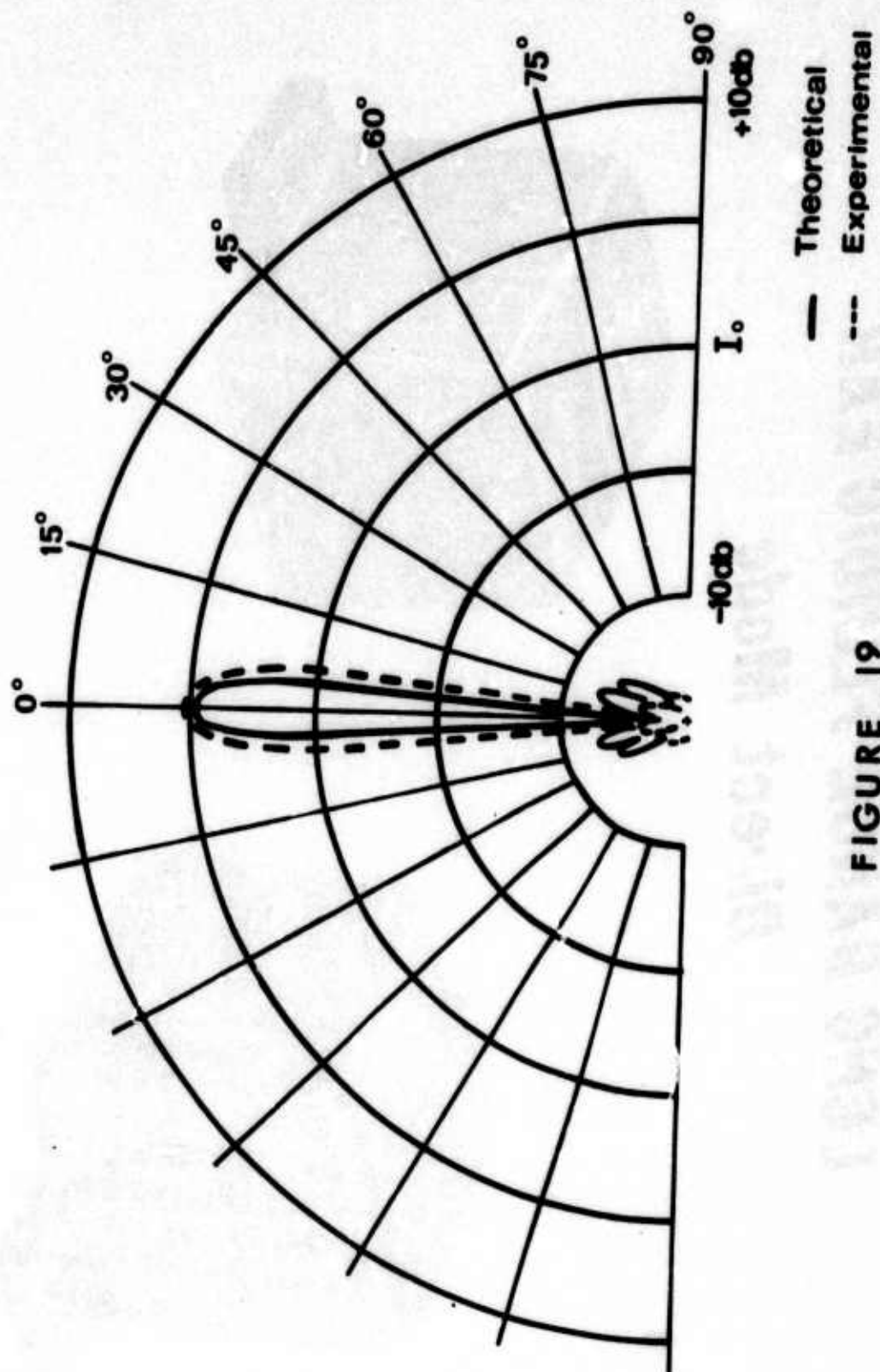


FIGURE 19

LONG RANGE FLUIDIC EAR

Direct Mode

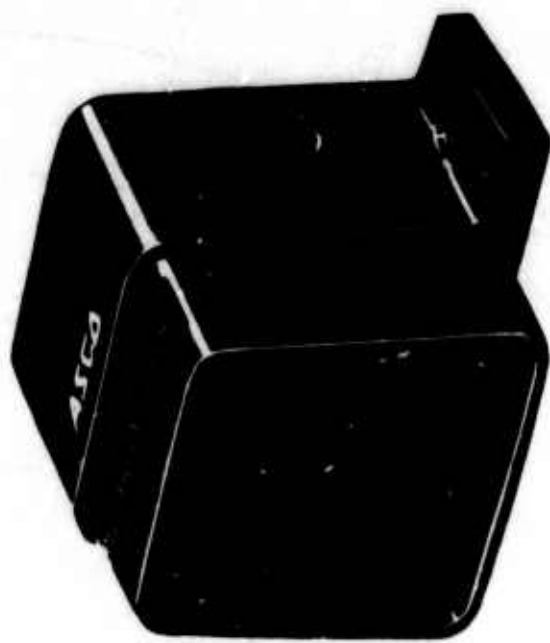
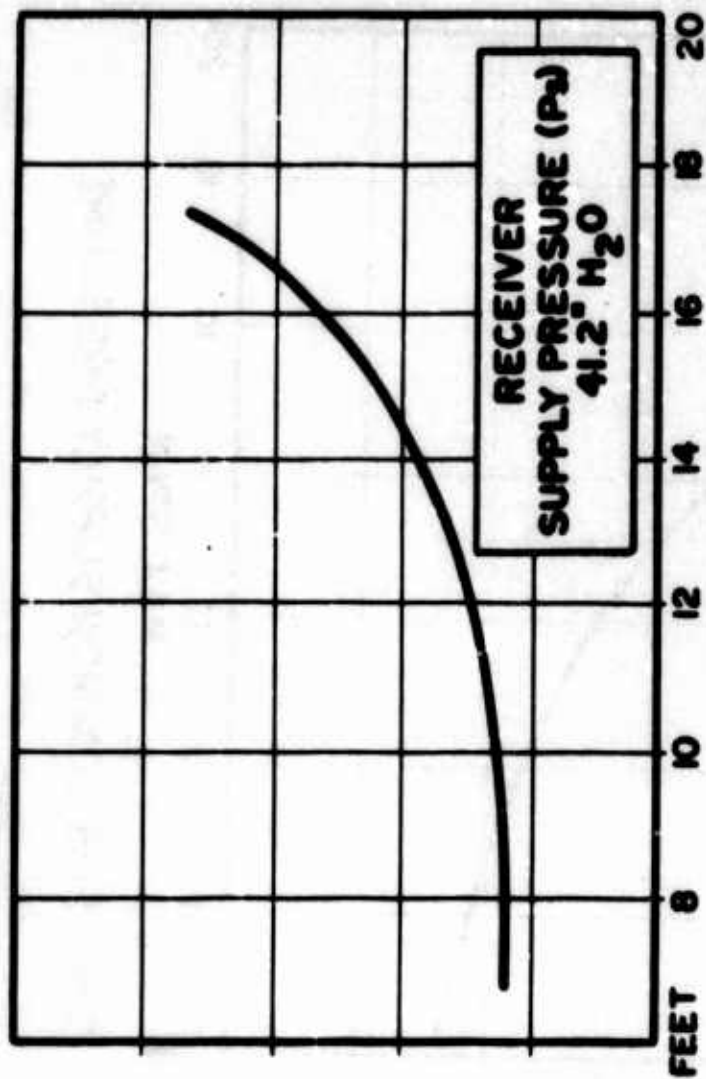


FIGURE 20

Long Range Fluidic Ear 6090028

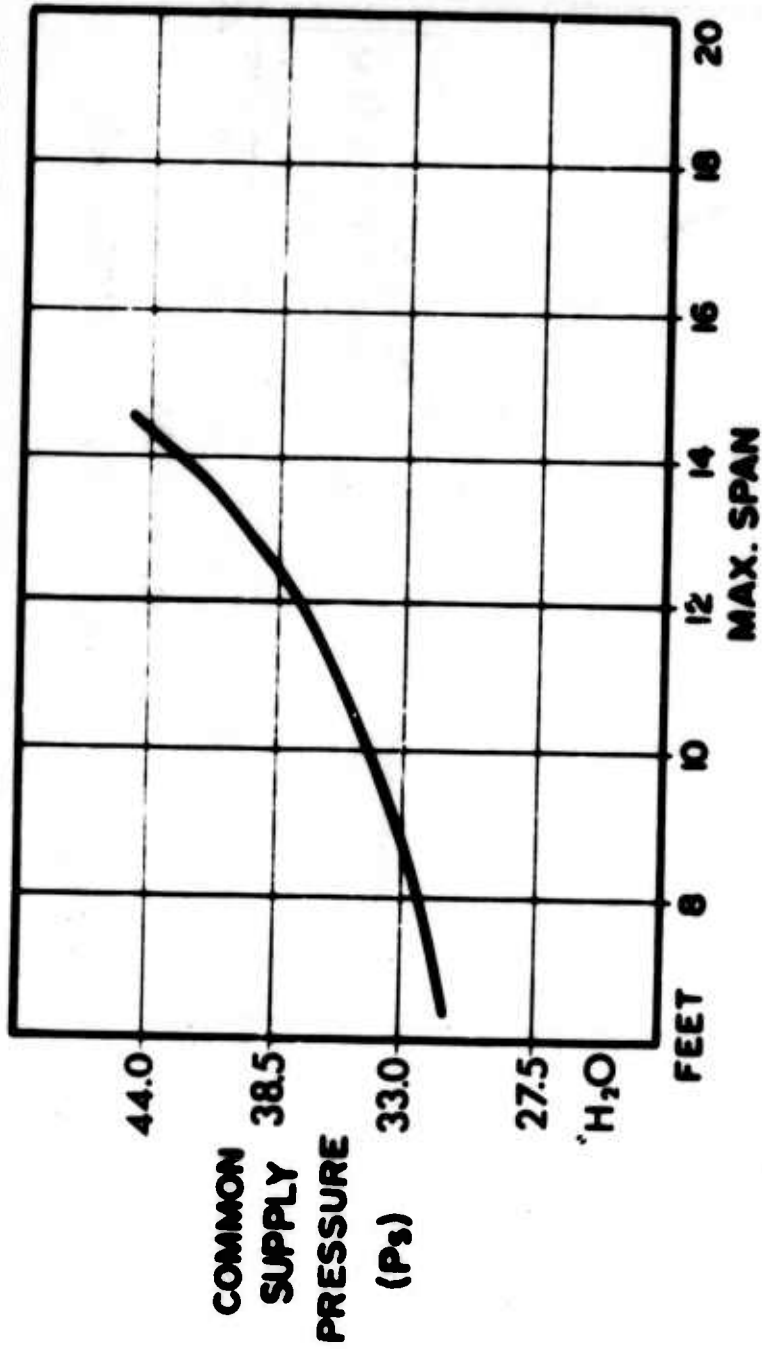
EMITTER
SUPPLY
PRESSURE
(PSI)



MAX. SPAN FOR SEPARATE SUPPLY PRESSURE

FIGURE 22

Long Range Fluidic Ear 8090028



MAX. SPAN FOR COMMON SUPPLY PRESSURE

FIGURE 21

FLUIDIG EAR

Area Coverage Sensor

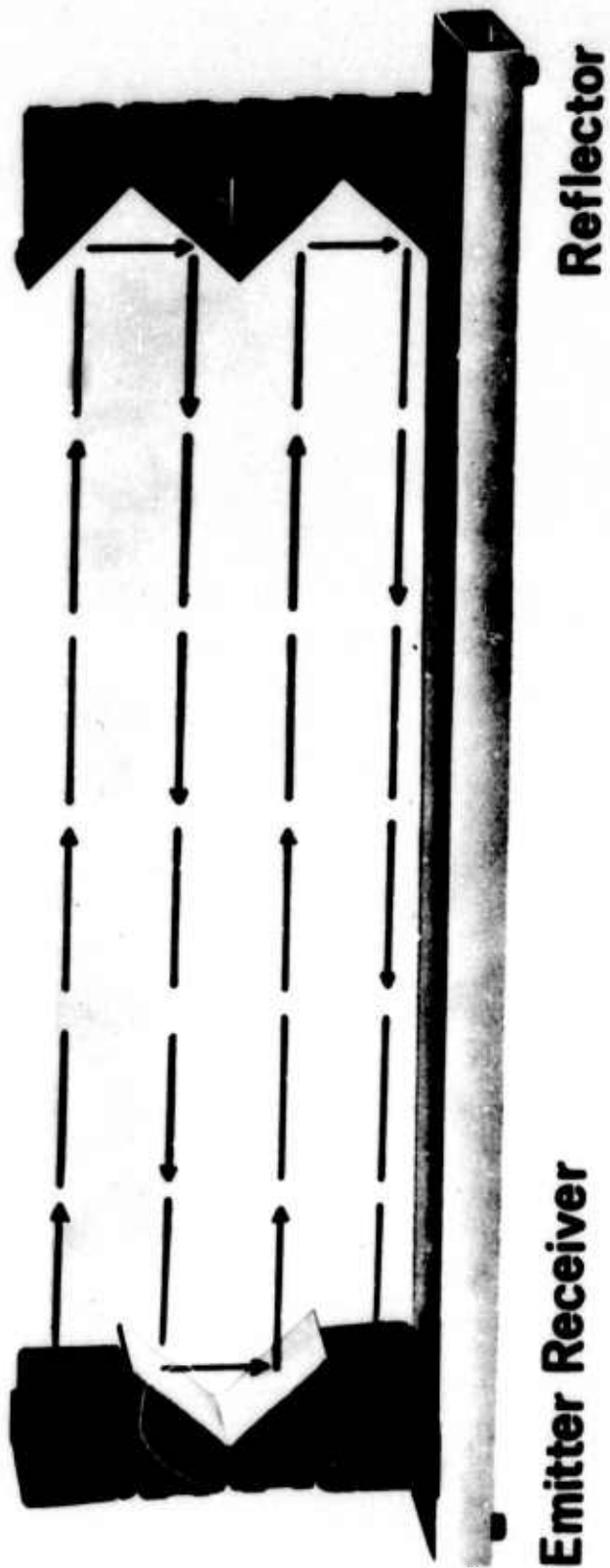


FIGURE 23

**PERFORMANCE AND APPLICATION
OF THE VORTEX RATE SENSOR**

**James O. Hedeer
Project Engineer
Honeywell Inc.
Government and Aeronautical Products Div.
Minneapolis, Minn.**

INTRODUCTION

The vortex rate sensor has now been under development for approximately fifteen years. During the first few years following its conception, development efforts were pointed toward defining mathematical models for sensor operation. This period was followed by experimental models which produced data showing the feasibility of the basic concept and which pointed out areas of needed improvement. These early development models were then applied to a variety of experimental inertial rate sensing and inertial rate damping systems. Some were a success and others were not. Those applications which were successful and which are still strong today are those which take advantage of one or more of the following strong points of the vortex rate sensor.

- . High reliability (no moving parts)
- . Operable in severe environments (vibration, shock, temperature and radiation).
- . Fast ready time

During recent years, methods of fabrication and producibility have been stressed. At the present time, the vortex rate sensor is an operational and producible inertial rate sensor with at least five major areas of application. This paper presents a description of present vortex rate sensor design, method of fabrication and level of performance and describes briefly those areas of application which show significant promise in the future.

PRINCIPAL OF OPERATION

The vortex rate sensor is a pure fluid device that senses angular velocity about its input axis and provides a fluid signal proportional to that velocity. There are no moving parts within the device and it employs a pattern of fluid flow to sense angular rotation.

The three basic parts of the vortex rate sensor are the coupling element, the vortex chamber, and the signal pickoff. The coupling element, the vortex chamber, the signal pickoff, and other secondary parts are shown in Figure 1. The fluid enters through the inlet and disperses around the annular plenum chamber. After passing through the coupling element, fluid flows towards the sink outlet and the pickoff. In some designs, as shown in Figure 1, a second sink outlet is added to increase the flow through the sensor thereby increasing sensor response.

The rate sensor coupling element imparts any turning motion of the case to the fluid flowing through the coupling element. The turning motion imparted to the fluid is amplified by free-vortex action as the fluid flows inward toward the sink outlets. This pattern of flowing fluid is contained within the vortex chamber and is made up of two superimposed flow fields:

- . A "sink" flow field, where the streamlines are radial and the flow path is straight to the center outlet.

- Superimposed upon the sink flow field is a rate-imposed tangential flow with a resulting vortex pattern.

In the resulting superimposed flow pattern, the streamlines assume a logarithmic spiral as they flow towards the center outlet.

The logarithmic spiral results from one of the basic principles of motion the conservation of angular momentum. This principle states that the total angular momentum of a body about an axis remains constant in the absence of restraining forces. Any turning rate about the input axis of the vortex rate sensor imparts a tangential velocity component at the outer ring to the already-present radial component.

The resulting angular momentum is conserved as the fluid is drawn towards the center outlet. Therefore, the component of tangential velocity increases to a maximum at the outlet. This amplified tangential velocity is detected by a pickoff in the outlet sink which is sensitive only to the tangential velocity component.

A major breakthrough in the development of the vortex rate sensor was the discovery of a pickoff which accurately sensed the magnitude of the vortex action without generating unwanted "noise". In detail, its configuration has changed during the development stages of the vortex rate sensor, however, its basic principle of operation has remained the same. The pickoff consists of an aerodynamic surface which protrudes into the flow stream in one of the sink outlets. In the absence of case rotation, the fluid flow over the pickoff is at zero angle-of-attack. With an input turning rate, the stream flows over the aerodynamic surface at some angle-of-attack proportional to the helix angle generated at the coupling element by the case turning rate.

This angle-of-attack produces a differential pressure across the airfoil, which is sensed by pressure ports located in the wall of the sink tube on opposite sides of the airfoil near the leading edge.

VORTEX RATE SENSOR THEORY

In most rate sensor applications, the important performance characteristics are sensitivity, accuracy, and response time. Performance with respect to these characteristics depends upon several parameters, the most important being the dimensions of the vortex chamber and the flow rate through it. A large vortex chamber, a small outlet, and a low flow rate generally result in a larger and more stable vortex motion. This is conducive to a more sensitive and accurate output signal. However, this also results in a slow response, for the response time of the vortex rate sensor is dependent upon the chamber volume and flow rate through it. A sensor with a fast response requires a small chamber volume and a fast flow rate; sensitivity is sacrificed. Because accuracy is dependent upon the size of the sensor, a tradeoff is generally necessary between size and power (flow rate) to obtain the best compromise between accuracy and response. The tradeoffs between the parameters of flow rate and size are determined by the application.

Mathematical models for some of these characteristics have been established allowing accurate prediction of device performance. Other characteristics have been established by empirical methods. The following describes the present knowledge in this area.

Sensitivity

The basic parameter used to express the sensitivity of the vortex rate sensor is scale factor. The following equation defines rate sensor scale meter for the presently used pickoff design.

$$S. F. = \eta_p Q_p \frac{R_o^2}{R_i^3} \times 10^{-4}$$

where

S. F. = Scale factor (psi/deg/sec)

η = Correction factor for viscous effects

ρ = Fluid density (slugs/ft³)

Q_p = Flow rate through primary sink (CFS)

R_o = Coupling inner radius (ft)

R_i = Radius of sink (ft)

The correction factor for viscous effects or viscous efficiency is:

$$\eta = \frac{1 - e^{-1/\beta}}{1/\beta}$$

Where the viscous parameter (β) is:

$$\beta = \frac{Q_t h}{12 \nu R_o^2}$$

Q_t = Total flow rate through sensor (CFS)

h = Plate spacing (ft)

ν = Fluid kinematic viscosity (ft²/sec)

R_o = Coupling inner radius (ft)

A correction factor is used to account for loading effects on the pickoff.

$$S.F. \text{ (loaded)} = \frac{S.F.}{1 + (C_L A_L / C_p A_p)^2}$$

where:

- A_L = Cross sectional area of load orifice or port
- A_p = Cross-sectional area of pickoff port
- C_L = Flow coefficient for load (approximately 0.65 for orifice)
- C_p = Flow coefficient for pickoff (approximately 0.35)

Accuracy

The accuracy of the vortex sensor is described by three parameters; threshold, noise, and linearity. Threshold defines the minimum detectable rate; noise defines the stability of the output signal; and linearity defines the deviation of the output from a nominal scale factor curve.

These parameters cannot be described theoretically but have been established from a large amount of empirical data. They are not amenable to theory because they depend upon the stability of the flow pattern. Turbulence-generating flaws such as sharp edges or protrusions on the coupling or non-symmetries of the pickoff cannot be predicted. To establish a reference point for determining accuracy, a large number of units of various sizes have been tested.

Threshold - Threshold of the VRS is limited by noise and the capabilities of the pickoff. The minimum swirl rate which it can detect is the limiting characteristic. Therefore, the larger the coupling diameter, the greater the swirl rate and the lower the threshold. Thresholds of less than 0.1 deg/sec are obtainable with present sensor designs.

Noise - Random perturbations (noise) develop within the flow pattern at sharp edges or protrusions and appear in the output signal as pressure fluctuations whose frequency and magnitude are both random in nature. The Reynolds number for incompressible fluids and Mach number for compressible fluids are important parameters for minimizing noise. For liquids, maintaining a Reynolds number of less than 4,000 in the outlet sink and avoiding cavitation reduces fluctuations due to large scale turbulence. Maintaining a Mach number less than one for gases eliminates fluctuations due to the development of shock waves.

Linearity - Non-linear rate sensor outputs result from two sources:

1. Nonsymmetries in the physical structure of the device.
2. Inherent saturation of the pickoff.

The former is generally the limiting characteristic. The most critical area for minimizing physical non-symmetries is in the exit and pickoff region. Maintaining sharp corners, smooth flow surfaces, and symmetrical bore and pickoff ports is of prime importance. With reasonable parts

control a linearity of $\pm 3\%$ is possible.

Saturation of the pickoff is reached when the flow angle of attack approaches about 30 degrees. Output linearity degradation due to pickoff saturation occurs at about 1/2 the fully saturated condition. The rate at which this occurs is approximately:

$$\text{L.R.} = \frac{5Q_p}{\eta R_o^2 R_1} \quad \text{deg/sec}$$

Response Time

The response of the vortex rate sensor is approximately a simple time delay. The time delay equals the emptying time for the sensor, which is the ratio of the vortex chamber volume to the volumetric flow rate through the chamber:

$$t = \frac{\pi R_o^2 h}{Q_t}$$

Where:

t = time response (sec)

R_o = coupling inner radius (ft)

h = plate spacing (ft)

Q_t = total flow rate through sensor (CFS)

The secondary sink provides a means of increasing the total flow through the sensor, and thereby increasing sensor response, without exceeding the primary sink flow limit. This primary sink flow limit would normally be sonic velocity, in a sensor run on gas, or the critical Reynolds number for the onset of turbulent flow in a sensor run on liquid. Therefore, the response of a given sensor can be increased, at the expense of power flow, by increasing the size of the secondary sink. A practical limit exists, however, at a secondary-to-primary sink flow ratio of approximately three to one. At higher flow ratios, the large flow rate through the secondary sink causes a skewed velocity profile in the vortex chamber, which prevents further increase in response and which may have adverse effects on sensor scale factor.

SENSOR DESIGN AND FABRICATION

The components of the vortex rate sensor are (1) the housing and manifold, (2) the coupling element, (3) the pickoff, (4) the null adjust and built-in-test (BIT) feature, and (5) the temperature compensation section. The last two components are optional, but they are now frequently included in the sensor design. The following is a description of these components and the method of fabrication.

Housing and Manifold

The housing normally contains the supply plenum, the upper and lower faces of the vortex chamber and the secondary sink (if one is included). The manifold, which is usually an integral part of the sensor housing, provides power to the supply plenum, collects the return flow from the sensor sink (s) and brings the pickoff signals out of the sensor. As shown in Figure 2 the housing consists of two pieces, a base and a cover. In the design of Figure 2, the base and cover are machined from aluminum with the manifolding drilled and O-ring seals used between the two pieces.

In the more recent design shown in Figure 3, the cover is machined with internal porting for the secondary sink flow. The base is a plate with the manifolding for the power, the return flow and the pickoff signals fabricated on the external surface using the electroform conductive wax (ECW) process. The ECW process uses a baseplate of stainless steel on which a conductive wax positive, in the shape of the desired manifold channels, is injection molded. Nickel is then electroplated onto the wax and baseplate. The wax is then removed resulting in a sealed assembly. The manifold side of the sensor base is shown in Figure 4.

Coupling Element

One coupling version consists of a cylinder of porous material placed inside the vortex chamber at as large a diameter as space permits (See Figure 1). The rotation is imparted to the fluid as it seeps through the fine porous passages of the coupling. Another version uses a stack of equally spaced "washers" (See Figure 3). Coupling is provided by viscous drag of the top and bottom faces of the washers on the fluid flowing between them. This causes exponential decay of any circumferential motion relative to the washers; i.e., the turning rate of the washers becomes imposed on the fluid.

The advantage of the porous coupling is that it can be used in very small devices and still provide good coupling. The advantage of the washer coupling is that it, in general, has lower bias and random noise. The washer coupling, if it is too small, or if the flow speed through it is too high, may not couple effectively. This latter effect has not been a problem in the general class of sensors used to-date, and therefore, the washer coupling design is most frequently used.

The design of a typical coupling element washer is shown in Figure 5. The washer, with spacer tabs, is chemically etched in one piece. A number of these elements are then stacked on alignment pins (see pins in pickoff of Figure 3) to obtain the complete coupling element.

As noted earlier under Response Time the response of the vortex rate sensor is dependent on the vortex chamber volume and, therefore, on the coupling element inner radius. The sensor response can therefore be characterized, to a degree, by variation in the inner radius of the various washers within the coupling element. Figure 6 shows one combination. Half of the coupling element has a constant inner radius, while the other half has an inner radius which decreases in steps to one third of the largest value. The smaller radius washers produce a faster response and lower sensitivity.

The resultant response of the total coupling element to an input turning rate is somewhat similar to that produced by a lag-lead dynamic shaping network.

Pickoff

The signal pickoff includes the primary sink tube, the airfoil and the pressure taps.

Figure 7 shows an electroformed pickoff. The base for the pickoff and entrance to the outlet sink are machined, and then the rest of the sink hole, the airfoil and the output pickoff ports are formed on the opposite side of the plate using the ECW process. The pre-electroformed pickoff of Figure 1 is shown in Figure 8. A slot, which divides the wax cylinder of Figure 8 into two halves, results, when electroplated, in the airfoil shown at the sink exit of Figure 7.

Figure 4 shows another electroformed pickoff design. This unit has two sets of pickoff ports, one on each side of the airfoil. These pickoff signals are summed in the sensor manifold to reduce the output impedance of the sensor.

Null Adjust and Built-in-test

Sensor null adjustment and test signal is accomplished with a small blade which extends into the vortex chamber downstream of the coupling element. By turning the blade, a small swirl, in either direction, can be imparted to the the flow which can be used to null the sensor output. With the sensor nulled, the blade is locked to prevent subsequent variations. A test signal can be introduced by rotating the blade a set amount. When combined with the null adjust, a second lock and rotational stop is provided for the test feature.

Temperature Compensation

In most applications the total flow through the rate sensor is held constant. Therefore, from the scale factor equation it can be seen that change in scale factor with change in fluid temperature occurs due to a change in the viscous efficiency (η). One method of compensating for this change in viscous efficiency is to push more flow past the pickoff when the viscous efficiency is low (high fluid viscosity) and less when the viscous efficiency is high. This is accomplished by transferring flow from the secondary sink to the primary sink as the fluid viscosity increases. A stack of small washers (see Figure 5) with integral spacers, similar to the coupling rings, are located at the exit and in series with the secondary sink hole. These form a viscous resistor which produces the desired effect of transferring flow from the secondary sink to the primary or pickoff sink as the fluid viscosity increases. By proper sizing of this viscous resistor, the rate sensor scale factor can be held relatively constant over a wide fluid temperature range.

SENSOR PERFORMANCE

The performance of the vortex rate sensor will depend, to a significant degree, on the sensor design, which in turn is based on the sensor application. The following data is not meant to represent the limits of attainable performance for a given parameter. It does represent, however, the level of overall performance obtainable from present vortex rate sensors.

Scale Factor

Figure 9 shows a scale factor curve for the rate sensor of Figure 2, using MIL-H-5606 hydraulic oil as the operating fluid. The data in Figure 10 shows the variation in scale factor with oil temperature and flow rate for this same sensor. The sensor has both a primary and a secondary sink with viscous resistor elements in the secondary sink to provide scale factor temperature compensation.

Figure 11 shows scale factor versus flow rate data for the sensor shown in Figure 4. This data is for MIL-H-5606 hydraulic oil at 120°F and 180°F.

The reduction in sensor scale factor when loaded with a fluidic amplifier having control port dimensions of .025 in. x .025 in is also shown. In this case the loaded scale factor is 42 percent of the dead ended scale factor. This device also has temperature compensation built into the secondary sink, however, in the configuration tested, it was not sufficient to completely eliminate variation in scale factor with change in oil temperature. The increasing slope of the scale factor versus flow rate curves at the higher flow rates is due to an increase in the viscous efficiency (η).

Accuracy

Figure 12 shows data for two parameters effecting sensor accuracy, noise and null shift. The data is for the sensor shown in Figure 4 and goes with the scale factor data presented in Figure 11. As shown, noise in equivalent degrees per second, remains approximately constant with changes in flow rate and fluid temperature, which means that the pressure fluctuation amplitude increases in proportion to the scale factor. The maximum Reynolds number in the primary or pickoff sink for the two curves shown is approximately 3000 (5.5 cis, 120°F) and 4750 (5.5 cis, 180°F). It should be noted that the data is plotted as a function of total sensor flow. At the 5.5 cis, 180°F point, the primary sink flow was measured at 1.8 cis.

The noise data presented in Figure 12 is for a frequency spectrum of less than approximately 20 Hz. The data is limited to this frequency range because of limitations in the standard pressure measuring instrumentation used and because most sensor applications have response limitations of less than 20 Hz.

When using a liquid as the operating fluid, as is the case with the data shown, care must be taken to eliminate air from the sensor signal lines and from the return plenum at the exit of the sensor sink (s). If not removed by designing the sensor lines to be self purging, the air will act as a capacitor which can set up oscillations or cause fluctuations in the two output ports to get out of phase and thereby produce noise.

The null shift data of Figure 12 was obtained by adjusting the sensor null, using the null adjust blade, at 2.0 cis and 120°F, and then recording the sensor null at the other flow and oil temperature conditions. The null shift is attributed to changes in the flow pattern in the sensor.

Response

Figure 13 shows frequency response curves at several flow rates for the sensor of Figure 2. This unit has a vortex chamber volume of approximately 0.04 cubic inches, which should produce a sensor delay time of 0.010 seconds or 90 degrees phase lag at 25 Hz with a total sensor flow rate of 4.0 cis. When tested in the normal two sink configuration, with a flow split of 1.5 cis through the primary sink and 2.5 cis through the secondary sink, the sensor exhibits considerably greater phase lag (90° lag at 15 Hz). Part of this increased lag is due to the flow split, as shown by the response curve for 4.0 cis flow rate with only one sink. With two sinks, and particularly when

a high proportion of the flow is going through the secondary sink, the signal transmission speed across the vortex chamber to the pickoff is reduced. The remainder of the increase in phase lag is attributed to lags in the sink and pickoff region of the sensor.

Although the actual sensor response does vary from the simplified theoretical value, sufficient empirical information is available to design a sensor to meet specific response requirements. In cases where high response has been required, such as the ejection-seat stabilization application, sensors with delay times of less than 0.005 seconds have been designed and successfully tested.

Reliability

In 1967, a program was initiated under the sponsorship of the U. S. Army Air Mobility R&D Laboratory to demonstrate the reliability of various fluidic components. During this program, the vortex rate sensor was subjected to over 48,000 operating hours without a failure. The test was conducted under typical MIL spec. operating environments such as 10-micron filtered oil, 50-micron filtered oil, -25° to +185°F temperature variations, and 0.5 to 2 g vibration. None of the 16 units tested failed the life test either by a catastrophic failure or a performance degradation failure, where the failure criteria was based on allowable rate sensor performance degradation for a typical aircraft stability augmentation system application. As a result of these tests a rate sensor MTBF in excess of 48,000 hours was demonstrated and a predicted rate sensor MTBF of 100,000 hours was established.

VORTEX RATE SENSOR APPLICATIONS

The following is a brief description of the major areas of application for the vortex rate sensor to date.

Aircraft Flight Controls

The most common area of application for the vortex rate sensor to date has been in aircraft flight controls, where it is the prime inertial sensor for stability augmentation.

Fluidic stability augmentation systems, operating on hydraulic oil from the aircrafts power supply, have accumulated over 325 single-axis flight hours on Army OH-58A and UH-1 type helicopters and have been tested on the S-58 and CH-54 helicopters. A number of systems (14 two-axis and 12 single-axis) are presently being built for field test on OH-58 and TH-57 helicopters, and additional prototypes are being built for evaluation on Sikorsky's UTTAS.

In the age of high reliability requirements and redundant flight control systems, the fluidic SAS, because of its reliability, offers advantages as either a primary or a backup system.

Turret/Cupola Stabilization

In the high vibration and shock environment of a helicopter gun turret or a cupola/turret of a ground vehicle, the environmental ruggedness of the vortex rate sensor offers significant advantages. In early 1974 a two-axis inertial rate damping system, containing two vortex rate sensors, was installed on the XM-28 turret of the AH-1G helicopter, and gun fire tests were successfully conducted. Under another program sponsored by the U.S. Army Weapons Command, Rock Island Arsenal, a single axis of a stabilization system for the cupola of an armored personnel carrier was built and bench tested. Both of these areas appear to be good applications for use of the vortex rate sensor.

Ejection Seat Stabilization

Where fast ready time is required of a stabilization system, the vortex rate sensor has the required capability. Feasibility of the fluidic control system concept for ejection seat stabilization was demonstrated in the flight test phase of the control system development program, ("Development of a Fluidic Control System For An Aircraft Ejection Seat", NADC Contract N00156-71-C-0226). The vortex rate sensor is the key component used in this fluidic solution to the ejection-seat stabilization problem.

Safing and Arming

In a number of safing and arming systems, inertial angular rate is the controlling parameter. An example of this is the case where a vortex rate switch was developed and a number of units were fabricated for a missile safing and arming application under contract DA-28-017-AMC-1524(A) and DAAA21-67-C-1111 for the U.S. Army, Picatinny Arsenal. The rate switch has a self-contained gaseous power supply and produces an electrical switch closure at a preselected roll rate of the missile. It has satisfactorily met the performance requirements of -65 to +160°F, 30g vibration, 30g acceleration and 15g shock.

Rate Sensor Packages

To cover other applications where the reliability, environmental capability and fast ready time advantages of the vortex rate sensor can be utilized, fluidic rate sensing packages are available. A typical two axis package contains two vortex rate sensors, two fluidic-to-electric transducers and the necessary electronics to produce a electrical output signal similar to electromechanical gyro packages. This type of package has been tested and additional development is in progress.

CONCLUSIONS

The vortex rate sensor has reached the level of development where a sensor can be designed using established theory, built using fabrication methods compatible with production and integrated into a control system with high confidence of satisfactory performance. In general, the level of performance attainable from present state-of-the-art sensors is lower than that which can be obtained from conventional electromechanical rate gyros. However, the vortex rate sensor does provide superior performance in the areas of reliability, environmental ruggedness and fast ready time. In applications such as aircraft stability augmentation, gun turret stabilization and safing and arming, where these advantages are being utilized, the vortex rate sensor shows significant promise.

For the future, increasing advances in the level of performance of the vortex rate sensor are visualized. Smaller sensors, operating from high pressure hydraulic supplies, will be more easily integrated with power control equipment. Lower noise and null shift, resulting from improved fabrication and packaging techniques should open additional areas of application.

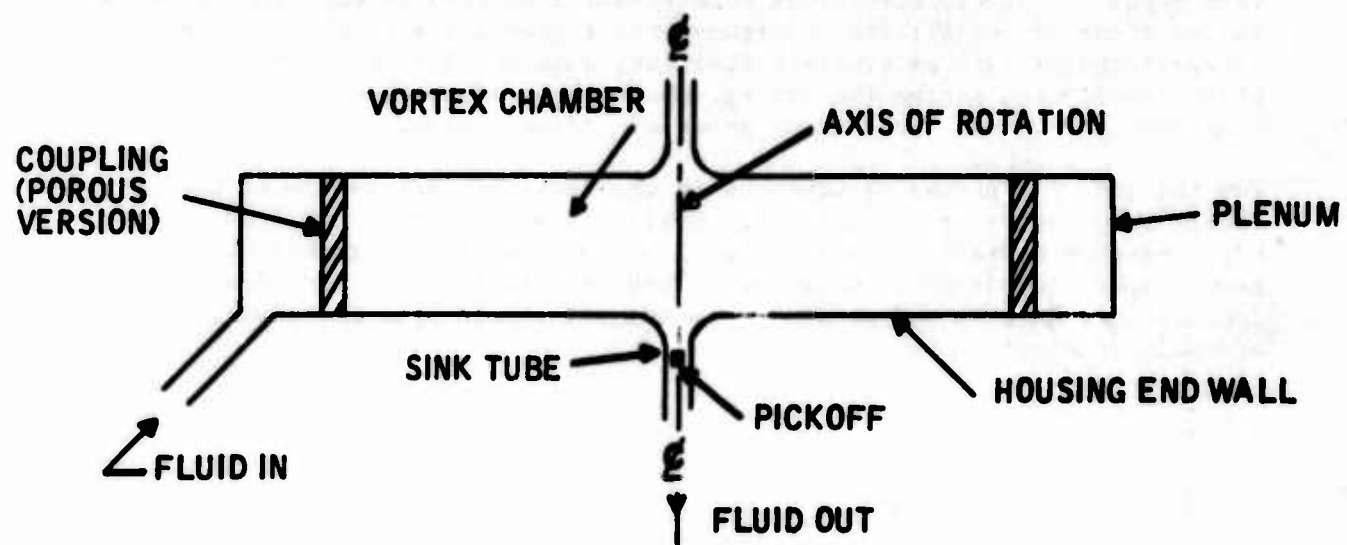


Figure 1. Cross-Section of Vortex Rate Sensor

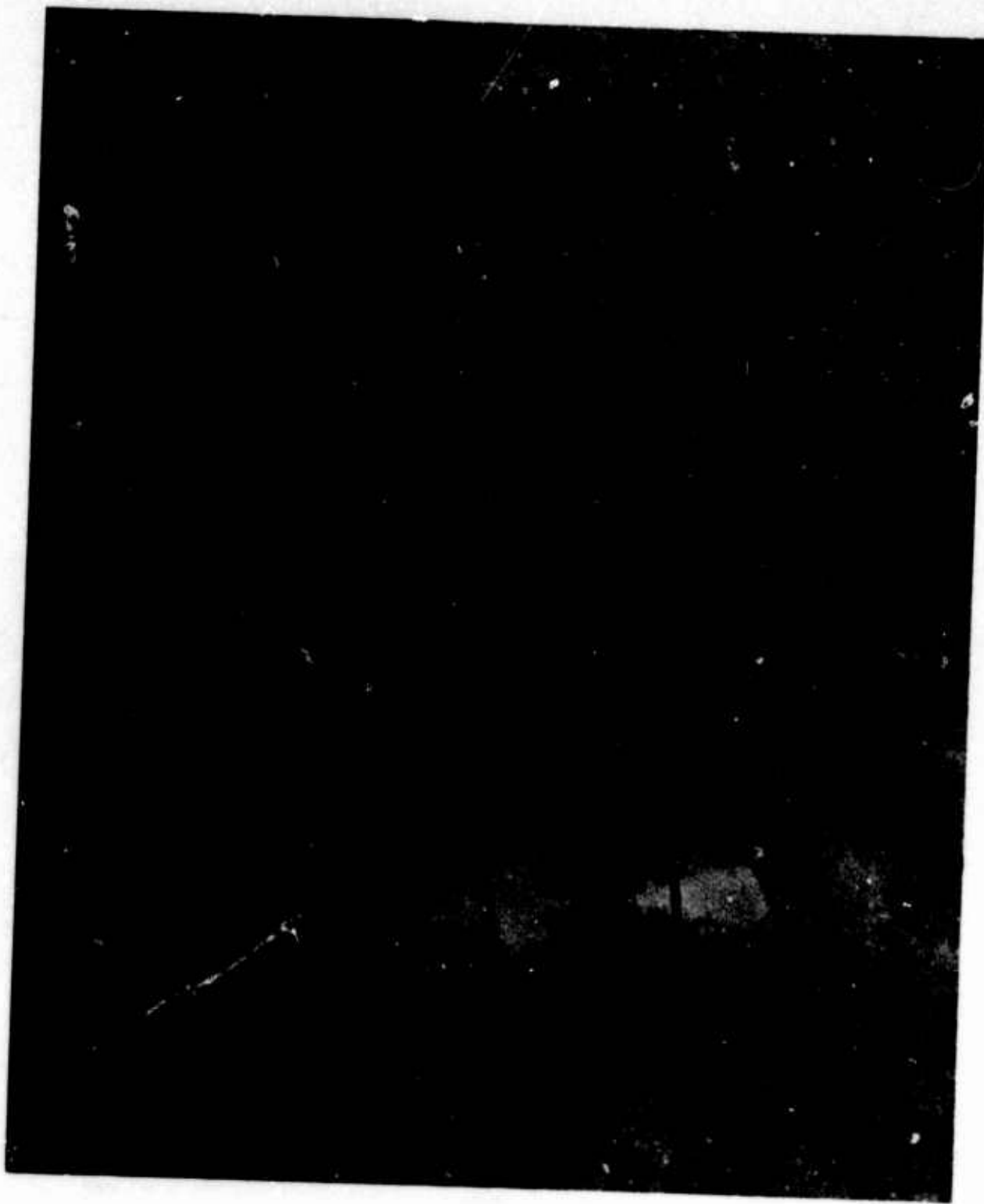


FIGURE 2. RATE SENSOR EXPLODED VIEW

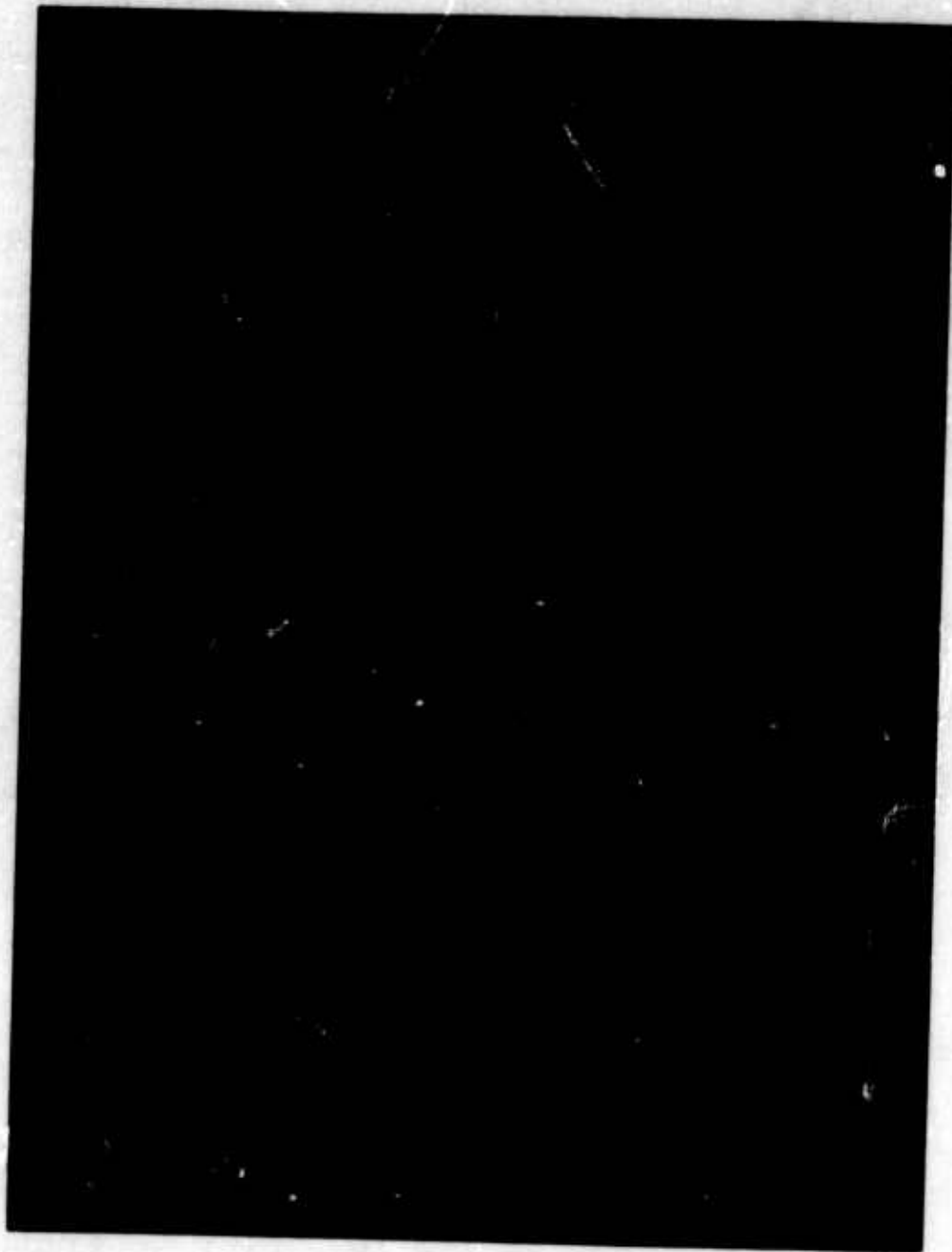


FIGURE 3. ADVANCED SENSOR DESIGN



FIGURE 4. ADVANCED SENSOR DESIGN



FIGURE 5. VARYING COUPLING DIAMETER

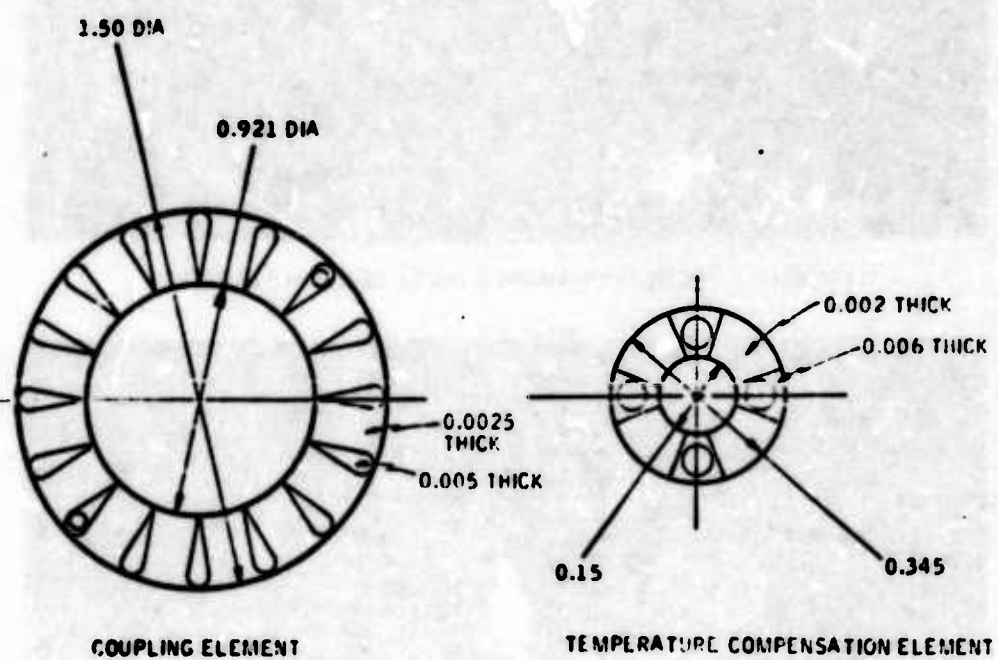


Figure 6. Rate Sensor Etched Elements



FIGURE 7. ELECTROFORMED RATE SENSOR PICKOFF

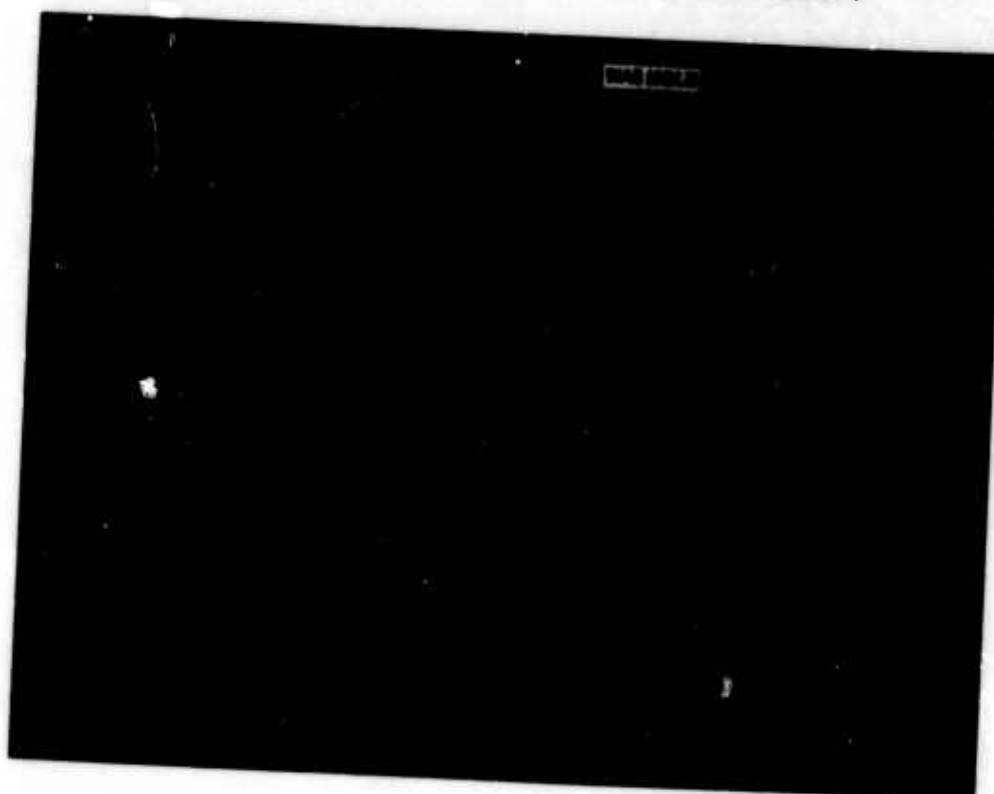


FIGURE 8. PRE-ELECTROFORMED RATE SENSOR PICKOFF

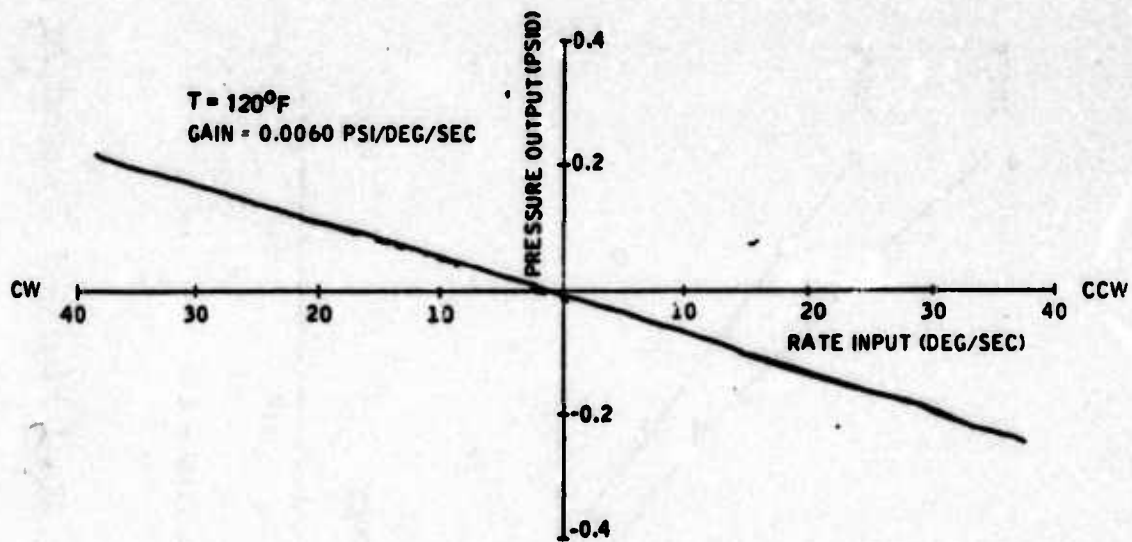


Figure 9 Rate Sensor Gain

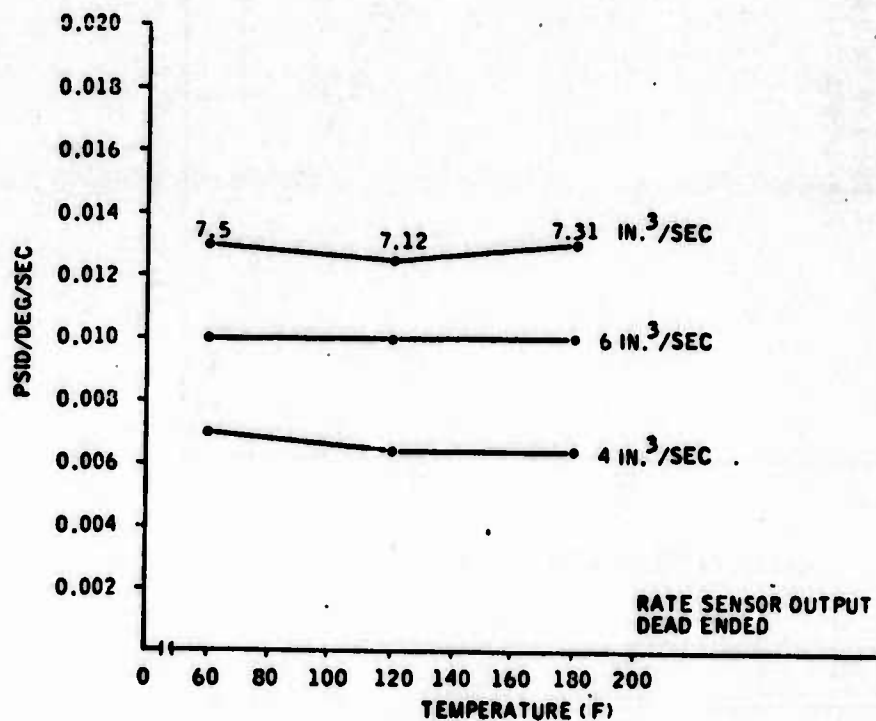


Figure 10 Rate Sensor Gain versus Temperature and Flow

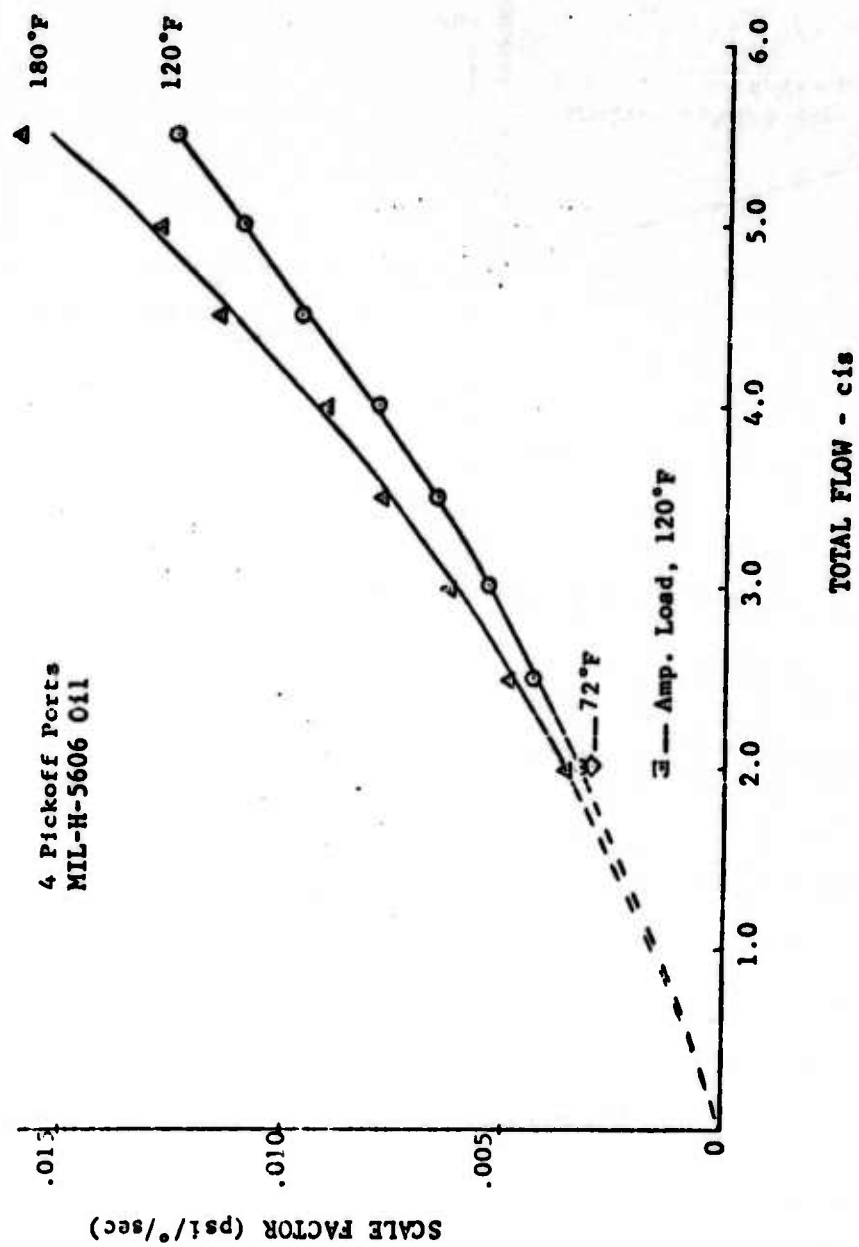


Figure 11 Scale Factor versus Fluid Flow and Temperature

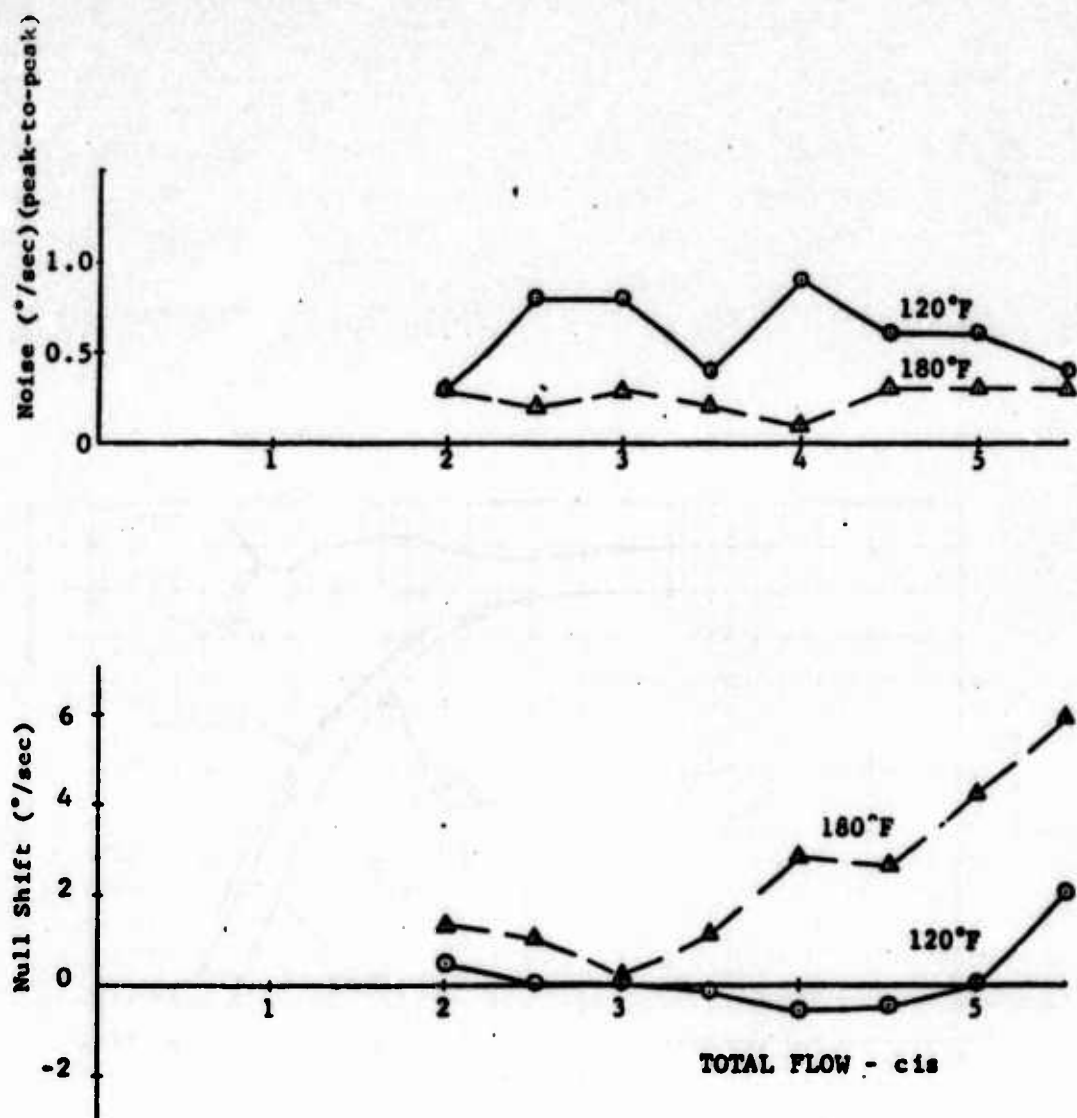


Figure 12 Rate Sensor Noise and Null Shift

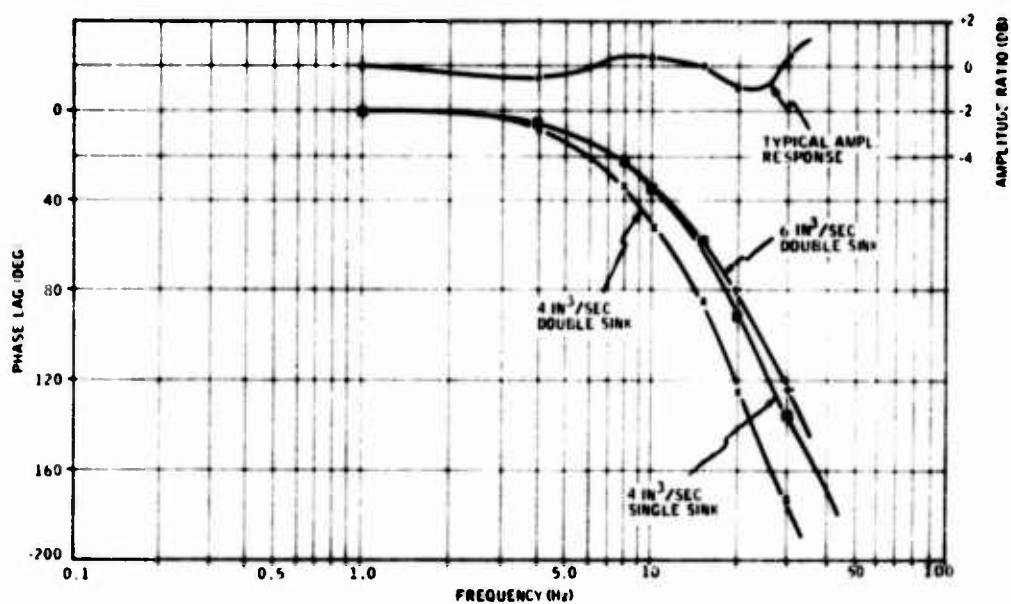


Figure 13 Rate Sensor Frequency Response Using Kistler Transducers

**THEORETICAL ANALYSIS
OF
TWO-DIMENSIONAL LAMINAR JET RATE SENSOR**

PAUL L. JACOBS

**GUIDANCE AND CONTROL DIRECTORATE
US ARMY MISSILE RESEARCH, DEVELOPMENT AND ENGINEERING LABORATORY
US ARMY MISSILE COMMAND
REDSTONE ARSENAL, ALABAMA 35809**

SYMBOLS

AR	Aspect ratio, nozzle height/nozzle width
B	Receiver spacing
d	Receiver width
h	Nozzle width
s	Virtual origin of Schlichting jet
t	Time
u	x direction velocity of similarity solution jet
v	y direction velocity of similarity solution jet
x	x direction variable
y	y direction variable
Δy	Jet deflection
Δx	Laminar resistor or nozzle length
C_1	Constant for calculating virtual origin distance
C_2	Constant in axisymmetric solution output
C_a	Speed of sound
K	Kinematic momentum
L	Sensor length
ΔP	Sensor differential pressure
P	Pressure
P_a	Ambient pressure
Q	Flow rate
Re_j	Reynolds number based on maximum nozzle exit velocity
T	Absolute temperature, °K
U_j	Centerline velocity of jet at nozzle exit
U_c	Centerline velocity of jet
γ	Specific heat ratio
ϵ	Similarity variable
μ, μ_0	Absolute viscosity, absolute viscosity at $T = 273^\circ K$

ν	Kinematic viscosity
ω	Angular rate, rad/sec
ω'	Normalized angular rate, $\omega h/U_j$
ρ	Density
τ	Jet transit time
τ_x	Jet transit time to station x

Subscripts

a	Atmospheric conditions
j	Nozzle exit centerline conditions
o	Orifice or standard or stagnation conditions
r	Laminar resistor
s	Supply
x	x direction variation

Superscripts

'	Normalized value
-	Average value

1. INTRODUCTION

Development of fluidic laminar rate sensors was begun approximately 5 years ago. The primary companies involved in this effort were General Electric, Hercules Powder, and Northrop. The aims of these development efforts were to obtain an angular rate sensor with very low noise, low power consumption, small size and weight, and low manufacturing cost. At that time these advantages had not been achieved in the vortex type sensors, which were still physically large, had low response, and consumed relatively large amounts of power. The threshold sensing level, although not of inertial quality, was projected to be adequate for the applications anticipated.

The primary problem with the laminar jet rate sensor is the low signal output. Early designs exhibited outputs an order of magnitude or more below that of a vortex rate sensor. More recent designs [1] exhibit much higher output than before, but still have to be amplified with three to five stages of proportional amplification to achieve useful signal levels.

The laminar jet rate sensor senses rotation by sensing the differential stagnation pressure across two receivers as the receivers rotate relative to the jet. The jet leaves the nozzle and continues on in inertial space (neglecting gravity and second-order effects) while the receivers have moved through an angle $\omega\tau$, where τ is the time taken by the jet to traverse the distance from the nozzles to the receiver. The output pressure differential is a linear function of the rate of rotation of the receivers. This is shown schematically in Figure 1.

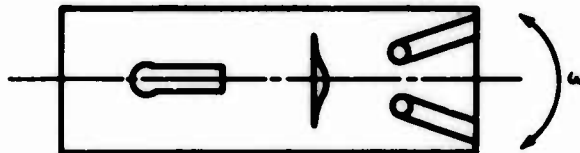


Figure 1. Output Pressure Differential
As a Direct Function of the Rate of
Rotation of the Receivers

This analysis is an attempt to predict the effects of physical design parameters on the output of a two-dimensional laminar jet rate sensor.

An analysis of this type was attempted by Reader et al. [2] at the beginning of the General Electric Company's rate sensor development work. He used Schlichting's [3] solution for a free jet with a match in flow rates and/or average flow velocity (Q/A) of the Schlichting jet and the nozzle flow at the nozzle exit. Using these criteria and a fully developed profile in the nozzle, he derived expressions for the momentum recovery downstream of the nozzle. The differential pressure or momentum recovered was calculated assuming the relative jet deflection under rotation of the receivers to be that of the centerline velocity vector under the Coriolis acceleration the fluid particles would experience in traversing the flow chamber from the nozzles to the receivers. The values used assumed parabolic profiles both in the nozzle and receiver and averaged their contributions. These results were compared to experimental results derived from model testing and are shown in Figure 2.

It is seen that the model overpredicts the experiments by about a factor of two. However, the slopes (gain) of the theoretical and experimental curves appear to be similar. The rate sensor tested was not optimized, and there was little discussion of the model limitations on experimental errors which would explain the discrepancy between theoretical and experimental results. The model did predict fairly accurately the measured jet centerline deflection, but not the output.

Recently, Griffin [4] performed analyses and experiments on an axisymmetric sensor also using Schlichting's axisymmetric free jet solution, but used the centerline velocity at the nozzle exit to match the similarity solution of the jet. The centerline velocity is again obtained by assuming fully developed laminar flow in the nozzle. His analysis neglects any jet distortion and the effects of the density gradient developed across the jet by the angular acceleration, and assumes that the jet deflection is determined by the deflection of a uniform stream whose velocity decays just like the centerline velocity of the Schlichting jet. Also, his analysis underpredicted optimum gain for pitot type receivers, which he attributed to jet spreading.

This analysis follows Griffin's axisymmetric analysis and redevelops it for a 2-D sensor. There are major differences in the actual flow phenomena, however, so that departures were necessary. The effect of aspect ratio (not a factor in a straight 2-D situation) has been shown to have a significant influence on sensor output in recent rate sensor tests [5]. These data were not available for comparison to previous analyses to determine the applicability of the 2-D assumption.

To date most of the experimental work on this sensor has utilized nitrogen as a working fluid. The effects of using different fluids (both liquid and gas) have not been fully determined. However, changes in temperature and ambient pressure have been found to affect performance adversely. Thus, an effective modeling of this phenomenon is needed.

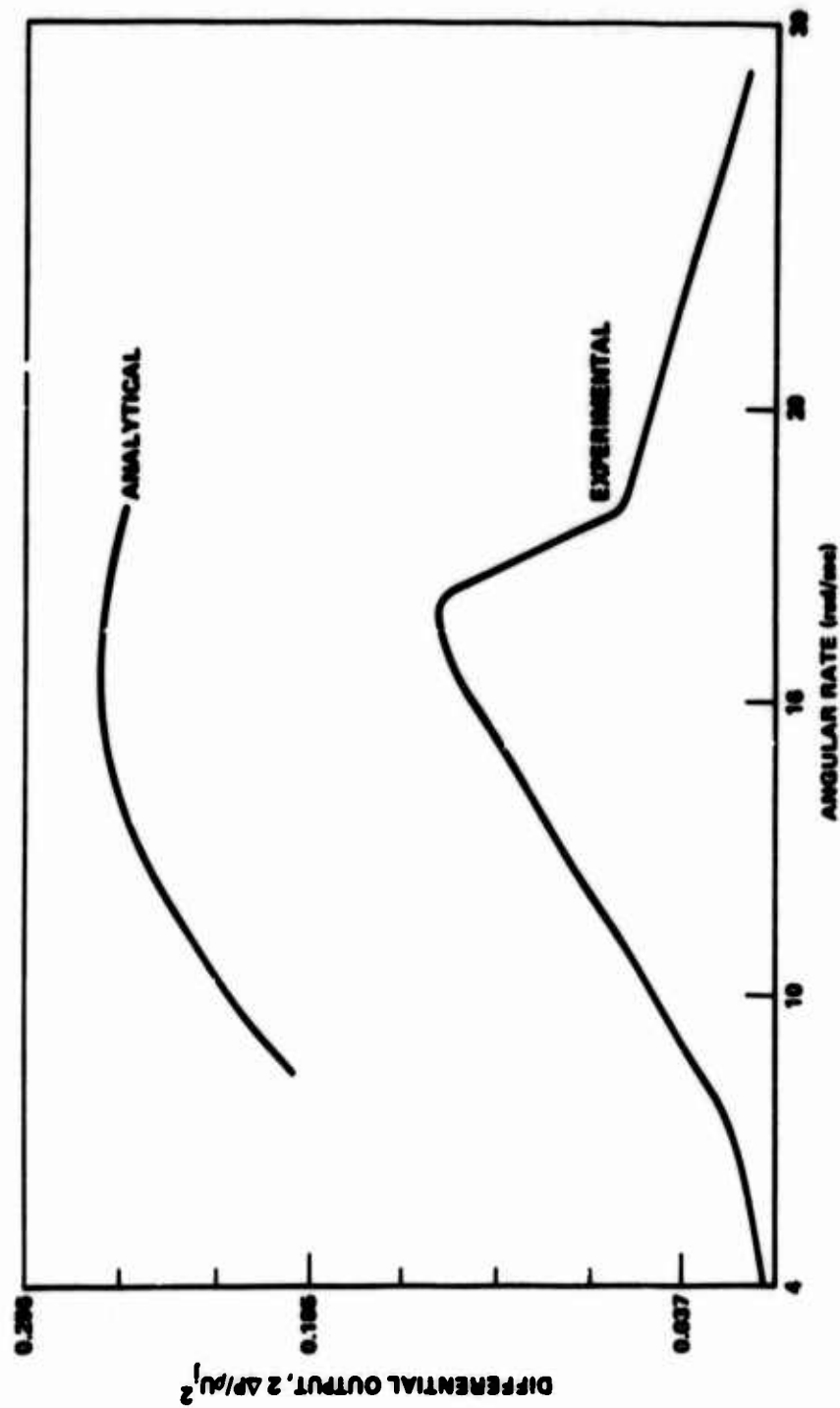


Figure 2. Comparison of Results [2] Analysis and Experiment

The General Electric Company, under contract to the US Army Missile Command, produced a roll rate control system which could be utilized in a high acceleration projectile. The basic sensor for this system was a planar laminar jet rate sensor. The analysis presented herein was an attempt to model the performance of this sensor with the air of optimizing the design and to determine analytically the effects of temperature, ambient pressure, working fluid, and geometry on sensor output.

To keep the model simple and to be able to use existing solutions to the Navier Stokes equations, the following assumptions were made:

- (1) Steady state operation -- no transients.
- (2) The effect of a hydrostatic density gradient due to rotation was neglected.
- (3) The geometry was modeled as two dimensional, and the wall and end effects were neglected.
- (4) The jet deflection at the receivers was considered to be that of the jet centerline (with no profile distortion) undergoing a Coriolis acceleration relative to the receiver over the length of the sensor.
- (5) Receiver size is small enough to have little effect on the jet profile.
- (6) The jet remains laminar throughout.

Examining these assumptions in turn, the restriction to steady state operation does not invalidate the predicted performance under some transient conditions. The performance predicted does not, however, give any criteria to determine when transient conditions will break down the jet. Some vibrational measurements have been made on limited geometries [6] and seem to indicate that, for aspect ratios >1 , limiting the nozzle Reynolds number to below 600 tended to prevent instability from occurring. Obviously, the closer the jet is to transition into turbulence, the smaller the transient input need be to cause instability.

The density of the ambient fluid will actually vary under rotation. A hydrostatic pressure gradient will set up a density gradient as the sensor rotates. Transient acceleration will also change densities. The effect of this gradient will be to spread and distort the jet. The analysis neglects this effect in order to use the solution for a submerged jet in a nonrotating media. Tests on an axisymmetric jet [4] show that the jet spreading does change predicted output.

The actual planar rate sensors presently developed are not two dimensional in their geometry. The effects of the boundary layer build-up along the top and bottom plates can have a significant effect on performance. In fact, lowering the aspect ratio of the nozzle (and sensor) has been shown to greatly increase performance for a fixed

nozzle Reynolds number and a particular geometry [1]. The results of the present analysis should be applicable to nozzles with aspect ratios greater than one.

Jet distortion will be a function of the actual sensor geometries, pressure and density gradient, effects of receiver size, vent location, secondary flows, entrainment flows, etc., and is hard to predict in a general manner. Actual jet profile measurement under dynamic conditions and analysis can be used to compare with the assumed profile used in the solution (Schlichting's). Better output predictions for the measured geometry could be obtained using curve-fitted profiles, but the essential sensor parameters and their influence on performance at other design conditions would probably not be shown. Some profile measurements are cited in [4], [7], [8], and [9] that are close to the one assumed in this analysis, so the prediction should give the right trends.

2. DISCUSSION

The geometry for this analysis is shown in Figure 3. The dimension s is the distance of the virtual origin of the Schlichting jet from the nozzle exit. The two-dimensional solution of the laminar jet spreading into a quiescent fluid assumes that fluid is entrained, and the jet spreads at such a rate to keep the momentum flux constant with distance downstream of the virtual origin. The acceleration and frictional terms in the momentum boundary layer equations are of the same order. For steady flow, the solutions to these equations yield the following relations for the components of velocity in the horizontal and vertical directions (in terms of the above-defined coordinate system).

$$u = 0.4543 \left[\frac{K^2}{v(x+s)} \right]^{1/3} \text{sech}^2 \xi \quad (1)$$

$$v = 0.5503 \left[\frac{Kv}{(x+s)^2} \right]^{1/3} (2\xi \text{sech}^2 \xi - \tanh \xi) \quad (2)$$

where

$$\xi \equiv \text{similarity variable} = 0.2752 \left(\frac{K}{v^2} \right)^{1/3} \frac{y}{(x+s)^{2/3}} \quad (3)$$

and

$$K \equiv \frac{J}{\rho} = \text{kinematic momentum} = \int_{-\infty}^{\infty} u^2 dy = \text{constant} \quad (4)$$



Figure 3. Geometry of Analysis

If the nozzle flow is assumed to be fully developed laminar flow (Poiseuille flow), a parabolic profile results. Using Equation (4) and the parabolic profile

$$u(y) = U_j \left[1 - \frac{y^2}{\left(\frac{h}{2}\right)^2} \right] \quad (5)$$

the value of the kinematic momentum K becomes

$$K = \frac{8}{15} h U_j^2 \quad (6)$$

where U_j is the maximum (centerline) velocity at the nozzle exit.

Under these conditions, Equation (1) becomes

$$u = 0.4543 \left[\frac{\frac{8}{15} h U_j^2}{\sqrt{\nu(x+s)}} \right]^{2/3} \text{sech}^2 \xi \quad (7)$$

and the similarity variable is

$$\xi = 0.2752 \left(\frac{\frac{8}{15} h U_j^2}{\nu^2} \right)^{1/3} \frac{y}{(x+s)^{2/3}} \quad (8)$$

For a uniform profile $u(y) = U_j = \text{constant}$, the value of K is $h U_j^2$, with appropriate modifications to u and ξ .

Selection of the proper criteria for matching the similarity solution profile to the nozzle exit flow conditions presents a problem, since the actual nozzle profiles will not coincide with the jet spreading solution. Markland and Beatty [7] have studied matching criteria for axisymmetric jets and tabulated values for pertinent parameters for three types. They tabulated values for flow rate match, kinetic energy match, and zero radial velocity match at the wall for both uniform and parabolic profiles.

A fourth matching criterion, that of centerline velocity, was used in Griffin's analysis and was discussed by Bell [9]. This criterion and flow rate matching were chosen for this analysis to attempt to match experimental performance.

Matching the centerline velocity of the nozzle exit profile and the Schlichting similarity profile at $\frac{y}{x} = 0$ ($\xi = 0$) yields an expression for the virtual origin length in terms of the fluid properties, velocity, and nozzle width. Defining a Reynolds number based on nozzle width and centerline velocity at the nozzle exit

$$Re_j = \frac{U_j h}{\nu} \quad (9)$$

and substituting $u = U_j$ into Equation (7)

$$U_j = (0.4543) \left(\frac{8}{15} \right)^{2/3} \left[\frac{h U_j^2}{(\nu s)^{1/2}} \right]^{2/3}$$

yields

$$\frac{s}{h} = 0.02667 Re_j \quad (10)$$

If the flow rate, $Q = \int_{-\infty}^{\infty} \rho u(y) dy$, were matched at the nozzle exit, using Equations (5) and (7), the resulting expression for the virtual origin is

$$\frac{s}{h} = 0.01543 Re_j \quad (11)$$

where the flow is based on a unit depth of nozzle. Thus, the virtual origin is proportional to the nozzle width and Reynolds number

$$s = C_1 h Re_j$$

where C_1 is the proportionality constant. For a uniform profile, $C_1 = 0.0278$ for flow rate match and 0.0938 for centerline velocity match at the nozzle exit.

The centerline velocity decay is assumed to be of the form

$$U_c = \frac{U_1}{\left(1 + \frac{x}{s}\right)^{1/3}} \quad (12)$$

which satisfies the requirements of the similarity solution. A comparison plot of profile matches for centerline velocity and flow rate is shown in Figure 4.

Jet deflection at point L is found by integrating the slope of the jet centerline from nozzle exit to L, assuming the deflection of the jet is the same as that of a "uniform" jet with the local centerline velocity of the similarity stream; that is,

$$y = \int_0^L \left(\frac{dy}{dx}\right) dx \quad (13)$$

The question arises as to what this slope is for the above-assumed conditions. Griffin uses the argument that the slope relative to a reference centerline velocity rotating with the sensor body at angular frequency ω is made up of two parts, one due to the physical rotation or relative displacement of the sensor physical centerline during time τ_x and the other due to the relative velocity of a point x on the sensor centerline with respect to the point on inertial space with which it coincides at that time. Consequently, the slope of the jet centerline is due to a rotation $\omega\tau_x$ of the sensor and an angle $\omega x/U_c$ due to the velocity of the point x on the sensor with respect to inertial space*

$$\frac{dy}{dx} = \omega\tau_x + \frac{\omega x}{U_c} \quad (14)$$

*The same results are obtained if one allows the sensor to rotate with frequency ω and the jet to propagate fixed in space, writes the equations in inertial space, and computes the relative deflection of the receivers, dy/dx . The slope in Equation (14) is found if the approximations $\sin \omega\tau \approx \omega\tau$, $\cos \omega\tau \approx 1$, and $U_c \gg \omega g$ are made. These approximations are valid for the small angular deflections considered here.

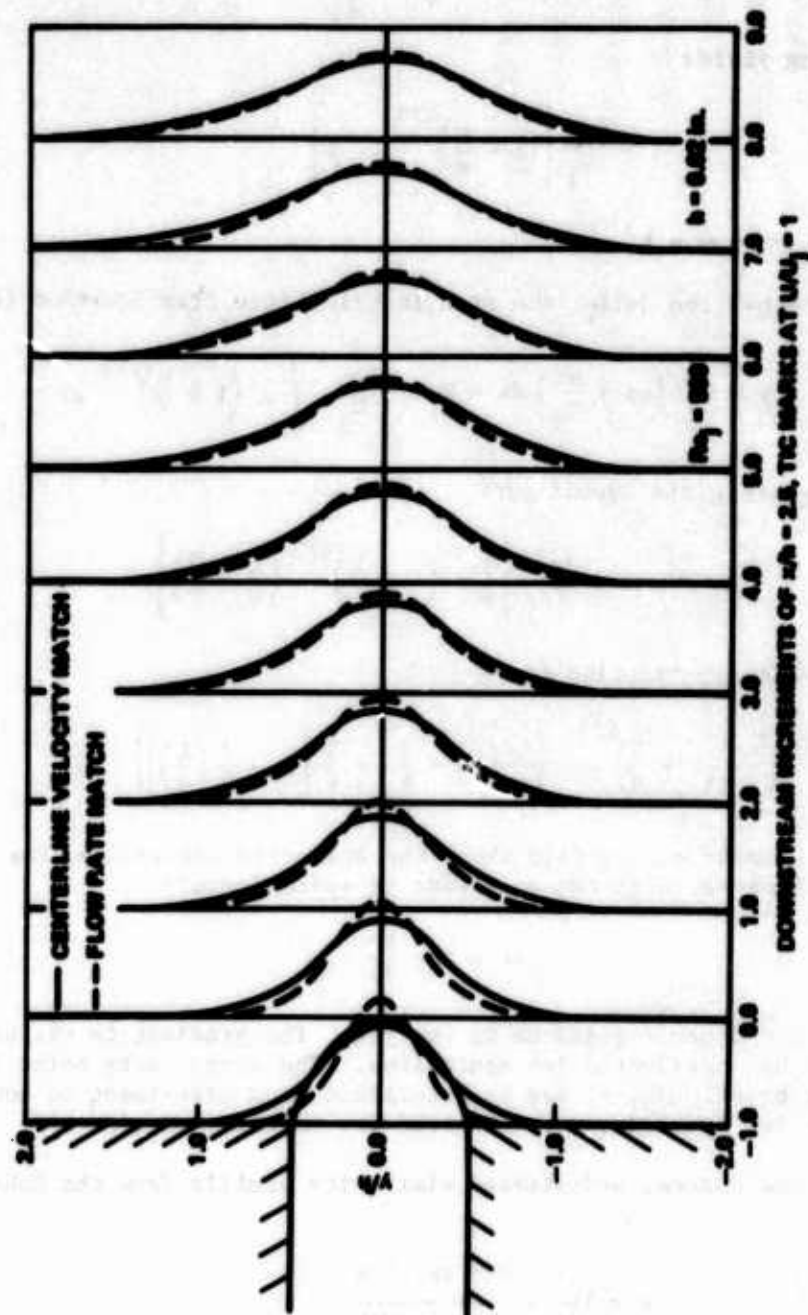


Figure 4. Schlichting Similarity Profiles for Nozzle Exit Match

Using these criteria, the jet transit time is found by integrating over time

$$\tau_x = \int_0^t dt = \int_0^x \frac{dx}{U_Q(x)} = \int_0^x \frac{\left(1 + \frac{x}{s}\right)^{1/3}}{U_j} dx \quad (15)$$

Integrating yields

$$\tau = \frac{3s}{4U_j} \left[\left(1 + \frac{L}{s}\right)^{4/3} - 1 \right] \quad (16)$$

where $\tau_x = \tau$ at $x = L$.

The centerline deflection at L is calculated from Equation (13)

$$\Delta y = \int_0^L \left(\omega \tau + \frac{\omega x}{U_Q} \right) dx = \omega \tau L + \frac{\omega}{U_j} \int_0^L x \left(1 + \frac{x}{s}\right)^{1/3} dx$$

Integrating the second part

$$\Delta y = \omega \tau L + \frac{3s^2\omega}{7U_j} \left[\frac{3}{4} + \left(1 + \frac{L}{s}\right)^{4/3} \left(\frac{L}{s} - \frac{3}{4}\right) \right]$$

Combining and substituting for τ

$$\Delta y = \frac{3s^2\omega}{7U_j} \left\{ \left(1 + \frac{L}{s}\right)^{4/3} \left[\frac{11}{4} \left(\frac{L}{s}\right) - \frac{3}{4} \right] + \frac{3}{4} \left[1 - \frac{7}{3} \left(\frac{L}{s}\right) \right] \right\} \quad (17)$$

For a symmetrical profile about the deflected centerline, the differential pressure in the receivers is approximately

$$\Delta P \approx 2\Delta y \frac{\partial P}{\partial y} \quad (18)$$

where P is the dynamic pressure in the jet. The gradient is evaluated at Δy from the undeflected jet centerline. The appropriate point (center of receiver or off center) may be determined from experiment to compensate for jet spreading not accounted for in the analysis.

Using the assumed undistorted similarity profile from the Schlichting solution

$$P = \frac{\rho U^2}{2} = \frac{\rho U_j^2 \operatorname{sech}^4 \xi}{\left(1 + \frac{L}{s}\right)^{2/3}} \quad (19)$$

Assuming the receiver in line with the velocity vector U , then

$$\frac{\partial P}{\partial y} = \frac{\partial P}{\partial \xi} \frac{\partial \xi}{\partial y} = \frac{\rho U_1^2}{2 \left(1 + \frac{L}{s}\right)^{2/3}} \left[4 \operatorname{sech}^3 \xi (-\operatorname{sech} \xi \tanh \xi) \frac{d\xi}{dy} \right] \quad (20)$$

From Equation (8)

$$\xi = 0.2752 \left(\frac{8}{15} \frac{h U_1^2}{v^2} \right)^{1/3} \frac{y}{(L+s)^{2/3}} = 0.2232 y \left[\frac{Re_1}{\sqrt{h} (L + C_1 h Re_1)} \right]^{2/3} \quad (21)$$

Substituting the virtual origin for the Re_j yields

$$\xi = 0.2232 \frac{y}{h} \left[\frac{1}{\left(\frac{L}{s} + 1\right) C_1} \right]^{2/3} \quad (22)$$

Differentiating this expression with respect to y and substituting into Equation (20) gives

$$\frac{\partial P}{\partial y} = \frac{0.4464 \rho U_1^2 \operatorname{sech}^4 \xi \tanh \xi}{C_1^{2/3} \left(1 + \frac{L}{s}\right)^{4/3} h} \quad (23)$$

Using Equations (17), (18), and (23) yields

$$\Delta P = 4.289 C_1^2 \omega \mu \operatorname{sech}^4 \xi \tanh \xi Re_j^3 B \quad (24)$$

where

$$B = \frac{11}{4} \left(\frac{L}{h} \right) \frac{1}{C_1 Re_j} - \frac{3}{4} + \frac{3}{4} \frac{\left[1 - \frac{7}{3} \left(\frac{L}{h} \right) \frac{1}{C_1 Re_j} \right]}{\left[1 + \left(\frac{L}{h} \right) \frac{1}{C_1 Re_j} \right]^{4/3}} \quad (25a)$$

or

$$B = \frac{11}{4} \frac{L}{s} - \frac{3}{4} + \frac{3}{4} \frac{\left[1 - \frac{7}{3} \left(\frac{L}{s} \right) \right]}{\left(1 + \frac{L}{s} \right)^{4/3}} \quad (25b)$$

in terms of the parameter L/s .

Normalizing this expression with the nozzle maximum jet momentum

$$\begin{aligned}\frac{\Delta P / \rho U_1^2}{2} &= 8.578 C_1^2 \frac{\omega h^2}{\nu} Re_j \operatorname{sech}^4 \xi \tanh (\xi) B \\ &= 8.578 C_1^2 \omega' Re_j^2 \operatorname{sech}^4 \xi \tanh (\xi) B\end{aligned}\quad (26)$$

where $\omega' \equiv \omega h / U_j$ gives the approximate normalized output of a two-dimensional laminar jet rate sensor rotating at frequency ω . This expression shows the influence of the geometric variables (nozzle width, receiver distance downstream, or receiver spacing), the dynamic variables (nozzle centerline velocity or jet momentum), and the fluid properties (density or viscosity).

The temperature dependence of this expression can be determined using ideal gas relations for $\rho(T)$ and empirical expressions for $\mu(T)$.

Equation (26) may be maximized with respect to y to determine an optimum receiver position. Differentiating it with respect to a non-dimensional distance y/h will yield the value of the similarity variable ξ (hence y) for maximum output at $x = L$ for an undistorted profile.

$$\frac{\partial(\Delta P) / \frac{\rho U_1^2}{2}}{\partial\left(\frac{y}{h}\right)} = 0 = \operatorname{sech}^6 \xi - 4 \operatorname{sech}^4 \xi \tanh \xi$$

which yields $\xi = 0.4812$ for maximum output. Receiver position for maximum output is then

$$\begin{aligned}\left(\frac{y}{h}\right)_{\text{receiver for maximum output}} &= 0.1918 \left(\frac{L}{s} + 1\right)^{2/3} \\ &= 0.1918 \left(\frac{L}{C_1 Re_j h} + 1\right)^{2/3}\end{aligned}\quad (27)$$

The maximum output for the sensor can now be determined as a function of Reynolds number, angular rate, fluid viscosity, and the parameter L/h . This expression is

$$\Delta P_{\max} = 1.2276 C_1^2 \omega \mu Re_j^3 \left\{ \frac{11}{4} \frac{L}{C_1 Re_j h} - \frac{3}{4} + \frac{3}{4} \left[\frac{1 - \left(\frac{7}{3}\right) \frac{L}{C_1} Re_j h}{\left(1 + \frac{L}{C_1 Re_j h}\right)^{4/3}} \right] \right\} \quad (28)$$

where $C_1 Re_j h$ indicates the virtual origin length s .

A plot of $y/h)_{\max}$ versus L/h for various values of sensor nozzle Reynolds number is shown in Figure 5. This figure indicates that a larger receiver spacing is necessary for operation at lower Reynolds numbers. This is consistent with the fact that the jet will spread more when it has a lower momentum, thus necessitating pickoffs at larger spacings for the same output. The effects of receiver loading will also be stronger at lower Re_j .

The expressions developed above, although algebraic, are somewhat cumbersome to examine and quickly determine qualitative effects. Some simplification is possible in the case of long sensors ($L/s \gg 1$).

If one is interested in quickly examining the effects of fluid properties, temperature, and geometry, on output, the above equations can be written as follows. The similarity variable, ξ , can be approximated by

$$\xi_{(L/s \gg 1)} = 2.500 \frac{y}{h} \left(\frac{L}{s} \right)^{-2/3} \quad (29)$$

and the optimum receiver spacing by

$$\frac{y}{h} = 0.1918 \left(\frac{L}{s} \right)^{2/3} \quad (30)$$

Using Equation (16), the jet transit time is

$$\tau_{(L/s \gg 1)} = \frac{3}{4} \frac{s}{U_j} \left(\frac{L}{s} \right)^{4/3} = \frac{3}{4 U_j} \left(\frac{L^4}{C_1 Re_j h} \right)^{1/3} \quad (31)$$

and the optimum sensor length is

$$\frac{L}{(L/s \gg 1)} = \left[\frac{4}{3} \tau U_j (C_1 Re_j h)^{1/3} \right]^{3/4} = \frac{1.241 C_1^{1/4} Re_j}{\sqrt{h}} \left(\frac{\tau \mu C_a^2}{P_a \gamma} \right)^{3/4} \quad (32)$$

where C_a is the sonic velocity at temperatures T , P_a is the ambient pressure, and γ is the specific heat ratio.

Thus, for a desired response time, the required sensor length can be determined in terms of the nozzle size and Reynolds number and the fluid properties. A similar set of equations developed in [4] for the axisymmetric sensor does not reflect an explicit dependence of the sensor length on nozzle diameter as these two-dimensional results indicate.

The optimum receiver location may be written in terms of the fluid properties using Equation (32).

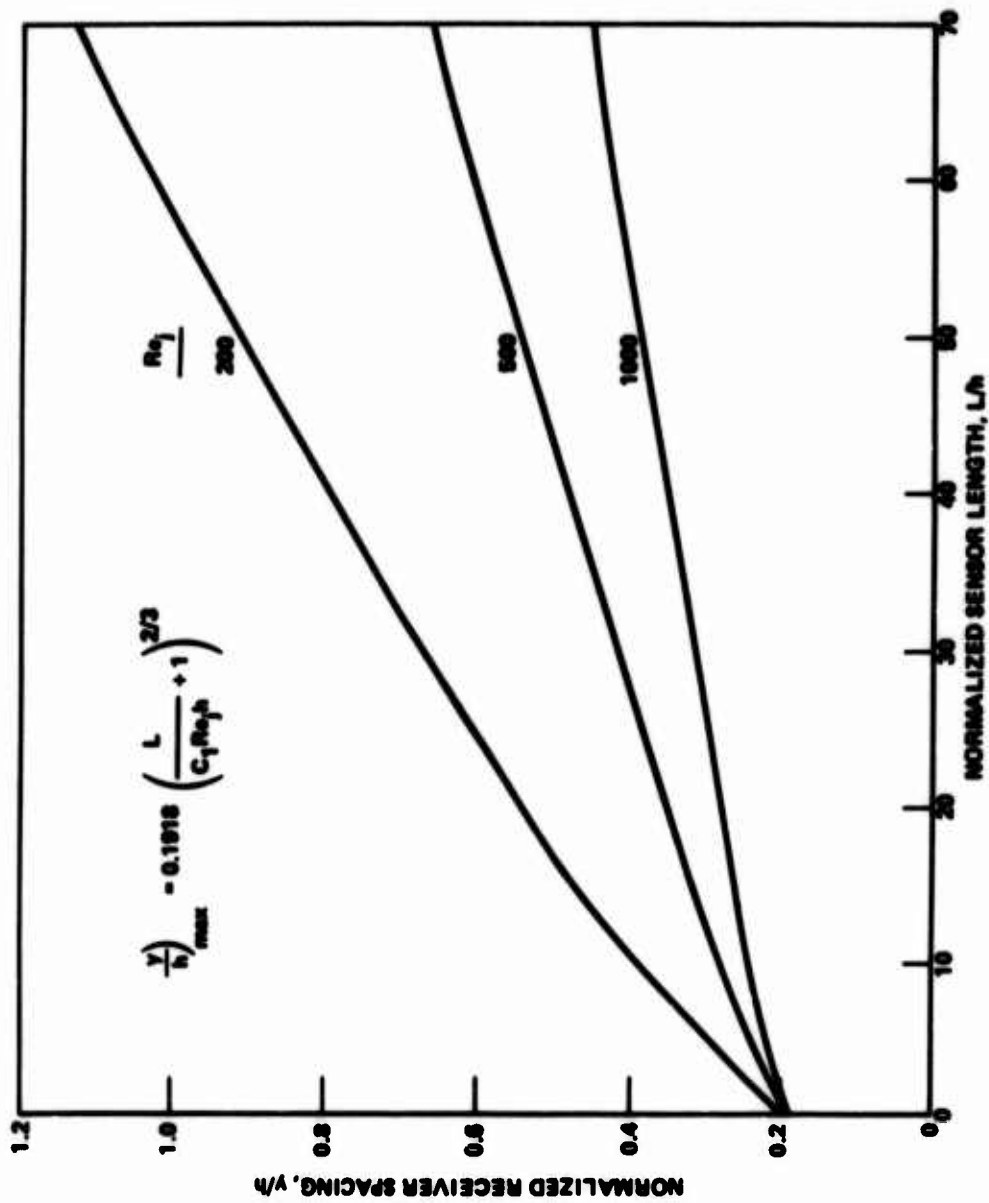


Figure 5. Receiver Spacing for Maximum Output

$$y_{\text{max output}} = \frac{0.2215}{\sqrt{C_1}} C_a \left(\frac{U}{P_a y} \right)^{1/2} \quad (33)$$

(L/s >> 1)

where the coefficient has the value 1.356 for the centerline velocity match. These results should be valid, as the jet similarity solution assumes that the profile described is far downstream from the virtual origin.

Little simplification is possible for the sensor output. The parameter B in Equation (25) becomes

$$B = \frac{1}{4} \left[\frac{11 L}{C_1 Re_j h} - \frac{7}{\left(\frac{L}{C_1 Re_j h} \right)^{1/3}} \right]$$

while the other parameters in Equation (28) remain the same. Hence, the influence of Reynolds number on output is not immediately apparent. Maximum output is still a function of Re_j , h , L , and ω . It is seen, however, that decreasing the nozzle size and increasing the sensor length for fixed Reynolds number increases output, but that there will exist an optimum Reynolds number for maximum output with a fixed geometry. These results are counter to those derived for axisymmetric long sensors in [4], which show increasing output with Reynolds number. The finite sensor axisymmetric relations do, however, exhibit an optimum Reynolds number for fixed geometry.

Examining the "long chamber" expressions, it is seen that for a fixed transit time the receiver location for maximum output is a function only of the fluid properties, a result that also applies in the axisymmetric case. The transit time depends upon the parameters L , Re , h , and U_j as shown in Equation (31). One can design an optimum spacing for a desired sensor response and then determine the operating conditions and L/h to achieve this response, subject, of course, to the restrictions of the model.

Griffin's analysis of an axisymmetric sensor followed similar reasoning and resulted in simpler expressions for output. He found that for an axisymmetric sensor

$$\frac{\Delta P / \rho U_1^2}{2} = \frac{C_2 \omega \left(\frac{D_j}{U_j} \right) \left(\frac{L}{D_j} \right)^2 \left(1 + \frac{L}{s} \right)}{\left(1 + \frac{L}{s} \right)^3}$$

where C_2 depends upon the choice of the value of the similarity variable ξ , D_j is nozzle diameter, and s is the virtual origin length, the value of which Griffin quotes as $3/80 Re_j D_j$. A value of $1/32 Re_j D_j$ is found if one matches the maximum velocity at the exit to a parabolic profile developed in a circular tube.

A comparison of the two-dimensional results and the corrected axisymmetric values is shown in Figure 6 for a fixed nozzle exit Reynolds number of 500. For one value of L/h (L/D_j in axisymmetric case), the effect of varying the receiver spacing is shown for both cases. Due to the difference in the profiles, the axisymmetric gives higher output at greater spacing than the two-dimensional sensor, but lower output as the spacing narrows. There are optimum receiver spacings for given values of the Reynolds number and L/h , which are exemplified by Figure 5. These optimum values are of course different for each type of sensor. Both analyses do show a linear dependence of output on angular rate.

3. RESULTS

a. Analysis Results

Figures 7 through 9 show normalized output performance predictions versus Reynolds number for various values of the geometric parameters y/h and L/h and the angular rate parameter ω' . These curves are plots of Equation (26) with the constant C_1 being equal to 0.02667, where the centerline velocity of the parabolic profile is matched at the nozzle exit to the centerline velocity of the Schlichting jet. The most striking feature of these predictions is the existence of an optimum Reynolds number to maximize output for a given geometric design. This optimum is not dependent upon ω' , but is a strong function of both y/h and L/h .

For the results presented, the optimum Reynolds number is seen to vary from 100 in Figure 7 to over 1000 in Figure 9.

Figures 10 through 12 show directly the sensor output versus the jet centerline deflection. Location of the receivers at the position of the curve maximum should yield the greatest output. The figures indicate that for the specific geometry depicted, physically achieving the maximum output would be difficult, as the positions are very close to the centerline and the receivers would have to be very small. This would create manufacturing difficulties and would limit the amount of power (flow) transmitted through the output. Designing for the optimum region would make repeatability extremely difficult. Present designs have receiver spacings ~ 0.015 to 0.060 inch, where the output is much reduced, but are fairly insensitive to manufacturing tolerances.

Figure 13 and 14 exhibit actual output differential values versus Reynolds number for the centerline velocity match case. The basic difference between these figures is the parameter y/h . Decreasing this value from 1.5 to 1.0 moves the optimum Reynolds number of operation significantly. The design in Figure 14 is substantially better than that of Figure 13, as the output at a given angular rate is higher and the sensitivity to changes in supply pressure (which changes the nozzle exit Reynolds number) is greatly reduced at the optimum Reynolds number.

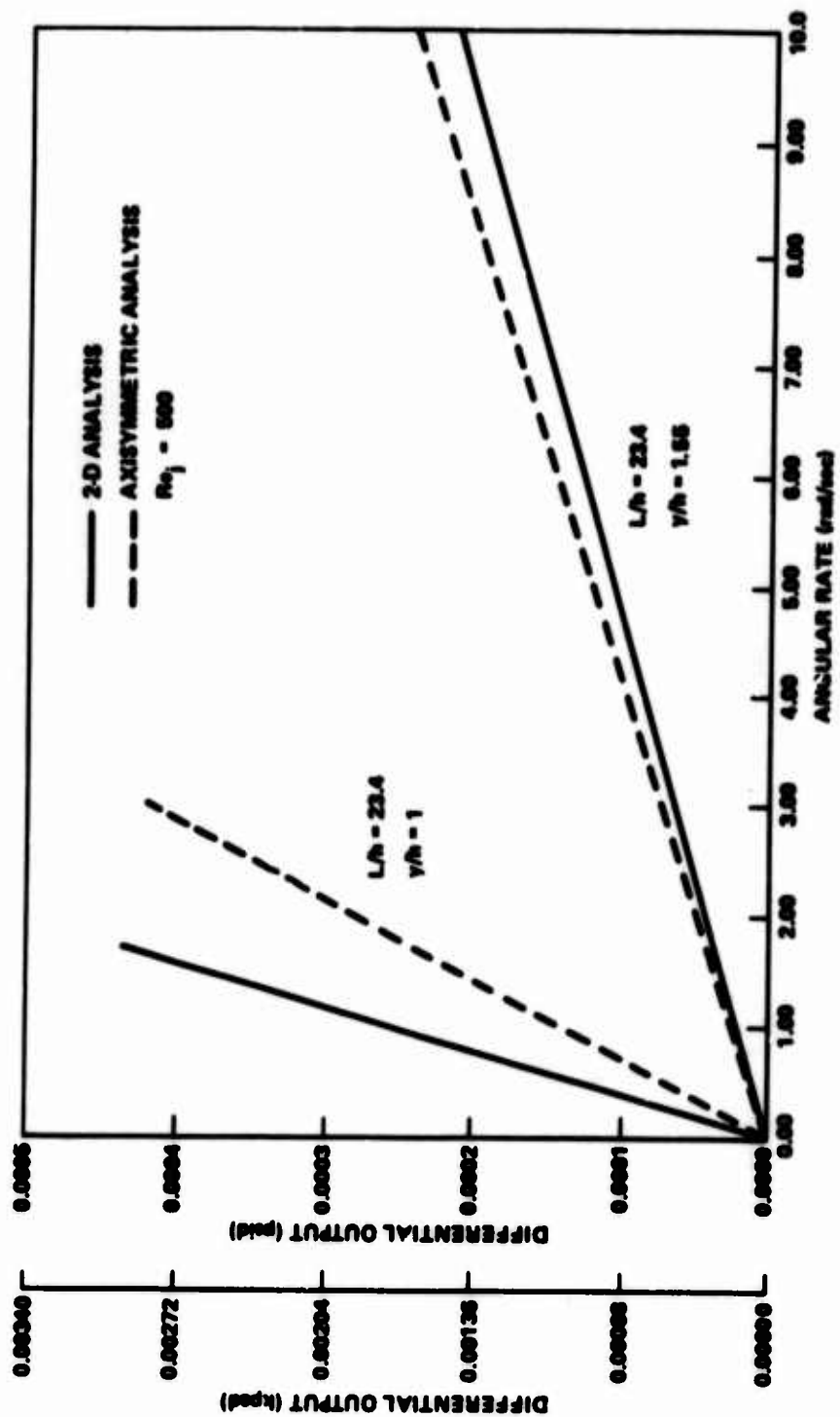


Figure 6. 2-D Versus 3-D Analytical Results

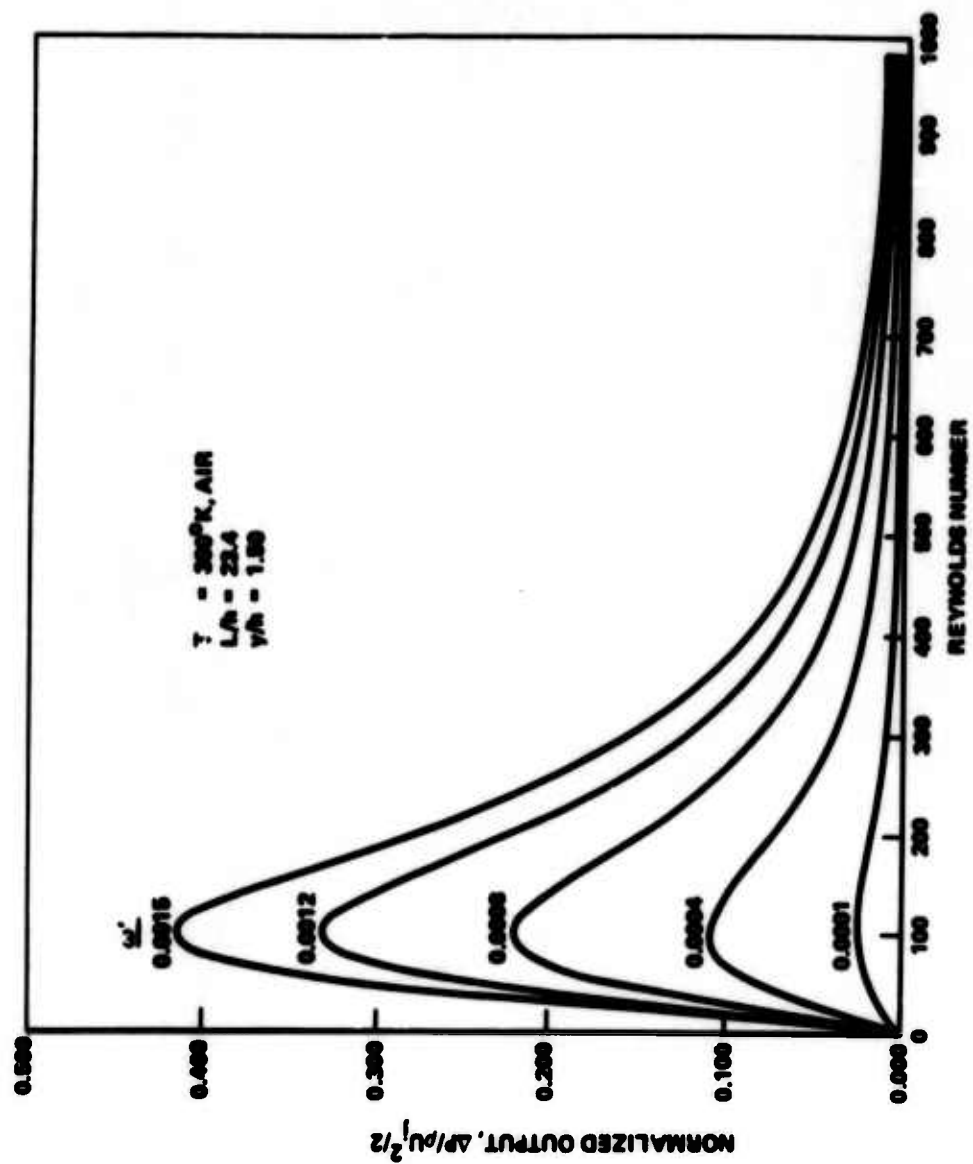


Figure 7. Laminar Rate Sensor Normalized Output

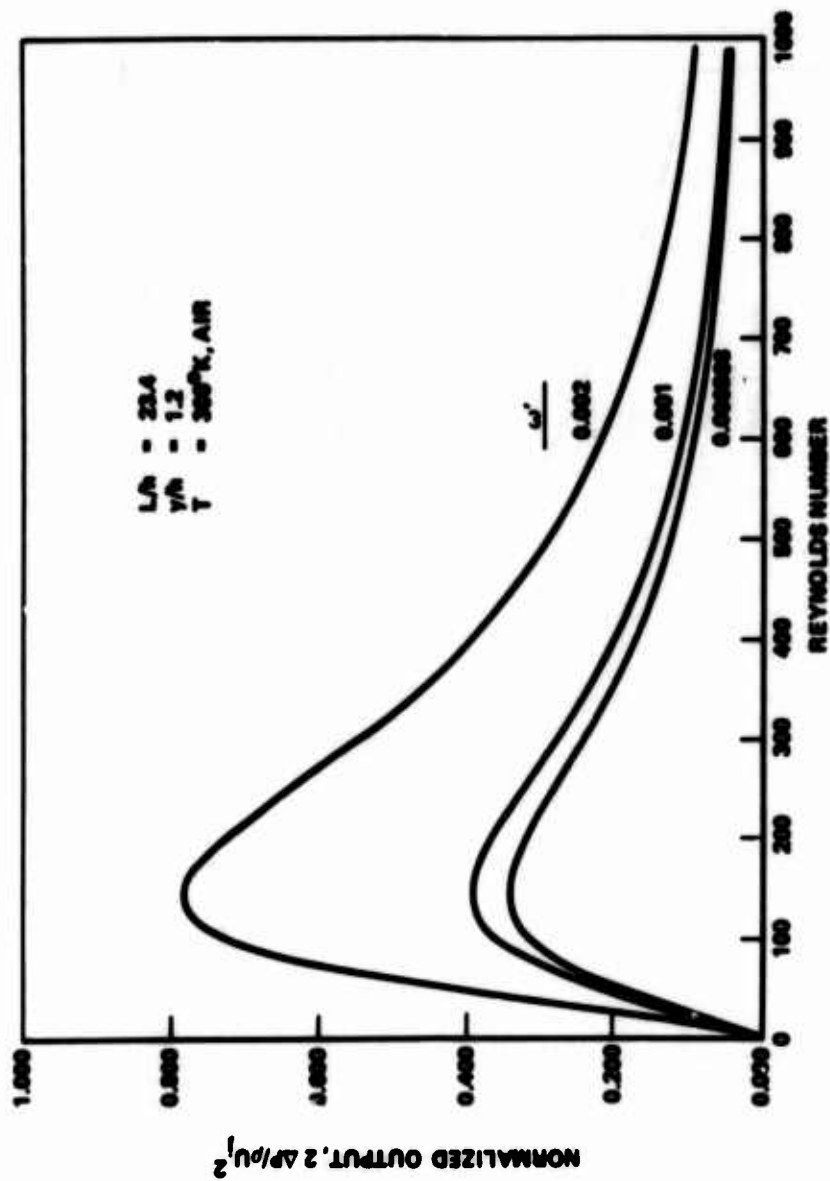


Figure 8. Laminar Rate Sensor: Normalized Output

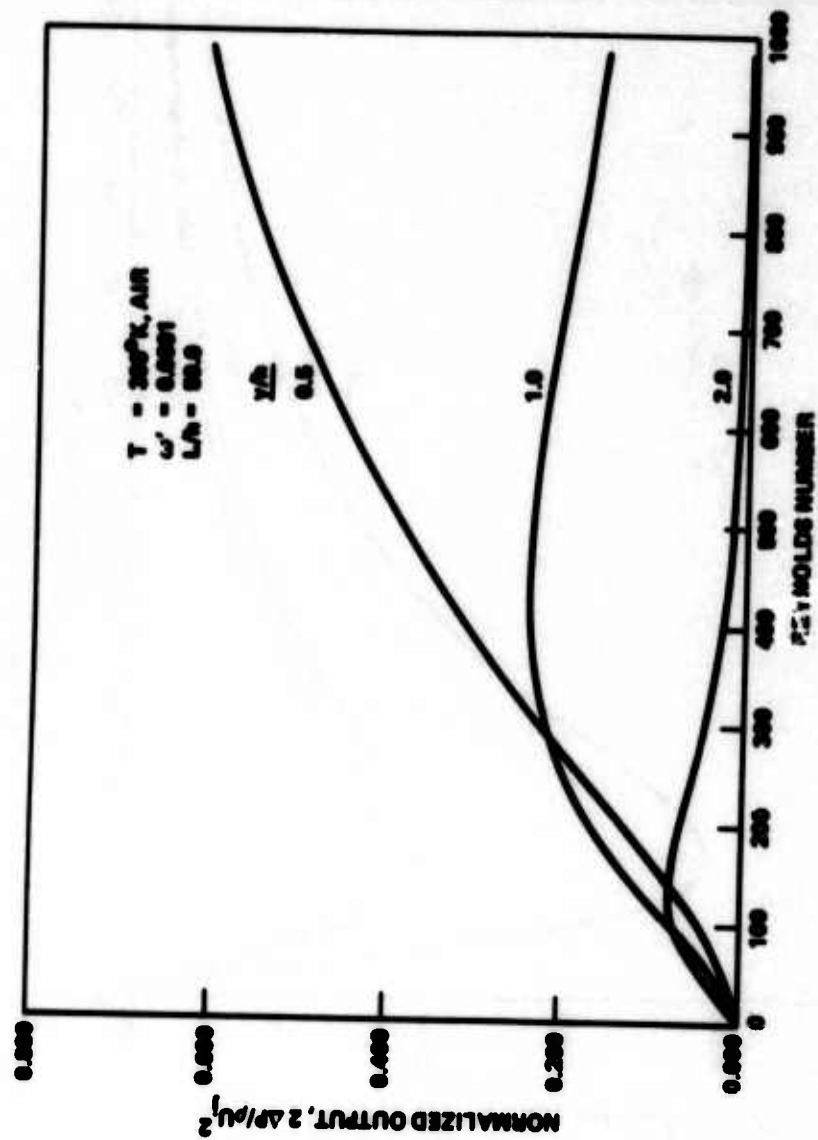


Figure 9. Laminar Rate Sensor Normalized Output

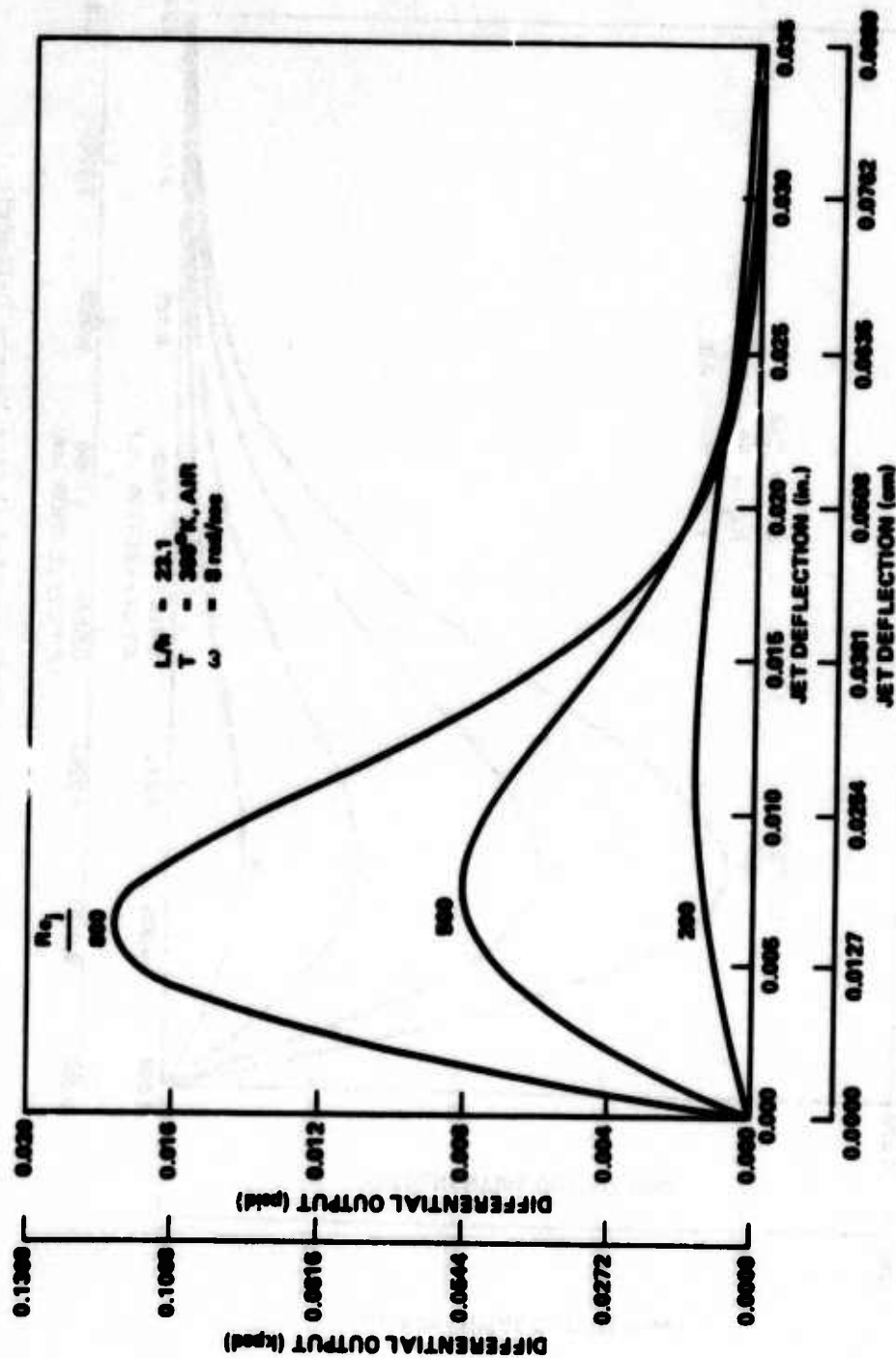


Figure 10. ΔP Versus y (Sensor Differential Output Versus Deflection)

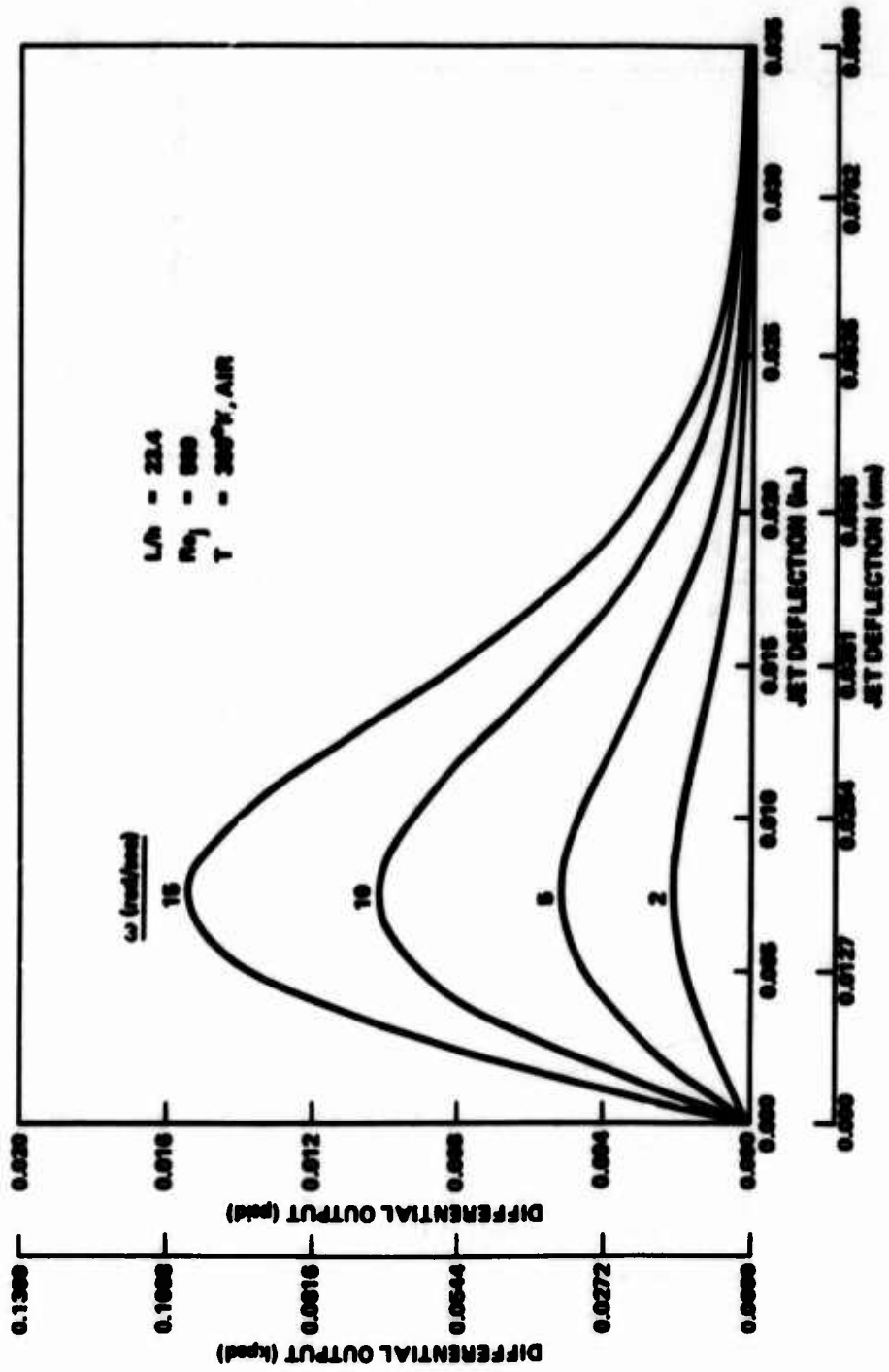


Figure 11. ΔP Versus y (Sensor Differential Output Versus Deflection)

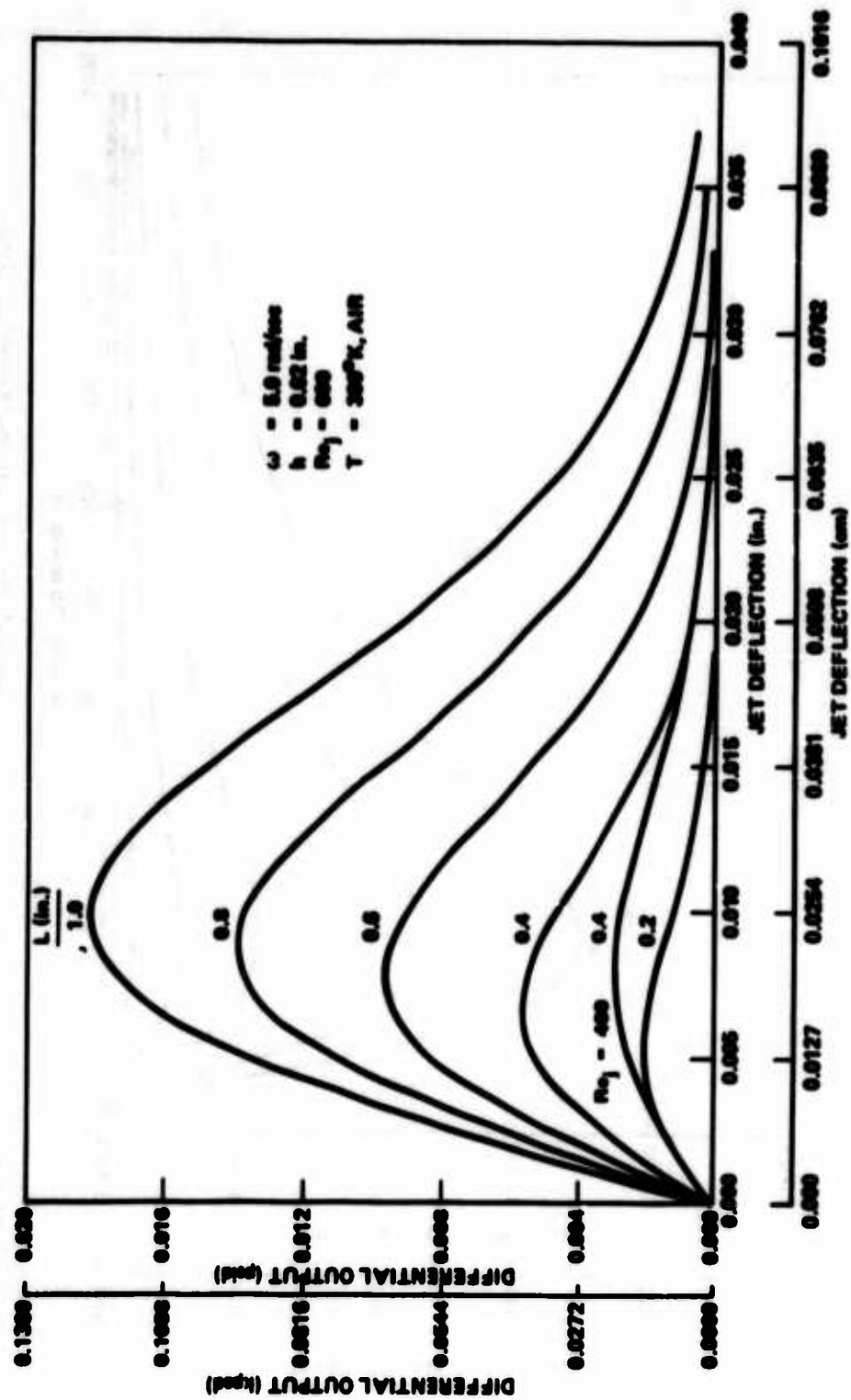


Figure 12. ΔP Versus y (Sensor Differential Output Versus Deflection)

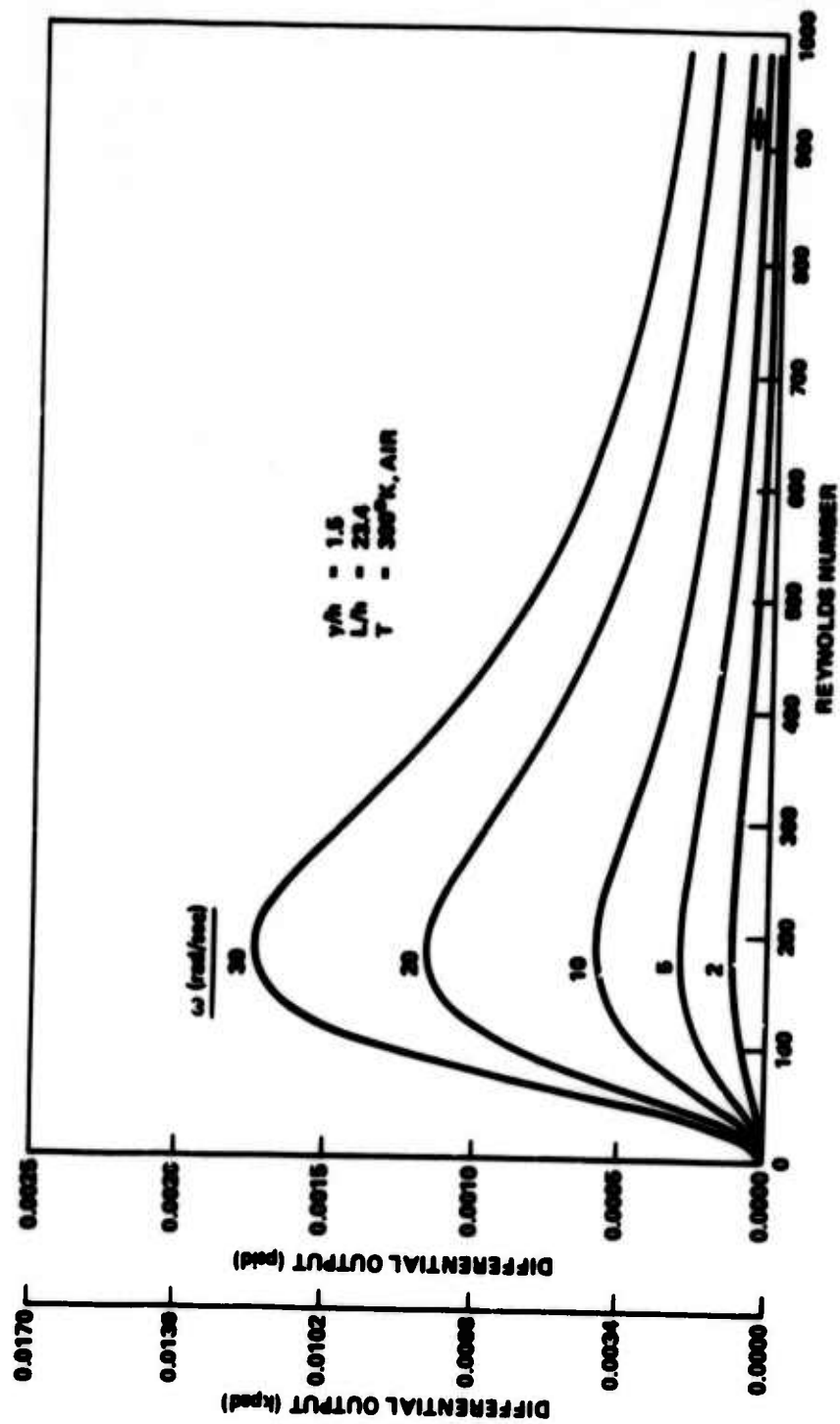


Figure 13. ΔP Versus Re_j (Sensor Differential Output Versus Reynolds Number)

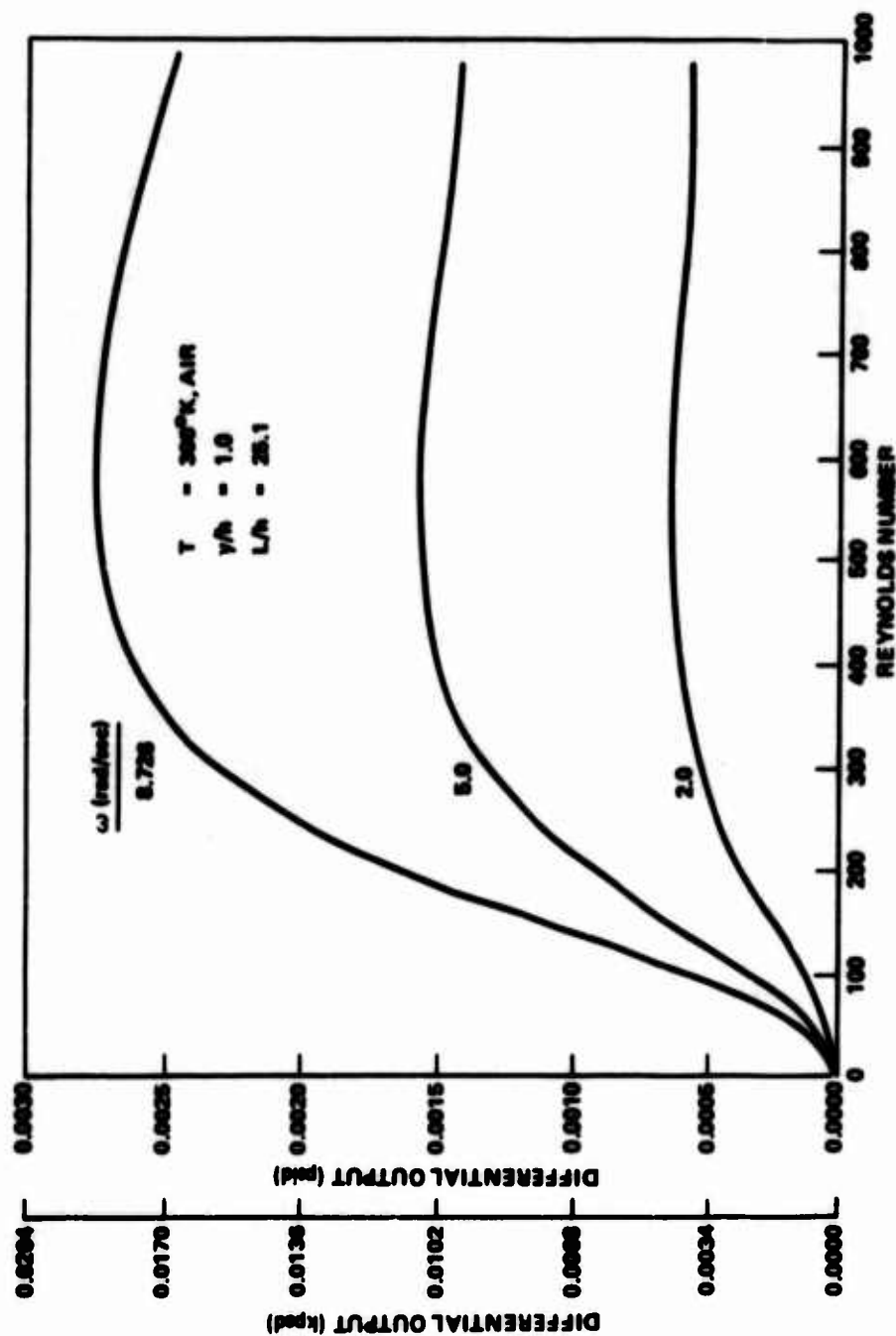


Figure 14. ω Versus Re_j (Sensor Differential Output Versus Reynolds Number)

Figures 15 and 16 exhibit the linear dependence of differential output on angular rate. A mixture of L/h and y/h ratios is shown to illustrate some typical tradeoffs. These data are for air at 300°K. For the geometry in Figure 15 the output increases with Reynolds number, while in Figure 16 the maximum output becomes reduced above a Reynolds number of 500.

b. Comparison to Experiment

Experimental data taken to date on the actual profiles of a rotating sensor have been restricted to only a few geometries. Griffin and Coultas [4] measured some profiles in the long ($L = 1.38$ inches) axisymmetric sensor, which agreed fairly well with Schlichting's solution with the exception that the centerline velocity was approximately 20% lower than predicted. The measured sensor output agreed with their axisymmetric prediction, but this was attributed to compensating errors, an increase in output due to jet spreading and a decrease due to the inefficient pickoff (flat plate receiver). The rederived results of the axisymmetric analysis do give higher output predictions than those cited in Griffin's paper. The actual profile shapes under rotation were not measured directly so direct comparison was not possible.

Profile measurements of nonrotating axisymmetric laminar jets have also been reported in [8] and [9], which conform to Schlichting's solution.

Data on planar sensors have been taken on long nozzle unit aspect ratio designs (3), and more recently on plug nozzle low aspect ratio (0.4, 0.6) designs (9). Significant gain variations are exhibited in these designs. The low aspect ratio designs can be operated at higher Reynolds numbers without breaking into turbulence than can the long nozzle designs, and thereby have higher gains.

All designs had side vents and the long nozzle designs also had center vents. The effects of vent receiver interactions and secondary flow phenomena are ignored in attempting to match data. However, they could cause significant profile distortion when the receivers are blocked, especially under transient conditions. The long nozzle exit profiles are considered to be parabolic, while the actual profile at the exit of a short nozzle ($\frac{L_{\text{nozzle}}}{h} \sim 4$) will fall between a uniform and a parabolic shape. The exact shape will depend upon inlet pressure, flow, and entrance conditions. The matching criteria that are the most appropriate will also depend upon the initial profile shape.

To attempt to match data for a given sensor, the dimensions must be accurately known. This analysis has shown that the most sensitive dimension is the receiver inlet evaluation point y. For recent low aspect ratio sensor designs, the splitter at the receiver protrudes

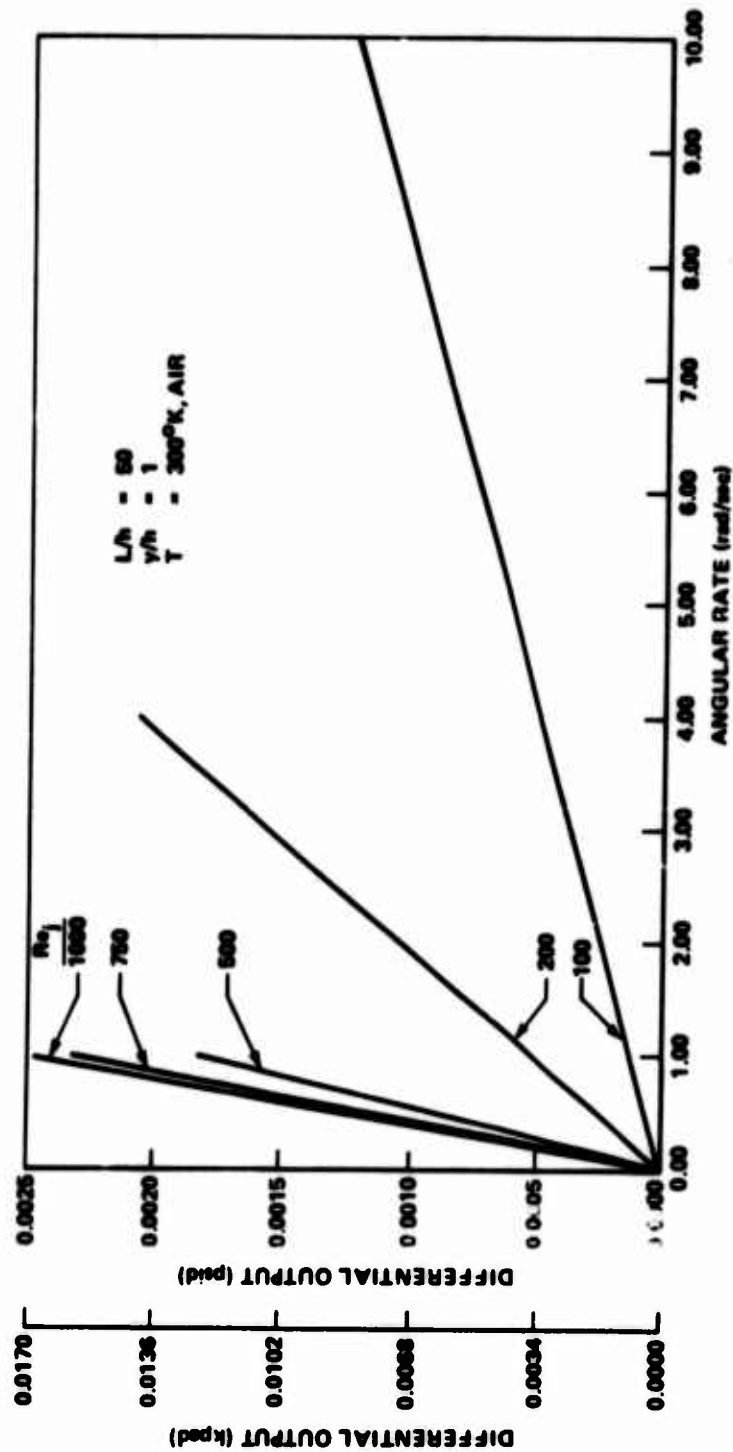


Figure 15. Δ^2 Versus $\dot{\theta}$ (Sensor Differential Output Versus Angular Rate)

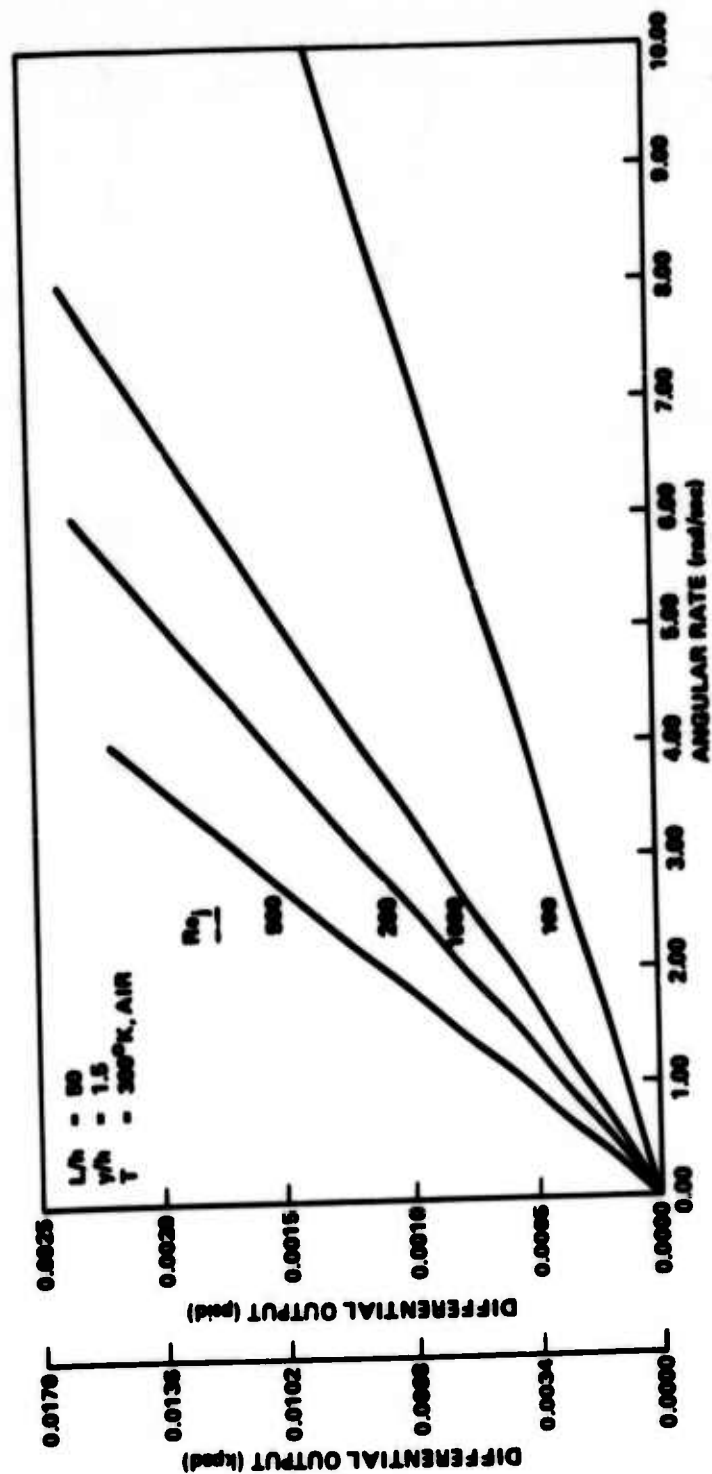


Figure 16. ΔP Versus ω (Sensor Differential Output Versus Angular Rate)

somewhat into the flow. A normal drawn from the splitter tip to the passage center yields a value of y approximately 30% less than that found if the passage center position at the receiver outside wall is selected. If the former position is selected as the pickoff point, the low aspect ratio data of [5] can be approximated by matching the centerline velocity using the nozzle width as the appropriate dimension.

Predictions of the effect of aspect ratio on sensor output were attempted using the hydraulic diameter as the appropriate dimension in the calculation of Re_j , y/h , and L/h . However, the results consistently underpredicted the experimental data by a factor of two.

The results of the analysis are compared with experimental data in Figure 17. The best gains (highest curve slopes) are achieved for the low aspect ratio designs, since higher velocities are achievable without transition into turbulence. For the range of sensor data available, use of a parabolic profile match at the nozzle exit predicts somewhat higher gains, because the predicted profile has a larger velocity gradient at the receivers. The data in [2] and [6] (Curves 1 and 2 in Figure 17) were for long nozzles ($L/h > 20$), so a parabolic profile is appropriate.

For the short nozzle data on $AR = 0.6$ sensor, the experimental data lie between curves calculated based on uniform (Curve 3) and parabolic (Curve 6) profiles, using centerline velocity as the matching criteria. The data for the lowest aspect ratio reported (Curve 5, $AR = 0.4$) are matched better with a parabolic profile. The uncertainty on these data is no better than 5%, primarily because of uncertainty in nozzle dimensions and drift with supply pressure. The data on Curve 4 [10] showed reduced gain compared with the earlier results, but exhibited a region of Reynolds number insensitivity which is a trend predicted by this analysis. Apparently the reduced wall roughness of this design (titanium metal etched) results in reduced wall friction and consequently a more uniform profile. The data are best fit with a uniform profile, flow rate match, being overpredicted ~30% by the parabolic profile, centerline velocity match.

It is seen that this simplified, two-dimensional analysis can yield predictions on obvious three-dimensional geometries which are substantiated experimentally.

4. SUMMARY AND CONCLUSIONS

The analysis presented in this paper, although simple, predicts sensor output with fair accuracy and yields some basic trends which a priori would be hard to predict. The equations depict a linear dependence of output on angular rate, which is the basis for using the device as a sensor. The more significant results, however, are the variations in maximum output as a function of L/h , y/h , and Re_j . For some geometries the variation is quite marked over a small

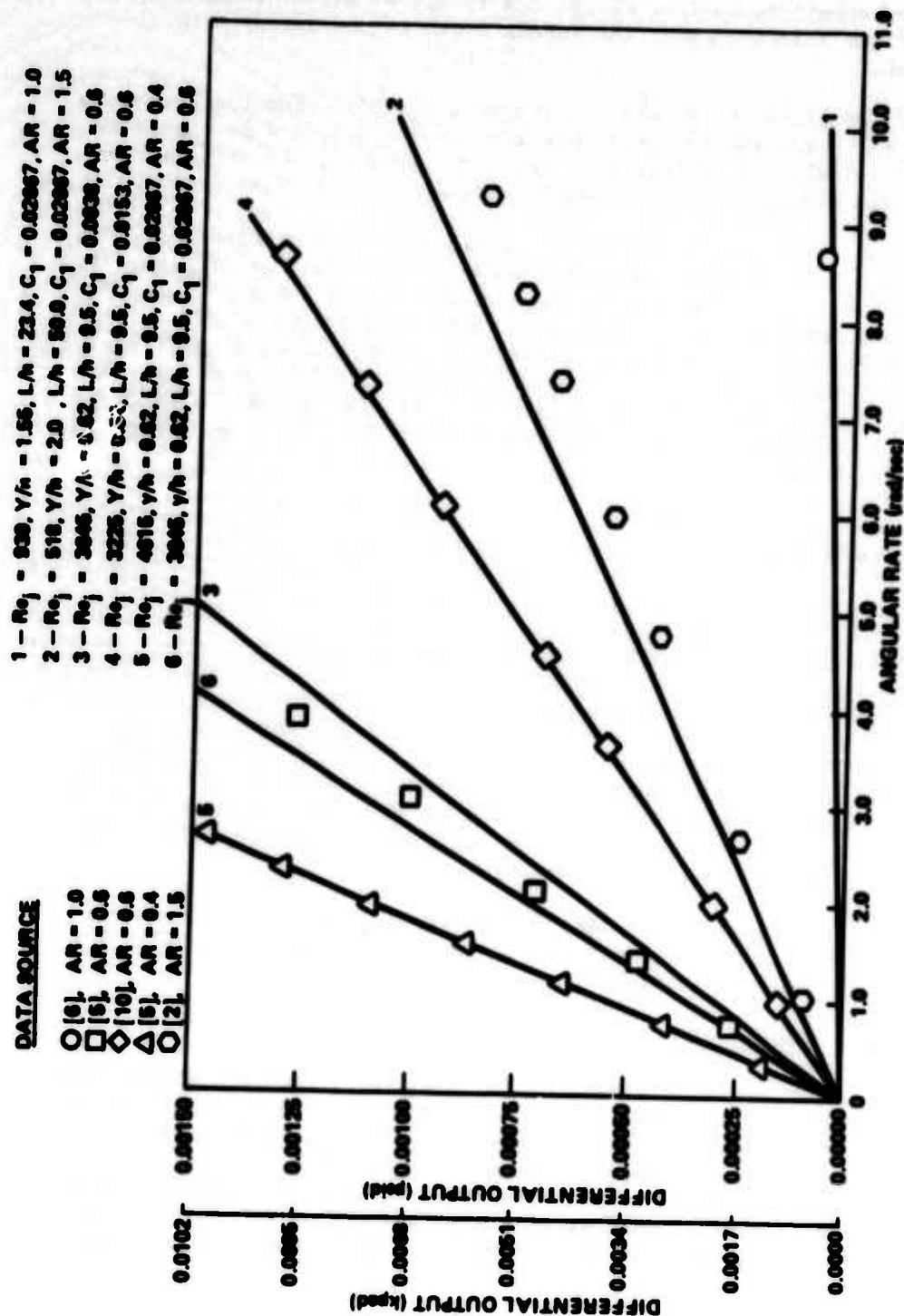


Figure 17. Comparison with Experiment

range of R_{aj} values, while others are insensitive to R_{aj} changes and thus are not as supply pressure sensitive (Figure 14). The analysis shows that maximum theoretical output would be difficult to achieve physically, as it requires very small and accurate spacing of receivers and small pickoff sizes. The model is also capable of determining the effects of environmental changes, and can be coupled with temperature compensation analyses to predict a given technique's effectiveness in stabilizing output during environmental changes.

REFERENCES

1. Young, R., Feasibility Investigation of a Laminar Rate Sensor, Phase IV, Interim Progress Reports 1-5 by the General Electric Company, to the Naval Air Systems Command, Washington, D. C., under Contract No. N00019-72C0231 for periods April-August 1972.
2. Reader, T. D., et al, Feasibility Investigation of a Laminar Rate Sensor, Phase I Report by General Electric Company, for the Naval Air Systems Command, Washington, D. C., under Contract No. N00019-69-C-0104, June 1969.
3. Schlichting, H., Boundary Layer Theory, 4th Edition, McGraw-Hill Book Company, New York, New York, 1960.
4. Griffin, W. S., and Coultas, R. K., The Axisymmetric Laminar Jet Angular Rate Sensor, Parts I and II, ASME Papers 72-FICS-4 and 72-FICS-5, presented at the Gas Turbine and Fluids Engineering Conference and Products Show, San Francisco, California, 26-30 March 1972.
5. Young, R., Feasibility Investigation of a Laminar Rate Sensor, (LARS), Phase IV Final Report by the General Electric Company, to Naval Air Systems Command, Washington, D. C., under Contract N00019-72-C-0231.
6. Bravo, V. O., Feasibility Investigation of a Laminar Rate Sensor, Phase III Final Report by the General Electric Company, for the Naval Air Systems Command, Washington, D. C., under Contract No. N00019-71-C-0900, December 1971.
7. Markland, E., and Beatty, E. K., "Feasibility Study of Laminar Jet Deflection in Fluidic Elements," 3rd Cranfield Conference Proceedings, Paper H-1, 1968.
8. Symons, E. P., and Labus, T. L., Experimental Investigation of an Axisymmetric Fully Developed Laminar Free Jet, National Aeronautics and Space Administration, Marshall Space Flight Center, Alabama, TN D-6304, April 1971.
9. Bell, A. C., An Analytical and Empirical Basis for the Design of Turbulence Amplifiers, Parts I and II, ASME Paper WA/FLCS, presented at the ASME Winter Annual Meeting, 26-30 November 1973.
10. Young, R., Private Communication.

BIBLIOGRAPHY

- Birkhoff, G., and Zarantonello, E. H., "Theory of Jets, Wakes, and Cavities," Applied Mathematics and Mechanics, Vol D, Academic Press, New York, 1957.
- Moore, A. G., and Schuemann, W. C., Fluidic Angular Rate Sensor Development, Final Report under Contract No. DAHC60-69-V-0127 to US Army Safeguard Systems Command, Redstone Arsenal, Alabama, January 1970.
- Pai, S. I., Viscous Flow Theory - Laminar Flow, Van Nostrand, Princeton, New Jersey, 1956.
- Shinn, J. N., et al, Fabrication of Integrated Fluidic Control Systems, Interim and Progress Reports by the General Electric Company, to USAF Materials Laboratory, Wright-Patterson AFB, Ohio, under Contract No. F33615-68-C-1700 (Project 861-8), covering periods March 1969 - March 1971.

748D2043
APRIL 1974

DEVELOPMENT OF A LAMINAR ANGULAR RATE SENSOR

by

Robert Young

GENERAL  ELECTRIC
Re-entry & Environmental
Systems Division
3128 Chestnut St., Philadelphia, Pa. 19101

Preceding page blank

357

I. INTRODUCTION

During the past few years, the need to substantially reduce the cost of guidance and control components, without sacrificing performance, has been a main forcing function in the development of advanced tactical missile systems. The angular rate sensor has been a part of this cost reduction thrust because conventional angular rate sensors (spring restraint gyros) cost between \$600 and \$1000 per unit and from one to six sensors are required per missile. In addition to costs, conventional rate gyros have inherent design limitations such as moving mechanical parts, low bandwidth, large size and weight, large input power and finite spin-up times. New techniques of sensing angular rate are presently being investigated in an attempt to obtain low cost angular rate sensors. Additional benefits desired from any new angular rate sensor are no-moving-part reliability and environmental hardness, large bandwidths, small size and weight, low input power and "instant-on". One rate sensing technique which has demonstrated its feasibility to be manufactured at low cost and which has all of the desired performance features listed above is the GE-RESD Laminar Angular Rate Sensor (LARS).

GE-RESD demonstrated the feasibility of the LARS in 1967. Since then, three prototype models of the LARS (with linear ranges from 50 degrees/second to 1000 degrees/second) have been developed under contract to the Naval Air Systems Command (NASC) under the technical direction of Mr. John Burns. Four phases of design, development, and testing effort have been performed during this period.

Phase I was composed of three tasks resulting in a clearer understanding of the design factors affecting the laminar jet. These tasks were:

- a. Task A - Supply Nozzle Design - The analysis and design activities centered on the parameters affecting the jet stream geometry and stability.
- b. Task B - Vent and Receiver Design - The objective was to improve the performance of a simple open loop laminar jet rate sensor by the application of techniques to isolate the laminar jet from unwanted external influences and increase the laminar jet rate sensor sensitivity to spatial angular rate.
- c. Task C - Test and Evaluation - The object was to perform functional and selected environmental tests on selected rate sensor designs.

The results of the Phase I Feasibility Investigation of a Laminar Angular Rate Sensor (LARS) are presented in GE-RESD Document No. 69SD698.

Phase II was composed of five tasks which resulted in the fabrication and testing of a selected laminar rate sensor design.

- a. Task A - Performance Design Goals - The objective of this task was to establish the performance design goals by selecting a suitable application for the laminar rate sensor. The design was then optimized with respect to the requirements of the application. Included in this task was the optimization of other design goals which were not intrinsically connected with the selected application but deemed essential to a component of this type.
- b. Task B - Scaling and Optimization - In this task, an analytical investigation was made to determine the effect of geometry changes on LARS performance.
- c. Task C - Overall Design - The objective of this task was to choose a material for flight hardware and design the equipment needed during Task E of this program.
- d. Task D - Detail Design - In this task, an analysis was performed to determine the optimum geometries required to satisfy the performance design goals established in Task A of this program.
- e. Task E - Fabrication and Testing - The objective of this task was to fabricate the laminar rate sensor out of chemically etched laminates and to assemble these laminates for test and evaluation. Testing of the LARS included the following:

<u>Functional Tests</u>	<u>Environmental Tests</u>
1. Threshold	1. Temperature
2. Range	2. Vibration
3. Frequency response	3. Acceleration
4. Transport lag	4. Noise
5. Power and flow consumption	5. Shock

Due to the very low pressure differentials involved, this last task included the simultaneous development of testing procedures and instrumentation requirements.

The results of the Phase II Feasibility Investigation of a Laminar Angular Rate Sensor (LARS) are presented in GE-RESO Document No. 70SD788.

Phase III was composed of five tasks which resulted in hard test data which substantiated the theoretical conclusions drawn from the earlier efforts.

- a. Task A - Detailed Performance Studies - The objective of this task was to perform static and dynamic testing of the rate sensor with three

stages of fluidic amplifiers cascaded in series and with all components centrally supplied.

- b. Task B - Sensitivity Studies - This task addressed itself to the effects of supply pressure and temperature.
- c. Task C - Noise Investigation - The objective of this task was to develop the pressure manifolds first used in the Phase II.
- d. Task D - Vibration and Shock Testing - Under this task, the rate sensor was subjected to a vibration test per MIL-STD-810B and a high g (> 12,000 g) shock test, non-operational.
- e. Task E - Analysis and Critique - The objective of this task was to analyze the test data generated during the Phase III effort and to recommend main objectives for a Phase IV effort.

At the conclusion of this effort, several questions still remained which were:

- 1. What is the minimum scale factor required from the LARS to make it a usable device in a fluidic system?
- 2. Can the above scale factor be obtained by a redesign of the basic rate sensor and/or a redesign of the gain block amplifier?
- 3. Can more amplifiers be added to the gain block to increase the scale factor? If so, what effect will this have on signal to noise level, null shift, transport lag, frequency response, and ease of fabrication.
- 4. How will the LARS perform in the anticipated service environments of: 1) temperature, 2) shock, 3) vibration, and 4) angular and linear acceleration?

The results of the Phase III Feasibility Investigation of a Laminar Angular Rate Sensor (LARS) are presented in GE-RESO Document No. 71-SD-2118.

Phase IV was a comprehensive program comprised of three main tasks. These tasks were designed to provide answers to the four questions from Phase III. The tasks were:

- Task A - Laminar Amplifier Development
- Task B - Staging Techniques
- Task C - Rate Sensor - Gain Block Optimization

In Task A, a determination was made of the required scale factor (Question 1) and a new high pressure gain laminar amplifier, based on the NASA Langley design, was developed. (Question 2) Based on the evaluation of the LARS as used in four fluidic

control systems, it was found that the scale factor of the Phase III LARS should be increased by 100 to 1000 times. During Task B, several different staged amplifier configurations were tested to determine the performance of the various staged gain blocks (Question 3). Task C was to improve the basic rate sensor design (Question 2), if possible, and to determine the operating characteristics and performance of the rate sensor and gain block combination (Question 4). This test data would allow an evaluation of the feasibility of the LARS when used in actual control systems.

II. PHASE I RESULTS

II-1. TASK A - SUPPLY NOZZLE DESIGN

At the start of this effort, the criterion of success used was that the best supply nozzle design would be the one that would provide the maximum Reynolds Number for stable laminar flow conditions. This criterion was selected for two reasons:

1. It was felt that the more stable the laminar jet the less sensitive it would be to unwanted external disturbances.
2. The highest Reynolds Number would give the highest laminar jet velocity. The higher jet velocity would allow the receiver to be located further downstream for a given dynamic pressure recovery. The further downstream the receiver, the more the laminar jet would be deflected at the receiver for a given angular rate input and, therefore, the better the sensitivity and scale factor of the sensor.

In order to determine laminar flow conditions for the various nozzle designs, water table and large scale air models were constructed.

Water Models

The use of submerged water models was particularly helpful in the investigation of supply nozzle design and interaction cavity design. Figure 1 is a photograph of the experimental apparatus used for testing submerged water models, and Figure 2 is a detailed photograph of a typical model. The experimental procedure used for submerged models is as follows:

- a. The channel width is set with the dial gauge adjuster.
- b. The ambient flow conditions are adjusted and recorded.
- c. A homogenized mixture of dye is run through the precision flow meters into the model.
- d. The flow from the model is then observed at an arbitrary distance (4 nozzle widths from the channel exit).
- e. The flow is gradually increased until unsteady flow exists at the arbitrary observation point.
- f. The critical Reynolds Number for this point is then calculated and recorded.

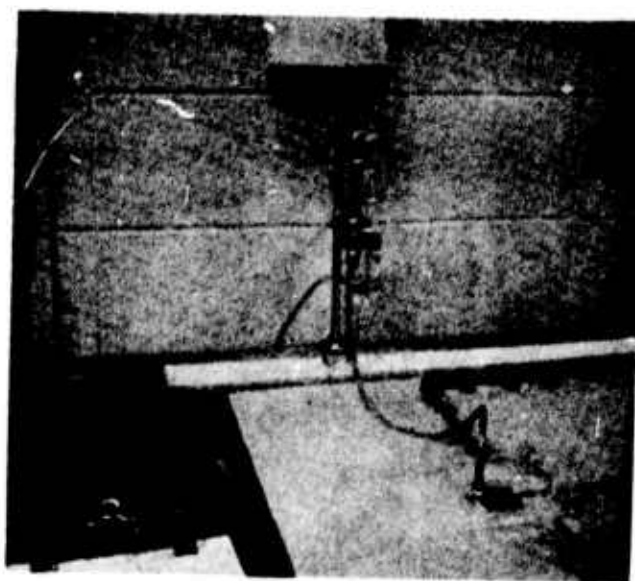
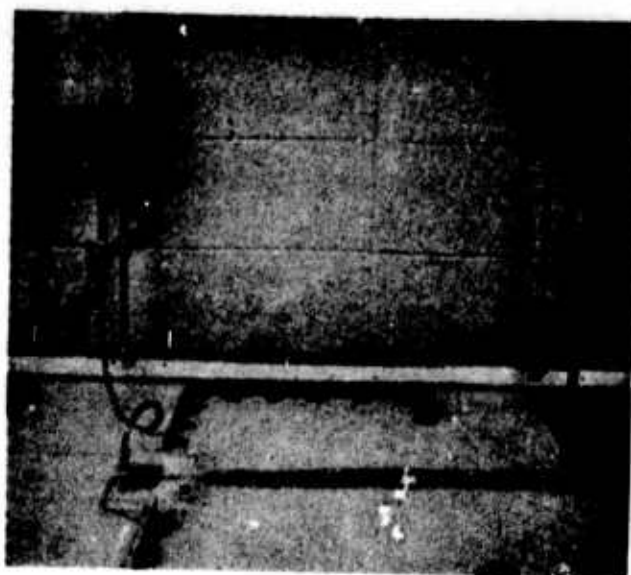


Figure 1. Laboratory Apparatus for Submerged Water Model Testing

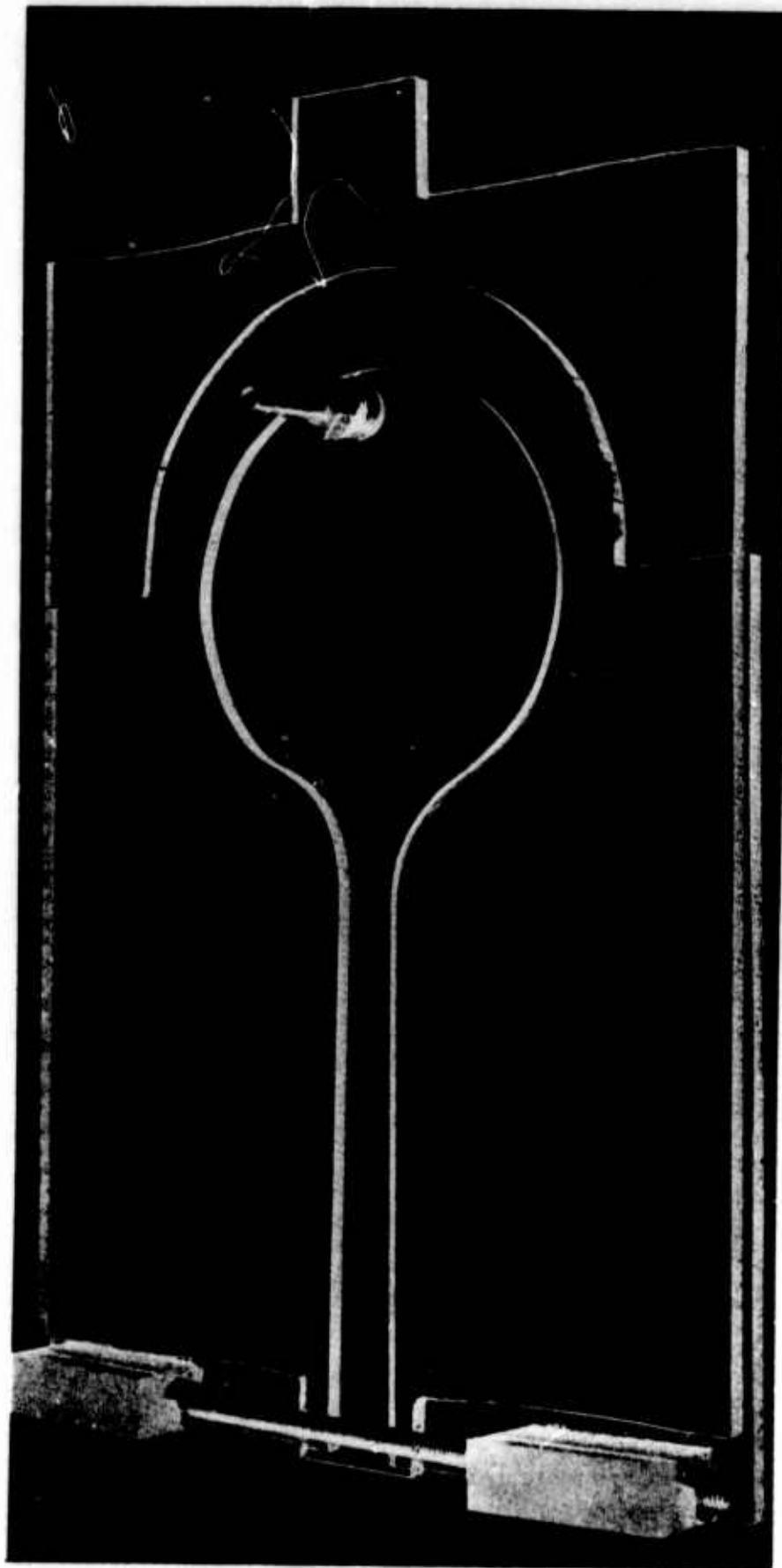


Figure 2. Typical Submerged Water Model without Dial Indicator

With respect to supply nozzle design, there are six areas of consideration that were tested using submerged models. They are as follows:

1. Inlet configuration
2. Length of nozzle
3. Convergence - divergence
4. Aspect ratio
5. Surface finish
6. Outlet Configuration

Several experiments were conducted on the open water table to further investigate the supply nozzle design. Dye was injected in a uniform manner at the inlet of the channel to increase visualization of streamlines. The exit of the channel was then observed for the formation of unsteady flow patterns.

Although a great deal of visibility was achieved by using open water models, some accuracy is lost in determining critical Reynolds Number values. The reason for the decrease in accuracy is that no convenient technique for determining the mean stream velocity (necessary for calculating Reynolds Number) is known; therefore, higher reliability was placed on submerged water model testing because the actual flow through the model could be determined by precision flow meters.

Air Model Experiments

Although it was possible to accurately determine flow rate using submerged models, there was still an uncertainty error in the observation technique of determining exactly when the flow became unsteady. Therefore, air model experiments were conducted in which flow rates and pressure losses could be accurately determined by using flow meters and manometers. Apparatus for air experiments is shown in Figure 3.

The first type of air experiment was done with pitot tubes placed perpendicular to the free stream jet flow. An increase in pitot tube reading would therefore indicate velocity components in orthogonal directions of the main jet. This condition constitutes unsteady flow. Unfortunately, even at very high flows, variations in pitot tube readings were so small that they weren't detectable using slant manometers.

Other air experiments were performed to determine the channel configuration which would provide the highest critical Reynolds Number within the channel. By recording and plotting pressure loss versus flow rate on log-log paper, a linear curve results with a discontinuous point at the transition point of steady

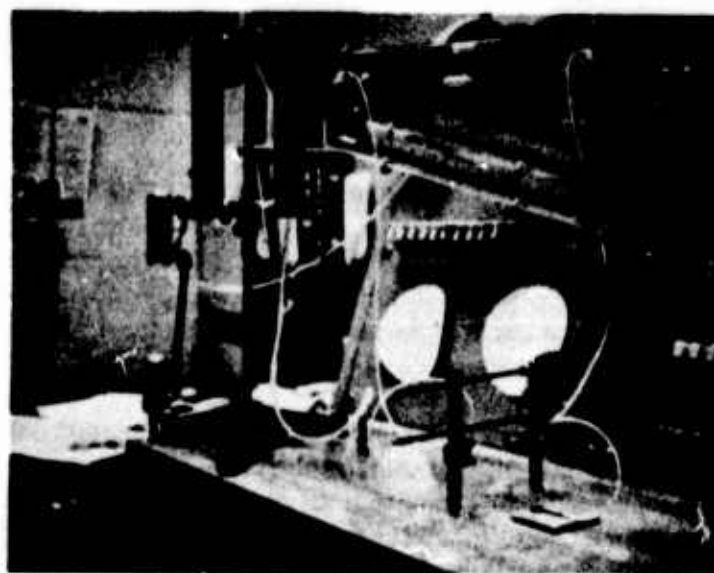
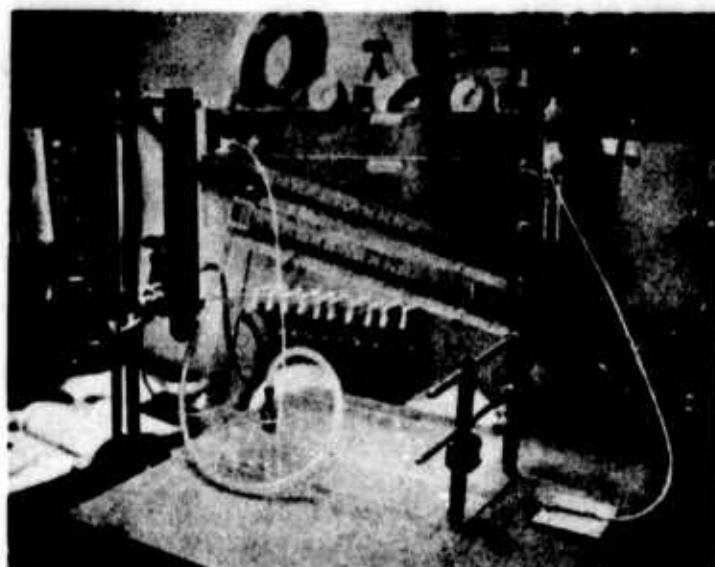


Figure 3. Air Model Test Apparatus

to unsteady flow. This discontinuity, characterized by an increase in the slope of the pressure versus flow curve, is a result of higher viscous losses per unit change of flow in the unsteady or turbulent flow region. However, this technique of determining the transition point can only be directly applied to straight walled channels where a negative linear pressure gradient exists. In the convergent and divergent cases, discontinuity points may not necessarily indicate a change in viscous losses but also kinetic changes. Another problem with this technique is that the stability is based on flow within the channel and not on flow development after the flow has issued from the nozzle exit.

Results

The experimental data, which was obtained using the water table and large scale air models, showed the following trends:

1. Inlet Configuration - The inlet configuration which is used on supply nozzles longer than 20 nozzle widths has very little effect on the critical Reynolds Number. However, as the length of the supply nozzle is decreased towards one nozzle width, the entrance design becomes more important with a light bulb shape giving the highest critical Reynolds Number.
2. Length of Supply Nozzle - The following relationship was determined between supply nozzle length and critical Reynolds Number. This relationship was experimentally verified for supply nozzle lengths from 1 to 50 nozzle widths.

$$N_{RCR} = 126 + 5.7 (1/w) - 0.008 (1/w)^2$$

$$N_{RCR} = \text{Critical Reynolds Number}$$

$$L = \text{Length of supply nozzle in inches}$$

$$w = \text{Width of supply nozzle in inches}$$

3. Supply Nozzle Convergence and Divergence - Experimental results showed that for aspect ratios greater than 0.25, a convergent supply nozzle with a slope of 25 to 1 gave the highest critical Reynolds Number. For aspect ratios equal to or less than 0.25, no effect was measured. These results are only valid for slopes from zero to 15 to 1, where the slope is defined as

$$\frac{W_o - W}{L}$$

$$W_o = \text{Entrance width}$$

W = Exit width

l = Nozzle length

4. Aspect Ratio - Test results showed that for aspect ratios of less than 3, the lower the aspect ratio the higher the critical Reynolds Number.
5. Surface Finish - Results were inconclusive for other than large surface finish roughnesses. It was found that surface roughness of 25 percent or greater in the direction of flow (not from top to bottom) caused a substantial reduction (>15 percent) in critical Reynolds Number.
6. Power Nozzle Outlet Configuration - Results of the outlet configuration investigation are shown in Figure 4.

II-2. TASK B - VENT AND RECEIVER DESIGN

An analytical description on the operation of a Laminar Angular Rate Sensor (LARS) has been given in a previous paper and is also presented in several reports which include "Feasibility Investigation of a Laminar Angular Rate Sensor" GE-RESO Document No. 693D698 and "Analysis of a Two-Dimensional Laminar Rate Sensor" by Dr. Paul Jacobs, Amicon Report RG-73-8. The second major effort, other than the analytical investigation, was to confirm the analytical model with actual test data. The test data was obtained using both water table models and actual size models using air as the supply medium.

Tests of a Submerged Water Model

Description of Experiments - Tests were conducted on a water table with a set-up shown in Figure 5. The water was supplied to the model from a reservoir placed at a constant height above the model so as to provide a constant pressure to the system. The inlet plenum of the model contains three successive screens to minimize the disturbances at the supply nozzle due to the inlet piping.

The vents and the receivers were vented into the water table except for a few cases where the receivers were blocked.

The supply flow-rate was controlled by a hand valve and the temperature in the reservoir was measured.

The Reynolds Number at the flow issuing from the supply nozzle was then calculated by the following relation:

$$N_R = \frac{Q D_h}{A \gamma}$$

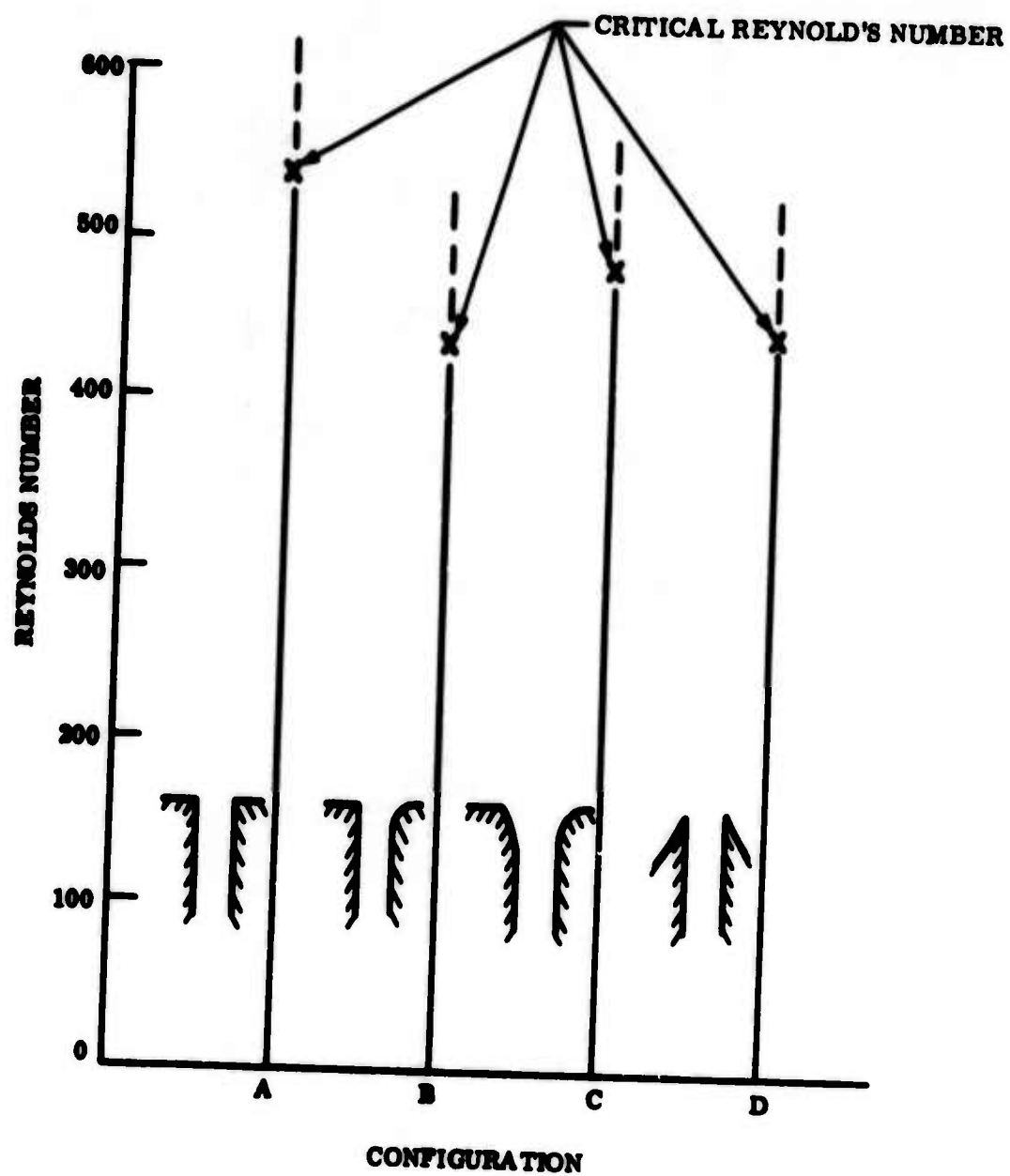


Figure 4. Effect of Outlet Configuration

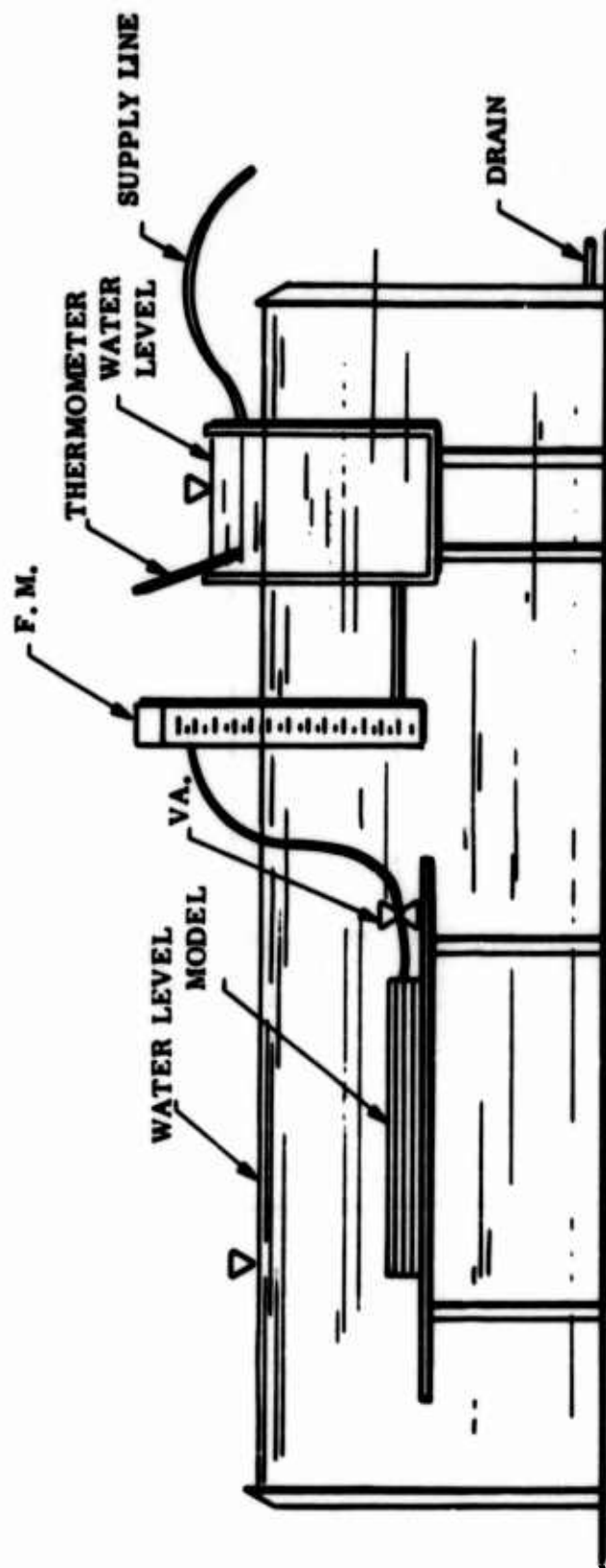


Figure 5. Water Table Setup for Submerged Water Model Testing

where

D_h is the hydraulic diameter of the supply nozzle (in)

A is the area of the supply nozzle (in^2)

Q is the flow rate measured at the supply line to the model (in^3/sec)

and

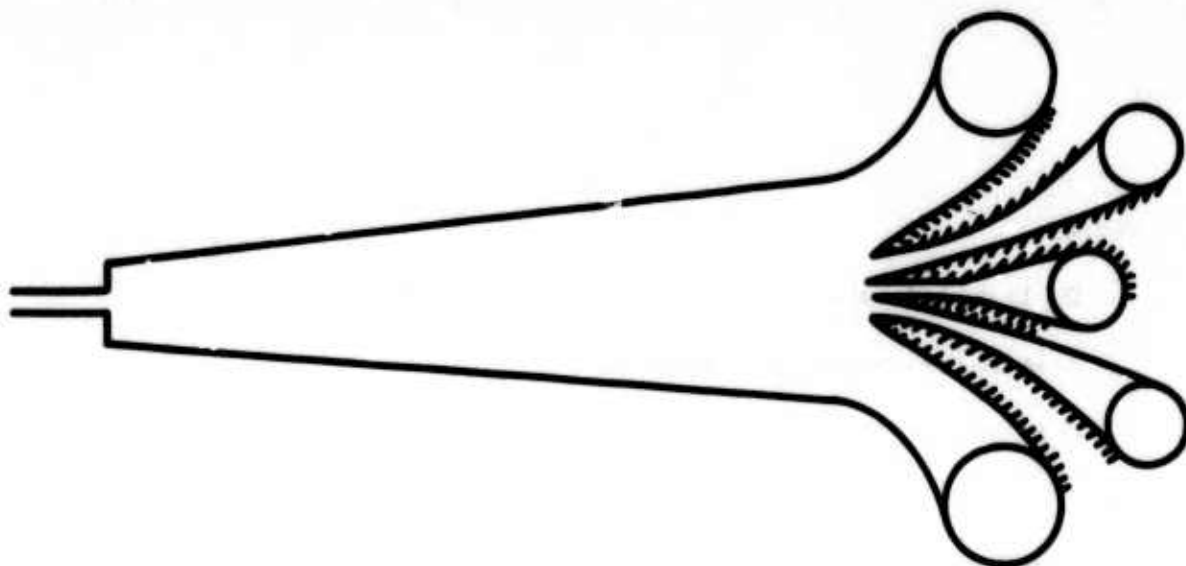
γ is the kinematic viscosity of the water at the measured temperature (in^2/sec)

The experimental procedure used during the tests was as follows:

- a. A steady flow and temperature were set at the supply nozzle.
- b. Dye was then injected into the inlet plenum.
- c. Two pictures were taken when the dye leaves the supply nozzle and when it enters the receivers, labeled A and B, respectively.
- d. A third picture, labeled C, was taken after the dye had been spread throughout the interaction cavity.
- e. For special cases where disturbances were introduced near the vents, a few more pictures were taken.
- f. Dye was also injected close to the exit of the supply nozzle and by the receivers, in some cases, to clarify the vortex formation at these points.

The above procedure was carried out for two types of shapes as shown in Figure 6. Shapes I and II were tested with an aspect ratio of unity and 2. Shape II was also tested with a deep interaction cavity having an aspect ratio of 3 while keeping the supply nozzle and the receivers at an aspect ratio of unity.

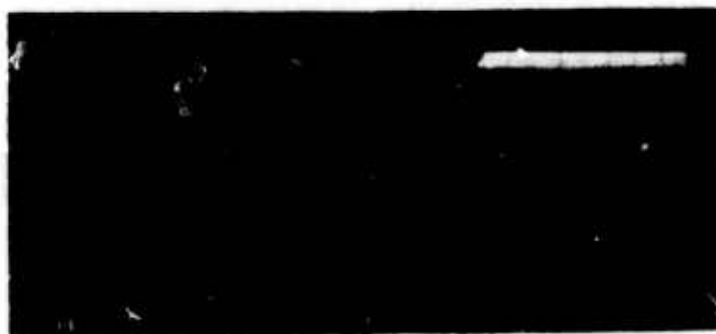
Model Design - The experiments were carried out on a water table with a model that had been enlarged by a scale factor of 12.5 over the anticipated actual size LARS.



Shape I



Shape II



Shape of deep cavity

Figure 6. Submerged Water Model Shapes

The dimensions of the model are as follows:

	<u>Model Dimension (Inches)</u>
Nozzle width (h)	0.25
Receiver width (d)	0.3
Receiver spacing (s)	0.3
Width of center vent	0.25
Distance from supply nozzle to receivers	10.0

The length of the straight portion of the supply nozzle was 3-1/2 inches ($1/h = 14$) which generates a fully developed parabolic flow for almost the entire range of Reynolds Numbers studies. Sample photographs of the water table tests are shown in Figures 7 and 8 and the data are tabulated in Tables I through V.

Tests of a Full Scale Rotating Rate Sensor

Procedure - The performance of a typical laminar rate sensor (Figure 9) was examined on a rotating wheel. The data collected during this test verifies part of the analysis that was done before.

Description of the Sensor - The dimensions of the rate sensor were as follows:

	<u>Dimension (Inches)</u>
Supply nozzle width (h)	0.02
Receiver width (d)	0.028
Receiver spacing (2s)	0.08
Distance from supply nozzle to receivers	1

Test Results

The experimental test results showed that the power jet centerline deflection angle versus angular rate of turn was in close agreement to the predictions of the analytical model. The momentum recovery and the rate sensor gain (scale factor), however, were much lower than was predicted when using the optimum vent/receiver design as determined by the analytical model equations

Aspect ratio = 1

Shape I



A



B



C

39.1 $N_R = 417$

Shape II



39.2 $N_R = 425$



A



B



C

39.3 $N_R = 485$



39.4 $N_R = 535$

Figure 7. Flow Patterns for Shapes I and II - Aspect Ratio = 1, $N_R = 417$ to 535

Aspect ratio = 1

Shape I



40.1 $N_R = 590$

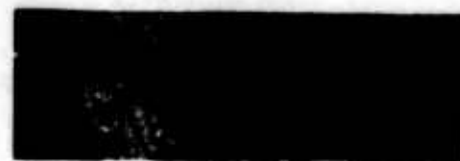


40.2 $N_R = 652$



40.3 $N_R = 857$

Shape II



40.4 $N_R = 586$



40.5 $N_R = 706$

Figure 8. Flow Patterns for Shapes I and II - Aspect Ratio = 1, $N_R = 586$ to 857

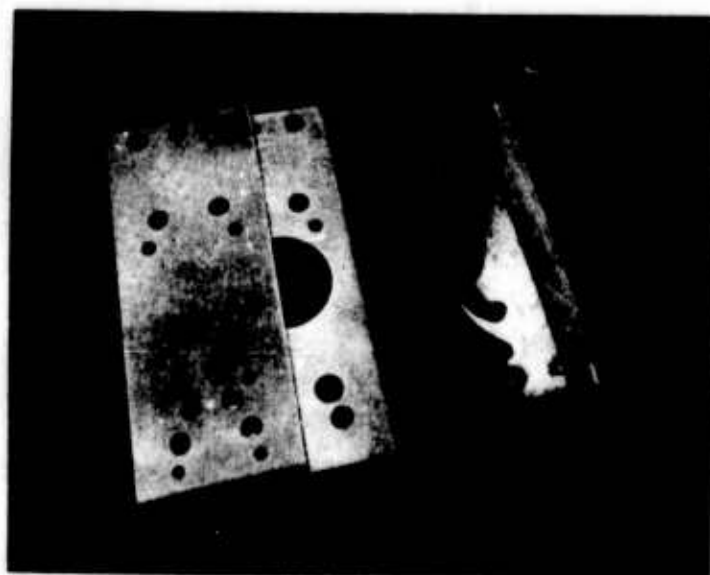
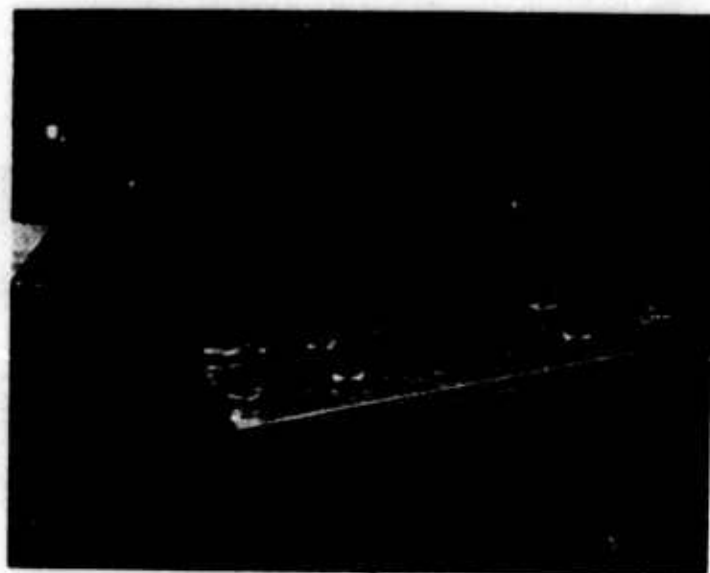


Figure 9. Full Scale Laminar Sensor

TABLE I. EXPERIMENTAL RESULTS FOR SHAPE I- ASPECT RATIO = 1

Figure	Q in ³ /sec	V in/sec	T °F	ν ft ² /sec	R _E
37.1	8.52·10 ⁻²	1.37	61.5	1.2x10 ⁻⁵	197
38.1	0.14	2.24	62.0	1.18	328
38.3	0.153	2.45	61.6	1.19	356
38.4	0.161	2.57	61.6	1.19	374
39.1	0.188	3.01	58.0	1.25	417
39.3	0.206	3.3	62.0	1.18	485
40.1	0.258	4.13	60.8	1.20	590
40.3	0.307	4.9	56.0	1.3	652
40.4	0.37	5.9	61.0	1.19	857
41.1	0.407	6.5	57.2	1.26	892

TABLE II. EXPERIMENTAL RESULTS FOR SHAPE I- ASPECT RATIO = 2

42.1	0.058	0.465	58.0	1.25x10 ⁻⁵	86
42.3	0.114	0.91	58.0	1.25	168
42.5	0.173	1.38	59.5	1.2	266
43.1	0.231	1.85	59.5	1.2	356
43.2	0.356	2.84	59.5	1.2	550

TABLE III. EXPERIMENTAL RESULTS FOR SHAPE II- ASPECT RATIO = 1

45.3	0.307	4.9	59.0	1.24x10 ⁻⁵	684*
37.2	0.073	1.16	60.0	1.2	168
37.3	0.102	1.63	59.7	1.22	231
38.2	0.142	2.27	59.9	1.2	327
39.2	0.188	3.0	59.7	1.22	423
39.4	0.232	3.71	59.9	1.2	535
40.2	0.254	4.06	60.3	1.2	586
40.5	0.307	4.9	59.9	1.2	706
41.2	0.316	5.05	60.0	1.2	730
45.1-46.1	0.188	3.0	60.3	1.2	432*

TABLE IV. EXPERIMENTAL RESULTS FOR SHAPE II
WITH A DEEP INTERACTION CAVITY

44.1	0.058	0.93	58.3	1.25x10 ⁻⁵	128
44.2	0.087	1.39	59.4	1.21x10 ⁻⁵	199
44.3	0.142	2.27	59.4	1.21	325
44.4	0.188	3.0	60.3	1.2	432
44.5-46.2	0.277	4.42	59.4	1.21	632
45.4	0.188	3.0	59.9	1.2	432*
45.2	0.142	2.27	60.4	1.2	342*

TABLE V. EXPERIMENTAL RESULTS FOR SHAPE II- ASPECT RATIO = 2

42.2-46.3	0.058	0.464	57.2	1.26x10 ⁻⁵	85.5
42.4-46.3	0.114	0.91	59.0	1.24	170
42.6-46.4	0.1575	1.26	59.7	1.22	240
43.3	0.23	1.84	57.2	1.26	338
43.4	0.29	2.32	59.7	1.22	440
43.5	0.356	2.81	59.0	1.24	530
47	0.20	1.6	59.0	1.24	300
43.6	0.422	3.37	59.7	1.22	640

*Blocked Output

(Figure 10). The reason for this discrepancy was never experimentally determined but indicated that the vent/receiver design was probably not optimum based on actual power jet spreading and/or losses that were different from the analytical model.

II-3. TASK C - TEST AND EVALUATION

The object of this task was to perform some selected environmental tests to determine the sensitivity of the LARS to variations in these selected environments. The environments which were selected for investigation were temperature, vibration, linear acceleration, angular acceleration, shock, and acoustic noise. The results of the tests performed during the above environmental variations were mostly of a qualitative nature and can be described as follows:

- Temperature Sensitivity - The LARS gain (scale factor) and null offset were sensitive to temperature and the LARS would require temperature compensation if it were to be a usable device.
- Vibration Sensitivity - There was no measurable output signal variation when the LARS was vibrated in all three axes at 0.5 g's over a frequency range of 5 to 1000 hertz.
- Acceleration Sensitivity (Linear and Angular) - The sensitivity of the LARS to acceleration was determined mainly by the vent cavity design. Improper vent design could cause bias of the LARS of up to 10 degrees/second at 2g accelerations.
- Shock Sensitivity - It was observed that the shape and duration of the shock input was observed on the output of the LARS.
- Acoustic Sensitivity - The noise level was set at 50 dB and varied from 5 to 20,000 hertz. The LARS power jet was very sensitive to the input noise at several frequencies when unshielded but was unaffected when a properly shielded vent cavity was used.

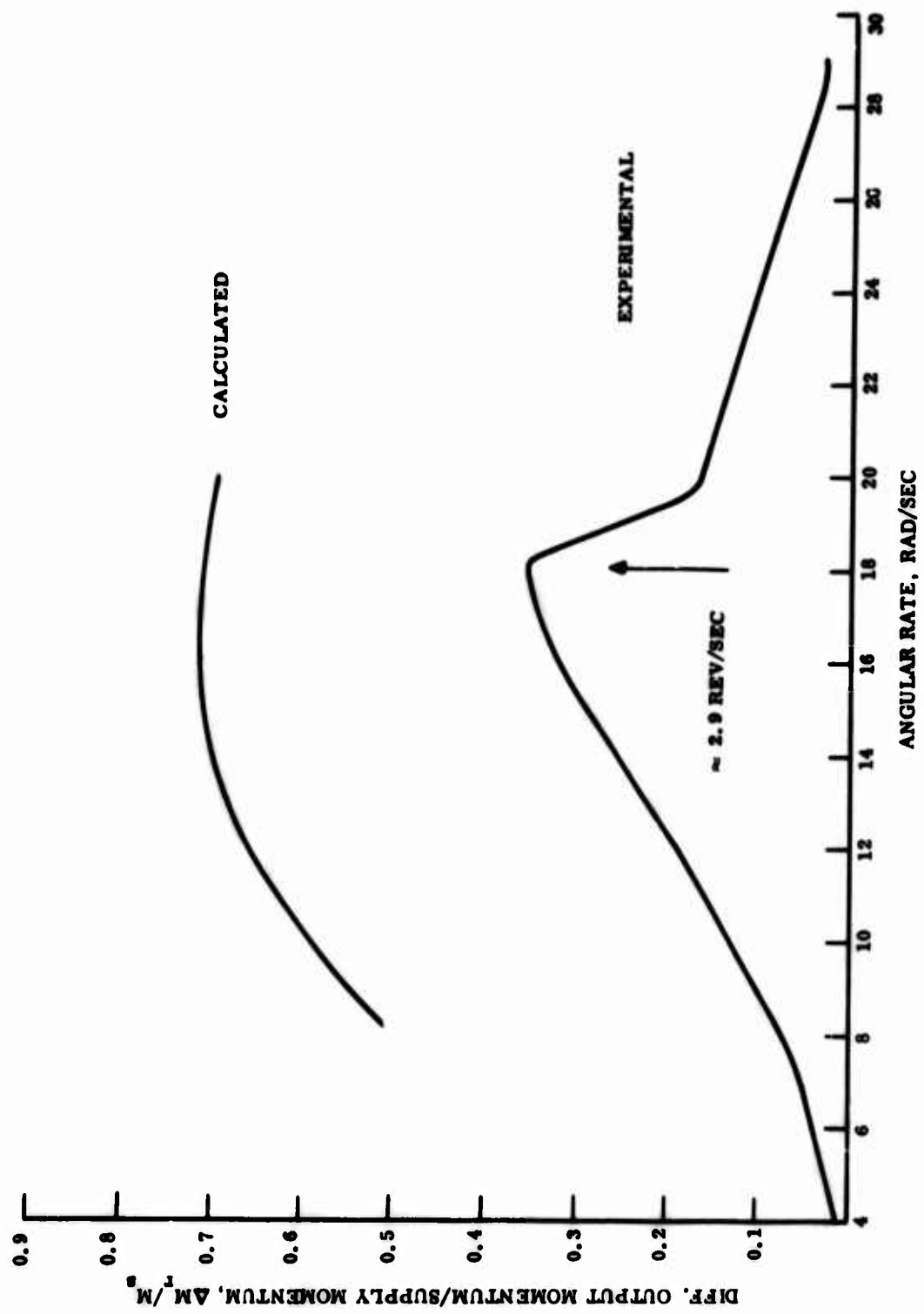


Figure 10. Momentum Recovery versus Angular Rate

III. PHASE II RESULTS

The major objectives of this phase were to (1) determine the LARS performance requirements, (2) design a breadboard LARS to meet those requirements, (3) fabricate the breadboard LARS, and (4) test the LARS at standard conditions and selected environments to demonstrate that the performance requirements had been met.

III-1. TASK A - LARS PERFORMANCE REQUIREMENTS

The object of the Phase I program was to demonstrate the feasibility of a laminar jet to sense angular rate and to determine some of the design parameters which effect the LARS performance. In this Phase, it was desired to have minimum performance requirements as a goal. The performance requirements for rate damping type control loops for tactical missiles was selected because:

- a. GE-RESO had contract effort in this area
- b. LARS potential for very low cost, size and weight
- c. Inertial quality sensor performance not required. Therefore, development effort to a preproduction design would be minimum.

Therefore, the following performance requirements for the LARS were established:

Threshold	0.05 degree/second
Hysteresis	0.05 degree/second
Resolution	0.05 degree/second
Linear Range	+ 500 degrees/second
Response	flat to 1000 radians/second
Noise	2% full scale

III-2. TASK B - SCALING AND OPTIMIZATION

Based on the water table and air model studies in Phase I, a LARS geometry was configured. This geometry was used as a starting point and the following geometric parameters were analyzed and a final LARS geometry was configured (Figure 11):

- a. Size - The power nozzle size and the distance to the receivers were determined to give the desired linear range.
- b. Vents - The vents are used (1) to eliminate vortices and secondary flows and (2) to remove the spillover from the receivers as efficiently as possible. The vent design in Figure 11 was found optimum when compared with circular walls, different vent wall setback and removal of the excess flow from the receivers at steeper angles.

- c. Receiver Widths - Based on the desired location of the receivers downstream of the power nozzle, the anticipated power jet spread angle and the desirability of obtaining the maximum rate of change of output pressure per angle of deflection, the receiver design in Figure 11 was configured with the aid of water table studies.

III-3. TASK C - MATERIAL SELECTION

A trade-off study was performed to select the optimum material for fabrication of the LARS. This trade-off study is as follows:

MATERIAL TRADE-OFF

<u>Material</u>	<u>Weight</u>	<u>Strength</u>	<u>Machin- ability</u>	<u>Bond Strength</u>	<u>Ability To Be Etched</u>	<u>Environmental Insensitivity</u>	<u>Total Points</u>
Aluminum	9	3	5	1	3	4	25
Titanium	7	8	4	10	8	9	46
Stainless Steel	4	9	6	3	6	8	36
Beryllium Copper	3	4	5	5	9	6	32

Points given on basis of 1-10 with 10 highest rating.

III-4. TASK D - DETAIL DESIGN

This task was an analytical investigation into the design determined in Task B in order to predicate LARS performance and potential unwanted environmental activities. The analysis showed that the LARS should meet the desired performance detailed in Task A.

III-5. TASK E - FABRICATION AND TEST

The LARS geometry (Figure 11), which was designed and analyzed in the previous tasks was fabricated, along with a 3-stage laminar gain block, by the photo-etch process. This unit was assembled and subjected to both functional operating tests and selected environmental tests.

Functional Operation Tests

The LARS and the 3-stage gain block were tested on a Genisco rate table using a Pace P90D pressure transducer to measure rate sensor performance. Results of the tests are as follows:

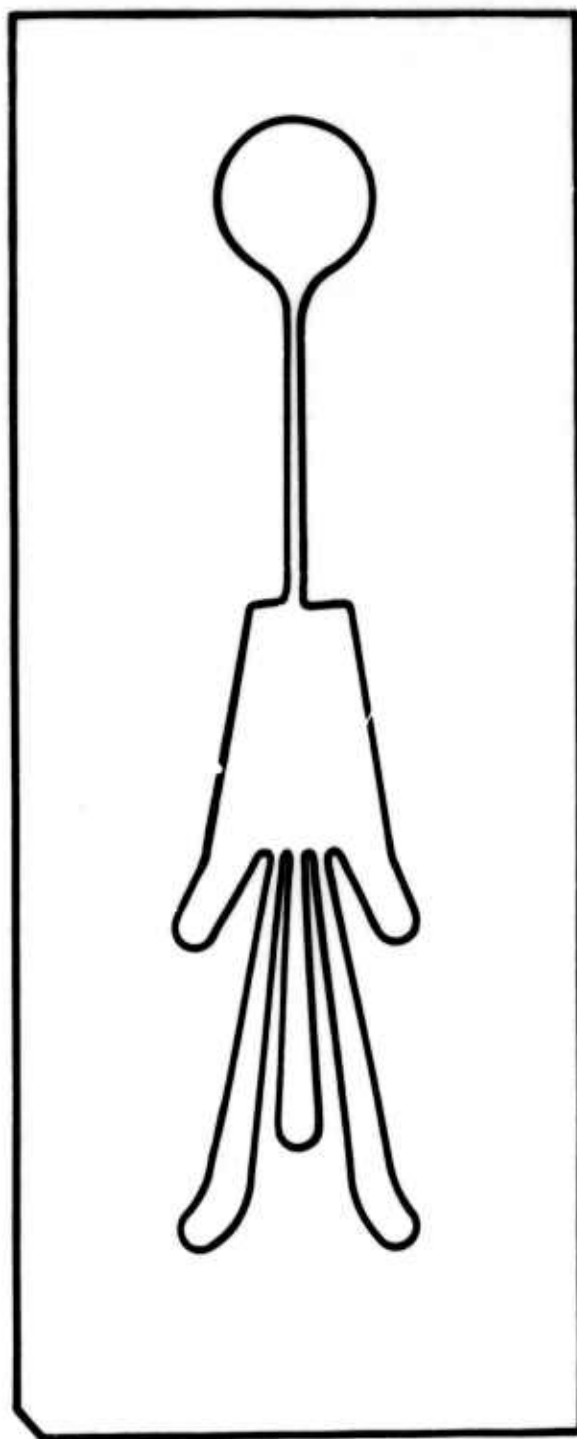


Figure 11. LARS Geometry

<u>Performance Parameters</u>	<u>Desired</u>	<u>Test Data</u>
Threshold	0.05	0.05 degree/second
Hysteresis	0.05	0.05 degree/second
Resolution	0.05	0.05 degree/second
Linear Range	± 500	± 700 degrees/second
Response	flat to 1000 radians/second	not tested
Noise	2% Full scale	none measured
Scale Factor	-	0.0011 mmHg/degree/second

Environmental Tests

The results of the environmental tests are summarized as follows:

- a. Temperature - For a temperature increase from 65°F to 315°F, there was a decrease in the LARS and gain block scale factor of 2.75. There was no temperature compensation in this LARS design.
- b. Acoustic Sensitivity - For the noise levels from 30 to 85 dB and the acoustic frequencies of 5 to 20K hertz, there was no measured effect on the LARS and gain block output signal when the vents were shielded.
- c. Vibration Sensitivity - The LARS and gain block were unaffected by vibrations of 0.5g at frequencies from 40 to 1000 hertz.

IV. PHASE III RESULTS

In this Phase, the basic LARS, the 3-stage laminar gain block, and a vent manifold were integrated into a prototype LARS package. This LARS package was then subjected to a complete evaluation and test program.

IV-1. TASK A - PERFORMANCE STUDIES

Optimum Supply Pressure

Both an analytical and test program were performed to determine the optimum supply pressure to each element in the LARS assembly. The supply pressure to the last stage amplifier was determined at 7.5 mmHg and the supply pressures to the other elements were orificed from this level to the optimum pressure.

Threshold Test - The LARS threshold test was conducted at NASA Langley. The measured threshold of the LARS was 0.04 degree/second using a Datametrix Pressure Transducing System.

Linear Range and Scale Factor Test - The linear range and scale factor of the LARS was measured on a Genisco rate table with a Kaman-Nuclear K-1100 Digi-Vit Pressure Readout. The measured linear range was 600 degrees/second with a scale factor of 0.0005 mmHg/degree/second. The linearity was within 2 percent of full scale.

Signal to Noise Ratio - The Signal to Noise Ratio (S/N) was measured using a Datametrix Pressure Transducing System. The electronic noise level (the noise level measured with the LARS turned off) was equivalent to a 0.4-degree/second peak-to-peak signal level. When the LARS was turned on, there was no change in the signal level as measured on an oscilloscope.

Frequency Response Tests - The LARS was mounted on an oscillating table and the oscillating table rate of turn was measured against the output of the LARS. The input frequency was varied from 20 to 250 hertz at a constant amplitude. The results of the tests were recorded on oscilloscope traces. The measured frequency response of the LARS with the gain block was flat to 100 hertz and was down 3 dB with a 90-degree phase shift at 150 hertz.

Transport Lag - The transport lag (pure time delay) of the LARS was determined by applying an impact acceleration to the oscillating table and measuring the time from impact to the first change in LARS output signal. This pure time delay was measured at 1.68 milliseconds.

IV-2. TASK B - SENSITIVITY STUDIES

Effects of Supply Pressure

It should be obvious by this time that the operating characteristics of the LARS are affected by the supply pressure level. A qualitative description of some of the effects of the supply pressure on the LARS performance characteristics is given below:

- a. Linear Range - Decreasing the supply pressure to the LARS gave an increase in linear range, and an increase in supply pressure gave a decrease in linear range (increase was limited to laminar flow range). No concise relationship between these two parameters was found but a combination of LARS gain and maximum pressure recovery appears to be the controlling factor.
- b. Noise - The output noise level remained below the sensitivity of the pressure transducer until turbulent flow was obtained. Then the output noise level increased with increasing supply pressure.
- c. Scale Factor - The scale factor (change in differential output pressure versus rate of turn) varied proportionally to the change in supply pressure. This relationship only holds in the laminar flow region.
- d. Null Uncertainty - The measured null output (differential output pressure versus supply pressure at zero rate of turn) behaved in a rather unpredictable manner.

Effects of Temperature

The performance of the LARS versus temperature variations was measured. Both an uncompensated and a temperature compensated (small orifice located upstream of the laminar supply nozzle) were tested with only scale factor and null variations being recorded.

- a. Scale Factor - When the temperature on the uncompensated LARS was varied from 65°F to 315°F, the scale factor dropped to 30 percent of its value at 65°F. When the above test was performed on the temperature compensated unit, the scale factor dropped to only 85 percent of its value at 65°F. Analysis showed that improvements could be made in the temperature compensation circuit and these improvements should maintain the scale to 95 percent of its 65°F value.
- b. Null Uncertainty - The temperature caused the null signal level to vary in both the uncompensated and compensated models. However, no precise relationship could be found.

IV-3. TASK C - NOISE INVESTIGATION

Two models were tested for acoustic noise sensitivity (see Figure 12). The first model had the vents of the rate sensor and gain block open to the ambient. The second model had all the vents captured in a manifold and then the vent flow exited through an orifice to ambient. The acoustic frequency was varied from 10 to 20,000 hertz at an average sound intensity of 105 dB. The first model had output signal levels equivalent to a 500 degrees/second rate of turn when the acoustic frequency was between 1400 to 2600 hertz, and had small output fluctuations (< 25 degrees/second) when the acoustic frequency was around 100 hertz. The second model had no measurable effects on its output signal through the complete test range.

IV-4. TASK D - SHOCK AND VIBRATION TESTS

The second model of the LARS with all the vents captured in a manifold was subjected to both vibration and shock.

Vibration

The LARS was subjected to the vibration test procedure detailed in MIL-STD-810B for equipment installed in air launched missiles. Resonance search, resonance dwell, and sinusoidal cycling were performed in all three axes. These tests showed that the LARS is unaffected by the above vibration levels.

Shock

Two LARS units were mounted on a bulkhead with their longitudinal axes rotated 90 degrees with respect to each other. An explosive charge was detonated which applied 12,500 g's to the LARS units. The functional tests performed on the LARS after the shock tests indicated that there was no apparent damage to the LARS.

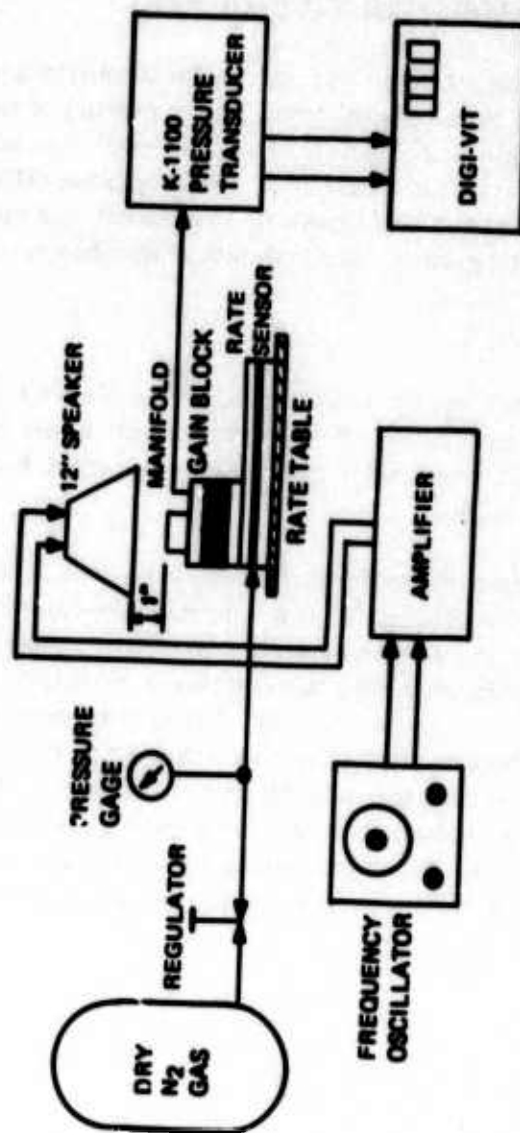


Figure 12. Noise Investigation Test Schematic

V. PHASE IV RESULTS

The main objectives of this phase were to (1) develop an optimum laminar proportional amplifier, (2) develop techniques and procedures for staging the laminar proportional amplifiers to obtain the desired gain block performance, and (3) optimize the design and fabrication of the rate sensor/gain block package to obtain a prototype LARS design with the desired operating performance.

V-1. TASK A - LAMINAR AMPLIFIER DEVELOPMENT

At the end of the LARS Phase III program, the major problem area to be solved was to greatly increase the output signal level (scale factor) of the LARS. Almost two orders of magnitude were desired over the level that was available with the 3-stage gain block used in Phase III. The stageable differential pressure gain of the amplifier used in the Phase III gain block was approximately 4. Therefore, it was desired to greatly increase this stageable gain.

Amplifier Test Results

Each of 10 amplifiers (2 each of the 5 different designs shown in Figure 13) was submitted to a differential pressure test. A comparison of the test results is shown in Table VI. The test results are given at the optimum bias level, supply pressure and aspect ratio (0.6).

After reviewing the data from the differential pressure test (Table VI), amplifier designs (B) and (C) were eliminated from further consideration because of their low stageable gain, i.e., too many stages to obtain required gain. (Note: Designs (B) and (C) incorporated a long narrow power nozzle.) When these amplifiers with the long power nozzle were subjected to maximum supply pressure test, they did remain laminar to higher Reynolds Numbers than the other designs. However, it appears that the velocity profile obtained at the exit of this type of power nozzle is not conducive to obtaining good gain using standard receiver designs. The test data on the remaining three designs was comprehensively reviewed and a comparison of the following major performance goals was made:

- a. Pressure gain
- b. Linearity
- c. Maximum linear range (function of pressure recovery and maximum supply pressure for laminar flow)
- d. Ease of fabrication (simplicity of design)
- e. Saturation characteristics



Figure 13. Amplifier Laminates

- f. Gain variations (as function of bias level, supply pressure, and output loading).

TABLE VI. AMPLIFIER TEST RESULTS

<u>Design</u>	<u>Maximum Block Load Pressure Gain</u>	<u>Maximum Stageable Pressure Gain</u>
(A)	7.5	6
(B)	5	4
(C)	4	2.5
(D)	13	10
(E)	8	5.5

Table VII gives a tabulated comparison of the three designs against the above performance criteria.

TABLE VII. PERFORMANCE CRITERIA COMPARISON

	<u>Design No. (A)</u>	<u>Design No. (D)</u>	<u>Design No. (E)</u>
Pressure Gain	Fair	Excellent	Fair
Linearity	Good	Poor	Fair
Maximum Range	Good	Good	Fair
Ease of Fabrication	Good	Good	Poor
Saturation	Poor	Excellent	Excellent
Gain Variations	Fair	Poor	Good

In reviewing the above table, no amplifier design becomes a clear cut choice as the one with the outstanding performance characteristics. However, the following general comments could be made about all three designs:

- a. The best stageable gain with minimal output noise is obtained when the amplifier is operated at the highest possible supply pressure without going turbulent.

- b. The maximum stageable gain is obtained at very low input bias levels. However, if the bias level gets too low, the maximum operating supply pressure is reduced.
- c. Equal amplifier gain for each design can be obtained at each aspect ratio tested at a corresponding supply pressure to maintain a fixed Reynolds Number. This was true for aspect ratios from 0.4 to 2.
- d. Higher amplifier gains are obtainable when the output load is less than one nozzle (i.e., the load approaches a blocked load condition). However, since there are no vents in the output legs, the amplifier tends toward instability at loads less than one nozzle.

Because of the high gain required by the gain block, design (D) was chosen for gain block tests because of its high stageable gain.

V-2. TASK B - STAGING TECHNIQUES

The purpose of this task was to optimize the performance of a 3-stage gain block with respect to gain, linearity, noise, and saturation. It was further desired to determine a method of predicting the expected performance of each amplifier design when interconnected into a gain block.

Gain Block Results

Keeping the above performance criteria in mind, a series of 3-stage gain blocks using amplifier design (D) were tested with various aspect ratio amplifiers for each stage. The gain blocks were made up of single stage amplifiers which were tubed together using soft wall tubing. The test configuration is shown in Figure 14. However, the test data obtained was poor and not repeatable. The poor results were due to: a) signal noise being generated by the interconnections, b) the interconnecting tubing getting bent or pinched, and c) failure to use the exact same piece of tube on the exact same connection points. Therefore, a special test manifold was designed to test the three-stage gain block coupled with the rate sensor in a "semi-integrated" package. Several different three-stage configurations were tested including the following aspect ratio combinations: a) 0.8, 0.6, 0.4, b) 0.4, 0.4, 0.4, c) 0.6, 0.6, 0.4, d) 0.6, 0.4, 0.4.

Table VIII gives the parameters of one of the better performing three-stage gain block configurations.

Pressure gains as high as 1000 were obtained for a 3-stage gain blocks but the gain was very sensitive to bias level and supply pressure to each stage. Gains of 550 to 610 were obtained fairly repeatably with a minimum sensitivity of the gain to input bias level and supply pressure variations. Signal to noise ratios of greater than 2000 were measured with the above configuration. The test instrumentation was the limiting factor for measuring better signal to noise

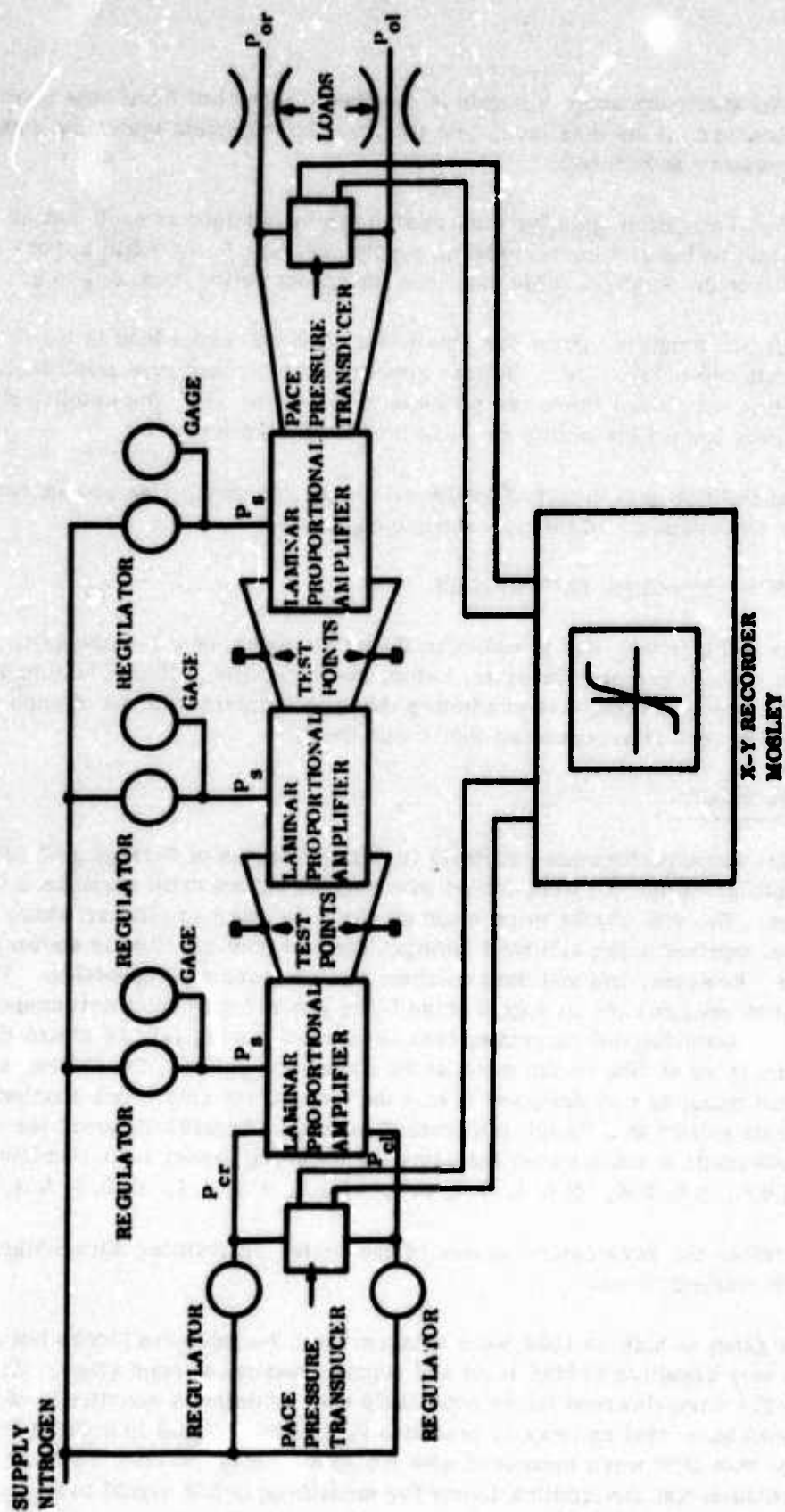


Figure 14. Test Setup - Three-Stage Gain Block

TABLE VIII. 3-STAGE GAIN BLOCK TEST RESULTS

	<u>Aspect Ratio</u>	<u>Supply Pressure</u>	<u>Bias Level From Sensor Rate</u>	<u>Output Load</u>	<u>Differential Pressure Gain</u>
Stage 1	0.6	8 mm Hg	1%		
Stage 2	0.6	20 mm Hg			
Stage 3	0.4	90 mm Hg		0.02"x0.01" Nozzle	610

ratios. During this test, supply pressures to each stage were independently regulated and the vents of each amplifier stage were individually bled unrestricted to the ambient. With the unrestricted vents, the 3-stage gain block was extremely sensitive to acoustic noise. Care had to be taken in keeping the room in which the tests were performed free of extraneous noise and room drafts.

The two other basic amplifier designs (A) and (E) were also tested in the 3-stage manifold similar to the procedure used to evaluate amplifier (D) described above. Design (E) is the standard GE-SFO design in an integrated configuration. This design had been used in Phase III with unity aspect ratio amplifiers in a vertically stacked arrangement. In this phase, the tests were performed using 0.4 and 0.6 aspect ratio amplifiers. The results showed that the 3-stage amplifier had a blocked load gain of 110 to 125 for both the aspect ratio 0.4 and 0.6 when it was operated in the laminar flow region (12 mmHg). Since this was substantially lower than amplifier (D), no further work was performed on this design during this phase of the contract. The final amplifier design that was tested was design (A). The basic amplifier had good blocked load pressure gain but when it was interconnected into the 3-stage gain block, very poor pressure gain resulted. By decreasing the aspect ratio for each downstream stage (increasing input impedance), results similar to the GE-SFO amplifier gain block were obtained. However, this device is much larger and more difficult to fabricate.

Gain Block Conclusions

At the end of the gain block tests, the following performance features of the (D) amplifier in a staged configuration were found:

- a. Very high pressure gain
- b. Relatively easy to fabricate by metal etch process

- c. Very high signal to noise ratio
- d. Very good saturation characteristics
- e. Overall pressure gain very sensitive to supply pressures to each stage

In spite of the supply pressure problem (which was not considered severe), this amplifier design was selected as the one to be used in the integrated Laminar Angular Rate Sensor (LARS). This amplifier design was based on a design submitted to GE-RESO by NASA Langley.

V-3. TASK C - LARS DESIGN OPTIMIZATION

During the Phase III effort, a breadboard laminar angular rate sensor and 3-stage gain block was designed, fabricated, and tested. This LARS is shown in Figure 15. In this Phase IV task, a prototype LARS, using the latest rate sensor and proportional amplifier designs, was to be fabricated and tested. This prototype LARS was to meet the rate sensor performance requirements (Table IX) which were specified for the three fluidic control systems which were under development at GE-RESO.

TABLE IX. SENSOR PERFORMANCE REQUIREMENTS

	Roll Rate Control for Advanced Navy Missiles	Roll Rate Control for High Acceleration Guided Missiles	Three Axis Autopilot for Advanced Navy Missiles
Scale Factor	0.04 mm Hg/deg/ sec	0.6 mm Hg/deg/ sec	0.04 mm Hg/ deg/sec
Linear Range	250 deg/sec	500 deg/sec	200 deg/sec
Frequency Response	500 rad/sec	1000 rad/sec	400 rad/sec
Threshold	2 deg/sec	0.5 deg/sec	0.1 deg/sec
Signal to Noise Ratio	100	500	20
Linearity	10%	5%	5%
Transport Lag	2 msec	2 msec	2 msec

Basic Rate Sensor Design

From Table IX the pressure gain requirement for a gain block coupled with the rate sensor developed in Phases I, II and III was as high as 75,000. Since the ability to obtain gains of this magnitude was deemed impossible in practical applications, an investigation was performed to increase the basic rate sensor

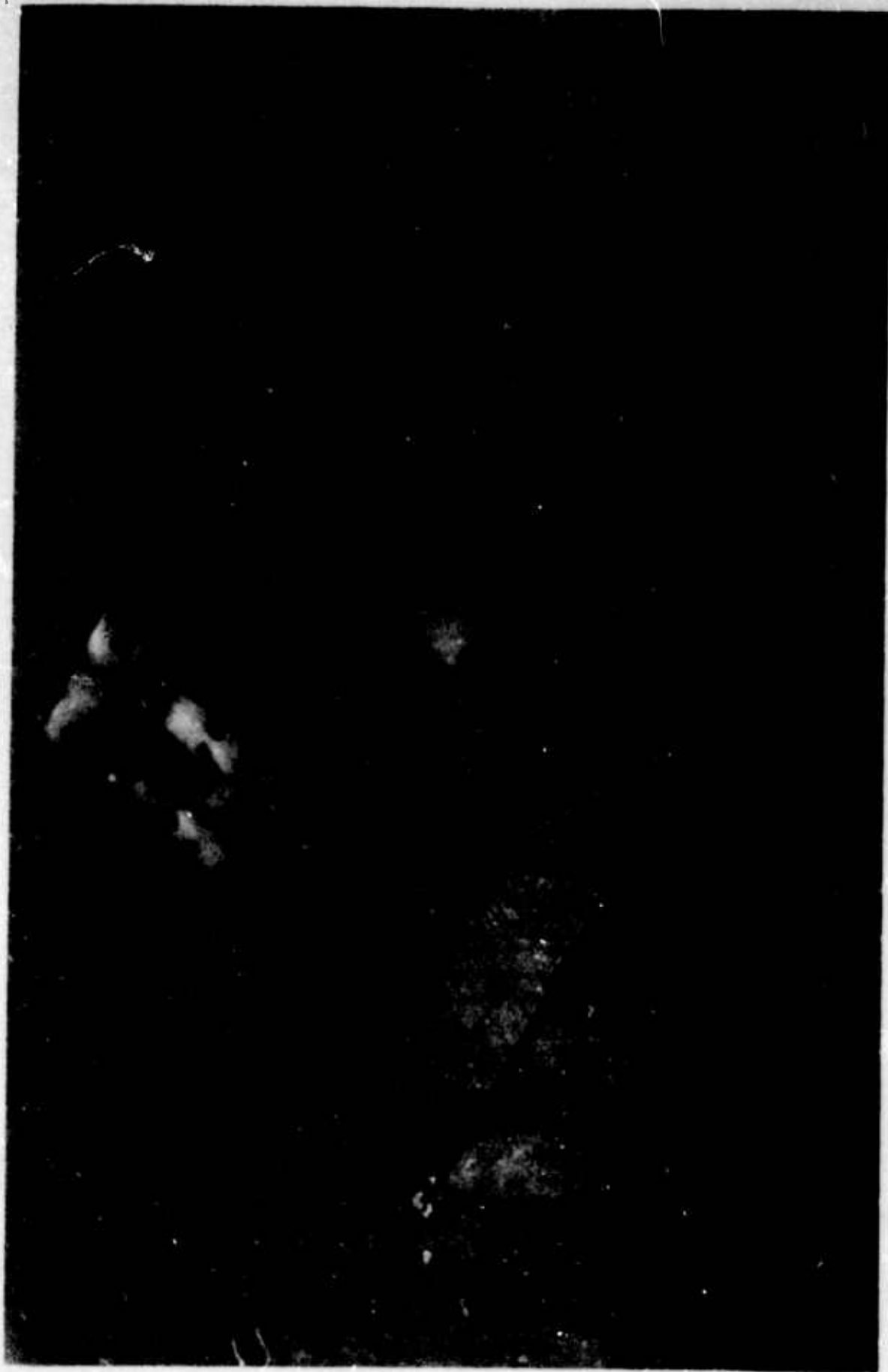


Figure 15. Original Rate Sensor Design

scale factor. The two main areas of this investigation were: 1) the effects of aspect ratio (AR), and 2) the effects of power nozzle and receiver design.

Aspect Ratio - During the previous three phases, the basic rate sensor was tested from aspect ratios of 1 to 3. To the best of the author's knowledge, aspect ratios of less than 1 were never tested. Therefore, an investigation was performed to determine the effect of aspect ratio on the rate sensor performance. The results of the tests are given in Table X.

TABLE X. TEST RESULTS - ASPECT RATIO VERSUS SCALE FACTOR

<u>Ratio Sensor Aspect Ratio</u>	<u>Scale Factor (mm Hg/deg/sec) (Blocked Loaded)</u>	<u>Linear Range (deg/sec)</u>
1 (original design)	8×10^{-6}	250
0.6	2×10^{-4}	700
0.4	4×10^{-4}	1000

An additional advantage of a lower aspect ratio sensor is a greatly increased speed of response. The reason for the increased response is due mainly to the increased power jet velocity at the much higher supply pressures used with the lower aspect ratios. A complete series of tests was performed to compare the performance data of the original rate sensor to the low aspect ratio units. The hysteresis, threshold, noise level, null drift, saturation, etc. of the low aspect ratio units were equal to or better than the original unit, except in one case. That is, from unit to unit, the effect of supply pressure variation on output pressure null was more severe for the lower aspect ratios.

Power Nozzle and Receiver Design - HDL had performed several tests on power nozzle and receiver designs - including the measurement of velocity profiles and the effects of nozzle and receiver design on amplifier gain. Based on these tests, HDL made the following recommendations to GE-RESO:

- a. To obtain the best amplifier gain for laminar flow amplifiers, use a short power nozzle.
- b. Better overall results will be obtained with a receiver design which does not use a center vent.

Therefore, it was decided to test amplifier design (D) as a laminar rate sensor. The rate sensor scale factor was 6×10^{-4} mm Hg/degree/second at an aspect ratio of 0.4. Also, the time delay was reduced from that measured for the original rate sensor because the receiver is only half as far from the power nozzle.

A much desired additional feature of this design when used as a rate sensor is the inclusion of control ports. The old rate sensor design had the disadvantage that it could not be trimmed. That is, the differential output pressure could not be nulled to zero for zero rates of rotation after the rate sensor had been assembled. In theory, this is not a problem. However, due to the practical limitations of the fabrication process, an inherent offset almost always exists and it is very difficult and time consuming to eliminate this offset by restacking and re-aligning the laminates. The addition of the control ports allows a differential pressure to be applied across the power jet to center it. This can be accomplished by bringing an external pressure into the ports or by placing an orifice between the control port and ambient (vent) pressure. For the Phase IV program, the orifice method was employed. Now the rate sensor can be assembled and adjusted to zero at any supply pressure.

The output of this task was to select a 0.6 aspect ratio, (D) amplifier design with a short supply nozzle and trim ports to perform the rate sensing function. The scale factor of this rate sensor design into a blocked load was 4×10^{-4} mm Hg/degree/second.

Laminar Gain Block Design

An integrated 3-stage gain block assembly was designed. This integrated assembly incorporated the 3-stage amplifier gain block developed in Section V-2 and detailed in Table VIII. Designed into this assembly was a common supply manifold and common vent plenum. The supply manifold used orifices to drop the manifold pressure to the level required by each amplifier. The vent plenum was used to capture all the vent flows from the rate sensor and amplifiers. The vent flow then passed through an orifice to ambient pressure. Capturing the vents "decoupled" the ambient variations from the performance of the LARS. The rate sensor and three stages of amplifiers were assembled in the integrated package and the package was tested. The tests showed a high noise level (≈ 20 degrees/second equivalent signal level) on the output of the LARS. Therefore, the LARS was disassembled and the amplifiers were placed in the test fixture used in Section V-2. The performance of the gain block exceeded the performance of the gain block described in Section V-2. The basic rate sensor was interconnected to the gain block and this package was tested. The performance of this package met the desired LARS performance including noise level (remember that each supply pressure and each vent were now independent). These components were then re-assembled into the integrated LARS package. The same high noise level problem existed. Several attempts were made to correct this problem by either modifying the vent plenum or changing the supply pressure to one or more of the amplifiers by changing the orifice size. Changing the vent plenum design had little effect unless the vents of the amplifiers were open to ambient. Then the noise level was substantially reduced but the LARS was very sensitive to ambient noise. Changing the supply pressures either (1) had little effect or (2) greatly reduced the noise level at a severe penalty of gain such that the LARS scale factor was unacceptable. The

reasons for the above noise problem were not found because every time we disassembled an integrated LARS and tested the components in the test fixture the unit worked fine. This same unit would not work in an integrated package and we were unable to instrument these packages.

Because of time and funding constraints, a new integrated LARS package was designed which incorporated the amplifier (D) design used as the rate sensor, one stage of amplifier (D) used a laminar proportional amplifier, and the amplifier (E) used as a laminar 3-stage gain block. The object of the new design was (1) to have separate vent plenums for the rate sensor and gain block and (2) to attempt to isolate the supply of the rate sensor from the gain block by redesigning the supply pressure manifold. Because of the design of the laminates and the desirability to "decouple" the vents of the rate sensor from the gain block, the rate sensor vents could not be internally shielded from the ambient. Therefore, a special metal shield was made and the 200-degree/second and 25-degree/second models were tested with this shield.

LARS Test Setup

Three models of the LARS were developed during this effort. The three models had a linear range of either 1000 degrees/second, 200 degrees/second or 25 degrees/second and are all similar to the unit shown in Figure 16. Tests were performed on each of the models to determine the following performance characteristics:

- a. Hysteresis
- b. Threshold
- c. Scale Factor
- d. Noise Level
- e. Linear Range
- f. Linearity
- g. Saturation Characteristics
- h. Null Drift
- i. Repeatable Null

Figure 17 shows the test setup for measuring d and h. The supply pressure was set and monitored. The tank was used to filter any noise in the supply line. Figure 18 shows the test setup for measuring the additional data listed above. Photographs of the setup are shown in Figure 19. Several problem areas were encountered in this test setup. In many cases, the test instrumentation limited our capability to determine the parameter of interest. Therefore, several parameters are given as "Limited By Test Equipment". This means that the parameter of interest is better than that stated. How much better could not be determined. The problem areas in this test setup were:



Figure 16. Fluidic Rate Sensor

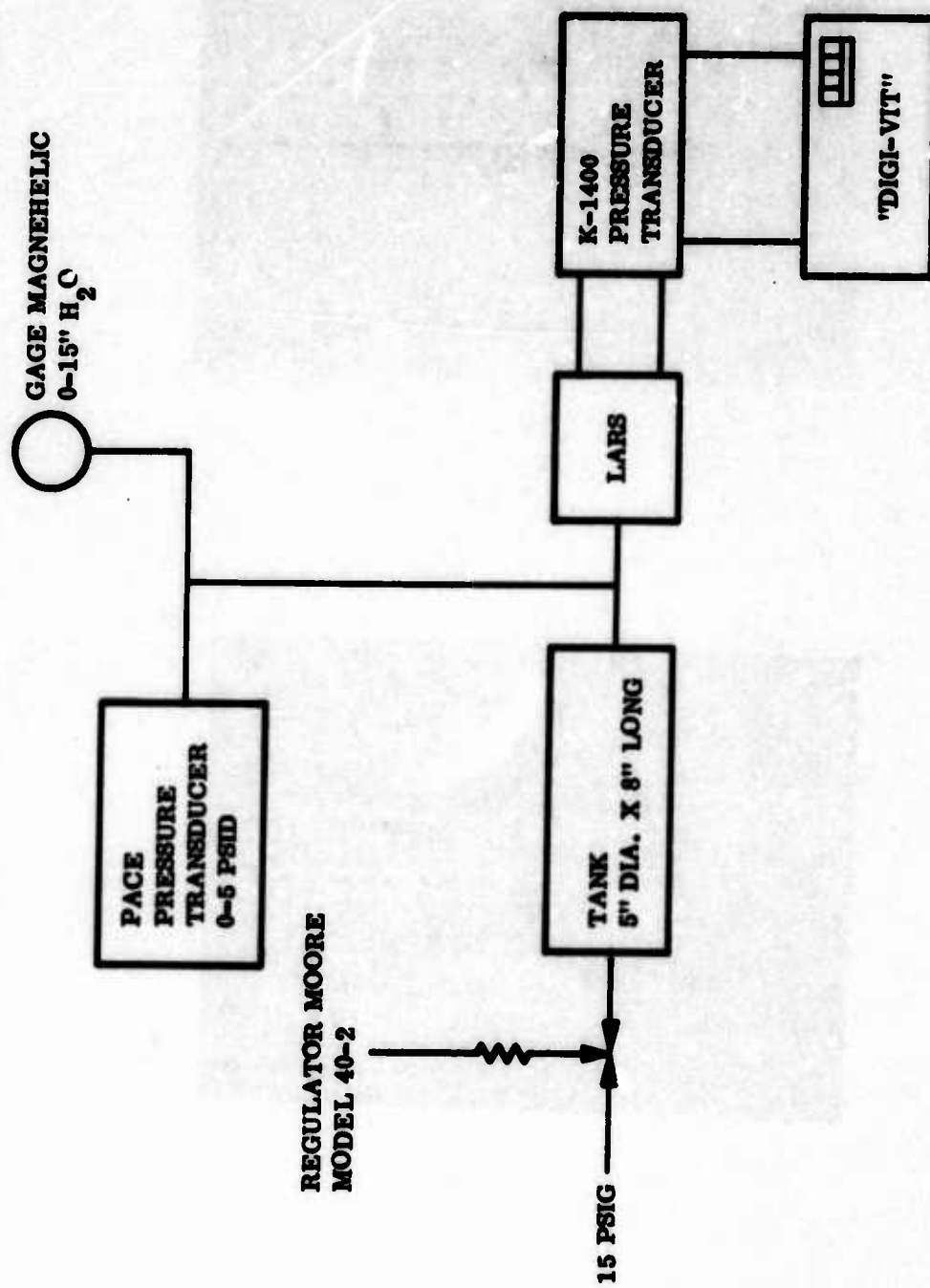


Figure 17. Test Setup - LARS Output Characteristics

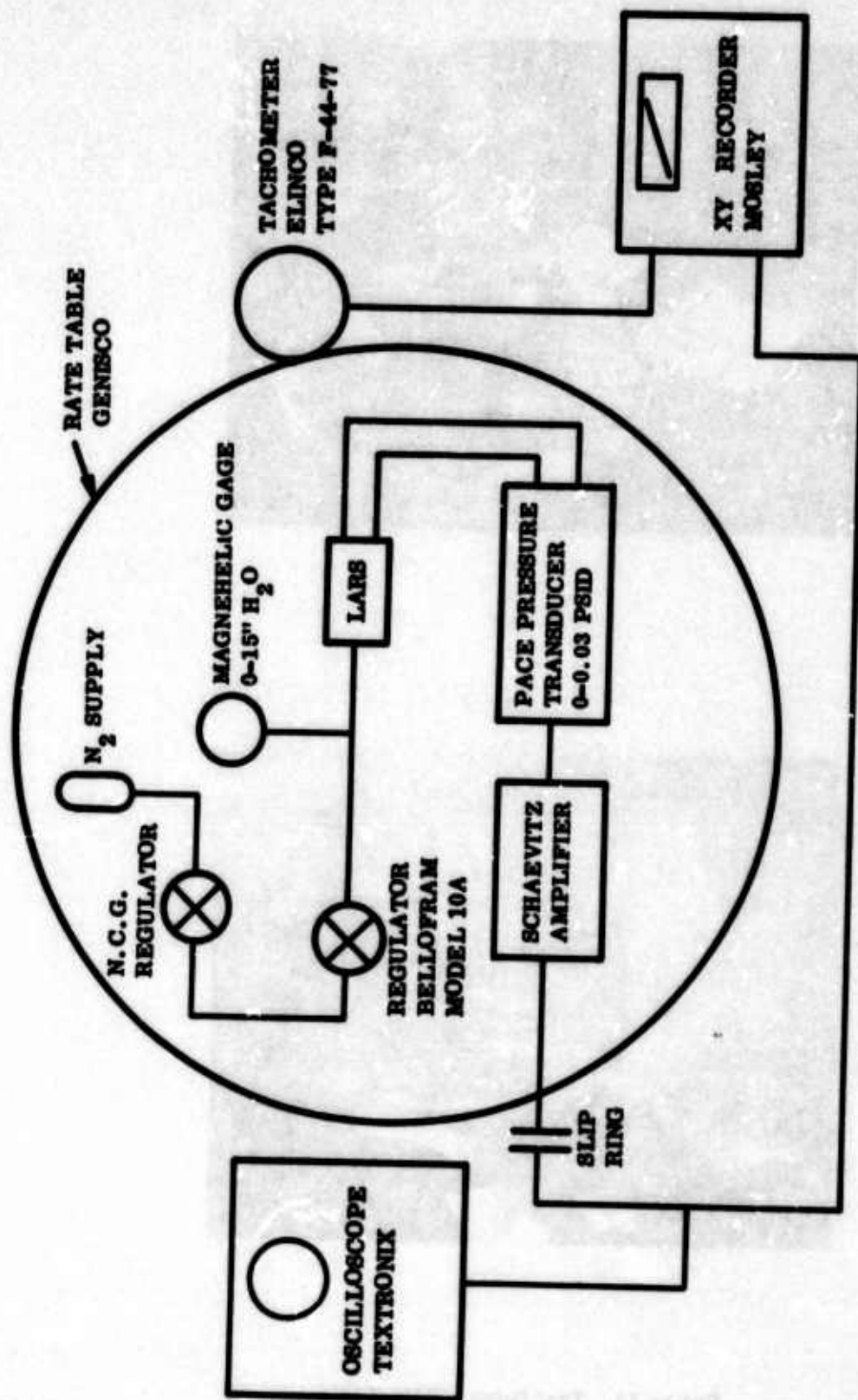


Figure 18. Test Setup Diagram - Rate Table



Figure 19. Test Setup - Rate Table

- a. Rates of less than 0.5 degree/second could not be measured. This was limited by both the tachometer and rate table.
- b. The linearity of the tachometer was approximately ± 10 percent. Two tachometers had been purchased and the one used was the better of the two.
- c. The tachometer was linear to 1000 degrees/second clockwise but only 200 degrees/second counter clockwise. Several tests were performed with this tachometer in this condition before it could be repaired.
- d. The pressure transducer had a minimum sensing capability of 0.001 mm Hg pressure differential. Pressure levels of at least an order of magnitude lower than that are needed for the threshold tests.
- e. The frequency response of the transducer is limited to 100 radians/second.
- f. A stored-gas, blow-down system was used as the air supply to the LARS. This gas system allowed tests of only a short duration (≈ 30 minutes) and caused supply pressure variations to the LARS.
- g. Due to the rate table slip rings, the electronic noise was appreciable.

Test Results of the 1000-Degree/Second Model

The test results of the 1000 degree/second model are given in Table XI. The results given are the average of the three units tested.

TABLE XI. PERFORMANCE - 1000-DEGREE/SECOND MODEL

Supply Pressure	13 mm Hg
Threshold	$< 0.5 \text{ deg/sec}^*$
Scale Factor	$\approx 0.0015 \text{ mm Hg/deg/sec}$
Hysteresis	$\approx 0.5 \text{ deg/sec}^*$
Linearity	10%
Linear Range	$< 1000 \text{ deg/sec}^*$
Noise Level	0.5 deg/sec* (Noise Measured)
Null Repeatability	1 deg/sec
Trim	0.5 deg/sec*

*The numbers given are the best capability of the test equipment. The actual LARS performance numbers could not be measured but are better than those given.

During the tests the following LARS performance was observed by the author:

- a. The design of the vent plenum successfully isolated the LARS from ambient conditions.
- b. The unit was easily trimmed. However, if the trim set screw was accidentally "bottomed", the LARS could not be trimmed because of damage to the trim mechanism.

Test Results of the 200-Degree/Second Model

The test results of the 200-degree/second model are given in Table XII. The results given are the average of the three units tested.

TABLE XII. PERFORMANCE - 200-DEGREE/SECOND MODEL

Supply Pressure	12 mm Hg
Threshold	0.5 deg/sec*
Scale Factor	0.015 mm Hg/deg/sec
Hysteresis	0.5 deg/sec
Linearity	10%*
Linear Range	200 deg/sec
Noise Level	0.5 deg/sec peak to peak
Null Repeatability	0.5 deg/sec
Trim	0.05 deg/sec

*See Table VII

During the tests, the following LARS performance was observed by the author.

- a. The null adjustment was difficult. The pitch of the threads of the set-screw must be changed for the higher sensitivity LARS units.
- b. Because of the redesign of the vent plenum, the LARS was now sensitive to ambient air disturbance unless the specially designed shield was used.

Test Results of the 25-Degree/Second Model

The test results of the 25-degree/second model are given in Table XIII. The results given are the average of the three units tested.

TABLE XIII. PERFORMANCE - 25-DEGREE/SECOND MODEL

Supply Pressure	12 mm Hg
Threshold	0.5 deg/sec*
Scale Factor	0.05 mm Hg/deg/sec
Hysteresis	0.5 deg/sec
Linearity	10%
Linear Range	50 deg/sec
Noise Level	1 deg/sec
Null Repeatability	2 deg/sec

*See Table XI.

During the tests, the following LARS performance was observed by the author.

- a. The null adjustment problem was the same as the 200 degree/second model.
- b. The basic unit was very sensitive to ambient air disturbances. This was due to the rate sensor vents being open to the ambient. These vents had to be enclosed using a specially designed shield to perform the tests.
- c. The zero null condition was difficult to maintain during these tests. Supply pressure variations of 0.1 percent were enough to cause measurable changes in the null signal.

The results showed that the LARS exhibits excellent performance in the areas of threshold, linearity, hysteresis, noise, etc. However, two problem areas existed in this rate sensor design which would limit the use of the rate sensor in control systems. The first problem was that the scale factor (rate sensor output versus rate of turn) had excessive variations with supply pressure and/or environmental variations (Figure 20). The second problem was the null signal level (output signal with zero rotation) varied outside acceptable limits with supply pressure and/or environmental variations (Figure 21).

It was believed that the above two problems were caused mainly by the photo etch fabrication process which was employed to make the LARS. However, a program to evaluate the effects of fabrication on the above problems was not performed prior to the end of the above phase on the prototype LARS units. Since evaluation of the original prototype LARS units, an investigation into the effects of the fabrication process on the above two problem areas has been performed. The test results showed that the variations in scale factor and null signal level with variations in supply pressure and/or environmental conditions

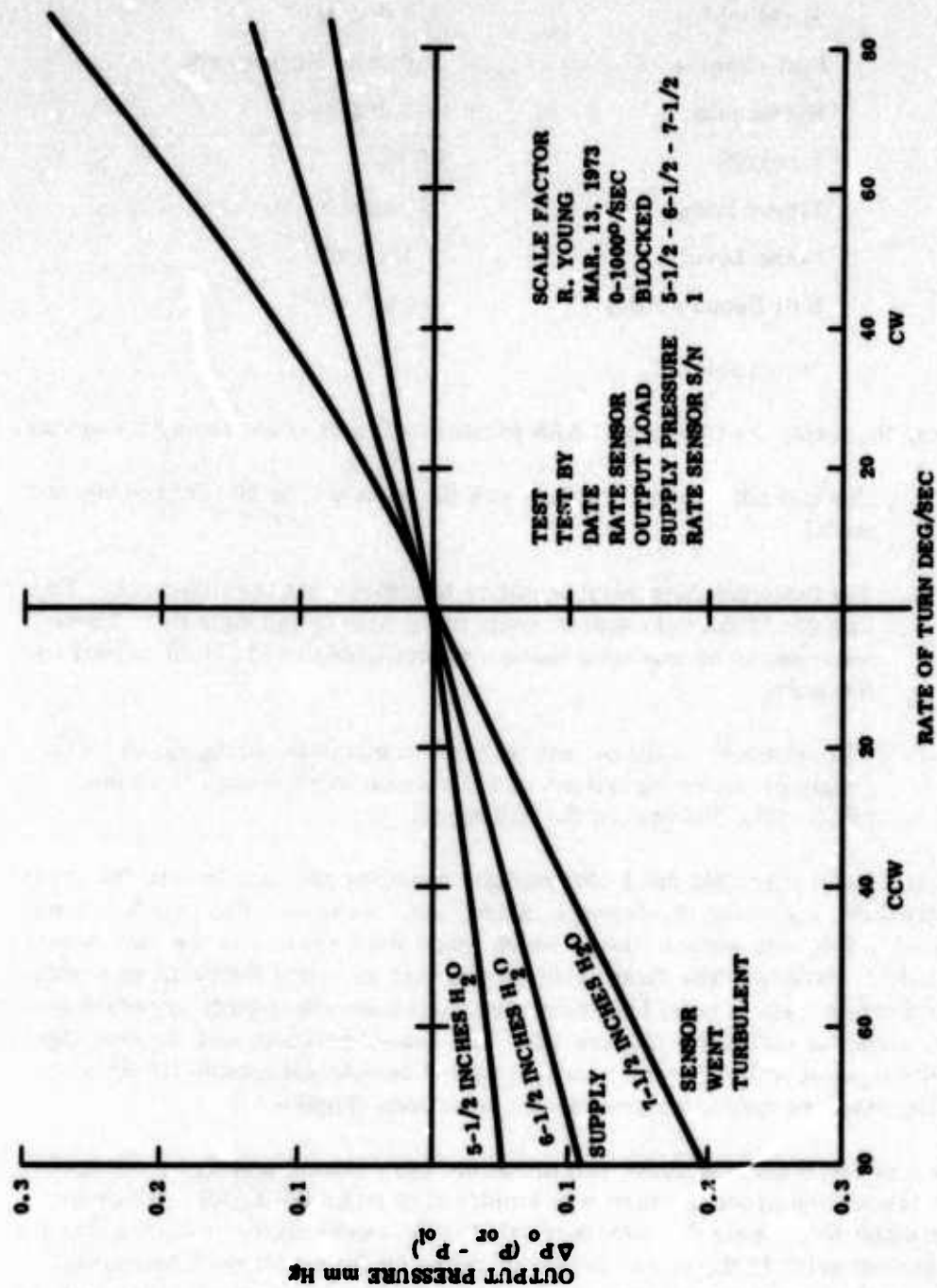


Figure 20. Scale Factor Test - 0 to 1000 Degree/Second Model

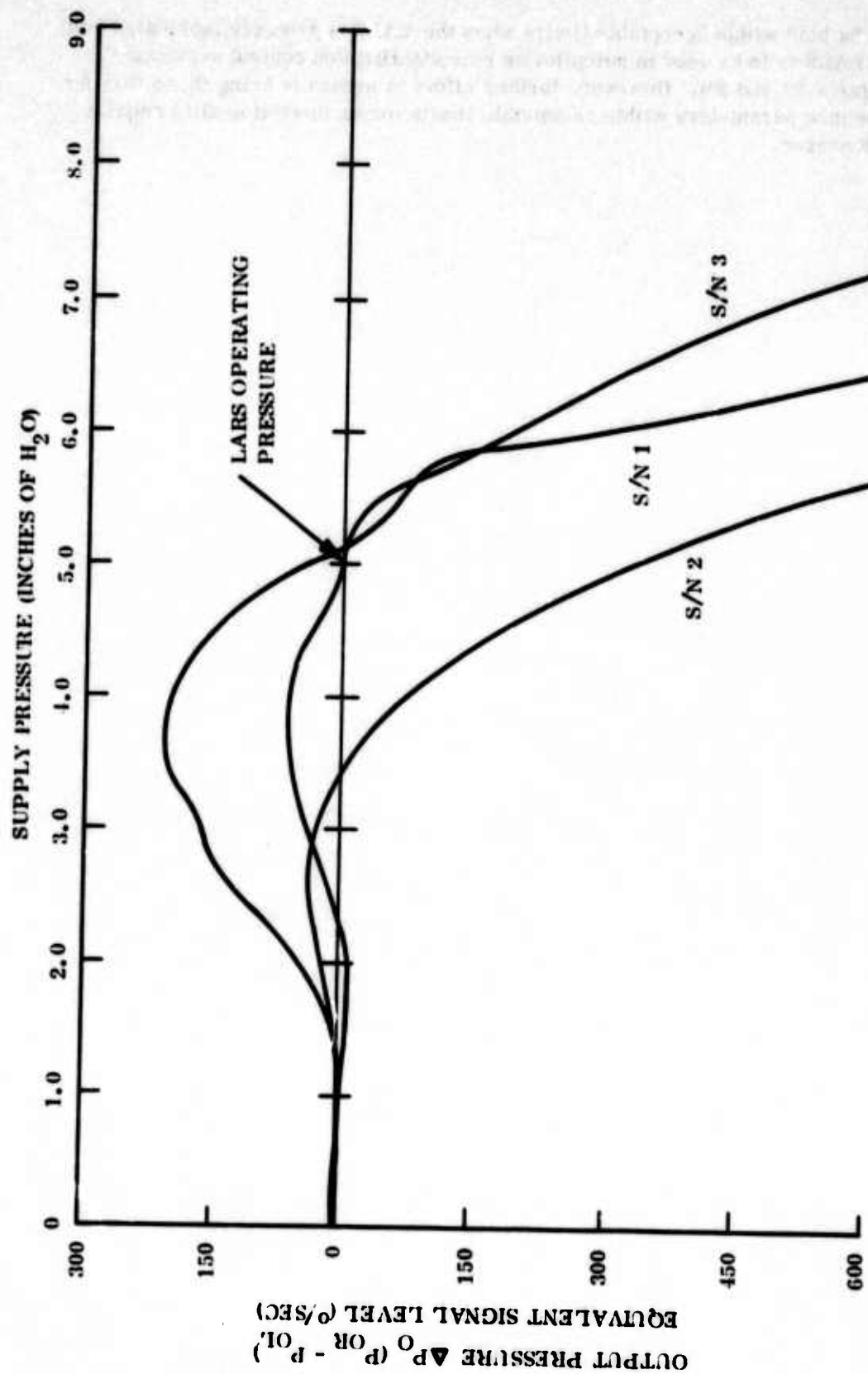


Figure 21. Graph of Zero Rate Error as a Function of Supply Pressure for 1000-Degree/Second Model LARS (Original Fabrication)

can be held within acceptable limits when the LARS is properly fabricated and the LARS is to be used in autopilot or rate stabilization control systems (Figures 22 and 23). However, further effort is needed to bring these two performance parameters within acceptable limits for an inertial quality angular rate sensor.

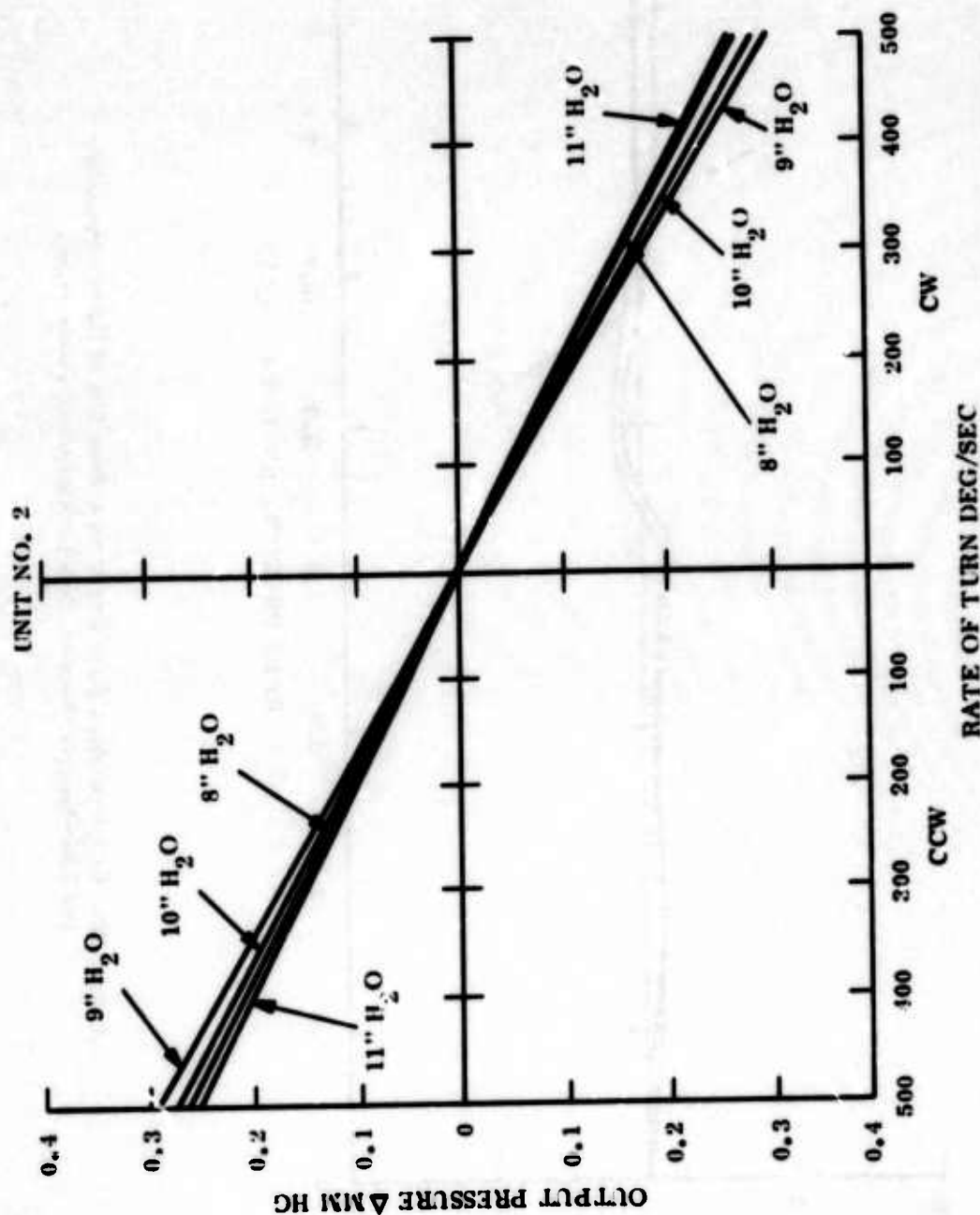


Figure 22. Graph of Differential Output Pressure versus Rate of Turn for 1000-Degree/Second Model LARS (with Small Diameter Supply Tube and Various Supply Pressures)

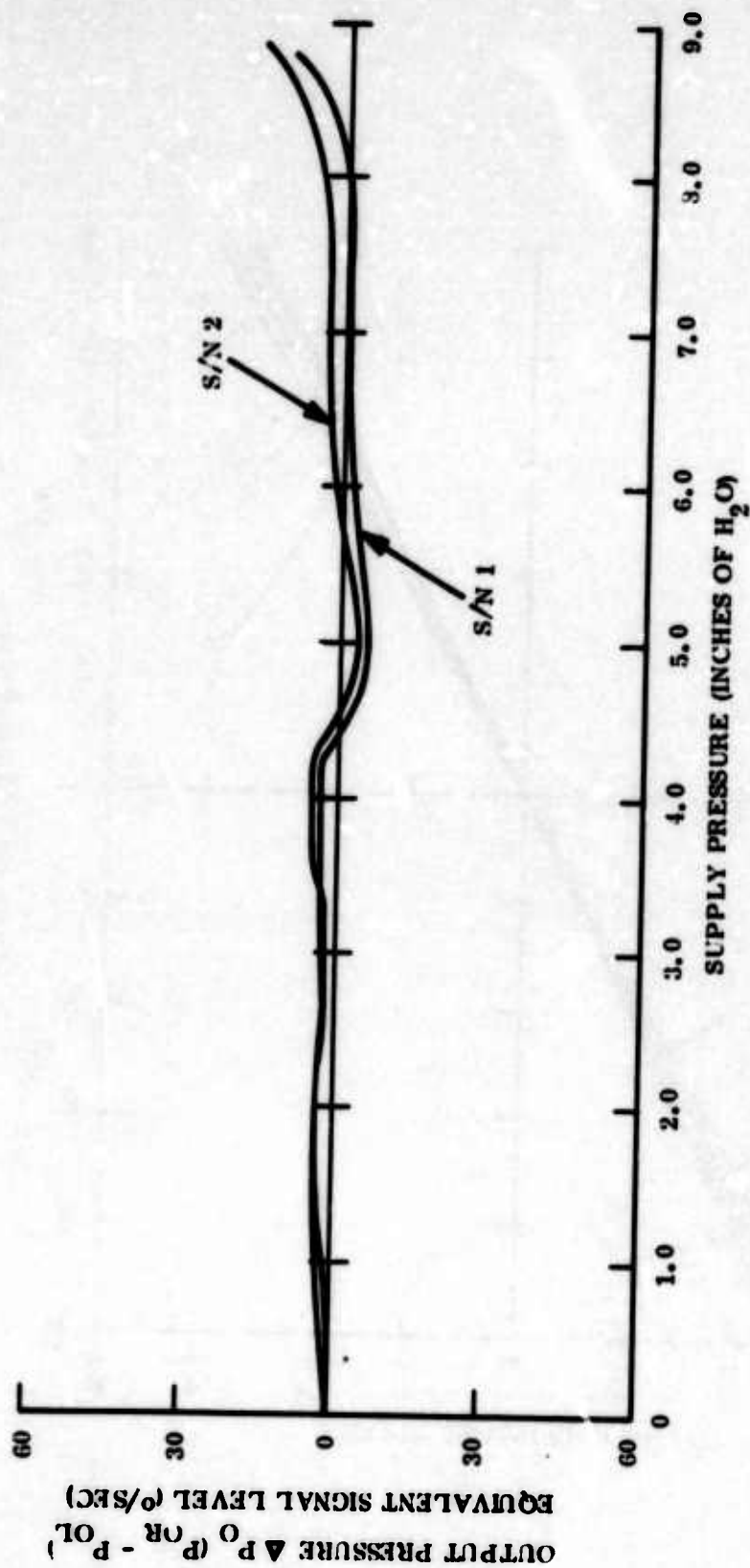


Figure 23. Graph of Zero Rate Error as a Function of Supply Pressure for 1000-Degree/Second Model LARS (New Fabrication)

VI. SUMMARY

To date, the previous effort has been to demonstrate the feasibility of a Laminar Angular Rate Sensor (LARS). GE-RESO performed several tasks to analyze, design, fabricate, test, and evaluate several models of a LARS. Analytical models, water table models, and actual prototype models have been employed to correlate anticipated performance with actual test data. Good correlation was obtained between theoretical analysis and actual test data for performance at both standard conditions and for selected environments. Power nozzle/receiver design, aspect ratio, and the fabrication process were determined to be the three most important parameters affecting the sensor performance and its sensitivities to environmental variations. The LARS has demonstrated itself to be a suitable device for use in rate stabilization type control systems.

The projected next step in the development of a Laminar Angular Rate Sensor package is to fabricate, test, and evaluate six preproduction models (four units of the 200-degree/second model and two of the 1000-degree/second model). The test and evaluation should be performed to confirm (1) that proper fabrication techniques will repeatedly keep the scale factor and null signal variations with supply and/or environmental variations within acceptable limits and (2) incorporating the above recommendations into the LARS design will reduce the environmental effects with no degradation in the other performance parameters previously measured on the prototype LARS units.

MATHEMATICAL MODELING AND COMPUTER AIDED DESIGN OF A FLUIDIC G SENSOR

by

Charles A. Belsterling* and Dr. Albertus E. Schmidlin**

ABSTRACT

One of the long-standing handicaps in the development of sophisticated fluidic devices and systems has been the difficulty in analyzing their behavior. Electronic computers have the capability of handling complex and cumbersome mathematical problems with ease. Obviously, the application of computers to the fluidics technology would minimize this handicap. The key to successful application is the development of valid mathematical models.

This paper is intended to illustrate, by the example of a fluidic G sensor (accelerometer), that valid models *can* be developed, and by more than one method. Furthermore it is to show how the behavior of these models can be analyzed and their performance optimized by means of both analog and digital computers. The results indicate the validity of the models and verify their value in improving the dynamic response and minimizing gas consumption of the G sensor.

*Franklin Institute Research Laboratories, Phila., Penna.

**Department of the Army, Picatinny Arsenal, Dover, New Jersey

LIST OF SYMBOLS

a	= acceleration of G Sensor, in/sec^2
A	= area, general, in^2
A_e	= effective area of piston (experimentally determined) in^2
A_o	= outlet orifice area, in^2
A_s	= supply orifice area, in^2
A_t	= total area of piston, in^2
A_{tv}	= area of top vent, in^2
A_v	= area of bottom vent, in^2
C	= capacitance, microfarads, compliance, in^5/lb .
C_1	= volume capacitance of lower chamber, in^5/lb
C_2	= volume capacitance of upper chamber, in^5/lb
d	= clearance above seismic mass, in
D	= damping coefficient, lb sec/in
E	= voltage, volts
F	= side force on the piston, lb
f	= sliding friction force, lb
g	= gravitational constant, in/sec^2
G	= acceleration, a/g , nondimensional
i	= current, amperes
K	= spring constant, lb/in
K_n	= vent nozzle coefficient, lb sec/in^4
L	= inductance, henries, inertance, $\text{lb sec}^2/\text{in}^5$
M	= mass of the piston, $\text{lb sec}^2/\text{in}$.
m	= mass flow, lb sec/in
P_a	= atmospheric pressure, lb/in^2
P_b, P_c	= generalized pressures lb/in^2
P_o	= output pressure, lb/in^2
P_s	= supply pressure, lb/in^2
P_1	= pressure in bottom chamber, lb/in^2

P_2	= pressure in top chamber, lb/in ²
ρ	= density of gas, lb sec/in ⁴
ρ_0	= density of gas in chamber, P_1/RT , lb sec/in ⁴
ρ_s	= density of gas at supply port, P_s/RT , lb sec/in ⁴
q	= volume flow, in ³ /sec
R	= gas constant, in ² /sec ² °R
R	= resistance, ohms, lb sec/in ⁵
R_b	= damping resistance, lb sec/in ⁵
R_L	= load resistance, lb sec/in ⁵
R_n	= vent nozzle resistance, lb sec/in ⁵
R_o	= output resistance, lb sec/in ⁵
R_s	= supply resistance, lb sec/in ⁵
s	= Laplace transform variable, 1/sec
T	= gas temperature, °R
v	= velocity, in/sec
V_1	= volume of bottom chamber, in ³
V_2	= volume of top chamber, in ³
W	= weight of the piston, lb
x	= displacement of mass w.r.t. vent nozzle, in
μ	= coefficient of sliding friction
γ	= ratio of specific heats

INTRODUCTION

The goal of any modeling effort is to develop a mathematical description that not only is valid but also is suitable for analysis by conventional techniques. One approach is to first describe a fluidic device in terms of its electrical analogies (equivalent electric circuit), then develop the nonlinear differential equations describing the circuit and finally apply standard circuit analysis and computing methods to the prediction of its behavior. (Ref 1) This is the approach used in the first part of this paper.

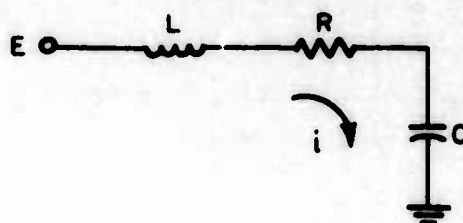
Another approach to modeling is by means of the classical equations of fluid mechanics. The coupled, nonlinear differential equations describing gas flow and mechanical motion are derived and solved with the aid of computers. This approach is illustrated in the latter part of the paper.

PART I. MODELING WITH ELECTRICAL CIRCUIT ANALOGIES

It is appropriate to begin with a description of analogous physical systems. In developing equivalent circuit models for fluidic devices, we are generally concerned with three types of physical systems, fluidic (pneumatic), mechanical and electrical. The analogous second-order differential equations are as follows:

ELECTRICAL

For the RLC electrical circuit shown below we have:



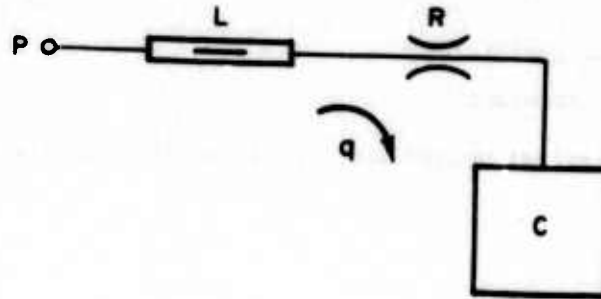
$$E = L \frac{di}{dt} + Ri + \frac{1}{C} \int i dt$$

where

- E = applied voltage
- i = instantaneous current
- L = inductance
- R = resistance
- C = capacitance

Fluidic (Pneumatic)

A similar combination of fluidic devices in the circuit shown below yields the differential equation:



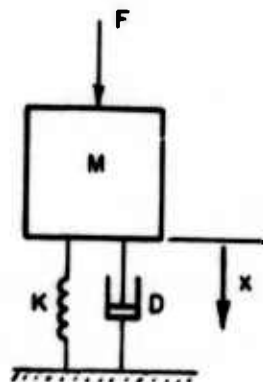
$$P = L \frac{dq}{dt} + Rq + \frac{1}{C} \int q dt$$

where

- P = total pressure
- q = instantaneous volume flow
- L = equivalent inductance
- R = equivalent resistance
- C = equivalent compliance

Mechanical

The differential equation describing the spring-mass-damper system shown below is:



$$F = M \frac{d^2 x}{dt^2} + D \frac{dx}{dt} + Kx$$

where

- F = sum of the forces on M
- x = instantaneous displacement
- M = mass
- D = damping coefficient
- K = spring constant

For the electrical equivalent circuit of the fluidic circuit we can let:

- P = E
- q = i
- L = L
- R = R
- C = C

in their appropriate units.

For the electrical equivalent of the mechanical system, it is most convenient to change the variable from displacement, x, to velocity, v, then:

$$F = Mdv/dt + Dv + K \int v dt$$

and we can use the analogies

- F = E
- v = i
- M = L
- D = R
- K = $\frac{1}{C}$

in their appropriate units.

PHYSICAL DESCRIPTION OF THE FLUIDIC G SENSOR

The physical model of the fluidic G sensor is shown in Figure 1. It operates as follows.

Supply flow enters the lower chamber through the supply restrictor and flows out either the vent nozzle or the output restrictor connected to

the load. There is a sealing diaphragm under the seismic mass to prevent flow leakage past the mass. In the upper chamber there is one vent to atmosphere through a restrictor which provides damping.

Assuming a vertical orientation as shown, the seismic mass exerts a downward force equal to Mg which tends to seal off the vent nozzle. When the output restrictor is relatively small, incoming supply flow will cause the pressure to build up in the lower chamber until it lifts the mass from the nozzle and allows more flow to vent out of the lower chamber through the nozzle. The seismic mass will begin to rise.

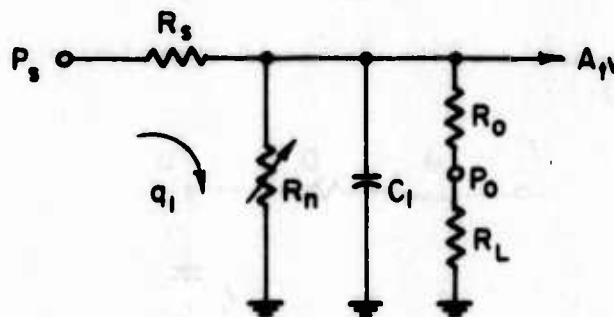
As the mass moves upward, it compresses air in the upper chamber, forcing it out through the damping restrictor. As the mass comes to rest in a stable position, the pressure in the upper chamber, P_2 , reaches atmospheric pressure. At equilibrium we have a force balance system in the lower chamber, where, neglecting sticking friction and diaphragm forces, the pressure in the lower chamber times the effective area, A_e , of the seismic mass must be equal to the mass, M , times the acceleration, a , or

$$P_1 = \frac{M}{A_e} a$$

That is, P_1 is a direct linear function of acceleration, provided M and A_e are constants. No other parameters or variables are involved in its static response. The proportional pressure, P_1 , is applied to the load, R_L , through the output restrictor, R_o .

EQUIVALENT ELECTRIC CIRCUIT

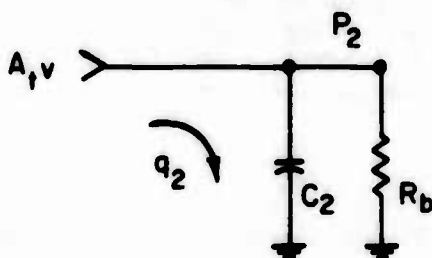
Assuming no flow from one end of the chamber to the other (sealed diaphragm), we have two convenient node points, 1 and 2, for summing flows. At node 1 (the lower chamber) there is only supply flow coming in, but there are several places for it to exit, as illustrated by the equivalent circuit that follows:



where

- R_n = variable vent nozzle resistance (function of x)
- C_1 = volume capacitance of lower chamber (function of x)
- A_t = total area of end of seismic mass
- v = velocity of seismic mass
- R_s = supply resistance
- R_o = output resistance
- R_L = load resistance

Similarly at node 2 (the upper chamber) we have the network



where

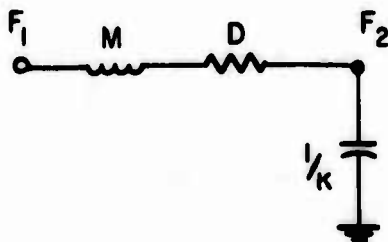
- R_b = damping resistance
- C_2 = volume capacitance of upper chamber (function of x).

Here vA_t is the only incoming flow and it is used to compress the air in the trapped volume capacitance C_2 and to bleed out the restrictor R_b to atmosphere.

Note that pressures, P_1 , and P_2 , are developed at the two nodes, and act on opposite ends of the cylindrical mass, M . Between the nodes 1 and 2 we have a mechanical system whose behavior will define the unknown velocity, v , connecting the two node equivalent circuits. Then

$$F_1 = Mdv/dt + Dv + K\int vdt = P_1 A_e$$

which can be represented by the electrical equivalent circuit (neglecting diaphragm forces).



To convert a circuit properly to pressure and flow variables we determined velocity of the mass by the equation

$$P_1 A_e - P_2 A_t = M \dot{v} + Dv$$

or in terms of the operator, s

$$P_1 A_e - P_2 A_t = v(sM + D)$$

or

$$v = \frac{P_1 A_e}{sM + D} - \frac{P_2 A_t}{sM + D}$$

However the increase in volume of the lower chamber and the decrease in volume of the upper chamber is determined by the velocity and total area A_t . That is:

$$Q_2 = A_t v = \frac{P_1 A_e A_t}{sM + D} - \frac{P_2 A_t^2}{sM + D} = \frac{P_1}{sM/A_e A_t + D/A_e A_t} - \frac{P_2 A_t/A_e}{sM/A_e A_t + D/A_e A_t}$$

Converting the mechanical impedances to fluidic impedances and compensating C_2 and R_b for the area ratio we have the modified impedances:

$$\begin{aligned} M' &= M/A_e A_t \\ D' &= D/A_e A_t \\ R'_b &= A_e R_b/A_t \\ C' &= A_t C_2/A_e \end{aligned}$$

Now the complete equivalent electric circuit for the G sensor is shown in Figure 2

External acceleration, a , produces a force equal to mass times acceleration into the mechanical circuit above. Since the device cannot react on the external acceleration (infinite input impedance and infinite reverse transfer impedance), it is introduced into the circuit through a pure voltage generator. To be compatible with the modified circuit, the force, Ma , is divided by the effective area, A_e , to produce an equivalent air pressure opposing P_1 .

MATHEMATICAL MODEL

The equivalent circuit in Figure 2 provides the means for developing the mathematical model for the fluidic G sensor using conventional mathematical procedures. To simplify the presentation we can make the following substitutions.

Let

$$Z_p = \frac{R_p / sC_1}{R_p + 1/sC_1} = \frac{R_p}{1 + sC_1 R_p} \quad (\text{parallel network in lower chamber})$$

where:

s = Laplace operator

and

$$R_p = \frac{R_n R_x}{R_n + R_x} \quad (\text{parallel resistances in lower chamber})$$

where;

$$R_x = R_o + R_L \quad (\text{sum of output and load resistances})$$

and

$$Z_2' = \frac{R_b' / sC_2'}{R_b' + 1/sC_2'} = \frac{R_b'}{1 + sC_2' R_b'} \quad (\text{parallel network in upper chamber})$$

The loop equations are

$$P_s = Q_1(R_s + Z_p) - Q_2(Z_p)$$

and

$$-\frac{Ma}{A_e} = -Q_1(Z_p) + Q_2(Z_p + sM' + D' + Z_2')$$

Now one can form the determinant of the 2 by 2 impedance matrix, set it equal to zero and determine the characteristic equation of the G sensor. By definition the characteristic equation defines the transient response of the G sensor as described in the linearized analytical study later in this paper.

Solving for Q_1 and multiplying it times Z_p defines the transfer function of the G sensor from which we can determine the dynamic response of P_1 to changes in acceleration and supply pressure.

ANALOG COMPUTER STUDIES

Referring to the equivalent electric circuit of Figure 2 and its component parts, we can formulate a set of equations most convenient for solution on an analog computer. They are the node equations

$$@P_1 \quad (P_s - P_1) / R_s = P_1 / R_n + C_1 dP_1 / dt + (P_1 - P_o) / R_o + vA_t$$

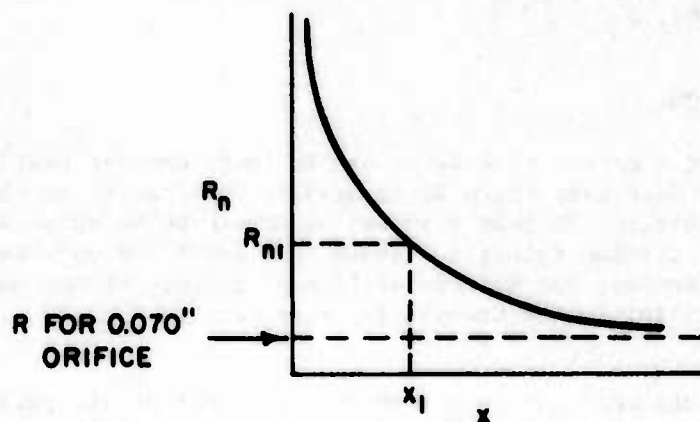
$$@P_2 \quad vA_t = C_2 dP_2 / dt + P_2 / R_b$$

$$@P_o \quad (P_1 - P_o) / R_o = P_o / R_L$$

and the forces acting on the mass, M.

$$@M \quad P_1 A_e - P_2 A_t = M (a + dv/dt) + Dv.$$

One more equation is necessary to the simulation of the G sensor. The nonlinearity of the vent nozzle restrictor is vital to the functioning of this force-balanced system. The value of this resistance, R_n , varies inversely with the nozzle gap, the distance, x , shown in Figure 1.ⁿ The characteristic of this vent nozzle resistance, R_n , is typically as shown below.



We assume the characteristic $R_n = \frac{K_n}{x}$ where

$$K_n = (R_n @ x_1) x_1.$$

The analog computer program based on the above five equations is shown in Figure 3.

Note that there are two other nonlinearities in the analog computing circuit. The first is in the generation of a friction term in the lower loop representing the mechanical system dynamics. Sliding friction is a nonlinear phenomenon which results in a restraining force in the direction opposite to the motion of the mass and it is at a relatively constant level. This phenomenon is generated by feeding the velocity signal into a comparator with a zero reference level whose output generates a changing sign or direction of the friction force. The potentiometer that follows is set to regulate the magnitude of the force, and the net result is a simulated friction level that changes its direction to always oppose the direction of motion of the mass.

The other nonlinearity is in the generation of the displacement, x of the mass, M . We have defined x as the distance between the mass and the vent nozzle, R_n . To avoid having the nozzle penetrate the mass during overtravel, we restrict the displacement x to positive values only, by inserting a diode in the signal output of the integrator. When x does go to zero, the vent restrictor is completely closed, so the value of R_n goes to infinity and P_1/R_n goes to zero.

Static tests of the analog computer program were run to correlate with experimental data, starting with the sensor at 1G with the supply pressure on. A step change of G was applied and a reading taken after transients had died out. Supply pressure was then removed and reapplied, after which a second reading was made. The step change in G was removed and the procedure repeated at 1G.

EFFECT OF ACCELERATION, G

A plot showing the effect of G level on the lower chamber pressure, P_1 , is in Figure 4. Note that there is an area of uncertainty in the pressure (non repeatability of test results) at levels below about 8 G due to the effect of sliding friction. Above this level the uncertainty disappears, perhaps because the system "stiffness" becomes strong enough to overpower any uncertainty, or because the mass settles with an oscillatory motion.

Other static tests were run to determine the effect of all parameters on the lower chamber pressure, P_1 . The following were effective:

- Acceleration, a
- Sliding Friction, f
- Effective Area, A_e
- Mass, M .

It was determined that the effect of the following variables on the chamber pressure, P_1 , under static conditions is negligible.

Damping Restrictor, R_d
 Supply Restrictor, R_s
 Output Restrictor, R_o
 Nozzle (Vent) Restrictor, R_n
 Lower Chamber Volume Capacitance, C_1
 Upper Chamber Volume Capacitance, C_2
 Supply Pressure, P_s (6-10 psi).

The output pressure P_o , is derived from P_1 . Therefore, to determine the effect of additional parameters on the output pressure, we need only investigate those parameters downstream of the lower chamber pressure, P_1 . Those parameters are the output resistance, R_o , and the load resistance, R_L . It was found that both parameters, R_o and R_L , have a significant effect on the output pressure, P_o .

The static tests confirmed that sliding friction can introduce serious errors in the output of the G sensor. At low levels of acceleration the errors are in the form of a band of uncertainty. At higher levels the errors appear to be always negative.

The static tests show that the only design parameters which affect the lower chamber pressure, P_1 , are sliding friction, f , mass, M , and effective area, A_e . The additional parameters that affect the output pressure, P_o , are the output restrictor, R_o , and the load restrictor R_L .

ANALOG COMPUTER STUDIES OF G SENSOR DYNAMICS

Dynamic tests were run with the computer program in Figure 3 starting at 1 G with the supply pressure on. A step change of G was applied, then when the transients had stabilized, the supply pressure was momentarily removed, then reapplied. Finally when the transients had stabilized again, the step change in G level was removed and the decay transient recorded.

Effect of Sliding Friction, f , at 10 G

Figure 5 shows the transient response of the G sensor with three values of sliding friction. Four characteristics are to be noted:

- (a) Sliding friction of 0.025 lb is required to produce acceptable damping @ 10 G;

- (b) Less damping is required for the response to a step input of 10 G than for a step input of 8 lb/in² supply pressure;
- (c) There is a critical level of *initial* disturbance beyond which more damping is required; the reason for the difference in required damping appears to be due to the nonlinearities.
- (d) The *undamped* natural frequency is approximately the same in both cases.

It is clear from the results of this test that stability of the fluidic G sensor with the parameters calculated from the present design is borderline. First, the value of sliding friction factor measured in the experimental unit is 0.60. With a cross axis acceleration of 1 G, this results in a force of 0.60×0.0274 lb or 0.017 lb. The computer performance shown in Figure 5 shows that this force is not enough to stabilize the G sensor. We could provide more sliding friction, but, as shown in the static case, this could introduce serious uncertainties into the response. Furthermore, in actual use in a missile, the cross-axis acceleration can be much lower than 1 G, in fact zero. This leads to the conclusion that sliding friction *cannot* be depended upon to stabilize the transient response of the G sensor. We must find ways to increase the effective "viscous" damping.

LINEARIZED ANALYTICAL STUDY

To aid in finding the means to increase the effective viscous damping most directly, an analytical study was carried out. This was a *linearized* analysis of the transient behavior of the G sensor in general mathematical form. The electrical equivalent circuit of Figure 2 was used to generate the characteristic equation of the complete system using standard algebraic processes. It was possible to factor the resulting cubic equation to establish the characteristic equation

$$\left[s^2 + \frac{1}{R_1} \left(\frac{1}{C_1} - \frac{1}{C_2} \right) s + \frac{1}{M C_1} \right] \left(s + \frac{1}{C_2 R_2} \right) = \text{Zero}$$

where

R_1 is the parallel combination of all restrictors connected to the lower chamber.

R_2 is the parallel combination of all restrictors in the G sensor.

From the characteristic equation we can derive:

$$\text{Undamped natural frequency} = \frac{1}{\sqrt{M'C_1}}$$

$$\text{Damping factor} = \frac{\sqrt{M'}}{2R_1\sqrt{C_1}} \left(1 - \frac{C_1}{C'_2} \right)$$

This leads to the following conclusions:

- (1) The undamped natural frequency is solely a function of mass, M , and volume of the lower chamber, C_1 .
- (2) The damping factor is primarily a function of the parallel combination of all restrictors connected to the lower chamber and the *ratio* of the volume of the lower chamber to the volume of the upper chamber;
- (3) The damping restrictor, R_b , acts with the volume capacitance of the upper chamber, C_2 , to reduce the energy in the second order system by attenuating the high-frequency components.

Tests were run using the *nonlinear* computer model to establish a rough correlation with the results of the *linearized* analytical study.

Figure 6 shows the transient response of the G sensor with various values of damping resistance, R_b . It is typical of the many other parameter studies conducted.

The response to G transients confirms that R_b provides *effective* damping by limiting the momentum of the mass as it approaches the nozzle. Then less energy is "injected" into the system and the oscillations are never severely excited and decay rather quickly. Note in Figure 6 the *frequency* of the oscillations is relatively unaffected by changes in R_b . This confirms that R_b is not a factor in determining the undamped natural frequency of the G sensor.

The response to supply pressure transients shows larger amplitudes of oscillation as R_b is increased, although the decrement of decay seems to be relatively constant. Larger amplitudes conflict with the hypotheses by the constant decrement confirms them.

It should also be noted that there is an *optimum* value for R_b which has the best combination of effects on G transients and supply pressure transients. We believe that this is due to the fact that with a high value of R_b the volume of flow through the restrictor is not large enough to extract a significant amount of energy from the system.

Summary of Analyses

The initial dynamic tests with sliding friction indicate the need for additional sources of damping to insure stability of the G sensor and to minimize static errors at low acceleration. The linearized analytical study led to the hypothesis that the restrictors connected to the lower chamber and the ratio of the volumes in the lower and upper chambers could be optimized to increase the damping factor. The study also predicted that the undamped natural frequency of the G sensor is dependent on the seismic mass and the volume capacitance of the lower chamber only.

The dynamic tests of the nonlinear mathematical model *consistently confirmed the hypotheses based on the linearized analysis* except for two cases due to nonlinearities.

- (1) Computed results indicate that the damping resistance, R_b , has an optimum value for damping, while the linearized analysis indicates the larger, the better.
- (2) Computed results indicate that the effect of the ratio of volume capacitances is of the form $(C_1/C_2 - 2)$ while the linearized analysis indicates $(1 - C_1/C_2)$.

The results of the linearized analysis have provided a clear insight as to additional sources for damping the nonlinear G sensor without introducing static errors and uncertainties. In addition the nonlinear analog computer program has proved to be of exceptional value in testing the effects of parameter changes and providing realistic static and dynamic responses.

G SENSOR EXPERIMENTAL TESTS

A model of the G sensor was constructed for a limited series of experimental tests. The dimensions are identical with those used in the computer studies so the test results could be correlated with computed results.

In the static tests to follow, the effect of acceleration on the G sensor is simulated by loading the top of the seismic mass with a controlled air pressure (P_2) applied and measured through the ports illustrated in the top chamber in Figure 7. The loading pressure is applied at one port and measured at a second port to avoid errors due to flow. The air is allowed to bleed normally through the damping restrictor, R_b . This method of loading the G sensor should introduce no static errors, but there will be dynamic errors due to decreased volume capacitance, C_2 , (inversely proportional to P_2) and increased incremental R_b (proportional to flow through the nonlinear damping restrictor).

Figure 8 is a photograph of the experimental G sensor set up for the test. Pressure is applied to the top through an interruptable jet and a motor-driven chopper wheel. Identical miniature pressure transducers are connected to continuously monitor the input pressure, P_2 , and the output pressure of interest and plot their relative values automatically.

Figure 9 shows the sensor static output pressure response plotted automatically. The loading was slowly increased to maximum, then slowly decreased to zero while the axis was oriented vertically. Note the exceptional linearity and the indication of hysteresis.

Comparison with Figure 4 shows good correlation in sensitivity but the absence of the effect of sliding friction, which for the computed case, was assumed at its maximum (axis horizontal).

A limited series of dynamic tests were conducted with the experimental G sensor. The sensor was oriented vertically so with zero loading pressure it was sensing one G.

Figure 10 shows the transient response of the G sensor to step changes in simulated acceleration. The upper trace is P_2 , representing acceleration and the lower trace is P_1 , the pressure in the lower chamber. Note that at 10 G the response shows a natural frequency of approximately 225 hertz and a characteristic nonlinear response. This is to be compared with the computed response for the nominal case shown in Figure 5. The computed natural frequency is about 240 hertz and we can see the same type of oscillatory response. Note also that adding friction by tilting the G-Sensor damps the response more nearly like the computed response (which included sliding friction).

Figure 11 shows the transient response of the G sensor to a step change in supply pressure. Note that the response is lightly damped as compared to the response to 10 G in Figure 10, and it is quite different in character. This is to be compared with the computed response in Figure 5. The similarity in amplitudes is quite good.

PART II. MODELING WITH THE BASIC PHYSICAL EQUATIONS

The fluidic "G" sensor can be described as a mass, air-spring, valve system. Three coupled, nonlinear, differential equations describe the gas flow and the motion of the mass.

Governing Equations

1. Summation of forces on the seismic mass, M:

$$\sum F = M\ddot{x} + M\dot{x}$$

Equation of motion for the mass, M:

$$\ddot{x} = -a + \frac{P_1 A_a}{M} - \frac{P_2 A}{M} - \frac{\mu F \dot{x}}{M |x|} \quad (1)$$

2. Mass rate of flow for a compressible fluid:

(Ref. 2)

$$\dot{m} = A_0 \left(\frac{P_b}{P_c} \right)^{\frac{1}{\gamma}} \sqrt{2g RT \frac{\gamma}{\gamma - 1} \left[1 - \left(\frac{P_b}{P_c} \right)^{\frac{\gamma - 1}{\gamma}} \right]}$$

To facilitate manual calculations, a simplified expression can be used. For $\gamma=1.4$ and $0.53 < P_b/P_c < 1.0$ the following expression is applicable with a maximum error of 1/4%.

$$\dot{m} = A_0 \sqrt{2g RT \frac{P_c - P_b}{P_c} \left[1 - \frac{3}{2\gamma} \left(\frac{P_c - P_b}{P_c} \right) \right]}$$

3. Equation of state for a perfect gas:

$$PV = mRT$$

4. Continuity equation for a chamber:

$$P\dot{V} + V\dot{P} = \dot{m}RT$$

Bottom chamber continuity equation:

$$\dot{P}_1 = \frac{P_s A_s}{V_1} \sqrt{2gRT \frac{P_s - P_1}{P_s} \left(1 - \frac{3}{2\gamma} \frac{P_s - P_1}{P_s}\right)} - \frac{P_1 (A_o + A_v)}{V_1} \sqrt{2gRT \frac{P_1 - P_a}{P_1} \left(1 - \frac{3}{2\gamma} \frac{P_1 - P_a}{P_1}\right)} - \frac{P_1 \dot{V}_1}{V_1} \quad (2)$$

3. Top chamber continuity equation:

a. $P_2 > P_a$ - flow out of the top vent

$$\dot{P}_2 = - \frac{P_2 A_{tv}}{V_2} \sqrt{2gRT \frac{P_2 - P_a}{P_2} \left(1 - \frac{3}{2\gamma} \frac{P_2 - P_a}{P_2}\right)} - \frac{P_2 \dot{V}_2}{V_2}$$

b. $P_2 < P_a$ - flow into the top vent

$$\dot{P}_2 = \frac{P_a A_{tv}}{V_2} \sqrt{2gRT \frac{P_a - P_2}{P_a} \left(1 - \frac{3}{2\gamma} \frac{P_a - P_2}{P_a}\right)} - \frac{P_2 \dot{V}_2}{V_2} \quad (3)$$

Assumptions

1. Gas flow through orifices is subsonic with negligible upstream velocity.
2. Gas temperature remains constant and uniform in both top and bottom chambers.
3. Sliding friction between the seismic mass and the barrel is present when operating in a horizontal position. In this case the side force is equal to the weight of the seismic mass; otherwise the side force is assumed to be negligible.
4. Effects of a pressure gradient along the diaphragm and flow force effects and diaphragm stiffness were approximated by experimental determination of an effective diaphragm area for force balance calculations.
5. Motion of the seismic mass is limited to positive values of x (see Figure 1). If the mass reaches $x=0$ at a finite velocity, the velocity becomes and remains zero until the acceleration becomes positive.

Discussion of Assumptions

The assumption of constant temperature was justified on the basis of a relatively low flow through the device and a relatively high ratio of surface area to volume in the top and bottom chambers. Although the static temperature of the gas will be lowered after throttling through the orifices, it is felt that this effect will be offset by the heat transfer from the metal.

In the case of the top chamber, for example, work by Daniels (Ref 3) on the acoustic impedance of enclosures suggests that the correction for deviation from isothermal will be negligible for this geometry at 10 Hz and only 10% at 100 Hz.

The use of an effective area for the diaphragm serves to correct for pressure and flow force effects on its surface. Since the test data were obtained with the sensor diaphragm oriented in its opening position the restraining forces within the diaphragm material were also included.

Limiting the motion of the seismic mass is necessary to satisfy the physical characteristics of the hardware. Nothing is sacrificed in the computer simulation as long as the mass remains within its nominal stroke between $x = 0^+$ and .020 in. In the event the mass approaches $x = 0$ at a finite velocity the rebound will not be simulated. This limitation in the computer model was accepted.

Analytical Results

The governing equations were solved for steady-state and transient cases (Ref 4). The steady state results were obtained using Newton's iteration technique. The transient results were obtained on a digital computer using a language called MIMIC which performs analog simulation. Two models of the "G" Sensor were investigated, a 15G and a 30G unit.

Static analysis is desirable here in order to confirm the nominal value of the scale factor (pressure per G of acceleration), the maximum supply pressure needed and the nominal travel of the seismic mass as a function of acceleration. The steady-state results for the 15G model are shown in Figure 12. The pressure versus acceleration curve was derived from the steady state form of equation(1), neglecting friction. The pressure versus displacement was derived from the steady state form of equation (2). The nonlinearities in the flow equation can clearly be seen in the pressure-displacement curve.

The transient response to the simultaneous application of supply pressure and a 10G step acceleration is shown in Figure 13. These results represent the 15G instrument which did not incorporate damping. The mathematical model was represented by equations (1) and (2); equation (3) was omitted. Regarding the hardware this means that both A_{TV} and d are sufficiently large so that $P_2 = P_a$.

The operation of the device can be interpreted directly from the figure. When the rising chamber pressure reaches the steady-state value, the mass begins to move. The pressure continues to rise until the mass reaches its steady-state displacement. The pressure begins to decrease, but is still above its steady-state value and the displacement of the mass continues to increase. As the pressure drops below the steady-state value, the displacement of the mass starts to decrease. When the displacement of the mass falls below the steady-state value, the pressure begins to rise again and the device limit-cycles. This lag between the pressure rise and mass displacement results primarily from the compressibility of the fluid and the kinetic energy of the mass.

The second instrument was designed for a full scale range of 30G. This unit incorporated damping by using the chamber above the seismic mass as a dashpot. This was accomplished by reducing the head clearance and the vent area, which had previously admitted ambient pressure to the upper side of the seismic mass. A comparison of the transient analytical and experimental results of the 30G unit are discussed later.

"G" SENSOR TEST PROGRAM

Static bench testing was conducted on the 15G Sensor to determine the relationship between a load on the seismic mass and the diaphragm pressure needed to support this load. In effect this test provided data for calculating the effective area of the diaphragm. The effective area was used in the analytical model also to compensate for the effects of pressure gradient, flow forces and diaphragm restraint.

The force was applied by means of a threaded rod which pushed downward on the mass of the sensor. An attempt was made to minimize side loading, thereby minimizing friction. The resulting load was measured by a weighing scale on which the sensor was placed. At specific points the load was read simultaneously with a reading of the pressure, P_1 , and a graph of force versus P_1 was plotted. The slope of this line is the numerical value of the effective area. This value was used in the design of the seismic mass for various g-levels. Based on these data, Figure 14 shows the plot of P_1 versus G labeled "characteristic curve". Also shown is a plot of data obtained from the centrifuge testing.

Centrifuge testing was performed to provide a known acceleration input for evaluating the G Sensor. The G Sensor was mounted horizontally at the periphery of the centrifuge table. Centrifuge testing was performed on both G Sensors and provided most of the data from which the G Sensor characteristics were determined. The results of tests on the 15G unit are shown on Figure 14 along with the "characteristic curve", a linear function derived from the static bench tests. The differences between the two curves may be due to the following factors.

1. Centrifuge tests include friction due to a side force equal to the weight of the seismic mass; characteristic curve assumes zero side force (vertical, static orientation). Hence, a hysteresis effect is present in the first case.
2. Bench tests were conducted with a special barrel. Hence, some variation may be due to dimensional variations between this special barrel and the unit tested on the centrifuge.
3. Centrifuge tests impose acceleration loads on the diaphragm which tend to keep it flat and possibly change its effective area, thereby increasing the slope of the curve. Static loading tests do not.

Dynamic tests on a 30G sensor revealed a limit cycling phenomenon as shown in Figure 15. In an attempt to eliminate this phenomenon, damping was added by utilizing the chamber above the mass as a dashpot. This was accomplished by reducing the clearance, d , and the size of the vent which previously had admitted ambient pressure into the top chamber.

The computer program was revised reflecting the addition of equation (3) as discussed earlier. Computer results with varied damping conditions are shown in Figure 16. The results show the effect of the top vent area, A_{tv} , on the damping characteristics. These cases can be compared with the experiments as follows:

1. Limit cycling - the experimental cycling frequency from Figure 15 is approximately 280 Hz. This compares very closely with computed results (Figure 16a Case I).
2. Damping - the transient response of the G sensor shown in Figure 15 illustrates the effect of the top vent and clearance on the response characteristic. The analytical results of Cases I and IV (Figures 16a and 16b) confirm the effect.
3. Response time - the fastest response to maximum pressure in Figure 15 is approximately 15 msec, while the computer runs indicate the first pressure peak in time periods between 1 and 4 msec. This difference is reasonable when the conditions of the experimental tests are considered. The gas flow to the G sensor was supplied through several feet of pneumatic tubing fittings that included a rotary coupling and a solenoid control valve which necessarily was remotely mounted on the bench. Therefore, there was a pneumatic lag in the experimental system while the computer runs reflect an instantaneous application of acceleration and supply pressure at the inlet port.

SUMMARY

As a result of this program it was concluded that this concept of the G Sensor was feasible as a means for monitoring the propulsion forces on a missile during the boost phase. Although the basic design is prone to limit cycle when damping is not provided, ample evidence both analytical and experimental was available to indicate practical solutions to this problem. The use of the top chamber volume as a dashpot is a simple remedy which does not require any additional gas consumption, any added size or weight or excessive cost for manufacture.

The parametric studies, centered primarily around the size of the supply orifice and on the size of the top vent, have indicated the effects of these variables. Of particular significance is the supply orifice size which determines the gas consumption of the device. These studies showed that a .010 orifice can be used in the sensor with acceptable results. In this way the gas consumption is extremely small (approximately 1/20 cubi. feet per minute) which is at least an order of magnitude less than required by other air-operated acceleration sensors (Ref 5).

CONCLUSION

In conclusion we have illustrated the development of mathematical models for fluidic devices, using the example of a fluidic G sensor. The value of these models in analyzing and optimizing the design with the aid of electronic computers has also been demonstrated. We believe that modeling and computer-aided analysis can provide the insight necessary for the successful application of fluidic devices in high-performance systems.

REFERENCES

1. Belsterling, C. A., *Fluidic Systems Design*, John Wiley and Sons, June 1971.
2. Shapiro, A. H. "The Dynamics and Thermodynamics of Compressible Fluid Flow," Vol. 1, Ronald Press, 1953.
3. Daniels, F. B. "Acoustic Impedance of Enclosures," *Journal of the Acoustical Society of America*, Vol. 19, No. 4, 1947.
4. Hover, J. and A. E. Schmidlin "Computer Aided Dynamic Analysis of a Fluidic G Sensor" Report No. SMUPA-TK-2011, Picatinny Arsenal, Feb 1971.
5. Schmidlin, A. E. "Fluidic Inertial Instruments" *ISA Aerospace Conference*, Las Vegas, May 1969.

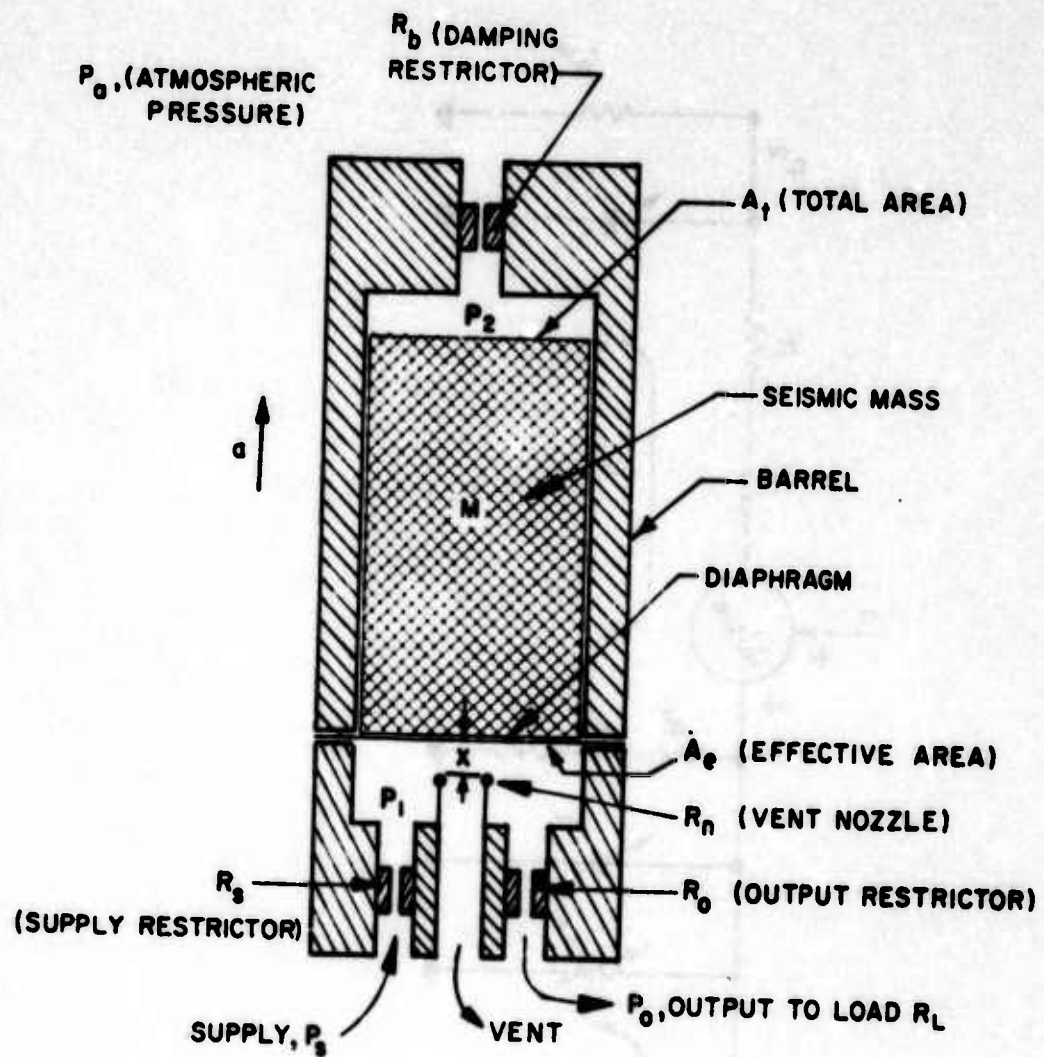


Figure 1. Physical Model of the G Sensor

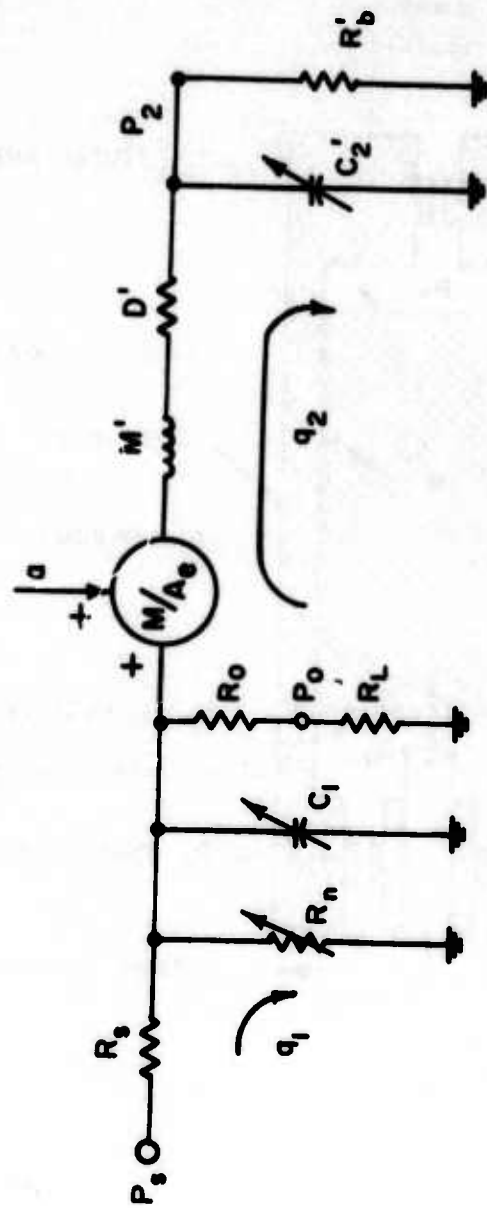
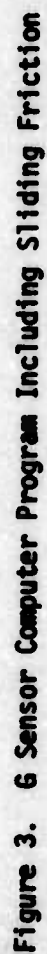


Figure 2. Equivalent Electric Circuit for the Fluidic G Sensor (Fig. 1)



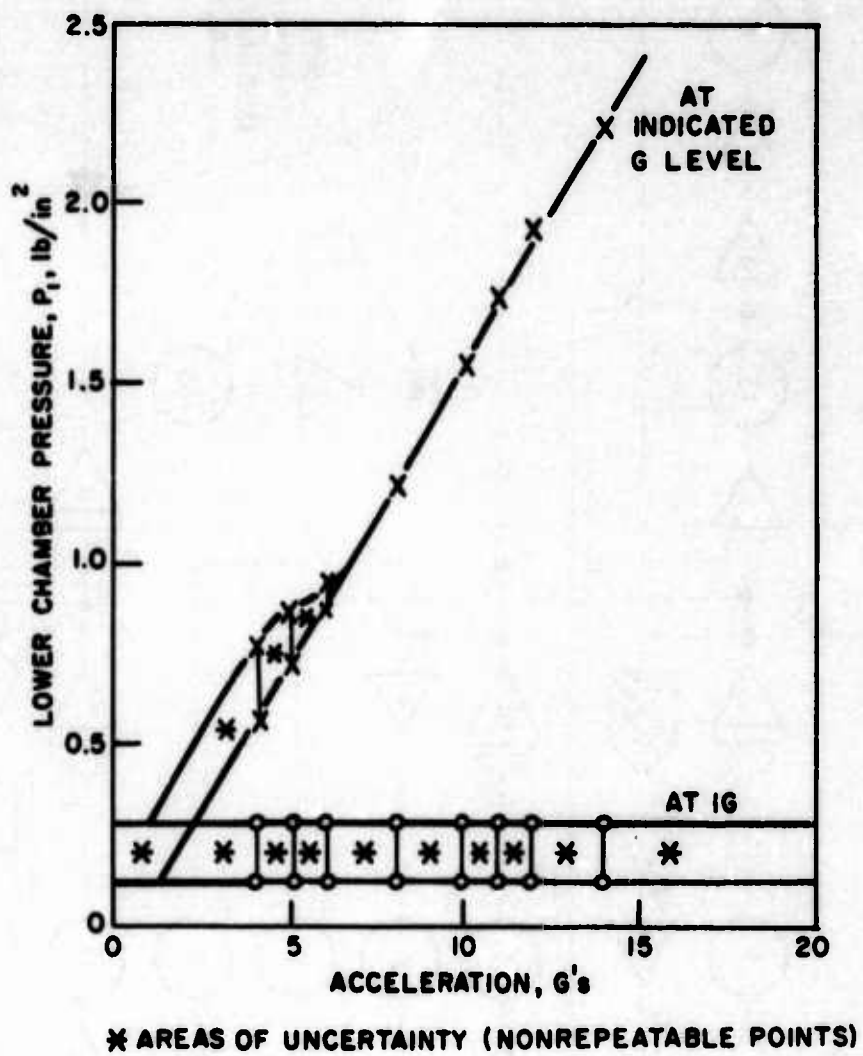


Figure 4. Static Effect of Acceleration, G

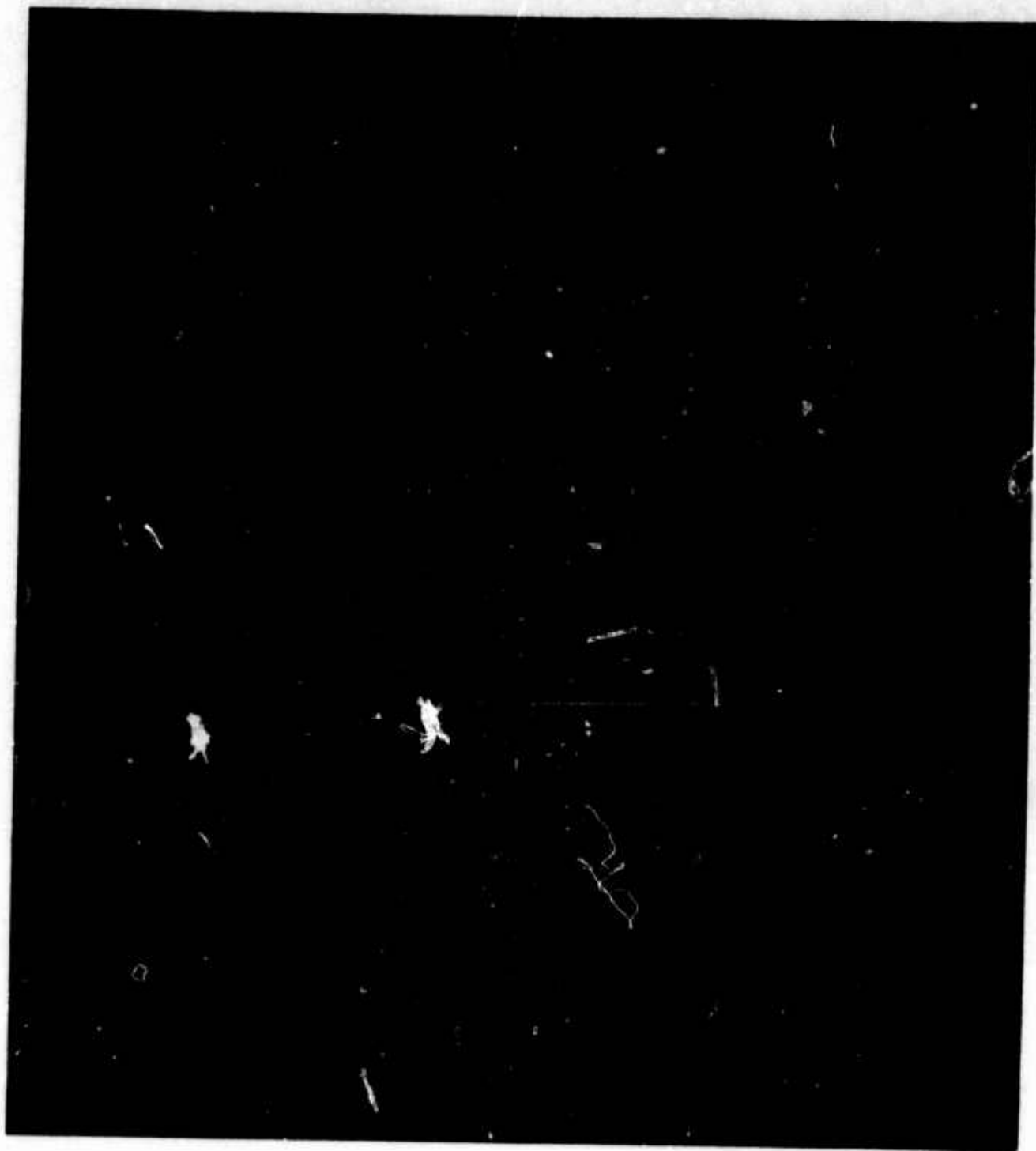


Figure 5. Dynamic Effect of Sliding Friction, f

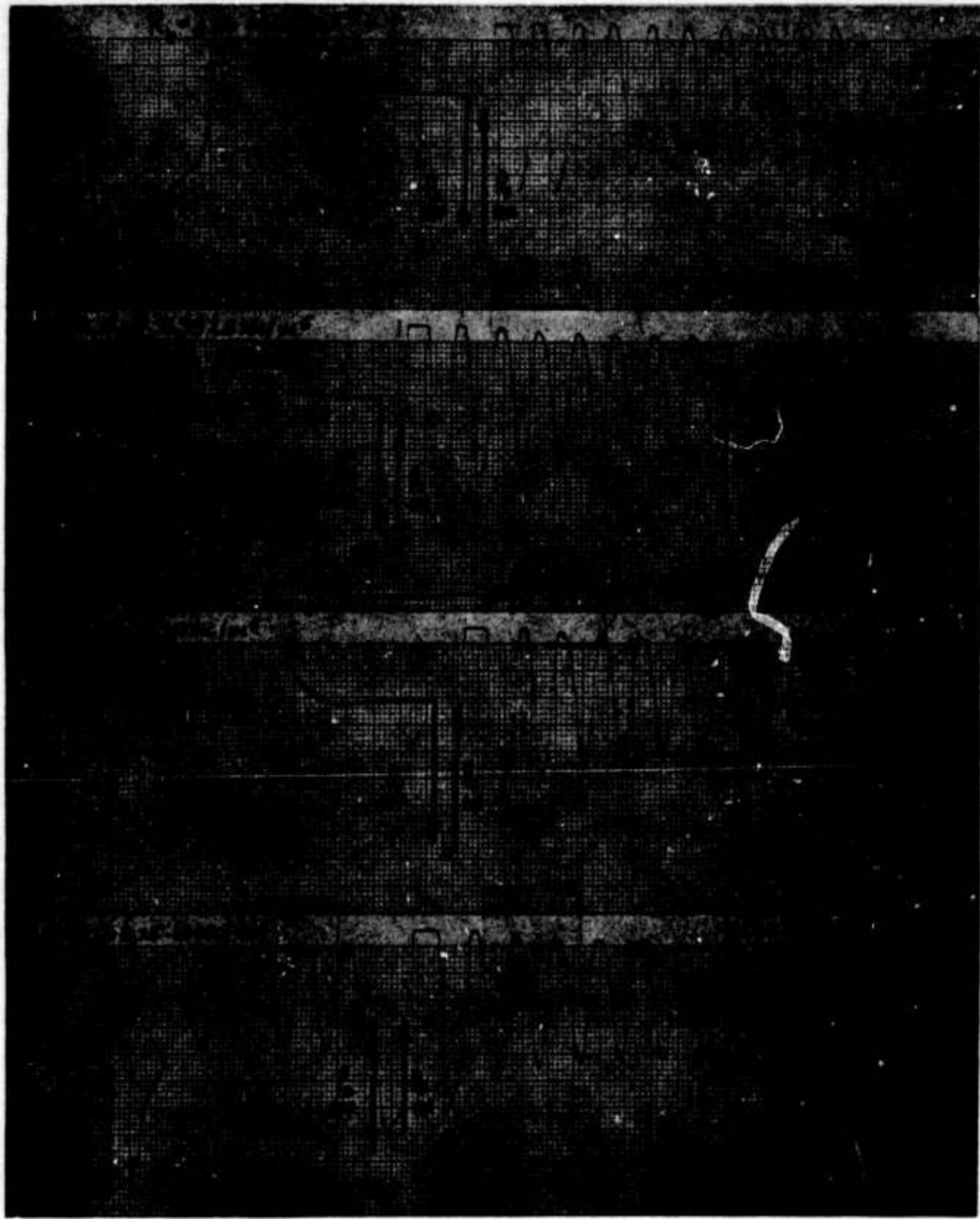


Figure 6. Dynamic Effect of Damping Resistance, R_b

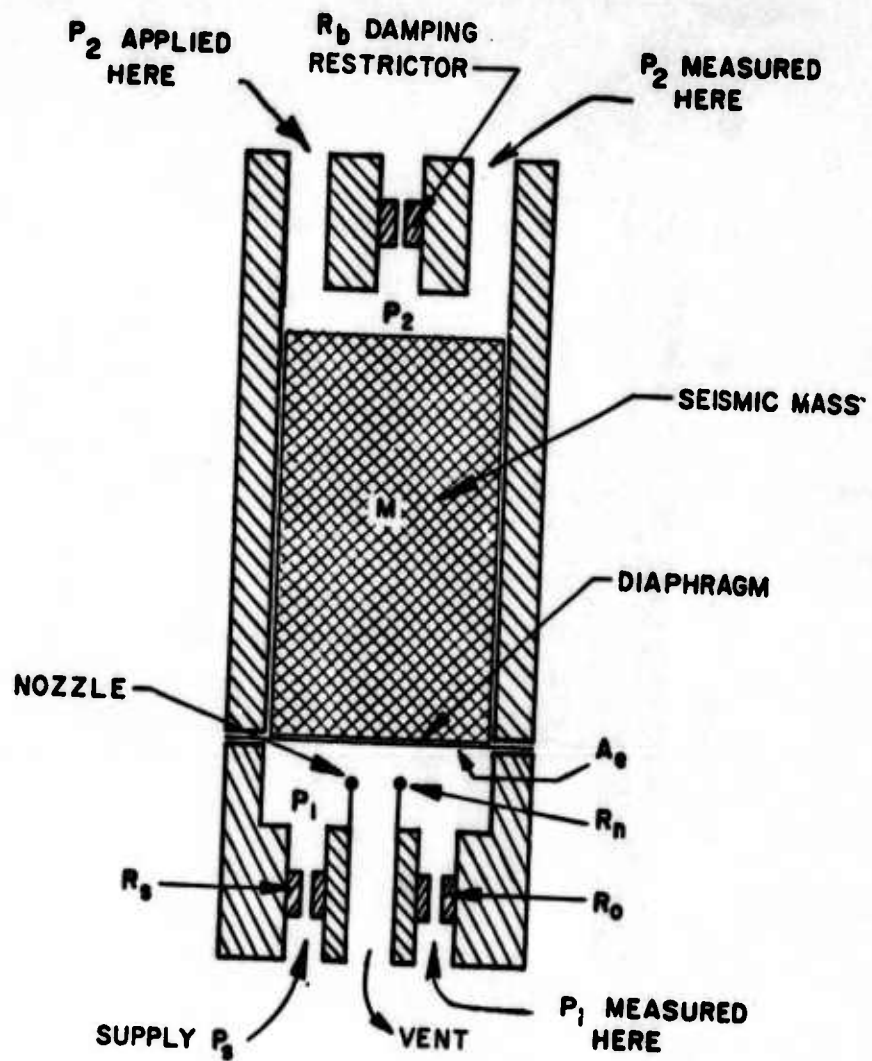


Figure 7. G Sensor Setup for Loading Tests

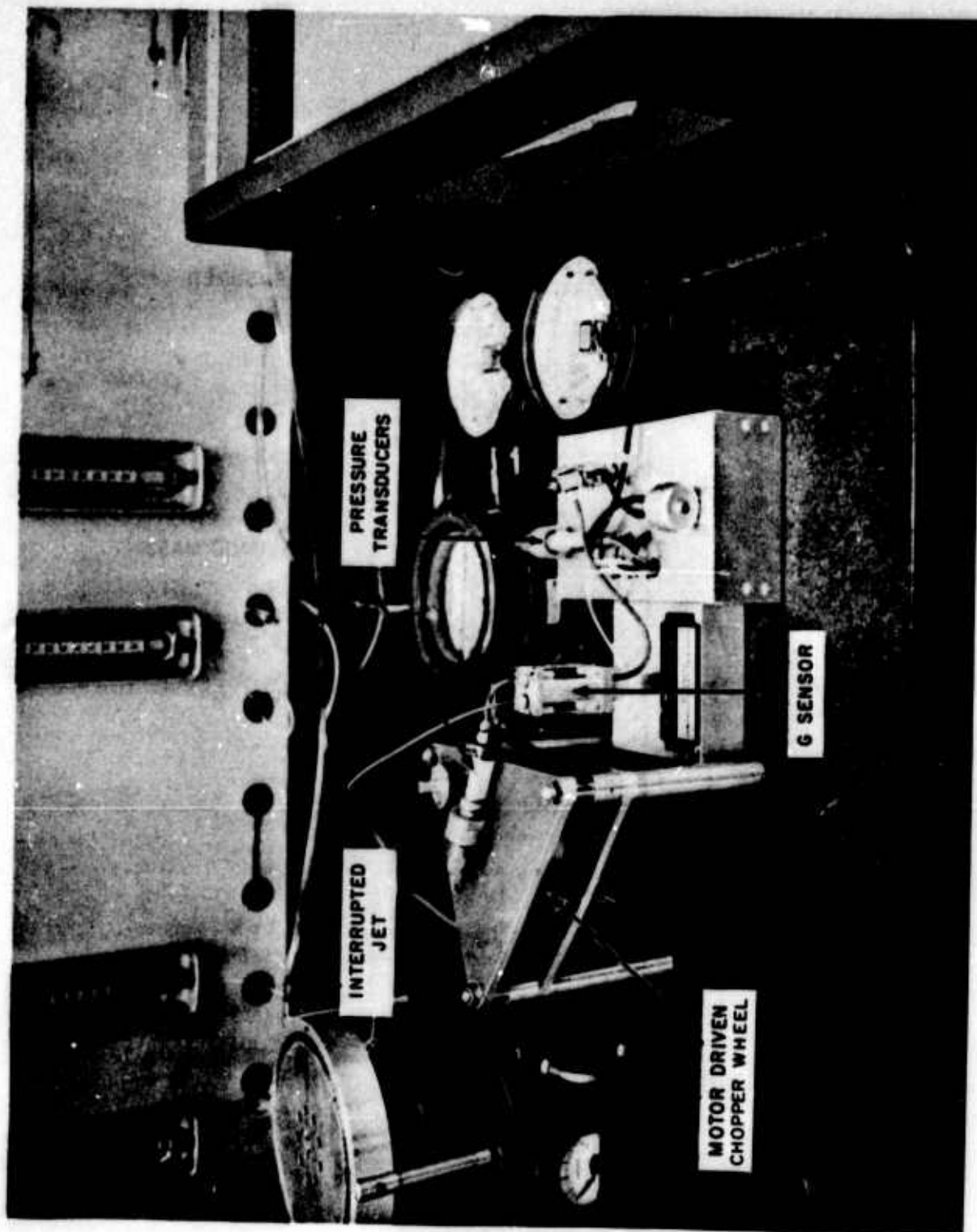


Figure 8. Photo of Experimental G Sensor on Test

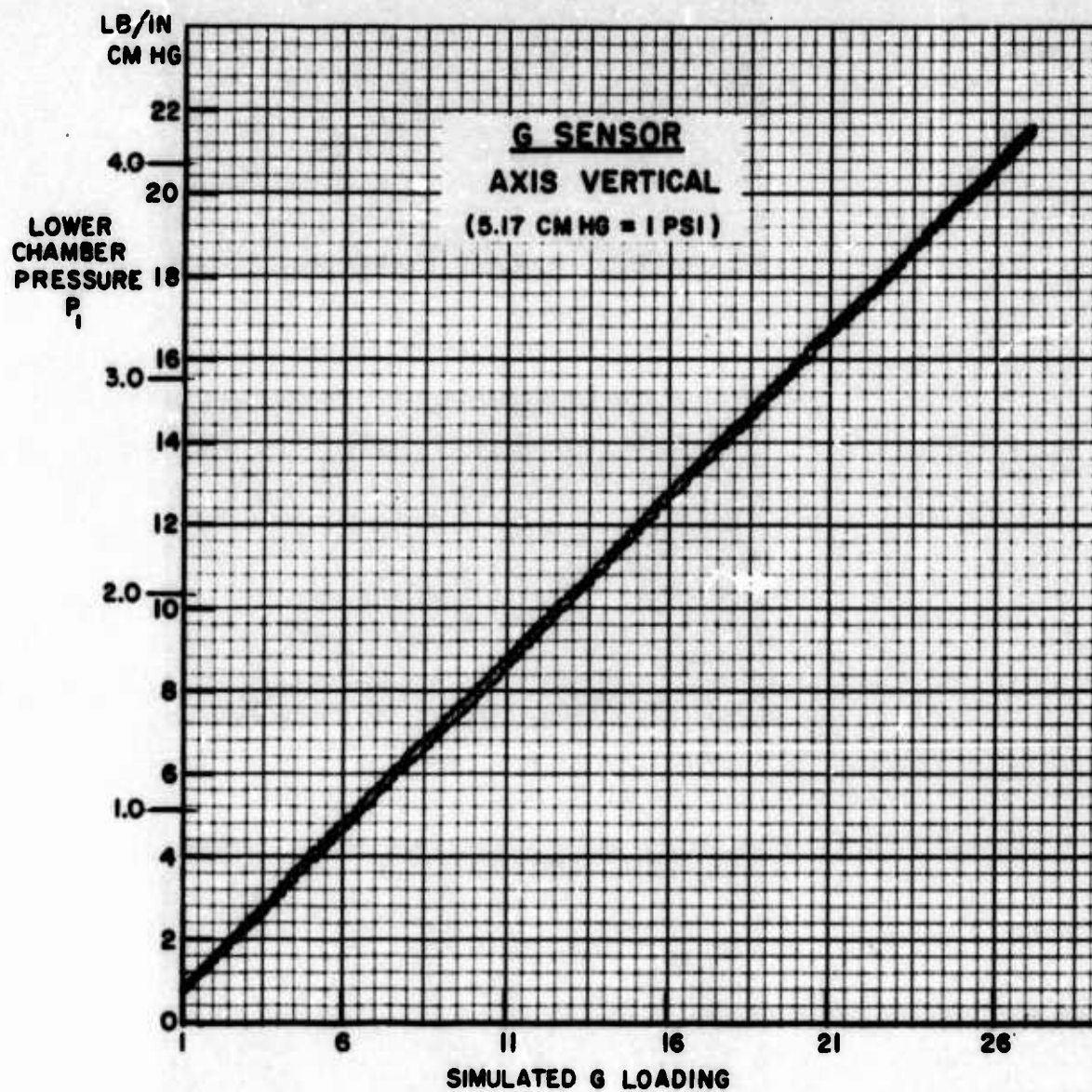


Figure 9. G Sensor Static Characteristics

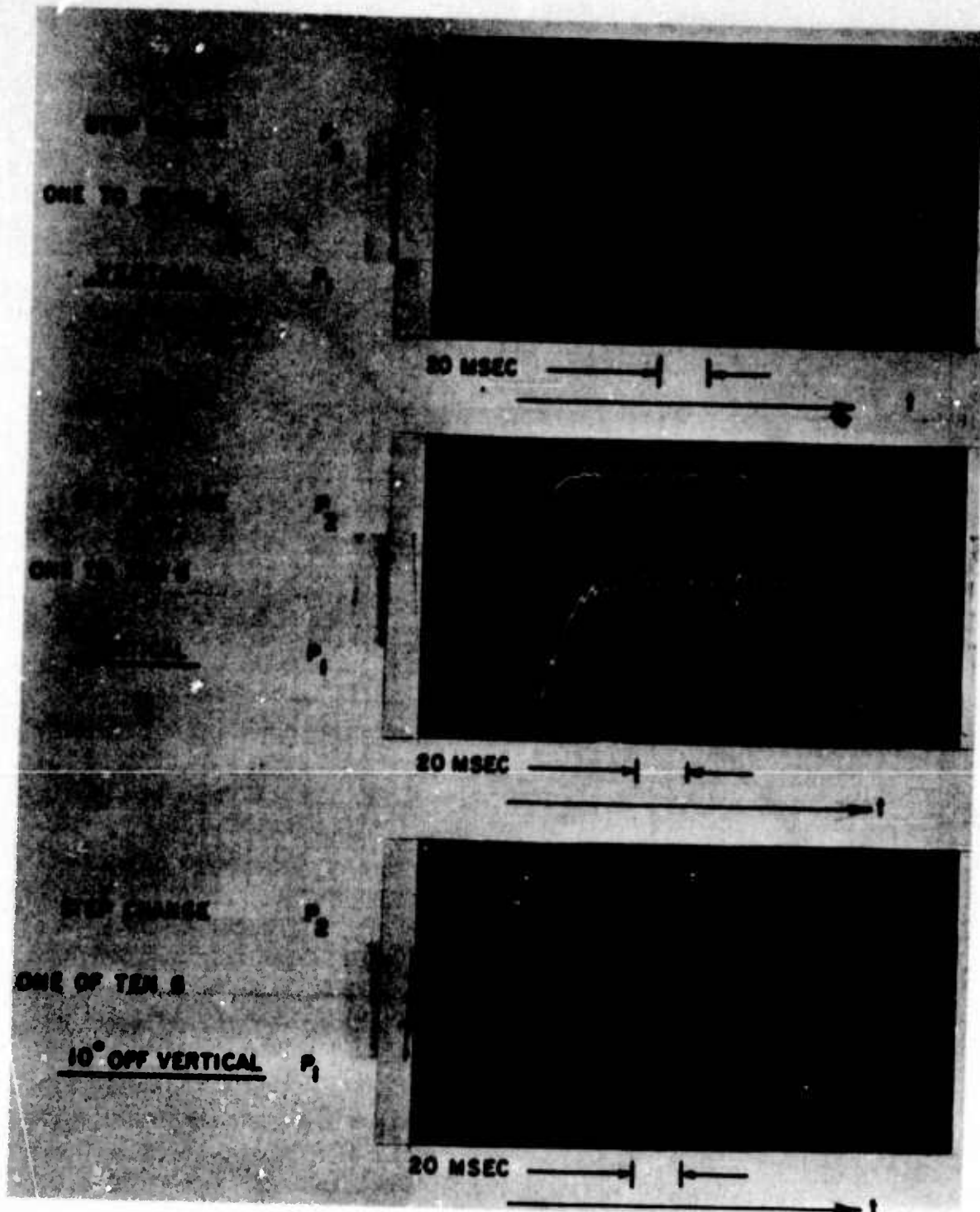


Figure 10. Experimental Response to G Transient

STEP CHANGE
0 TO 8 LB/IN² SUPPLY
AT 10 G
AXIS VERTICAL

P₂

P₁

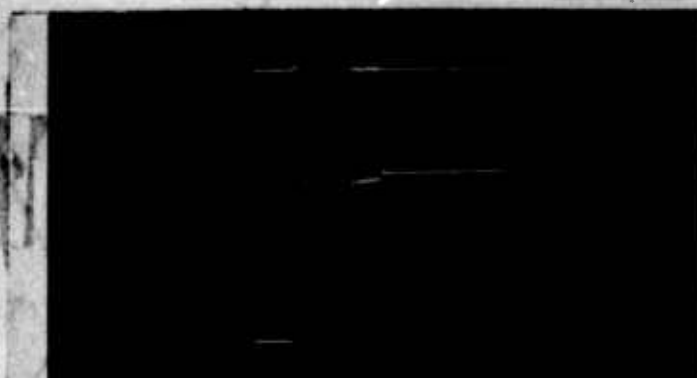


0.2 SEC ————| |————→ t

STEP CHANGE
0 TO 8 LB/IN² SUPPLY
AT 10 G
AXIS 10° OFF VERTICAL

P₂

P₁



0.2 SEC ————| |————→ t

Figure 11. Experimental Response to Supply Pressure Transient

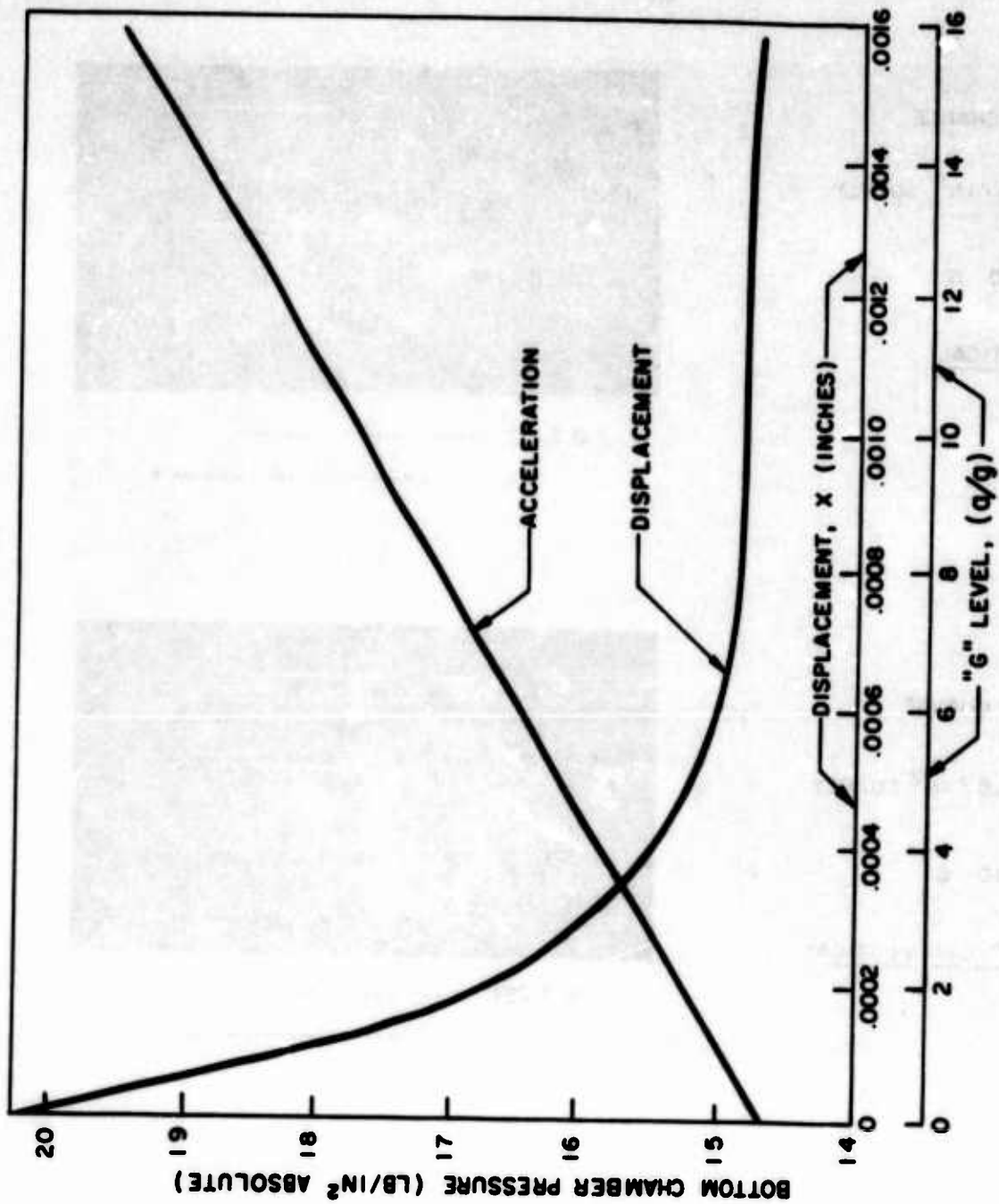


Figure 12. Steady State Data - 15 G Sensor

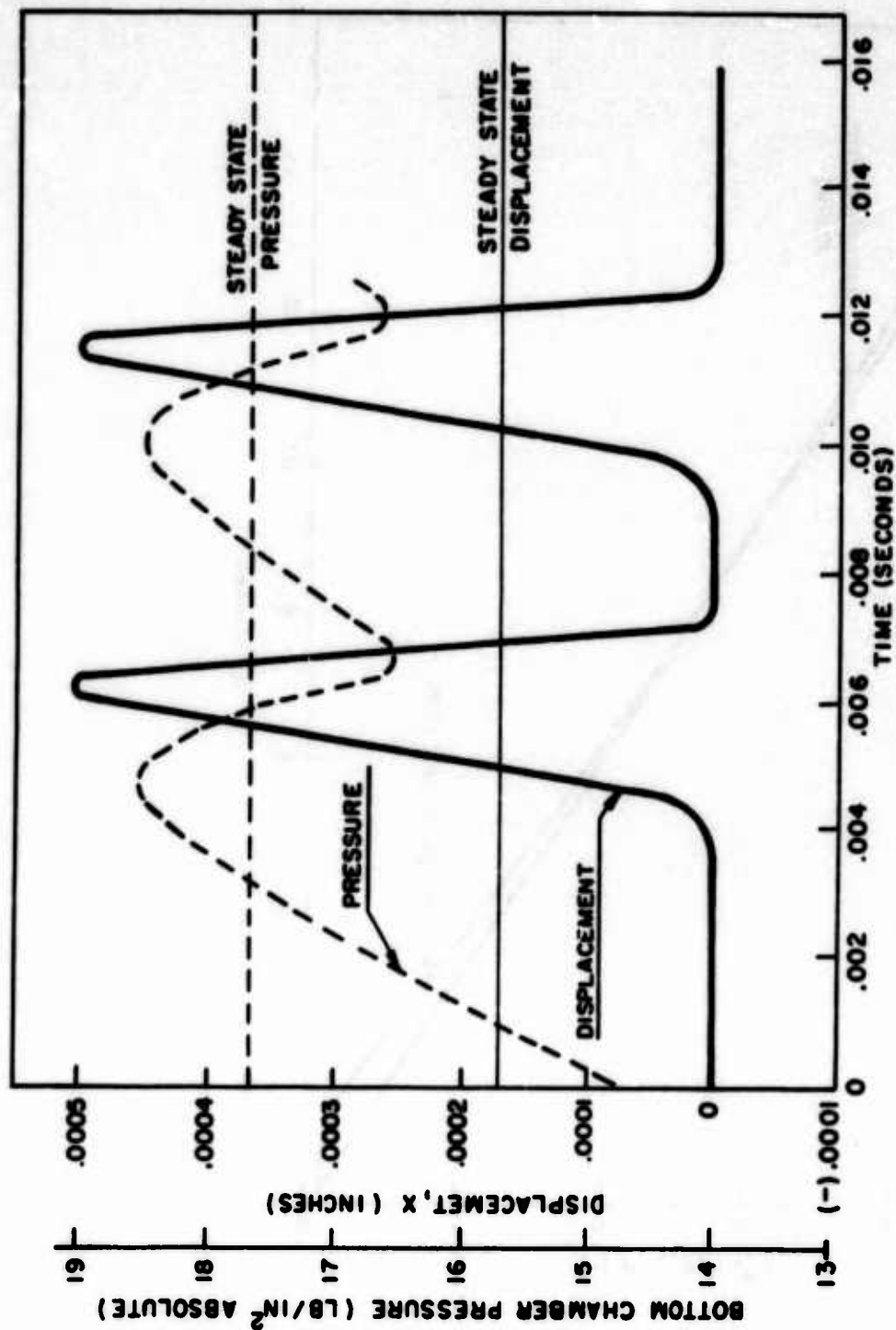


Figure 13. Transient Data - 15 G Sensor

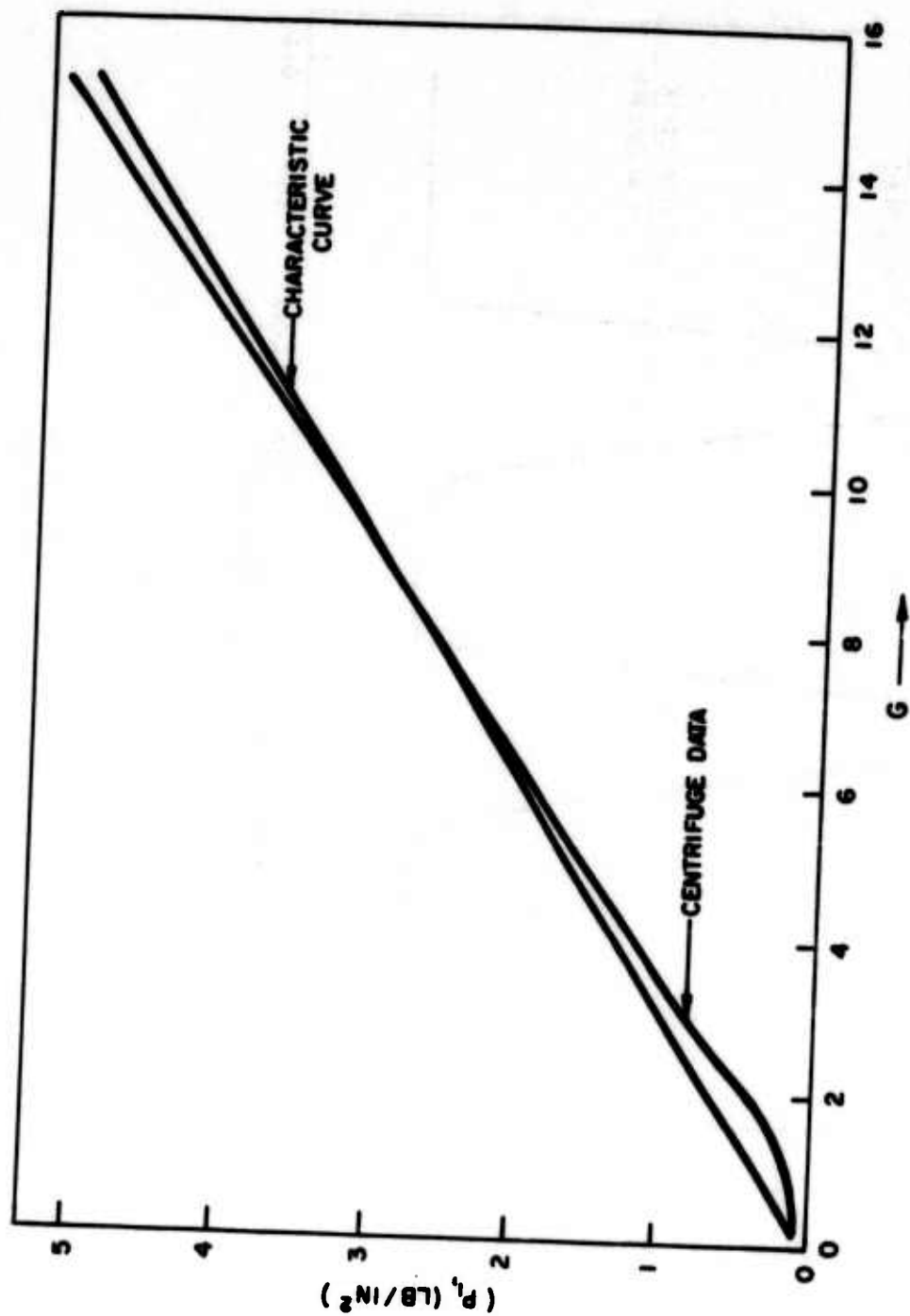


Figure 14. Bottom Chamber Pressure vs. G Level 15 G Sensor

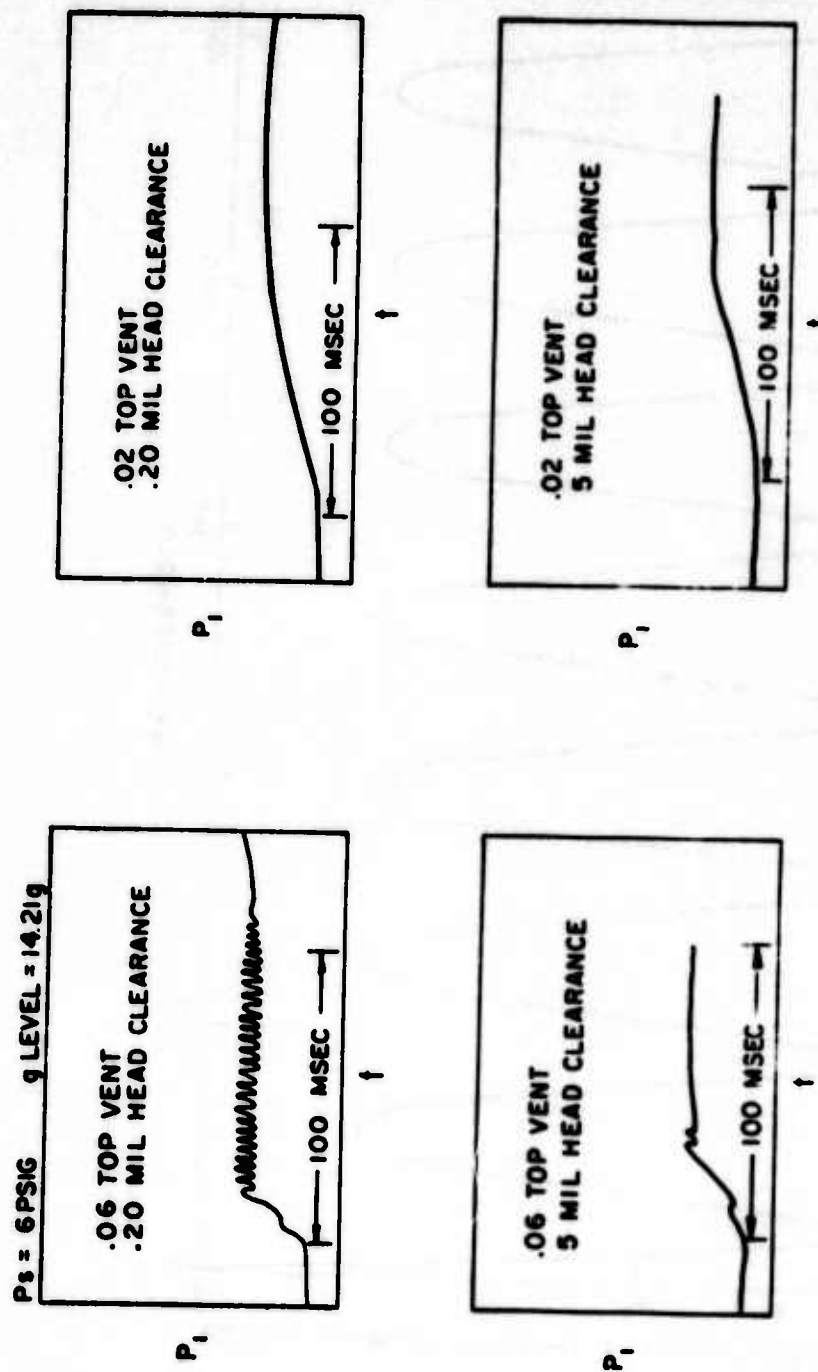


Figure 15. Experimental Test Results With High & Low Damping

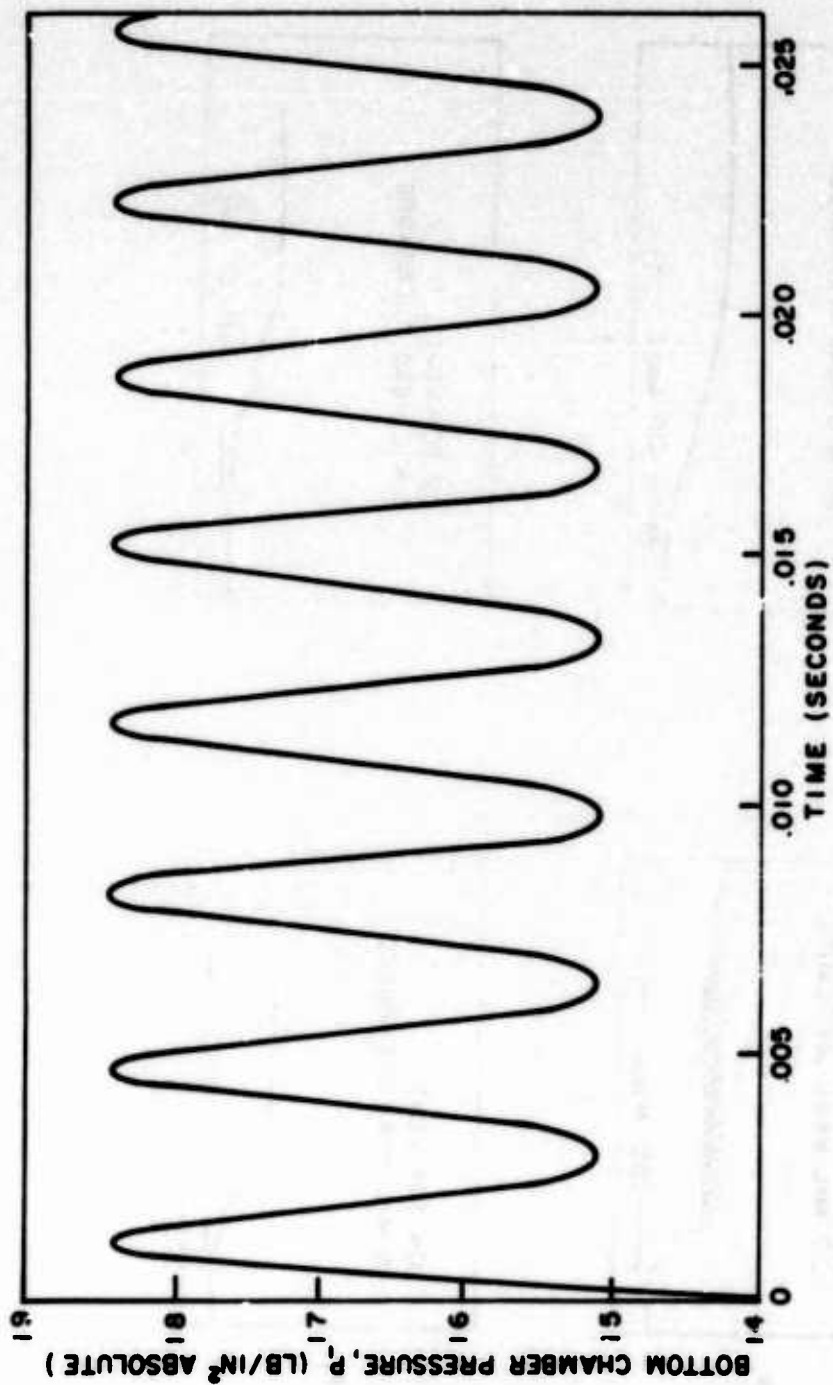


Figure 16A. Transient Data-Case I-Top Vent 0.060" Dia.

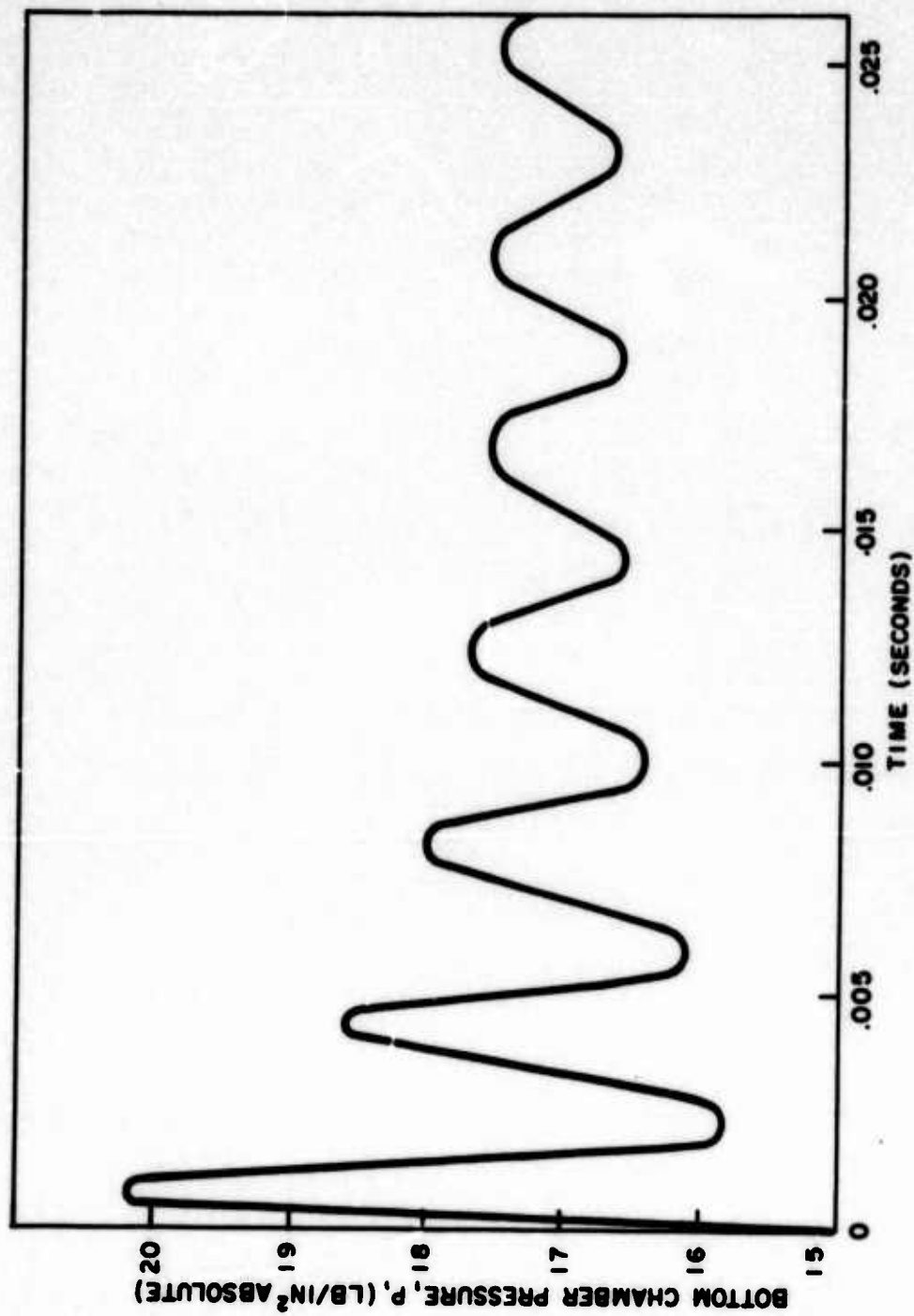


Figure 16B. Transient Data-Case IV-Top Vent 0.010" Dia.

PNEUMATIC RATE/ACCELERATION SENSOR

C. J. Bell* and L. R. Hester**

I. INTRODUCTION

With the advent of the fluidic amplifier, fluidic computation, and fluidic sensors there has developed considerable interest in the application of all-fluidic control systems to aircraft and missiles. One area in this application that has presented problems and has inspired considerable development work is that of fluidic rate and acceleration sensors. These sensors are a necessary and vital part of control systems whether they are used for stability augmentation or automatic controls. Fluidic rate and acceleration sensors have utilized many different concepts from electro-mechanical sensors with fluidic interfaces to pure fluidic sensors such as the vortex rate sensor.

This paper is concerned with presenting the results obtained from a prototype rate/acceleration sensor that utilizes a rotating solid mass for sensing rates and accelerations and through a somewhat unique concept provides an output fluidic signal. This device, the pneumatic rate/acceleration sensor (RAS), has been under development at Mississippi State University for the past 2 years. The device is capable of sensing two angular rates and three linear accelerations. This paper presents only the preliminary test results obtained with a somewhat arbitrarily selected configuration for a prototype. Optimization with regard to sensitivity, compactness, and output signal levels would require considerable further development work. Nevertheless, the initial prototype performance indicates that the concept is viable.

II. DESCRIPTION OF THE PNEUMATIC RATE/ACCELERATION SENSOR

The pneumatic rate/acceleration sensor (RAS) consists of a rotor supported by two opposed conical air bearings. The first working model of the device may be seen assembled on a rate table for testing in Figure 1. In Figure 2, the major components of the device are shown. Figure 3 is a schematic diagram of the device.

Referring to the schematic, the device functions as follows. The rotor is supported on the air films between the stator cones and the rotor cones. There are four feed orifices spaced 90° apart around each stator cone for a total of eight feed orifices. These feed orifices are individually supplied from their corresponding feed chambers.

* Professor - Mechanical Engineering - Mississippi State University

** Associate Professor - Aerophysics & Aerospace Engineering - Mississippi State University

The feed chambers are supplied by supply orifices which are connected to common supply manifolds in each stator cone. A signal port from each feed chamber provides the primary signal pickoffs. Assuming a constant supply pressure P_s , the feed chamber pressures P_{A1} , P_{Bk} , will each depend upon the rotor cone position with respect to the stator cones. For example, if the device is accelerated in the y-direction, pressures P_{A1} and P_{B1} will rise, while pressures P_{A3} and P_{B3} will fall. The linear acceleration in the y-direction is a function of $(P_{A1} + P_{B1}) - (P_{A3} + P_{B3})$. With proper design, the linear acceleration will be proportional to the algebraic sum of pressures indicated above, over some range of acceleration level. Linear accelerations in three mutually perpendicular directions may be obtained by summing (algebraically) the proper combination of signal pressures.

Consider next a torque acting in a clockwise direction on the rotor and about the z-axis. Pressures P_{B1} and P_{A3} will rise to resist this torque, while pressures P_{A1} and P_{B3} will decrease. The sum $(P_{B1} + P_{A3}) - (P_{B3} + P_{A1})$ will be a function of the torque about z. A torque about z arises when the entire device is rotated about the y-axis. The torque about z depends upon the usual gyro parameters of rotor speed, rotor moment of inertia and angular velocity about y. Of course, in rotating the unit about y, a torque is also imposed on the rotor about y. However, the precessional torque about z is much larger than the rotational torque about y in a properly designed device. A similar function of the pressure P_{A2} , P_{B4} , P_{A4} , P_{B2} will yield a signal which is a function of the angular velocity about z.

This abbreviated discussion indicates how fluid signals are generated by the RAS. These pressure signals must be processed by the appropriate fluidic circuits. The circuitry for each output signal desired consists basically of differential summing amplifiers followed by any additional stages of proportional amplification required. A typical network for angular rate sensing is shown in Figure 4.

III. EXPERIMENTAL SYSTEM AND RESULTS

The RAS was mounted on a rate table as shown in Figure 1. The table was powered by a D.C. motor, and the angular rate was determined with a frequency counter. The RAS was mounted so that the orientation of the y-axis (see Figure 3) with respect to the axis of rotation of the table could be set at any angle from 0° to 90° .

The output signals from the device were processed by a summing amplifier as shown in Figure 4. Each summing amplifier was followed by a single stage proportional for further amplification. The tests

reported have included fluidic circuits for two angular rates only. Linear acceleration tests have not been conducted.

In order to record the outputs, the fluidic signal from the final amplifier in each channel was fed to a Kulite pressure transducer, through a preamp and finally to a Sanborn 320 dual channel recorder.

Results and Conclusions: The output versus input results for the RAS as an angular rate sensor are shown in Figures 5 and 6. In Figure 5, the outputs about the principle axis of rotation are shown for the cases of rotation about the device y-axis and the device z-axis. Results for rotational of the device about an axis mid-way between the RAS y and z axes are presented in Figure 6.

As indicated by Figure 5, the sensitivity about each axis is essentially linear up to 15 degrees per second. The somewhat erratic results beyond the 15 deg/sec point could be due to limitations of this prototype, to limitations of the data gathering system, or to limitations of the fluidic signal processing circuitry. No attempt has been made to determine which of these segments, if any, contributes most to this behavior. One facet of the device performance which is not indicated in Figure 5 is that of crossfeed. The raw data indicated that with rotation about, say, the y-axis, there is approximately 10% crossfeed into the z-axis. The RAS was subjected to angular rotation with zero rotor speed, and no output signal could be detected during this test. It appears, therefore, that increased precision in manufacture and mounting can virtually eliminate any crossfeed between axes.

In Figure 6, the simultaneous outputs from both the y and z axes are presented for rotation about an axis at 45° to y and z. There are two important characteristics indicated from this data. First, the RAS can resolve an angular rate in a plane into its two components. However, the outputs are not proportional to the angles of orientation of respective axes.

The tests of this prototype RAS indicate that it is, in principle, a feasible concept for angular rate sensing. It is also clear that further work, analytical and experimental, is required before the device can be commercially useable.

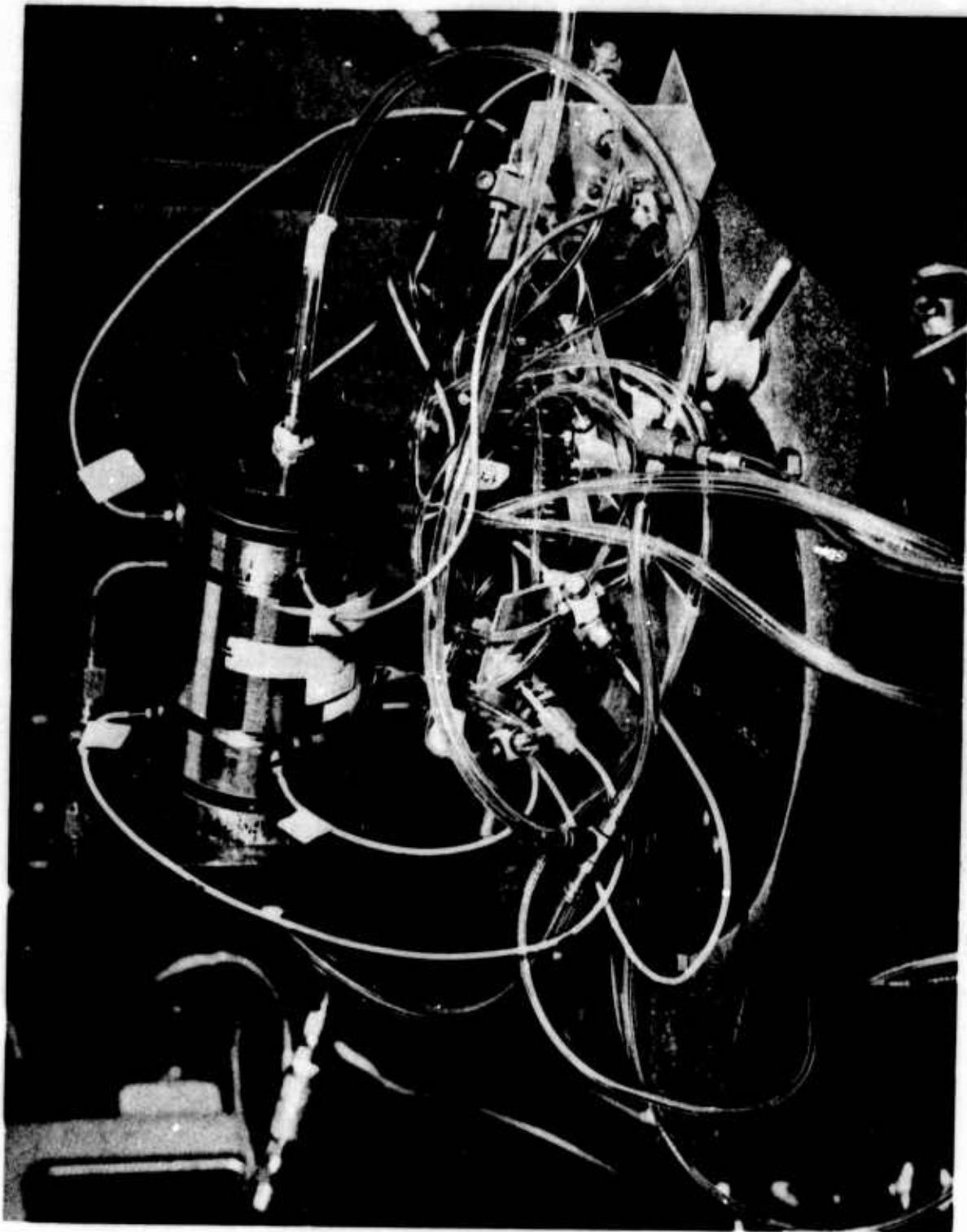


Figure 1. RAS Mounted on Rate Table

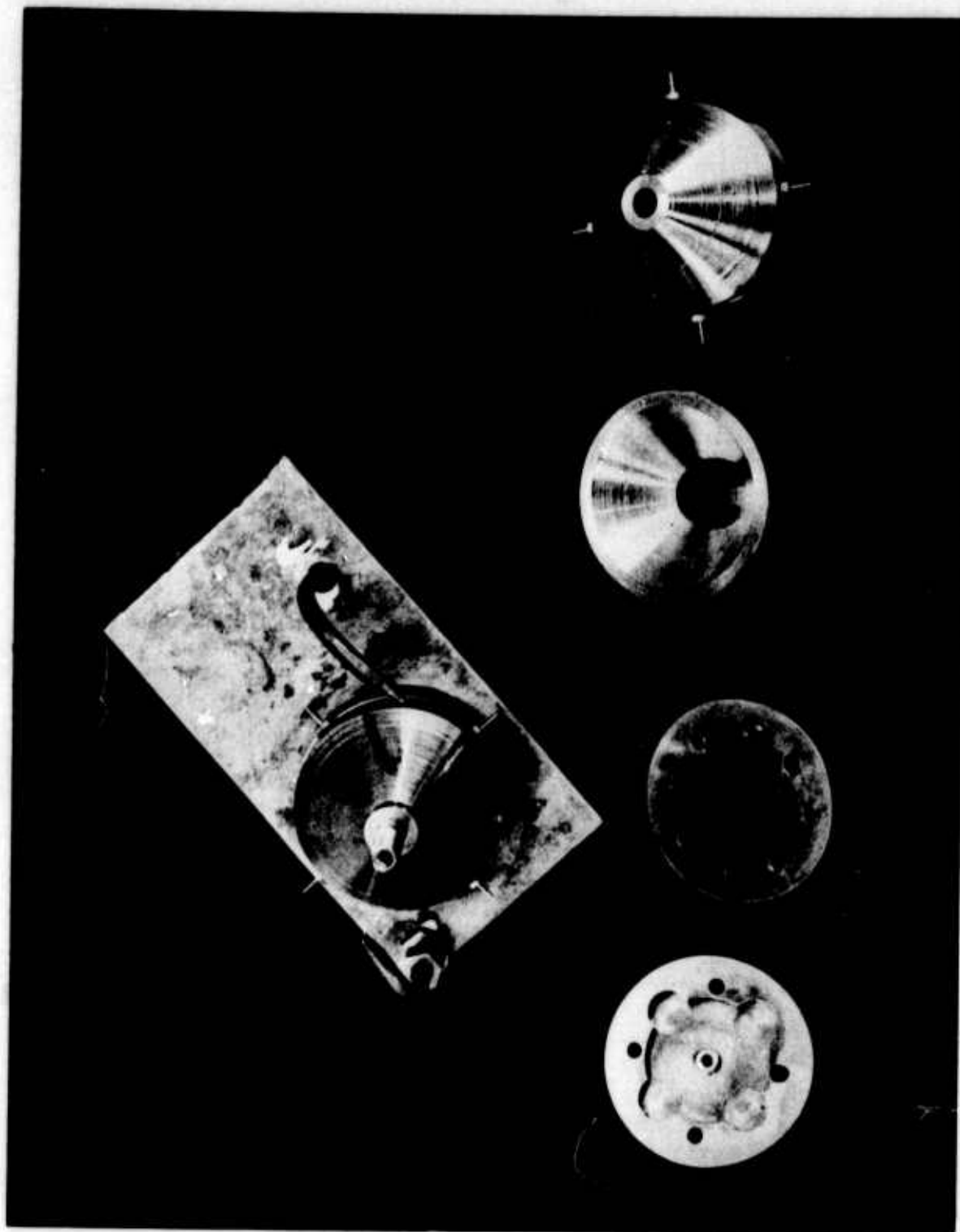


Figure 2. Major Components of RAS

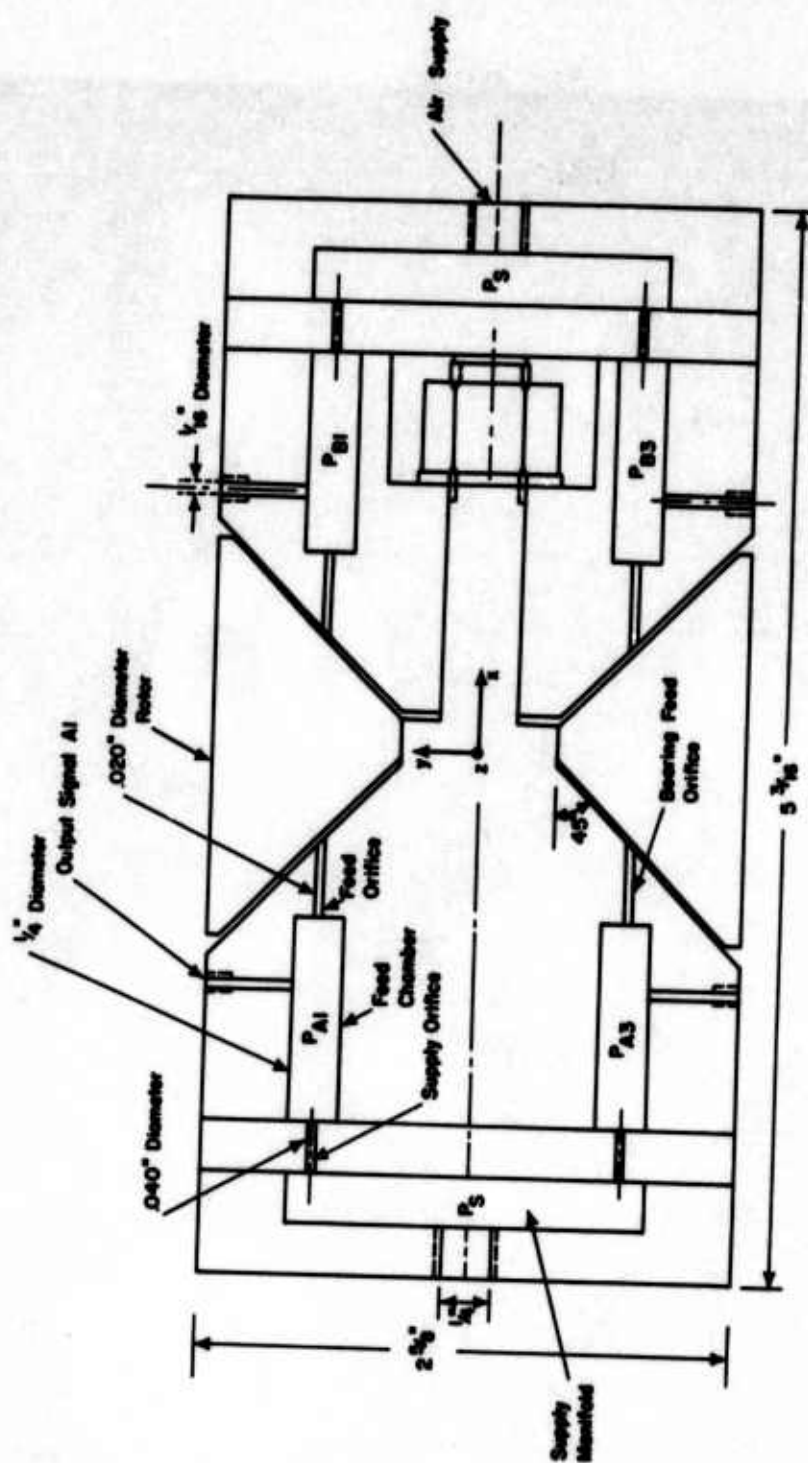


Figure 3. RAS Schematic

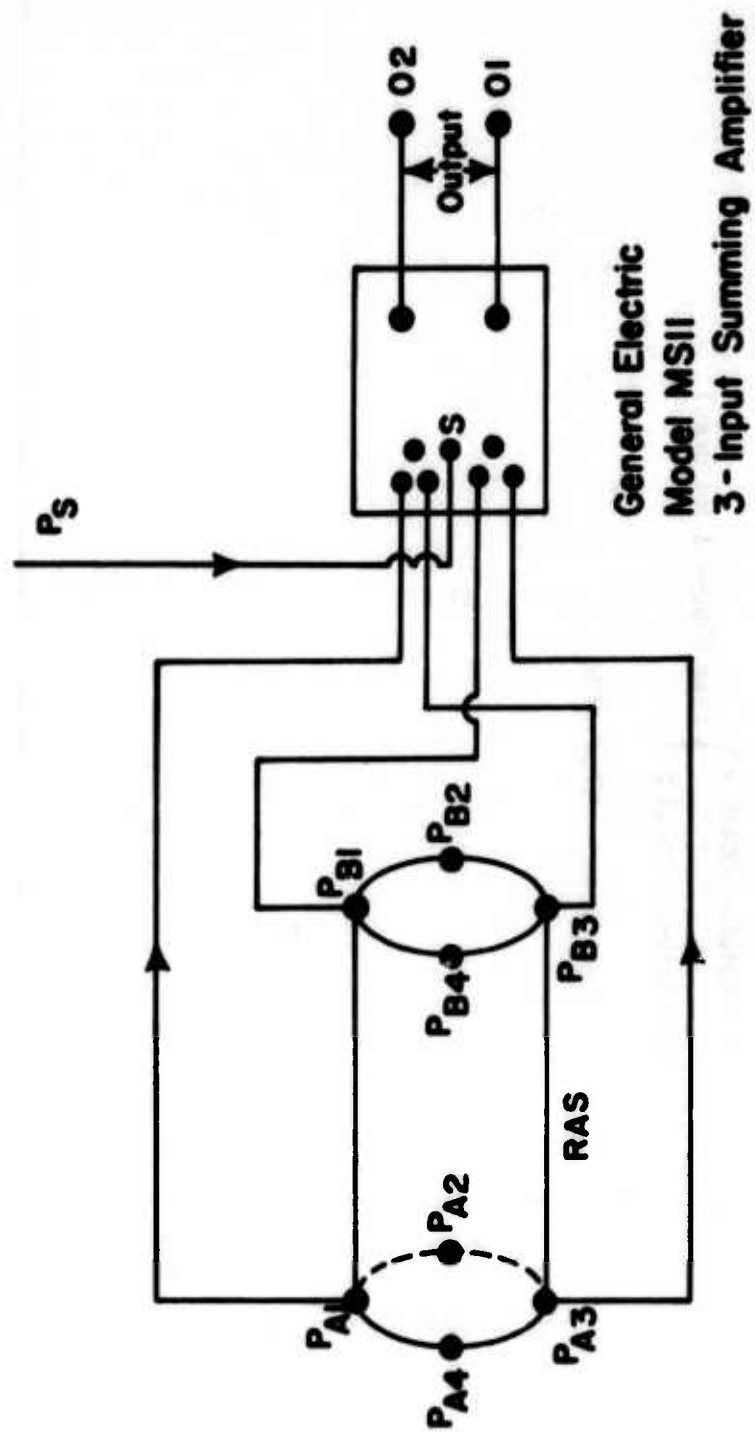


Figure 4. Typical Fluidic Circuit For One Angular Rate Signal

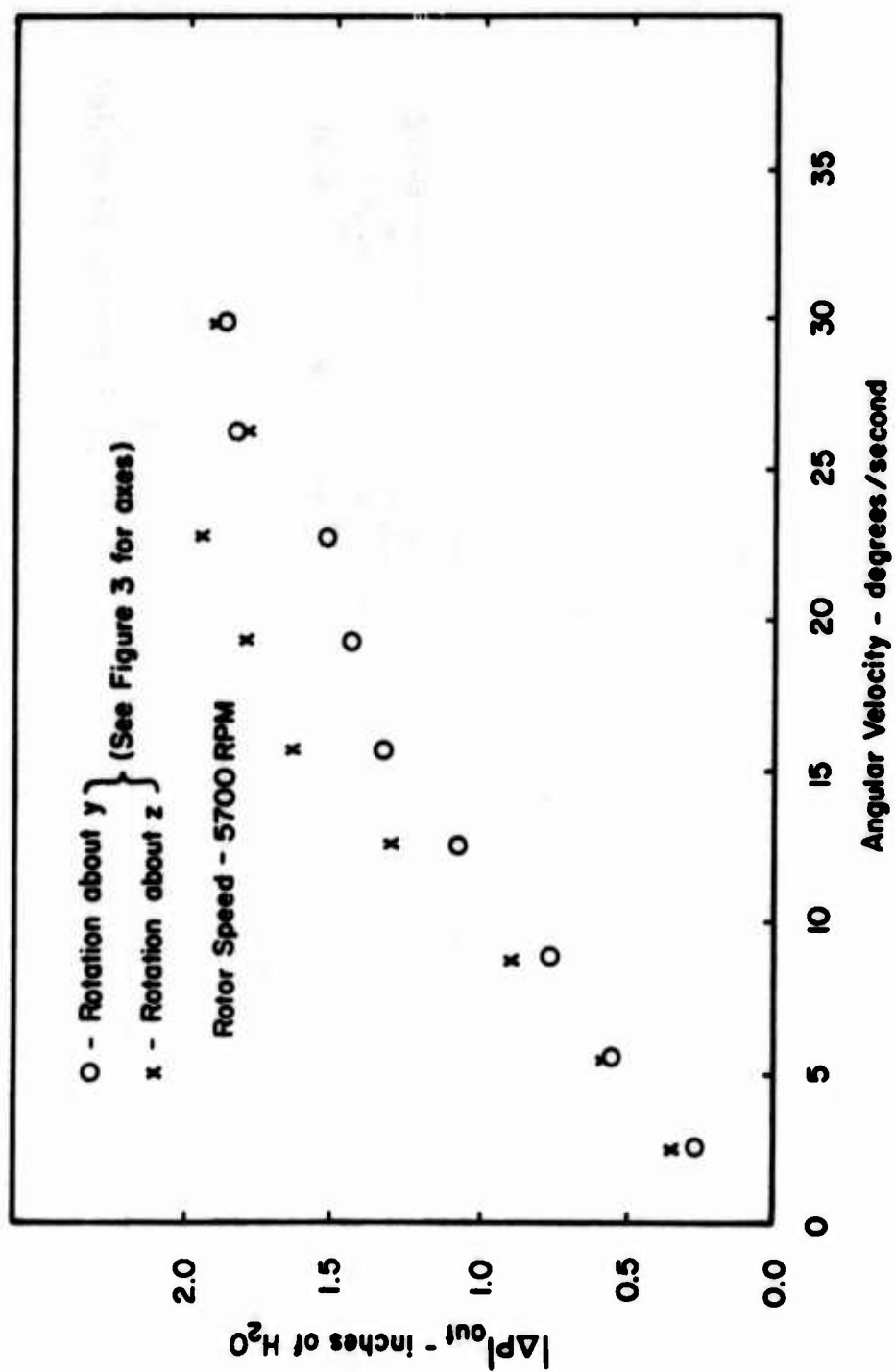


Figure 5. Outputs For Rotation About Sensitive Axes of RAS

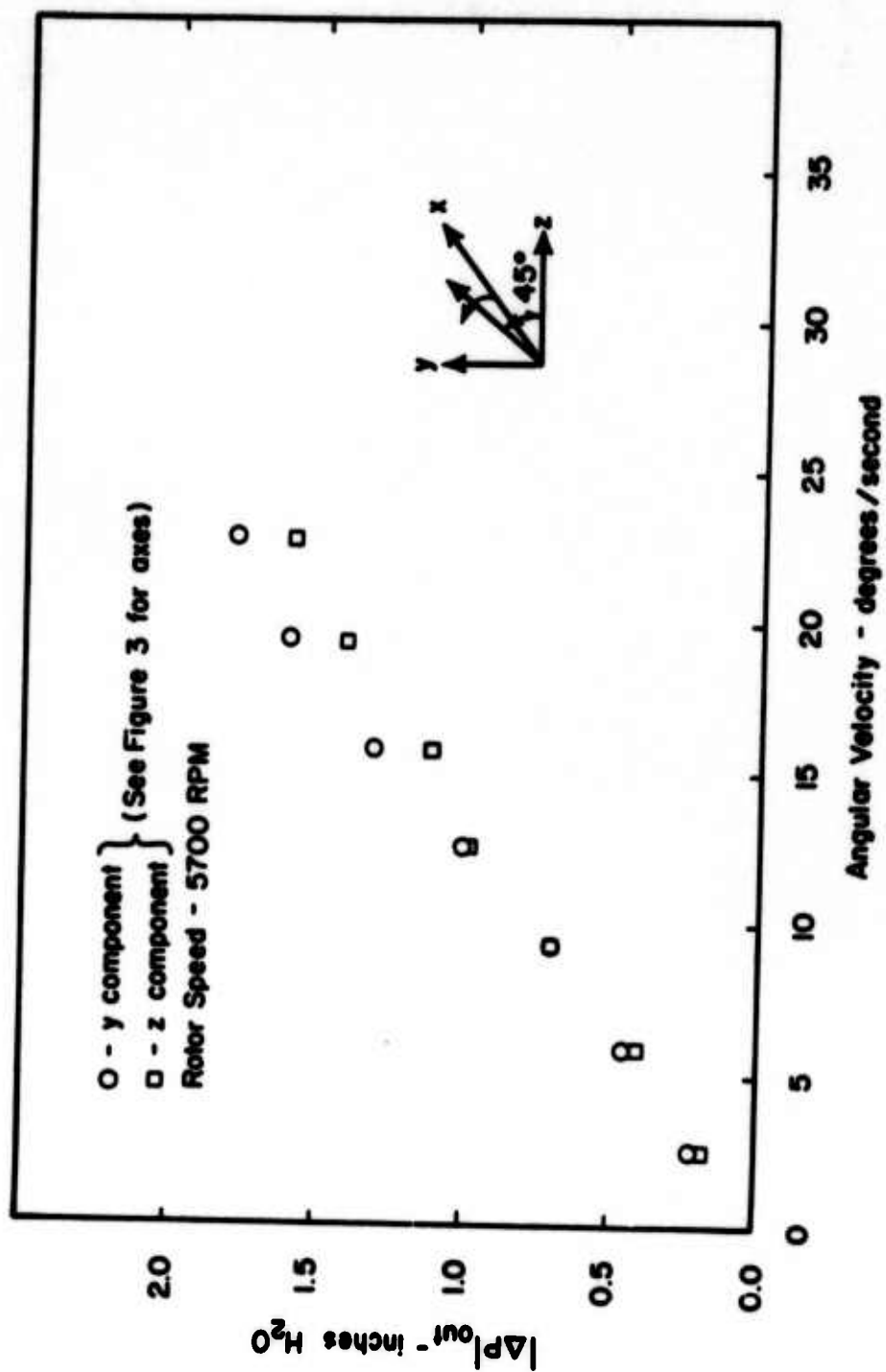


Figure 6. Outputs For Rotation About Axes 45° to RAS Sensitive Axes

FLUIDIC NONCONTACT GAGING

W. R. Schurman
Monsanto Research Corporation
Mound Laboratory*
Miamisburg, Ohio

ABSTRACT

A fluidic noncontact method of gaging using low pressure air (less than 1 psig) was developed for measuring compacted powder heights of loaded detonators. Conventional air gages which used air flow indicators and back pressure sensors were investigated; however the minimum recommended operating pressure of 5 psig of gages of this type would disturb the compacted powder surface.

Two gaging systems using extremely low back pressures coupled with a fluidic logic network were built and evaluated. Maximum sensing pressure and optimum gaging distance were established. Tooling for gaging the compacted powder heights for two different loaded detonators was developed. The relationship of back pressure and powder heights was determined over a 0.003 in. range. One fluidic gage was outfitted with a five-stage proportional amplifier. Another gage used fluidic indicator lights to indicate parts which were in tolerance, above tolerance, or below tolerance. The gages were also outfitted with a precision pressure transducer and digital display graduated in 0.001 psig divisions for obtaining actual back pressure readings. Other applications which could take advantage of gaging and sensing at extremely low pressures as they apply to detonator fabrication were also investigated.

*Mound Laboratory is operated by Monsanto Research Corporation for the U. S. Atomic Energy Commission under Government Contract No. AT-33-1-GEN-53.

TABLE OF CONTENTS

ABSTRACT

INTRODUCTION

BASIC OPERATION OF CONVENTIONAL AIR GAGES

COMBINING FLUIDIC AMPLIFICATION WITH BACK PRESSURE SENSORS

**FLUIDIC POWDER HEIGHT GAGE WITH VISUAL INDICATOR -
CASE HISTORY**

**FLUIDIC POWDER HEIGHT GAGE WITH PROPORTIONAL AMPLIFIER
CASE HISTORY**

OTHER APPLICATIONS OF FLUIDIC GAGING

Measurement of Pellet Height
Depth-to-Powder Gage
Well Depth Gage

CONCLUSIONS

REFERENCES

NOMENCLATURE

psig	- Pounds per square inch gage
in.	- inch
"d"	- Orifice diameter
"D"	- Sensing distance
PA	- Pressure ambient
PR	- Pressure restricted
R_1	- Resistor #1
C_1	- Control #1
O_1	- Output #1
P_{O1}	- Pressure at output #1
P_s	- Pressure or power supply
P/A_1	- Proportional amplifier #1
O/N_1	- OR/NOR gate #1
N_1	- Needle valve #1
G_p	- Pressure gain
CA	- Capacitor
Q	- Flow rate

INTRODUCTION

Since its introduction in the late 1920's, gaging of components with air has been widely used on single repetitive measurements as well as on many automatic multiple inspections where the inspection department is essentially part of the production line. With automatic gaging, the parts are continually inspected and corrective actions can be made by automatic machines.¹ Air gaging has been used to measure such conditions as diameter, out-of-roundness, bevels, taper, concentricity, center distances, camber, parallelism, shaft runout, squareness, etc. In the past all air gaging was performed with a supply pressure of 5-20 psig. However, with the advent of fluidics, low pressure sensing and fluidic amplification have become possible. The new techniques of fluidic switching and amplification provide additional versatility, range, and precision to air gaging. Back pressure sensing with pressures less than 1.0 psig are used in fluidic gaging. Noncontact gaging is necessary when powder surfaces or delicate electronic surfaces must be gaged. Fluidic noncontact gaging appears to fulfill this requirement in certain applications. In its broadest definition, gaging is the art of determining the size of an object, the quantity thereof, or capacity. Techniques used to sense size, position, flow, level (liquid or solids), etc. are considered to be included in this broad field of gaging.

BASIC OPERATION OF CONVENTIONAL AIR GAGES

Throughout their history, air gages have proven to be an extremely accurate method of determining single and multiple dimensions. Ease of operation and calibration, coupled with relatively low cost and endurance, are some of the reasons for their widely accepted use. The basic operation of conventional air gaging is relatively simple; however, it should be thoroughly understood in order that an intelligent comparison can be made between it and fluidic gaging.

In its simplest form the heart of the most popular air gaging instrument is essentially an air-flow indicator. An air supply of 60 to 125 psig is supplied to the instrument

through a filter and regulator. The air is regulated to approximately 10 psig and flows through a glass or plastic tube where it suspends a float. The float rises and falls in the tube as determined by the air flow through the tube. A hose is connected from the top of the tube to the gage head itself. Rate of air flow, as indicated by the position of the float in the column, is proportional to the clearance between the gage head and the work being measured. The gage is calibrated by determining the upper and lower float positions which represent the maximum allowable tolerance limits.

At first glance the gage head, normally used to check an internal diameter, physically resembles a common plug gage; however, it has a central air passage with a series of air jets exiting at its diameter. When inserted into the hole to be checked, the gage checks the true diameter of the hole based on the clearance between the gage head and the inside diameter of the hole. The larger the diameter the greater the air flow; therefore, the float will rise in the tube. A typical system of this type, shown in Figure 1, can also be adapted for making external diameter checks as well as other dimensional checks.

Another widely used air gaging instrument uses the back pressure sensor in conjunction with a dial indicator. It is connected to an air supply through a filter and regulator. Supply air is regulated to approximately 20 psig. The indicator is essentially a limited-range bourdon tube which immediately shows the back pressure. As in the case with the flowmeter gage, the pressure changes are determined by the clearance between the gage head and the component being measured. Extremely fast responses and remote sensing are advantages of a liquid-filled bourdon tube. A typical back pressure gage used for checking an internal diameter is shown in Figure 2.

COMBINING FLUIDIC LOGIC WITH BACK PRESSURE SENSORS

When gaging small delicate surfaces, we are usually faced with the problem of sensing a physical parameter with extremely low pressure air and minute air flows and of amplifying the signal to achieve a working output. Fluidics can

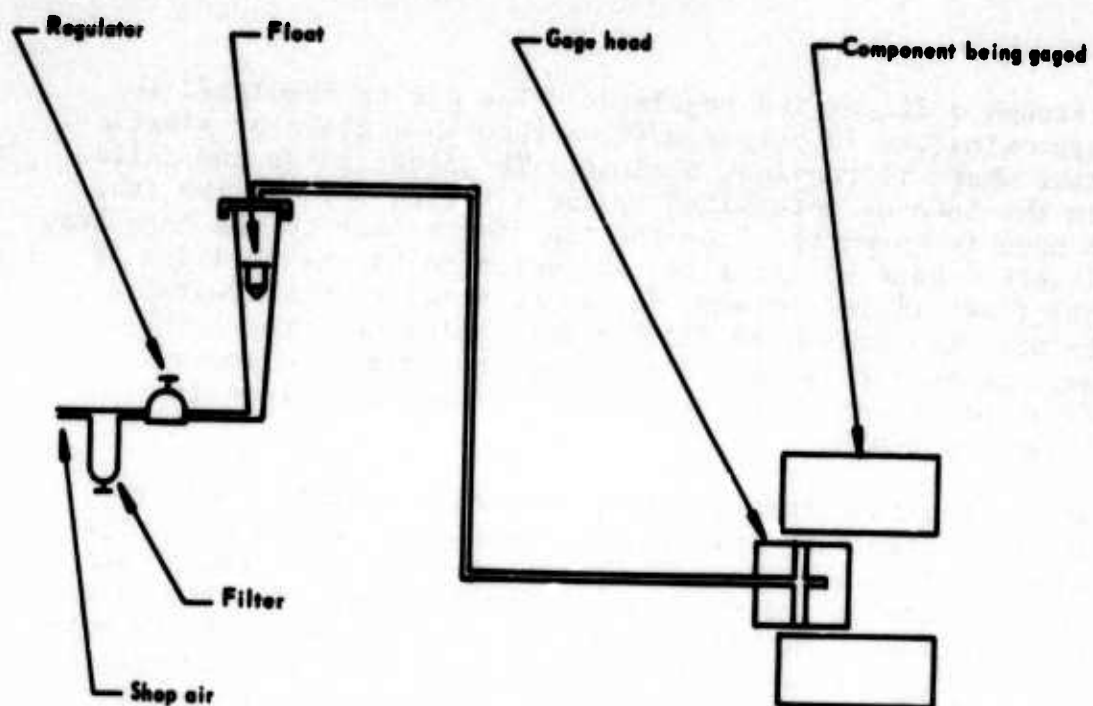


FIGURE 1 - Air flowmeter used for gaging.

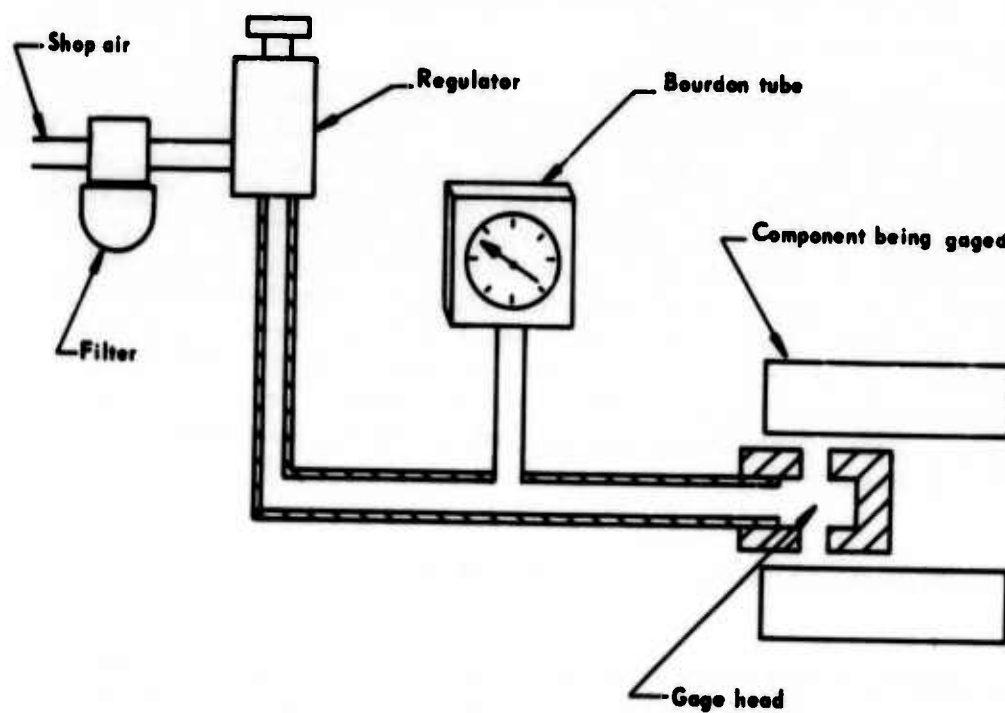


FIGURE 2 - Back pressure gage used to gage inside diameter.

be quite satisfactorily combined with back pressure sensors to amplify the low back pressure signal.

The sensor uses a flow of air which is filtered, regulated, and metered through an orifice. The output of the sensor, which is back pressure in the line, is proportional (over a limited range) to the distance of the item being gaged from the orifice.

Back pressure sensors are considered proximity switches because it is not generally necessary that complete closure of the sensing port occur in order to obtain an output signal. It should be understood, however, that the back pressure method is generally limited to distances of less than $1/4$ the probe diameter. Figure 3 shows a typical relationship between back pressure and the distance of the

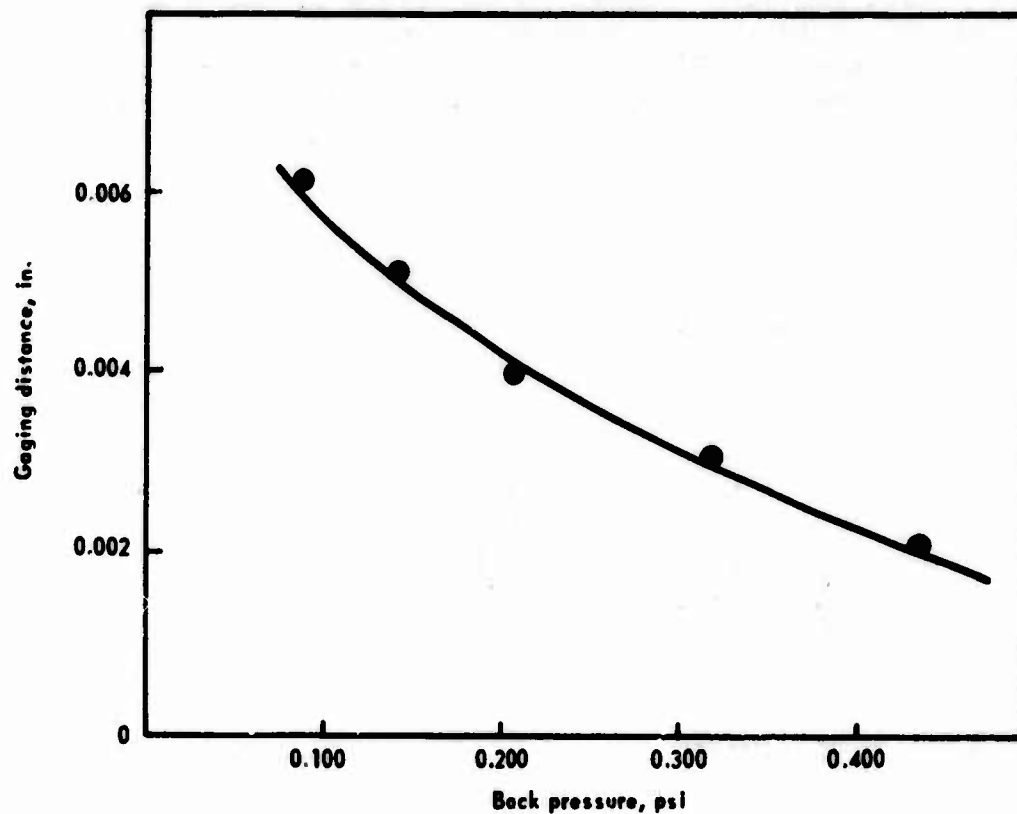


FIGURE 3 - Typical relationship between back pressure and gaging distance.

object being gaged. As shown, the back pressure output signal generated varies inversely with the gaged distance and directly with the supply pressure (over a limited range).

Back pressure venturi devices² can be custom designed for sensing or gaging small, precision parts and powdery surfaces as well as liquid surfaces. The venturi nozzle shown in Figure 4 has the ideal geometry for back pressure sensing. It should be noted that the diameter of the sensing orifice "d" should be approximately five times the sensing distance of "D".

The coupling of low pressure fluidic elements to perform signal amplification, digital switching, and logic functions provides wider versatility and range to air gaging applications which use back pressure heads.

It is possible to combine the proportional amplifier with the back pressure sensors to achieve a pressure amplification of up to several hundred to one.³ A simple example of this is shown in Figure 5. This system as shown consists of a needle valve, a pressure chamber, and the sensing orifice.

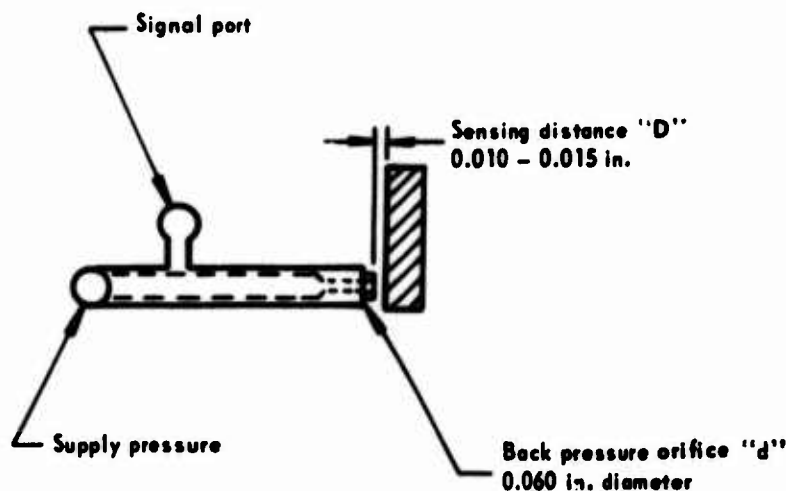


FIGURE 4 - Ideal nozzle geometry for back pressure sensing.

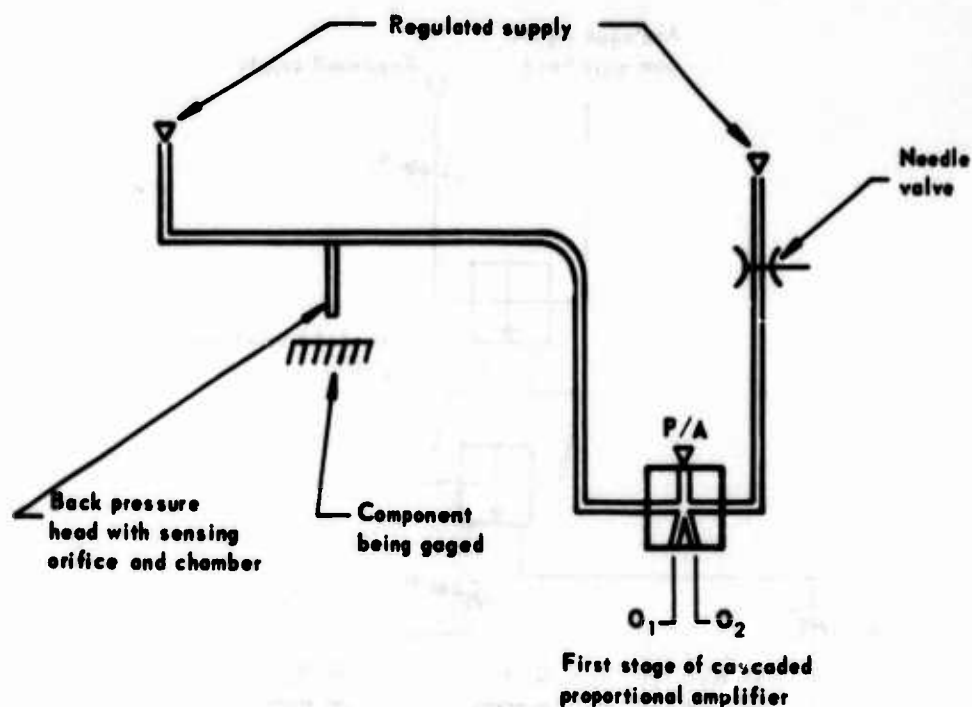


FIGURE 5 - Combination of back pressure sensor with proportional amplifier.

The component being gaged is slid under the orifice; it partially impedes the flow of air from the orifice causing a rise of pressure in the sensing chamber thereby increasing the pressure in the control jet of P/A. The output from O₂ of P/A can then be further amplified by cascading with other proportional amplifiers.

A Go/No Go indication can be accomplished by converting the analogue output of the proportional amplifiers to a digital signal. A system of this type is shown in Figure 6. In this example the low pressure leg of the proportional amplifier is used to determine when the part is at its tolerance limit. The OR/NOR gages O/N₁ and O/N₂ are held in a switched condition (output O₂) when an in tolerance part is being gaged. If the part varies out of tolerance, O/N₁ and O/N₂ will switch to O₁ indicating a reject component. The entire tolerance band can be shifted by adjusting the bias on the needle valve N₁. The high and low limits can be shifted by adjusting N₂ and N₃. For example, closing N₂ will raise

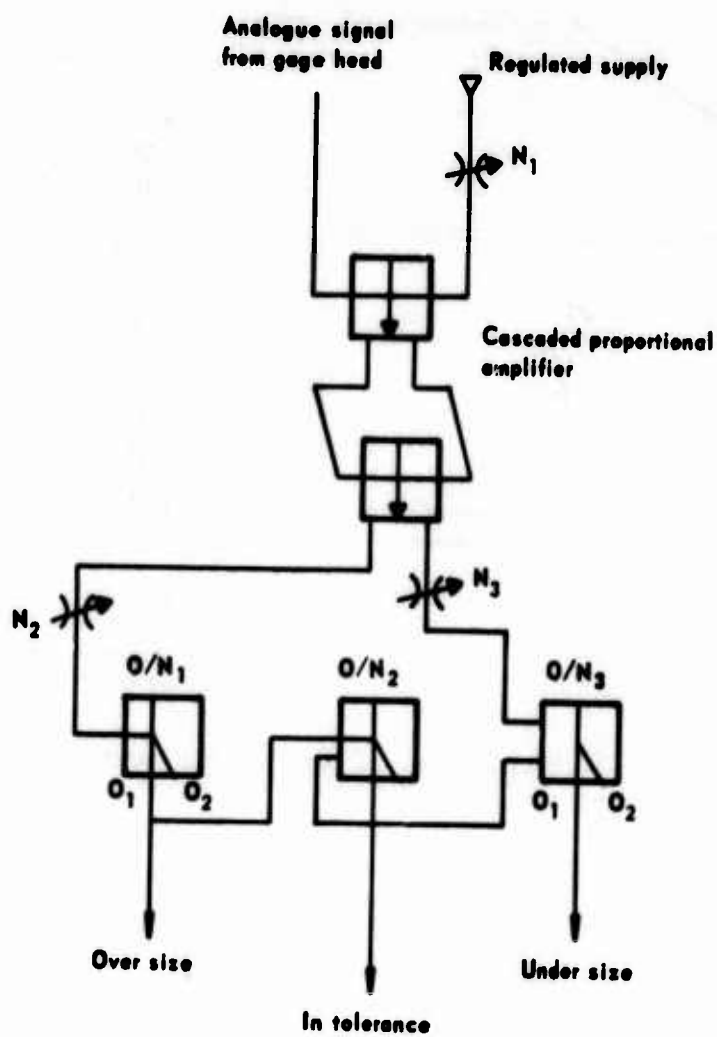


FIGURE 6 - Conversion of analogue to digital signal.

the undersize limit; i.e., O/N_1 will switch back (output O_1) sooner because the signal is restricted. This system as described can provide a noncontact gaging method with digital display without delicate instrumentation or electronic amplification when its input signal comes from a back pressure head.

Since there are no moving parts in the fluidic gaging circuit it is virtually maintenance free. With a three-stage amplifier it is possible to detect dimensional changes of less than 0.0001 in. After the tolerance limits have been established the system can be calibrated with gage masters.

A fluidic comparator circuit can also be designed by adding an additional gage head with a built-in master. This can be of benefit when the problems of providing a constant air pressure and maintaining the set points must be eliminated. A fluidic comparator gaging circuit, as shown in Figure 7, can be used for extremely accurate gaging. This system uses two gage heads, one for the master and one for the component being gaged. The back pressure from the two heads is connected to a cascaded proportional amplifier which can be used to power indicator lights, bourdon tubes, or pressure transducer system.

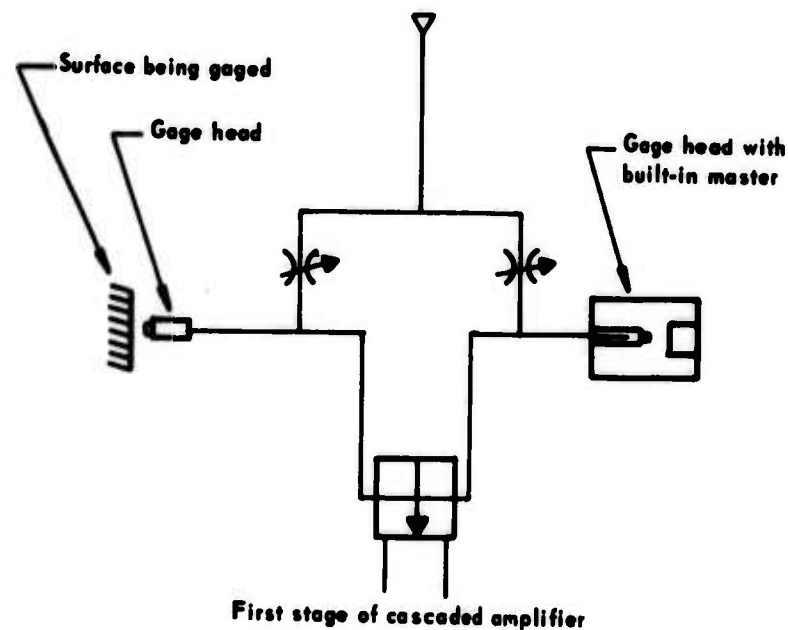


FIGURE 7 - Fluidic comparative gaging.

These examples show some of the gaging systems which are possible when back pressure sensing is combined with fluidic amplification. In most cases the descriptions given are brief to show only the basic operating principles.

FLUIDIC NONCONTACT POWDER HEIGHT GAGE WITH VISUAL ACCEPTANCE INDICATOR - CASE HISTORY

An important physical parameter requiring measurement during the manufacture of detonators is the explosive powder extension (Figure 8). This measurement must generally be controlled and verified within several thousands of an inch. Techniques used for the measurements of the heights of the extremely fluffy powder in loaded detonators have remained virtually unchanged since the original gaging method (the "snake eye" gage) was developed in the 1950's. This gage (Figure 9) consists of a cup which has two protruding pins whose lengths match the maximum and minimum allowable powder extension. The pressed powder height is gaged by placing the snake eye gage over the loaded cylinder. The loading would then be microscopically inspected and the presence of

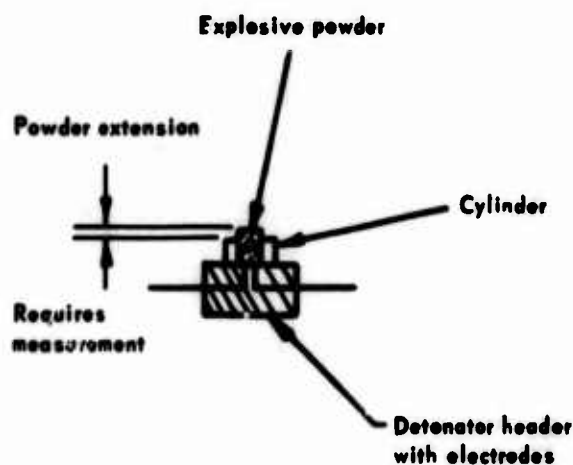
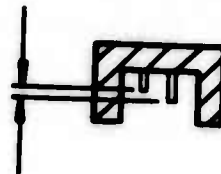


FIGURE 8 - Location of explosive powder measurement.



Pin lengths match the maximum
and minimum powder extension

FIGURE 9 - Snake eye gage used for
powder height verification.

one indentation in the powder surface would indicate an acceptance component. No indentations or two indentations would indicate a reject part. In addition to undesirable gage marks on the powder surface, this method relies on visual inspection to accept or reject an extremely critical fabrication parameter. Various noncontact methods of gaging this dimension have been evaluated such as light section microscope, light reflection, capacitance, and laser. The light section microscope is accurate; however, operation is slow and performed only by trained gage inspectors. It is not considered an in-line type of inspection. The light reflection method did not repeat well enough to reliably gage powder heights. Capacitance and laser gages remain under evaluation.

Prior work with fluidics, in the areas of machine control, process control, parts sensing, and position sensing, provided the background required to conceive the combination of fluidic logic and back pressure sensing to design a powder height gage.*

*Work performed by Corning, Bendix, Pitney Bowes, Johnson Service, and others in the area of sensing and gaging proved to be beneficial when background information was being collected.

A back pressure head was designed which would not contact the critical powder surface. This design, shown in Figure 10, incorporated an adjustable center probe and an outside retainer which would reference on a noncritical area of the component being gaged. Air was supplied to the slightly recessed center probe where it would exit along the powder surface being gaged. Air escapement flutes along the side of the retainer would allow the air to exit unrestricted.

Prior to finalizing the design, a development study was undertaken to establish the optimum gaging parameters such as orifice diameter, gaging distance, air escapement size, and gaging pressure. The original prime design requirements for this gage were that it 1) would not contact the powder; 2) would gage a part in not more than 15 sec; 3) could be operated by unskilled personnel; 4) would give visual indication of the condition of the part, i.e., in tolerance; 5) would be portable; and 6) could be easily calibrated and maintained. A simplified block diagram of this gage is shown in Figure 11. Some of the design parameters selected were the sensing orifice at 0.052 in., the sensing distance

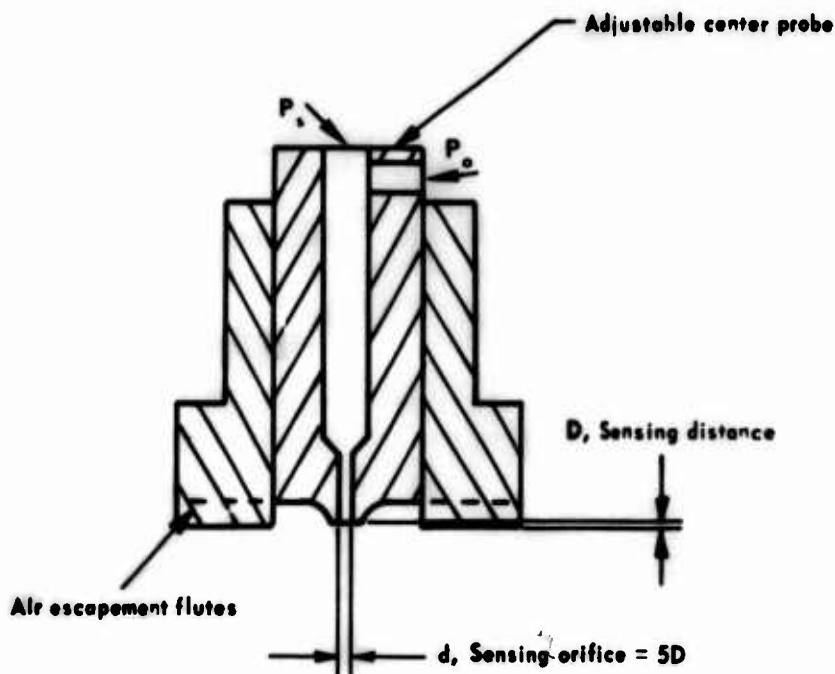


FIGURE 10 - Cross section of back pressure gage head.

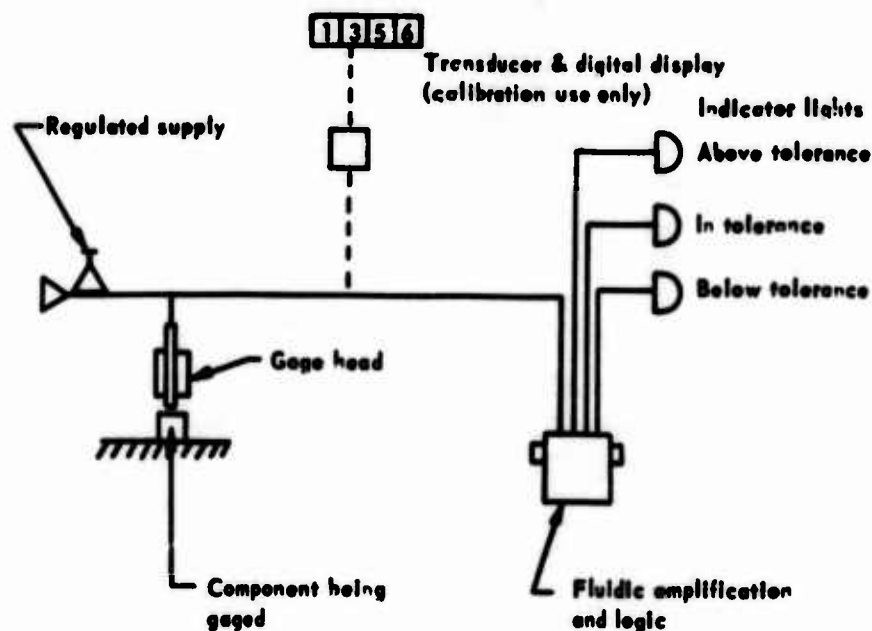


FIGURE 11 - Block diagram of a powder height gage.

at 0.010 in., and the back pressure at 0.100 psi. The pressure distance relationship was also established with sensor pressure varying from 0.050 to 1.0 psig. As a result of these studies a fluidic noncontact powder height gage was designed for measuring the explosive powder extension in a detonator. The gage which was built is shown in Figure 12. In actual use fluidic indicator lights visually indicate whether the component being gaged is in or out of tolerance.

Calibration with masters was used to establish the relationship between back pressure and simulated powder extension. This relationship is shown in Figure 13. The masters (Figure 14) were fabricated from hardened steel in a configuration to match the detonator being gaged. In order to calibrate the gage accurately, it was interfaced with a precision transducer and digital pressure display which had a full scale reading of 2.0 psig graduated in 0.001 psi increments.

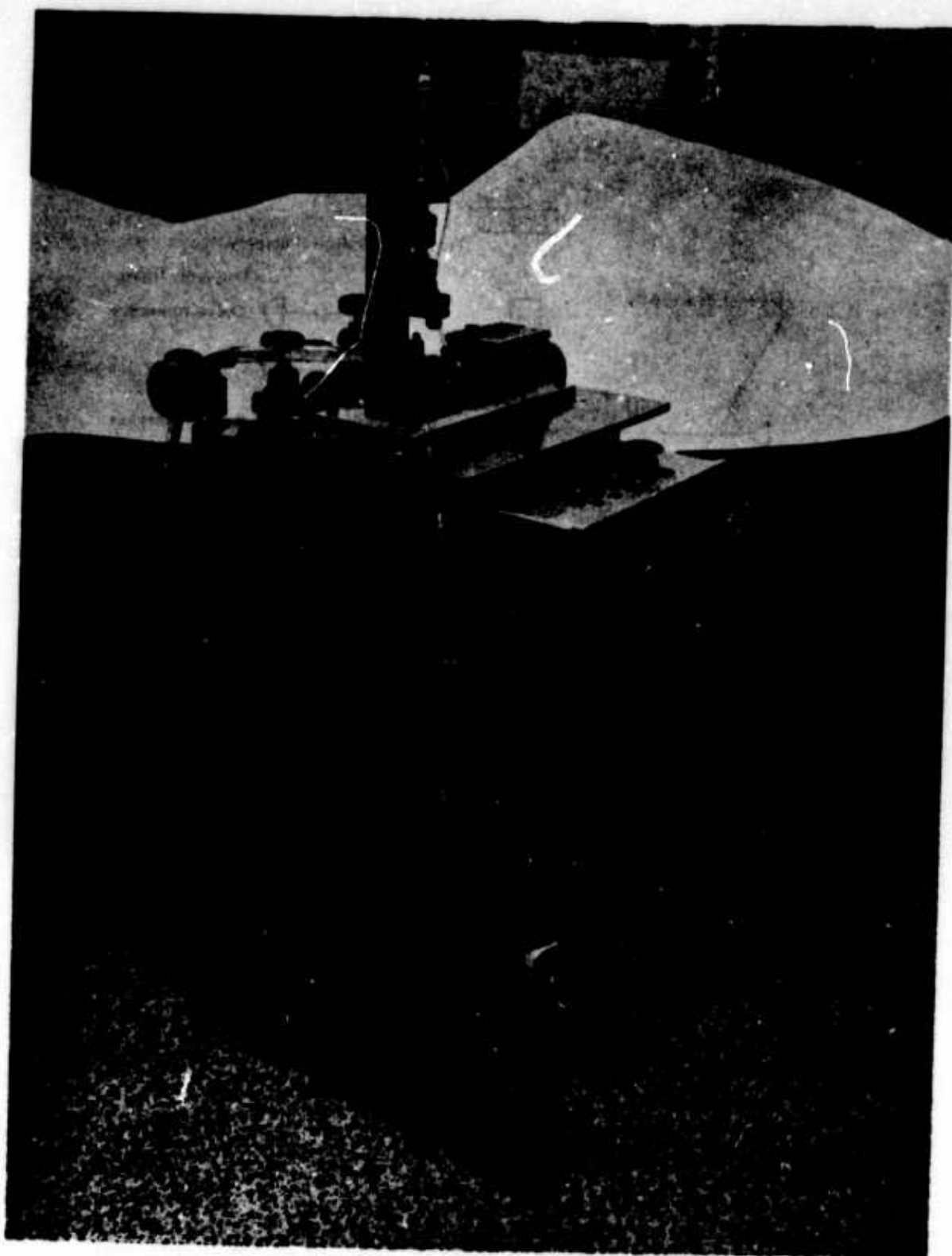


FIGURE 12 - Fluidic powder height gage with visual indicator.

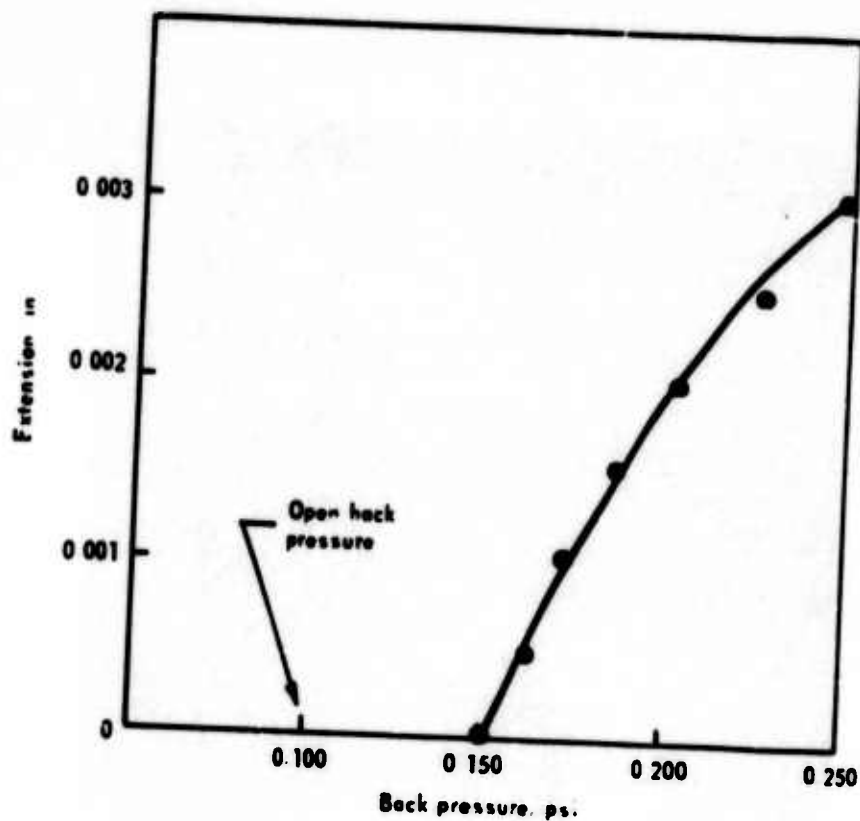


FIGURE 13 - Calibration curve obtained with steel masters.

The complete gaging system checked loaded detonators of the type shown in Figure 15. A series of detonators was loaded to various powder heights ranging from -0.001 to +0.006 in. These units were used to further calibrate the gage to determine the relationship of back pressure to actual powder height. This relationship is shown in Figure 16. Over the normal gaging range (i.e., flush to +0.003) the readability of the gage was determined to be equivalent to 0.000080 in.

In production use the digital display was not used because of the small back pressures which had to be measured. The hardened steel masters were used for daily checks of the Schmitt triggers in the gage circuit.

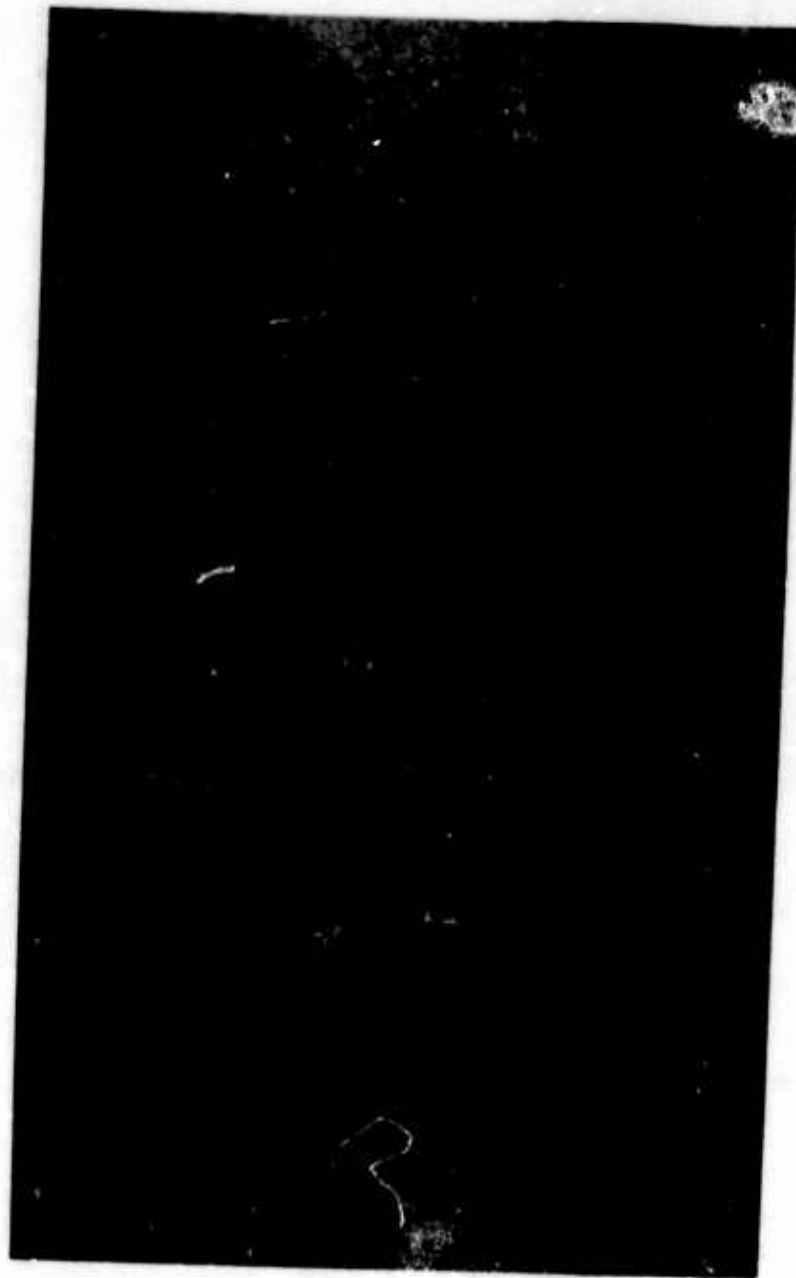


FIGURE 14 - Hardened steel masters used for gage calibration.



FIGURE 15 - Detonator loaded with compacted explosive.

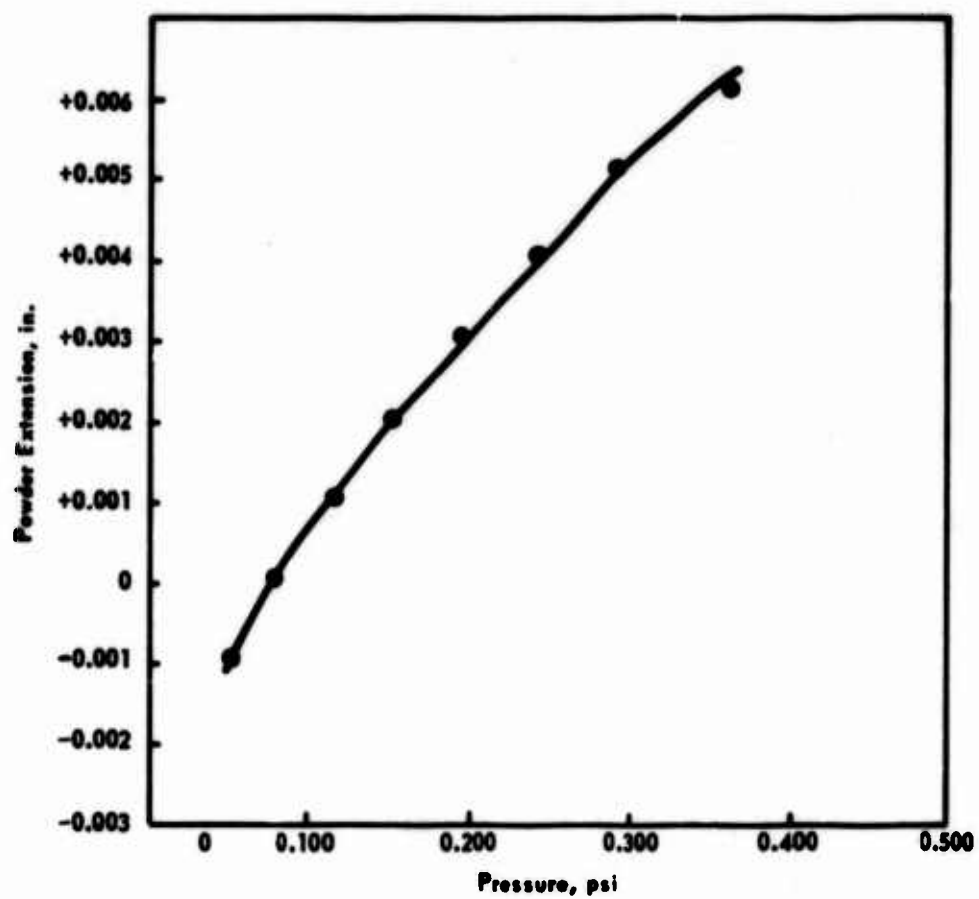


FIGURE 16 - Relationship between back pressure and powder extension in a detonator.

When a below tolerance master was in the nest, the set point on the Schmitt trigger was set to indicate "Below Tolerance." A similar procedure was followed when setting the Schmitt triggers for "in tolerance" and "above tolerance" conditions as shown by the indicator lights.

FLUIDIC POWDER HEIGHT GAGE WITH PROPORTIONAL AMPLIFIERS CASE HISTORY

There were stability problems associated with adjusting the set points of the Schmitt triggers and with production drifts of the powder extension that could not be detected in time to make necessary tooling adjustments.

Because of the low back pressures involved, direct reading of the back pressure was not attempted in production use. The unique feature of the proportional amplifier, i.e., to amplify a low level signal, was used in the design of an improved powder height gage where the actual back pressure could be monitored. The improved design also eliminated drifting set points on the Schmitt triggers. This gage incorporated a Corning 5-stage, 3-input summer with fixed resistors giving pressure gains (G_p) of 2.5, or 10. This summer (proportional amplifier) is shown schematically in Figure 17. The pressure at output #2 (P_{o2}) is expressed in the following equation:

$$P_{o2} = \frac{R_1}{R_{12}} P_{e2} + \frac{R_1}{R_{14}} P_{e4} + \frac{R_1}{R_{16}} P_{e6} - \frac{R_1}{R_{15}} P_{e5} \text{ or}$$

$$P_{o2} = 2.45 P_{e2} + 5.13 P_{e4} + 11.0 P_{e6} - 1.15 P_{e5}$$

where the flow rates of the fixed resistors are listed as follows:

$$\begin{aligned} Q \text{ of } R_1 &= 14.3 \text{ std. cm}^3/\text{min} \\ Q \text{ of } R_{12} &= 35.0 \text{ std. cm}^3/\text{min} \\ Q \text{ of } R_{14} &= 73.4 \text{ std. cm}^3/\text{min} \\ Q \text{ of } R_{15} &= 16.4 \text{ std. cm}^3/\text{min} \\ Q \text{ of } R_{16} &= 157.7 \text{ std. cm}^3/\text{min} \end{aligned}$$

The actual P_{o2} to P_e relationship as supplied by Corning is shown in Figure 18. An amplification G_p of up to 10X is noted.

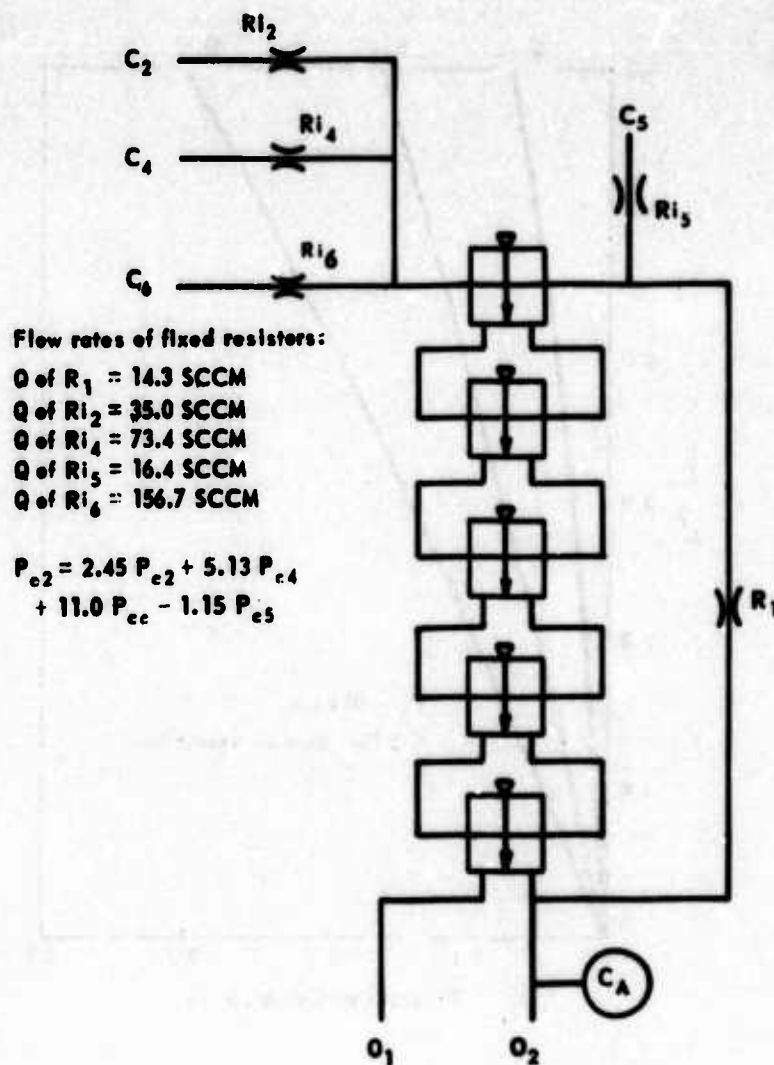


FIGURE 17 - Three input summer circuit (proportional amplifier) with fixed gains.

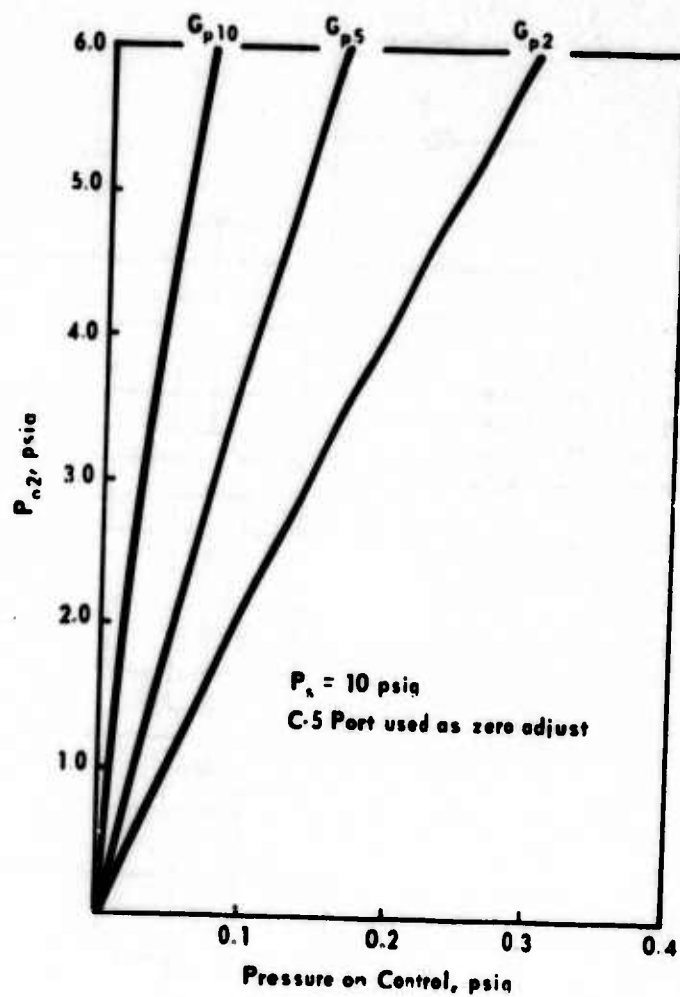


FIGURE 18 - Relationship of control input to pressure output of proportional amplifier.

With the use of the P/A, then the relatively small ΔP of 0.100 from the back pressure head during aging can be amplified up to a much higher, more readable level, detected with a precision transducer and displayed on a digital display.

The powder height gage which incorporated the P/A is shown in Figure 19. After the operator places the component to be gaged in the nest, the operator depresses the start button. The air cylinder lowers the gage head; the amplified back pressure is then indicated on the digital display. The control circuit which was designed for this gage is shown in Figure 20. With the use of the selector valves the operator can select amplifications of 0, 2, 5, and 10.

The actual calibration curves at the various amplification levels using hardened steel masters are shown in Figure 21. From these curves, tables showing the back pressure and corresponding powder extension were established. An operator can use the tables to determine the actual powder height after reading the back pressure. A binary-coded decimal output on the digital display also allows the option for interfacing with a computer, punched cards, or punched paper tape for more permanent recording or computation.

OTHER APPLICATIONS OF FLUIDIC GAGING

The combination of back pressure gaging with fluidic logic affords many advantages over other gaging methods. One major advantage for use in inspection of high explosive pellets and pressings is that no electrical accessories are required. A partial list of applications which relate to detonator fabrication include measurements of pellet heights, pellet diameters, depth to powder, well depth, liquid levels, and powder surface area.⁵ The techniques used are all similar and major differences occur only in fixturing and tooling. Some of these applications will be briefly described.

Measurement of Pellet Height Explosive pellet heights are measured by the combination of back pressure sensors and

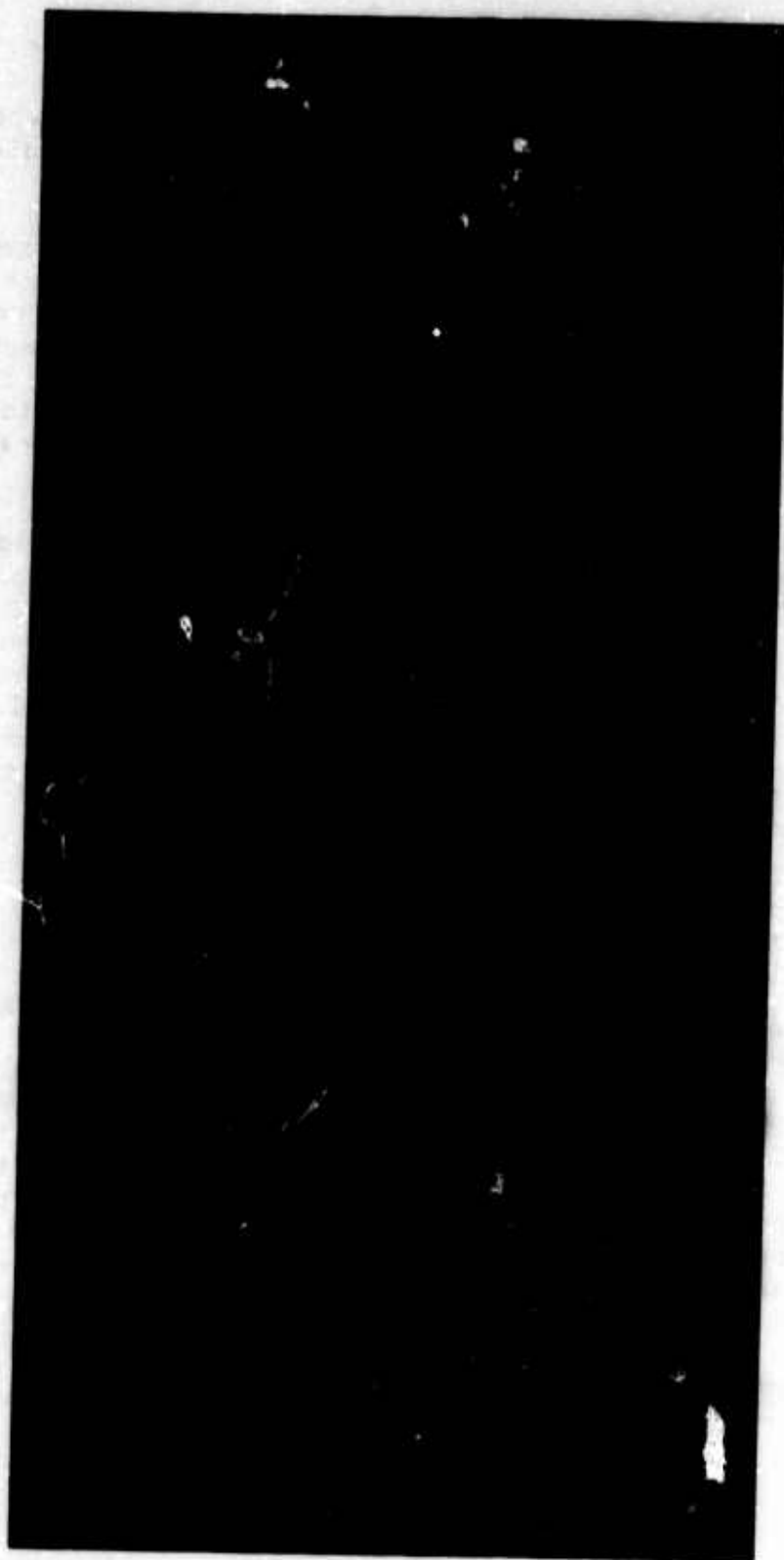


FIGURE 19 - Fluidic powder height gage with proportional amplifier.

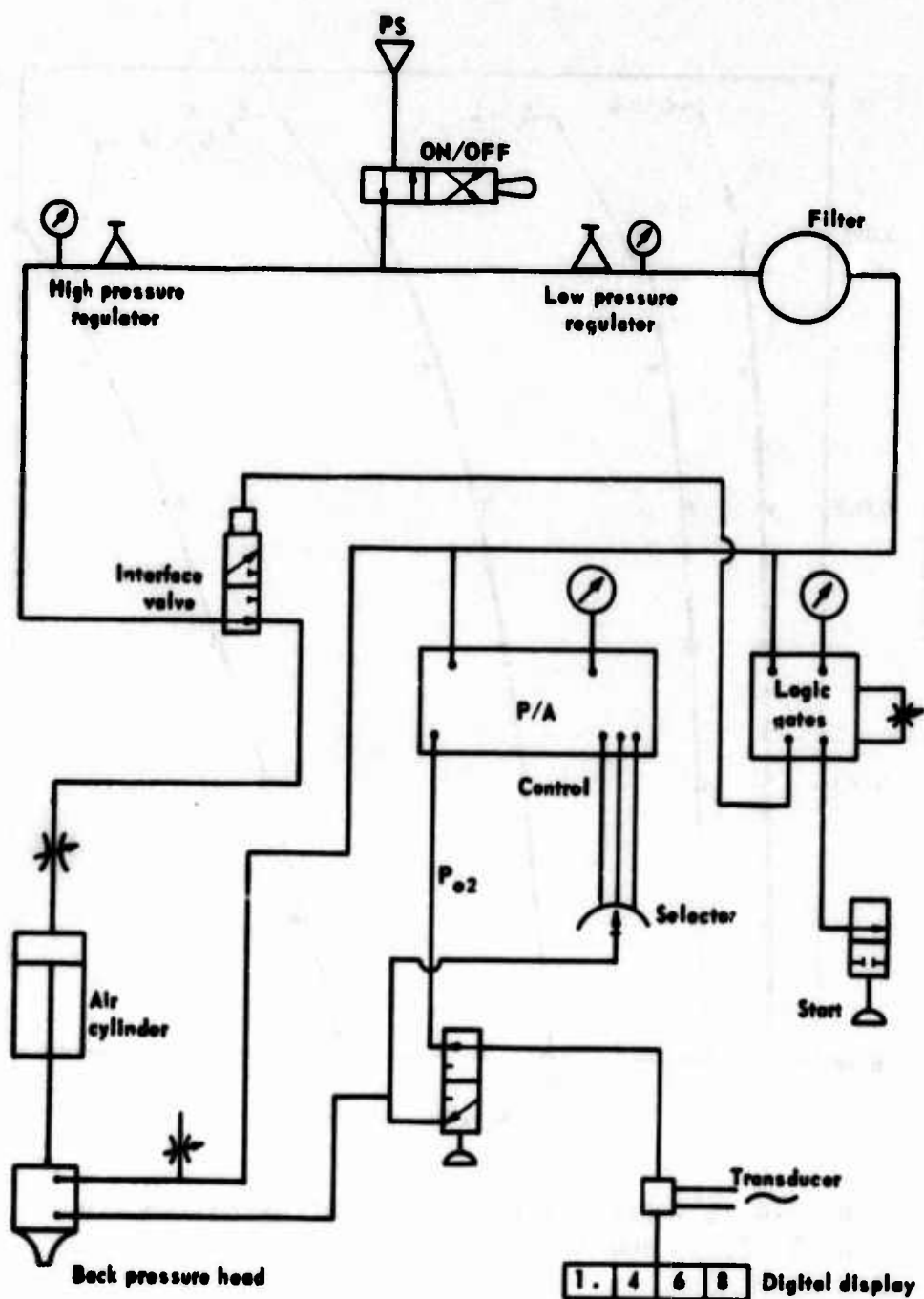


FIGURE 20 - Control circuit designed for powder height gage with proportional amplifier.

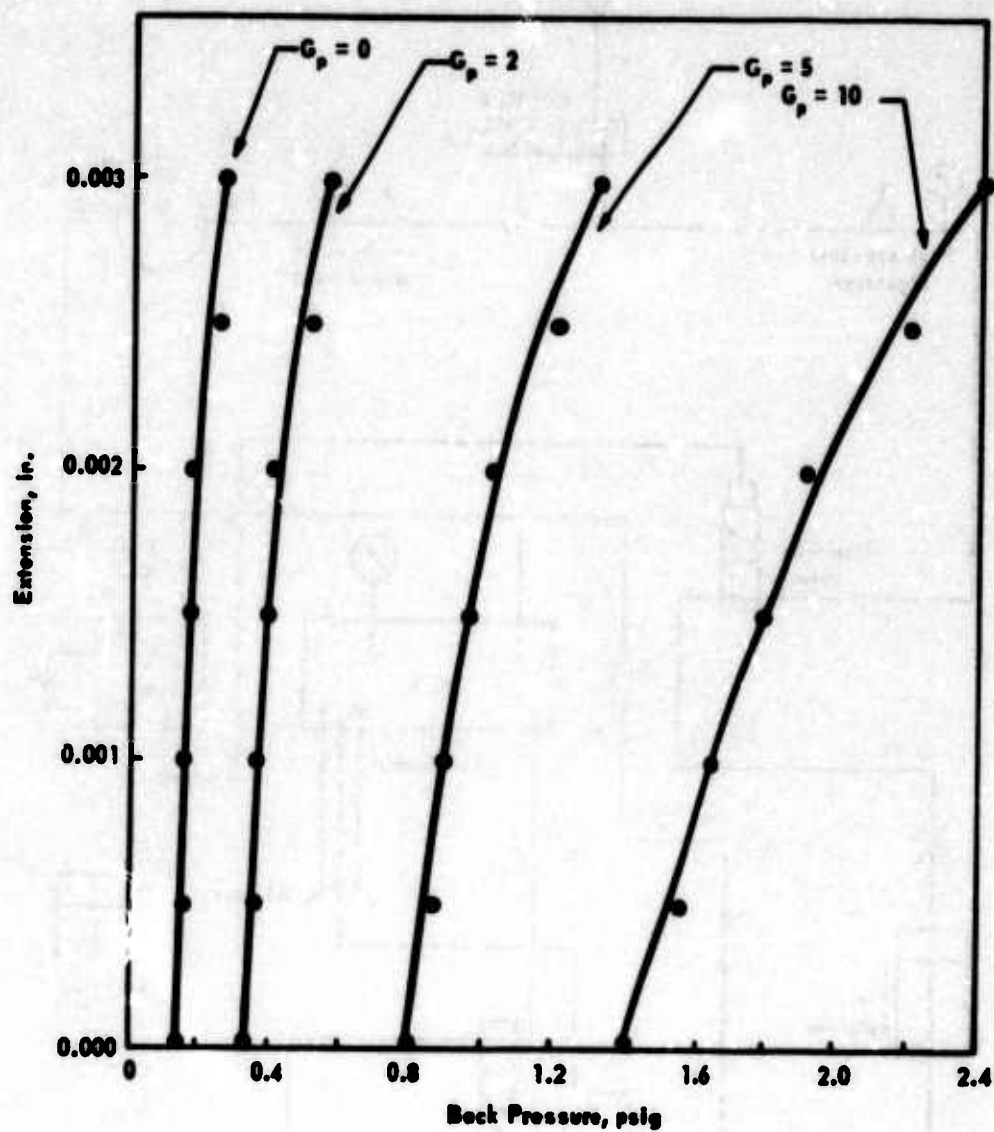


FIGURE 21 - Calibration curves at amplification of 0, 2, 5, and 10.

fluidic logic. A system of the type shown in Figure 22 gages pellet height without contacting the pellets. This system consists of a gage head where the pellets are inspected and a nest which holds the pellet. The inspection gage head is connected to an identical gage head with a permanently installed master which serves as a standard.

The outputs of these gage heads are then fed into a staged amplifier cascaded to the OR/NOR elements O/N_1 , O/N_2 , and O/N_3 . When an acceptable pellet is in the gage head, elements O/N_1 and O/N_2 are held in a switched condition (i.e., output O_2) and O/N_3 shows an in-tolerance pellet. If an unacceptable pellet is in the gage head elements, the outputs of elements O/N_2 and O/N_1 or O/N_3 switch and indicate an out-of-tolerance condition. The tolerance limits can be adjusted by adjusting needle valves N_1 and N_2 . An inspection system of this type is easily mechanized and could be interfaced into the operation of the press.

The above system provides simple accurate gaging without expensive gaging equipment. There are no moving parts as such in the fluidic gaging circuit. With a three-stage proportional amplifier, it is possible to determine pellet height with an accuracy of 0.0001 in. depending on the range being measured.

A similar system could be employed to determine pellet diameter. Identical in operation, the only major difference would be the gage head itself.

Depth-To-Powder Gage The powder in many detonators is pressed to a recessed condition for later placement of a high density pellet. The measurement, commonly referred to as the "depth-to-powder" dimension, has been taken with contact methods such as snake eye gages, ball-operated variable resistors, and feather-touch dial indicators. A modification to the gage design described in previous sections is used to measure recessed powder heights. An example of how this is incorporated is shown in Figure 23. A gage head fabrication with a known machined step would reference against the end of the cylinder; however, the step length would be slightly less (0.010 in.) than the maximum depth-to-powder. During gaging the back pressure readings correlate to the actual powder height. The back pressure received is connected to

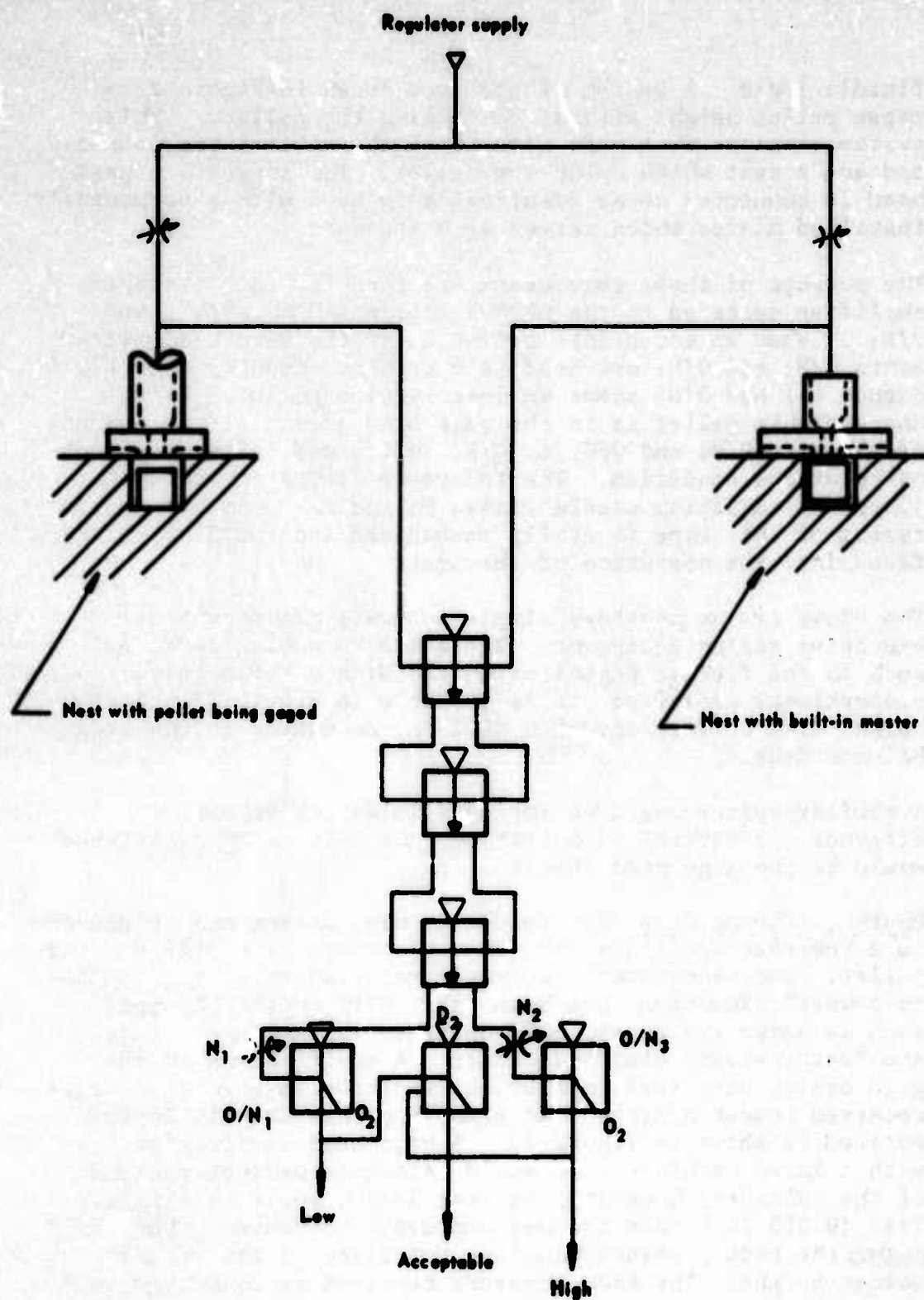


FIGURE 22 - Gaging system for measurement of explosive pellet height.

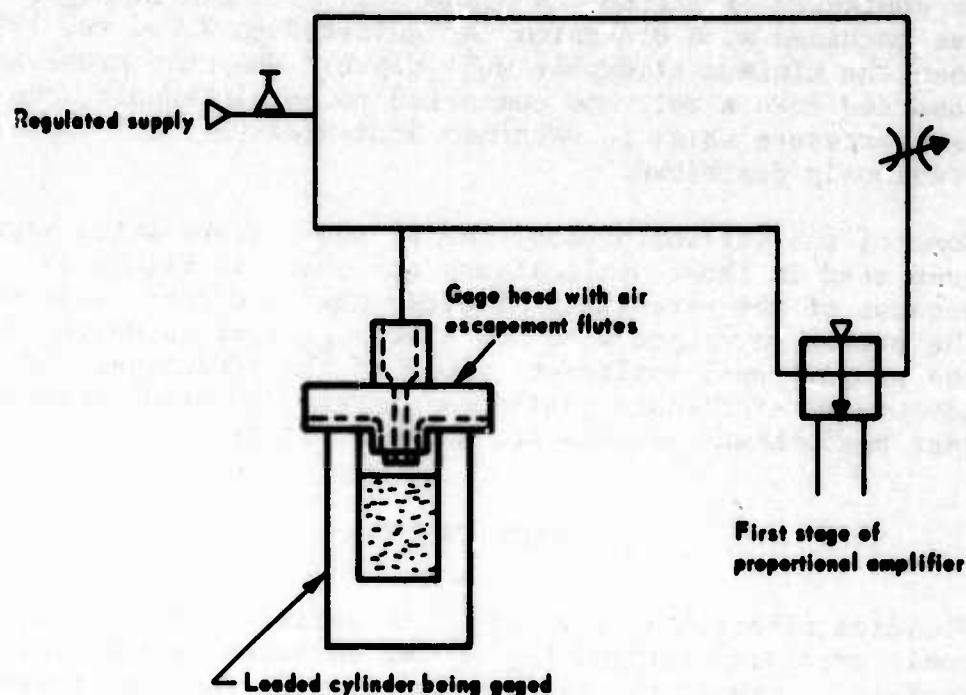


FIGURE 23 - Gaging of depth to powder of loaded cylinder.

a proportional amplifier and coupled to a digital display. The gage head is machined with air escapement flutes along the sides so that the air can escape freely. This technique can be used to measure compacted powder heights, either extended or recessed. A noncontact method of gaging which will not disturb the powder is necessary in the manufacture of many small bore detonators where even a minute disturbance in the powder surface can be of significant size compared to the total area of the exposed powder surface.

Well Depth Gage Well depth measurements of detonators have been taken with dial indicator or Sheffield Precisionaire¹ air gages where a properly designed tip is lowered into the well contacting the surface being gaged. In most cases the tip is shaped to avoid contact with areas which could be damaged. This method has become unacceptable when the measurement must be taken from delicate vapor-deposited, printed-circuit, or silk-screened surfaces which should not

be contacted or marred. A probe such as shown in Figure 24 was machined with dimension "A" adjusted to 0.010 in. less than the minimum allowable well depth. When the probe is inserted into a well and connected to an air supply, the back pressure which is obtained indicates the well depth as previously described.

Some of the various probes, nests, and masters which have been used in these applications are shown in Figure 25. Because of the versatility fluidic gaging offers, most of the probes were used with the same gage console which used the proportional amplifier. Some of the advantages and disadvantages of fluidic gaging as compared to other noncontact measurement systems are shown in Table 1.

CONCLUSIONS

Fluidics offers many advantages to assist in the gaging of small precision components, powder surfaces, and delicate surfaces. One of the major advantages is that the gaging pressure and/or flow can be directly connected to the fluidic logic elements. Speed is another advantage; fluidic amplifiers can react to changes in input in approximately 1 msec. This eliminates delay times which means high speed gaging can be accomplished. Other advantages such as no moving parts and inherit insensitivity to temperature extremes, shock, and vibration are also beneficial in eliminating downtime and maintenance.

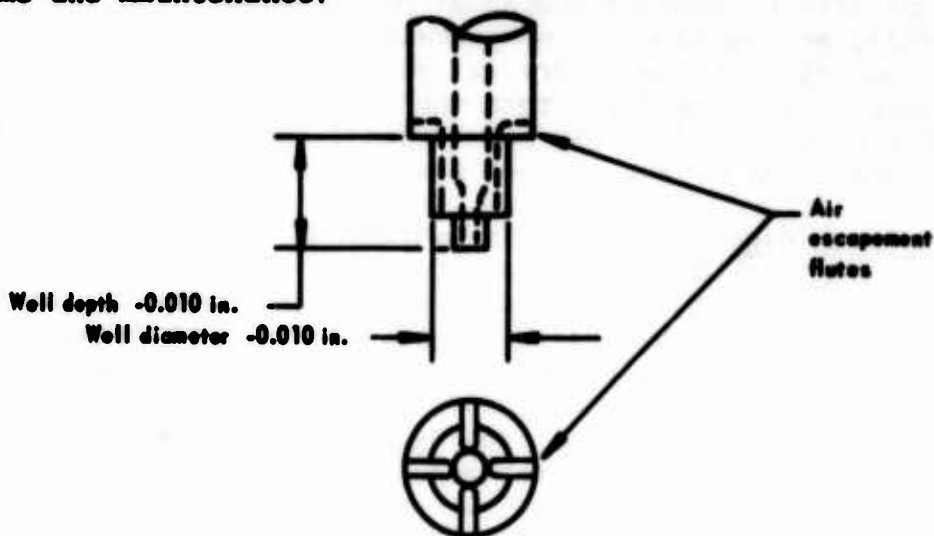


FIGURE 24 - Details of nozzle used for measurement of well depth.



FIGURE 25 - Various probes nests, and masters used for pellet heights, well depths and powder height measurements.

Table 1

COMPARISON OF FLUIDIC WITH OTHER NONCONTACT GAGING METHODS

Design Feature	Fluidic Gage	Light Section Microscope	Capacitance Gage	Light Reflection
Initial Cost	\$1,200	\$2,500	\$1,500 up	\$2,000 up
Gage Time Maximum	10 sec	3 min	5 sec	5 sec
Operator	Manual or Automatic	Skilled Manual	Manual or Automatic	Manual or Automatic
Effect of Surface Being Measured	Should be relatively smooth	Independent of surface	Very dependent upon material	Very dependent upon surface and color
Accuracy	0.000050	0.000050	0.0001	0.0001
Adaptable to Multiple Gage Head	Yes	No	No	No
Can be Coupled to E.D.P.	Yes	No	Yes	Yes
Gage Distance (in.)	<0.010	<0.007	<0.030	<0.030
Remote Gage Possible	Yes	No	Yes	Yes
Warm Up Time	None	None	10-15 min	10-15 min
Explosion Proofing	None Required	Available at additional expense	Available at additional expense	Available at additional expense

REFERENCES

1. "Sheffield Modular Gauging," Bendix Corporation, Dayton, Ohio, p. 4, 1967. (Product Literature)
2. Doug St. Clair, "Fluidics," Sylvania Electrical Equipment Group, Waltham, Mass., pp. 5-4, 1970.
3. Ronald H. Sutter, "Fluidic Gaging," ASTM Technical Paper #MS-69-54, 20501 Ford Rd., Dearborn, Michigan 48128.
4. R. A. Humphrey, F. T. Brown, "Dynamics of a Proportional Amplifier," Journal of Basic Engineering, Vol. 92, 1970, p. 303.
5. W. R. Schurman, "Fluidic Noncontact Gaging," MLM-1940, Monsanto Research Corp., Miamisburg, Ohio (June 15, 1973), p. 24.

A FLUIDIC SENSOR APPLIED TO THE
HYDRAULIC CONTROL OF ROTATIONAL SPEED

R. J. Stuart
Graduate Student*

R. W. Mayne
Assistant Professor
Department of Mechanical Engineering
State University of New York at Buffalo
Buffalo, New York 14214

ABSTRACT

This paper is concerned with a fluidic speed sensor consisting of a submerged fluid jet and a rotating disk. The jet is parallel to the rotational axis of the disk and near its periphery. The fluid velocity produced by the disk rotation deflects the jet and changes the recovery pressure at a downstream receiver. In this effort, performance of the speed sensor is studied experimentally using hydraulic oil as a working fluid and an analytical procedure similar to that suggested by Katz and Hastie is applied to estimate that performance.

The remainder of the paper deals with a breadboard application of the speed sensor controlling the output speed of a hydrostatic transmission. The speed sensor signal is compared to the desired output speed in a pilot operated valve which drives a ram adjusting the displacement of the transmission pump. The dynamic design of this feedback controller is considered and ideal and actual transient responses of the system are compared.

*Presently: Design Engineer, Zinsco Electrical Products, Division of GTE-Sylvania, Hampton, Virginia.

NOMENCLATURE

A_R	ram area	P_L	ram load pressure
A_V	area of valve spool end	P_O	sensor output pressure, $\omega = 0$
B_R	ram viscous damping	P_S	sensor supply pressure
B_V	valve spool damping	dq/dx	jet flow entrainment rate
C	Albertson's constant	r	radius within jet
C_R	ram capacitance	R	disk radius
C_V	capacitance at valve spool end	Re	Reynolds Number, $U_e D_e / \nu$
D_e	jet diameter at exit	R_v	sensor output resistance
D_O	receiver diameter	T_D	disk thickness
F_L	load force	$u(r)$	axial velocity at radius r
F_O	valve spring force at null	U_e	jet velocity at exit
K_C	pressure-flow coefficient	v	crossflow velocity
K_q	flow gain	V	a constant crossflow velocity
K_s	speed sensor gain	x	distance from exit
K_V	valve spring coefficient	x_o	distance at flow establishment
L	jet length	X_v	valve displacement
\dot{m}_e	jet flowrate at exit	y	jet deflection
M_j	jet axial momentum	Y_R	ram displacement
M_R	mass of ram and load	Z	distance from disk edge
M_V	valve spool mass	θ	jet deflection angle
M_y	jet crossflow momentum	ν	kinematic viscosity
P	sensor output pressure	ρ	mass density
		ω	disk speed

INTRODUCTION

Rotational speed has been controlled by fluid power in many applications employing various approaches for sensing and control. In a traditional controller arrangement described by Raven [1], engine speed is sensed mechanically by a fly ball governor and that signal is transferred to a hydraulic actuator which adjusts the engine throttle. Latson et al. [2] have controlled a hydromechanical transmission to maintain good prime mover performance by maintaining a desired transmission input speed at varied output speeds. A hydraulic pump was employed as the rotational speed sensor. In a similar application, Reid and Woods [3] have utilized an air powered fluidic speed sensor (based on frequency to analog conversion) and a pneumo-hydraulic servovalve in the control of a hydrostatic transmission. Boothe et al. [4] have described the use of phase discrimination techniques for the control of rotational speed and have developed air powered fluidic controllers using that approach.

The purpose of this paper is to investigate the application of a hydraulic fluidic sensor for the control of rotational speed. The sensing principle to be considered is based on the air operated device studied by Leathers and Davis [5] and shown schematically in Figure 1. Fluid moving in the boundary layer attached to the rotating disk interacts with the jet flowing near the disk from source to receiver and reduces the recovered pressure. As the disk speed increases, the jet deflection increases and the recovered pressure decreases.

A similar air powered sensor has also been proposed by Katz and Hastie [6] for application to machines containing spur gears. In this sensor the jet is directed as in Figure 1 but instead of flowing near the disk edge, the jet passes through the path of the rotating gear teeth. Recovery pressure is either zero (when a tooth is in the path) or equal to the pressure recovered from the jet which is being deflected by the velocity of fluid trapped between the rotating teeth. The output circuit filters the pressure variations and the average output pressure becomes a decreasing function of rotational speed. Other work with jet deflection linear velocity sensors has been performed by Tanney [7]. He indicates that improved sensor linearity and a direction sensitive output can be obtained by using two receivers producing a differential output pressure signal.

This paper focuses on the basic configuration proposed by Leathers and Davis as a simple sensor for use in the hydraulic control of rotational speed. The static characteristics of the sensor are first studied using hydraulic oil as the working fluid, then, the application of the sensor in a hydraulic speed controller is considered. It should be mentioned that the alternative configurations suggested by Katz and Hastie and also by Tanney may be similarly employed and might be quite attractive for particular applications.

THE SENSOR CHARACTERISTICS

Geometry and details of the jet deflection hydraulic speed sensor are presented in Figure 2. In this study the disk radius was typically $R = 1.37$ in. the jet length $L = .56$ in. and the exit orifice diameter $D_e = .054$ in. Supply pressures were normally less than 10 psi and the entire disk, supply and receiver arrangement were submerged in hydraulic oil. The experimental results are summarized in Figures 3-5 which are in normalized form. The ratio of the blocked output pressure to the blocked output pressure at zero speed is given by P/P_0 and the tangential velocity of the disk edge is referenced to the average jet velocity as $R\omega/U_e$. Figures 3-5 show the effects of distance from the disk edge and disk thickness on sensor performance. These figures do not show experimental data points since they were obtained by drawing curves through actual X-Y plots of output pressure vs. speed as measured by a tachometer. These plots were continuous but somewhat noisy. A typical noise level of the sensor pressure is shown in the pressure-time plot of Figure 6. It was possible to manage the effects of this noise on speed control by adjusting the closed loop system dynamics.

It should be clear that the sensor geometry can be adjusted to obtain various sensitivities and to produce reasonably linear behavior over different ranges of shaft speed. The final dimensions and calibration chosen for use in the breadboard controller to be considered later in this paper are presented in Figure 7.

ANALYSIS OF SENSOR PERFORMANCE

The ultimate objective of an analysis of this sensor is to be able to predict the sensor output pressure as a function of speed for all geometric configurations of interest. The analysis presented here is an initial step in that direction. It focuses primarily on the jet behavior and on cases where the effect of the disk rotation can be simply represented by a region of crossflow at the velocity of the disk periphery. This effort can be readily extended to the more general situation by describing the appropriate crossflow velocity at all points between the jet source and receiver but this requires a detailed study of the flow field surrounding the rotating disk.

The deflection angle of a jet with respect to its original axis has been shown by Keffer and Baines [8] to be proportional to the ratio of momentum flux in the crossflow direction to the momentum flux of the jet:

$$\theta(x) = \frac{M_y(x)}{M_j} \quad (1)$$

The jet momentum is essentially constant at

$$M_j = \dot{m}_e U_e = \rho \frac{\pi D_e^2}{4} U_e^2 \quad (2)$$

and the crossflow momentum at any point along the jet results from the velocity of the flow entrained by the jet up to that point

$$M_y(x) = \rho \int_0^x \frac{dq}{dx} v dx \quad (3)$$

where dq/dx is the entrainment rate of the jet and v is the crossflow velocity at the point of entrainment. Equation (1) thus becomes

$$\theta(x) = \frac{4}{\pi U_e^2 D_e^2} \int_0^x \frac{dq}{dx} v dx \quad (4)$$

and to calculate the deflection angle in a given crossflow only the entrainment rate remains to be determined. Albertson et al. [9] present expressions for the entrainment rate of a submerged free jet based on the assumption of a Gaussian velocity distribution within the jet. These expressions are:

$$\left(\frac{dq}{dx}\right)_0 = .785 C U_e D_e \left(1 + \frac{4Cx}{D_e}\right) \quad (5)$$

in the zone of flow establishment and

$$\left(\frac{dq}{dx}\right)_{es} = \pi C U_e D_e \quad (6)$$

in the zone of established flow. The constant C is experimentally determined for a particular jet flow by a method which will be described. Figure 8 defines the zones of flow establishment and established flow. The flow is considered established when the core of the original jet has disappeared at $x_0 = D_e/2C$.

Combining Equations 5 and 6 with 4, the angle θ can be determined for a given crossflow velocity distribution. Assuming that the crossflow velocity is a constant V over the full length L of the jet and realizing that for the jet length under consideration the flow does not become established ($L < x_0$), Equations 4 and 5 yield

$$\theta(x) = \frac{V C}{U_e D_e} \left[x + \frac{2Cx^2}{D_e}\right] \quad (7)$$

Integrating Equation 7 over the length of the jet then gives the jet centerline deflection at the receiver as

$$y = C \frac{VL^2}{U_e D_e} \left(\frac{1}{2} + \frac{2CL}{3D_e} \right) \quad (8)$$

Knowing the centerline jet deflection at the receiver, Katz and Hastie [6] have shown that the output pressure recovered by the receiver is

$$P = \frac{4}{\pi D_o^2} \left[\int_0^{\frac{D_o}{2} - y} 2\pi r P(r) dr + \int_{\frac{D_o}{2} - y}^{\frac{D_o}{2} + y} 2r \cos^{-1} \left(\frac{r^2 + y^2 - D_o^2/4}{2ry} \right) P(r) dr \right] \quad (9)$$

for $y \leq \frac{D_o}{2}$

and

$$P = \frac{4}{\pi D_o^2} \int_{y - \frac{D_o}{2}}^{y + \frac{D_o}{2}} 2r \cos^{-1} \left(\frac{r^2 + y^2 - D_o^2/4}{2ry} \right) P(r) dr \quad (10)$$

for $y \geq \frac{D_o}{2}$

In Equations 9 and 10, $P(r)$ represents the pressure recovery due to the fluid velocity at a given radius r within the jet. According to Reid [10], for $L/D_o > 10$, this pressure may be calculated by

$$P(r) = \frac{1}{2} \rho [u(r)]^2 \quad (11)$$

where $u(r)$ is the jet velocity at radius r computed for the free jet at the receiver. The velocity distribution according to Albertson et al. [9] is

$$u_o(r) = U_e \exp \left[\frac{-(r + Cx - \frac{D_o}{2})^2}{2C^2 x^2} \right] \quad (12)$$

for the region of flow establishment and

$$u_{es}(r) = \frac{U_e D_e}{2 C x} \exp\left[\frac{-r^2}{2C^2 x^2}\right] \quad (13)$$

after the flow has been established.

Combining Equations 11 and 12 or 13 with Equation 9 or 10 produces the desired relationship between output pressure and jet deflection. For the problem at hand, the receiver is quite close to the region of established flow and Equation 13 has been used for the velocity distribution. The output pressure in normalized form is thus

$$\begin{aligned} \frac{P}{P_o} = & .637 \frac{P_s}{P_o} \left(\frac{D_e}{C D_o L} \right)^2 \left[\int_0^{\frac{D_o}{2} - y} \pi r \exp\left(\frac{-r^2}{C^2 L^2}\right) dr \right. \\ & \left. + \int_{\frac{D_o}{2} - y}^{\frac{D_o}{2} + y} r \cos^{-1}\left(\frac{r^2 + y^2 - D_o^2/4}{2ry}\right) \exp\left(\frac{-r^2}{C^2 L^2}\right) dr \right] \\ & \text{for } y \leq \frac{D_o}{2} \text{ and} \end{aligned} \quad (14)$$

$$\begin{aligned} \frac{P}{P_o} = & .637 \frac{P_s}{P_o} \left(\frac{D_e}{C D_o L} \right)^2 \int_{y - \frac{D_o}{2}}^{y + \frac{D_o}{2}} r \cos^{-1}\left(\frac{r^2 + y^2 - D_o^2/4}{2ry}\right) \exp\left(\frac{-r^2}{C^2 L^2}\right) dr \\ & \text{for } y \geq \frac{D_o}{2}. \end{aligned} \quad (15)$$

The pressure P_o is the recovered pressure with zero jet deflection. The constant C is evaluated by forcing Equation 14 to agree with the recovered pressure at zero deflection. In this study, $C = .042$ has been obtained which is low compared to [6 and 9] but seems reasonably consistent with the low Reynolds Number and rather high pressure recovery

(about 2/3) characterizing the sensor. Numerical integration has been applied for evaluating Equations 14 and 15.

Results of the analysis using the above approach are compared to the experimental results in Figure 9. The computations for disk thickness $T_D = 1/2$ in. have been carried out as described above using a crossflow velocity of R_w over the total jet length. This result agrees reasonably well with the actual performance at $Z/D_e = 1$ which is the closest that the disk was approached. For $T_D = 1/4$ and $1/16$ in., the analysis was modified to apply the R_w velocity only over the disk thickness. This approach seems to be reasonable for the thicker $1/4$ in. disk but apparently for $T_D = 1/16$ the crossflow velocity caused by boundary layers attached to the disk becomes very significant. This effect could be considered by defining the flow field completely and returning to Equation 4.

THE HYDRAULIC SPEED CONTROLLER

In order to study the sensor's performance in a hydraulic controller a breadboard system was developed using the speed sensor to control the output speed of a hydrostatic transmission. A diagram showing the general nature of the system is given in Figure 10. The hydraulic signal produced by the fluidic sensor is compared to the desired speed setting in a pilot operated interface valve. The output of this valve drives a piston and cylinder which adjusts the transmission pump displacement to achieve the proper output speed. The controller will attempt to maintain the desired output speed with changing input speeds and with changing loads on the transmission output.

A schematic of system components is shown in Figure 11 where P is the blocked output pressure of the speed sensor and Y_R is the position of the output piston controlling pump displacement. The spring shown within the interface valve sets the desired output speed and moving the base of this spring left or right changes the setpoint. Changes in setpoint could be accomplished by other methods including the introduction of bias pressure, etc., but that has not been considered in this effort.

In developing a dynamic model of this control system for design purposes it was first necessary to identify the plant. This was done by observing the response of the transmission output speed to small step changes in the position of the piston controlling pump displacement. The resulting second order transfer function is shown in Figure 12.

A model of the sensor-valve-ram combination begins by writing the following equations:

continuity on the left side of the valve;

$$C_V \frac{d}{dt} P_V = \frac{P - P_V}{R_V} - A_V \frac{d}{dt} X_V \quad (16)$$

continuity for the piston;

$$C_R \frac{d}{dt} P_L = K_q X_V - K_c P_L - A_R \frac{d}{dt} Y_R \quad (17)$$

motion of the valve;

$$M_V \frac{d^2}{dt^2} X_V = A_V P_V - B_V \frac{d}{dt} X_V - K_V X_V - F_0 \quad (18)$$

and motion of the piston;

$$M_R \frac{d^2}{dt^2} Y_R = A_R P_L - B_R \frac{d}{dt} Y_R - F_L \quad (19)$$

Here:

C_V = valve capacitance	$P_L = P_1 - P_2$ = ram load pressure
C_R = ram capacitance	A_V = valve spool area
P_V = pressure on valve left	X_V = valve displacement
P = sensor blocked output pressure	A_R = ram area
K_q = valve flow gain	F_0 = spring force at $X_V = 0$
K_c = valve pressure-flow coefficient	M_R = piston mass
Y_R = ram displacement	F_L = load force
M_V = valve mass	B_R = piston damping
B_V = valve damping	K_V = spring rate
	R_V = sensor output resistance

Since this will be a relatively low performance and low pressure system, it is reasonable to assume that the hydraulic oil is incompressible

($C_v = C_R = 0$) and also that the inertial forces are small. Under these conditions, Equations 16 and 17 become

$$\frac{d}{dt} \Delta X_v = \frac{(\Delta P - \Delta P_v)}{R_v A_v} \quad (20)$$

and

$$\frac{d}{dt} \Delta Y_R = \frac{K_q}{A_R} \Delta X_v \quad (21)$$

where Δ 's have been introduced as a reminder that these linearized equations are valid only for small perturbations about an operating point. Combining Equations 18 and 20 yields

$$(R_v A_v^2 + B_v) \frac{d}{dt} \Delta X_v = A_v \Delta P - \Delta P_o - K_v \Delta X_v \quad (22)$$

Inserting the dependence of sensor pressure on transmission speed ω gives

$$(R_v A_v^2 + B_v) \frac{d}{dt} \Delta X_v = A_v K_s \Delta \omega - \Delta P_o - K_v \Delta X_v \quad (23)$$

The transfer function equivalents of Equations 21 and 23 have been included in the block diagram of Figure 12. This diagram shows the desired output speed as the spring force at zero valve displacement being summed at the valve spool with the fluidically sensed actual speed. Also indicated in this figure are the final values of all the parameters. A Bode plot design procedure was used to check the dynamic characteristics of the system and open loop plots are shown in Figure 13. The vertical dashed lines in this figure indicate the corner frequency associated with the sensor valve dynamics and the transmission natural frequency. Three different amplitude plots are shown for values of K_q corresponding to valve supply pressures of 100, 200 and 300 psi. It can be seen that reasonable phase margins exist for the lower supply pressures but at the valve gain corresponding to 300 psi stability is questionable.

The actual performance of the hydraulic control system is shown in Figure 14 for small step inputs in desired speed. These recorder plots agree exactly with the conclusions of Figure 13 showing good response at the lower pressures but very light damping for the 300 psi supply. Computer solutions for the step response of the mathematical model have also been obtained and compare favorably to the actual performance. A

typical comparison is shown in Figure 15 for the valve supply pressure at 200 psi.

It might be noticed in Figure 13 that the time constant associated with the sensor output impedance and interface valve provides the dominant dynamic effect in the control loop. This time constant could be readily decreased by reducing the sensor output resistance. However, it was desired to keep the system bandwidth somewhat less than 1 cps to reduce the influence of the sensor noise (at several cps) on the controller and this could be accomplished with the sensor dynamics as indicated in Figure 13. The crossover frequencies (points where $|G(j\omega)| = 1$) and thus the bandwidths of the systems shown in Figure 13 are in the 1 cps neighborhood. Accuracy of the speed controller with this sensor-valve configuration could be held to ± 1 rad/sec despite the appreciable sensor noise plotted in Figure 6. As expected, a reduction of the sensor-valve time constant by decreasing the sensor output impedance and the corresponding increase in closed loop bandwidth resulted in increased steady state error.

CONCLUSIONS

This paper describes the performance, analysis and laboratory application of a hydraulic fluidic sensor for rotational speed. The sensor is simple and its application in hydraulic control is straightforward. It can be powered by any constant pressure hydraulic supply by using a suitable dropping resistor.

In the breadboard application considered here, the dynamic performance of the speed control loop was somewhat limited to provide adequate steady state accuracy. With reductions in the sensor noise level, the dynamic performance of the controller can no doubt be improved. It should be noted that no serious attempt to reduce sensor noise has been made to date and that progress in this aspect of sensor performance is quite likely.

REFERENCES

1. Raven, Frances, H., Automatic Control Engineering, McGraw-Hill Book Co., Inc., New York, 1961.
2. Latson, D.M., Gordanier, M., Dorgan, R.J. and Rio, R.L., "A Hydromechanical Transmission Development," SAE Journal, Vol. 76, June 1968.
3. Reid, K.N. and Woods, R.L., "Fluidic Control of a Hydrostatic Transmission in a Vehicle Propulsion System," ASME Trans., J. of Dyn. Sys., Meas. and Cont., Vol. 95, No. 2, 1973.
4. Boothe, W.A., Ringvall, C.G., and Shinn, J.N., "New Fluid Amplifier Techniques for Speed Control," SAE Aerospace Fluid Power Systems and Equipment Conference, May 1965.
5. Leathers, J.W. and Davis, J.C.H., "A New Rotational Speed Sensor for Fluidics," Proc. of the 4th Cranfield Fluidics Conf., Vol. 2, BHRA, Cranfield, 1970.
6. Katz, S. and Hastie, E., "Fluid Sensing of Rotational Speed Using Spur Gears," ASME Paper No. 72-FLCS-6, 1972.
7. Tanney, J.W., "Three Fluidic Sensors Using Unbounded Turbulent Jets," Proc. of the 4th Cranfield Fluidics Conf., V. 2, BHRA, Cranfield, 1970.
8. Keffer, J.F. and Baines, W.D., "The Round Turbulent Jet in a Cross-Wind," J. of Fluid Mechanics, Vol. 15, Part 4, April 1963.
9. Albertson, M.L., Dai, Y.B., Jensen, R.A. and Rouse, H., "Diffusion of Submerged Jets," ASCE Trans., Vol. 115, 1950.
10. Reid, K.N., "Static and Dynamic Interaction of a Fluid Jet and Receiver Diffuser," Sc. D. Thesis, MIT, 1964.

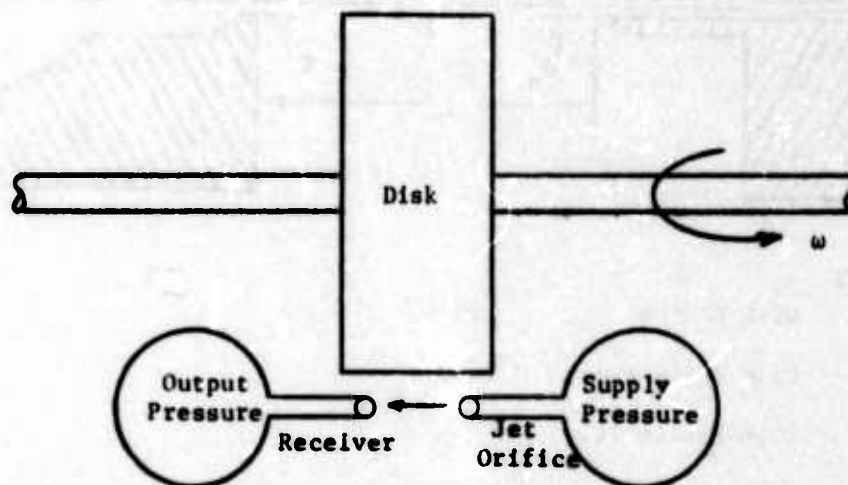
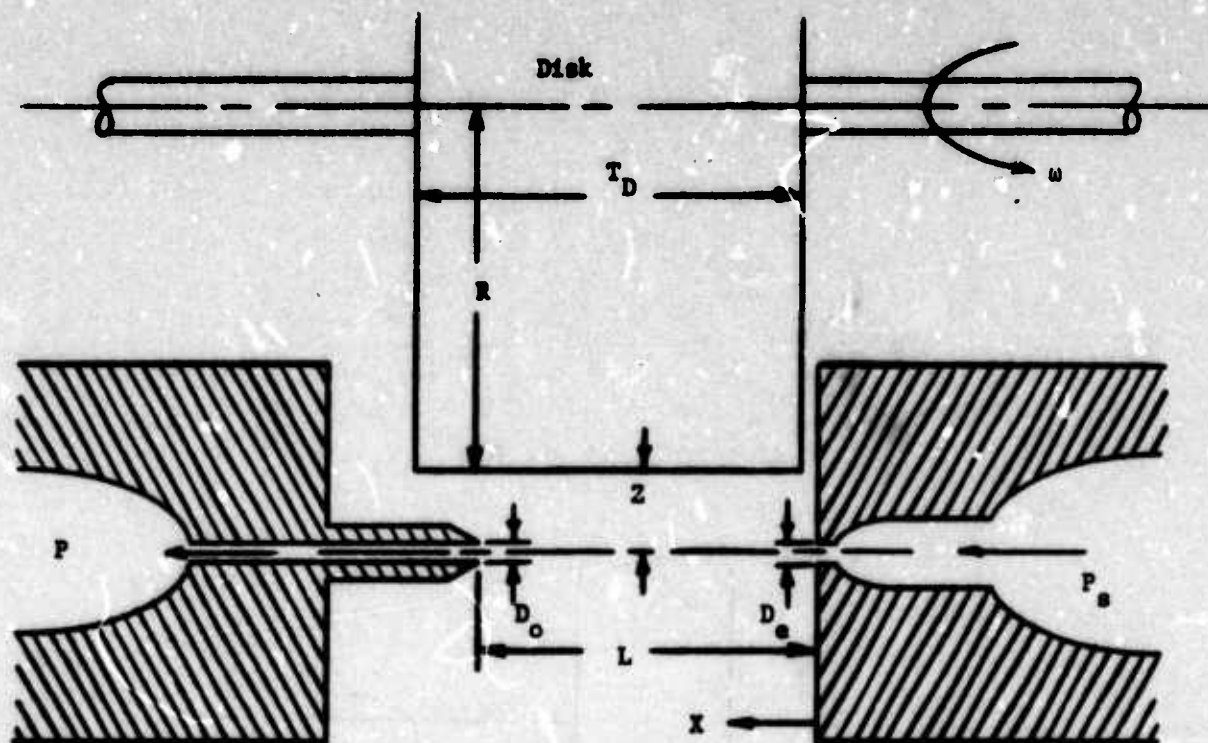


Figure 1

Basic Configuration



- R = Disk Radius
- T_D = Disk Thickness
- ω = Disk Rotational Speed
- P_s = Jet Supply Pressure
- P = Receiver or Sensor Output Pressure
- P_o = Receiver Pressure at Zero Disk Speed
- X = Distance from the Jet Orifice Measured Along the Jet Axis
- L = Orifice to Receiver Distance
- Z = Disk Edge to Jet Centerline Distance
- D_e = Orifice Diameter
- D_o = Receiver Diameter

Figure 2 Oil Powered Experimental
Rotational Speed Sensor

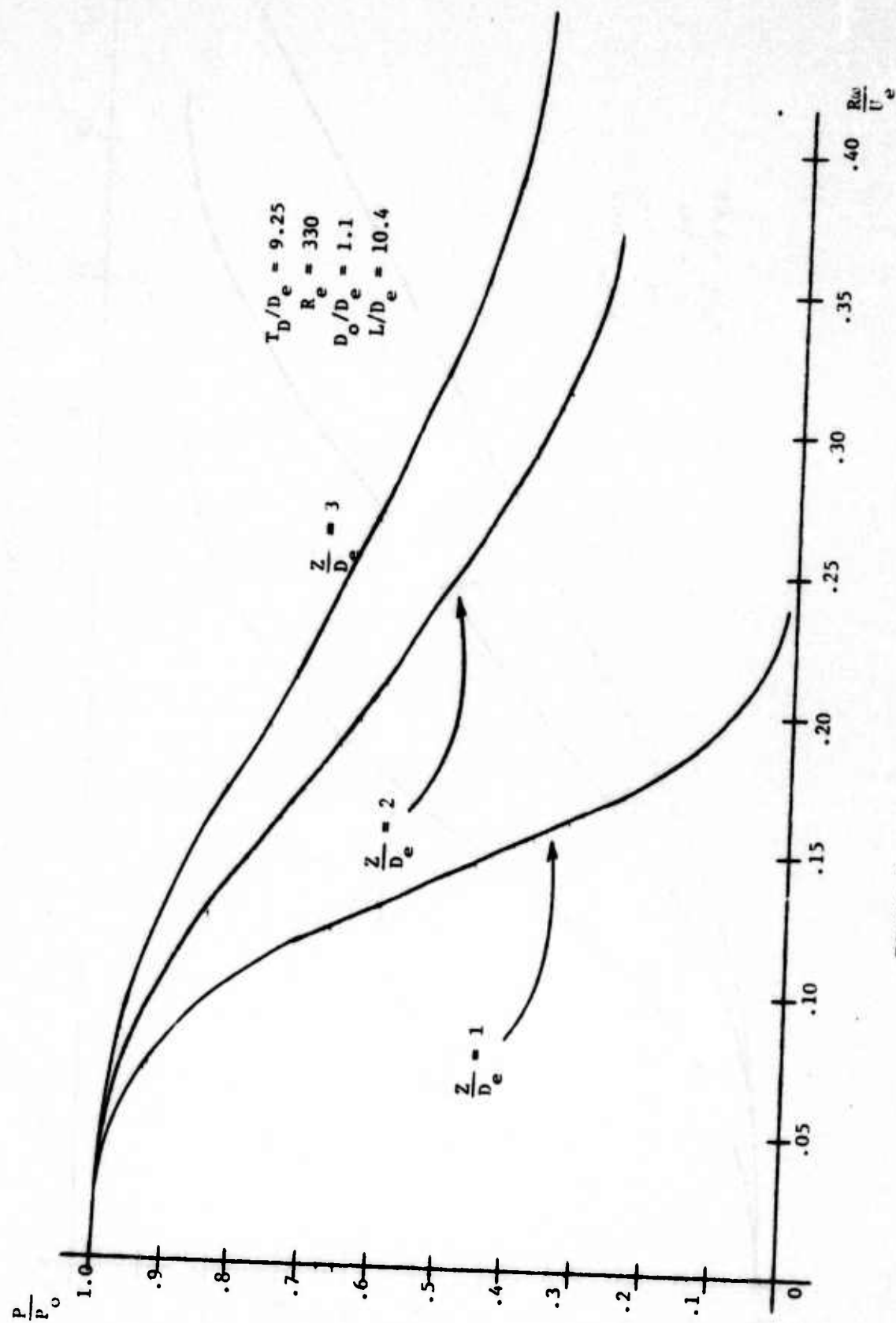


Figure 3 Variation of Sensor Characteristics With Jet to Disk Spacing

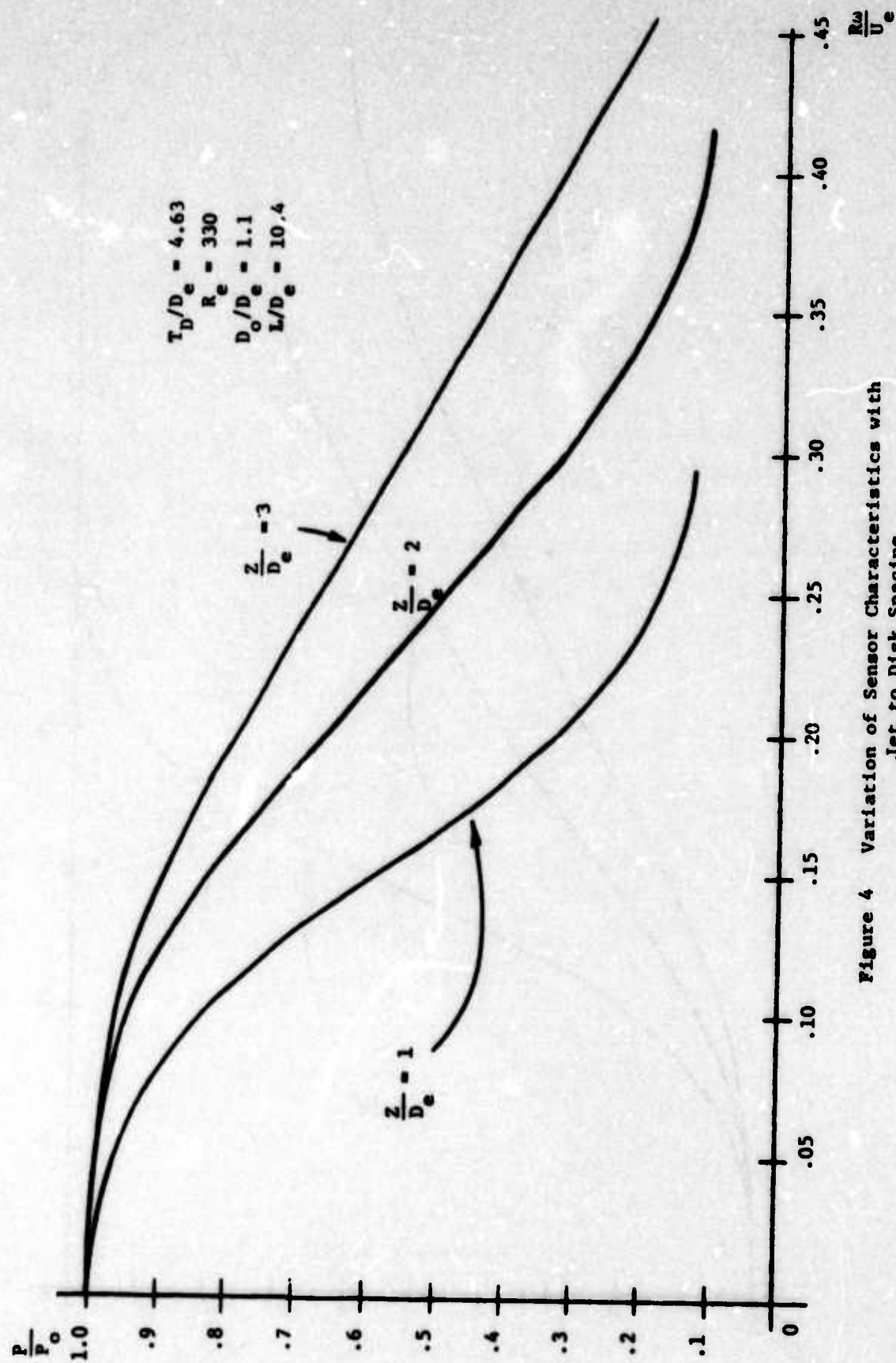


Figure 4 Variation of Sensor Characteristics with Jet to Disk Spacing

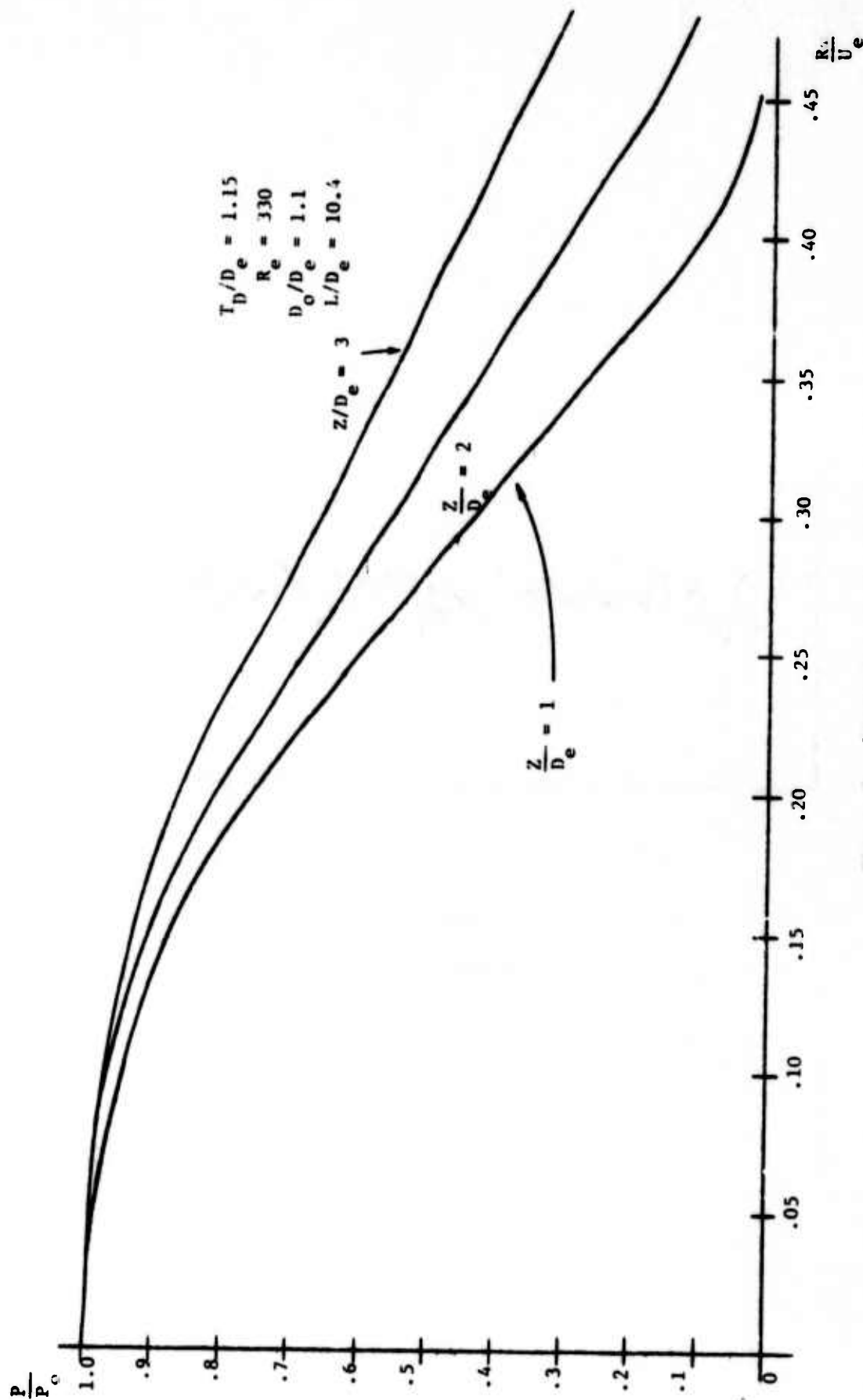


Figure 5 Variation of Sensor Characteristics With Jet to Disk Spacing

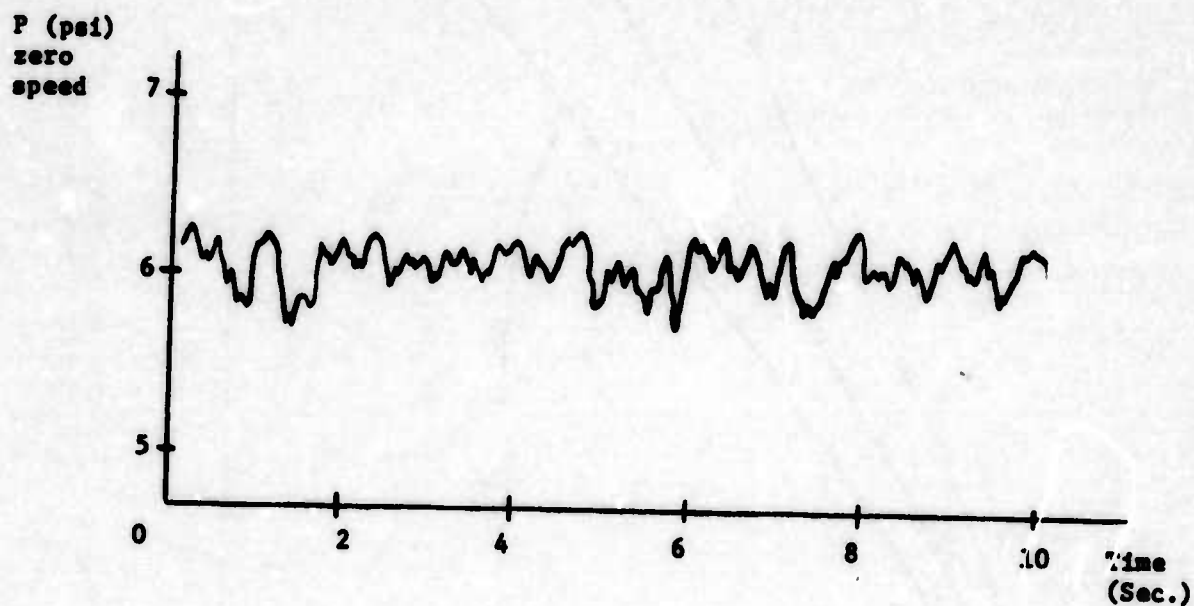


Figure 6
Typical Sensor Noise

Supply Pressure = 8.9 psi
 Jet Reynolds Number = $U \rho_e / \mu$
 = 372
 $T_D = 1/4"$
 $R = 1.37"$
 $z/D_e = 2.0$
 $L/D_e = 10.4$
 $D_e = 0.054"$
 $D_o = 0.060"$

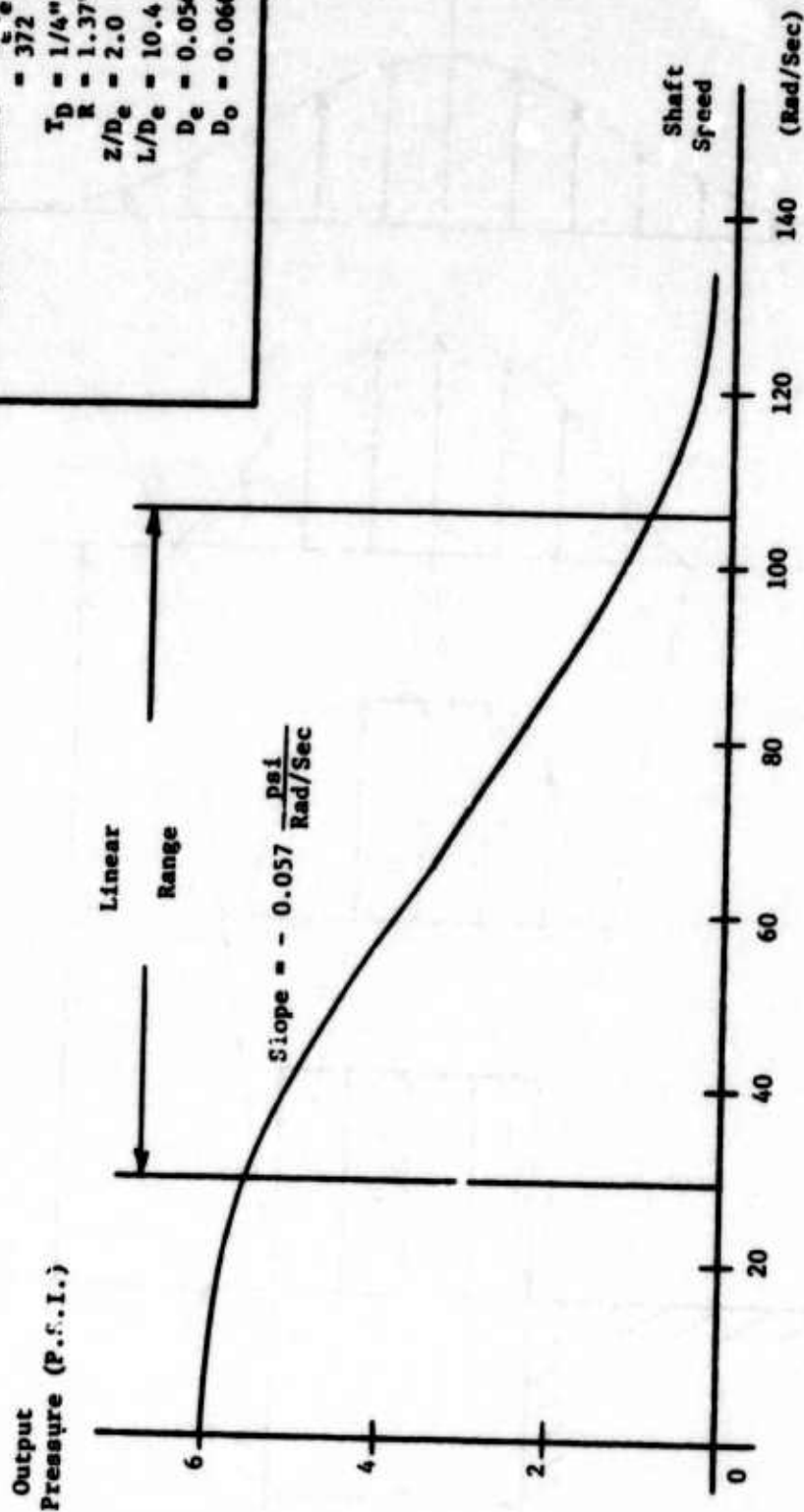


Figure 7 Final Sensor Characteristics

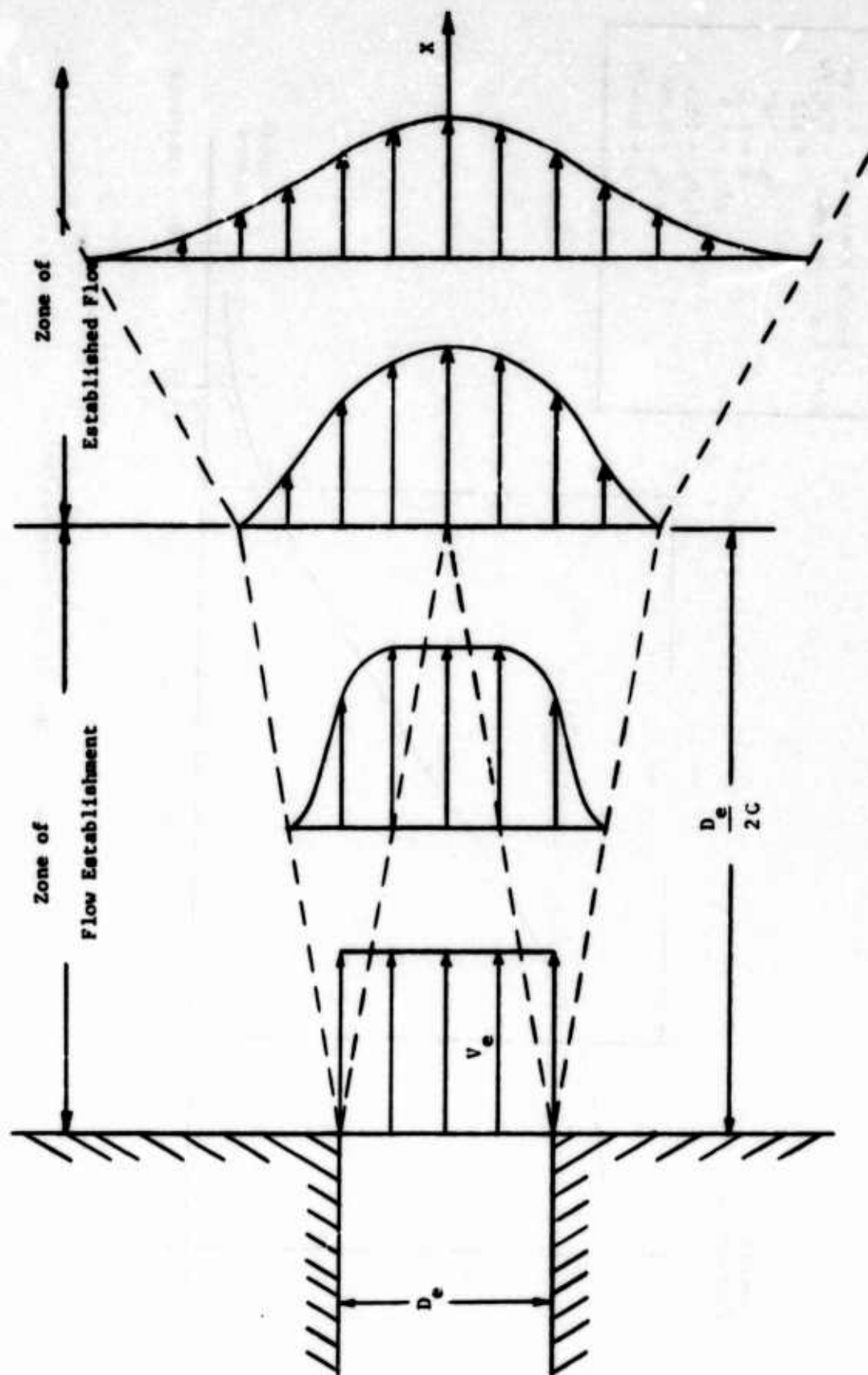


Figure 8 Diffusion of a Submerged Jet

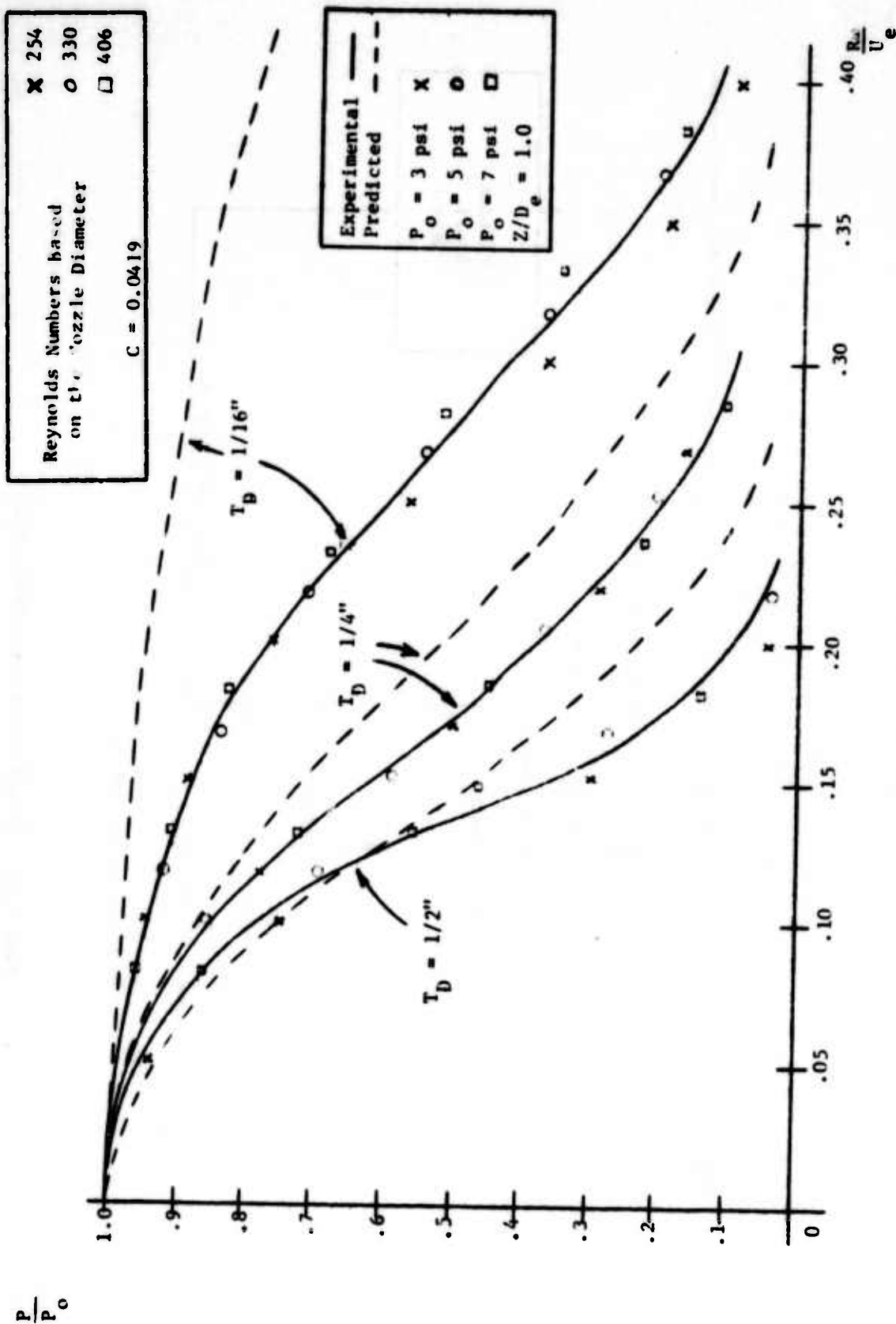


Figure 9 Experimental and Predicted Results

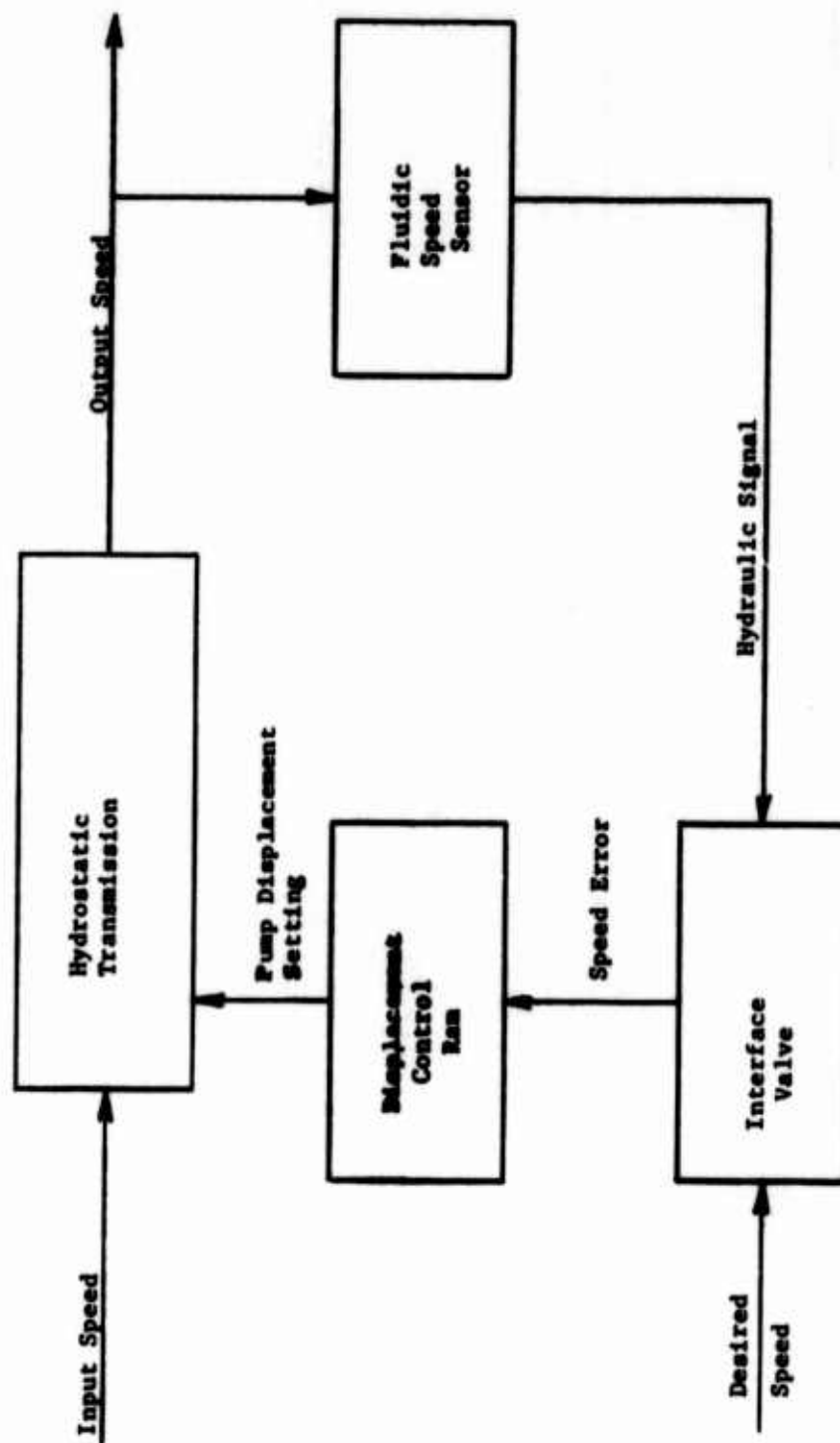
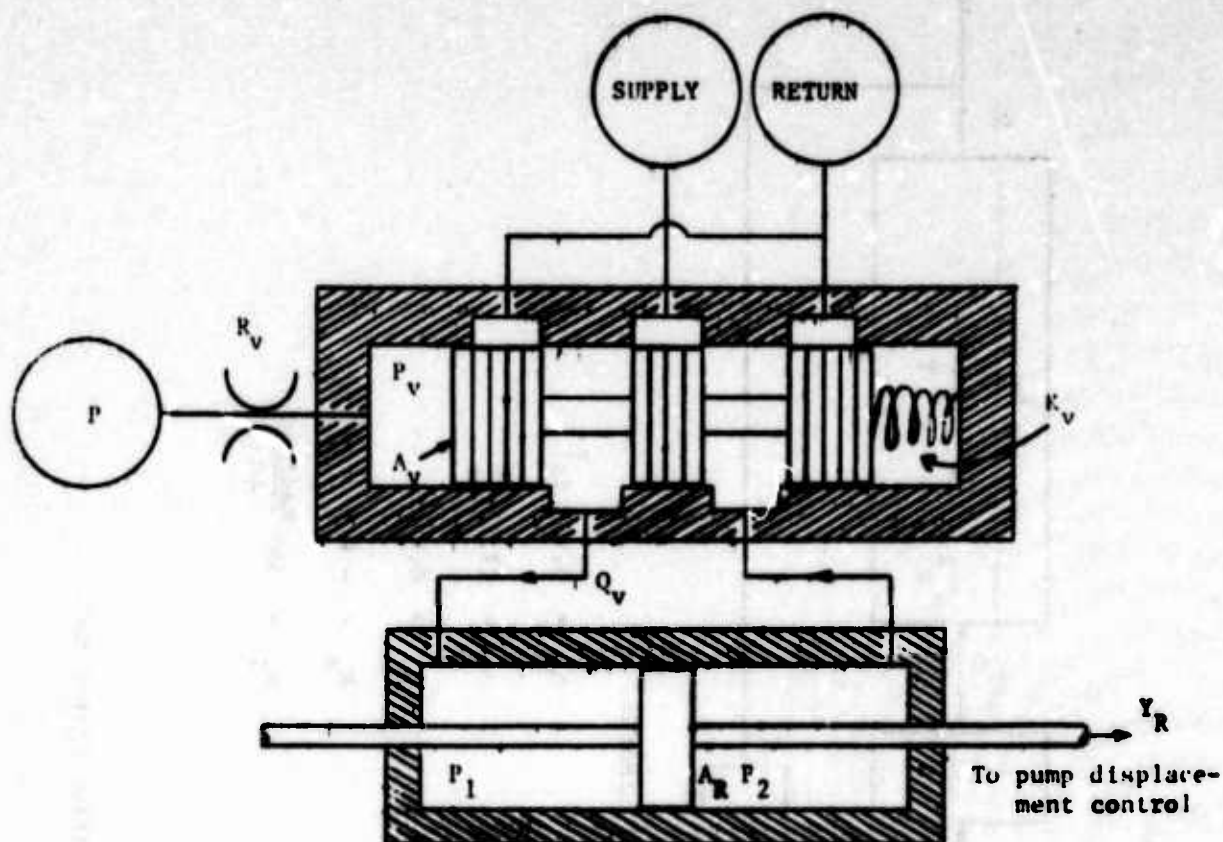
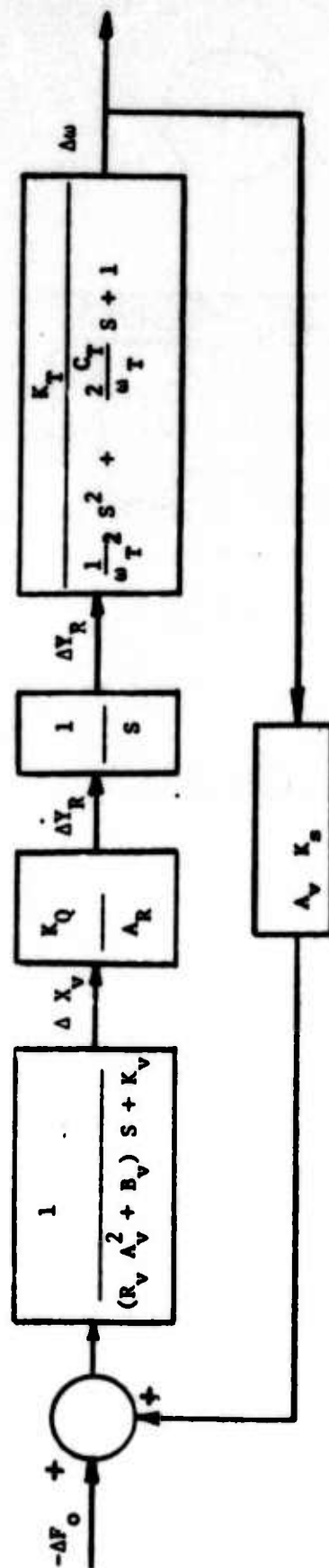


Figure 10 Transmission Speed Controller



- P = Sensor output pressure
- P_v = Pressure on the end of the valve spool
- P_L = $P_1 - P_2$ = Load pressure
- X_v = Spool position measured from null
- y_R = Ram position
- A_v = Spool cross-section area
- A_r = Ram piston cross-section area
- Q_v = Flow from the valve to the ram
- K_v = Valve spring constant
- R_v = Hydraulic resistance of the tube connecting the sensor to the valve.

Figure 11 Valve-Ram Combination



Linearized Parameter Values

$$R_v = 31.3 \frac{\text{lb} \cdot \text{sec}}{\text{in}^5}$$

$$A_v = 0.785 \text{ in}^2$$

$$B_v = 0.1 \frac{\text{lb}}{\text{in}/\text{sec}}$$

$$K_v = 83.3 \frac{\text{lb}}{\text{in}}$$

$$K_Q = 10.6, 19.0, 30.2 \frac{\text{in}^3/\text{sec}}{\text{in}}$$

$$A_R = 0.393 \text{ in}^2$$

$$\omega_T = 17.7 \frac{\text{Rad}}{\text{Sec}}$$

$$C_T = 0.46$$

$$K_s = -0.057 \frac{\text{psi}}{\text{Rad}/\text{Sec}}$$

$$K_T = 300 \frac{\text{Rad}/\text{Sec}}{\text{in}}$$

Figure 12 Linearized and Simplified System Model

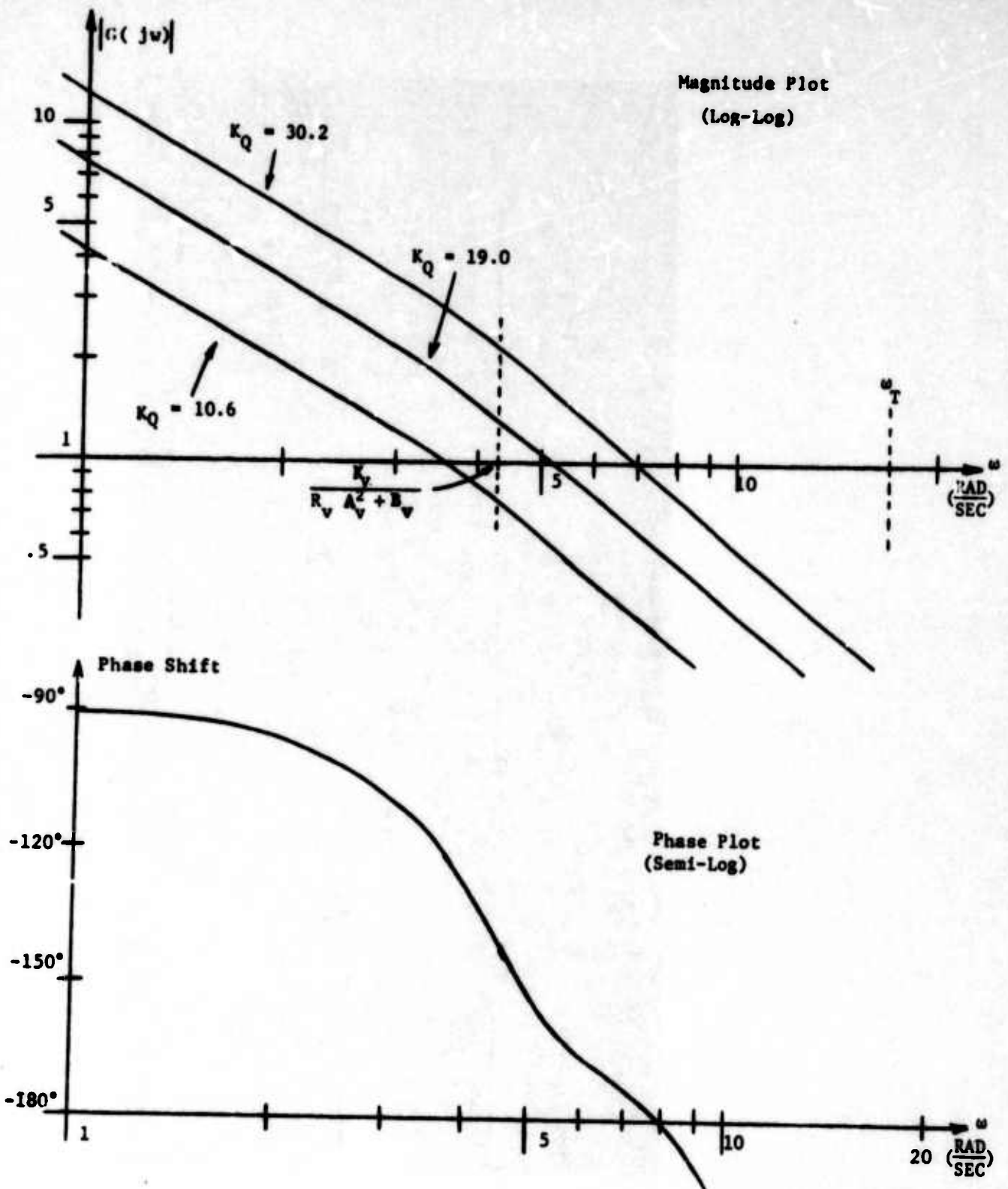
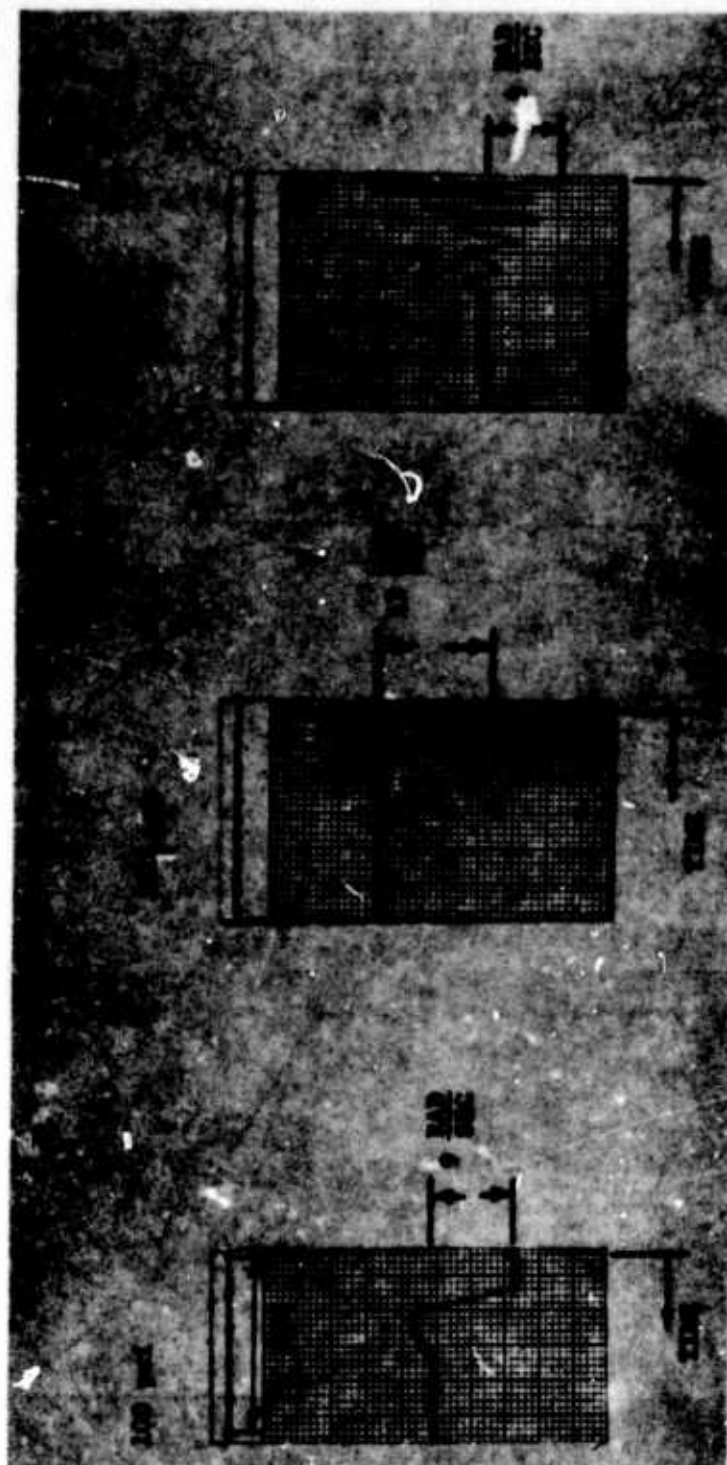


Figure 13 Bode Plot of the Linearized System



Valve Supply Pressure = 200 psi

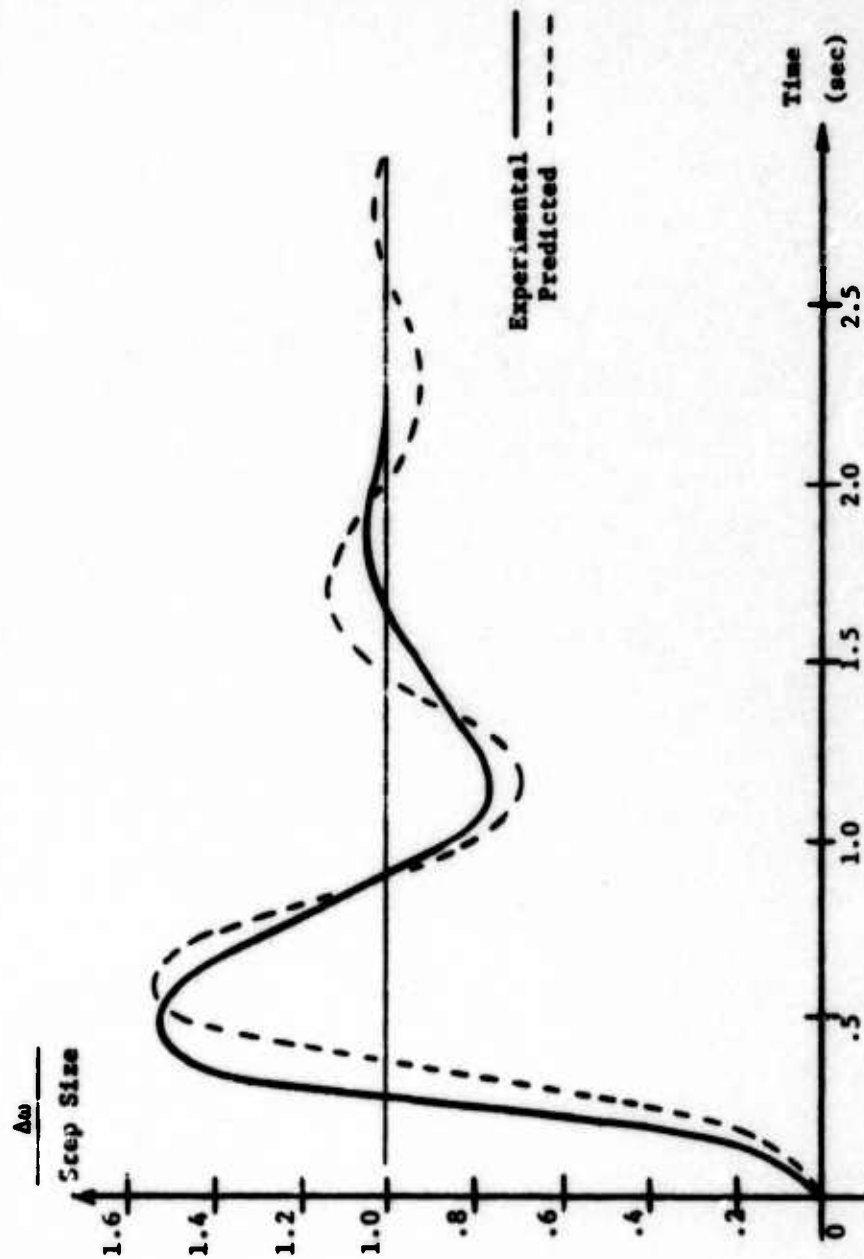


Figure 15 Actual and Predicted Step Response

A FLUID AMPLIFIER REYNOLDS NUMBER

by

TADEUSZ M. DRZEWIECKI

Submitted for presentation at:
The Harry Diamond Laboratories
Fluidic State-of-the-Art Symposium
30 Sep - 4 Oct 1974
Adelphi, Maryland

ABSTRACT

This paper presents a short analysis of and comprehensive experimental verification for the existence of a new dimensionless group, that relates fluid amplifier characteristics, called the fluid amplifier Reynolds number, N_{Ra} . It is defined as

$$N_{Ra} = [b_s \sqrt{2P_s/\rho/\nu}] / [\ell_{th}/b_s + 1)(1 + 1/\sigma)^2]$$

where:

- b_s - amplifier supply nozzle width
- P_s - amplifier supply pressure
- ρ - fluid density
- ν - fluid kinematic viscosity
- ℓ_{th} - amplifier supply nozzle throat length
- σ - amplifier supply nozzle aspect ratio

In addition to showing that this is a valid scaling parameter for many fluidic devices, both digital and analog, it is also shown that a critical value of N_{Ra} exists, $N_{Ra} = 1000$, such that fluidic operation is virtually independent of Reynolds number (supply flow, pressure) above that value. It is argued that this condition defines the lower limit of fully established turbulent flow in a fluidic device.

NOMENCLATURE

- A - cross-sectional area, (m²)
- b - nozzle width, (m)
- B - width, (m)
- c_d - nozzle discharge coefficient, (dimensionless)
- d_h - hydraulic diameter, 2bh/(b + h), (m)
- D - geometric constant, (dimensionless)
- G_R - pressure gain, (dimensionless)
- h - nozzle height (m)
- K - constant, (dimensionless)
- ℓ - length, (m)
- L - characteristic dimension, (m)
- N_R - Reynolds number, $\frac{L}{\nu} \sqrt{\frac{2P}{\rho}}$, (dimensionless)
- P - pressure, (kPa)
- Q - volumetric flow, (m³/s)
- r - radius, (m)
- R - fluid resistance, (kg/(m⁴ · s))
- S - normalized distance along a nozzle wall
- U - characteristic fluid velocity, (m/s)

Greek Symbols

- ν - fluid kinematic viscosity, (m²/s)
- ρ - fluid density, (kg/m³)
- σ - aspect ratio, h/b, (dimensionless)
- X - dummy variable of integration, (dimensionless)

Subscripts

- a - amplifier
- c - control
- eff - effective
- FET - fully established turbulence
- h - height
- i - integer count, 1 or 2
- n - nozzle
- id - ideal
- p - plenum
- s - supply
- st - static
- S - stretched
- th - throat
- 1 - refers to condition on converging walls
- 2 - refers to condition on plane walls
- ∞ - nozzle exit condition

INTRODUCTION

In fluidics, as in other areas of fluid mechanics, it is often useful to consider dimensionless groups (scaling parameters) which provide a means for comparison of various phenomena in differing physical circumstances. The most familiar such group is perhaps the Reynolds Number, N_R , which provides a measure of the ratio of inertial to viscous forces in a moving fluid. N_R is defined as the quotient of the product of a characteristic velocity U and characteristic dimension, L , with the kinematic viscosity ν . In general the characteristic dimension is an obvious quantity, for example the length of a plate, the diameter of a cylinder, or the width of a two-dimensional channel. In each case it is the only important dimension. One begins to run into trouble, however, when considering three-dimensional flow or internal flow with a complex geometry. Which dimension should be chosen to be most representative of a flow phenomena, when there is more than one dimension? In pipe flow the hydraulic diameter is used. Hydraulic diameter, d_h , is proportional to the ratio of the flow-through area to the wetted perimeter. Zumens [1] shows this to be generally true in his very lucid presentation. Already, however, one begins to see the complexity involved if more than one dimension is involved, since the definition of hydraulic diameter is not obvious. In the case of fluidic flow problems involving jets there are at least seven dimensions common to most devices: supply nozzle width, b_s , supply nozzle height, h_s , length of throat, l_{th} , overall nozzle length, l_n ; nozzle-to-splitter distance; amplifier width, B_a ; and control nozzle width, b_c . It is conceivable that there are more if one wishes to consider such dimensions as outlet channel width, attachment wall length, and offset; and control nozzle shape. Applying the Buckingham π theorem only produces as many Reynolds numbers as dimensions so that it does not appear that dimensional analysis is going to help.

With this background, then, it is clearly evident that a problem exists. The solution lies in finding the simplest relation possible which is still universal enough to be a valid scaling parameter in as many instances as possible. Drzewiecki's [2] analysis of discharge coefficients shows that, even for simple nozzle flow, the Reynolds number based on nozzle width does not reduce the data to a single curve. Kelley and Boothe's [3] data on proportional amplifier gain show that hydraulic diameter, used as the characteristic dimension, does not produce a suitable Reynolds number. Manion and Mon's [4] data on proportional amplifier gain indicate that to use the nozzle height as the characteristic dimension is fairly good, but scatter is still evident, and it, too, is therefore not entirely satisfactory. Because combinations now become somewhat more arbitrary, it is the present purpose to determine analytically a good characteristic dimension, and so to define a fluid-amplifier Reynolds number, N_{Ra} .

ANALYSIS

In general the predominant feature of a jet fluid amplifier or gate is the supply jet issuing from a nozzle, so that if the discharge coefficient of a nozzle can be expressed in terms of a single variable then this variable may include the characteristic length being sought.

F. Manion, HDL, suggested that the simple form of discharge coefficient, c_d , from reference [2] be multiplied out and a dominant group pulled out of there. This is the form found in eq. 1.

$$c_d = [1 - 2D_1/\sqrt{N_R}] [1 - 2D_2/(\sigma\sqrt{N_R})] \quad (1)$$

where

$$\begin{aligned} N_R &= \sqrt{2P_s/\rho} b/v \\ \sigma &= \text{aspect ratio, } h/b \\ P_s &= \text{amplifier supply pressure} \\ \rho &= \text{fluid density} \\ v &= \text{fluid kinematic viscosity} \end{aligned}$$

The value of D_1 involves an integral of the axial freestream velocity over the entire length of the nozzle. If a simple relation between geometry and this velocity exists then the integral may be replaced by the effective length of straight duct to which the nozzle is equivalent so that:

$$D_1 = K(\ell_{\text{eff}}/b + \ell_{\text{th}}/b)^{1/2} \quad (2)$$

where

$$\begin{aligned} K &= 1.75 \\ \ell_{\text{eff}} &= \text{effective-length contribution of the contraction} = \int_0^S (u/U_w)^5 d\chi \\ &\quad \text{on fig. 1 that portion of the nozzle between the straight sections.} \\ S &= \text{distance along wall from start to end of contraction} \\ \chi &= \text{dummy variable for } S \end{aligned}$$

Substituting eq. (2) into (1), the equation for discharge coefficient becomes

$$c_d = \left[1 - 2K \sqrt{\frac{\ell_{\text{eff}}/b + \ell_{\text{th}}/b}{N_R}} \right] \left[1 - \frac{2K}{\sigma} \sqrt{\frac{\ell_{\text{eff}}/b + \ell_{\text{th}}/b}{N_R}} \right] \quad (3)$$

Multiplying out yields the following equation:

$$c_d = 1 - 2K \sqrt{\frac{(\ell_{\text{eff}} + \ell_{\text{th}})/b}{N_R}} \left(1 + \frac{1}{\sigma}\right) + \frac{4K^2}{\sigma} \frac{(\ell_{\text{eff}} + \ell_{\text{th}})/b}{N_R} \quad (4)$$

For the normally expected case

$$\frac{\ell/b}{N_R} \ll 1, \ell = \ell_{\text{eff}} + \ell_{\text{th}}$$

$$c_d \approx 1 - 2K \sqrt{\frac{\ell/b(1 + 1/\sigma)^2}{N_R}} \quad (5)$$

From eq. 5 it can be seen that the discharge coefficient, for large Reynolds numbers, is a function of a single variable group such that

$$c_d = f \left(\frac{N_R}{\ell/b(1 + 1/\sigma)^2} \right) \quad (6)$$

Numerical experiments with various nozzles indicate that the effective length of the nozzle contraction, ℓ_{eff}/b is under most circumstances no greater than the order of 1. In that case one can define a modified Reynolds number, or a fluid amplifier Reynolds number,

$$N_{Ra} = N_R / [(\ell_{\text{th}}/b + 1)(1 + 1/\sigma)^2] \quad (7)$$

It can therefore be seen that if the supply jet is the predominant part of a device the characteristic dimension to be used is $L = b/[(\ell_{\text{th}}/b + 1)(1 + 1/\sigma)^2]$.

EXPERIMENTAL VERIFICATION

To justify, not only that this characteristic length is truly characteristic but also that the supply jet characteristics predominate in fluid amplifiers of many types, the experimental data following is presented.

Four nozzles of the planview shown in fig. 1, with $b \approx 1.0$ mm and $h \approx 0.5, 1.0, 1.5, 2.0$ mm, and a moderately long throat, $\ell_{\text{th}} \approx 4.0$ mm were used in the experimental measurement of the discharge coefficient. The plenum chambers were made long in order to allow the flow from a fitting, making a right angled turn, to become uniform. The static pressure in the plenum was measured by using a static wall tap located at the start of the contraction. Electronic manometers were used to measure this pressure as well as the pressure differential across a calibrated laminar flow-meter. The data were recorded on an X-Y plotter as volumetric flow rate, Q , versus plenum static pressure, P_{st} . Figure 2 shows the raw data. The supply stagnation pressure, P_s , was then calculated from the plenum dimensions and the flow, as:

$$P_s = P_{st} + \frac{1}{2} \rho \bar{U}^2$$

or by noting that the average velocity is the quotient of flow and area:

$$P_s = P_{st} + \frac{\rho}{2} \left[\frac{Q}{B_p h} \right]^2$$

where

B_p - width of the plenum chamber

ρ - fluid density

The experimental value for discharge coefficient is the ratio of the actual flow through the nozzle to the ideal flow [2, 2a].

$$c_d = \frac{Q}{Q_{id}} = Q / (bh \sqrt{2P_s / \rho})$$

The resultant experimentally determined values of discharge coefficients are shown in fig. 3. As can be seen the discharge data all collapse to one curve except in the case of the low-aspect-ratio nozzle, $\sigma = 0.5$. Close examination of the actual nozzle used for $\sigma = 0.5$ showed that glue bonding the cover plate had seeped into the channel forming a considerable fillet thus reducing the cross-section, increasing the impedance to flow and hence yielding a low value of c_d based on the ideal nozzle exit area.

The experimental data taken for proportional amplifier pressure gain given by Kelley and Boothe [3], was collapsed by them to approximately one curve by use of a stretched Reynolds number $N_{RS} = N_R (\sigma d_h / b)$, where $d_h = 2bh / (b+h)$, is the hydraulic diameter. Their data are shown in fig. 4, which also shows how their data collapse on the fluid-amplifier Reynolds number, N_{Ra} of eq. 7. The scatter of the data is about the same. Kelley and Boothe did not give the length of their nozzle so that the dimensionless group N_R'' , used is simply

$$N_R'' = N_R / (1 + 1/\sigma)^2 \quad (8)$$

because ℓ does not vary in their experiment. Expanding their "stretched" Reynolds N_{RS} number shows that it is simply,

$$N_{RS} = N_R / \left[\frac{1}{\sigma} \left(1 + \frac{1}{\sigma} \right) \right]$$

which is only different from N_R'' , by a factor of one (1) in the denominator, in that Kelley and Boothe have $1/\sigma$ and the present analysis has $(1 + 1/\sigma)$. For low values of the aspect ratio, σ , this apparently does not result in too great a difference.

The data of Manion and Mon [4], also for proportional amplifier pressure gain, is plotted against Reynolds number based on nozzle height N_{Rh} . Their data are shown in fig. 5 as is a comparison using the fluid-amplifier Reynolds number of eq. 8. As can be seen the data are tighter around the modified Reynolds number. Scaling with nozzle height was not bad, however. If the fluid-amplifier Reynolds number of eq. 8 is expanded to have a Reynolds number based on nozzle height (rather than width) the result is:

$$N_R'' = N_{Rh}/(\sqrt{\sigma} + 1/\sqrt{\sigma})^2$$

The quantity $1/(\sqrt{\sigma} + 1/\sqrt{\sigma})^2$, for the aspect ratios of 0.4 - 1.0 used, varies only from 0.2041 to 0.25, hence the choice of nozzle-height Reynolds number was fortuitous, in that it was only off by a factor that didn't vary much.

Referring now to the work of McRee and Moses [5] and McRee and Edwards [6] it can be determined from their data on attachment point distance that at a constant value of the fluid-amplifier Reynolds number

$$N_{Ra} = N_R/((L_{th}/b + 1)(1 + 1/\sigma)^2) = 1000$$

there is no longer any appreciable Reynolds number dependence. In other words the jet entrainment is constant, which is tantamount to the establishment of fully-turbulent flow in the device. Considering this point a little further, one can observe the data on the flow required to cause a switch in a digital device as a function of supply pressure as taken by Müller [7] and Warren [8]. When this flow becomes independent of supply pressure it, too, is an indication that fully established turbulent flow or constant entrainment has occurred. For Müller's data on sharp splitter digital devices using a throat length $L_{th}/b_+ = 1.0$ with an aspect ratio, $\sigma = 1$, the Reynolds number, N_{Ra} , at which the switch flow becomes constant is 1000. For Warren's data on latching vortex-type digital devices with an aspect ratio $\sigma = 2$, a throat length $L_{th}/b = 2.5$, and a nozzle width of 0.8 mm, the switch flow becomes approximately constant at 12.4 kPa (1.8 psi). This, too, corresponds to a value of fluid-amplifier Reynolds number of 1000. A trend has appeared. To pursue it further the data of Weinger [9] on turbulence level in proportional amplifiers show that there, too, for various aspect ratios from 2 to 7 the point at which a constant level of turbulence was achieved corresponds to a $N_{Ra} = 1000$. (The throat length used in Weinger's experiment was $5.3 b_s$. The data for aspect ratios from .5 to 1.0 did not go high enough in supply pressure to insure constancy of the turbulence level).

The indication from the latter five independent sets of data is that there appears to be a constant value of N_{Ra} which predicts the onset of fully-established turbulence in a fluidic device. Examining this statement, it appears that the value of $N_{Ra} = 1000$ describes a minimum-stability laminar velocity profile at the exit of the nozzle that immediately becomes turbulent

upon exiting. One can see from this that an increase in throat length will cause the nozzle-width Reynolds number to be higher for fully-established turbulence. Similarly a decrease in aspect ratio will do the same thing. These were the things done based on experience to promote laminarity and low noise. Now there is some analytical-empirical justification. The cause of this laminarization is quite evident. If the throat is long or the aspect ratio is low, the exit-velocity profile is fairly well developed and the gradient of velocity (\sim shear) is low so that the flow is more stable than a flow with high free-shear interface. This is the case for a low discharge coefficient. Apparently the combination of the adjacent (top and side) boundary layers has an effect for if it were only the sides undergoing separation that were critical then the critical number would be different (e.g. $N_R / (\ell_{th}/b + 1)$). The value therefore of the fluid amplifier Reynolds number for fully-established turbulence $N_{Ra}|_{FET}$ is

$$N_{Ra}|_{FET} = 1000$$

SUMMARY AND CONCLUSIONS

The analysis has indicated that there is a characteristic dimension for many fluid amplifiers such that the Reynolds number using that dimension collapses all amplifier discharge coefficient data, regardless of nozzle shape or aspect ratio, to a single curve. This has been experimentally verified. In addition this same modified Reynolds number has been found to relate to other fluid-amplifier characteristics. It collapses the gain curves for laminar proportional amplifiers of different aspect ratios, and more importantly a constant value of 1000 established the Reynolds-number-independent operating region of turbulent fluid amplifiers, both digital and proportional.

This modified Reynolds number therefore is truly representative of a fluid amplifier - it includes such important parameters as aspect ratio and supply nozzle shape, as well as throat length, which were lacking from previously used dimensionless groups.

In conclusion, then, a new Reynolds number for fluid amplifiers has been established from a rational analysis of supply jet flow issuing from a power nozzle, and a constant has been experimentally determined that determines the region of Reynolds-number-independent flow.

ACKNOWLEDGEMENT

Sincere appreciation is extended to Frank Manion, HDL, for his help and comments regarding the establishment of the modified Reynolds number.

BIBLIOGRAPHY

- [1] Zuments, G., "Study of the Validity of the Hydraulic Radius Concept for Viscous Flow in Non-circular Ducts," AIAA Student Journal, Vol. 2, no. 2, Oct 1964, pp. 19-25.
- [2] Drzewiecki, T. M., "Planar Nozzle Discharge Coefficients," Developments in Mechanics, Vol. 7, Proc. 13th Midwestern Mechanics Conference, Aug 1973, also:
[2a] "Fluerics 33: Planar Nozzle Discharge Coefficients," HDL-TM-72-33, 1973.
- [3] Kelley, L. R. and Boothe, W. A., "Hydraulic Fluidics," ASME publication no. 68-WA/FE-26, New York, 1968.
- [4] Manion, F. M. and Mon, G., "Fluerics 33: Design and Staging of Laminar Proportional Amplifiers," HDL-TR-1608, Sept 1972, AD-751182.
- [5] McRee, D. and Moses, H., "The Effect of Aspect Ratio and Offset on Nozzle Flow and Jet Reattachment," Advances in Fluidics, ASME Fluidics Symposium, Chicago, IL, May 1967.
- [6] McRee, D. and Edwards, J., "Three-Dimensional Jet Reattachment," ASME publication no. 70-WA/Flcs-5, Nov 1970.
- [7] Müller, H. R., "A Study of the Dynamic Features of a Wall Reattachment Fluid Amplifier," ASME publication no. 64-FE-10, May 1964.
- [8] Warren, R. W., "The Digital Amplifier," Proc. IFAC/IFIP Symposium, Munich, Germany, Oct 1965.
- [9] Weinger, S., "Effect of Aspect Ratio on Noise in Proportional Amplifiers," Advances in Fluidics, ASME, Fluidics Symposium, Chicago, IL, May 1967.

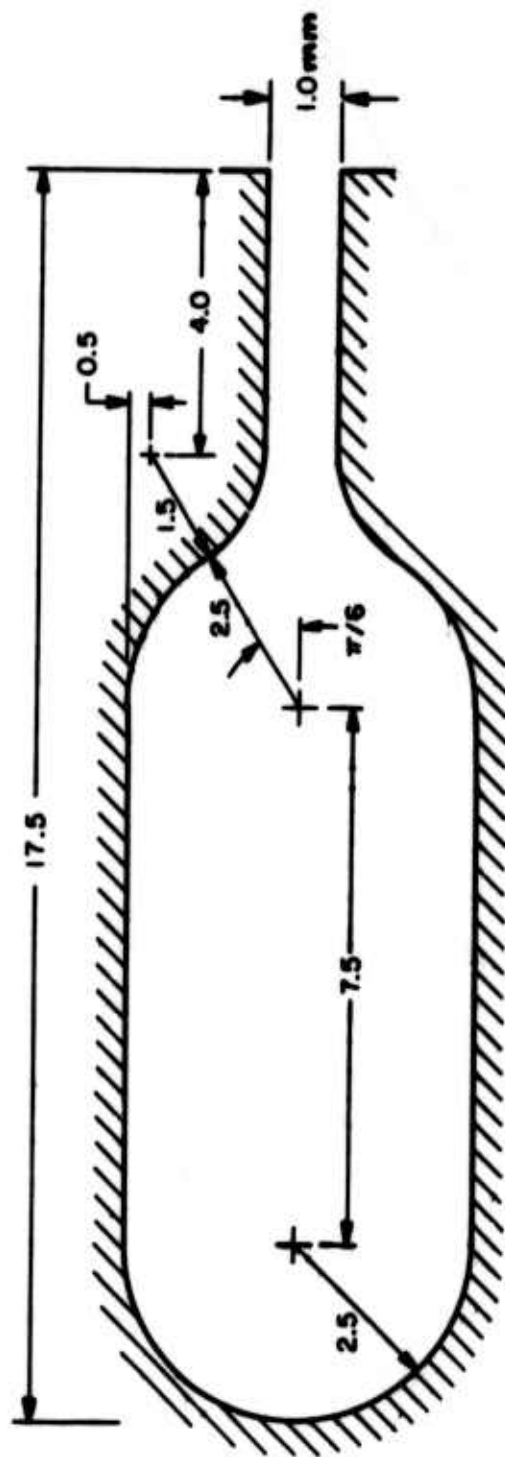


Figure 1. Planview of the planar nozzle used in the experiments

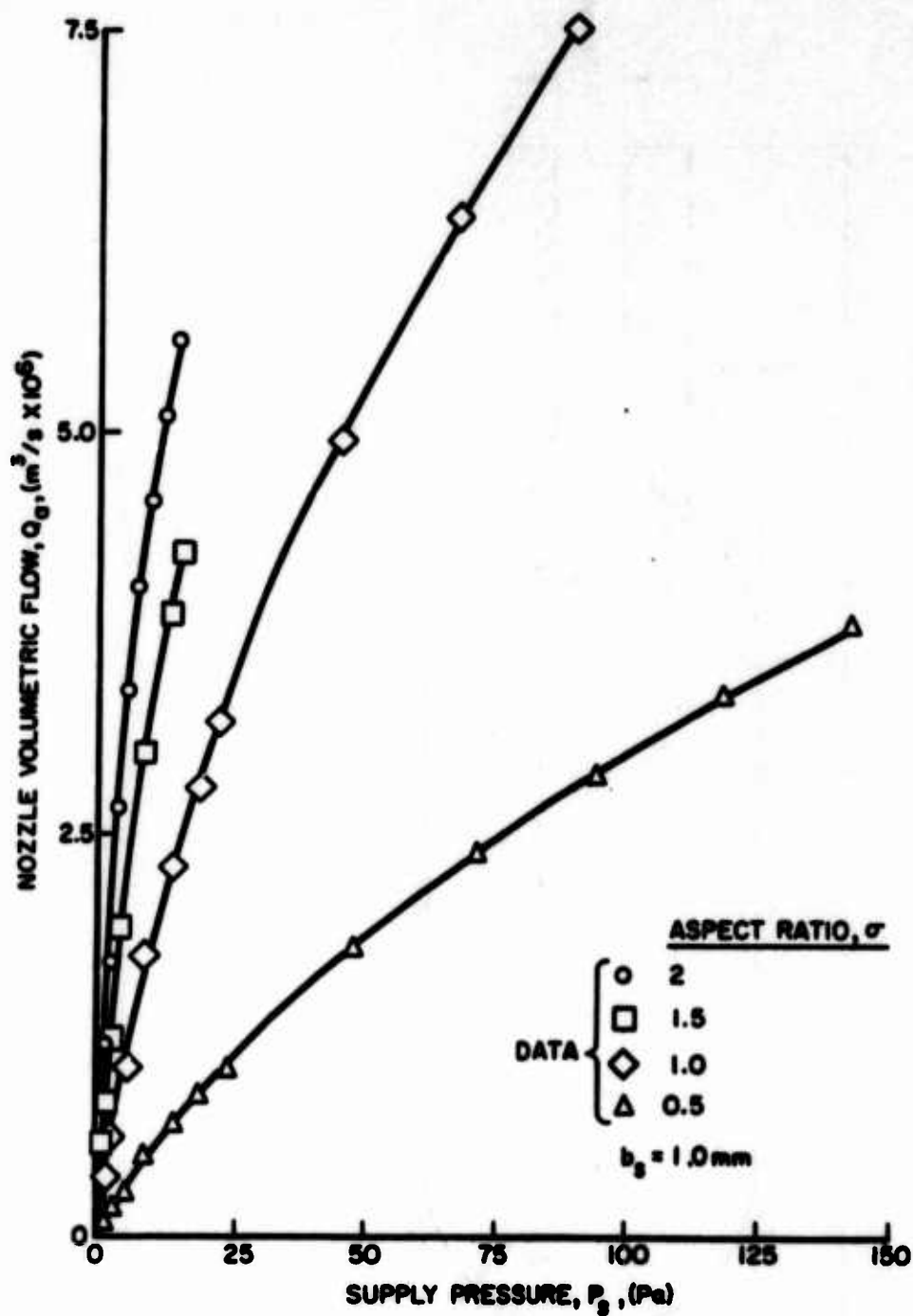


Figure 2. Raw flow-pressure data for the experimental nozzle

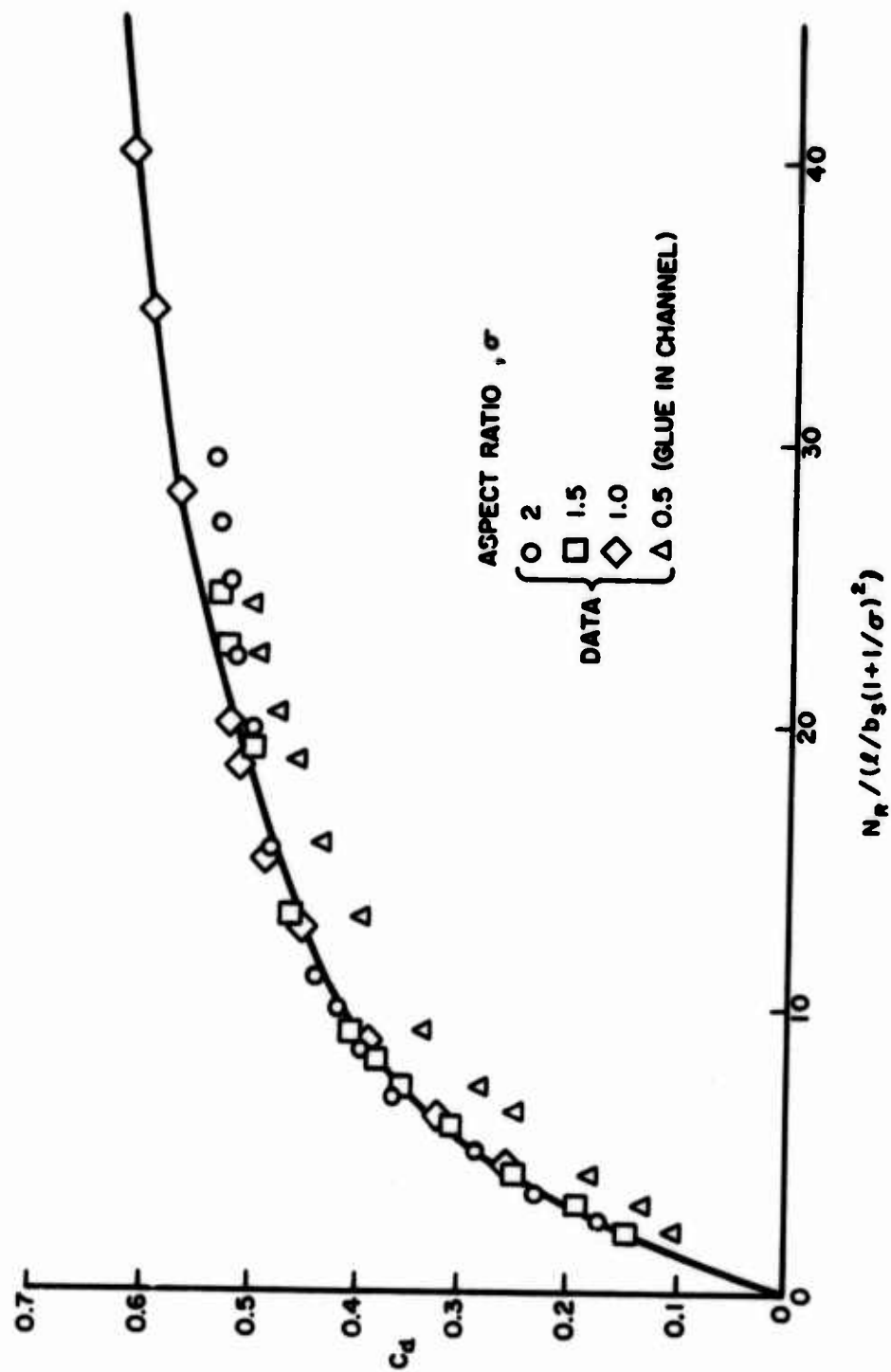


Figure 3. Collapsing of discharge coefficient data on modified Reynolds number

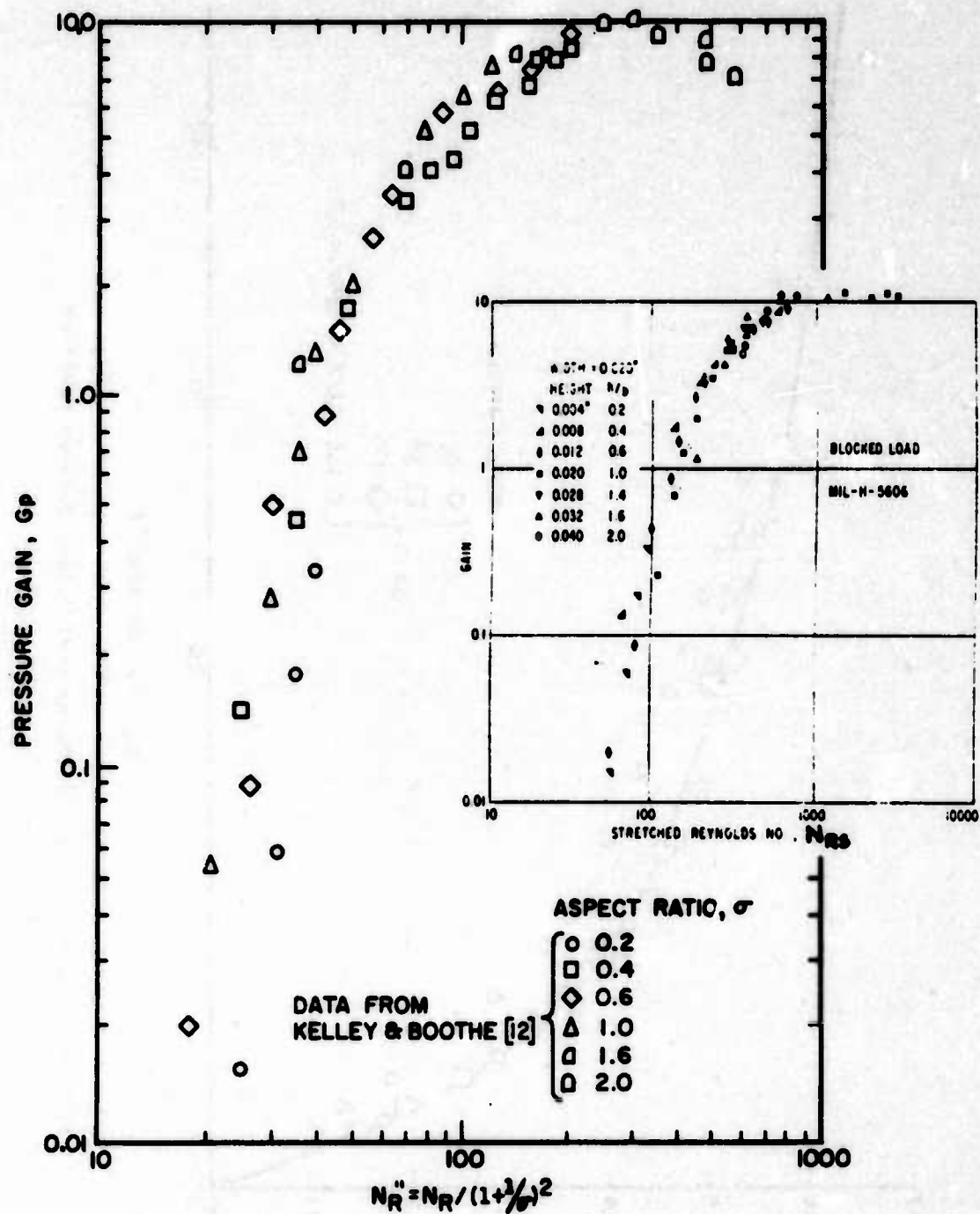


Figure 4. Comparison of pressure gain data for Kelley and Boothe's stretched Reynolds number and the modified Reynolds number

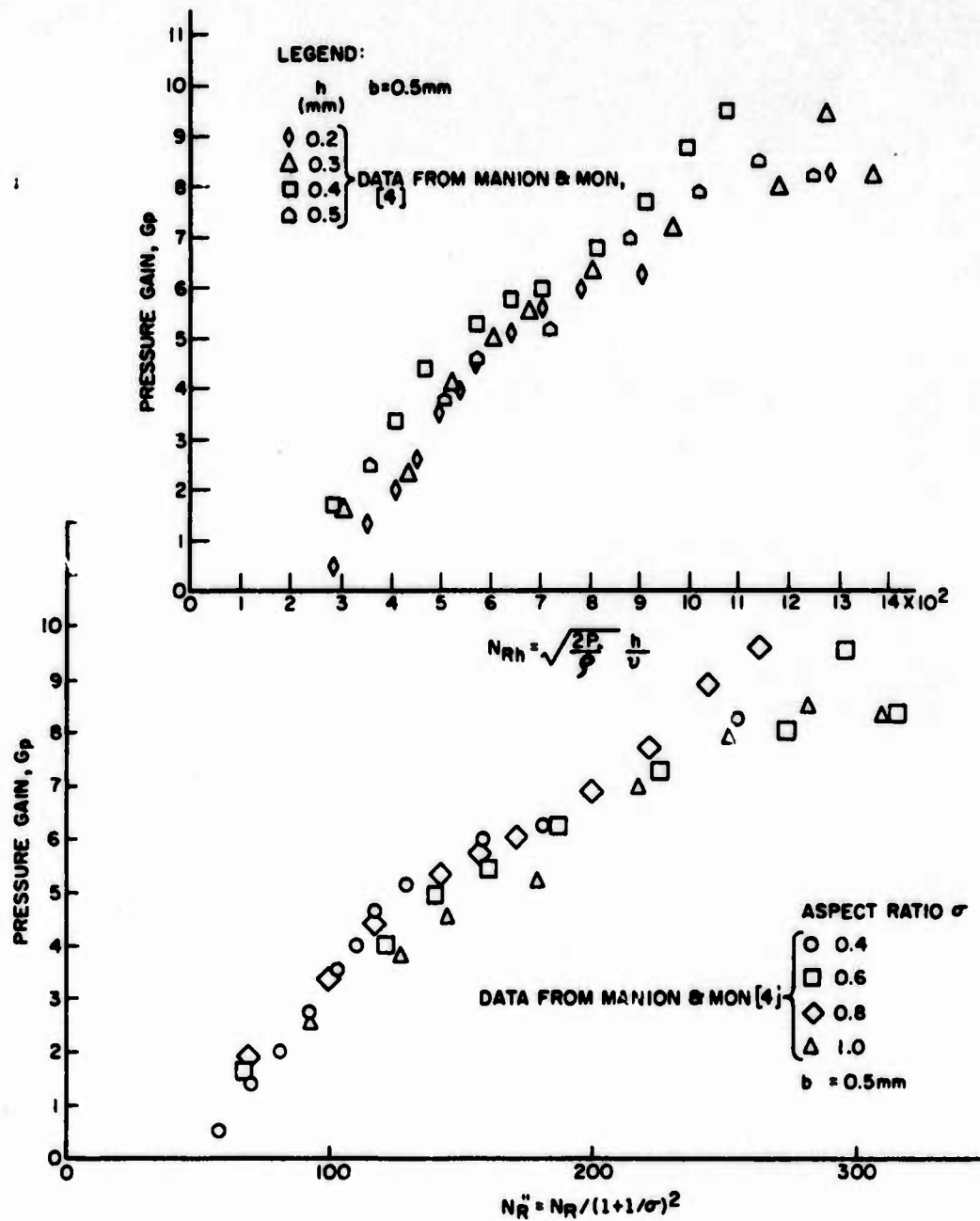


Figure 5. Comparison of pressure gain data for Reynolds number based on height and modified Reynolds number

**EFFECTS OF ASPECT RATIO AND LOW REYNOLDS
NUMBER ON RECOVERY AND FLOW REGIMES
IN A PLANE-WALL DIFFUSER**

A. S. Dighe¹

A. T. McDonald²

May 1974

¹**Reader in Mechanical Engineering
Department of Chemical Technology
University of Bombay
Bombay, INDIA**

²**Professor
School of Mechanical Engineering
Purdue University
West Lafayette, Indiana 47907**

EFFECTS OF ASPECT RATIO AND LOW REYNOLDS
NUMBER ON RECOVERY AND FLOW REGIMES
IN A PLANE-WALL DIFFUSER

A.S. Dighe¹ and A.T. McDonald²

ABSTRACT

The flow regime and pressure recovery behavior of a plane wall diffuser were studied experimentally to determine the effects of low Reynolds number and aspect ratio. Tests were performed for flow conditions (Reynolds numbers between 3,000 and 28,000, based on hydraulic diameter) and aspect ratios ($0.21 < AS < 2.65$) typical of those found in fluidic devices.

The pressure recovery coefficient for fixed geometry was found to increase monotonically with Reynolds number. At the highest Reynolds number tested, the recovery for $AS \geq 1$ was comparable to that obtained by Reneau, et al, at high Reynolds number. For constant Reynolds number, the pressure recovery coefficient first increased and then decreased with aspect ratio; optimum values of aspect ratio were identified for three representative Reynolds numbers. Flow regime behavior was found to depend on both Reynolds number and aspect ratio.

NOTATION

Symbol

A	geometric cross-sectional area
A_B	blocked area, $A - A_E$
A_E	effective area, $\dot{m}/\rho V$
AR	area ratio, A_2/A_1
AS	aspect ratio, b_1/W_1
B	blocked area fraction, A_B/A

¹Reader in Mechanical Engineering
Department of Chemical Technology
University of Bombay
Bombay, INDIA

²Professor
School of Mechanical Engineering
Purdue University
West Lafayette, Indiana 47907

b	diffuser height
C_p	pressure recovery coefficient, $p_2 - p_1 / \frac{1}{2} \rho \bar{U}_1^2$
d_p	hydraulic mean diameter, $2A/(b+W)$
E	effective area fraction, A_g/A
\dot{m}	mass flowrate
p	static pressure at a cross-section
p_o	stagnation pressure
Re	Reynolds number, $\bar{U}_1 d_1 / \nu$
\bar{U}	core velocity
\bar{U}	average velocity
V	maximum velocity at a cross-section
W	diffuser width

Greek Symbols

δ^*	displacement thickness of boundary layer, $\int_0^\delta \left(1 - \frac{u}{U}\right) dy$
θ	momentum thickness of boundary layer, $\int_0^\delta \frac{u}{U} \left(1 - \frac{u}{U}\right) dy$
θ	diffuser half angle
ν	kinematic viscosity
ρ	density

Subscripts

1	diffuser inlet section
2	diffuser outlet section

INTRODUCTION

Diffusers have been studied experimentally for many years; however, a design guide for efficient diffusers is far from completion, mainly because of the large number of governing parameters on which diffuser performance depends. Analytical prediction techniques for flow behavior fail for most practical diffuser geometries because flow in these diffusers is often separated.

A survey of the existing literature on diffusers indicates that most experimental work on diffusers of various geometries and shapes was done at high Reynolds number ($Re > 60,000$), because in applications such as turbine draft tubes, aircraft inlets, and turbomachinery passages, diffusers generally operate at high Reynolds numbers.

Diffusers working at low Reynolds numbers (possibly with laminar inlet boundary layers) were not of practical interest until recently when fluidic applications gained increased importance. Many fluidic devices such as fluid amplifiers, rate and temperature sensors were developed as

control system elements to compete with their corresponding electronic counterparts. These units have diffusing passages at the output sections. Because of their miniature sizes and low flowrates these units operate at low Reynolds numbers (of the order of a few thousand) and their aspect ratios are also low (of the order of unity).

The purpose of this experimental study was twofold: (1) to evaluate the pressure recovery coefficient of a plane wall diffuser at varying aspect ratio ($0.21 \leq AS \leq 2.65$) in the low Reynolds number range ($3,000 \leq Re \leq 25,000$), and (2) to study the effects of aspect ratio and low Reynolds number on the flow regime behavior.

LITERATURE REVIEW

The pressure recovery of a diffuser has been found to depend upon both geometric parameters and flow parameters. For plane wall diffusers, the length ratio, divergence angle (or area ratio), and aspect ratio are the geometric parameters while Reynolds number, Mach number (in the case of compressible flow), inlet boundary layer thickness, etc. constitute flow parameters.

Reneau, Johnston and Kline¹ prepared extensive pressure recovery charts for plane wall diffusers using the performance data then available. They also realized that the aspect ratio of a plane wall diffuser can influence the pressure recovery. They made analytical computations using the integral momentum method to predict boundary layer growth for unstalled diffusers. Their results suggested that for aspect ratios above about 10, the predicted pressure recovery remains unaffected by aspect ratio. The analytical results also suggest that in the case of low aspect ratio diffusers, short units have better pressure recovery than long ones of the same area ratio.

Sovran and Klomp² correlated the inlet blocked area fraction to determine the pressure recovery coefficient for optimum recovery diffuser geometries. Their correlation works well for two dimensional as well as conical diffusers so long as the inlet boundary layer is maintained turbulent and thin. The blocked area coefficient, B_1 , is defined by the equation

$$B_1 = 1 - \frac{A_E}{A} \quad (1)$$

where A represents the geometric cross-section of the diffuser at inlet and A_E , the effective cross-section calculated from the equation

$$A_E = \frac{\dot{m}}{\rho V_1} \quad (2)$$

In Eq. 2, V_1 represents the maximum centerline velocity at the inlet of the diffuser.

The first experimental measurements of the effects of aspect ratio on two dimensional diffusers were reported by Johnston and Powars.³ They selected five aspect ratios and three different geometries; one in the unstalled flow regime, another with peak recovery and the third in the transitory stall regime. Their results indicate that the pressure recovery for the diffuser geometry with transitory stall increases as the aspect ratio is lowered, a result contradicting the trend predicted analytically by Reneau et al. for unstalled diffusers. However, Johnston and Powars used boundary layer control to maintain their inlet displacement thickness, δ^* , on all the four walls.

Further experiments were performed by Runstadler⁴ using diffusers with aspect ratios of 1/4, 1, and 5. Inlet Mach number, M_1 , and inlet blocked area fraction, B_1 , were the primary flow parameters varied. From one of the cross-plots showing peak pressure recovery versus aspect ratio with inlet blockage fraction, B_1 as a parameter, it appears that C_p rolls off on either side of a maximum value obtained at $AS = 1$. All of these experiments were conducted at high Reynolds number ($Re > 10^5$).

Recent work by McMillan and Johnston⁵ concentrated on one aspect ratio ($AS = 0.1$) with fully-developed inlet flow for diffusers with $N/W_1 = 6$ and seven different area ratios. They found C_p to be Reynolds number dependent and to increase with increasing Re , in the range $20,000 < Re < 70,000$. They attributed the low values of C_p to inefficient diffusion owing to increasing dissipation caused by turbulent shear. The failure of the Sovran and Klomp correlation technique in these low aspect ratio diffusers was mainly because of inefficient diffusion. McMillan and Johnston also studied the flow patterns and found that diffusers in the transitory stall regime exhibited flow pattern variations. The flow pattern changed from transitory stall to fixed stall and finally to bistable stall as the Reynolds number increased.

In fluidic devices, the role of aspect ratio as a controlling parameter for noise reduction has been considered by several investigators. Glaettli, et al.⁶ and Comparin, Glaettli and Mitchell⁷ conducted studies on noise reduction of fluid jet amplifiers and found that reduced aspect ratio attenuated the noise level. The investigation of Tamulis⁸

on jet knife edge amplifiers showed that low aspect ratio ($AS \approx 1$) in general adversely affected the establishment of jet knife-edge noise. Thus amplifiers of near unity aspect ratio have an advantage over high aspect ratio amplifiers.

In many fluidic devices, the output legs incorporate diffusing passages and the working range of Reynolds number is low ($3,000 < Re < 25,000$). Recent experimental results of Drzewiecki⁹ have shown that flows in the nozzle exit region of close wall bistable amplifiers exhibit diffuser flow regime behavior. The mean flow and boundary layers in these units may be either laminar or in the transition zone from laminar to turbulent. Many investigators have qualitatively predicted a low pressure recovery at lower Reynolds number but an experimental evaluation of C_p has not yet been undertaken.

EQUIPMENT DESIGN AND PROCEDURE

By using a suitable experimental setup, both of these governing parameters (low Reynolds number and aspect ratio) can be studied to determine their influences on pressure recovery coefficient and on flow regime behavior. A plane wall diffuser unit with $N/W_1 \approx 18$ and $2\theta = 8^\circ$ was selected for this investigation because at high Reynolds number this geometry gives high pressure recovery.

Clear plastic sheets in nominal thicknesses of 1/4, 1/2 and 1 inch were machined to form diffuser strips and corresponding filler plates. To ensure uniform thickness, sheets were milled on both sides. Using machined strips it was easy to assemble the unit free from leakage. The diffuser holder was also fabricated from clear plastic to permit flow visualization. Suitable combinations of diffuser strips and filler plates were used to obtain twelve different aspect ratios in the range $0.21 < AS < 2.65$.

Static pressure taps 0.016 inch in diameter were drilled carefully along the axis of the top cover plate on 2 inch centers and also at the diffuser throat and exit planes. An access hole of 5/16 inch diameter served to admit a pitot tube used to measure the velocity profile normal to the parallel walls. No provision was made to control the boundary layer as this is beyond control in the normal application of diffusers to fluidic devices. A pictorial view of the diffuser unit is shown in Fig. 1.

The general layout of the experiment setup is shown schematically in Fig. 2. Water is circulated around the

system by a small centrifugal pump. The diffuser assembly joins the two constant water level tanks.

The pressure rise through the diffuser was very small at low Reynolds numbers, so a micromanometer with a least count of 0.001 inch of water was used.*

For flow visualization, dye was injected at the diffuser inlet and exit planes using hypodermic needles. The pressure taps were also used to inject dye when needed to observe flow patterns. The most important flow patterns were also photographed in super 8 format color movies.

The water flowrates were generally low, so they were measured by collecting the flow of water over the downstream weir during a measured time interval. Using the measured mass flowrate, \dot{m} , the mass average velocity, \bar{U}_1 , was calculated from the equation,

$$\dot{m} = \rho A_1 \bar{U}_1 \quad (3)$$

The pressure recovery coefficient, C_p , was then calculated for a given Reynolds number, from

$$C_p = \frac{P_2 - P_1}{\frac{1}{2} \rho \bar{U}_1^2} \quad (4)$$

Sufficient time (as much as 1/2 hour) was allowed to let each reading stabilize.

RESULTS AND DISCUSSION

Variations in C_p with increasing Reynolds number were measured for each of 12 aspect ratios. Representative plots are shown in Figs. 4 through 8.

* Since this micromanometer used a liquid as gauge fluid, it could not be coupled directly to the diffuser pressure taps. A three fluid coupling (water-air-manometer fluid) arrangement with a converter section between the pressure taps and manometer was used. A pictorial view in Fig. 3 shows the test setup. For accurate measurements of small pressure differentials, sufficient time was allowed for the air temperatures in the converter section to equalize.

In each of Figs. 4 through 8, a steep increase in C_p occurs in the low Reynolds number range below $Re \approx 7,000$. The performance remains fairly independent of Reynolds number above a value of about 15,000.

At low Reynolds number, viscous forces tend to dominate over the inertia forces in internal flow. The loss due to viscous dissipation accounts for inefficient diffusion thus decreasing C_p considerably. The bulk flow at low Reynolds number was observed to be laminar. No boundary layer trips were used at the diffuser inlet, so the boundary layer remained laminar, as made clear by dye traces injected in the boundary layer. As the Reynolds number was increased by increasing the flowrate, the boundary layers became turbulent, and the recovery coefficient increased. A turbulent boundary layer is thus found to improve the pressure recovery coefficient for a fixed aspect ratio.

The cross-plot in Fig. 9 illustrates the effect of aspect ratio on the performance of a diffuser at constant Reynolds number. C_p increases as aspect ratio increases for each fixed Reynolds number up to an optimum aspect ratio. With further increases in aspect ratio, C_p decreases slightly. The curves shown in Fig. 9 suggest a trend for the optimum aspect ratio as the Reynolds number of the flow increases. For $Re = 5,000$, the optimum $AS \approx 1.6$; for $Re = 10,000$, the optimum aspect ratio is about 1.5, while at $Re = 20,000$, $AS \approx 1.33$ gives maximum C_p . Thus as Reynolds number increases, best recovery is obtained with lower aspect ratio units. For the diffuser geometry ($N/W_1 \approx 18$ and $2\theta = 8^\circ$), $AS \approx 1.33$ appears best for $Re \geq 20,000$.

The inlet blocked area fraction, B_1 , was measured as a function of Reynolds number for 3 different aspect ratios. The results are shown in Fig. 10. Some scatter in these data is apparent at lower Reynolds numbers, due to the very small dynamic pressure values measured at low flowrates. However, the data show a consistent trend toward lower blockage as Reynolds number is increased.

As noted earlier, the Sovran and Klomp correlation was based on diffuser data obtained with turbulent boundary layers and high Reynolds numbers. Therefore the correlation should agree only with some of the present data, those measured at high Reynolds number. Table 1 shows the predicted C_p values, using the measured blocked area fraction B_1 , from Fig. 10, in the SK correlation, against the experimentally calculated values of C_p . For $AS \approx 0.94$ the agreement between the predicted and experimentally calculated values of C_p is within 10 percent, when $Re \geq 10,000$.

TABLE 1

Reynolds Number	Aspect Ratio	$C_{p_{SK}}^*$	C_p	Percent Error (absolute)
20,000	2.65	0.754	0.709	6.30
	0.94	0.766	0.704	8.80
	0.40	0.808	0.578	39.8
10,000	2.65	0.718	0.686	4.66
	0.94	0.737	0.671	9.83
	0.40	0.747	0.531	40.6
5,000	2.65	0.702	0.610	14.1
	0.94	0.710	0.610	16.4
	0.40	0.716	0.365	96.1

*Calculated from correlation of Sovran and Klomp, Ref. 2

i.e. with turbulent inlet boundary layers. For lower aspect ratio however, there is considerably better agreement. This can be explained by studying more closely how Sovran and Klomp derived their correlation. At the inlet and exit planes of a diffuser,

$$p_{o_1} = p_1 + \frac{1}{2} \rho V_1^2 \quad \text{and} \quad p_{o_2} = p_2 + \frac{1}{2} \rho V_2^2 \quad (5)$$

where, V_1 and V_2 represent maximum velocities at these planes. From Eqs. 5

$$p_2 - p_1 = \frac{1}{2} \rho V_1^2 \left(1 - \frac{V_2^2}{V_1^2} \right) - (p_{o_1} - p_{o_2}) \quad (6)$$

Using effective area fractions E_1 and E_2 as designated by Sovran and Klomp,

$$\frac{\dot{m}}{\rho} = A \bar{U}_1 = E_1 A_1 V_1 = E_2 A_2 V_2 \quad (7)$$

Then Eq. 6 can be written

$$p_2 - p_1 = \frac{1}{2} \frac{\bar{U}_1^2}{E_1^2} \left(1 - \frac{E_1^2 A_1^2}{E_2^2 A_2^2} \right) - (p_{o_1} - p_{o_2}) \quad (8)$$

Finally, using the definition of recovery coefficient,

$$C_p = \frac{p_2 - p_1}{\frac{1}{2} \rho \bar{U}_1^2} = \frac{1}{E_1^2} - \frac{1}{E_2^2 AR^2} - \frac{p_{o1} - p_{o2}}{\frac{1}{2} \rho \bar{U}_1^2} \quad (9)$$

The ideal one-dimensional pressure recovery coefficient, C_{p_i} , depends only on the area ratio, AR . It can be easily shown that

$$C_{p_i} = 1 - \frac{1}{AR^2} \quad (10)$$

Thus, the coefficients E_1 and E_2 in Eq. 9 account for velocity profile distortion at the diffuser inlet and exit planes. This velocity profile distortion is attributed to insufficient diffusion. However, the stagnation pressure loss, $p_{o1} - p_{o2}$, or the loss coefficient $p_{o1} - p_{o2} / \frac{1}{2} \rho \bar{U}_1^2$, is due to inefficient diffusion. In general diffuser losses are due to both insufficient and inefficient diffusion.

Sovran and Klomp assumed negligible stagnation pressure loss in arriving at their correlation and thus allowed for only insufficient diffusion as the principal factor in predicting the pressure recovery coefficient.

Thus the actual recovery coefficient could be written

$$C_p = C_{p_{SK}} - \frac{p_{o1} - p_{o2}}{\frac{1}{2} \bar{U}_1^2} \quad (11)$$

$$\text{where } C_{p_{SK}} = \frac{1}{E_1^2} - \frac{1}{E_2^2 AR^2} \quad (12)$$

The results shown in Table 1 suggest, for high aspect ratio diffusers ($AS > 0.94$), operating at high Reynolds numbers, insufficient diffusion was the main contributing factor in determining C_p . At lower Reynolds numbers ($Re < 5,000$) the inefficient diffusion effect was no longer negligible. For low aspect ratio diffusers in fact, velocity profile distortion as well as stagnation pressure loss terms were comparable at all Reynolds numbers. The "potential core" was practically absent. The actual C_p thus was much less than the predicted value of Sovran and Klomp.

A study of flow patterns in the diffuser was also undertaken at increasing Reynolds number for all the aspect ratios. Figure 11 represents the flow pattern at $Re = 3,760$ for a diffuser with $AS = 0.21$. The stalled and reversed flow areas were seen clearly using dye tracers. The separation bubble remained stationary for a few seconds and

then slowly marched upstream before it was washed out. When the Reynolds number was increased beyond 5,000 the stall disappeared.

An interesting type of stall pattern which exhibited a periodic behavior was observed for $AS = 0.46$ at $Re = 3,890$. The stall developed on one wall near the exit plane of the diffuser and was washed out later with no stall for small time duration. It then developed on the other wall and was eventually washed out. This shifting of stall from one wall to another was not observed with any other geometry. At $Re = 4,300$ switching was not observed and stall preferred one wall. No stall was observed beyond $Re = 5,300$.

Figure 12 shows the flow pattern for nearly a square diffuser ($AS = 1.12$) at $Re = 2,220$. A two dimensional stall was observed on one wall but it was not bistable in nature. Introduction of dye through a pressure tap 2 inches downstream from the throat also indicated the existence of the stall. At $Re = 4,700$ the two dimensional stall disappeared and small local spots of recirculation were observed. No stall was seen above $Re = 5,600$.

In Fig. 13 a flow pattern for $AS = 1.37$ at $Re = 2,440$ is shown. Dye injected in the exit plane traveled upstream along the diffuser floor. Stall was also observed on one diverging wall. No stall however was found at Reynolds numbers beyond 5,400.

A two dimensional stall was observed at $Re = 3,500$ for $AS = 2.21$ as shown in Fig. 14. This stall was not bistable in nature and as the Reynolds number was increased stall disappeared as in all the previous cases.

CONCLUSIONS

Experiments were performed on plane wall diffusers with $N/W_1 = 18$ and $2\theta = 8^\circ$ for twelve different aspect ratios. Results of measurements of pressure recovery coefficient and flow regime behavior, revealed the following:

1. At constant aspect ratio, the pressure recovery coefficient, C_p , increased monotonically with Reynolds number for all aspect ratios tested. C_p increased rapidly in the Reynolds number range between 3,000 and 7,000. The increase was less rapid at Reynolds numbers above 10,000.

2. At constant Reynolds number, recovery first increased and then decreased with steadily increasing aspect ratio. The aspect ratio for optimum recovery decreased slightly as Reynolds numbers increased.
3. Flow regime changed with increasing Reynolds number. At low Re, jet flow was observed in some low aspect ratio diffusers, while a two dimensional stall pattern was exhibited in diffusers with $AS \geq 0.94$ up to $Re = 5,000$. Above $Re = 5,000$ none of the diffuser units tested exhibited stall.

REFERENCES

1. Reneau, L. R., Johnston, J. P. and Kline, S. J. (1964), "Performance and Design of Straight, Two-Dimensional Diffusers," Report PD-8, Thermosciences Division, Department of Mechanical Engineering, Stanford University, September 1964.
2. Sovran, G. and Klomp, E. D. (1967), "Experimentally Determined Optimum Geometries for Rectilinear Diffusers with Rectangular, Conical or Annular Cross-Section," in Fluid Mechanics of Internal Flows, G. Sovran, ed., Elsevier Publishing Co., New York, 1967, pp. 270-319.
3. Johnston, J. P. and Powars, C. A. (1967), "Effects of Aspect Ratio on the Performance of Straight Walled, Two-Dimensional Diffusers," Report PD-13, Thermosciences Division, Department of Mechanical Engineering, Stanford University, 1967.
4. Runstadler (Jr.), P. W. (1969), "Pressure Recovery Performance of Straight-Channel, Single-Plane Divergence Diffusers at High Mach Numbers," U.S. Army Aviation Material Laboratories, Fort Eustis, Virginia, Technical Report 69-56, 1969.
5. McMillan, O. J. and Johnston, J. P. (1970), "Performance of Low Aspect Ratio Diffusers with Fully Developed Turbulent Inlet Flows," Report PD-14, Thermosciences Division, Department of Mechanical Engineering, Stanford University, 1970.
6. Glaettli, H. H., Müller, H. R. and Zingg, R. H. (1964), "Remarks on the Limitations of Pure Fluid Elements," in Proceedings of the Fluid Amplification Symposium, Harry Diamond Laboratories, Washington, D.C., Vol. 1, pp. 217-232, 1964.

7. Comparin, R. A., Glaettli, H. H. and Mitchell, A. E. (1962), "On the Limitations and Special Effects in Fluid Jet Amplifiers," in Proceedings of the Symposium on Fluid Jet Control Devices, New York, American Society of Mechanical Engineers, November 1962.
8. Tamulis, J. C. (1967), "Sources of Signal Noise in Fluid Amplifiers," Ph.D. Thesis, Department of Mechanical Engineering, Pennsylvania State University, December 1967.
9. Drzewiecki, T. M., "The Interpretation of Surface Static Pressure Distributions in Fluid Amplifier Applications," U. S. Army Materiel Command, Harry Diamond Laboratories, Washington, D.C., NDL-TR-1627, July 1973.

LIST OF FIGURES

- Fig. 1 Photograph of Diffuser Unit Showing "Sandwich" Construction.
- Fig. 2 Schematic Layout of Experimental Setup.
- Fig. 3 Overall View of Test System.
- Fig. 4 Effect of Reynolds Number on Pressure Recovery Coefficient; $AS = 0.21$.
- Fig. 5 Effect of Reynolds Number on Pressure Recovery Coefficient; $AS = 0.63$.
- Fig. 6 Effect of Reynolds Number on Pressure Recovery Coefficient; $AS = 0.94$.
- Fig. 7 Effect of Reynolds Number on Pressure Recovery Coefficient; $AS = 1.37$.
- Fig. 8 Effect of Reynolds Number on Pressure Recovery Coefficient; $AS = 2.65$.
- Fig. 9 Influence of Aspect Ratio on Pressure Recovery Coefficient at Constant Reynolds Number.
- Fig. 10 Variation of Inlet Blocked Area Fraction, B_1 , with Reynolds Number at Constant Aspect Ratio.
- Fig. 11 Stall Pattern for $AS = 0.21$ at $Re = 3,760$.
- Fig. 12 Stall Pattern for $AS = 1.12$ at $Re = 2,200$.
- Fig. 13 Stall Pattern for $AS = 1.37$ at $Re = 2,440$.
- Fig. 14 Stall Pattern for $AS = 2.21$ at $Re = 3,550$.



Fig. 3 Dighe and McDonald

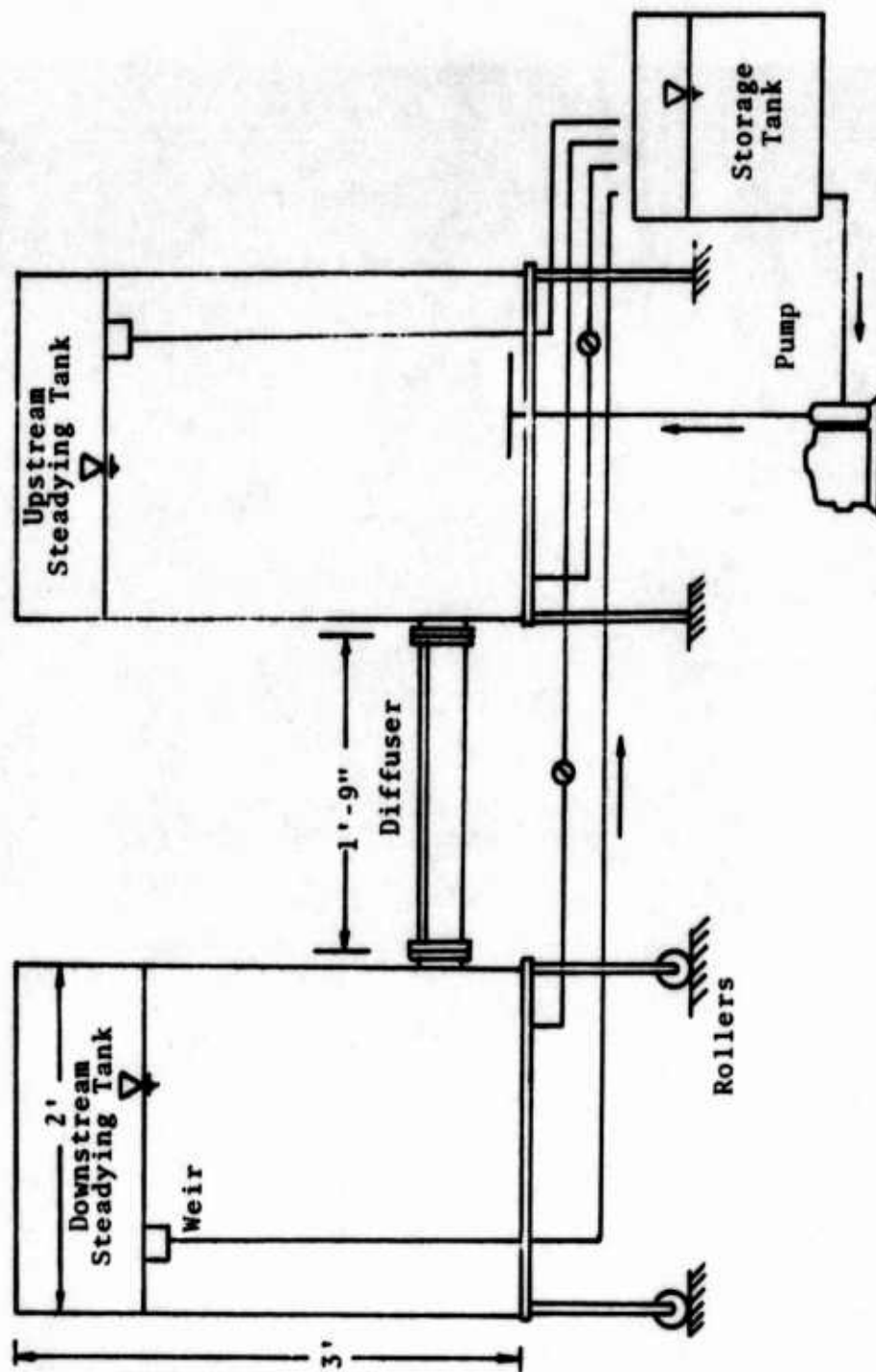


Fig. 2 Dighe and McDonald

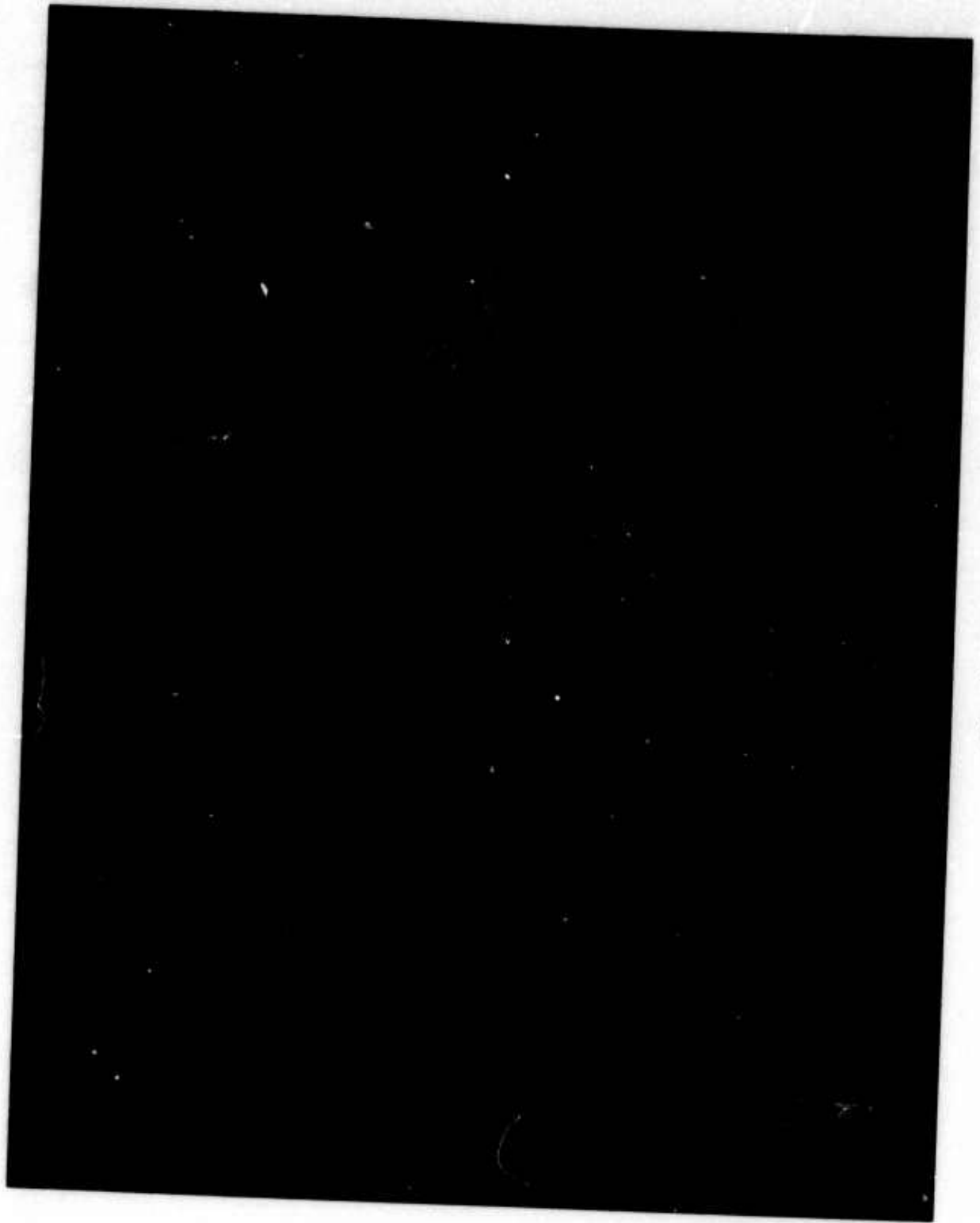


Fig. 1 Dighe and McDonald

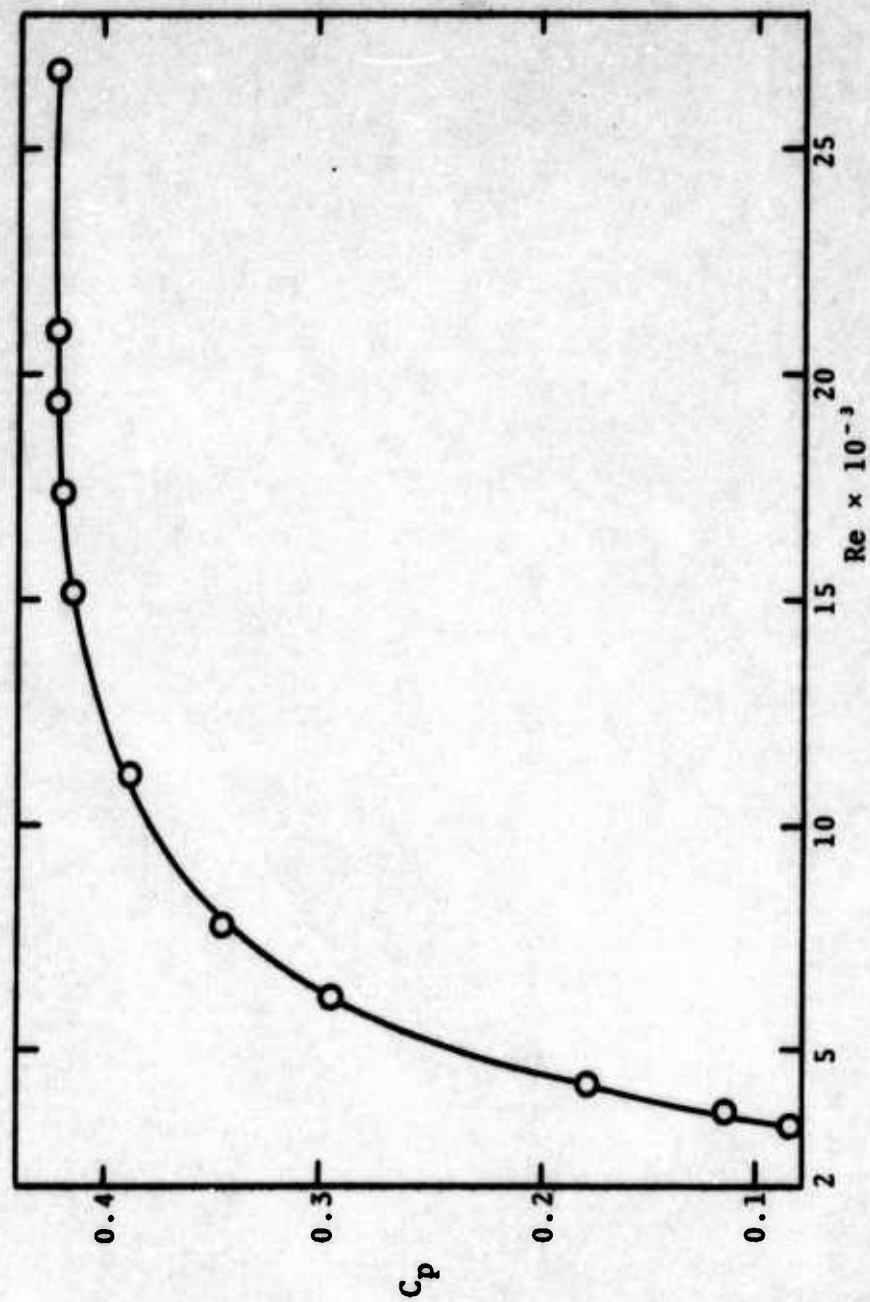


Fig. 4 Dighe and McDonald

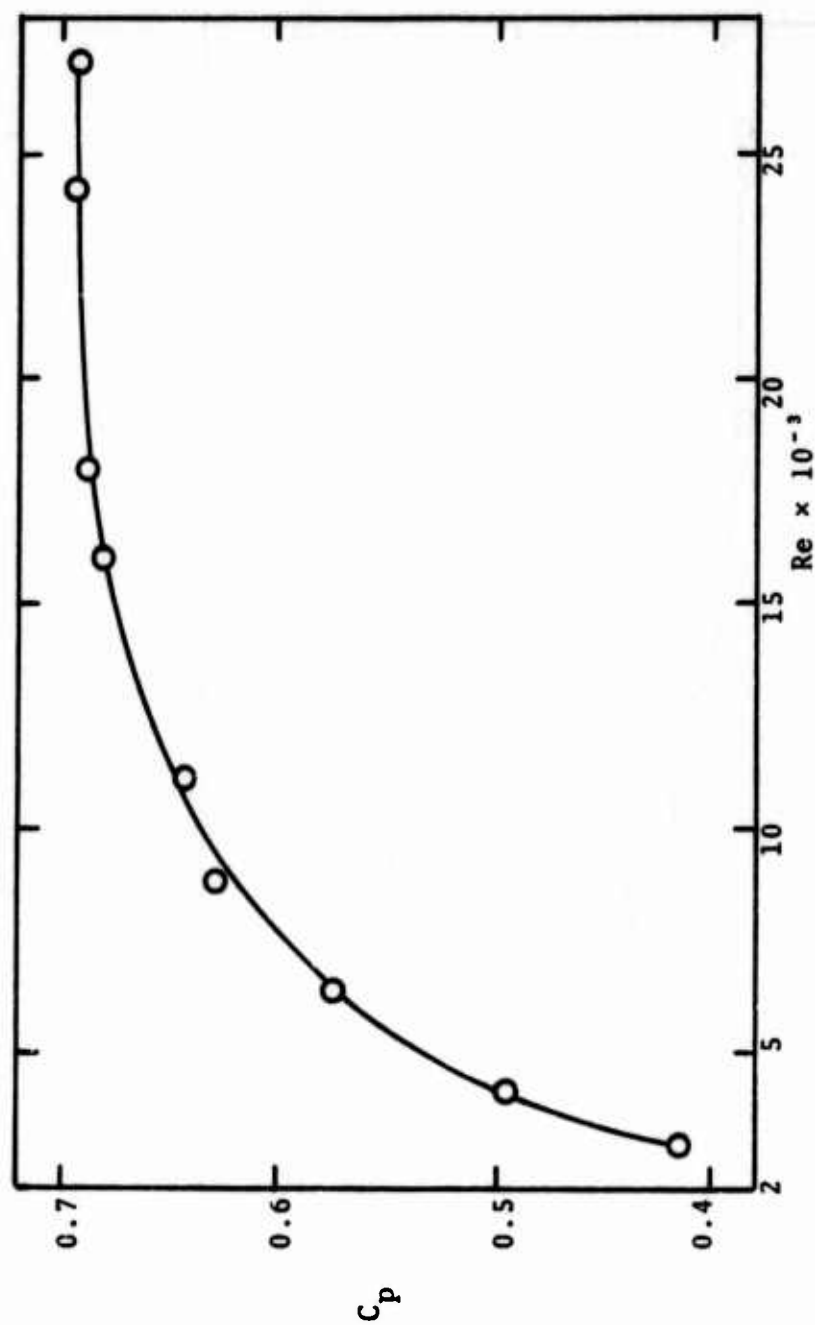


Fig. 5 Dighe and McDonald

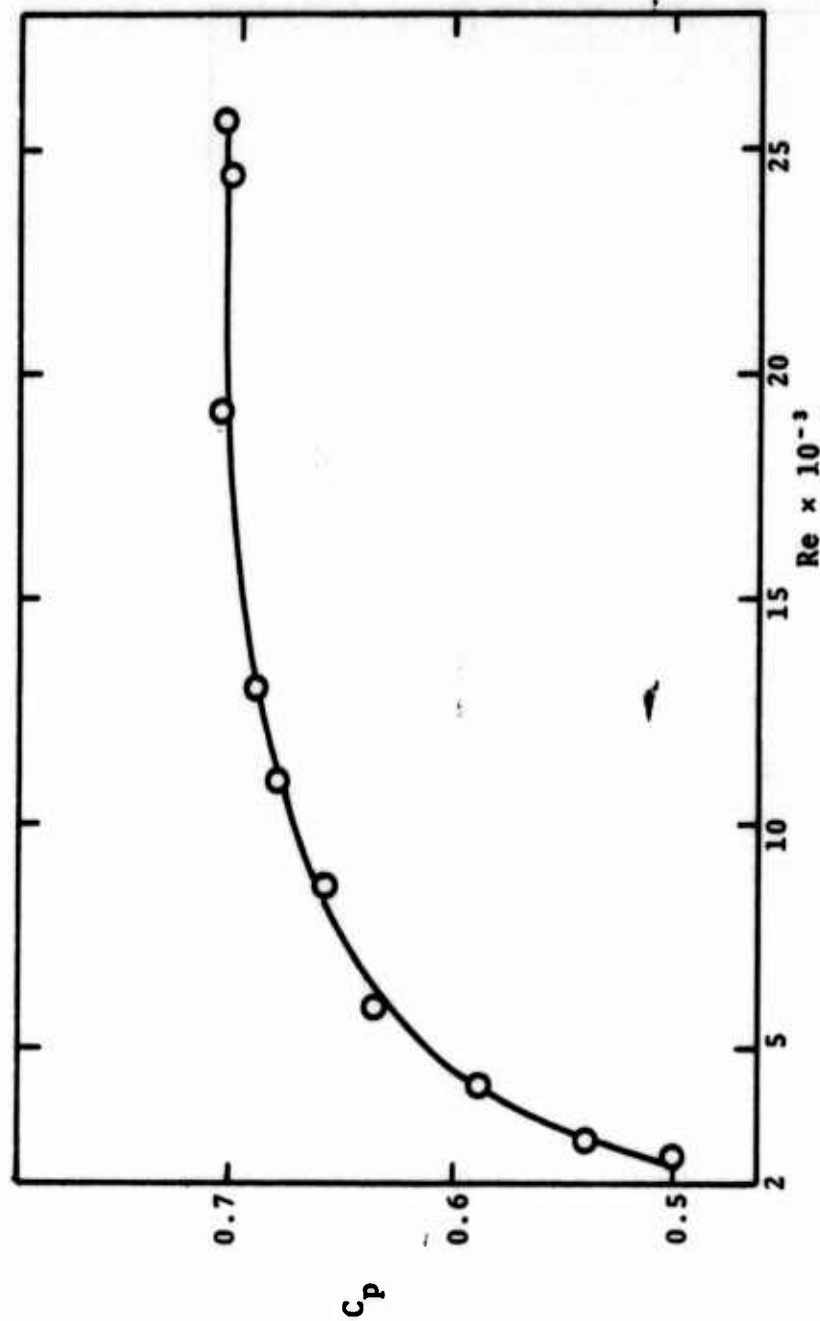


Fig. 6 Dighe and McDonald

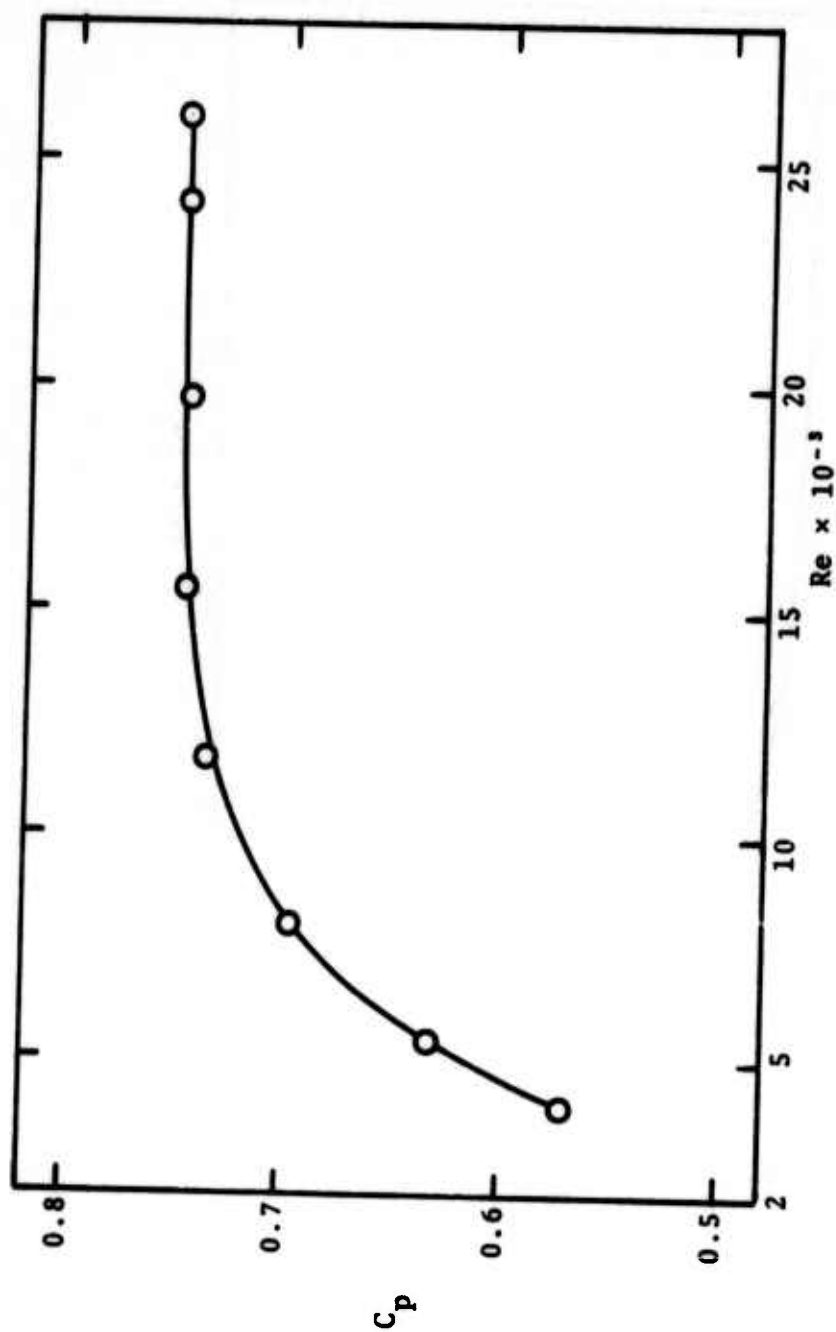


Fig. 7 Dighe and McDonald

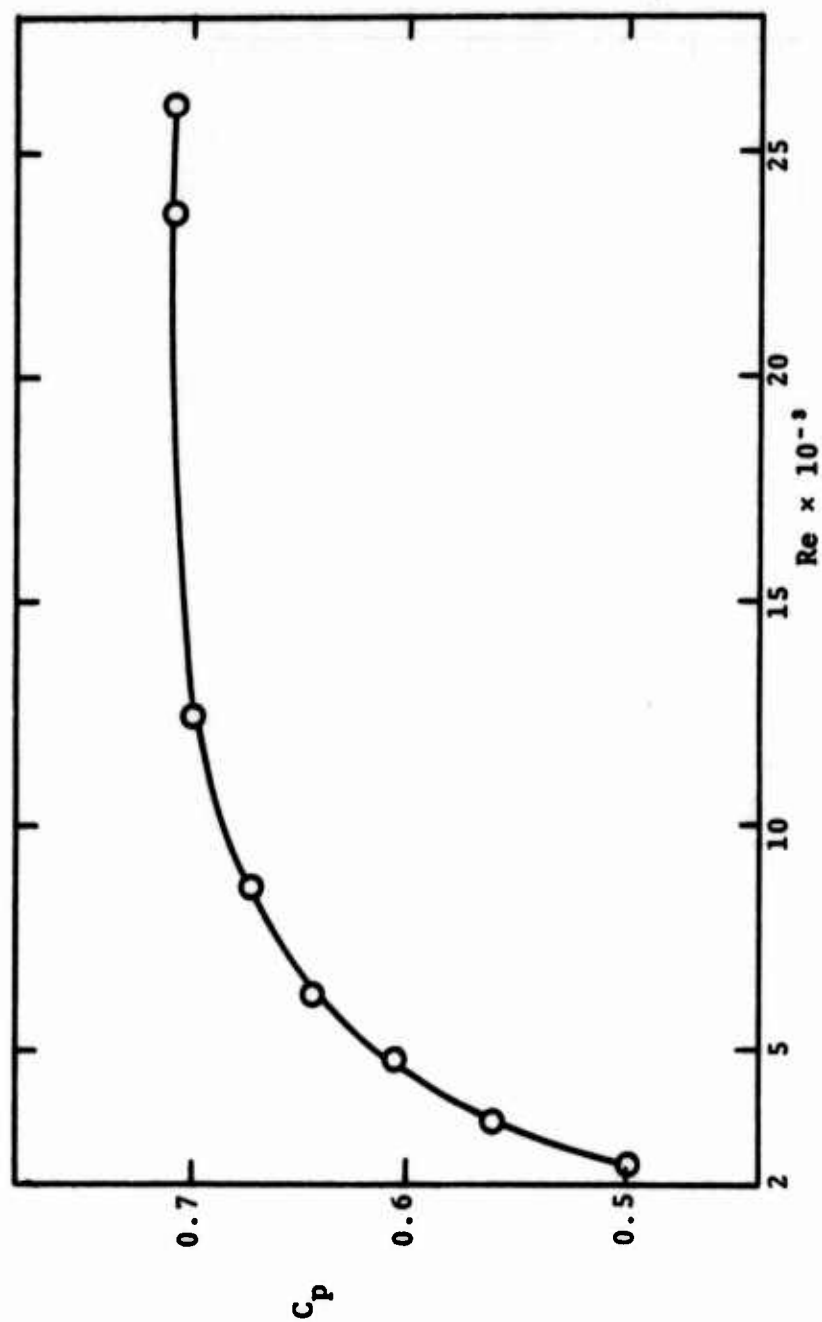


Fig. 8 Dighe and McDonald

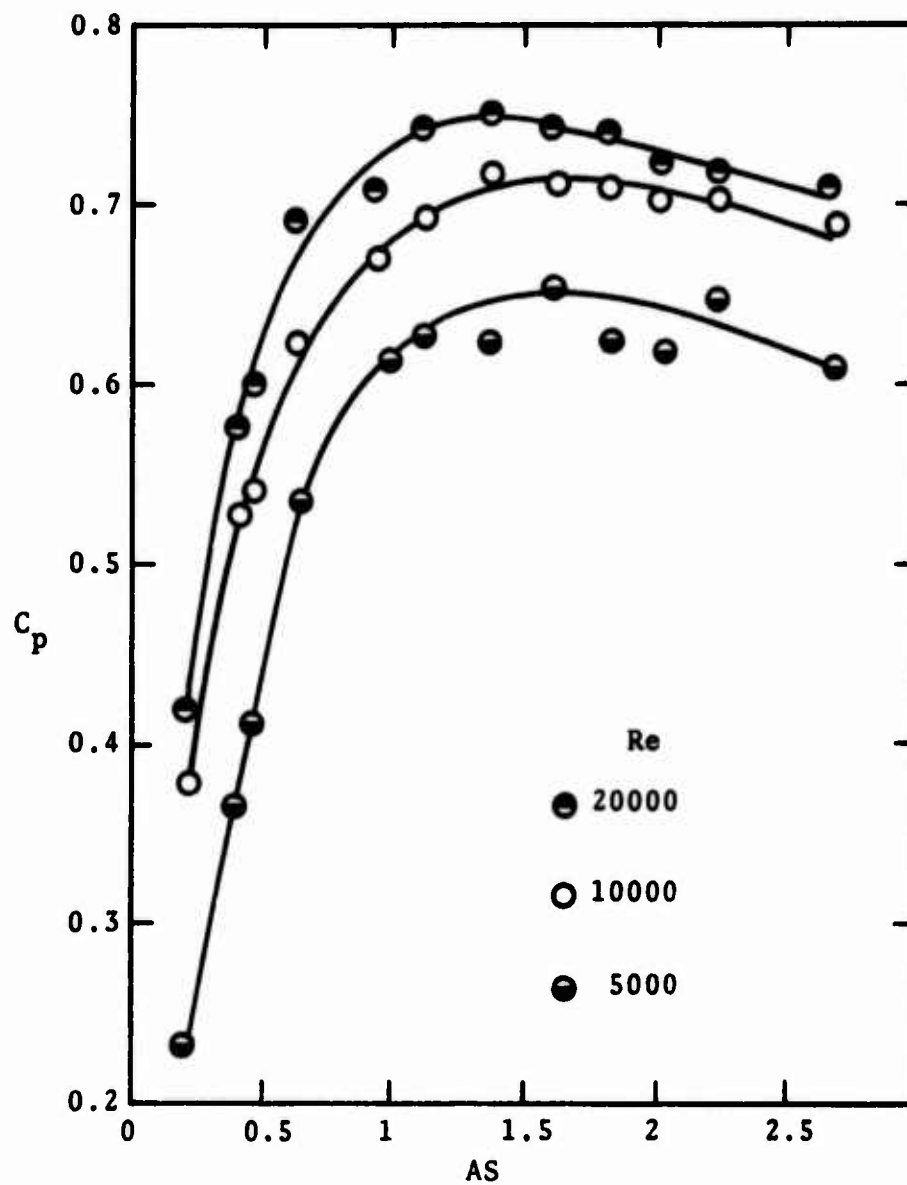


Fig. 9 Dighe and McDonald

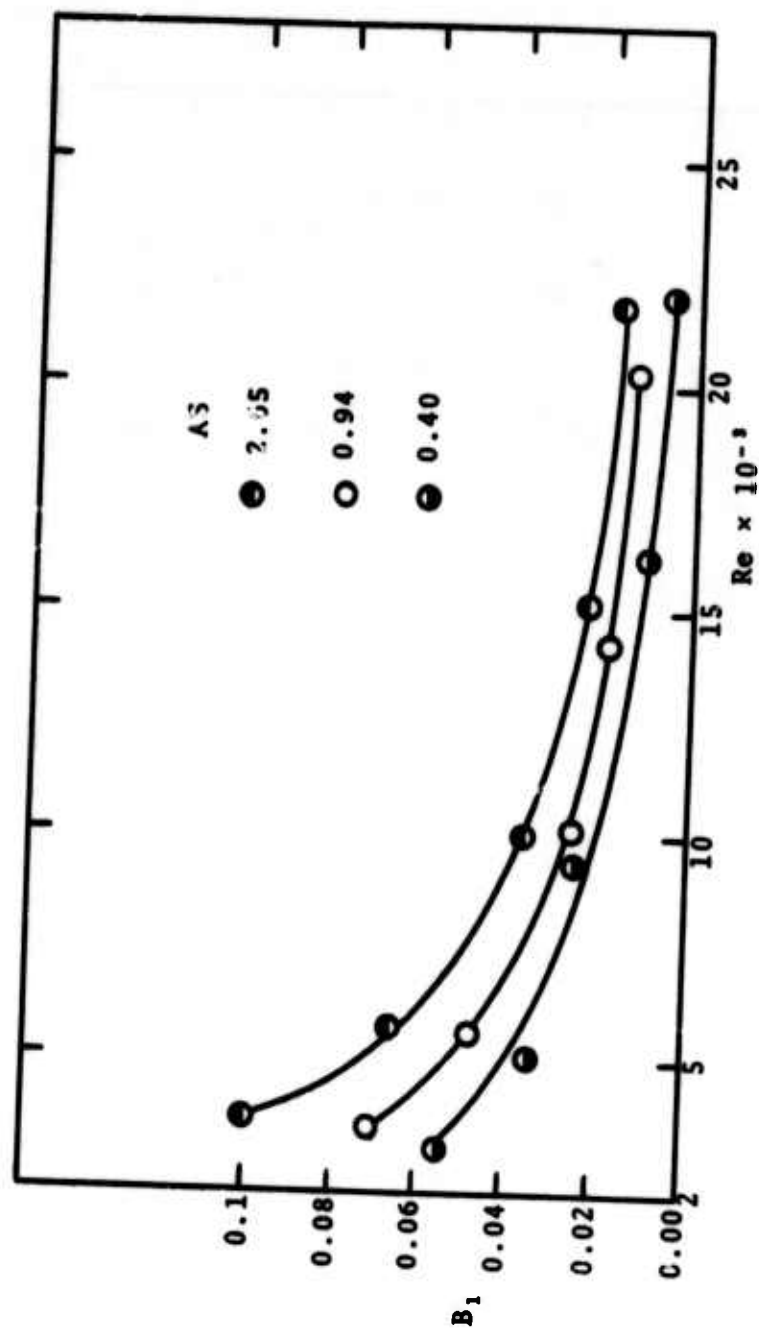
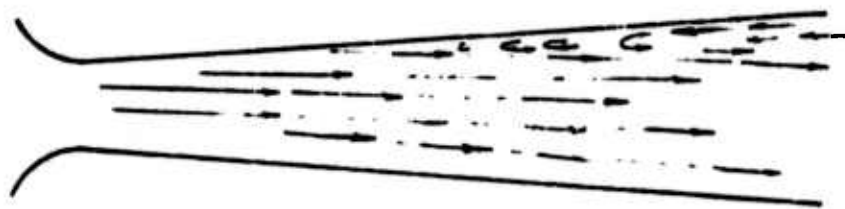
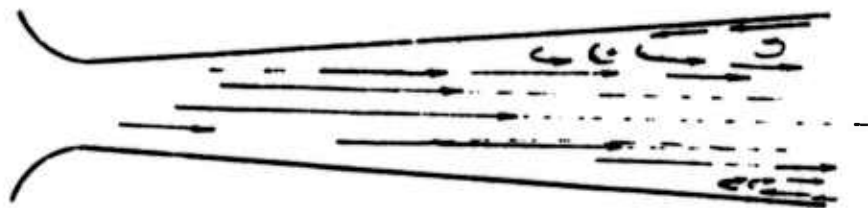
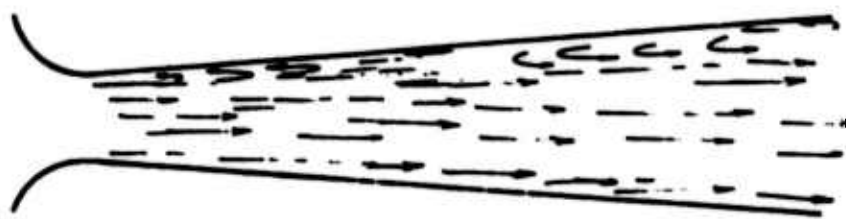
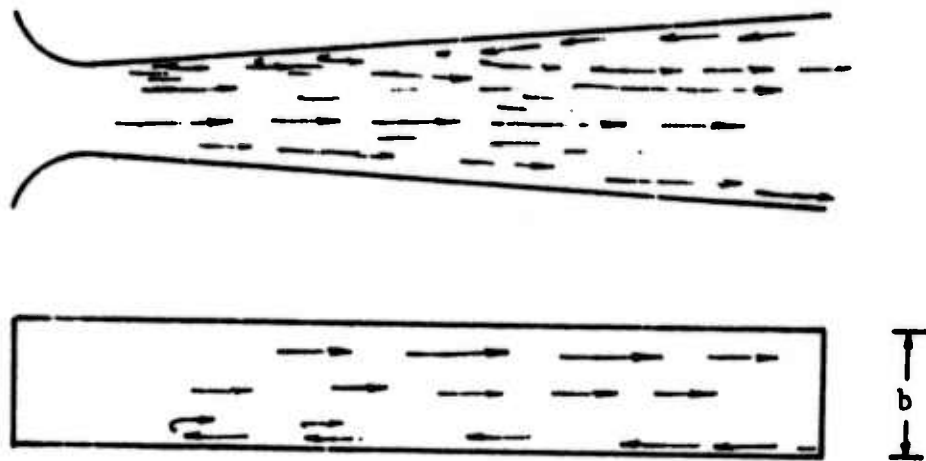


Fig. 10 Dighe and McDonald



Figs. 11 & 12 Dighe and McDonald



Figs. 13 & 14 Dighe and McDonald

HEAT AND MASS TRANSFER AS CONTROL PARAMETERS IN FLUIDIC CIRCUITS

by

Sui Lin
Assistant Professor
Department of Mechanical Engineering
Sir George Williams University
Montreal, Canada.

Abstract

An analytical study of the effect of heat and mass transfer on the flow properties of a gas stream flowing through a duct with constant cross-sectional area in both the subsonic and supersonic regions is reported. A relation of equivalence between the dimensionless heat and mass transfer which influence the dimensionless flow properties is established. The mass transfer has the same effect on the pressure ratio, between the down-and-up stream, as the heat transfer. In the subsonic region, the increase of heat or mass supplied to the flow causes the decrease of the pressure ratio. The increase of the withdrawal of heat or mass from the flow causes the increase of the pressure ratio. In the supersonic region, the effects are reversed.

1. Introduction

The transfer process consists of momentum, heat and mass transfer. In fluidic circuits, momentum transfer has been effectively utilized. However, the use of heat and mass transfer lags far behind that of momentum transfer. In the present work, an analytical study of the effect of heat and mass transfer on the flow properties of a gas stream through a duct with constant cross-sectional area is reported.

In general, one-dimensional compressible flows in ducts with variable cross-sectional areas may have chemical reaction, change of phase, transfer of heat, mass, and work, etc. Shapiro [1] described such a problem with differential equations and his end results were carried out numerically. Under certain simplifications, a one-dimensional compressible, isentropic flow with heat and mass transfer was treated by Lin [2] using integral equations to get approximate closed solutions. In this paper, a method similar to that in [2] is used. However, the friction loss in the duct is considered. The advantage of the method used is that from the closed solutions, a clear view of the effect of heat and mass transfer on flow properties can be obtained.

2. One-dimensional flow with heat and mass transfer

For calculating a one-dimensional compressible steady flow in a duct with constant cross-sectional area, and with heat and mass transfer, the following assumptions are made:

- (1) The heat and mass transferred to the stream in the duct are uniformly distributed over the whole cross-sectional area; the upstream state is kept constant during the heat and mass transfer into the stream.
- (2) The gases of the mainstream and of the supply are perfect gases with constant specific heats. To simplify the problem, it is assumed that the gas supplied is the same as that in the mainstream, or that the quantity of gas supplied, which is different from that in the mainstream, is small in comparison to that of the mainstream. The change in chemical composition can then be ignored.
- (3) There is no body force acting on the fluid and no change in elevation.

The system of governing equations for the flow in the duct between two sections can be expressed as follows:

-the continuity equation:

$$\rho_1 V_1 A + \int_{x_1}^{x_2} \dot{m}(x) dx = \rho_2 V_2 A, \quad (1)$$

-the momentum equation:

$$(p_1 + \rho_1 V_1^2) A - \int_s \tau_w ds = (p_2 + \rho_2 V_2^2) A, \quad (2)$$

-the energy equation:

$$\begin{aligned} \rho_1 V_1 A \left[c_p T_1 + \frac{V_1^2}{2} \right] + \left[c_p T_s + \frac{V_s^2}{2} \right] \int_{x_1}^{x_2} \dot{m}(x) dx \\ + \int_{x_1}^{x_2} \dot{q}(x) dx = \rho_2 V_2 A \left[c_p T_2 + \frac{V_2^2}{2} \right], \end{aligned} \quad (3)$$

-and the equation of state:

$$\frac{p_1}{\rho_1 T_1} = \frac{p_2}{\rho_2 T_2}, \quad (4)$$

where ρ is the density, V the velocity, A the cross-sectional area, x the axial coordinate of the duct, $\dot{m}(x)$ the mass transferred in the direction perpendicular to the x -coordinate per unit time and unit length, p the pressure, τ_w the shear stress at the duct wall, s the surface of the duct wall between the sections 1 and 2, c_p the specific heat at constant pressure, T the absolute temperature, and $\dot{q}(x)$ the heat supplied per unit time and unit length. The subscripts 1, 2 and s refer to the states at positions respectively upstream of, downstream of, and in the region where the heat and mass are being transferred. Due to

$$\tau_w = f \frac{\rho V^2}{2}, \quad (5)$$

the term of the shear stress in eq. (2) can be expressed as

$$\int_s \tau_w ds = \int_s f \frac{\rho V^2}{2} ds = \pi D \int_{x_1}^{x_2} f \frac{\rho V^2}{2} dx, \quad (6)$$

where f is the friction coefficient. By making use of an average value of $\frac{f \rho V^2}{2}$ the above integral term can then be integrated

$$\int_s \tau_w ds = \pi D (x_2 - x_1) \frac{\overline{f \rho V^2}}{2} = \frac{2(x_2 - x_1)A}{D} \overline{f \rho V^2}. \quad (7)$$

To obtain an explicit expression of the average value of $\overline{f \rho V^2}$, the following linear relationship is assumed:

$$\overline{f \rho V^2} = \bar{f}_{12} (\rho_1 V_1^2 + \beta \rho_2 V_2^2), \quad (8)$$

where \bar{f}_{12} and β are constants. Substituting eq. (8) into eq. (7) gives

$$\int_s \tau_w ds = A \alpha (\rho_1 V_1^2 + \beta \rho_2 V_2^2), \quad (9)$$

$$\text{where } \alpha = \frac{2(x_2 - x_1)\bar{f}_{12}}{D} \quad (10)$$

For the above approximation, it is understood that there is no shock wave taking place in the region between positions 1 and 2.

Introducing the following dimensionless variables

$$m = \frac{\int_{x_1}^{x_2} \dot{m}(x) dx}{\rho_1 V_1 A}, \quad (11)$$

$$q_o = \frac{\int_{x_1}^{x_2} \dot{q}(x) dx}{\rho_1 V_1 A \cdot c_p T_{01}}, \quad (12)$$

$$e_o = \frac{c_p T_s + v_s^2/2}{c_p T_{01}}, \quad (13)$$

$$\Gamma = (1 + m)^2 \frac{\rho_1}{\rho_2}, \quad (14)$$

$$\psi = (1 + m) \frac{v_2}{v_1}, \quad (15)$$

$$\theta = (1 + m)^2 \frac{T_2}{T_1}, \quad (16)$$

$$P = \frac{P_2}{P_1}, \quad (17)$$

and using the Mach number relationships

$$\frac{v_1^2}{c_p T_1} = (\kappa - 1) M_1^2, \quad (18)$$

$$\rho_1 v_1^2 = \kappa p_1 M_1^2, \quad (19)$$

$$\frac{T_{01}}{T_1} = \left(1 + \frac{\kappa - 1}{2} M_1^2\right), \quad (20)$$

where T_{01} is the stagnation temperature of state 1, and κ the ratio of the specific heats, the system of equations (1) to (4) becomes

$$\Gamma = \psi, \quad (21)$$

$$\frac{1}{\kappa M_1^2} + (1 - \alpha) = \frac{1}{\kappa M_1^2} P + (1 + \alpha\beta) \frac{\psi^2}{\Gamma}, \quad (22)$$

$$(1 + \frac{\kappa-1}{2} M_1^2)(1 + me_o + q_o) = \frac{1}{(1+m)} (\theta + \frac{\kappa-1}{2} M_1^2 \psi^2), \quad (23)$$

$$P = \frac{\theta}{\Gamma}. \quad (24)$$

This system of equations can be solved as follows:

$$\Gamma = \frac{1 + (1-\alpha)\kappa M_1^2}{2(\frac{\kappa+1}{2} + \alpha\beta\kappa)M_1^2} \left[1 \pm \sqrt{1 - \frac{1+E}{1 + E_{\max}}} \right], \quad (25)$$

$$\psi = \Gamma, \quad (26)$$

$$P = 1 + \kappa M_1^2 [(1-\alpha) - (1+\alpha\beta)\Gamma], \quad (27)$$

$$\theta = P\Gamma, \quad (28)$$

$$\text{and } \frac{M_2^2}{M_1^2} = \frac{\Gamma}{P}, \quad (29)$$

$$\text{where } E = (1+m)(1 + me_o + q_o) - 1, \quad (30)$$

$$\text{and } E_{\max} = \frac{[1+(1-\alpha)\kappa M_1^2]^2}{4(\frac{\kappa+1}{2} + \alpha\beta\kappa)M_1^2(1 + \frac{\kappa-1}{2} M_1^2)} - 1. \quad (31)$$

The above solutions indicate that the heat and mass transfer are combined in a single energy term E in eq. (30), which is denoted hereafter as the total energy.

3. Determination of the constant β

The heat and mass transferred to the mainstream always act to move the Mach number at the downstream position, M_2 , towards unity,

irrespective of whether the flow is subsonic or supersonic. Therefore, it is expected that M_2 will be equal to one, when the total energy reaches its maximum value, which is called the critical total energy.

From eq. (25), it is evident that E_{\max} is the maximum amount of total energy that can be added to the flow since imaginary results are obtained for $E > E_{\max}$. For such a case, $E = E_{\max}$, M_2 can be calculated from eq. (29) as follows:

$$M_{2,E_{\max}}^2 = \frac{1}{1 + \alpha\beta\kappa} . \quad (32)$$

Because M_2 must satisfy the above requirement,

$$M_{2,E_{\max}} = 1 , \quad (33)$$

hence, the value of β must be:

$$\beta = 0 . \quad (34)$$

Therefore, the solutions of the problem, eqs. (25) to (31), become

$$\Gamma = \frac{1 + (1-\alpha)\kappa M_1^2}{(\kappa+1) M_1^2} \left[1 \pm \sqrt{1 - \frac{1+E}{1+E_{\max}}} \right] , \quad (35)$$

$$\psi = \Gamma , \quad (36)$$

$$P = 1 + \kappa M_1^2 [(1-\alpha) - \Gamma] , \quad (37)$$

$$\theta = P\Gamma , \quad (38)$$

$$\frac{M_2^2}{M_1^2} = \frac{\Gamma}{P} , \quad (39)$$

$$E = (1+m)(1+me_0+q_0) - 1 , \quad (40)$$

$$E_{\max} = \frac{[1 + (1-\alpha)\kappa M_1^2]^2}{2(\kappa+1)M_1^2(1+\frac{\kappa-1}{2} M_1^2)} - 1 . \quad (41)$$

4. Equivalence between the heat and mass transfer

$$\text{Let } Q = me_o + q_o \quad (42)$$

be the dimensionless total heat transferred to the mainstream. Then the total energy can be expressed as

$$E = (1 + m)(1 + Q). \quad (43)$$

From this equation, it is obvious that the effect produced by the mass transfer, m , on the dimensionless flow properties (Γ , ψ , P , θ and M_2) is the same as that produced by the total heat transfer, Q . However, in the real case, the mass transfer has other functions which directly influence the ratios of density, velocity, and temperature, but do not influence the ratio of the pressure, as indicated in eqs. (14) to (17).

5. Discussion of the value of α

In eqs. (35) to (41), the value of α , which is defined by eq. (10), is unknown because the mean value of the friction coefficient, \bar{f}_{12} , between the sections 1 and 2 is unknown. In general, the value of \bar{f}_{12} has to be determined experimentally. However, if the quantity of heat or mass transferred to or from the control circuit is relatively small in comparison with the total enthalpy or mass of the mainstream, respectively, then the effect of the heat or mass transfer on the friction coefficient can be neglected. For such a case, the mean value of the friction coefficient can be determined by Shapiro's work [1].

For the purpose of discussion of the effect of the heat and mass transfer on the flow properties downstream, a fixed value of 0.1 will be assigned to α .

6. Critical total energy

From eq. (35), it is seen that E_{\max} is the maximum amount of the total energy that can be transferred to the flow since imaginary results are obtained for $E > E_{\max}$. In Figs. 1 and 2, E_{\max} is plotted as a function of M_1 in the subsonic and supersonic regions for $\kappa = 1.4$ and $\alpha = 0.1$. In the region $0.675 < M_1 < 1.866$, the Mach number at section 2 has already reached sonic velocity due to the friction effect. Therefore, no energy is allowed to supply the flow in this region. It is also seen that there is no limitation of E_{\max} when M_1 approaches zero. However, when M_1 approaches infinity, there exists an asymptote as follows:

$$(E_{\max})_{M_1 \rightarrow \infty} = \frac{(1-\alpha)^2 \kappa^2}{(\kappa^2 - 1)} - 1 \quad (44)$$

7. Change in properties

Because of the approximation used in eq. (9), a shock wave relationship should be excluded. Therefore, only the minus sign in eq. (35) can be used. Figs. 3 to 10 show the effect on the flow properties of the total energy transferred to the flow in both the subsonic and supersonic regions. The following table summarizes the relationship for increasing the total energy supplied:

	In subsonic flow $M_1 < 1$	In supersonic flow $M_1 > 1$
Γ	increase	decrease
ψ	increase	decrease
P	decrease	increase
θ	increase	increase
M_2	increase	decrease

Figs. 11 to 18 show the effect on the flow properties of the withdrawal of the total energy. The following table also summarizes the relationship for increasing the withdrawal of the total energy:

	In subsonic flow $M_1 < 1$	In supersonic flow $M_1 > 1$
Γ	decrease	increase
ψ	decrease	increase
P	increase	decrease
θ	decrease	decrease
M_2	decrease	increase

For increasing the withdrawal of the total energy, there exists a limitation because the mass flow rate and the stagnation enthalpy carried by the mass flow rate are limited. Therefore, Γ and θ in Figs. 11 and 13, respectively, in the subsonic region, and P and θ in Figs. 16 and 17 in the supersonic region, do not reach to the zero point.

8. Control in Fluidic Circuits

The effect of heat and mass transfer on the pressure of the flow is a major interest in the control of fluidic circuits. From the definition, eq. (17), the dimensionless parameter P does not include the parameter m . Therefore, the effect produced by the mass transferred, m , on the parameter P is exactly the same as that produced by the total heat transferred, Q . In the subsonic region, the increase of heat or mass supplied to the flow causes the decrease of the parameter P . However, the increase of the withdrawal of heat or mass from the flow causes the increase of the parameter P . In the supersonic region, the effects are reversed.

9. Conclusions

Heat and mass transfer as control parameters in fluidic circuits are analyzed. The relation of equivalence between the dimensionless heat and mass transfer which influence the dimensionless flow properties is established. The mass transfer, m , has exactly the same effect on the pressure ratio between sections 2 and 1 as the heat transfer, Q . In the subsonic region, the increase of heat or mass transferred to the flow causes the decrease of the pressure ratio P . The increase of heat or mass transferred from the flow causes the increase of the pressure ratio P . In the supersonic region, the effects are reversed.

Acknowledgement

This work was supported by the National Research Council of Canada under Grant no. A7929.

References

1. Shapiro, A.H. "The dynamics and thermodynamics of compressible fluid flow", The Ronald Press Co., New York, 1953, Vol. 1, Chapters 6, 7 and 8.
2. Lin, S. "One-dimensional compressible flow with supply of heat and mass", Proceedings of Symposium on Internal Flows, Ottawa, October 29, 1971, sponsored by NRC.

List of Symbols

A	cross-sectional area
c_p	specific heat at constant pressure
D	diameter

List of symbols (cont'd)

e_0	dimensionless total enthalpy per unit mass transferred defined in eq. (13)
E	total energy defined in eq. (40)
E_{\max}	maximum total energy defined in eq. (41)
f	friction coefficient
\bar{f}_{12}	mean value of the friction coefficient between x_1 and x_2
m	dimensionless mass transfer defined in eq. (11)
$\dot{m}(x)$	mass transfer per unit time and unit length
M	Mach number
p	pressure
P	dimensionless pressure defined in eq. (17)
$\dot{q}(x)$	heat transfer per unit time and unit length
q_0	dimensionless heat transfer defined in eq. (12)
Q	dimensionless total heat transferred defined in eq. (42)
s	surface at the duct wall
T	temperature
V	velocity
x	axial coordinate
α	constant defined in eq. (10)
β	constant
Γ	dimensionless density defined in eq. (14)
θ	dimensionless temperature defined in eq. (16)
κ	ratio of specific heats
ρ	density
τ_w	shear stress at duct wall
ψ	dimensionless velocity defined in eq. (15)

Subscripts

- 1, 2, s referring to the states at positions respectively upstream of, downstream of, and in the region where heat and mass are being transferred
- 0 referring to stagnation state

Fig. 1: Maximum total energy as a function of upstream Mach number in subsonic flow for $\alpha = 0.1$ and $\kappa = 1.4$.

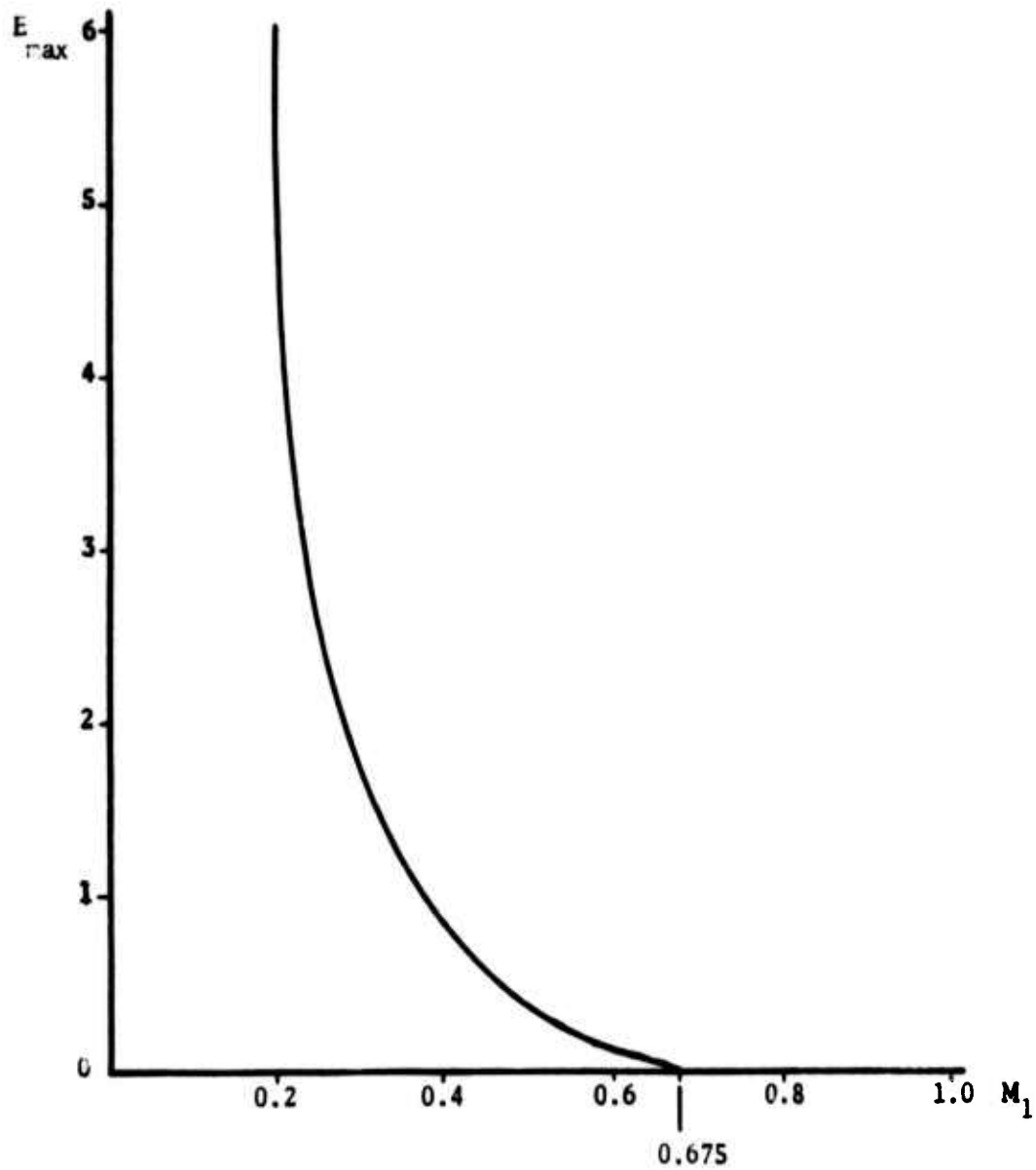


Fig. 2: Maximum total energy as a function of upstream Mach number in supersonic flow for $\alpha = 0.1$ and $\kappa = 1.4$.

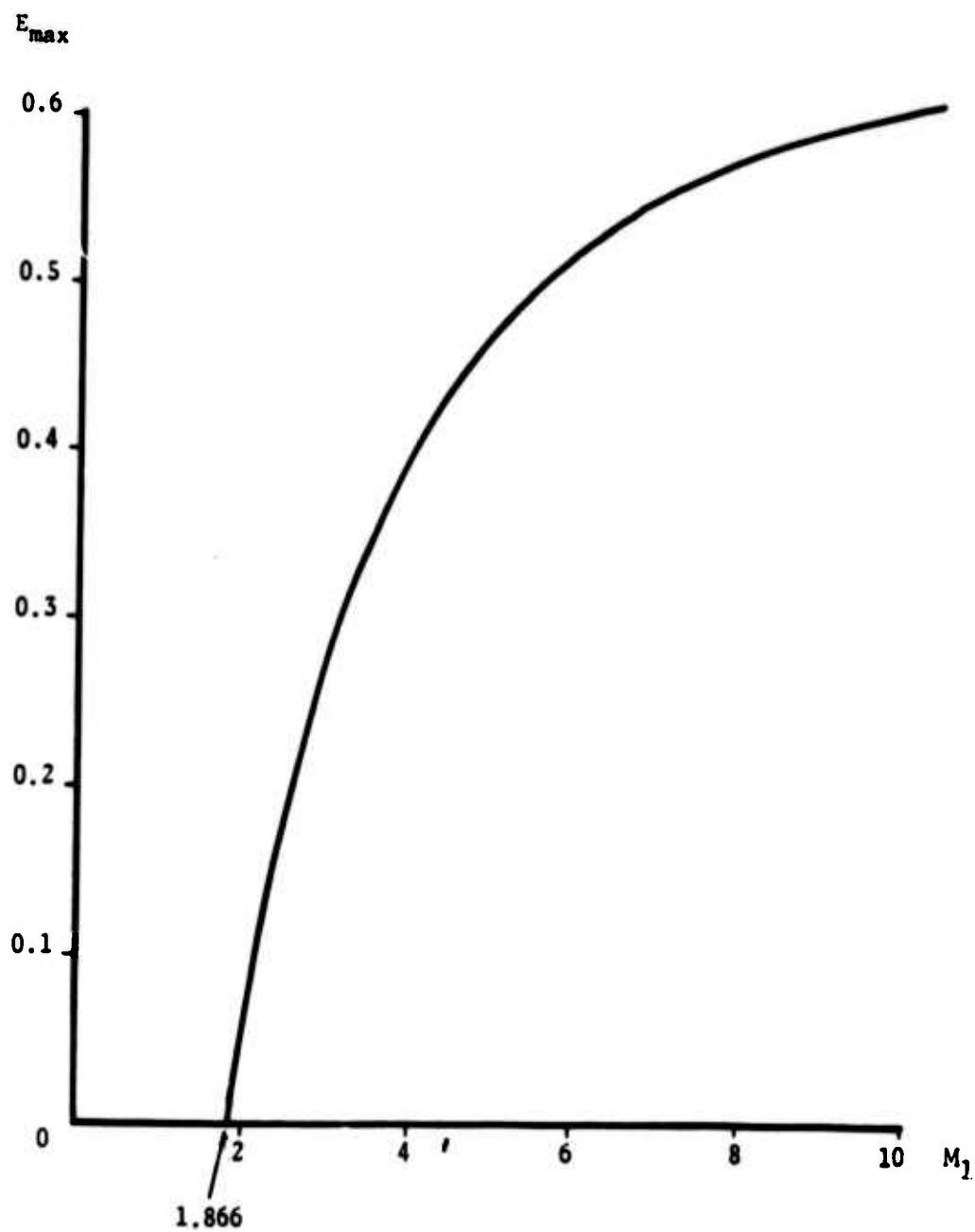


Fig. 3: Dimensionless density as a function of upstream Mach number in subsonic flow with positive E/E_{\max} as parameter for $\alpha = 0.1$ and $\kappa = 1.4$.

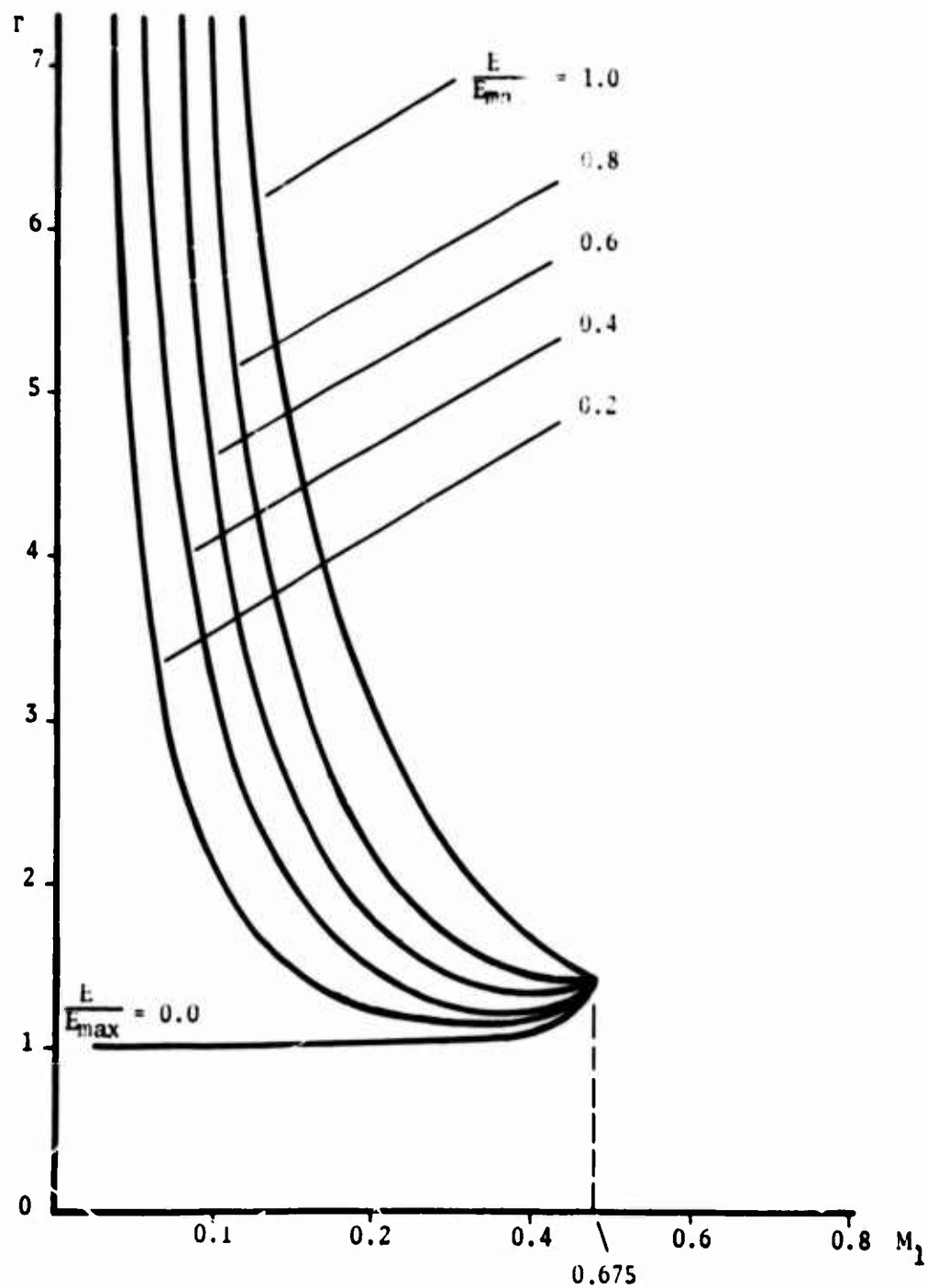


Fig. 4: Dimensionless pressure as a function of upstream Mach number in subsonic flow with positive E/E_{\max} as parameter for $\alpha = 0.1$ and $\kappa = 1.4$.

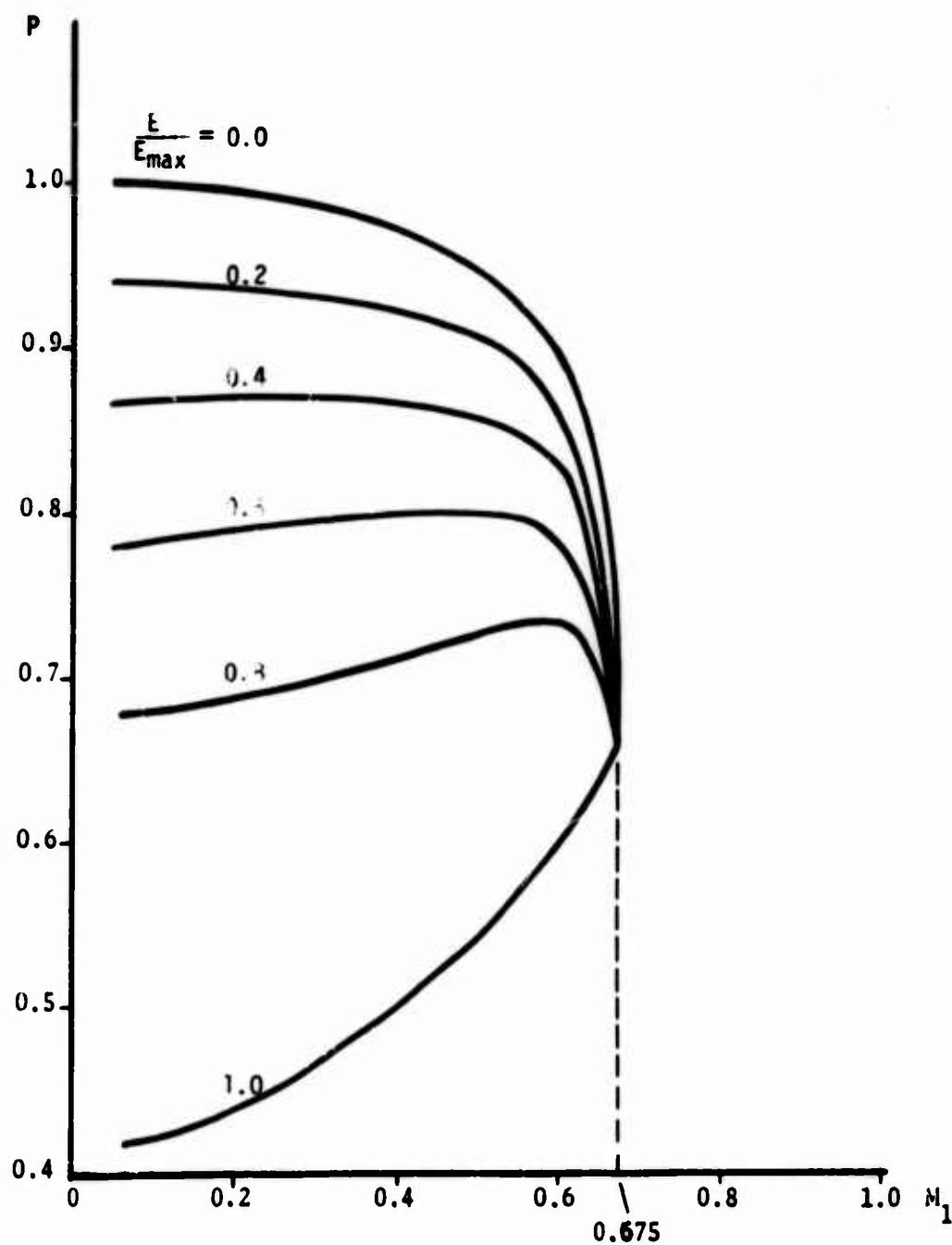


Fig. 5: Dimensionless temperature as a function of upstream Mach number in subsonic flow with positive E/E_{\max} as parameter for $\alpha = 0.1$ and $\kappa = 1.4$.

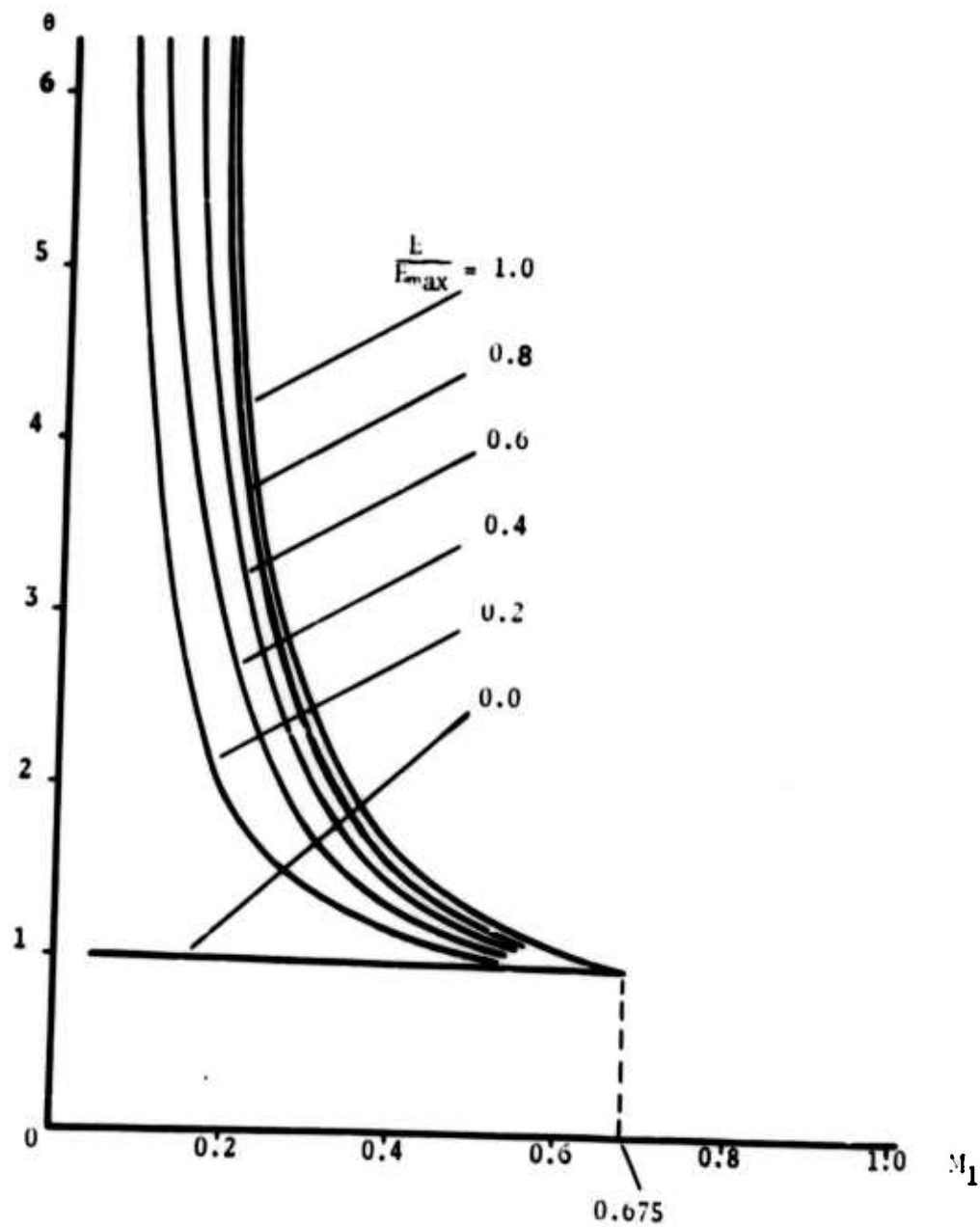


Fig. 6: Downstream Mach number as a function of upstream Mach number in subsonic flow with positive E/E_{\max} as parameter for $\alpha = 0.1$ and $\kappa = 1.4$.

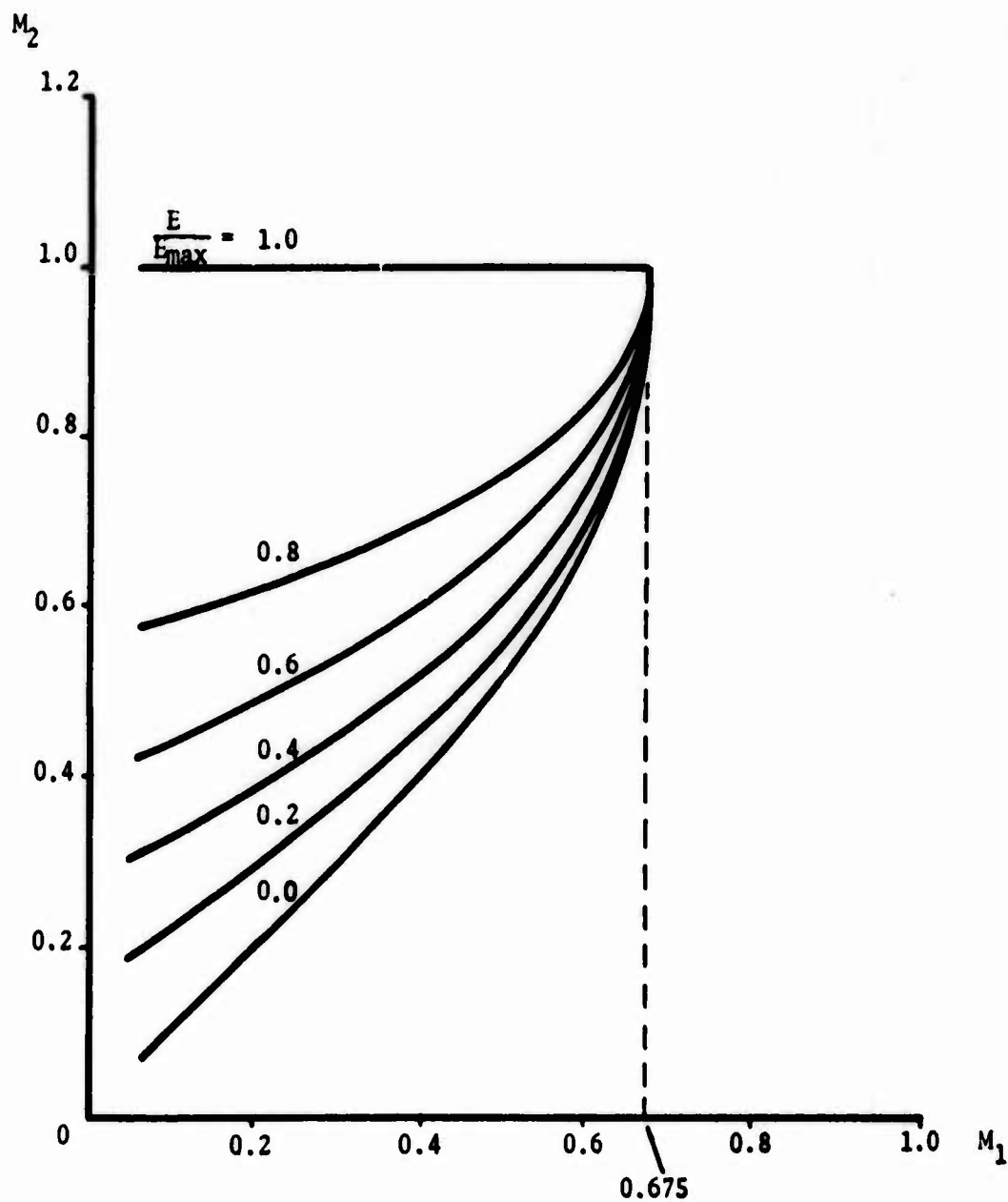


Fig. 7: Dimensionless density as a function of upstream Mach number in supersonic flow with positive E/E_{\max} as parameter for $\alpha = 0.1$ and $\kappa = 1.4$.

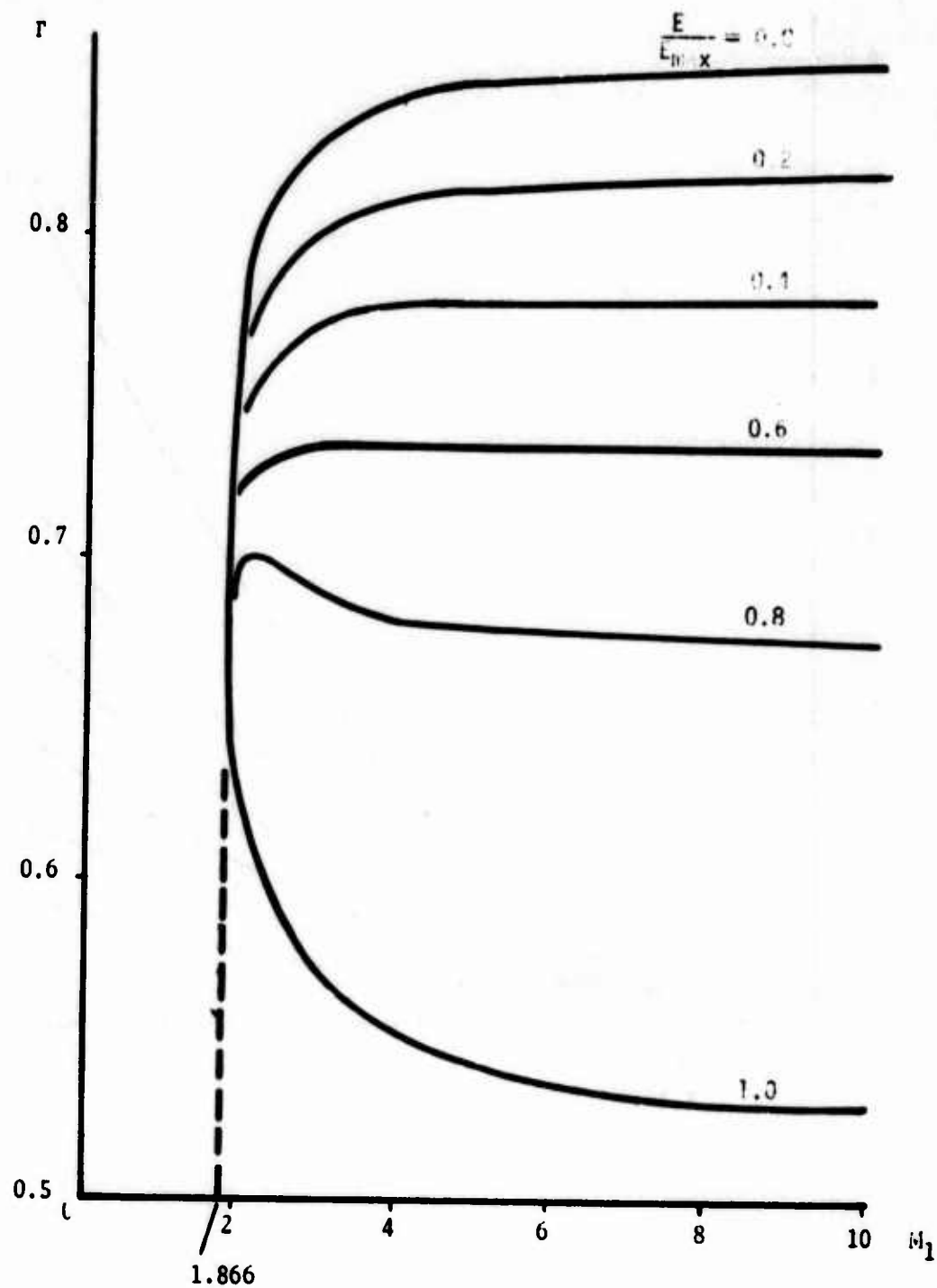


Fig. 8: Dimensionless pressure as a function of upstream Mach number in supersonic flow with positive E/E_{\max} as parameter for $\alpha = 0.1$ and $\kappa = 1.4$.

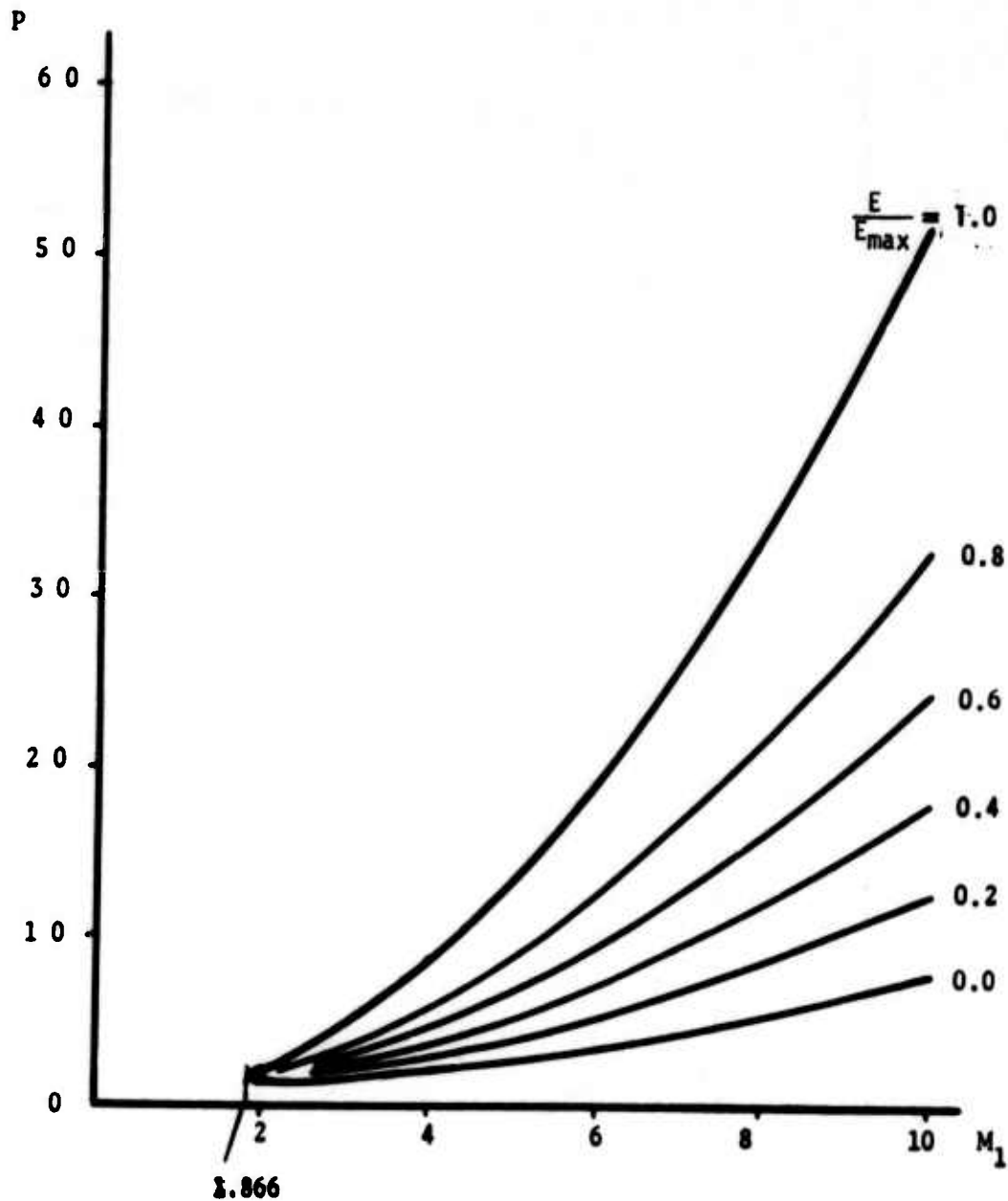


Fig. 9: Dimensionless temperature as a function of upstream Mach number in supersonic flow with positive E/E_{\max} as parameter for $\alpha = 0.1$ and $\kappa = 1.4$.

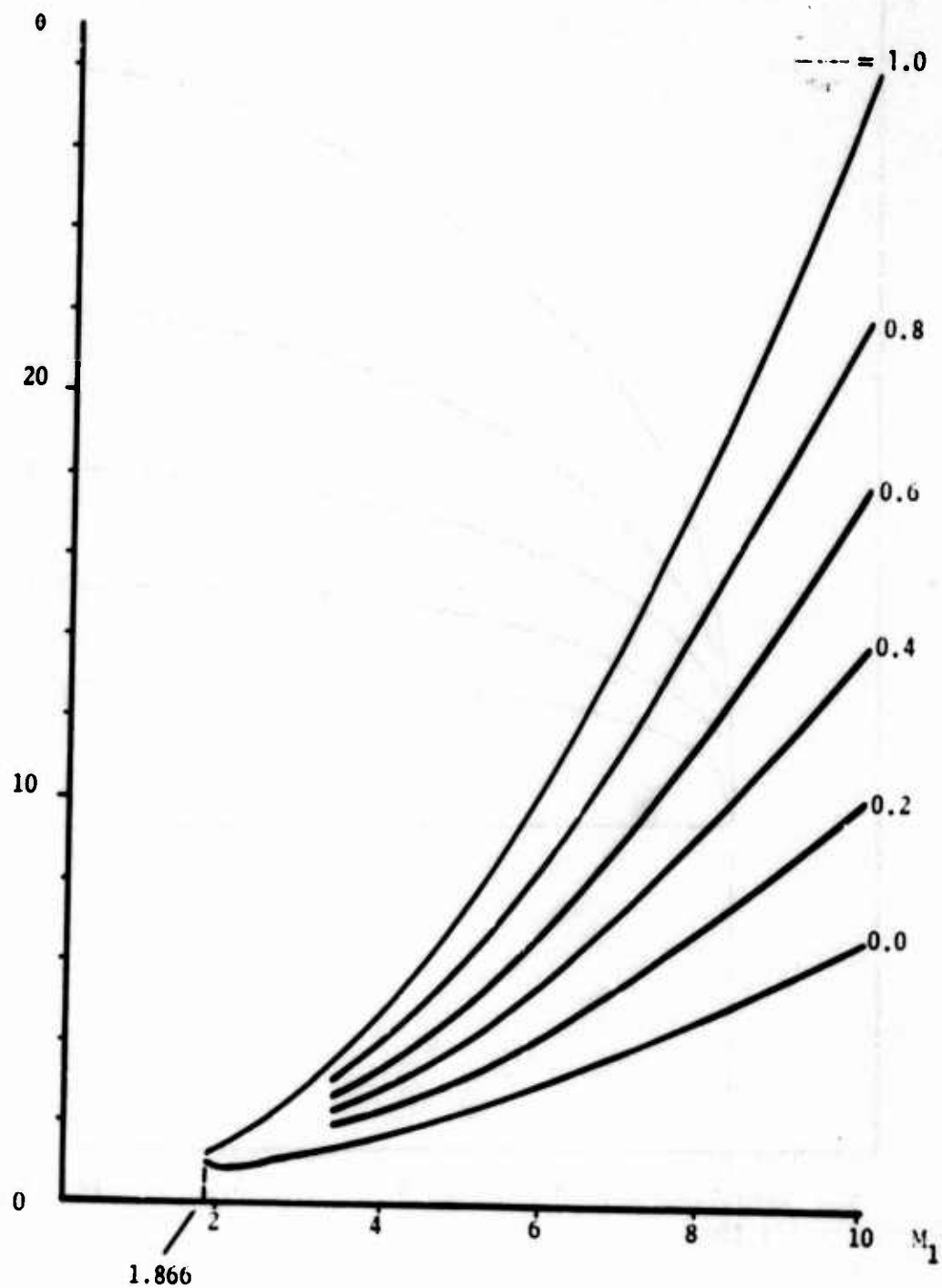


Fig.10: Downstream Mach number as a function of upstream Mach number in supersonic flow with positive E/E_{\max} as parameter for $\alpha = 0.1$ and $\kappa = 1.4$.

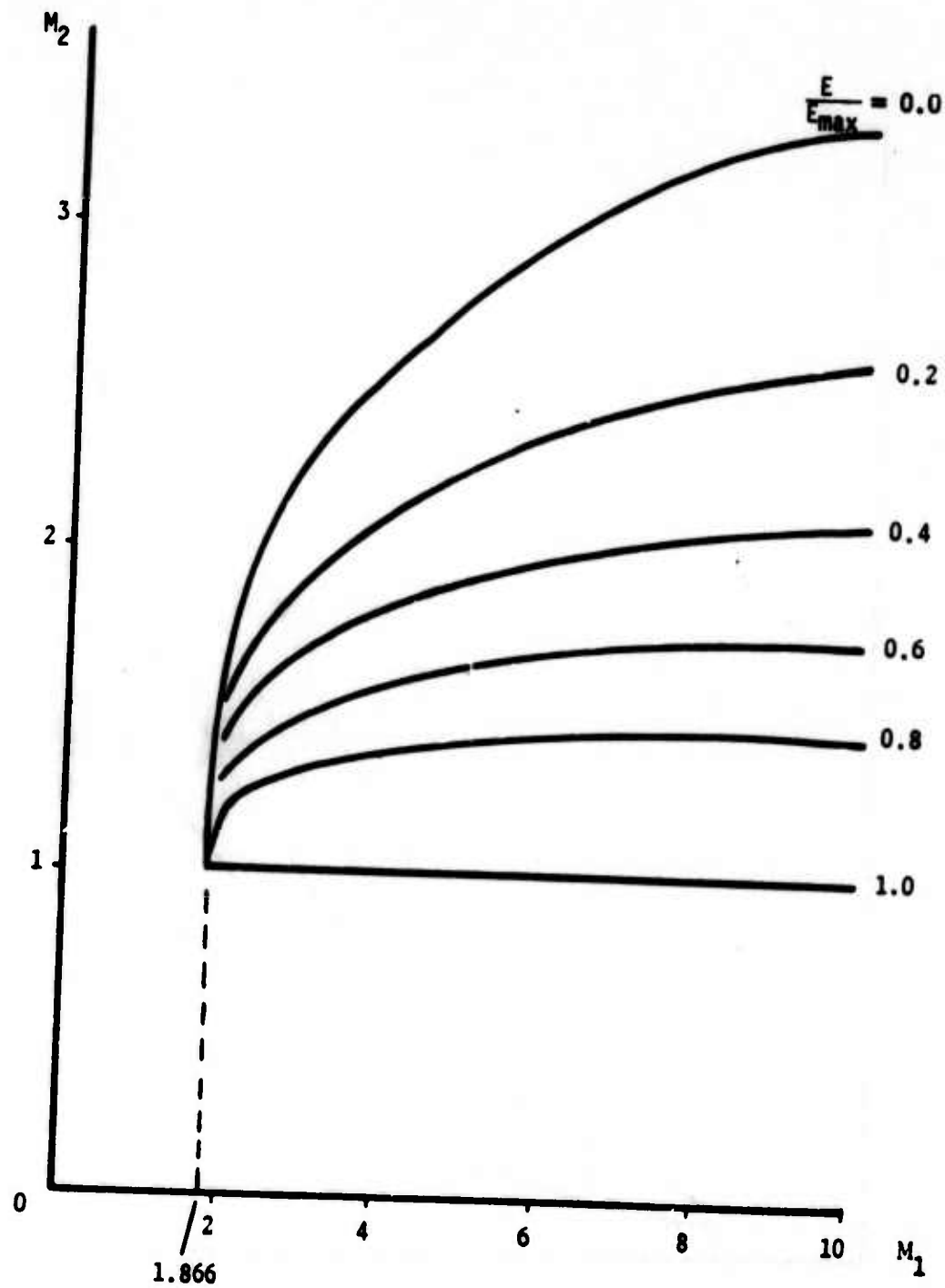


Fig.11: Dimensionless density as a function of upstream Mach number in subsonic flow with negative E/E_{\max} as parameter for $\alpha = 0.1$ and $\kappa = 1.4$.

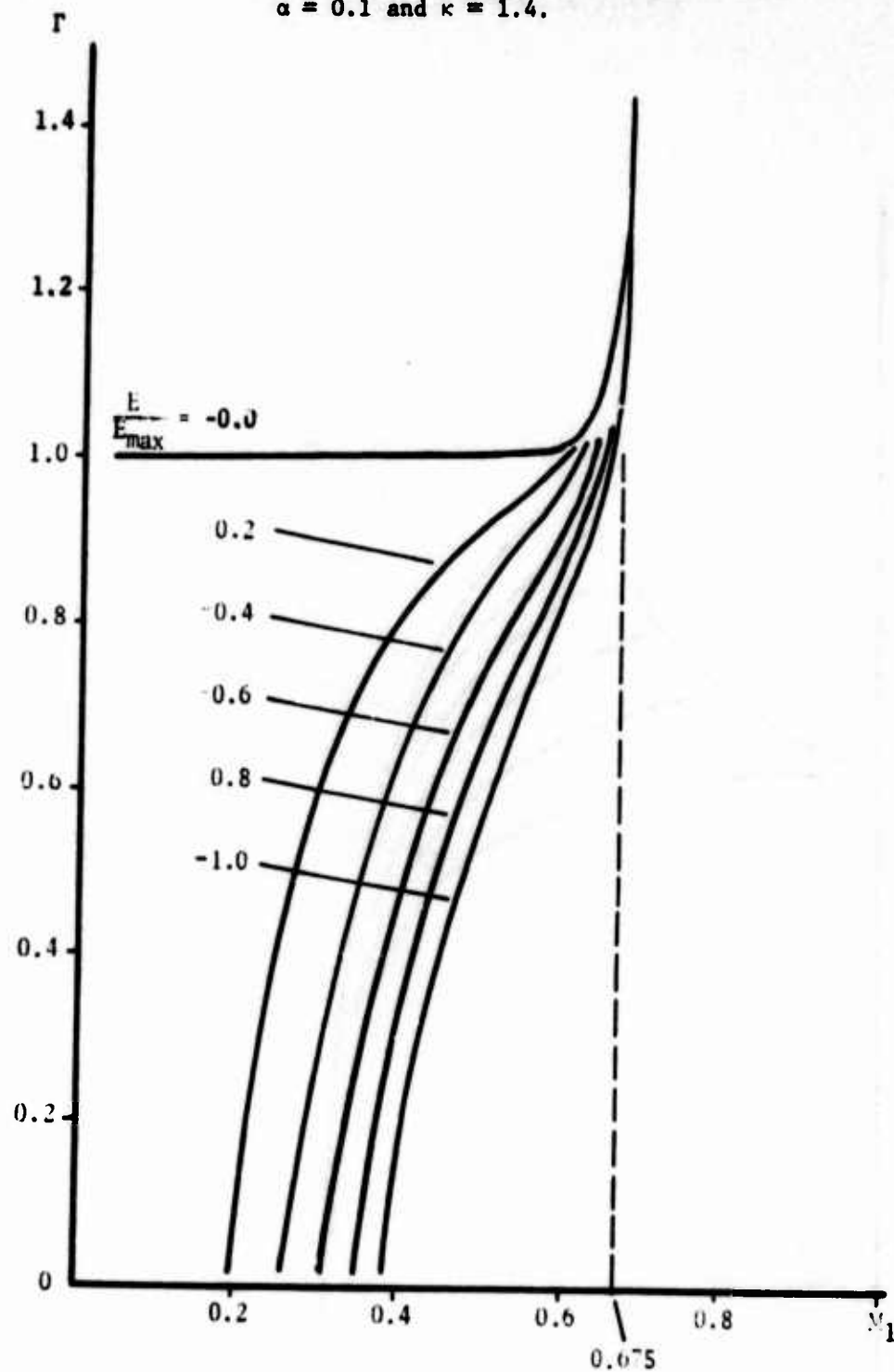


Fig.12: Dimensionless pressure as a function of upstream Mach number in subsonic flow with negative E/E_{\max} as parameter for $\alpha = 0.1$ and $\kappa = 1.4$.

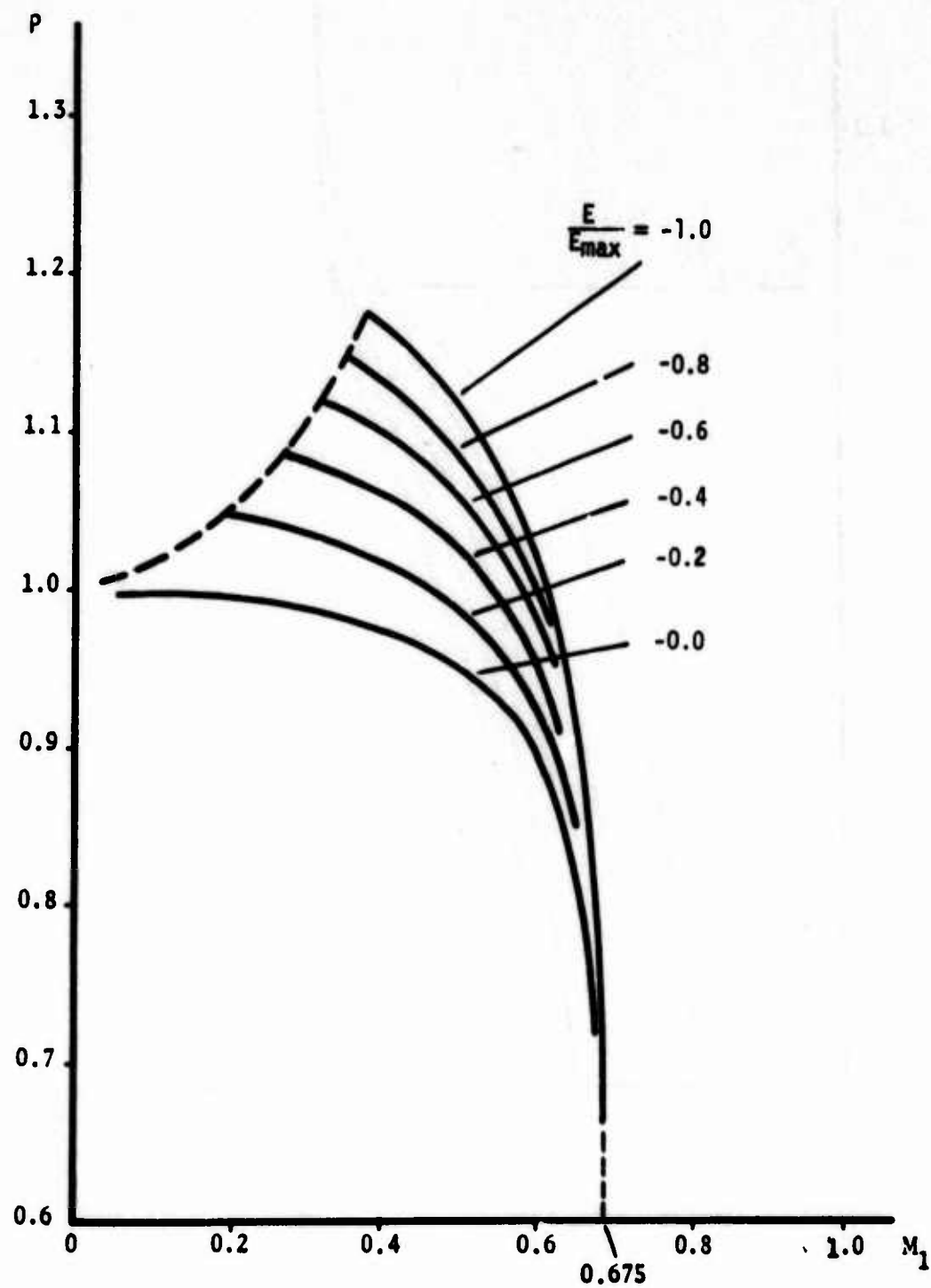


Fig.13: Dimensionless temperature as a function of upstream Mach number in subsonic flow with negative E/E_{\max} as parameter for $\alpha = 0.1$ and $\kappa = 1.4$.

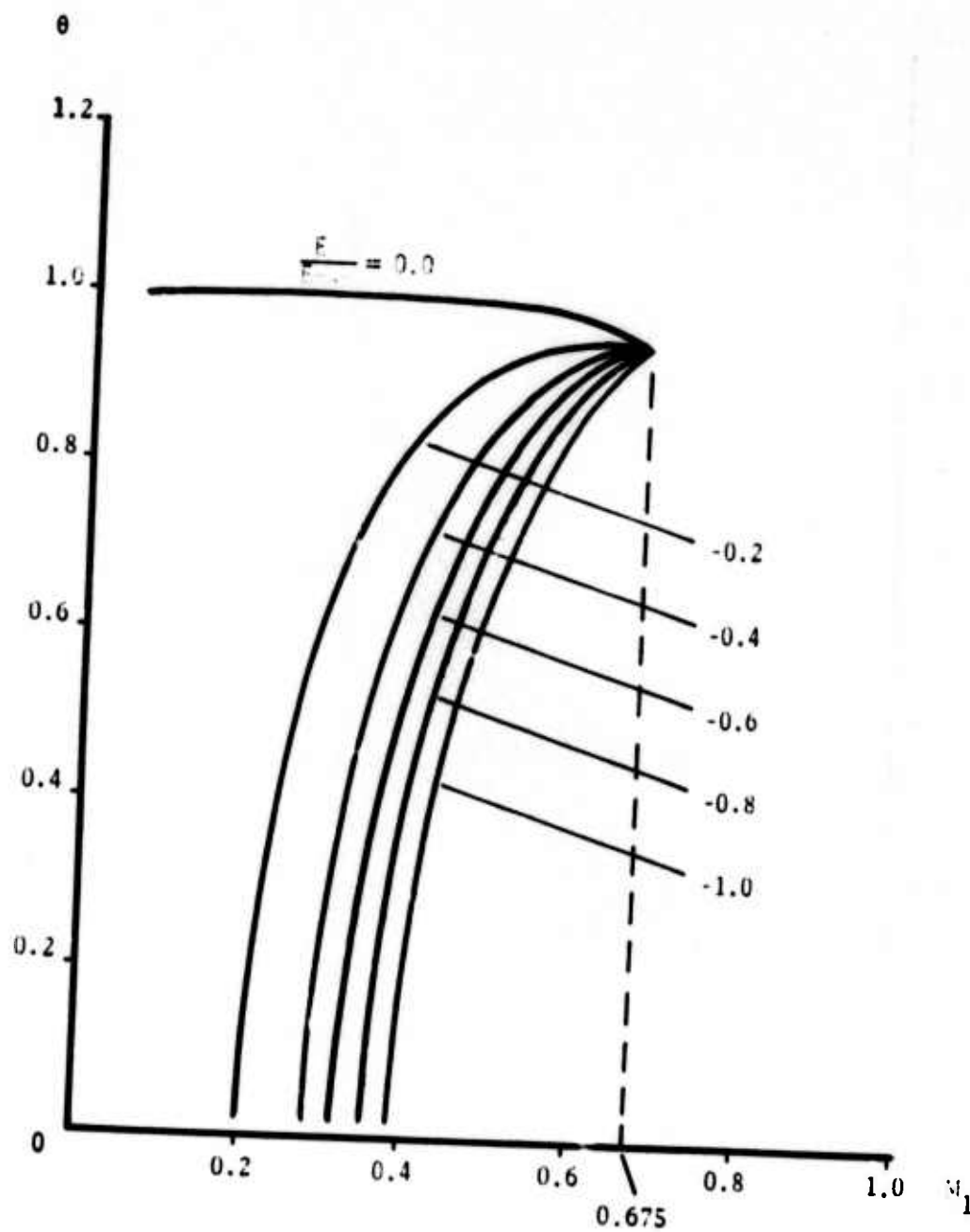


Fig.14: Downstream Mach number as a function of upstream Mach number in subsonic flow with negative E/E_{\max} as parameter for $\alpha = 0.1$ and $\kappa = 1.4$.

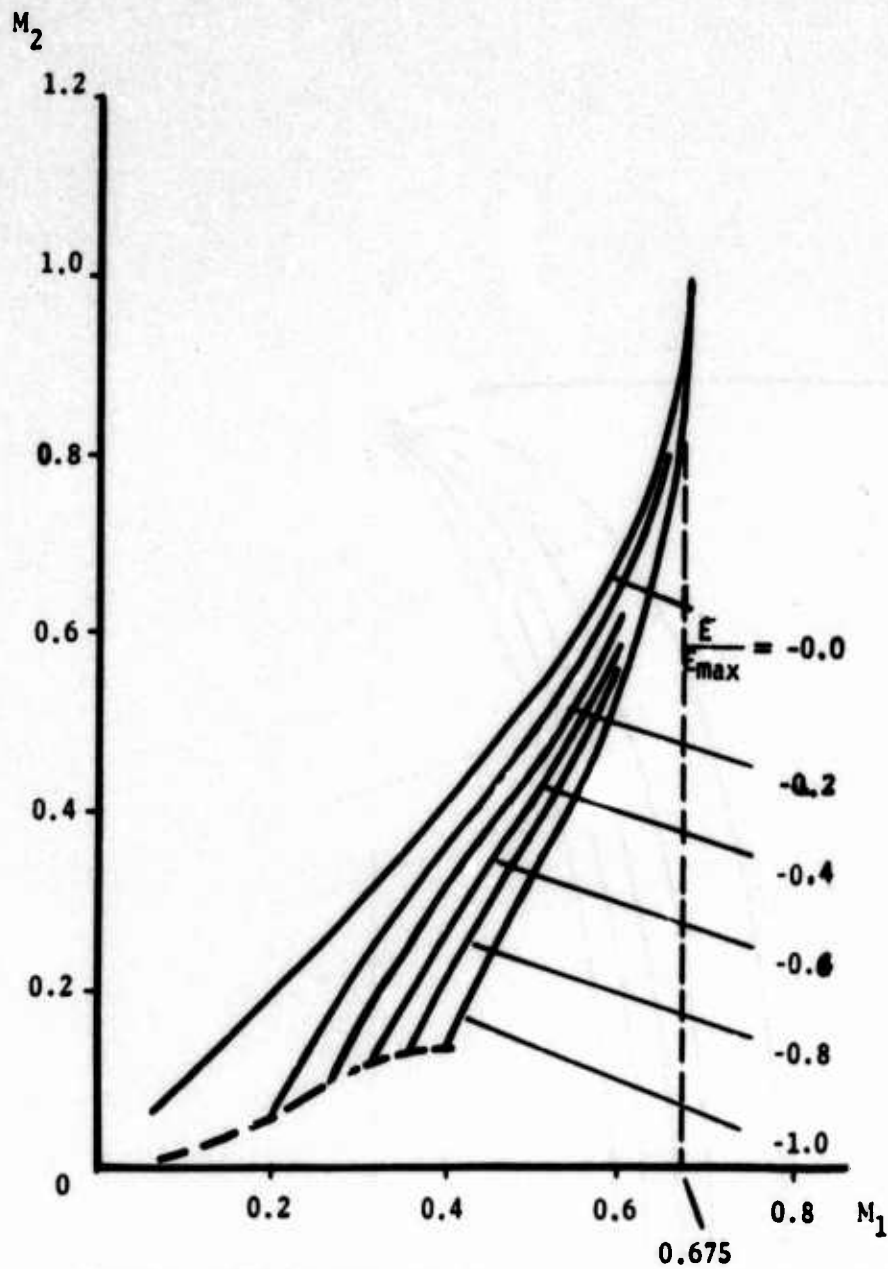


Fig.15: Dimensionless density as a function of upstream Mach number in supersonic flow with negative E/E_{\max} as parameter for $\alpha = 0.1$ and $\kappa = 1.4$.

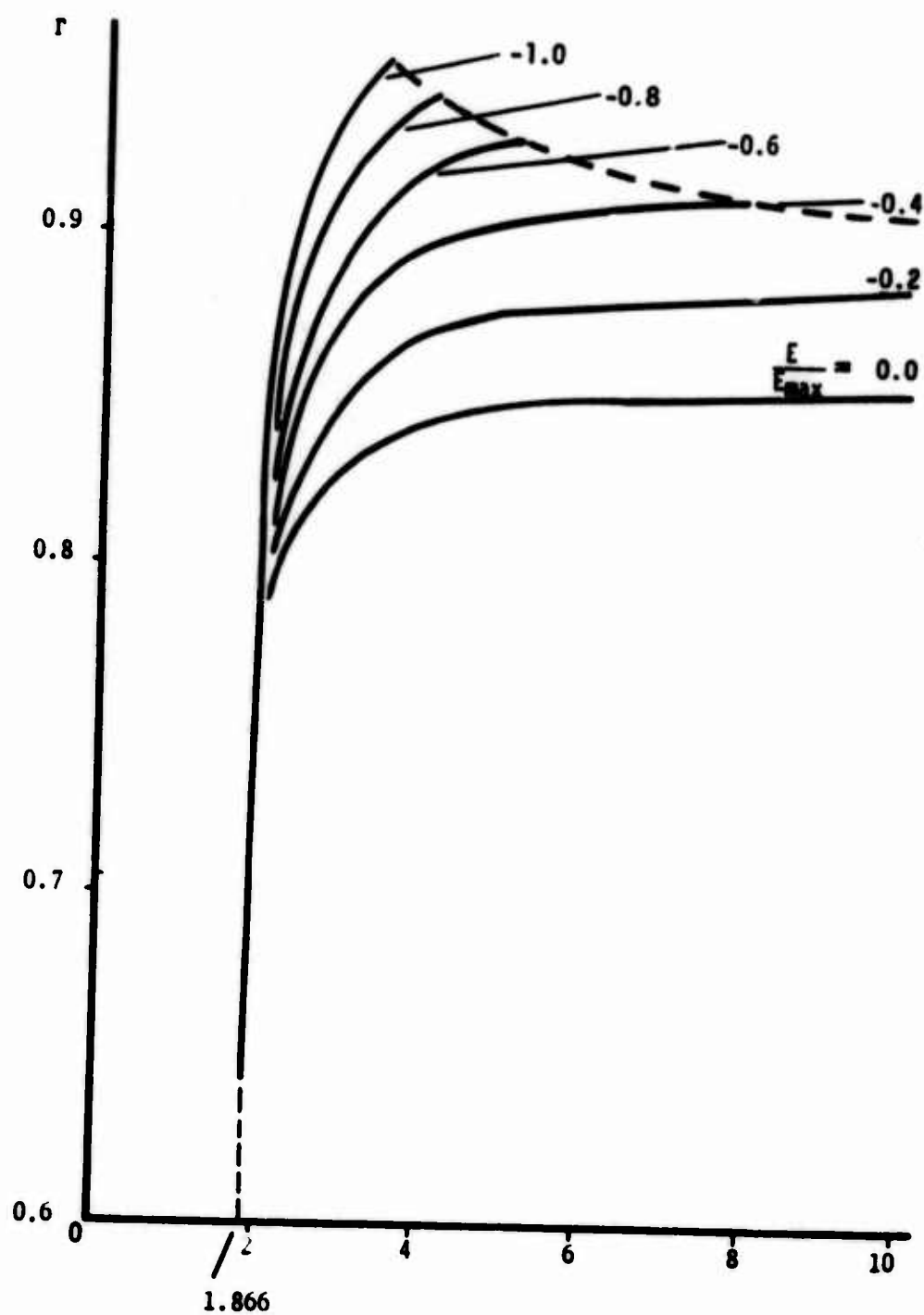


Fig.16: Dimensionless pressure as a function of upstream Mach number in supersonic flow with negative E/E_{\max} as parameter for $\alpha = 0.1$ and $\kappa = 1.4$.

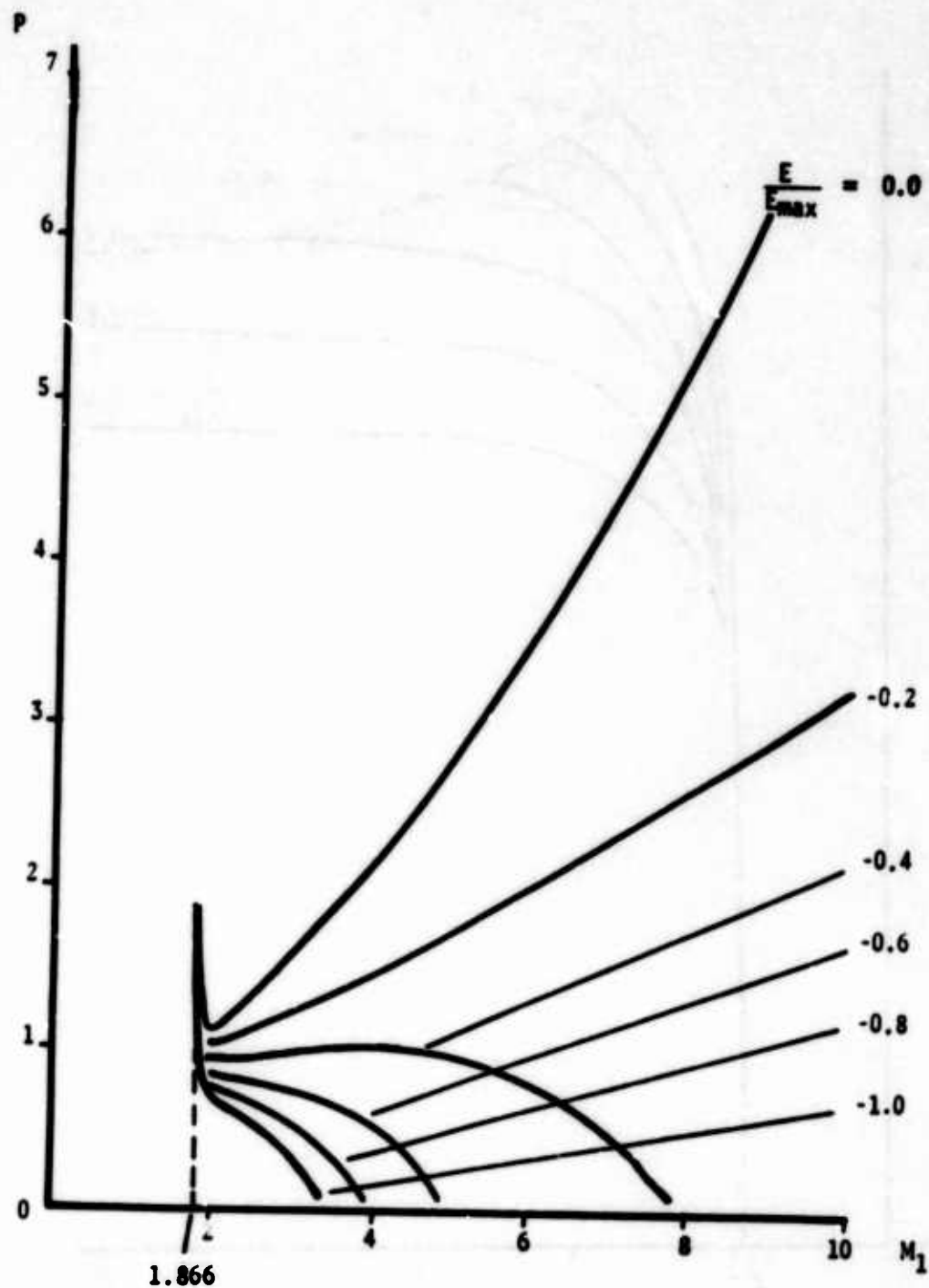


Fig.17: Dimensionless temperature as a function of upstream Mach number in supersonic flow with negative E/E_{\max} as parameter for $\alpha = 0.1$ and $\kappa = 1.4$.

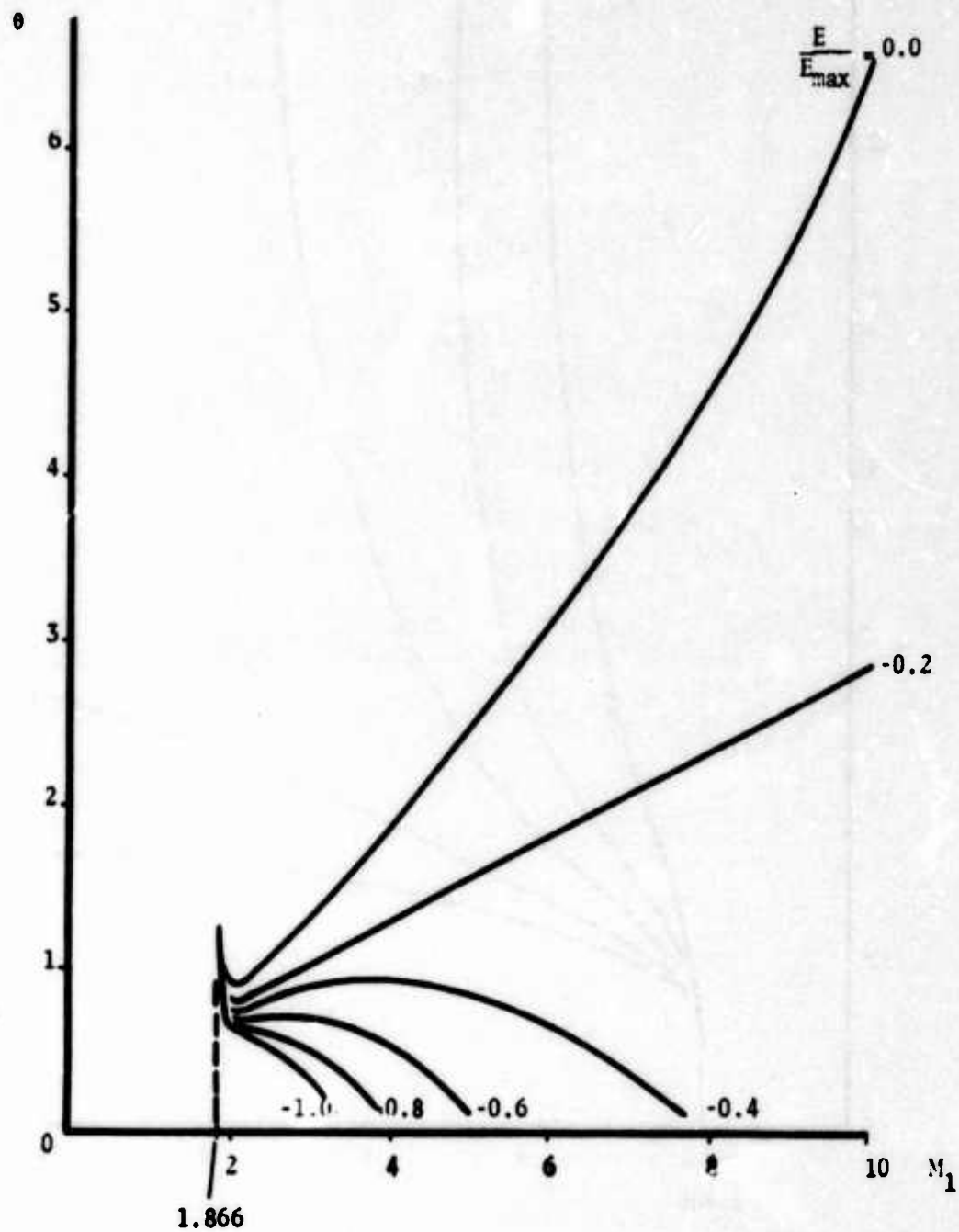
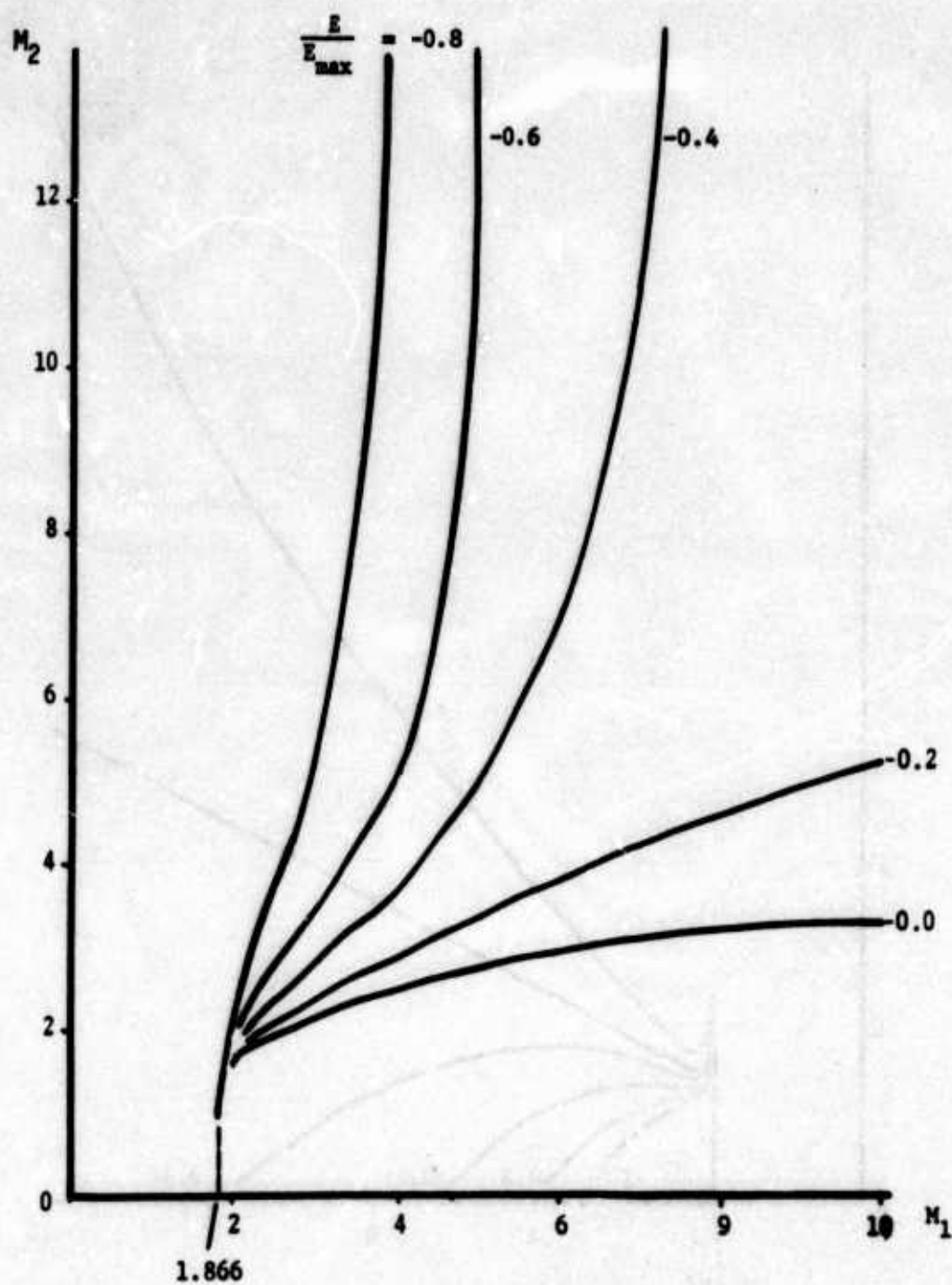


Fig.18: Downstream Mach number as a function of upstream Mach number in supersonic flow with negative E/E_{\max} as parameter for $\alpha = 0.1$ and $\kappa = 1.4$.



THRUST AND ASSOCIATED PHENOMENA OF FREE AND SUBMERGED JETS

Ernest A. Taylor, Jr.
Monsanto Textiles Company

During a series of discussions about jet propelled boats a number of years ago, I was able to demonstrate that a free jet has more thrust than a submerged jet. I adjusted the pistol grip nozzle on a garden hose to produce a high velocity jet. When I held the hose about three feet back from the nozzle and turned the water on, the thrust of the vertical jet raised the nozzle about six inches. When the nozzle was lowered into a bucket of water, the nozzle dropped some two or three inches when the tip touched the water surface. This simple, repeatable demonstration was convincing "proof" that a free jet produces more thrust than a submerged one, although I could not explain why.

In recent years, some of my work has been involved with the flow of liquid into various types of diffusers. When I ran into several bottle-necks, I kept remembering the experiment with the garden hose nozzle. So I wrote letters to three authorities on fluid flow asking for their comments on this problem. All three wrote me considered replies explaining the reason for this phenomenon. When I was given an opportunity to prepare this paper, I had to verify for myself the reason for this behavior. As a result of my work, I have learned that neither my correspondents nor I were fully informed on the problem. Like many other things in life, this problem is simple only at first blush.

Many years ago, Lord Kelvin said, "...when you can measure what you are speaking about, and express it in numbers, you know something about it; but when you cannot measure it, when you cannot express it in numbers, your knowledge is of a meager and unsatisfactory kind."⁽¹⁾ Until this time, I did not have any numbers for the thrusts involved, only repeated observations. The first order of the day was to upgrade my knowledge of the problem. A carefully performed backyard experiment with my garden hose nozzle revealed that the thrust of the free jet was three ounces and the thrust of the submerged jet was two ounces. The problem now was simply to explain why submerging the tip of the nozzle beneath a water surface would reduce the thrust of the jet by one-third.

My three correspondents, each in his own way, had suggested that the decreased thrust of the submerged jet was because of reduced pressure at the nozzle exit created by induced secondary flow. I designed three nozzles of one-quarter inch tubing, each with a flat plate of a different area welded to the tip of the nozzle. By carefully measuring water flow to the nozzle and the nozzle thrust both free and submerged, I was confident that I could easily determine the reduced pressure at the face of each plate due to the induced secondary flow. Imagine my astonishment when I discovered that the thrusts of these jets were identical for the same flow rate whether they were free or submerged.

It was obvious that I had failed to identify the problem. An examination of my garden hose nozzle revealed what I had missed. The tip was cone shaped. Aha! So I added an identical cone to the tip of a quarter inch tube. But the free and submerged jets still had identical thrusts.

A searching reexamination of the garden hose nozzle led me to take serious consideration of the center plunger for the first time. The position of this plunger determines whether the water from the nozzle is a fine spray or a high velocity stream. When the nozzle was adjusted to produce a high velocity jet, I became aware that there was a bubble trapped inside the jet and attached to the tip of the plunger. It is really strange that I had never observed that before. With sudden insight, I modified a one-quarter inch tube by centering a one-eighth inch rod in it with the tip of the rod retracted $5/32$ inch from the nozzle exit. With this nozzle, I was able to measure a distinct difference between the thrusts of the free and submerged jets for the first time. By using a slightly larger rod and adjusting its retraction inside the nozzle, I was able to improve the thrust and increase the difference in thrust between the free and submerged jets. However, it was quite difficult to install the rods and keep them centered in the tubes.

In analyzing the data from these modified jets, I calculated the jet exit velocity from the flow and thrust data. I found the exit velocity of the free jet to be higher than that of the submerged jet for the same flow rate. I also observed that the trapped air bubble inside the free jet disappeared when the tip of the nozzle was submerged. However, it reappeared when the nozzle tip was lifted clear of the water. The highest thrust valued occurred in the free jet with the trapped air bubble. In my reading, I learned that the friction factor of a jet passing over a region of low velocity fluid can be up to about twenty times the friction factor of a turbulent boundary layer along a smooth wall.(2) This higher friction factor increases the shear stress at the jet boundary. When the nozzle tip is submerged, the jet exits from the nozzle into a relatively low velocity fluid. The resulting high shear stress at the jet boundary, as mentioned above, increases the turbulence inside the jet. This is one reason that a submerged jet spreads more rapidly than a free jet. The trapped air bubble is aspirated away by the now turbulent jet and is replaced by a short separation bubble of fluid. The jet now spreads inward to close itself around the envelope of this separation bubble. Since the mass flow rate remains essentially constant, the jet velocity decreases as the cross sectional area of the jet increases. Some of this jet spreading and the resulting velocity decrease occurs before the jet reaches the nozzle exit. The thrust, being a function of the velocity squared, is therefore reduced. When the submerged jet is lifted clear of the water, the high shear stress at the jet boundary is eliminated. Jet turbulence is diminished and the jet spreading is reduced. This lowers the pressure in the separation bubble. Apparently, the jet ruptures to admit air and relieve this low pressure at the center of the jet, thus reestablishing the trapped air bubble at the end of the rod and increasing the jet exit velocity and thrust thereby.

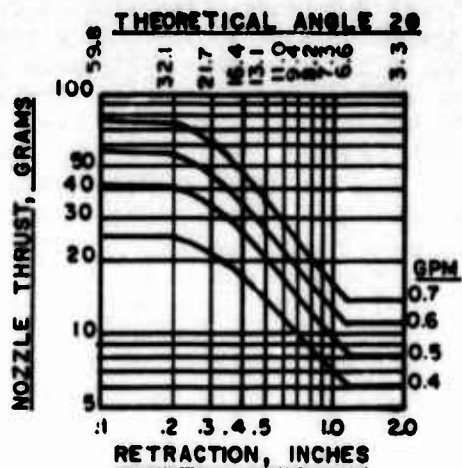
In a solid jet, the thrust for a given flow rate is constant whether the jet is free or submerged. In a garden hose nozzle, the center plunger produces a hollow jet with the hollow extending into the nozzle. The thrust of the free jet is high. When this nozzle is submerged, the accentuated jet spreading extends into the nozzle, reducing the thrust.

This answered one question but now there is another. How much vacuum is in the separation bubble. Alas! There is no way to measure it.

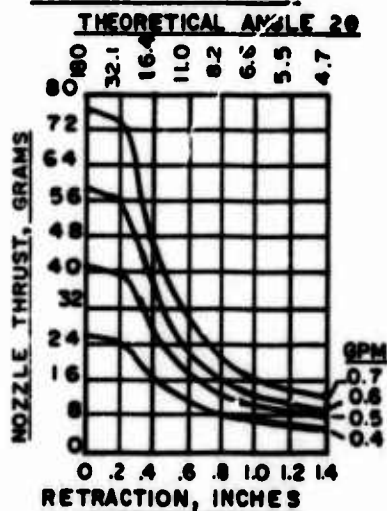
But, wait! Suppose the jet is turned inside out! I decided to use a one-eighth inch tube inside a one-quarter inch tube. The small tube would carry the water for the jet and the large tube would confine the separation bubble. I designed and built a nozzle on this basis with a connection for a vacuum gauge at the top of the large tube. Using a vernier caliper with a depth gauge, I could set the end of the small tube any distance inside the large tube and measure the retraction to one-thousandth of an inch. With the one-eighth inch tube, I was limited to water flow rates of 0.4, 0.5, 0.6 and 0.7 gallon per minute. With this nozzle, I measured the water flow, thrust and separation bubble vacuum of the submerged jet at various retractions up to two inches. When I began to plot data from these tests, I found it quite nonlinear. In looking for correlations, I decided to examine the performance of this nozzle as a diffuser. The inside diameter of the small tube was 0.075 inch and that of the large tube was 0.190 inch. For every retraction increment, I calculated the angle between imaginary lines from the exit diameter of the small tube to the exit diameter of the large tube. These imaginary lines defined an imaginary conical diffuser. The angle between these lines, two theta, is shown on the graphs of the data.

The data taken with this nozzle is plotted as graphs on the following page. Graph number 1, on logarithmic paper, shows that the curve of thrusts for each flow rate has two constant values with a true logarithmic section in between. For retractions between 0.2 inch and zero, the thrust is maximum and is the same whether the nozzle is submerged or free. There is a smooth transition to the logarithmic curve of decreasing thrust which terminates abruptly at a retraction of about 1.2 inches at the minimum thrust value for the submerged jet. For the free jet, there is no change in thrust or vacuum with any retraction as long as the jet does not touch the sides of the large tube. Graph number 2 shows that there is no vacuum in the separation bubble of the submerged nozzle until the small tube is retracted more than 0.2 inch. Then, it increases rapidly, reaching a maximum value at a retraction of 1.2 inches. The cause for this behavior is shown in figures 1, 2 and 3. These figures show the tip of the small tube retracted inside the one-quarter inch tube. In practice, these tubes are vertical. In figure number 1, the jet is shown entraining fluid from the space between the jet boundary and the inside wall of the large tube. However, there is ample room for a flow of make-up water to replace that aspirated by the jet. Thus, there is no established separation bubble and no measurable vacuum. The jet has not spread, since there is no change in thrust. In figure number 2, at a retraction of 0.6 inch, there is a considerable reduction in thrust with a corresponding jet spread. The equation for thrust makes it possible to calculate the jet diameter. This larger jet diameter partly closes the exit of the large tube, reducing the make-up water flow to the separation bubble, which is now well established. As graph number 2 shows, there is a considerable vacuum in the separation bubble at this point. In figure number 3, the jet has spread to essentially fill the exit of the large tube. No make-up water can now flow to the separation bubble. At this point, the thrust has reached its lowest value and the vacuum its highest. Further retraction causes no change in either.

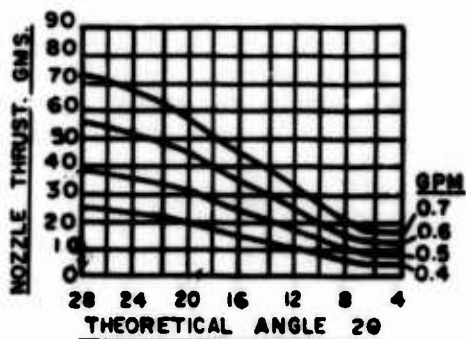
Graph number 3 shows the thrust plotted on rectangular coordinate



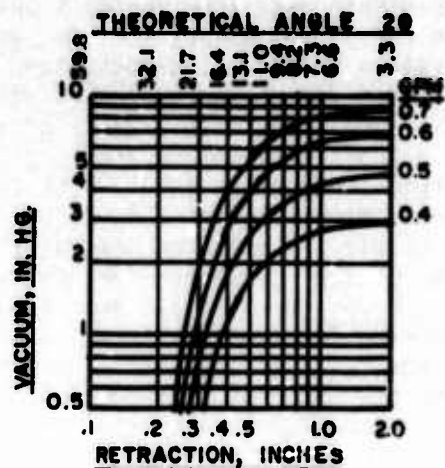
GRAPH NUMBER 1



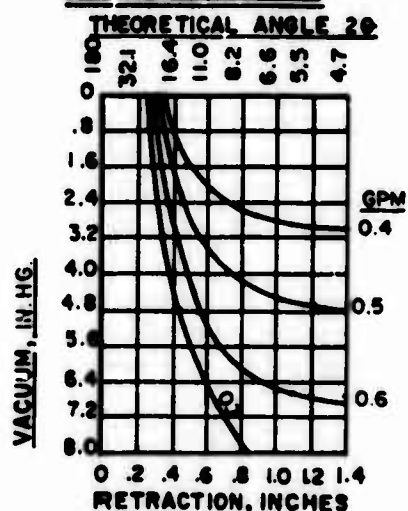
GRAPH NUMBER 3



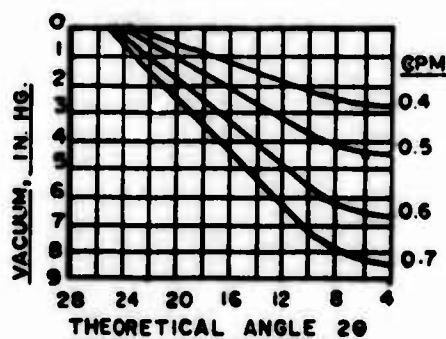
GRAPH NUMBER 5



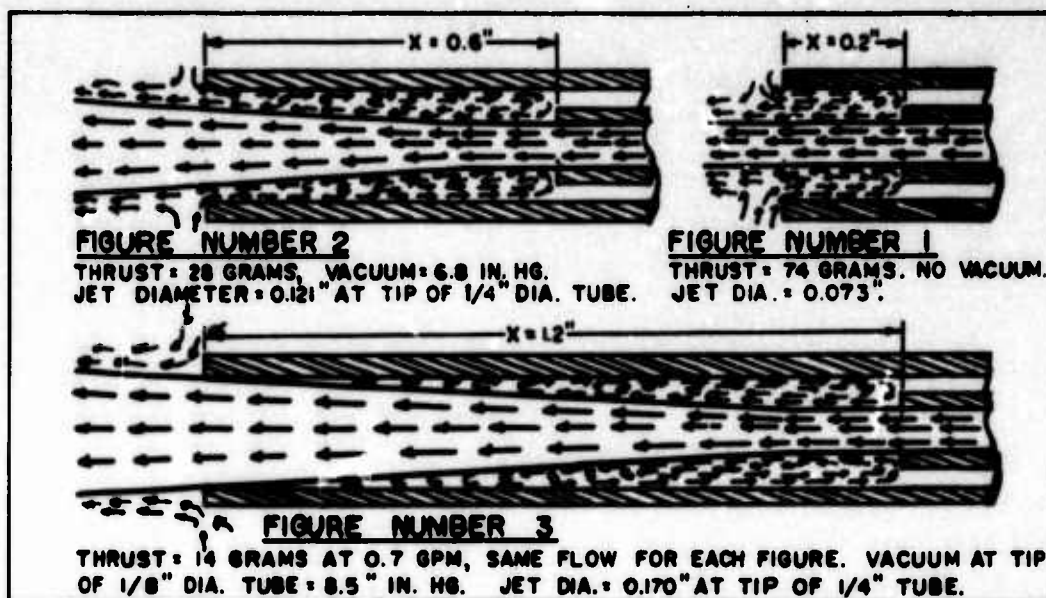
GRAPH NUMBER 2



GRAPH NUMBER 4



GRAPH NUMBER 6



paper and graph number 4 shows the separation bubble vacuum plotted on the same paper. These four graphs have the retraction of the small tube as the abscissa. At the top of these graphs, the theoretical diffuser angle two theta is shown for reference.

Graphs number 5 and 6 show the theoretical diffuser angle two theta as the abscissa. In both of these graphs, it is intriguing that both the thrust and separation bubble vacuum plot as straight lines, although at different slopes, over the major portion of each graph. I cannot account for this. It is very significant that both of these curves flatten out at a theoretical diffuser angle of less than six degrees. This shows that the jet spread angle is identical with the most efficient diffuser angle. It is also highly significant that the logarithmic portion of the thrust curve occurs between the theoretical diffuser angles of about six and twenty two degrees. This agrees with the investigations of Cochran and Kline(3) who found that the flow through a straight walled diffuser was attached to both walls until the diffuser angle was increased to almost twenty one degrees, although the flow began to be unsteady at about seventeen degrees.

I have also discovered other correlations which are impossible to discuss in these few pages. I am convinced that thrust is a tool that can be employed with profit in defining jet spread and other parameters required for the most efficient design of fluidic equipment.

Bibliography

- (1) Chilton's Instruments and Control Systems, December, 1971, Vol.44, No. 12, top of page 3.
- (2) Streeter, V. L., Handbook of Fluid Dynamics, 1st edition, McGraw-Hill Book Company, Inc., New York, 1961, page 11-10.
- (3) Cochran, D. L. and Kline, S. J., Use of Short Flat Vanes for Producing Efficient Wide-Angle Two-Dimensional Subsonic Diffusers, NACA Technical Note 4309, September, 1958, page 29.

FLOW OF PARTICLES IN A SUBMERGED FLUIDIC DEVICE

P. I. Chen
Applied Science and Engineering Department
Portland State University

M. L. Marcott
Bureau of Sanitary Engineering
City of Portland

Portland, Oregon

The phenomena of particle flow in a bistable wall attachment fluidic device were first investigated by Chen and Hogland. Their studies were mainly concerned with the two-phase flows of solids in gas streams. This study, however, is concentrated on the hydraulic aspects of solid flow in a fluidic device which is submerged in liquid.

In our study, experiments were conducted in order to evaluate the effect of solid/fluid density ratio, supply pressure, and the depth of submergence upon the percentage of particle recovery at the active output. Results show a higher recovery efficiency for lower density ratios which in fact confirm the original observations. Entrainment strength also plays an important role in determining the efficiency. These findings are described in detail and substantiated by a graph.

This study demonstrates that non-moving part bistable fluidic devices can be employed with high levels of efficiency in directing the flow of particles moving in a liquid stream. It is expected that this project could lead to applications in industrial processes and slurry controls.

INTRODUCTION

The bistable fluid device is a non-moving part device which utilizes the wall attachment phenomenon, commonly known as Coanda effect, to control flow direction between two possible outputs. The Coanda effect is primarily used in designing the digital type of fluidic devices. However, this study is concerned with the investigation of a bistable device capable of transporting solid particles. The investigation of such a device which can be used to perform this function was first attempted by Chen and Hogland (1,2). In their studies, solid particles were sent through a bistable fluid device, and the collecting efficiency for particle of various sizes under different pressures were computed. They defined the collecting efficiency as the ratio of the number of particles collected at the active output to the total number of particles received at both outputs. Their study mainly was concentrated on the flow of light particles in the air stream.

The device described in their first study (referred to as the basic device) was incapable of obtaining a 100% collecting efficiency. Their

second study involved the design and testing of three modifications of the basic device. The designs included: (a) Lifted legs, (b) Blocking vane, and (c) Guiding vane. All three modifications reported a nominal 100% collecting efficiency.

In this on-going study, water is used as the transporting medium. No modification of any kind to the so called basic device was employed up to this point of experimentation. Since the density of particles is different from that of the working fluid, particle tends to move with different velocity as compared to its surrounding fluid. A particle moving along a straight streamline which does not have a significant difference in transverse velocity gradient, tends to stay on the streamline. In this case, the forces acting on the particles are the drag force and inertia force. When a particle moves towards a curved jet stream, the forces acting on the particle in addition to drag and inertia forces are centrifugal force, lift force in the longitudinal direction, and drag force in the transverse direction.

Factors holding the particle in the jet stream are the lift force created by the velocity distribution and the transverse drag force which resists the tendency of the particle to move across the jet stream. Neglecting wall interference, the momentum of the particle becomes the dominating factor for the particle to detach from the jet stream. That is, when the momentum of the particle overcomes its drag force in the transverse direction, the particle will flow towards the apex of the splitter and may strike the inactive side of the output leg.

EXPERIMENTAL SET-UP AND TESTINGS

For the experiment, a bistable fluid device as shown in Fig. 1 was constructed of plexiglas. The dimensions of this device are as follow:

Size.....8.5" long, 5.0"wide, 1" high
Throat area.....0.5" deep, 0.5" wide
Throat length.....3.0"
Outlet wall angle.....19° from centerline
Vents.....0.25" downstream from the splitter apex
Output leg.....0.5" wide, 0.5" deep

Also, a splitter position of 2 inches away from the centerline of the control ports was used as a result of an earlier study (2).

Particles used in testings were round in nature in order to reduce the complexity involved in motion. The average weight, diameter and density are contained in Table I.

TYPE OF PARTICLE	WEIGHT gm	DIAMETER cm	VOLUME cm ³	DENSITY gm/cm ³
Glass Beads	0.085	0.370	0.0265	3.207
Lead Shot	0.203	0.330	0.0188	10.798
Plastic Beads	0.039	0.381	0.0290	1.345

TABLE I The Physical Characteristics of Particles

The test set-up as shown in Fig. 2 included a plexiglas tank 43.8 cm wide, 80.0 cm long and 41.3 cm deep. Clear plexiglas was chosen for constructing the tank in order to allow observation from the sides and the bottom of the tank. It also made possible for high speed movie filming from the tank bottom.

City tap water was used as the working fluid. The depth of water in the tank was controlled by an adjustable "morning glory" type overflow drain.

Tests were conducted by first setting the supply pressure to the device and then measuring flow rates under steady state condition by timing and weighing of the overflow. With the depth of submergence set at a controlled level, particles were introduced into the supply port of the device via a Y connection. Particles were placed in the stream one at a time in order to eliminate possible interaction among each other. A collection trough was located downstream near the device output for the purpose of collecting particles after each test run. When sufficient tests were conducted for one flow rate, the supply pressure was changed in order to study the same phenomenon under a different flow rate. The range of supply pressure varied from 3 psig to 12 psig which provided a calculated velocity range from 5.25 feet per second to 8.6 feet per second at the throat section.

During some test runs, a 16 mm movie filming at the rate of 64 frames per second was taken. This movie was then viewed at the rate of 24 frames per second in order to observe a greater detail of the particle behavior in the device. At lower supply pressures, the motion of particle was clearly visible, especially at the region downstream from the throat section, without the aid of the high speed movie.

EXPERIMENTAL FINDINGS

The result of the test runs is shown on Fig. 3. Each point on the graph represents an average of some 6 to 8 runs for a given supply pressure setting. We notice that this figure contains no information on the depth of submergence. Little or no indication was shown that there was any effect contributed to the collecting efficiency by the depth of submergence. This apparently implies that hydrostatic pressure above the device does not affect the strength of entrainment flow. Nevertheless, it was observed that when the device was not fully submerged, the liquid jet would split between the two outputs. But as soon as the vents were submerged the wall attachment phenomenon took place immediately.

A comparison of collecting efficiency among three types of particles used in the testings shows that the lead shot recovery rates were about 75%; the recovery rates of glass beads were ranged from 85% to 90%; and plastic beads were close to 100% recovery at the active leg. These results provide a good indication that the density of particle in stream, that is, the momentum of the particle plays an important role in determining the collecting efficiency. The low recovery efficiency of the lead shot is caused by its high density thus its high momentum, as compared to particles of other types. Thus momentum was a dominating factor in deciding the forward motion of the particle relative to that by other forces.

The momentum would tend to carry the particle in a straight line due to the relatively long straight nozzle. If the particle struck the splitter on the side of active output, the particle would be carried out the active output. However, if the particle struck the splitter on the inactive side, the momentum of the particle would then have to overcome the strength of the reverse flow in order to escape through the inactive output. This accounts for the observation that particles which entered the inactive leg were sometimes forced to return to the active output, after moving in a circular motion within the inactive leg near the splitter.

Figure 3 shows that for both the glass beads and lead shot a higher recovery rate was observed at the lower flow rates. This is believed to be caused by the lower particle momentum which could not overcome the strength of the reverse flow. The reverse flow affects the lighter particles more than the heavier ones. This also leads to a greater collection efficiency for the lighter particles.

Although data shown reflects tests conducted without the presence of a control jet, it was observed that, in general, recovery rates were higher when the control jet was present. The reason is the control jet momentum can serve to deflect those particles which tend to detach from the jet stream.

SUMMARY

The study of particle flow in a bistable device was investigated in this paper. The results indicate that wall attachment phenomenon can affect the particle flow in such a device.

The momentum of the particles plays an important role in the movement of the particle in the fluid stream. Particles of lower density can be collected more efficiently than higher density ones. Lesser collecting efficiency was caused by the momentum of the heavier particles which dominates the forward motion of the particle.

Thus for a particle to not reach the active output, it must possess enough momentum to not only escape the inactive leg, but also to overcome the reverse flow.

From all observations it was found that recovery rate was not influenced by the depth of submergence. Because of the limitation of the test tank, a steady flow condition could not be maintained for supply pressures higher than 12 psig, this leaves the question of "whether or not the supply pressure affects the recovery rate" yet to be answered.

ACKNOWLEDGMENTS

The authors wish to express their thanks to T.C. Wildschut for his help in constructing the flow tank and the fluidic device for the experiment.

REFERENCES

- (1) Chen, P.I., Hogland, G.H., "Designs of a Bistable Fluid Device for Transporting Solid Particles". ASME paper 72-MH-27, 1972.
- (2) Hogland, G.H., Chen, P.I., "Flow of Particles in a Bistable Fluid Device". ASME paper 72-MH-28, 1972.



Fig. 1 A Bistable Fluidic Device



Fig. 2 The Experimental Set-Up

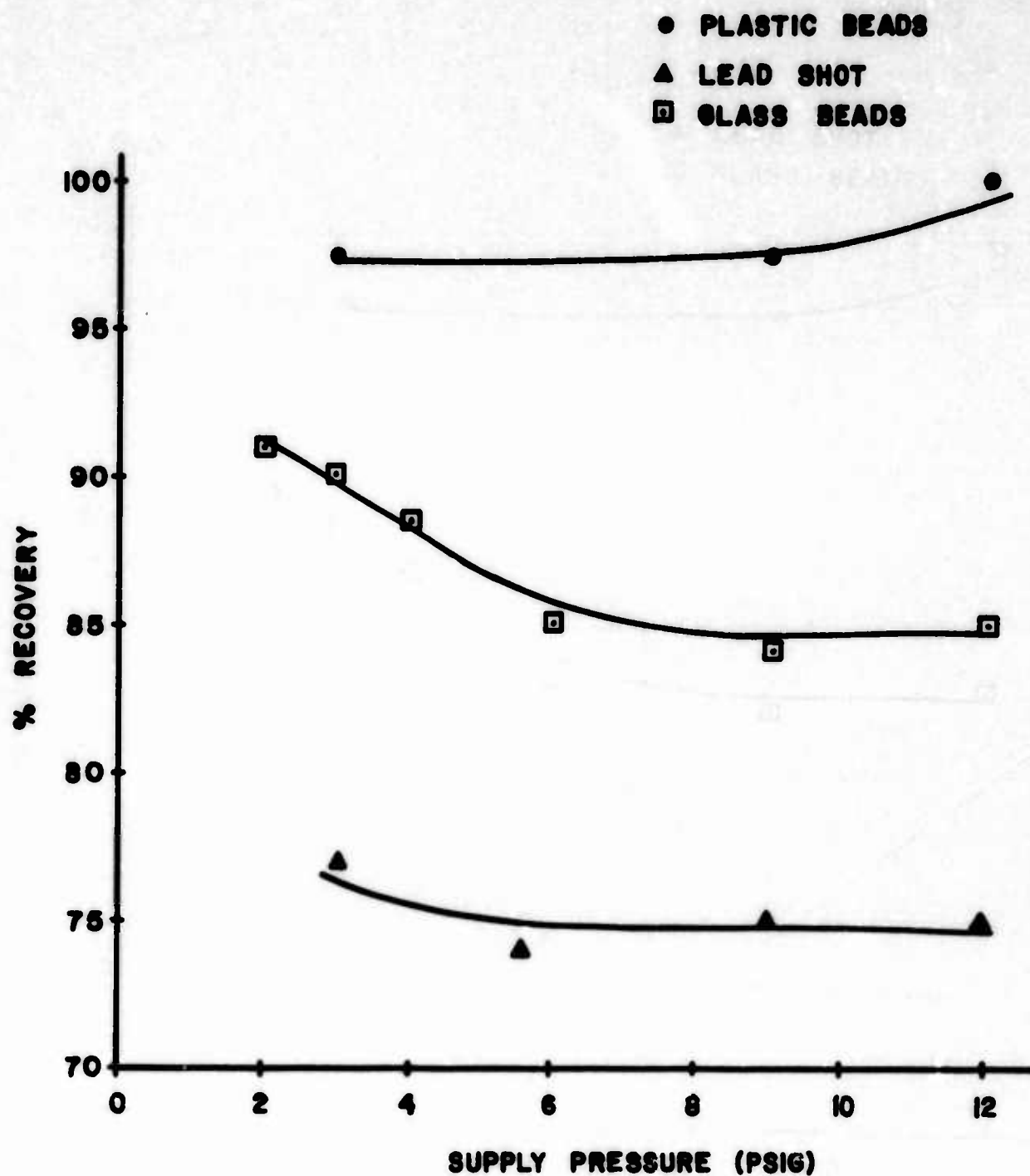


Fig. 3 The Collecting Efficiency vs. the Supply Pressure

SUPERSONIC BOUNDARY LAYER CONTROL AND ITS APPLICATIONS

R V Thompson Ph.D., M.Eng., B.Sc., F.I.Mech.E.

Marine Industries Centre
University of Newcastle upon Tyne, England

ABSTRACT

The phenomenon of supersonic boundary layer separation and subsequent reattachment, with particular emphasis on its application to Fluidic/Flueric devices, is briefly explained.

Details are provided of concepts developed, including monostable, bistable and three dimensional devices involving operating media of pressures and temperatures up to and including 5000 psia and 6000°F. Past, present and future missile systems, utilising the phenomenon, are described together with a detailed analysis of the advantages to be gained by extrapolating the concept to vertical lift devices, stabilised platforms and decoy systems.

Although an attempt has been made to be informative the prime objective of the paper is to stimulate a re-assessment of the direction in which boundary layer control appears to be moving in this field.

INTRODUCTION

This paper concerns itself with the control and application of phenomena associated with supersonic boundary layers.

The research into this particular aspect of Boundary Layer Control commenced at the University of Strathclyde in the early 1960's with the intention of developing an alternative form of missile wing surface control system to that already in existence. The system was somewhat unusual in that it was to be completely pneumatic (operating on hot exhaust gases), self-supporting and, more importantly, was to form an integral part of the actual wing assembly.

To transfer the idea into a working proposition it was necessary to develop a control device capable of directing hot gas supplied at supercritical pressure ratios according to a given bandwidth of demand. The prime result of the applied effort was the successful development of a component capable of switching supersonic jets in a bistable mode by alternatively venting and closing control vents to the atmosphere. Furthermore, a fundamental understanding, together with an intuitive mathematical solution of the phenomenon of boundary layer separation and reattachment was both evolved and subsequently substantiated.

During this period interest was shown in the development by Missile Companies in the U.K., Scandinavia and the U.S.A. resulting in the design and development of various permutations on the original theme. Applications included jet reaction and hot gas secondary injection steering of missile systems, together with cold gas single stage power actuator arrangements.

Early success encouraged further exploration of the phenomenon leading to the construction of three dimensional thrust vector control and vertical lift devices. Even a non-moving part single element thrust and pressure ratio computer suitable for gas turbine monitoring requirements has been demonstrated.

In view of the apparently limitless application of the phenomenon, an attempt has been made in this paper to outline the principles involved, devices developed and possible future applications, in the hope that the interest of others will be stimulated to a sufficient degree to warrant the expenditure of their own effort, thereby reaping benefits yet unknown.

To obviate a totally insular presentation a list of references detailing the efforts of others known by the Author to have made contributions in this field have been included at the end of this publication.

BOUNDARY LAYER EFFECTS

Separation

Figure 1 describes a two dimensional convergent divergent duct subjected to a gas flow supplied at supercritical pressure ratio, viz. $P_o/P_a > 2$.

Ordinarily, propulsion ducts or nozzles are designed for adapted flow, i.e. the process of expansion of the supersonic gases is allowed to continue until the pressure at exit is identical to ambient. In the case shown, the duct has been extended beyond this critical length to the degree that boundary layer separation has been encouraged to occur.

Process is basically as follows.

The Mach number of gases expanding through a convergent-divergent duct will exceed unity provided the pressure ratio between throat of supply reaches a clearly defined minimum value - of the order of 0.500. The flow in the divergent portion may be subdivided into two main flow regions - main stream and boundary layer flow. The former is assumed to be inviscid and isentropic with zero transverse velocity gradient, the latter viscous flow with a large transverse velocity gradient. The velocity at the wall of the duct is zero and at the outer edge of the boundary layer is approximately that of the main stream. If the Mach number of the main stream is in excess of unity, then somewhere in the width of the boundary layer occurs a stream layer moving with the velocity of sound in the fluid. Nowhere in the main stream can the downstream conditions be transmitted directly upstream, i.e. the main flow has no indication of the conditions appertaining downstream because of its supersonic velocity. However, the fluid trapped between the sonic line and the duct wall is conscious of the prevailing downstream conditions and, more important, provides a feedback path for this information.

An adverse or positive pressure gradient will cause a slowing down of the subsonic flow stream causing, in turn, a general thickening of the boundary layer, i.e. the sonic line moves nearer the centre of the main stream. If the adverse pressure gradient is of sufficient magnitude the boundary layer may separate from the duct wall, causing a series of compressive wavelets which combine to form an oblique shock. This has a distinct effect on the main stream flow. Symmetrical separation is shown in Figure 1.

It is interesting to note that although the interruption to flow is severe the resulting thrust from the situation shown is still significant. Naturally, the optimum thrust condition occurs when duct is adapted, with a loss in power being noted either side of this position. Maximum power, however, will occur when the gas is on the point of separating at the exit when the immediate pressure in the stream will be

given by

$$p_a/p_s = \left[\{kn/(n+2)\} + 1 \right] \quad \text{--- (1)}$$

which, for most situations of turbulent boundary layer flow, results in an ambient/separation pressure ratio near to 2. Further expansion by increasing the length of the duct, however, will not necessarily result in further loss in thrust simply because, under ideal conditions, the pressure immediately after separation increases rapidly to ambient thereby minimising pressure drag. It should be remembered also that rate of change of momentum is still increasing with continuous expansion of the gases, substantially negating separation losses.

The above observations are considered to be of some importance to applications detailed later.

A unique mathematical evaluation of the separation problem is contained in Appendix I, together with an explanation of the process involved. It should be noted that the theory applies to both laminar or turbulent flow situations and provides reasonable approximations to three dimensional expansions.

Re-Attachment

Although mathematically elusive, the effects of boundary layer separation have been well known to Aero and Gas Dynamicists for many years. It was only comparatively recently, however, that the effects of gross over-expansions were fully appreciated. Figure 2 shows a duct of length at least two and a half times that required to permit ordinary boundary layer separation to take place. It may be seen that subsequent to separating in the normal way, asymmetric boundary layer reattachment has occurred with useful consequences. Before exploring these further it is considered prudent to detail the factors influencing the reattachment process.

Proceeding from the conditions of symmetrical separation shown in Figure 1, the developments leading to reattachment are as follows.

Referring to Figure 2, sketch (a) details the flow situation following a step input of applied pressure P_0 . The gas may be seen to have separated symmetrically from both divergent walls describing the pressure distribution shown. The flow situation is highly unstable due to turbulent pressure fluctuations occurring along the separated stream lines. Furthermore, a process of entrainment occurs along these exposed edges because of visco/molecular attraction creating the vortex flow indicated. Naturally, an increase in velocity of the gas in these areas is accompanied by a reduction in pressure thereby intensifying the transverse instability of the jet. Ordinarily, the process will prove more virulent on one flank to the detriment of the other, hence encouraging the growth of a transverse pressure gradient. The pressure which originally caused boundary layer separation fails in sympathy with entrainment

pressure and so the position of separation iterates downstream in a continuous attempt to maintain the status quo as shown mathematically in Appendix I and pictorially in Figure 2(b). The combination effect of transverse pressure gradient and intensifying entrainment encourages the main stream to move toward the wall adjacent to the most active area, finally culminating in reattachment. The vortex or reverse flow region is at maximum intensity and is 'locked in', resulting in a stable flow situation which may only be destroyed by the application of external forces. Figure 2(c) identifies the salient flow and pressure characteristics which are further amplified in Figure 3. The whole process occurs in approximately one millisecond.

SPECIFIC APPLICATIONS

All the applications detailed briefly below depend upon the separation-reattachment phenomenon discussed previously. Of specific importance is the relationship which exists between vortex and ambient pressures, i.e. the former being substantially lower than the latter at any real absolute pressure. The first six applications are realities in that devices have been made, tested and installed in systems. Further substantiating details of their capabilities are provided in the text.

Bistable Switch

Referring to Figure 2c it may be seen that the stable flow situation indicated is susceptible to external influences, e.g. the placing of a suitably sized orifice adjacent to the latching vortex region permits ambient air to be introduced at comparatively high pressure. The continuous entrainment process taking place in the region will have access to an inexhaustible supply of air at a flow rate predescribed by the orifice impedance. Ordinarily, the pressure within the vortex will increase carrying with it physical growth. The pressure ratio across the jet decreases causing movement toward the opposite divergent wall as a result of an increase in curvature. The entrainment process between that wall and the jet free surface becomes more active; pressure drop more intense, resulting in a mirror image of the process of attachment detailed earlier. The total switching process, although a function of orifice (control port) area may be caused to occur in less than one millisecond.

Obviously, the placing of a further orifice in the wall to which jet has switched its allegiance will permit a reversal of the process to take place providing the original control port is simultaneously closed.

Figure 5 shows an experimental switch with a supply operating range from 70 to 130 psi. Devices have been built by the Author to operate on pressures up to 2200 psia and temperatures in excess of 3000°F. In all cases air at atmospheric conditions was the sole means of control power. Worthy of note is the fact that control air is drawn into the operating region and, in consequence, the control circuit is virtually

Isolated from the main power medium. Further details of this device are contained in References 4, 12, 13, 14.

A considerable amount of effort was applied to proving that the separation reattachment region may be isolated from excessive back pressures. Details of the experimentation and the results obtained are shown in Reference 6. The amplifier specifically designed was used to actuate a large piston against substantial loads. A frequency response of 0 to 40 cycles/second at $\pm \frac{1}{4}$ of an inch was obtained and a piston thrust in excess of 200 lbs. achieved. The device was operated simply by alternately venting the control ports to atmosphere. Figure 6 shows a diagram of the circuit involved.

Mono Stable Switch

A natural extension of the above device was single port control thereby halving the control requirements. Although the power consumption involved in the control circuit is minimal, a reduction in the relative complexity results in significant advantages. Figure 8 shows a schematic diagram of the device. The geometry has been modified slightly, as shown at the exit of the throat. The setback in this area provides bias to the expansion of the main gas jet to the extent that when the control port is closed the jet will attach to the adjacent wall.. Opening of the control port encourages switching to the opposing divergent wall by the process detailed previously. Subsequent closure of the port will cause the gas jet to return to its initial position due to the effect of asymmetrical geometry. The device has much the same capabilities as the Bistable Switch in that it will operate at extremely high pressures and temperatures with high speed of response.

A further extension of the research has shown that it is quite possible to build a device which will switch from one divergent wall to the other at a pre-described supply pressure without the assistance of control ports. A further increase in supply pressure will cause the jet to return to its original position. The range between the two critical pressures is variable both in absolute terms and in relation to supply pressure.

Missile System Application and Development

The concepts detailed in previous sections may be applied with advantage to missile control schemes; the alien environmental conditions normally associated with the field being compatible with the mode of operation of the devices under review. Methods employed to date include secondary injection, jet reaction steering, a combination of both and direct boundary layer control of missile exhaust flux. Obviously, there are further 'indirect' applications, e.g. the supersonic device may be used as the final operating element in a piston-yoke assembly or to direct gases to boundary layer bleed areas on missile skin or control surfaces. Permutations are, apparently, endless and depend upon the immediate need and the resourcefulness of the designer.

An attempt is made to detail concepts, together with appropriate applications, in the following sections.

Secondary Injection

Figure 8 shows a diagrammatic sketch of a supersonic bistable device installed in the vicinity of the exhaust nozzle of a substantial missile. The mode of operation is reasonably evident. Combustion chamber products are bled off on a continuous basis to a series of possibly four bistable devices which are operated either in a 'bang-bang' or pulse width modulated mode directly in response to gyro stabilisation or guidance control demands. A typical design consists of the required number of amplifiers being vented to the atmosphere by small, electrically operated solenoids; the basic power pack being batteries rated at 30 volts and 1 amp for a duration of at least six seconds.

The type of device required for this application demands special attention to the design of exhaust impedance, etc, for, invariably, the point of injection into the missile main thrust nozzle is at elevated pressures in comparison with prevailing atmospheric conditions.

Typical design requirements are:

Valve supply pressure	1000 - 1500 psia
Inlet Temperature	5000 - 6000°F
Pressure (impedance) at point of injection into missile nozzle	150 - 500 psia
Range of ambient pressure to be incorporated	14.7 - 8 psia

Ordinarily, secondary injection control concepts may be subdivided into four basic derivations dependent upon auxiliary power source:

- (a) hot gas (4000 - 6000°F)
- (b) warm gas (below 2500°F)
- (c) cold gas (ambient temperature)
- (d) liquid (ambient temperature)

(a) infers tapping main engine; (b) and (c) ordinarily infer the carriage of a secondary charge and (d) entails a regulated gas/liquid accumulator system or possibly tapping of main fuel tanks.

Therefore, questions may be raised regarding the efficiency and durability of a system which incorporates a continuous demand cycle, e.g. flow through the device is continuous immediately upon ignition of main propulsion system. Figure 9 shows the results of a parametric study relating to a hypothetical missile rated at 30,000 - 50,000 lbs. of boost thrust requiring control thrusts ranging from 150-500 lbs. over a period of some six seconds.

It may be seen that cold gas shows the least advantage in overall weight of the control system and hot gas bleed the most economical. All systems shown which may be controlled in a discontinuous manner, i.e. lending themselves to control by normal on/off valves, are rated at a 40% duty cycle whereas warm gas and hot gas systems are considered on a 100% basis. The total weight of a two axis, battery source, hot gas system designed to satisfy the above requirements approximates to 24 lbs.

It may be noted from Figure 8 the redundant gases emitted by the valve are being exhausted in the axial sense. In reality, some additional advantage may be obtained by venting tangentially through the skin of the missile. A combined secondary injection jet reaction system is, thereby obtained.

A monostable design has been conceived which satisfies the control requirements detailed above and offers the obvious advantages of halving the actuating requirements, i.e. only one electrically operated solenoid system is required per hot gas valve. A system of intrinsic, passive pressure feed forward is required to overcome transverse impedance problems occurring within the valve and the imposition of adverse fluctuation in atmospheric pressure. It is worth noting that all systems using warm or hot gas as the power medium impose penalties associated with accumulated debris resulting from combustion. Apart from 'clogging' fierce erosion usually occurs and new materials or methods of manufacture have had to be developed in concert with application of fluoric control. Figure 10 shows a device which underwent warm gas testing for a period of four minutes indicating that adequate directional control of exhaust material may be obtained for quite considerable periods by the use of carbon base materials.

Jet Reaction Steering

Simple jet reaction steering involves reversing the secondary injection design, i.e. exhausting gas through missile skin for a control phase and axially when in the passive situation. The mass flow involved are larger than those required in the B.L.I.C. concept mentioned previously as substantial lateral thrusts are required to perform abrupt engagement manoeuvres. As before, some augmentation from skin boundary layer interference is always in evidence but the larger percentage of power is derived from momentum considerations.

The design of such a valve is simple and quite straightforward and may be derived from curves typified by Figure 11 due principally to the fact that exhaust log impedances are, to all intents and purposes, similar, thereby obviating the need for applying specialised matching techniques. The device may be designed to be self-compensating for altitude changes by judicious selection of geometric parameters and, in consequence, successful first time operation may be expected.

Boundary Layer Interference Control (B.L.I.C.)

Figure 12 shows a further variation on a theme and combines jet reaction steering with boundary layer interference control. It should be noted that only one wall exists in the device. The exhaust flux from the monostable amplifiers provides some degree of lateral thrust by integrating rate of change of momentum per unit time but provides a larger measure of thrust augmentation due to its effect on boundary layer flow over the missile skin. The exhaust flux essentially exerts a similar influence to the imposition of an obstruction in the external stream, effectively damming the local flow resulting in a pressure rise upstream of outlet orifice which, in turn, creates a transverse force on the missile.

Such a system could have application to a trim/glide duty cycle requirement after boost phase has been completed, as gas requirements are relatively small. A demonstration prototype missile system is shown in Figure 13.

Exhaust Flux Control

All the devices discussed above involve the control and utilisation of gases undergoing two dimensional expansion, a logical expansion of the effort is obviously the development of three dimensional systems. A specific example is the direct control of missile main nozzle exhaust flux, the method involved being as follows.

The exhaust nozzle is designed for gross over-expansion permitting not only separation but subsequent reattachment to take place: an obvious method being to increase the overall length of the nozzle to a scale appropriate with achieving the necessary degree of expansion and stability of reattachment.

Conventional nozzles consist of circular cross section and, although the phenomenon still applies, reattachment can occur anywhere around the wall thereby making thrust vector control extremely complicated, if not impossible. The feasibility of obtaining missile thrust vector control by means of boundary layer control in an over-expanded nozzle was first demonstrated in a device of square cross section in the U.K. in 1964. The results are shown, diagrammatically, in Figure 14. It may be seen that the exhaust gas tended to attach to one of the sides of the nozzle and, although remaining discreet suffered from lack of integrity resulting in low thrust efficiency. Furthermore, although switching by atmospheric venting was shown to be possible the control ports tended to be large with obvious consequences on actuator design.

Rounding of the corners produced a most interesting and important result. The gas jet adhered to one of the corners, as shown in Figure 15, maintaining a high degree of integrity and, hence, controllability. It may be seen from the Figure that the exhaust jet always offers allegiance to the control port which is closed, the other three remaining open. Switching is effected in the usual manner simply by closing vent to which jet is required to adhere simultaneously with opening vent in the corner to which it is already attached.

In a correctly designed application switching time is limited only by the response of the control system and not by the inertia of the gas attachment phenomenon itself. Figure 16 shows a series of geometric shapes which have undergone exploratory tests and Figure 17 indicates the degree of control which may be exercised over such a device simply by closing the appropriate control vent to the atmosphere by the application of finger pressure alone. Other designs have been tested which offer advantages in terms of nozzle length and efficiency but these may not be offered for general publication.

Significant advantages offered by the above system include high lateral thrust generation, immense power gains and fast response. Figure 18 shows the results of tests completed to date with a nozzle of specific design and range of expansion angles. Lateral to axial thrust ratios of 30% are indicated with negligible input control demands. Typically, a missile exerting 6000 lbs. of thrust on boost has a 1500 lbs. lateral thrust capability using this method providing the designer with an unusual headache as, ordinarily, control systems exert too little rather than too much influence on missile guidance.

Perhaps the most significant result applicable to this area of activity is the relatively high axial thrust efficiency to be obtained despite the gross deviation from accepted design principles which normally apply to thrust nozzles. Furthermore, a correctly designed system is self-compensating for changes in altitude and, therefore, has direct applicability to air to air combat missiles.

Boundary Layer Lift and Thrust Augmentation

In parallel with the fluidic device type developments referenced above, a high degree of experimental effort has been applied to the effect of supersonic gas flows on aerofoil type sections with particular emphasis on the generation and control of lift. Figure 19 shows a cross-section through a circular flat plate over which gas at supersonic velocity is allowed to expand. The resulting pressure profile, although three dimensional, is to all intents and purposes identical to that detailed in previous Sections.

Integration of the shaded area determines the vertical thrust generated by exhausting gases in this way. Generating lift by this method is relatively inefficient with respect to direct thrust; the former having an $F/P_o A_t$ of approximately 0.5 which is to be compared with 1.3 - 1.4 for an adapted bell-mouthed nozzle

where

- F = vertical thrust
- P_o = stagnation supply pressure
- A_t = area of throat

If, however, the flat plate is replaced by a conical surface the value increases to 0.7. Theory has shown that free three dimensional expansion cannot compare in lift efficiency with two dimensional flow hence the device shown in Figure 20 has been investigated. Optimisation of the geometric profile involved in generating lift has formed the basis of the effort involved.

$F/P_0/A_f$ values in the range 1.3 - 1.4 have been recorded with specific profiles over a range of pressures P_0 of 80 psi to 550 psi. Due to the anticipated application efforts were centralised around 130 psi which could logically be generated by a gas turbine compressor bleed system. Although the thrust factors measured compare favourably with those generally hoped for in a well designed nozzle, the main area of interest is in the method available to control lift and with it attitude.

Attitude Control

The nature of the basic vehicle design promotes a neutrally stable situation in hover. The four leg cruciform configuration allows two axis attitude control to be readily effected by varying the lift on one or more of the appropriate lift surfaces. This is accomplished by venting the low pressure region on the lifting surface to atmospheric pressure with simple vent valves which can be proportionally controlled in a continuous or time modulated manner. The nature of jet attachment to the lifting surface is such that the switch from the lift mode to the vent mode can occur in 0.001 second. Assuming axis designations similar to those on conventional manned aircraft the lift surface control described above can rotate the vehicle about its pitch and roll axes. Yaw control can be effected with small bleed jets or trim tabs in the compressor bleed air flow or turbine discharge gas flow. Figure 21 shows an artist's impression of a man carrying vehicle considered suitable for forward area surveillance.

Advantages

Assuming that a gas turbine system formed the basis of the lift vehicle shown the control technique involved offers advantages of simplicity, cost and response time over alternative developments, e.g. helicopter, jet thrust control and augmentation, etc.

The engine could be 'run up' to cruise speed relatively slowly on a comparatively simple acceleration schedule with all control vents open. Although the engine would be developing full power corresponding thrust would be insufficient to cause lift off. Closure of vents would provide a step input of thrust causing lift off to occur in approximately three milliseconds. Horizontal flight would be generated by inclining vehicle in required direction of motion simply by time modulation of the control ports. Altitude control would be similarly effected.

A further advantage of the device is, of course, the lack of rotor and transmission equipment required which very frequently accounts for a

substantial proportion of the overall cost of any vertical lift machine. The vehicle is unlikely to present any constructional difficulties and it must be assumed that it could be easily concealed and stored on board a vessel or vehicle. Figure 22 gives an indication of the flight envelope which may be expected from the simplest design. Figure 23 gives an estimate of related costs between this device and the helicopter. Further information regarding anticipated pay load to fuel load ratio is provided in Figure 24. In fairness it must be stated that the helicopter shows distinct advantages over any vertical lift machine using direct thrust with respect to fuel consumption. To the author's knowledge, apart from fixed wing aircraft, there is no way of competing with the lift capabilities of a well designed rotor system.

A substantial quantity of research has been applied to optimising the expansion surface with respect to generating lift. However, a great deal remains to be evaluated, particularly with respect to the effect of vehicle/wind velocity - an attachment phenomenon.

OTHER APPLICATIONS

Lift augmentation for aircraft faced with the problem of landing on short runways at high elevation, pressure ratio sensing, flow measurement and control, power actuation, etc, are all within the scope of involvement. As an example, consider Figure 25 jet attachment through an angle of 90° is shown to be quite stable for a range of geometric parameters and pressure ratios, indicating that thrust directional control may be obtained with some gain in economy over more conventional methods thereby providing perhaps a broader spectrum of design possibilities.

It is postulated that the range of application of the phenomenon discussed in this paper is limited only by the skill and ingenuity of the engineer involved and if some interest has been kindled the effort has been worthwhile.

ACKNOWLEDGEMENT

The Author wishes to record his appreciation to the Management of Chandler Evans Inc., West Hartford, Connecticut, U.S.A. for permission to publish certain illustrations contained within this paper.

APPENDIX

BRIEF THEORETICAL PREMISE

Invoking the assumption that the boundary layer reaches a position of constant velocity at the point of incipient separation, i.e. true physical separation occurring at subsequent deceleration condition a solution may be evolved as follows.

The two dimensional Navier Stokes equations may be simplified to the extent of equating rate of change of momentum to the resisting force created across a plane perpendicular to the boundary layer flow direction between the limits of $y = 0$ to $y = \delta_s$ where δ_s is equal to the transverse boundary layer displacement to the sonic stream line from the solid boundary. This results in the expression

$$\rho U^2 / (n+2) M^2 = p_b - p \quad \text{--- (1)}$$

where M = the Mach No. corresponding to incipient separation

ρ = local density

n = the power index of similarity profile

U = main stream velocity corresponding with M

p = local pressure, i.e. corresponding to M

Eliminating ρU and p in terms of Mach No. and stagnation supply pressure P_0 by utilising the adiabatic, isentropic identities and universal gas equation, expression (1) becomes

$$M^2 = 2 \left\{ \left[\frac{kn}{(n+2)} + 1 \right] \cdot (P_0/p_a)^{1/k} - 1 \right\} / (k-1) \quad \text{--- (2)}$$

where k = ratio of specific heats.

For turbulent boundary layer flow with air as the base fluid $n = 7$, $k = 1.4$ and (2) simplifies to

$$[6.17 (P_0/p_a)^{0.286} - 5]^{0.5} = M \quad \text{--- (3)}$$

Substitution of the overall pressure ratio (P_0/p_a) acting upon a supersonic fluidic device results in a value for the main stream Mach No. at the point of boundary layer incipient separation. Worthy of note is that a 40% change in n results in a variation of the Mach No. M of only 1%.

The actual position of incipient separation may be found by substituting determine value of M in the following expressions.

$$\frac{A}{A_t} = \left\{ 1 + \frac{[(k-1)/2] M^2}{(k+1)/2} \right\}^{(k+1)/2 (k-1)} \frac{1}{M} \quad (4)$$

$$a = (A/A_t - 1) t_n/2 \quad (5)$$

$$x_t = a \operatorname{cosec} (\alpha/2) \quad (6)$$

where x_t = distance to point of separation along divergent wall
measured from throat

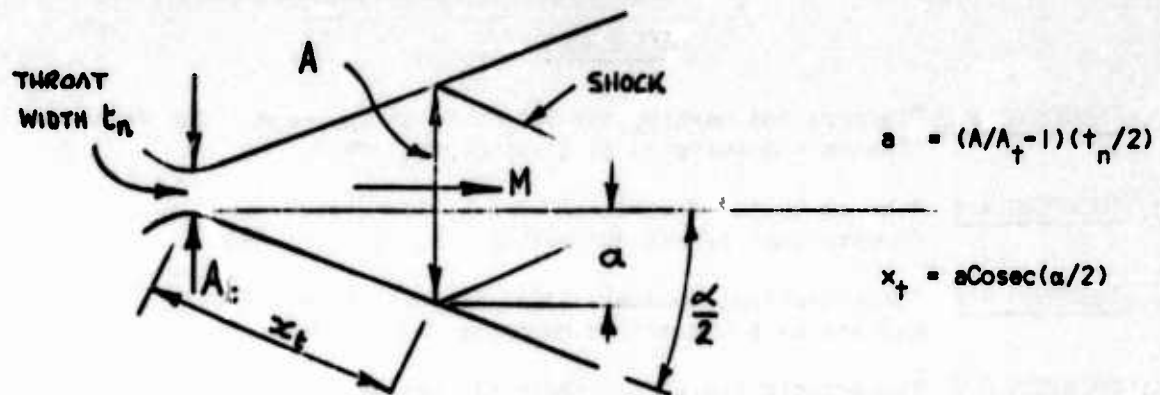
A_t = Area of throat

t_n = Throat width

α = Total divergent angle

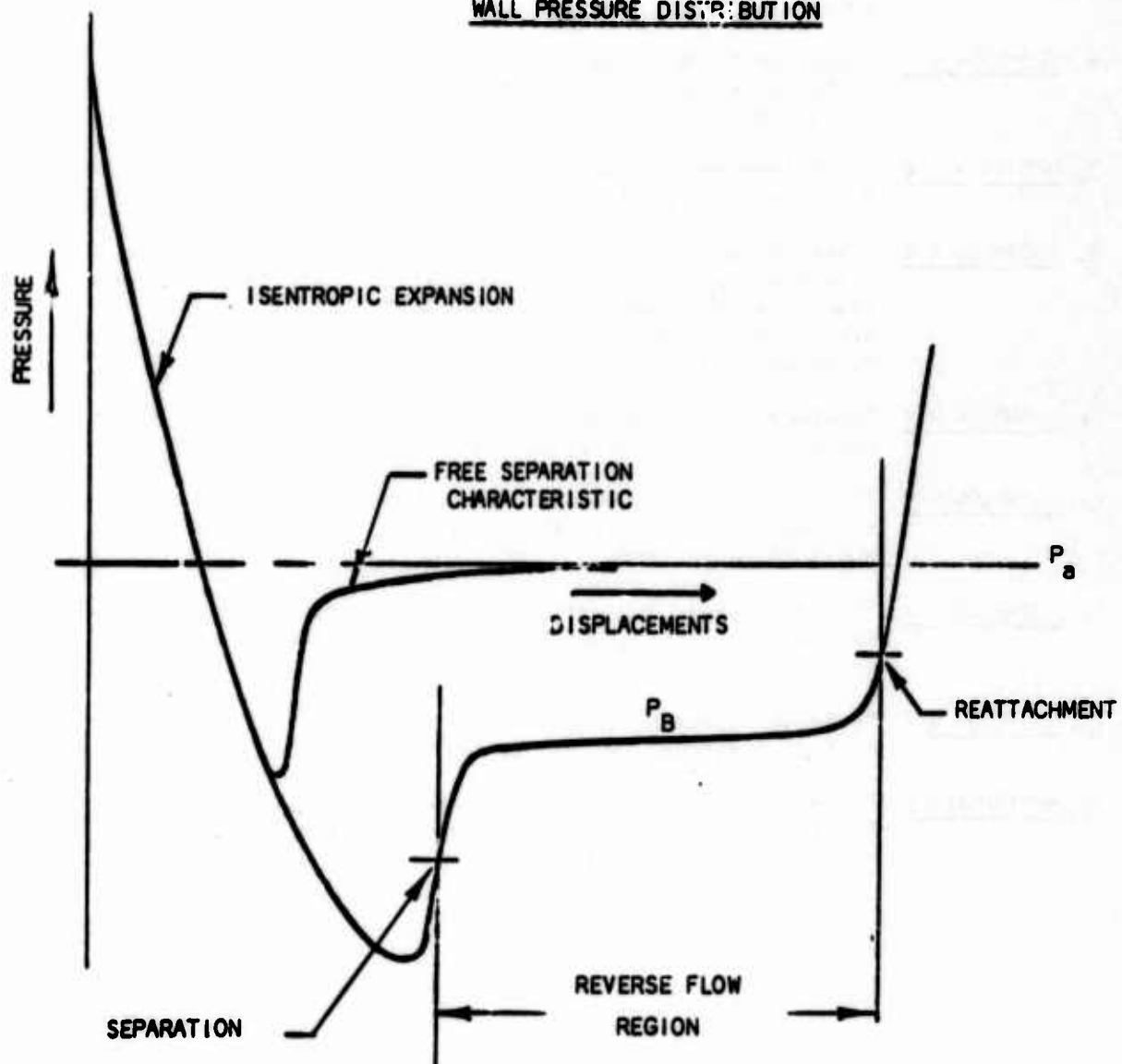
The total flow situation occurring in the supersonic bistable device may be further evaluated by solving the curved shock/main flow compatibility situation caused by the separation of the boundary layer from the free wall i.e. that wall having separation not followed by reattachment. Impingement of the curved shock on the opposite wall causes separation to occur prior to this point which will cause, in turn, a further oblique shock to be generated as shown in Figure 3. This resultant shock interacts with the original curved shock tending to increase the radius of curvature, resulting in a minor shift of the reattachment point which modifies the whole situation in a process akin to a control feedback compensating loop. Fortunately, convergence is rapid and the number of iterations of the shock equations required is small.

Applying to a convergent divergent duct



where x_t = distance from throat to position of separation. Derived pressure profile shown in the following Figure.

WALL PRESSURE DISTRIBUTION



REFERENCES

1. THOMPSON R V "Factors Influencing the Switching of Supersonic Gas Jets"
Thesis - University of Strathclyde 1967
2. THOMPSON R V "Thrust Vector Control and the Fluid Switch"
Process Control and Automation 13, 7, 37, 1966
3. THOMPSON R V "Understanding Boundary Layer Separation in a Fluid Switch"
Hydraulics & Pneumatics Magazine March 1968
4. THOMPSON R V "Supersonic Fluidics: Empirical Design Data"
4th International Conference on Fluidics - Coventry
March 1970
5. THOMPSON R V "The Switching of Supersonic Gas Jets by Atmospheric
Venting" 2nd Cranfield Fluidics Conference - Cambridge
January 1967
6. THOMPSON R V "Experiments Relating to Pressure Recovery in Supersonic
Bistable Switches" 3rd Cranfield Fluidics Conference -
Turin May 1968
7. MARTIN A P W "Some Improvements to the Supersonic Bistable Switch"
4th Cranfield Fluidics Conference March 1970
8. THOMPSON R V "Theoretical Determination of the Point of Separation in a
Compressible, Turbulent, Supersonic Boundary Layer Sub-
jected to an Adverse Pressure Gradient" Annual A.S.M.E.
Winter Meeting and Energy Systems Exposition - Philadelphia
November 1967
9. THOMPSON R V "Application of Boundary Layer Control to V.T.O.L." A.S.M.E.
University of Hartford, Connecticut November 1969
10. THOMPSON R V "The Phenomenon of Boundary Layer Separation and Reattach-
ment Applied to Fluidics" A.S.T.M.E. Seminar on Fluidics
New York June 1969
11. THOMPSON R V "Boundary Layer Separation Applied to Thrust Vector Control"
Proceedings of E.S.R.O. Summer School, Denmark September
1966
12. THOMPSON R V "A Fresh Approach to Fluid Power Switching" Process
Control & Automation 13, 2, 33 1966
13. WETTERSTAD L "Experimental Investigation of the Pitot Fluidistor and
Other Supersonic Amplifiers" 4th Cranfield Fluidics Con-
ference Coventry March 1970

14. THOMPSON R Y Supersonic Fluidic Switch Patent No. 3570 512
Patented 16th March 1971 Washington U.S.A.
15. THOMPSON R Y Monostable Fluidic Switch Patent No. 3606 901
Patented 21st September 1971 Washington U.S.A.
16. METRAL M "L'effet Coanda" Proceedings 5th International Congress
on Applied Mechanics p.258 1938
17. MULLER H R "A Study of the Dynamic Features of a Wall-reattachment
Amplifier" Fluids Engineering Conference, Philadelphia
18th-21st May 1964
18. SHER N C "Jet Attachment and Switching in Bistable Amplifiers"
Fluids Engineering Conference, Philadelphia, 18-21 May
1964
19. MUELLER T J "An Experimental Investigation of the Reattachment of
Compressible Two-dimensional Jets" Fluids Engineering
Conference, Philadelphia, 18-21 May 1964
20. DUNAWAY and "A Status Report on the Experimental Development of a
AYRE Hot Gas Valve" Proceedings of the Fluid Amplification
Symposium H.D.L. (Washington D.C. 1964) p.459
21. HOLMES and "Supersonic Fluid Amplification with Various Expansion
FOXWELL Ratio Nozzles" Proceedings of the Fluid Amplification
Symposium H.D.L. (Washington D.C. 1965)
22. CAMPAGNUOLO, "Experimental Analysis of Digital Fluoric Amplifiers
C.J. and for Proportional Thrust Control" 2nd Cranfield Fluidics
HOLMES A.B. Conference, Cambridge (Paper K.3) 3rd-5th January 1967
23. DAHLEN G "Further Developments of a Fluidic Injection Valve for
Thrust Vector Control of a Rocket Motor" Svenska Flyg-
motor, A.B. Report No. RF.5:1997 (in Swedish) 15th June
1966
24. WARREN R W "Some Parameters Affecting the Design of Bistable Fluid
Amplifiers" A.S.M.E. Paper
25. HACKER R Unpublished Report to Weapons Division, Royal Aircraft
Establishment Farnborough, Hants.
26. FEHRMANN Technische Hochschule, Institut f. Regelungstechnik,
Karl Marx Stadt, Deutsche Demokratische Republik, March
1967
27. ROSIC R Communications, Thompson Manufacturing Company, Los
Angeles, California 90023, U.S.A.

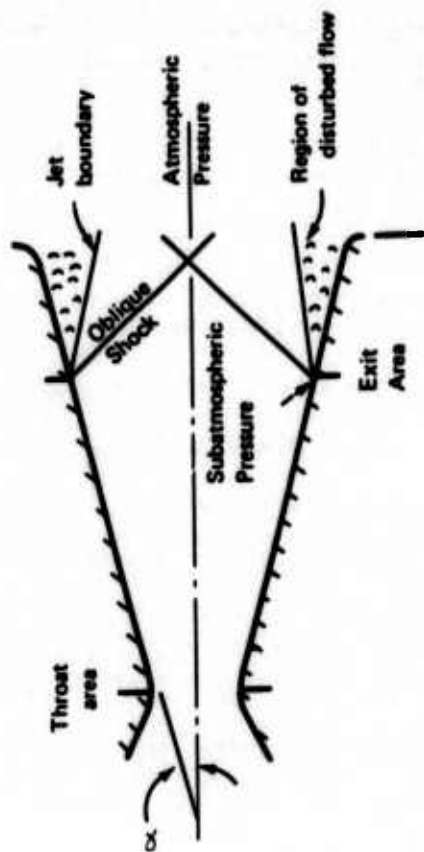


FIG. 1 OVEREXPANDED JET: DIAGRAM OF BOUNDARY LAYER SEPARATION WITH OBLIQUE SHOCK

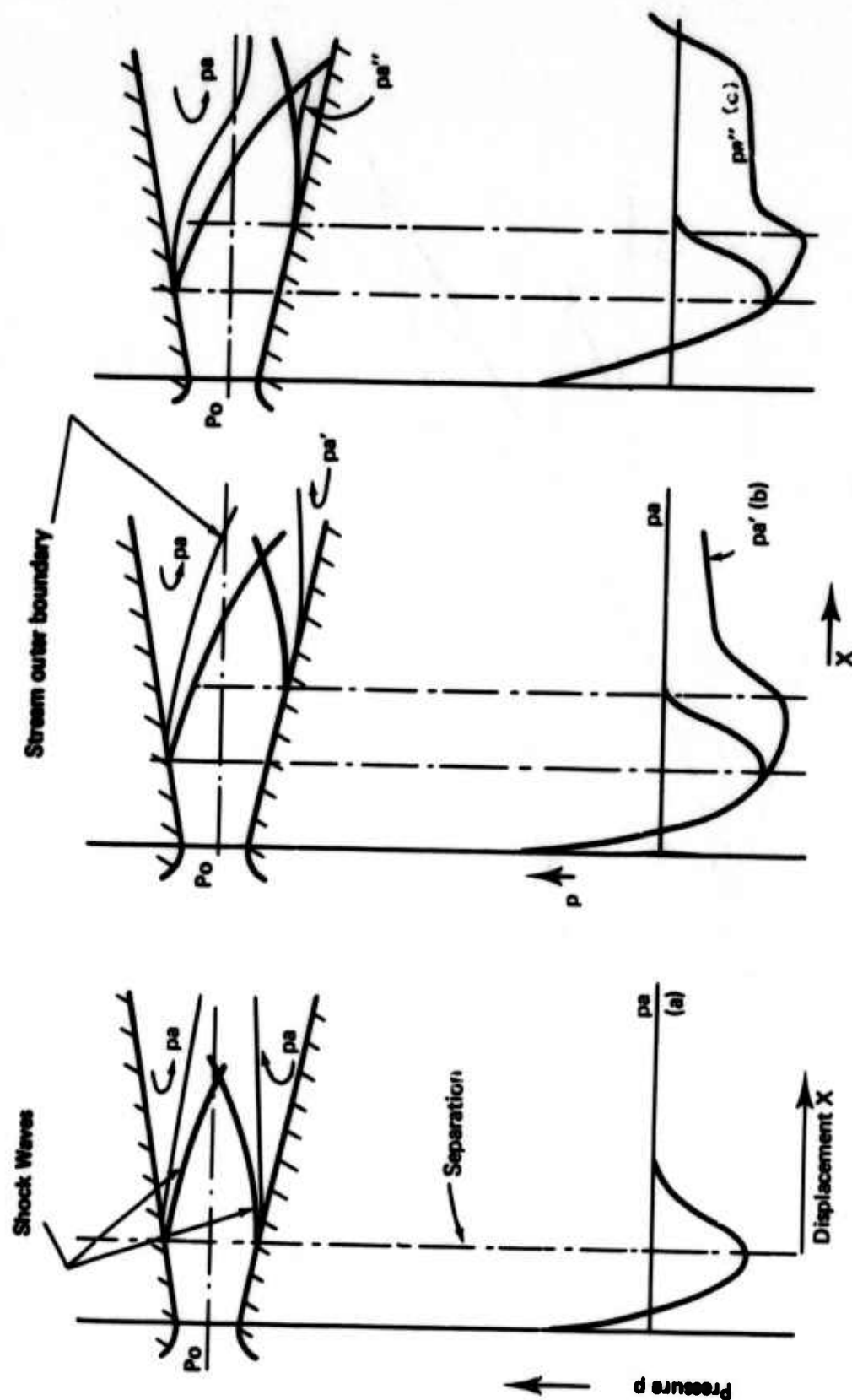
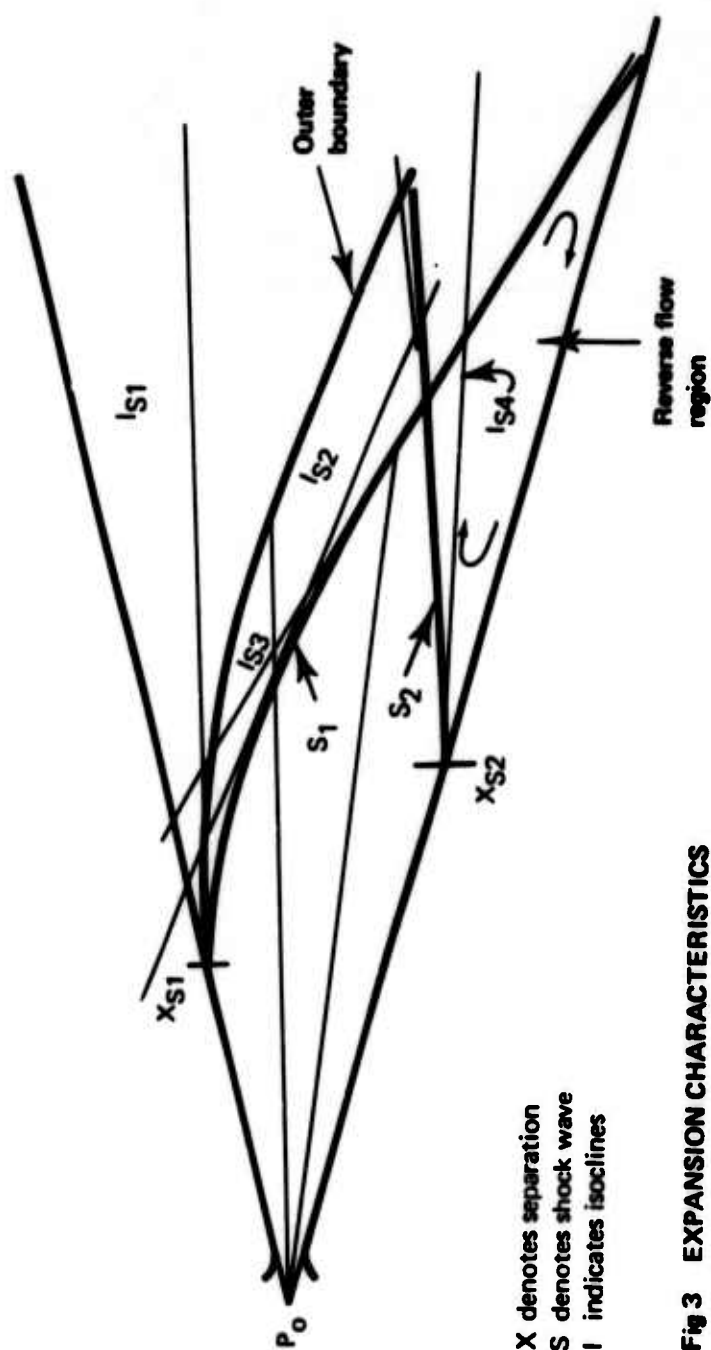
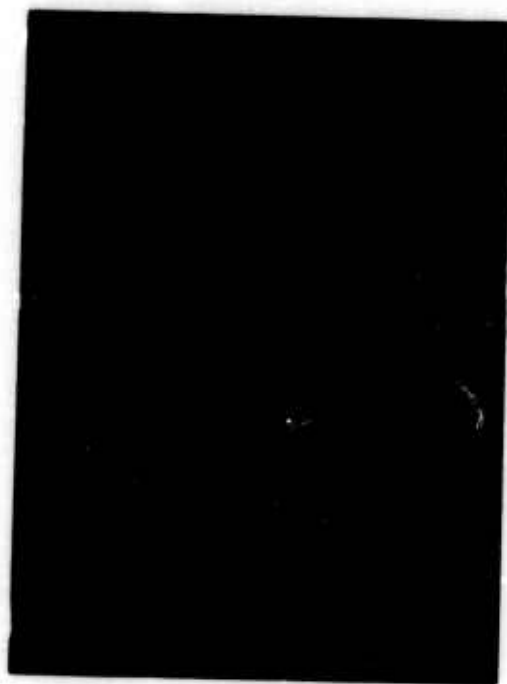


Fig 2 THE RE-ATTACHMENT PROCESS



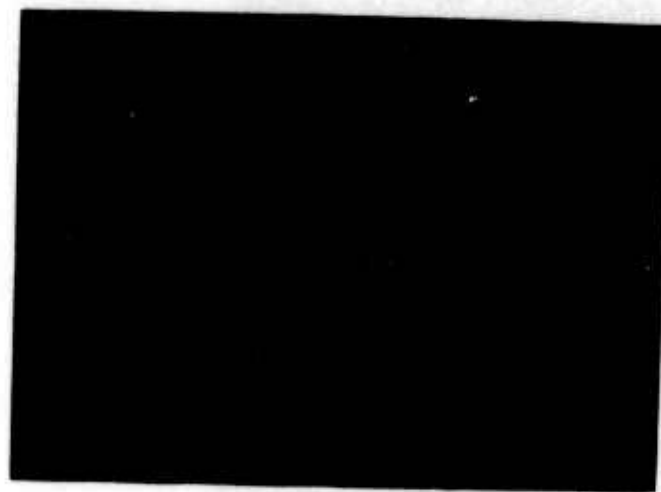
X denotes separation
 S denotes shock wave
 I indicates isoclines

Fig 3 EXPANSION CHARACTERISTICS



SCHILIEREN PHOTOGRAPH
WITH REATTACHMENT

FIGURE 4



Experimental Switch

Figure 5

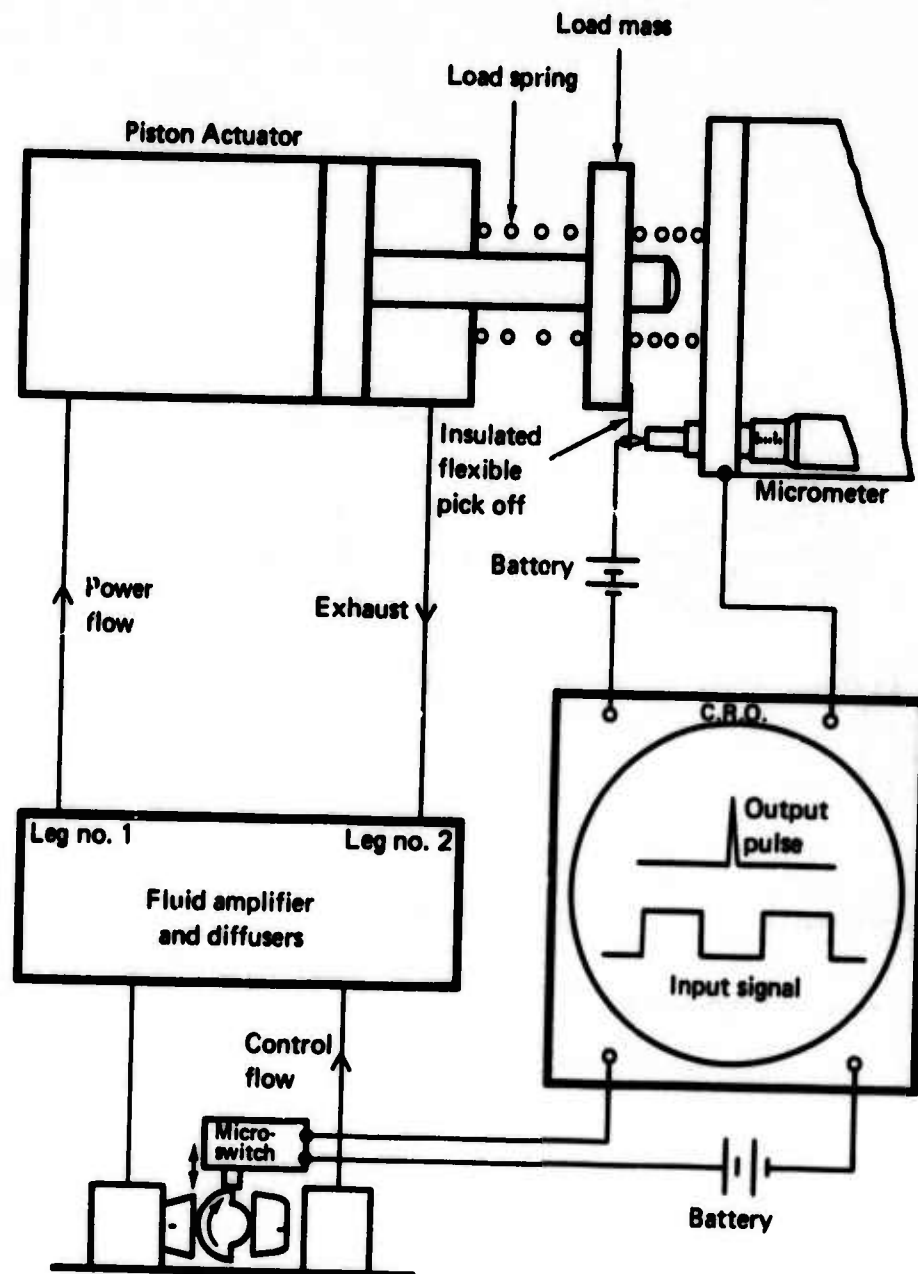


Fig. 6 DIAGRAM OF PRESSURE RECOVERY CIRCUIT



Control Port
Initially Closed



Control Port
Initially Open

Fig 7 SINGLE PORT CONTROL

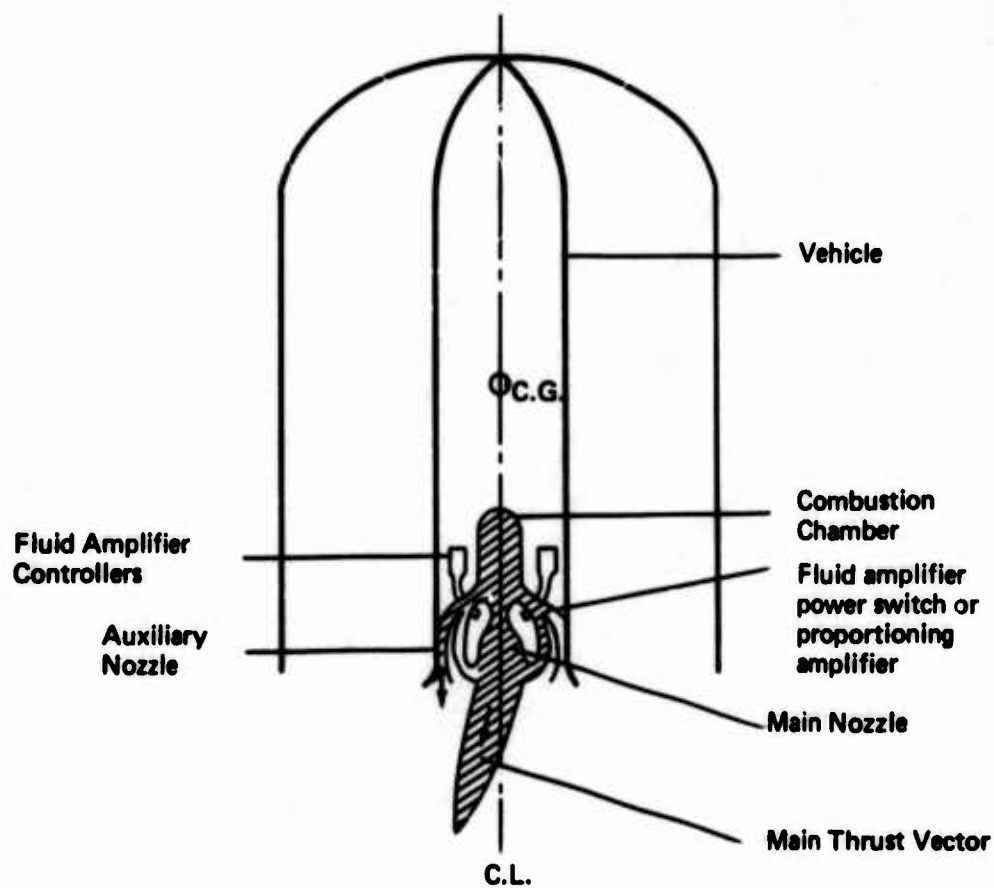


Fig 8 MISSILE WITH SECONDARY INJECTION

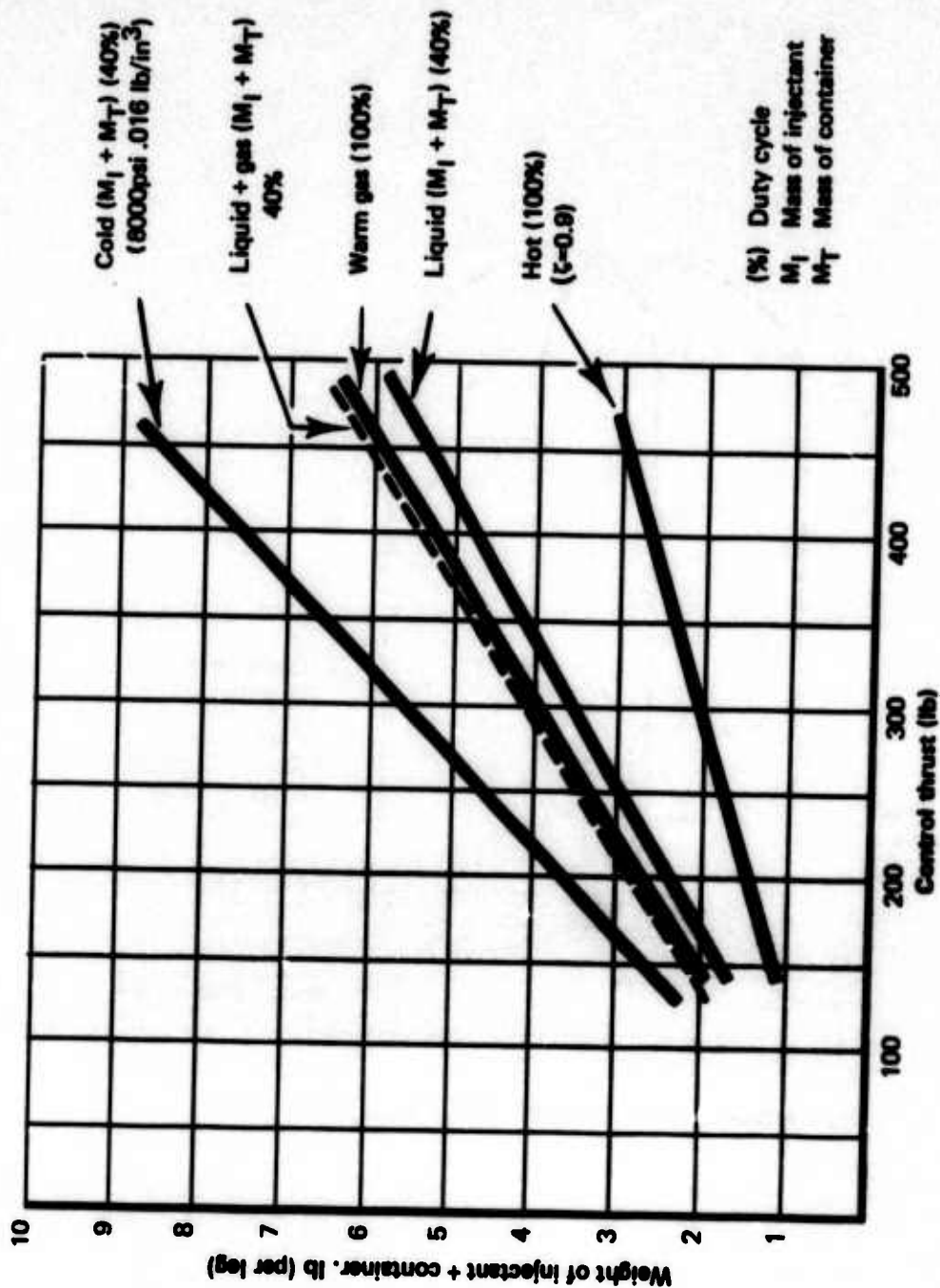
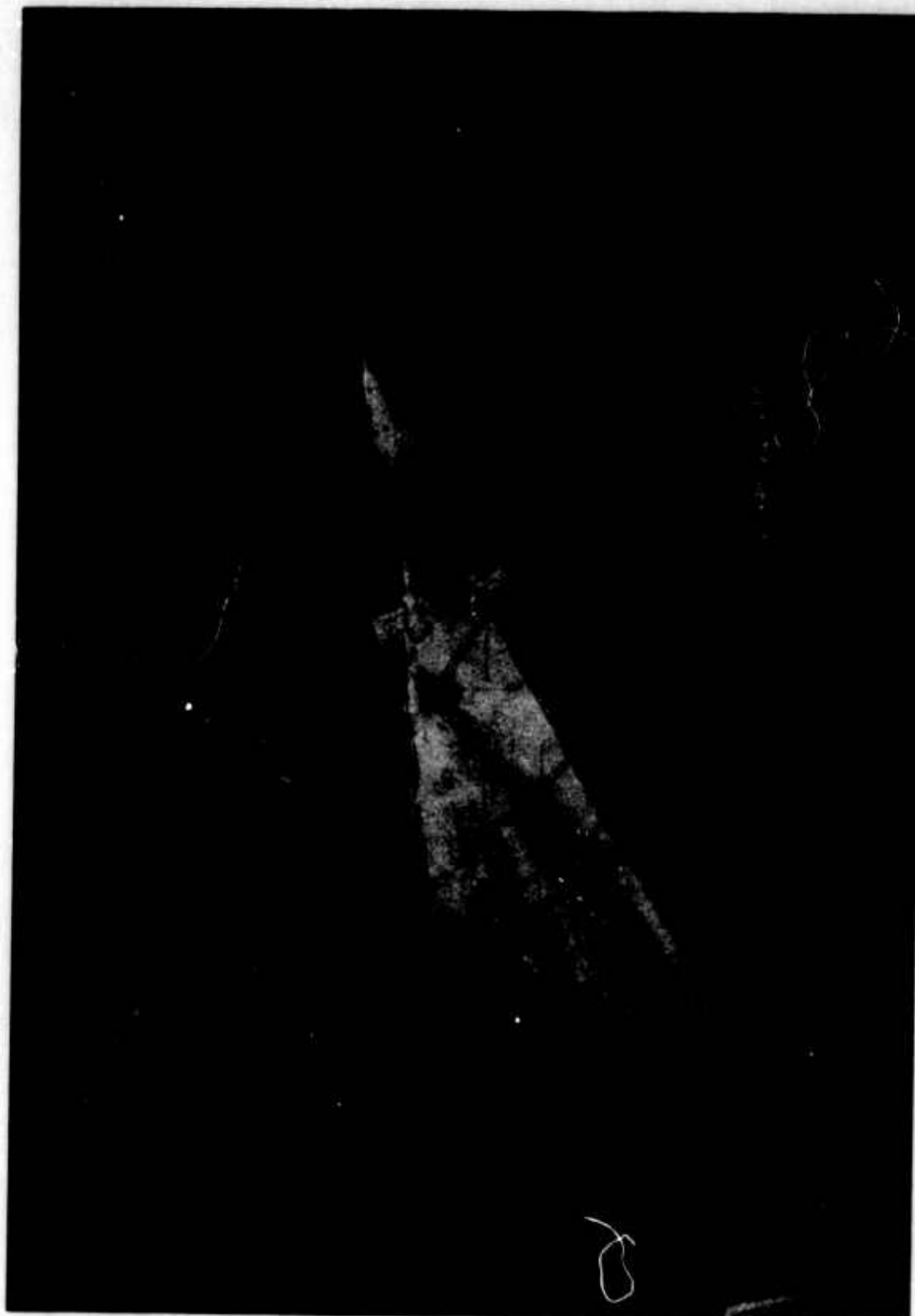


Fig 9 SECONDARY INJECTION: COMPARISON OF PERFORMANCE



'Warm' Gas Device After Test

Figure 10

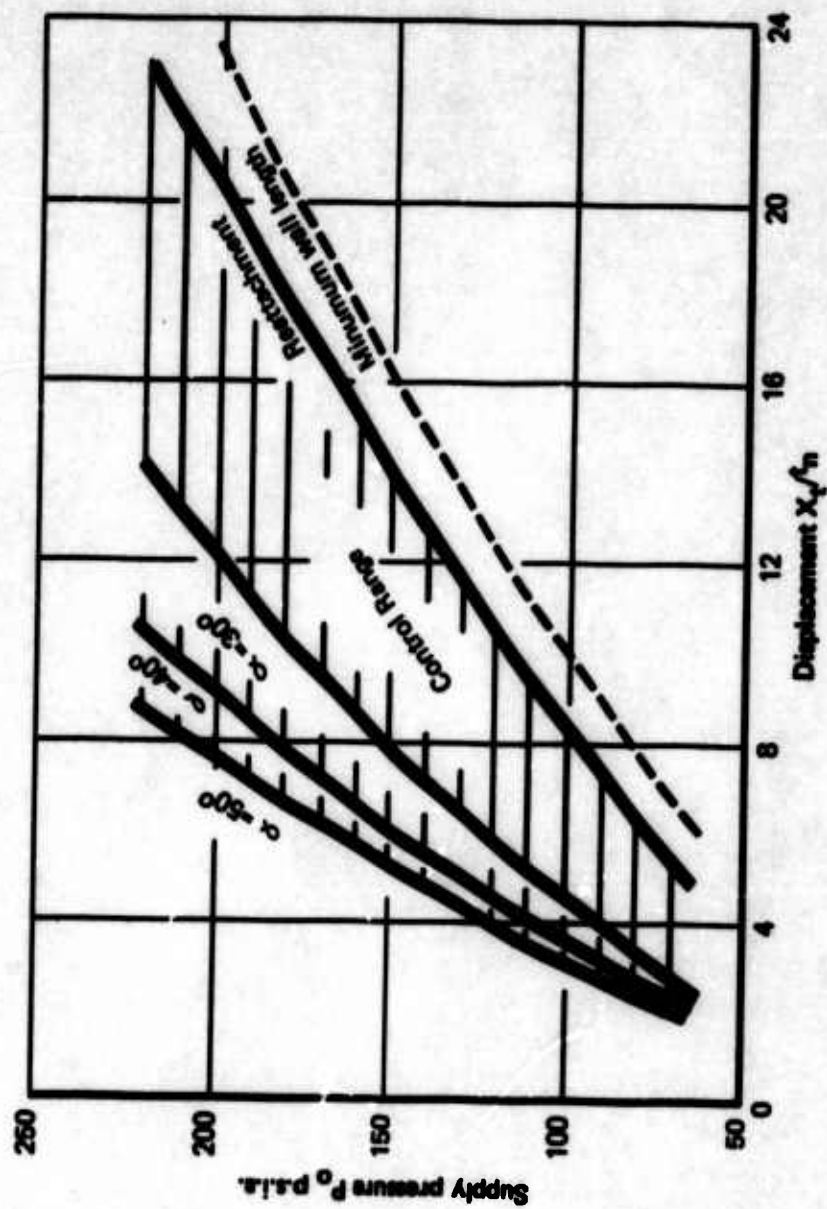


Fig 11 SUPERSONIC BISTABLE SWITCH: BASIC DESIGN CRITERIA

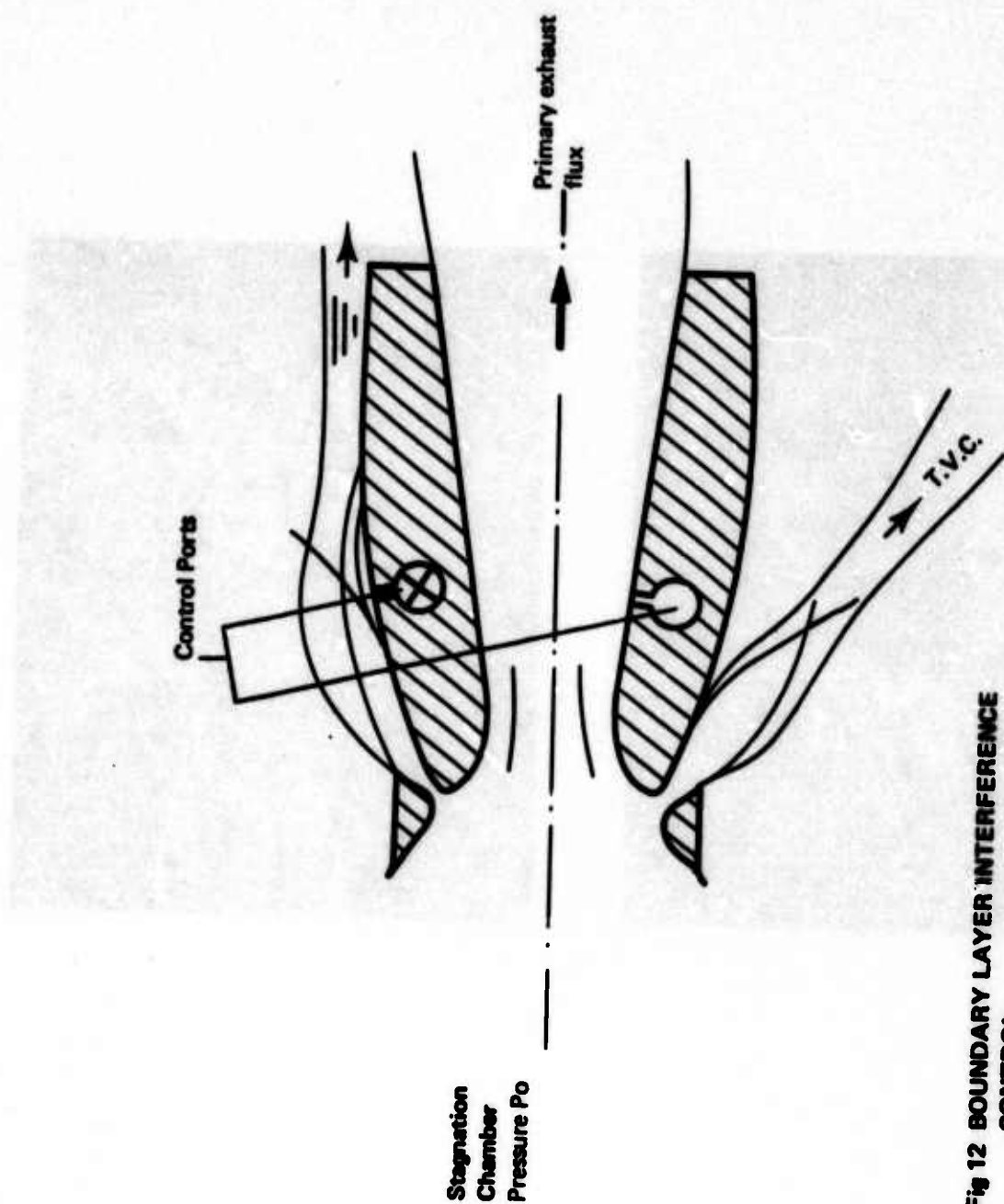
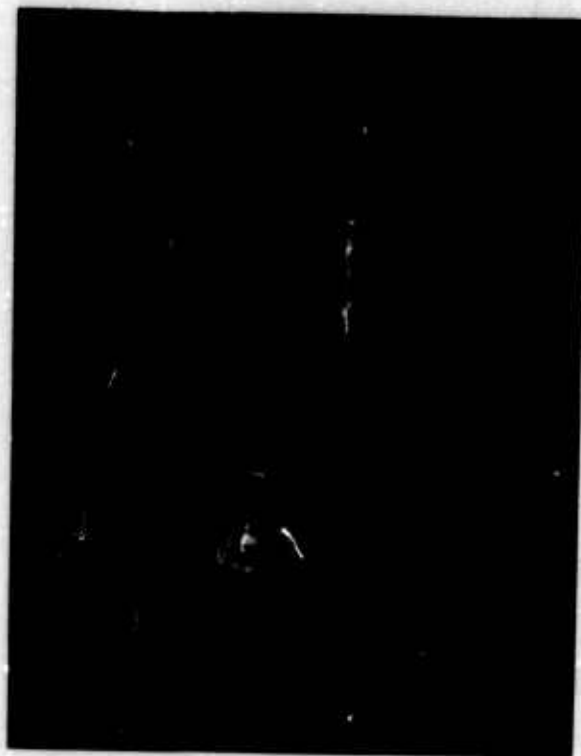


Fig 12 BOUNDARY LAYER INTERFERENCE CONTROL



Prototype Missile Boundary Layer
Interference Control System

Figure 13

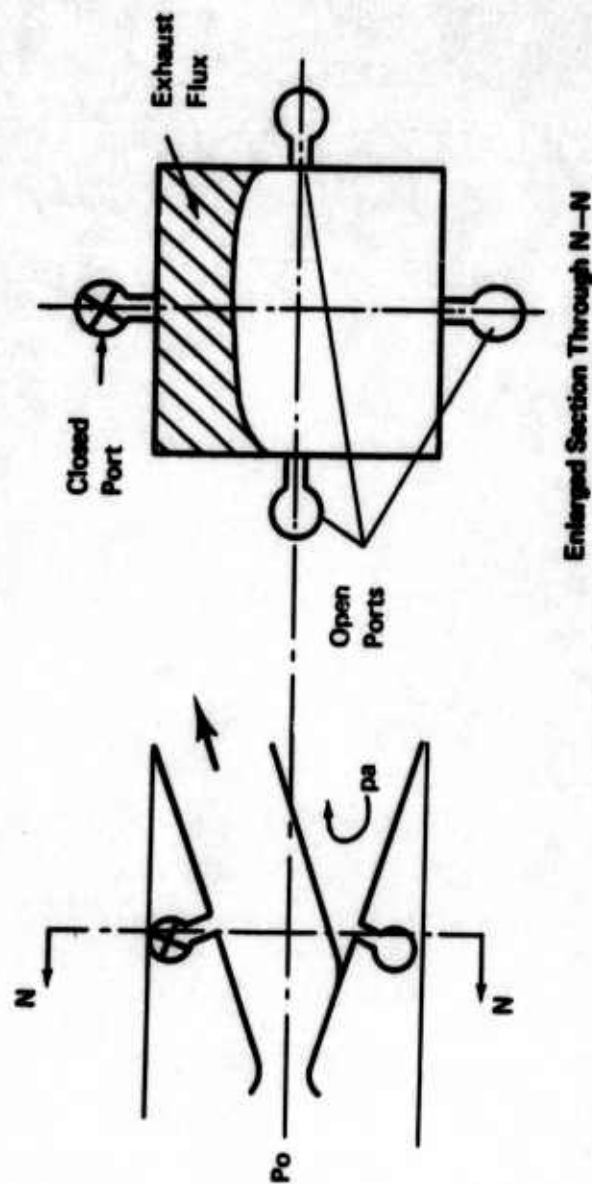


Fig 14 THRUST VECTOR CONTROL: DIAGRAM OF EXHAUST GAS ATTACHMENT AND VECTOR

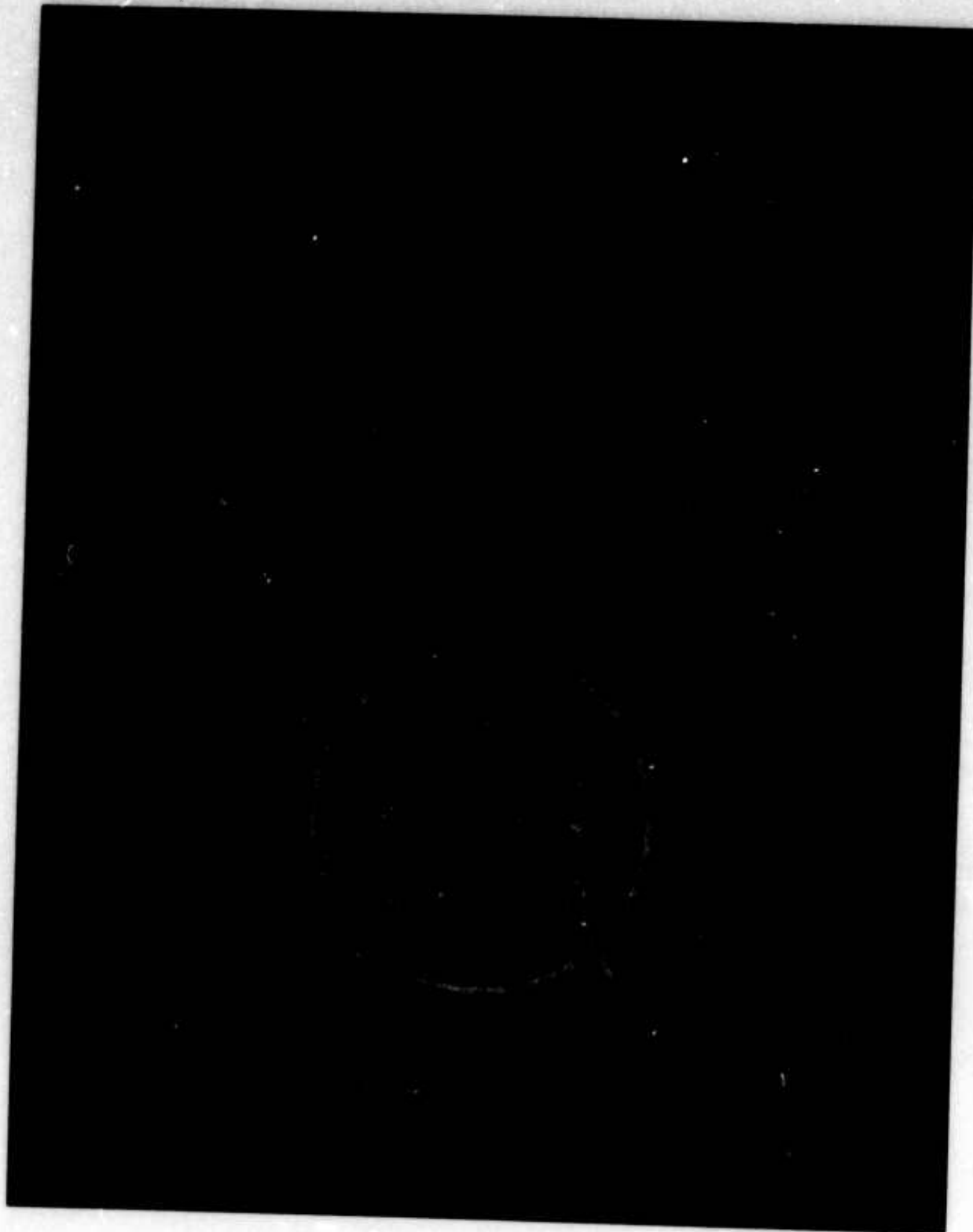


Figure 15



Figure 16. Nozzle Cross-sectional Shapes

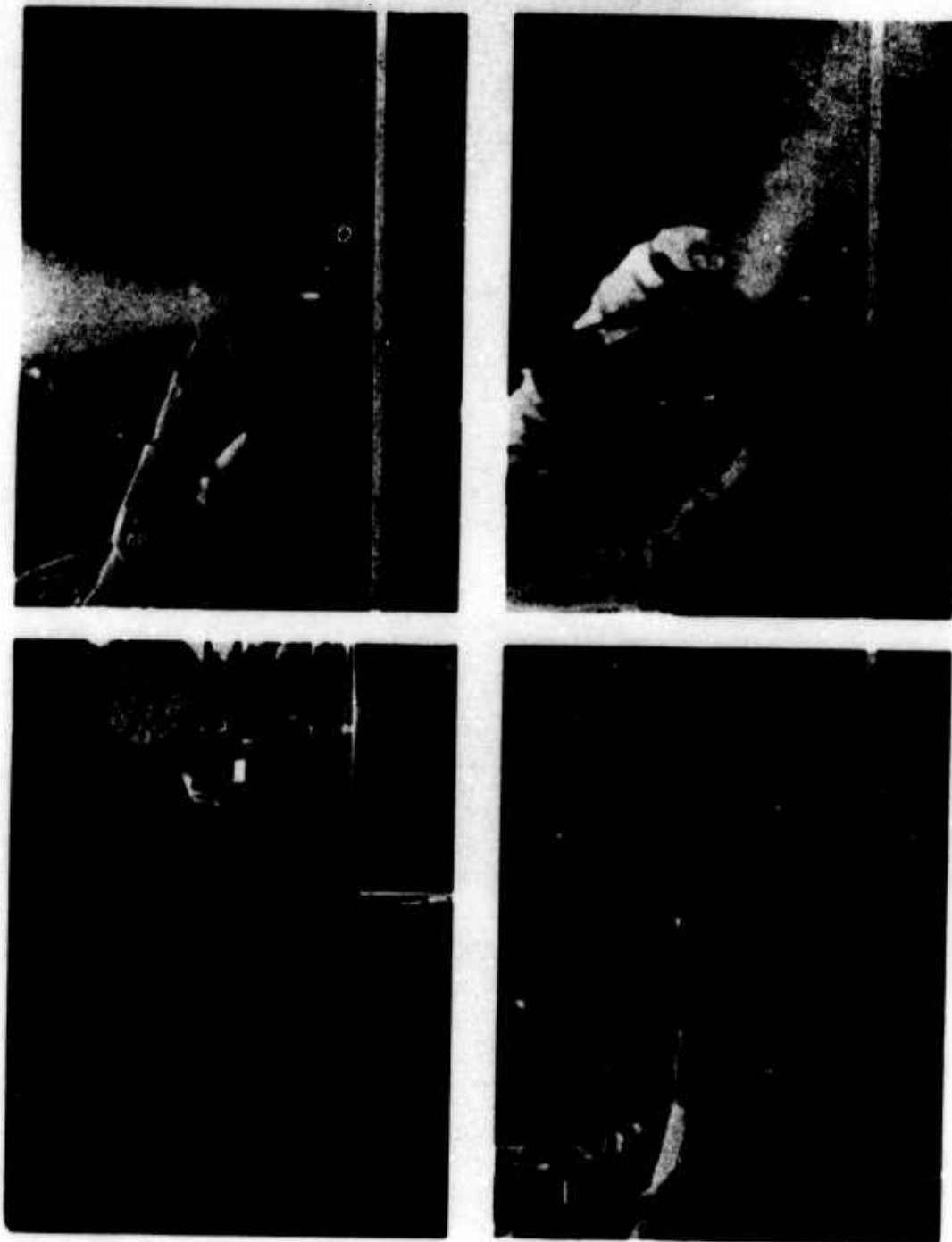


Figure 17. Thrust Vector Control

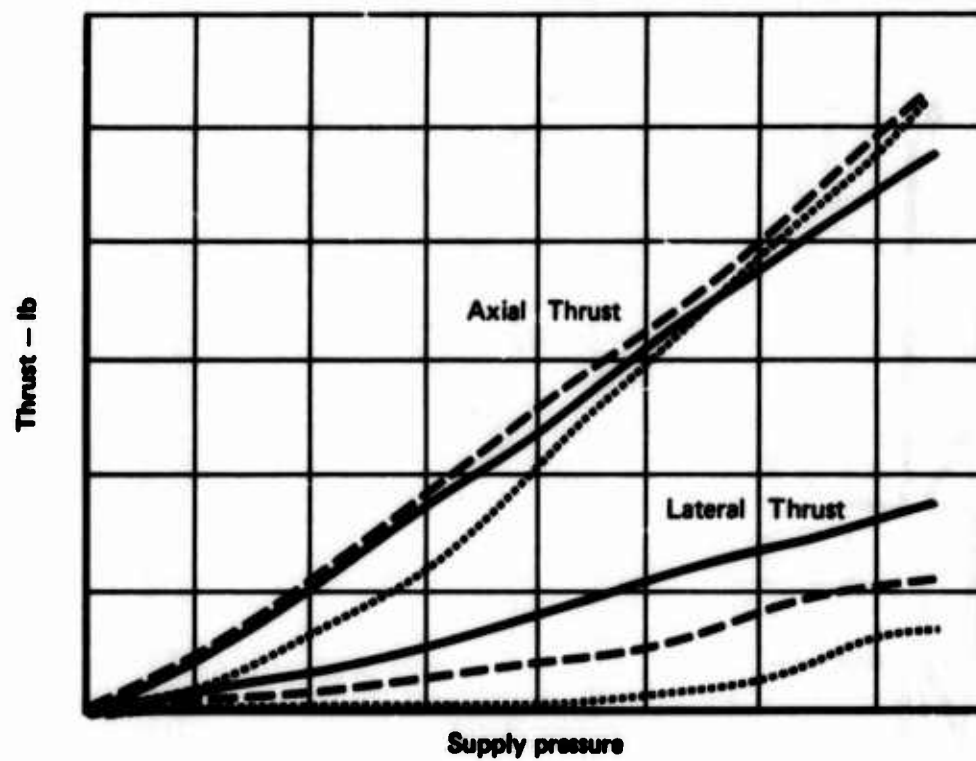


Fig 18 THRUST OF NOZZLES WITH VARIOUS EXPANSION ANGLES

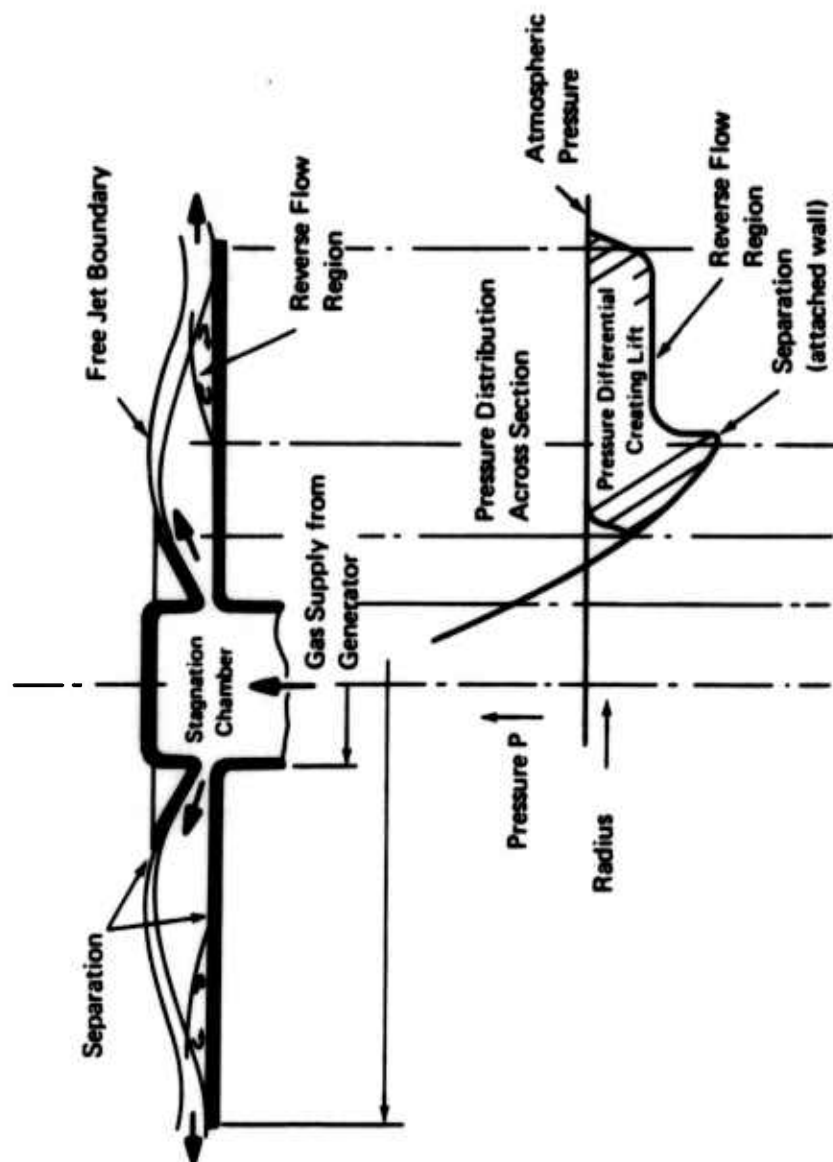


Fig 19 MODEL UTILIZED IN EXPERIMENTAL EVALUATION OF LIFT
GENERATED BY PRESSURE DIFFERENTIAL ALONE

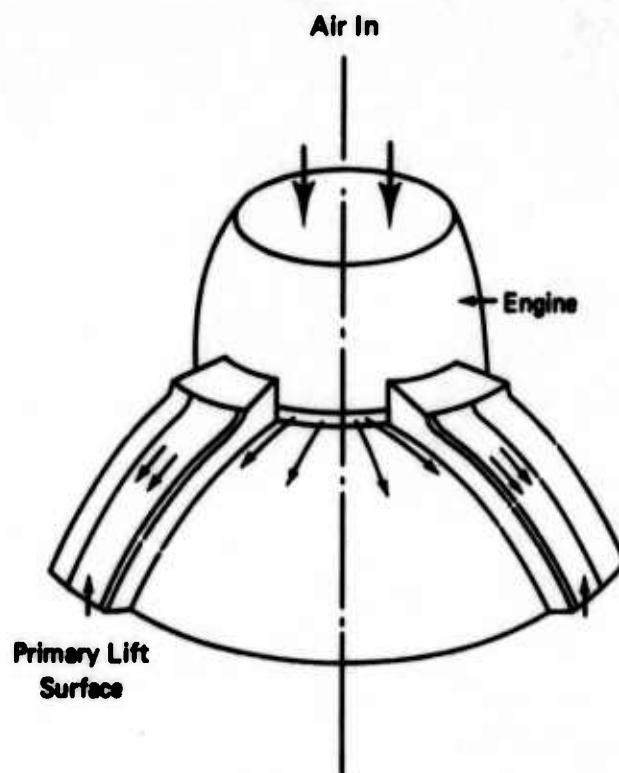


Fig 20 BASIC LIFT VEHICLE CONFIGURATION



FIGURE 21

Lift Factor = Vertical thrust amplification
of lift vehicle concept

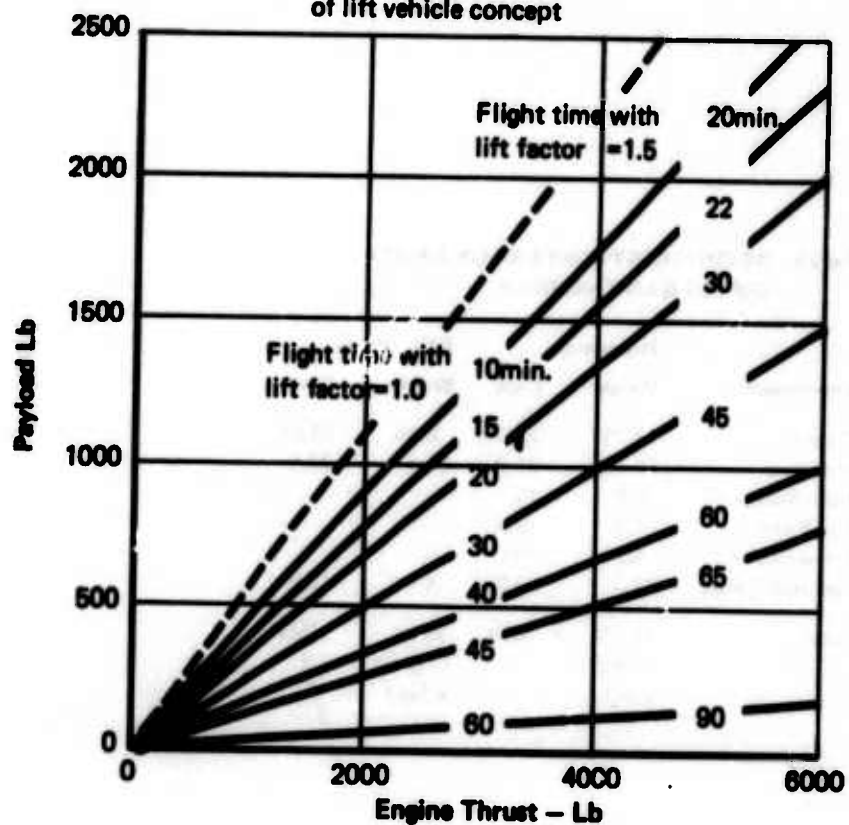


Fig 22 LIFT VEHICLE PAYLOAD

**Fig 23 WEIGHT-COST COMPARISON OF HELI-
COPTER & LIFT VEHICLE**

Component	Helicopter		Lift Vehicle	
	Weight	Cost	Weight	Cost
Engine	7.7%	21.3%	8.4%	53.6%
Structure	24.7%	21.3	26.1	33.5
Main Rotor	8.9	14.3	-	-
Tail Rotor	1.8	2.9	-	-
Transmission	9.9	16.0	-	-
Controls & Misc.	12.0	24.2	4.4	12.9
Total	65.5% of gross weight	100%	38.9% of gross weight	100%

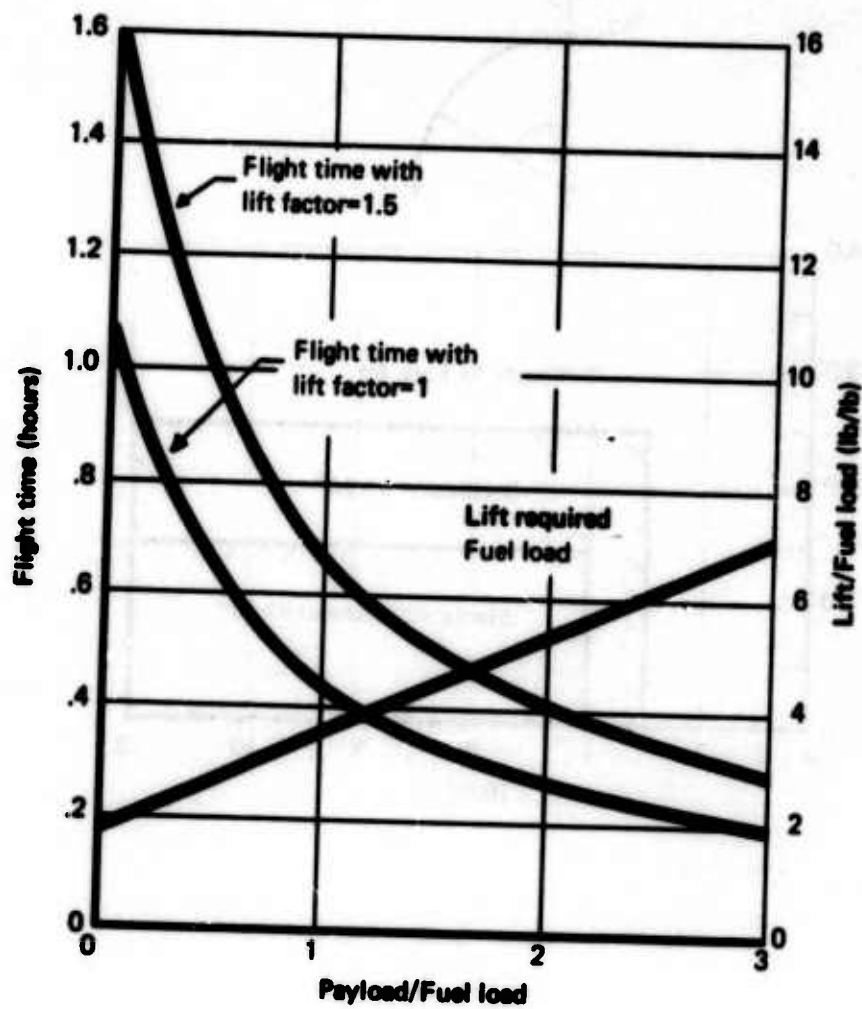


Fig 24 FLIGHT TIME AND LIFT

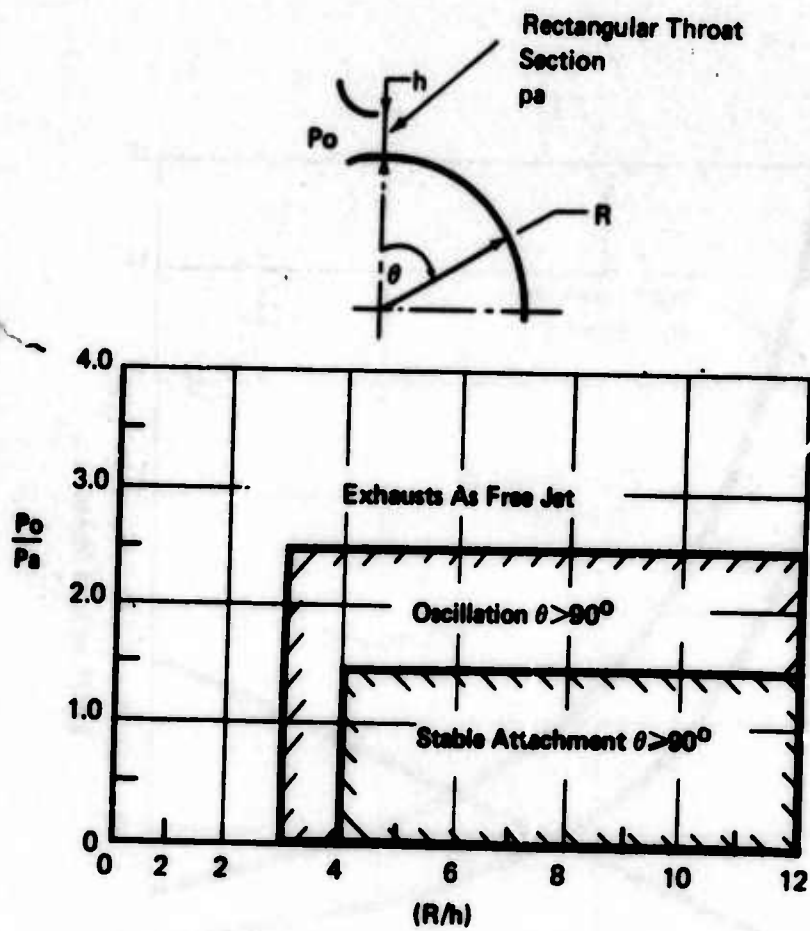


Figure 25

Jet Attachment Stability Criteria